

The Investigation of Organic Nitrogen Species and Inorganic Constituents in Particulate Matter in Polluted Asian Megacities

Stefan James Swift

Doctor of Philosophy

University of York

Chemistry

March 2021

Abstract

Delhi and Beijing are known to experience exceedingly high and often dangerous levels of outdoor ambient air pollution, ubiquitously spread as to expose tens of millions of inhabitants. Particulate Matter of diameter $< 2.5 \mu\text{m}$ ($\text{PM}_{2.5}$) is one of the most harmful and abundant pollutants, adversely affecting both human health and the environment. The inorganic constituents comprise a substantial (and often dominant) fraction of $\text{PM}_{2.5}$ which directly affects the particle's physical and chemical properties. In addition, Organic Nitrogen (ON) species are a highly carcinogenic and mutagenic class of species known to be present in megacity $\text{PM}_{2.5}$ and contribute greatly to the toxic nature of Asian megacity $\text{PM}_{2.5}$.

Ion Chromatography (IC) was used on filter samples collected during the Air Pollution and Human Health (APHH) campaigns during Delhi pre- (DPEM) and post-monsoon (DPOM) seasons and Beijing winter (BWIN) and summer (BSUM) seasons. A substantially higher fraction of ionic species were present during the warmer months of DPEM (78.5 %) and BSUM (62.5 %), compared to the cooler months of DPOM (33.7 %) and BWIN (35.7 %) which was attributed to higher photooxidation under higher solar flux, temperatures and differing emission sources.

This thesis also explores the reaction of highly abundant BVOCs and the NO_3 radical in the formation of Org- NO_3 species during chamber experiments of the NO_3 ISOP campaign using a Particle-Into-Liquid-Sampler coupled to IC (PILS-IC). The identification of acid catalysed hydrolysis of these species has indicated that the formation of Org- NO_3 within Asian megacities may be a contributing factor to NO_3^- . A comprehensive Two-Dimensional Gas Chromatography Coupled to Nitrogen Chemiluminescence Detection ($\text{GC} \times \text{GC} - \text{NCD}$) technique was also exploited to assess the concentration of nitrosamines during BWIN. It was found that inhabitants in Beijing are at significantly higher risk of developing cancer from $\text{PM}_{2.5}$ compared to London.

Contents

Abstract	2
Contents	3
List of Tables	8
List of Figures	9
Acknowledgements	22
Declaration	24
1 INTRODUCTION	25
1.1 Atmospheric Pollution	25
1.2 Atmospheric Aerosol and PM_{2.5}	27
1.2.1 Aerosol Effects on Climate	28
1.2.2 Particle Size and Deposition in the Respiratory Tract	28
1.2.3 Illnesses and Mechanisms Attributed to PM _{2.5} Exposure	29
1.2.3.1 Induced Oxidative Stress	29
1.2.3.2 Inflammation, Asthma and Infection	30
1.2.3.3 Cardiovascular disease	30
1.2.3.4 Mutagenicity, Genotoxicity and Carcinogenicity	31
1.3 Chemical Composition of PM_{2.5}	31
1.3.1 Inorganic Fraction	32
1.3.1.1 Chloride	32
1.3.1.2 Nitrate	35
1.3.1.3 Sulfate	38
1.3.1.4 NOR and SOR	42
1.3.1.5 Ammonium	44
1.4 Overview of inorganic PM_{2.5} aerosol in India and China	45
1.4.1 India Summer (Pre-Monsoon)	50
1.4.2 India Post-Monsoon – Winter	51
1.4.3 China Winter	52
1.4.4 China Summer	53
1.5 PM_{2.5} in Delhi and Beijing (and APHH)	55
1.5.1 APHH Delhi and Beijing	55
1.5.2 Experimental Methods and Contribution of this Thesis to APHH	55
1.5.2.1 Ion Chromatography	55
1.5.2.2 GC × GC – NCD	56
1.5.2.3 PILS	57
1.5.3 Aims and Hypotheses of PhD Thesis	58
1.5.3.1 Literature Knowledge Gaps	58
1.5.3.2 Research Aims and Objectives	60
1.5.3.3 Research Hypotheses	61
1.5.4 Thesis Outline	62
2 ION CHROMATOGRAPHY THEORY OF OPERATION AND METHOD DEVELOPMENT: EXPERIMENTAL TECHNIQUES, METHOD DEVELOPMENT AND DATA QUALITY ASSURANCE.	64

2.1	Introduction	64
2.2	Experimental and Method Development	65
2.2.1	Sample Collection.....	65
2.2.2	Comparison Data from APHH partners.....	68
2.2.3	Filter Extraction.....	68
2.2.4	Calibration Standards.....	69
2.2.5	Ion chromatographic analytical procedure.....	69
2.2.6	Quality Control.....	71
2.2.6.1	Calibration Correction.....	71
2.2.6.2	Blank Correction.....	72
2.2.6.3	Recovery Correction.....	74
2.2.6.4	Limit of Detection.....	76
2.2.7	Calculation Method Development.....	81
2.2.7.1	Iteration 1: Initial Atmospheric Concentration Calculation: (Initial Calculation).....	81
2.2.7.2	Iteration 2: Atmospheric Concentration Calculation 2 (Improved Calculation).....	82
2.2.7.3	Iteration 3: Atmospheric Concentration Calculation 3.....	83
2.2.7.4	Comparison and Evaluation of Calculation Methods.....	85
2.2.8	Calculation of IC Errors.....	87
2.2.8.1	IC Sample Concentration Error.....	87
2.2.9	Blank Subtraction Error.....	88
2.2.9.1	Recovery Correction Error.....	89
2.2.9.2	Mass of Ionic Species Error.....	89
2.2.9.3	Air Volume Error.....	90
2.2.9.4	Final Atmospheric Concentration Error.....	90
2.2.10	Ionic PM _{2.5} Ion Chromatography Inter-Laboratory Comparison Study.....	91
2.2.10.1	Overview and Results.....	91
2.2.10.2	Specific Contribution of this work to the Intercomparison.....	96
2.2.10.3	Critiques Surrounding the IC Inter-Laboratory Comparison Study.....	96
2.2.11	Cement Analysis for Inter-Instrument Comparison.....	97
2.2.12	Validity of Measuring Nitrite on Filters.....	97
2.2.13	Evaluation and Validity of using a Quadratic fit for Calibrations.....	99
2.2.14	Other Issues.....	99
2.3	Conclusions and Suggestions for Future IC Users	101
3	ATMOSPHERIC CONCENTRATIONS AND CHARACTERISTICS OF THE MAJOR IONS FOUND IN PM_{2.5} DURING THE APHH BEIJING AND DELHI CAMPAIGNS	104
3.1	Introduction	104
3.2	Experimental	106
3.3	Results and Discussion	106
3.3.1	Meteorological Conditions.....	106
3.3.1.1	Delhi Winds.....	106
3.3.1.2	Delhi Temperature and Relative Humidity.....	107
3.3.1.3	Beijing Winds.....	108
3.3.1.4	Beijing Temperature and Relative Humidity.....	108
3.3.2	Gas and Particle Phase Composition in Delhi and Beijing.....	110
3.3.2.1	Time Series of Major Gas mixing ratios and Daily PM _{2.5} concentrations.....	110
3.3.2.2	Delhi.....	110
3.3.2.3	Beijing.....	113
3.3.2.4	Comparison of Gas Phase Species and PM _{2.5} in Beijing and Delhi.....	116
3.3.3	Time series of ionic species in PM _{2.5}	117
3.3.3.1	Delhi Pre-Monsoon.....	117
3.3.3.2	Delhi Post-Monsoon.....	120

3.3.3.3	Beijing Winter.....	122
3.3.3.4	Beijing Summer	125
3.3.4	Average Inorganic PM _{2.5} Concentrations Comparison in Delhi and Beijing.....	127
3.3.4.1	Building a Violin Plot	128
3.3.4.2	Delhi and Beijing Day and Night Concentration Comparison.....	129
3.3.4.3	Chloride	132
3.3.4.4	Nitrate	133
3.3.4.5	Sulfate	134
3.3.4.6	Ammonium	136
3.3.4.7	Oxalate.....	137
3.3.4.8	Other Ions	138
3.3.5	Composition of PM _{2.5} in Delhi and Beijing during the APHH Campaigns	138
3.3.6	Inter-Instrumental Comparison of Inorganic Species	143
3.3.6.1	Delhi Pre-Monsoon.....	143
3.3.6.2	Delhi Post-Monsoon	146
3.3.6.3	Beijing Winter.....	152
3.3.6.4	Beijing Summer	156
3.3.6.5	Summary of Inter-Instrument Comparison	160
3.3.6.6	Summary of Expectations <i>vs</i> Observations between Sampling Methods.....	160
3.3.6.6.1	Delhi Pre-Monsoon.....	161
3.3.6.6.2	Delhi Post-Monsoon	161
3.3.6.6.3	Beijing Winter	162
3.3.6.6.4	Beijing Summer.....	162
3.3.7	Further analysis of the AMS and IC Comparison.....	163
3.3.7.1	Artefacts.....	163
3.3.7.2	Beijing.....	164
3.3.7.2.1	Beijing Winter	166
3.3.7.2.2	Beijing Summer.....	168
3.3.7.2.3	Delhi	169
3.4	Conclusion	171
4	CONCENTRATION AND COMPOSITION OF PM_{2.5} COMPARISON TO PREVIOUS STUDIES IN DELHI AND BEIJING	175
4.1	Introduction.....	175
4.2	Experimental	176
4.2.1	Studies Reviewed for Delhi and Beijing.....	176
4.2.2	Heights and Types of Sampling Sites	179
4.2.3	Full Review Compilation.....	181
4.3	Results and Discussion.....	181
4.3.1	History of Major Ionic Species in Delhi and Beijing.....	181
4.3.1.1	Delhi.....	182
4.3.1.2	Beijing.....	182
4.3.1.3	Historical change in [PM _{2.5}] in Delhi and Beijing.....	182
4.3.1.4	Historical [ion] change in Delhi.....	185
4.3.1.5	Historical [ion] change in Beijing	189
4.3.2	Particle Composition Comparison of PM _{2.5} in Delhi and Beijing (Timelines).....	191
4.3.2.1	Delhi Pre-Monsoon.....	191
4.3.2.2	Delhi Post-Monsoon	194
4.3.2.3	Beijing Winter.....	197
4.3.2.4	Beijing Summer	200
4.3.3	Comparison Challenges	203
4.4	Conclusion	205

5	INVESTIGATION AND INTERPRETATION OF THE INORGANIC PM_{2.5} SPECIES CONCENTRATIONS AND COMPOSITIONS WITHIN DELHI AND BEIJING: IMPLICATIONS AND COMPARISONS ON THE AMMONIUM AEROSOL SYSTEM	207
5.1	Introduction	207
5.2	Experimental	208
5.3	Results and Discussion	208
5.3.1	Chloride	208
5.3.1.1	Non-Sea Salt Chloride	208
5.3.1.2	Major Chloride Sources	209
5.3.1.3	Delhi.....	209
5.3.1.4	Delhi Pre-Monsoon.....	211
5.3.1.5	Delhi Post-Monsoon	212
5.3.1.6	Beijing.....	213
5.3.1.7	Beijing Winter.....	214
5.3.1.8	Beijing Summer	215
5.3.1.9	Challenges in Cl ⁻ source identification.....	215
5.3.2	Nitrate and Sulfate	216
5.3.2.1	[NO ₃]/[SO ₄ ²⁻] Ratio	216
5.3.2.2	[NO ₃]/[SO ₄ ²⁻] Ratio Comparison between Delhi and Beijing.....	218
5.3.2.3	SOR and NOR in Delhi and Beijing	221
5.3.2.4	Delhi Pre-Monsoon.....	223
5.3.2.5	Delhi Post-Monsoon	224
5.3.2.6	Beijing Winter.....	224
5.3.2.7	Beijing Summer	225
5.3.2.8	NOR and SOR (Inter-Campaign) Average Comparisons	225
5.3.2.9	NOR and SOR Correlations	232
5.3.2.10	Temperature	232
5.3.2.11	Relative humidity.....	234
5.3.2.12	Concentrations of precursor oxidants.....	236
5.3.2.13	Particle Size and Surface Area.....	236
5.3.2.14	Uncertainties in [NO ₃]/[SO ₄ ²⁻], NOR and SOR.....	237
5.3.3	Ammonium and Particle Acidity	241
5.3.3.1	Beijing Winter Day	241
5.3.3.2	Beijing Winter Night.....	244
5.3.3.3	Beijing Summer Day.....	245
5.3.3.4	Beijing Summer Night	247
5.3.3.5	Delhi Pre-Monsoon Day	247
5.3.3.6	Delhi Pre-Monsoon Night.....	248
5.3.3.7	Delhi Post-Monsoon Day.....	250
5.3.3.8	Delhi Post-Monsoon Night	252
5.3.3.9	Role of Weak Acids	253
5.3.3.10	Challenges in Analysis.....	254
5.4	Conclusion.....	254
6	THE QUANTIFICATION OF ORGANO-NITRATE SPECIES USING A PILS-IC METHOD AT THE SAPHIR SMOG CHAMBER DURING THE NO₃ISOP CAMPAIGN.....	256
6.1	Introduction.....	256
6.2	Experimental	259
6.2.1	Sampling Site and SAPHIR Smog Chamber	259

6.2.2	PILS Denuder Preparation	260
6.2.3	Sample Collection and IC Analysis	260
6.2.4	Sample Evaporation and Reanalysis on the IC	261
6.2.5	IC Analysis and Atmospheric Concentration Calculation	261
6.2.6	Org-NO ₃ Hydrolysis in Water	262
6.3	Results and Discussion	263
6.3.1	Org-NO ₃ Hydrolysis	263
6.3.1.1	Org-NO ₃ Dissociation in 25 ppm LiF	263
6.3.1.2	Effect of light on Org-NO ₃ Dissociation in 25 ppm LiF (Pilot Tests)	269
6.3.1.3	Comparison of Org-NO ₃ Dissociation in Water and LiF solution (compounds 1-3)	271
6.3.1.4	Hydrolysis Reaction Kinetic Orders and possible Mechanisms for compounds 1-3	273
6.3.1.5	Compound 4 Hydrolysis Mechanism	277
6.3.2	PILS IC results from the SAPHIR Chamber	281
6.3.2.1	Limit of Detection	281
6.3.2.2	Uncertainty of PILS-IC Measurements	281
6.3.2.2.1	Uncertainty of Dilution Factor, R	281
6.3.2.2.2	Uncertainty of NO ₃ ⁻ and SO ₄ ²⁻ Atmospheric Chamber Concentrations	282
6.3.2.2.3	Uncertainty of PILS-IC Org-NO ₃ Atmospheric Chamber Concentrations	284
6.3.2.3	Quantitative Inorganic AMS Measurement and Uncertainty Evaluation	284
6.3.2.4	NO ₃ ISOP Experimental Results	285
6.3.2.4.1	17 th August (Blank Chamber)	287
6.3.2.4.2	15 th August (High Concentration Experiment Example)	287
6.3.2.4.3	16 th August (Low Concentration Experiment Example)	291
6.3.2.4.4	18 th – 23 rd August	292
6.3.2.4.5	Ratio of Organic to Inorganic Nitrate	299
6.3.2.5	Comparison of PILS-IC [Org-NO ₃] concentrations to Speciated Measurements	301
6.3.2.6	Comparison of Techniques and Uncertainties in Measuring Org-NO ₃	302
6.3.2.7	Improved Future Methods of [Org-NO ₃] Analysis	304
6.3.2.8	Work Intensity to Data Benefit Analysis of PILS-IC vs AMS Methods	305
7	TIME-RESOLVED CHARACTERIZATION OF ORGANIC NITROGEN IN PM_{2.5}: AN INVESTIGATION INTO BEIJING'S AIR QUALITY AND CANCER RISK	309
7.1	Introduction	309
7.2	Experimental	312
7.2.1	Sampling Site Method and Meteorology	312
7.2.2	Formation of GC × GC – NCD MegaMix Standard	312
7.2.3	Filter Extraction and sample preparation	314
7.2.3.1	Preparation of ASE Extraction Cells and Vials	314
7.2.3.2	Sample Preparation with Accelerated Solvent Extraction	314
7.2.4	GC × GC – NCD Method	315
7.2.5	Data Quality Assurance	315
7.2.5.1	Method Blank Correction	316
7.2.5.2	Method Recovery Correction	316
7.2.5.3	Limit of Detection	316
7.3	Results	316
7.3.1	ON MegaMix	316
7.3.2	Kovats Retention Indices	322
7.3.3	ON Time Series and Concentrations	324
7.3.4	Calculating Nitrosamine Concentration Error	329
7.3.5	Comparison to Other Studies	332
7.3.6	Coelution of N-tert-butylformamide and NDEA	335
7.3.7	Total Nitrosamine Concentration	337
7.3.8	Cancer Risk Factor	338

7.3.9	Cancer Risk Assessment assuming low [NDEA]	343
7.4	Conclusion.....	344
8	CONCLUSIONS.....	346
8.1	Findings and Conclusions.....	346
8.1.1	Use of Ion Chromatography for Inorganic PM _{2.5} Quantification.....	346
8.1.2	Inter-Instrument Comparison.....	347
8.1.3	Inorganic Aerosol Formation in Delhi and Beijing.....	347
8.2	Recommendations	351
8.3	Future Work.....	353

List of Tables

Table 2.1.	Table showing the campaign sampling start and end times, the number of filters and the number of blocked filters recorded for the Delhi pre- and post-monsoon campaigns and the Beijing winter and summer campaigns.	67
Table 2.2.	Blank concentrations for APHH IC analysis for extractions carried out between 2017 -2019 (ppm).	73
Table 2.3.	Recovery % correction values for the APHH Delhi (2019) and Beijing (2017) IC analysis.	75
Table 2.4.	LOD and LOQ concentrations (ppm) determined for the Delhi filter analysis in 2019 (with % of samples for each ion which where over the LOD and LOQ).....	78
Table 2.5.	LOD and LOQ concentrations (ppm) determined for the Beijing winter and summer filter analysis conducted in 2017 and 2018, respectively (with % of samples for each ion which where over the LOD and LOQ).....	78
Table 2.6.	Table showing the anion LOD (ppm) values before and after replacement of the column and suppressor.	81
Table 2.7.	Comparison of Weighted Averages ($\mu\text{g m}^{-3}$), StDevs ($\mu\text{g m}^{-3}$) as well as R ² regression analysis between calculation iteration and the AMS.	86
Table 2.8.	Table of LODs (ppm) reported from 10 different laboratories for anion and cation species from Xu et al., (2020) ²⁶⁷	95
Table 2.9.	Comparison of LOD (ppm) calculated in this work to the method by Xu et al., (2020) ²⁶⁷	95
Table 3.1.	TEOM-FDMS PM _{2.5} (UoB) statistical parameters for the APHH Delhi and Beijing campaigns ($\mu\text{g m}^{-3}$).	116
Table 3.2.	Day, Night, Day/Night and Total campaign [Cl ⁻] means ($\mu\text{g m}^{-3}$).	132
Table 3.3.	Day, Night, Day/Night and Total campaign [NO ₃ ⁻] means ($\mu\text{g m}^{-3}$).	133
Table 3.4.	Day, Night, Day/Night and Total campaign [SO ₄ ²⁻] means ($\mu\text{g m}^{-3}$).....	134
Table 3.5.	Day, Night, Day/Night and Total campaign [NH ₄ ⁺] means ($\mu\text{g m}^{-3}$).....	136
Table 3.6.	Day, Night, Day/Night and Total campaign [C ₂ O ₄ ²⁻] means ($\mu\text{g m}^{-3}$).....	137
Table 3.7.	Comparison of the IC 'other' fraction to the AMS PM ₁ organic fraction.	142
Table 3.8.	R ² regression coefficients of the IC (UoY) vs the AMS (CEH) and IC (UoB) DPEM datasets....	145
Table 3.9.	R ² regression coefficients of the IC (UoY) vs the AMS (CEH) and IC (UoB) for the DPOM datasets.	149
Table 3.10.	R ² regression coefficients of the IC (UoY) vs the AMS (CEH) and IC (UoB) for the BWIN datasets.	154
Table 3.11.	R ² regression coefficients of the IC (UoY) vs AMS (CEH and IAP) and IC (UoB), BSUM datasets.	158
Table 4.1.	Sampling sites reported by the reviewed studies in Delhi.	177
Table 4.2.	Sampling sites reported by the reviewed studies in Beijing.	179
Table 4.3.	Table showing the sampling site region classification as depicted on google maps, sampling site height above sea level (S.L) and ground level (G.L) for each publication reviewed, as reported by the specific study, for Delhi.....	179

Table 4.4. Table showing the sampling site region classification as depicted on google maps, sampling site height above sea level (S.L) and ground level (G.L) for each publication reviewed, as reported by the specific study, for Beijing.....	180
Table 5.1. $[\text{NO}_3^-]/[\text{SO}_4^{2-}]$ ratios reported by other studies in Beijing from $\text{PM}_{2.5}$ measurements.....	219
Table 5.2. Number of data points used to calculate the NOR and SOR values across the APHH campaigns.	228
Table 5.3. Review of NOR and SOR across other studies in Delhi	229
Table 5.4. Review of NOR and SOR across other studies in Beijing.	230
Table 5.5. Linear Correlation Coefficient values between NOR and SOR against other Key Oxidation Variables. Values in Red, Amber and Green are $R^2 > 0.5, 0.7$ and 0.9 , respectively. Within these values, those underlined demonstrated negative gradients. The number of data points used for correlation calculation are also given for each value (N).	233
Table 5.6. The Role of Weak Acids in NH_4^+ Neutralization during the day and night of the DPEM, DPOM, BWIN and BSUM Campaigns.	253
Table 6.1. Evaluation of Chamber conditions during the NO_3 ISOP campaign as taken from Dewald et al., (2020) ⁴⁸¹ over the PILS sampling period.....	260
Table 6.2. Hydrolysis reaction kinetics of a range of Org- NO_3 (compounds 1-4) synthesised by UEA.....	264
Table 6.3. Comparison to orders of reaction and hydrolysis rates between the Org- NO_3 hydrolysis experiments within an LiF (25.4 ppm) and neutral water (18.2 M Ω) for compounds 1-3.	272
Table 6.4. Percentage of samples (out of the sample set) that were below LOD for $[\text{NO}_3^-]$ and $[\text{SO}_4^{2-}]$ for each day, as well as the Correlation Regression Coefficient values for each day between the PILS-IC values and the time averaged AMS values for $[\text{NO}_3^-]$ and $[\text{SO}_4^{2-}]$	286
Table 7.1. Table of contributing mixes to MegaMix standard. N.B. Mix 8 and Mix 10 have been removed from the table as these compounds were not suitable for GC \times GC – NCD analysis.....	313
Table 7.2. Summary of the statistical parameters for nitrosamines species within the 7-day period sampled for the APHH Beijing winter campaign (ng m^{-3}).	328
Table 7.3. Comparison of mean nitrosamine concentrations (ng m^{-3}) during the clean and polluted period within the 7-day period sampled (between 22 nd - 28 th Nov).	329
Table 7.4. Summary of the mean and standard deviations of nitrosamines within atmospheric aerosol (ng m^{-3}) within the literature.....	332
Table 7.5. Comparison of the mean and standard deviation of Σ [nitrosamines] concentrations between the WHO IARC groups between Beijing and London.	338
Ap Table. A. Specification of Reviewed Studies (India).	355
Ap Table. B. India $\text{PM}_{2.5}$ and Major Anion concentrations in Reviewed studies.....	358
Ap Table. C. India Minor Anion concentrations in Reviewed studies.	360
Ap Table. D. India Cation concentrations in Reviewed studies.	361
Ap Table. E. Specification of Reviewed Studies (China).	363
Ap Table. F. China $\text{PM}_{2.5}$ and Major Anion concentrations in Reviewed studies.....	368
Ap Table. G. China Minor Anion concentrations in Reviewed studies.	370
Ap Table. H. China Cation concentrations in Reviewed studies.....	373
Ap Table. I. Specification of Reviewed Studies (Delhi).	375
Ap Table. J. Delhi $\text{PM}_{2.5}$ and Anion concentrations in Reviewed studies.....	377
Ap Table. K. Delhi Cation concentrations in Reviewed studies.	378
Ap Table. L. Specification of Reviewed Studies (Beijing).	379
Ap Table. M. Beijing $\text{PM}_{2.5}$ and Major Anion concentrations in Reviewed studies.	383
Ap Table. N. Beijing Minor Anion concentrations in Reviewed studies.	385
Ap Table. O. Beijing Cation concentrations in Reviewed studies.	388

List of Figures

Fig. 1.1. NO_x and RO_x Cycles for O_3 production as depicted by Wang et al., (2017) ²⁰	26
Fig. 1.2. Depictions of the PM_{10} and $\text{PM}_{2.5}$ size ranges compared to a grain of sand a strand of hair taken from the EPA ⁴⁸	27
Fig. 1.3. Possible methylchloride formation mechanism based on the methylhalide formation mechanism from soil origin reported in Keppler (2000) ¹³⁴	34

Fig. 1.4. Map of India showing the distribution of ionic PM _{2.5} particle composition across India (Summer - Monsoon) from reviewed studies. A key denoting the segment species colours is shown in the top left corner with the major ions listed in the bottom right corner. Red markers on the map of India show the different cities. Studies presented in red text represent studies which solely took place over the summer period as opposed to summer-monsoon period (black text). Text shown above each study presents the details of each study.	46
Fig. 1.5. Map of India showing the distribution of ionic PM _{2.5} particle composition across India (Post - Monsoon - Winter) from reviewed studies. A key denoting the segment species colours is shown in the top left corner with the major ions listed in the bottom right corner. Red markers on the map of India show the different cities. Text shown above each study presents the details of each study.	47
Fig. 1.6. Map of China showing the distribution of ionic PM _{2.5} particle composition across China (Winter) from reviewed studies. A key denoting the segment species colours is shown in the top left corner with the major ions listed in the bottom right corner. Red markers on the map of China show the different cities. Text shown above each study presents the details of each study.	48
Fig. 1.7. Map of China showing the distribution of ionic PM _{2.5} particle composition across China (Summer) from reviewed studies. A key denoting the segment species colours is shown in the top left corner with the major ions listed in the bottom right corner. Red markers on the map of China show the different cities. Text shown above each study presents the details of each study.	49
Fig. 1.8. Orthogonal GC × GC Schematic.....	56
Fig. 1.9. NCD System Schematic.....	56
Fig. 1.10. Schematic of the BMI PILS System used during the NO3ISOP Campaign (Chapter 6).	57
Fig. 2.1. Map of Delhi and the location of the Indira Gandhi Delhi technical University for Women indicated by the red star.	66
Fig. 2.2. Map of Beijing and the location of the Institute of Atmospheric Physics (Chinese Academy of Sciences) indicated by the red star.....	67
Fig. 2.3. Flow chart of general filter sample extraction protocol used in these IC analyses.	68
Fig. 2.4. Chromatogram of 50 ppm Salt Mix calibration standard for the Delhi Analysis in Anion Mode.	70
Fig. 2.5. Chromatogram of 50 ppm Salt Mix calibration standard for the Delhi Analysis in Cation Mode.	70
Fig. 2.6. 50ppm NH ₄ Cl IC Chromatogram demonstrating the contaminant ions present from the manufacturer.....	71
Fig. 2.7. Column degradation of IC overtime producing a noisier baseline.	80
Fig. 2.8. Change in calibration gradient dependant on region of calibration concentrations chosen to demonstrate how the gradient changes at different sections of a calibration curve for IC analysis.....	82
Fig. 2.9. Quadratic calibration shapes observed during the APHH IC analysis.	84
Fig. 2.10. Change and improvement in time series through iteration 1 (pale green), iteration 2 (pale orange), iteration 3 (black) and comparison of time series to the AMS (bright blue). The associated errors for iteration 3 are shown as black error bars in the y-axis. These errors are calculated using the calculation described in section 2.2.8. The grey vertical lines represent the time of 00:00 for the respective date shown on the x-axis.	85
Fig. 2.11. Ionic Atmospheric Concentration Comparison Results from Xu et al., (2020) ²⁶⁷ . The results for each lab are shown via the key above the time series. The grey vertical lines represent the dates of sampling (shown on the bottom charts and are vertically identical). Red error bars have been added to the time series of Lab-9 (results from this thesis) to demonstrate the ±30% range.	93
Fig. 2.12. Filter sample sent by the University of Birmingham for the IC inter-laboratory comparison study.	96
Fig. 2.13. IC Chromatogram representing NO ₃ ⁻ to NO ₂ ⁻ partitioning in a mixed standard over the course of ca. 1 month.....	100
Fig. 2.14. NaCl, NaNO ₃ and NO ₂ SO ₄ mixed salt solution were ran on IC at 100 ppm (black), 200 ppm (dark blue), 300 ppm (pink), 400 ppm (brown), 500 ppm (green) and 650 ppm (light blue).	100
Fig. 3.1. Wind Rose Plots showing the overall wind speeds (legend, m s ⁻¹) and wind directions across the APHH DPEM and DPOM campaigns.	106
Fig. 3.2. Time series of Temperature (Orange) and Relative Humidity (Blue) across the APHH DPEM and DPOM campaigns. Error ca. < 1 %.....	107
Fig. 3.3. Wind Rose Plots showing the overall wind speeds (legend, m s ⁻¹) and wind directions across the APHH BWIN and BSUM campaigns.....	108
Fig. 3.4. Time series of Temperature (Orange) and Relative Humidity (Blue) across the APHH Beijing BWIN and BSUM campaigns. Error ca. < 1 %.....	109
Fig. 3.5. Time series of the major gases and [PM _{2.5}] measured during the APHH Delhi pre- and post-monsoon campaigns. The errors for the gas phase are NO (4.58 %), NO ₂ (5.72 %), SO ₂ (3.12 %), O ₃	

(4.04 %) and CO (9.14 %). TEOM-FDMS error was unavailable. Species concentrations are shown on the y-axes with time on the x-axes. The grey vertical lines represent midnight time points. The red error bars for [PM _{2.5}] show the time of sampling. The x-axes are identical for each time series and are shown in the bottom chart ([PM _{2.5}]).	111
Fig. 3.6. Time series of the modelled boundary layer height (ECMWF) ³³⁶ during the Delhi post-monsoon campaign.	112
Fig. 3.7. Time series of the major gases and PM _{2.5} measured during the APHH Beijing Winter and Summer campaigns. The errors for the gas phase are NO (4.58 %), NO ₂ (5.72 %), SO ₂ (3.12 %), O ₃ (4.04 %) and CO (9.14 %). TEOM-FDMS error was unavailable. Species concentrations are shown on the y-axes with time on the x-axes. The grey vertical lines represent midnight time points. The red error bars for [PM _{2.5}] show the time of sampling. The x-axes are identical for each time series and are shown in the bottom chart ([PM _{2.5}]).	114
Fig. 3.8. Bar charts showing the mean major gas concentrations of NO (light blue), NO ₂ (dark blue), SO ₂ (red), O ₃ (green), CO (grey) and PM _{2.5} (black) measured during the APHH DPEM, DPOM, BWIN and BSUM campaigns. The errors for the gas phase are NO (4.58 %), NO ₂ (5.72 %), SO ₂ (3.12 %), O ₃ (4.04 %) and CO (9.14 %). The error bars shown for [PM _{2.5}] values demonstrate the SD of the dataset.	116
Fig. 3.9. Time series of the major ions measured by offline ion chromatography during the APHH Delhi pre-monsoon campaign. Ion concentrations are shown on the y-axes with time on the x-axes. The grey vertical lines represent midnight time points. The red error bars show the time of sampling and the blue error bars show the error of each concentration measurement in the y-axis. The x-axes are identical for each time series and are shown in the bottom chart (oxalate).	118
Fig. 3.10. Time series of the major ions measured by offline ion chromatography during the APHH Delhi post-monsoon campaign. Ion concentrations are shown on the y-axes with time on the x-axes. The grey vertical lines represent midnight time points. The red error bars show the time of sampling and the blue error bars show the error of each concentration measurement in the y-axis. The x-axes are identical for each time series and are shown in the bottom chart (oxalate).	121
Fig. 3.11. Time series of the major ions measured by offline ion chromatography during the APHH Beijing Winter campaign. Ion concentrations are shown on the y-axes with time on the x-axes. The grey vertical lines represent midnight time points. The red error bars show the time of sampling and the blue error bars show the error of each concentration measurement in the y-axis. The x-axes are identical for each time series and are shown in the bottom chart (oxalate).	123
Fig. 3.12. Time series of the major ions measured by offline ion chromatography during the APHH Beijing Summer campaign. Ion concentrations are shown on the y-axes with time on the x-axes. The grey vertical lines represent midnight time points. The red error bars show the time of sampling and the blue error bars show the error of each concentration measurement in the y-axis. The x-axes are identical for each time series and are shown in the bottom chart (oxalate).	126
Fig. 3.13. Build-up of a violin plot. (A) Data segregated into large bin size; (B) Data segregated into smaller bin sizes; (C) Data segregated into smaller bin sizes with kernel distribution overlay; (D) Final violin plot with box plot.	128
Fig. 3.14. Bar Charts representing Day and Night Ionic PM _{2.5} data in Delhi. The orange bars represent the daytime mean, the green bars represent night-time mean, and the purple bars represent the total campaign mean. The lighter 3 bars (3 bars to the left of each species) represent the DPEM campaign, and the darker bars represent the DPOM campaign. The associated errors for these data may be found in Fig. 3.9 - Fig. 3.10.	130
Fig. 3.15. Violin Plots demonstrating Day (yellow distribution) and Night (blue distribution) ionic PM _{2.5} distribution data in Delhi. The distribution density displayed is calculated by the kernel distribution function. The boxplot represents the inter quartile range and the white line within the boxplot represent the median atmospheric concentration for each species (labelled along the bottom axis). High concentration ions are shown on the left and low concentration ions to the right. The pre-monsoon data is presented on the top and the post-monsoon data is shown on the bottom.	130
Fig. 3.16. Bar Charts representing Day and Night ionic PM _{2.5} data in Beijing. The yellow bars represent the daytime mean, the red bars represent night-time mean, and the blue bars represent the total campaign mean. The lighter 3 bars (3 bars to the left of each species) represent the BWIN campaign, and the darker bars represent the BSUM campaign. The associated errors for these data may be found in Fig. 3.11 - Fig. 3.12.	131
Fig. 3.17. Violin Plots demonstrating Day (yellow distribution) and Night (blue distribution) ionic PM _{2.5} distribution data in Beijing. The distribution density displayed is calculated by the kernel distribution function. The boxplot represents the inter quartile range and the white line within the boxplot represent the median atmospheric concentration for each species (labelled along the bottom axis). High	

	concentration ions are shown on the left and low concentration ions to the right. The winter campaign is presented on the top and the summer campaign is shown on the bottom.	131
Fig. 3.18.	Pie charts representing the averaged composition of PM _{2.5} aerosol during the APHH Delhi pre- (top left) and post-monsoon (top right), and Beijing winter (bottom right) and summer (bottom left) campaigns. The species are presented as F ⁻ (gold), CH ₃ SO ₃ ⁻ (orange), Cl ⁻ (green), NO ₂ ⁻ (dark blue), Br ⁻ (medium blue), NO ₃ ⁻ (light blue), PO ₄ ³⁻ (yellow), SO ₄ ²⁻ (red), C ₂ O ₄ ²⁻ (brown), Na ⁺ (pink), NH ₄ ⁺ (lilac), K ⁺ (purple), Mg ²⁺ (black), Ca ²⁺ (grey) and other (amber). Percentage contributions are also labelled underneath each species in each pie chart. The average [PM _{2.5}] from a TEOM-FDMS (UoB) is also given underneath each pie chart for the respective campaign.	139
Fig. 3.19.	Inter-instrument time-series comparison for the major ions Cl ⁻ (top left), NO ₃ ⁻ (top right), SO ₄ ²⁻ (bottom left) and NH ₄ ⁺ (bottom right) during the DPEM campaign. The IC (UoY) is shown as the blue dot points and the AMS (CEH) is shown as the grey line. Atmospheric concentrations are displayed on the y-axis and time is displayed along the x-axis. The grey vertical lines represent midnight time points. The errors associated with the IC (UoY) are found in Fig. 3.9. Error values for the other instruments were unavailable.	144
Fig. 3.20.	Bar Charts presenting the weighted averages between the IC (UoY, blue) and AMS (CEH, grey) during the DPEM campaign, as well as IC (UoB, yellow) during the same season. The errors of measurements are shown for the IC (UoY), although the error values for the AMS (CEH) and IC (UoB) were unavailable.	145
Fig. 3.21.	Inter-instrument time-series comparison for the major ions Cl ⁻ (top left), NO ₃ ⁻ (top right), SO ₄ ²⁻ (bottom left) and NH ₄ ⁺ (bottom right) during the DPOM campaign. The IC (UoY) is shown as the blue dot points; the AMS (CEH) is shown as the grey line; and the IC (UoB) is shown as the yellow dot points. Atmospheric concentrations are displayed on the y-axis and time is displayed along the x-axis. The grey vertical lines represent midnight time points. The errors associated with the IC (UoY) are found in Fig. 3.10. Error values for the other instruments were unavailable.	147
Fig. 3.22.	Bar Charts presenting the weighted averages between the IC (UoY, blue), AMS (CEH, grey) and IC (UoB, yellow) during the DPOM Campaign. The errors of measurements are shown for the IC (UoY), although the error values for the AMS (CEH) and IC (UoB) were unavailable.	149
Fig. 3.23.	Screen shot of replicate IC Chromatograms of UltraTech Cement displaying very high SO ₄ ²⁻ response (large peak) with the incorporation of much lower concentration ions. The x-axis is time and the y-axis is peak area (μS*min).	150
Fig. 3.24.	Diurnal profiles of other ions which may exist in cement. The blue time series shows the average diurnal averaged across the available data and the beige lines on each side demonstrate the ±SD of these values. Atmospheric concentration of ionic species is on the y-axis, with time of day on the x-axis. The crosses represent a single measurement for midnight.	151
Fig. 3.25.	Inter-instrument time-series comparison for the major ions Cl ⁻ (top left), NO ₃ ⁻ (top right), SO ₄ ²⁻ (bottom left) and NH ₄ ⁺ (bottom right) during the BWIN campaign. The IC (UoY) is shown as the blue dot points; the AMS (CEH) is shown as the grey line; the IC (UoB) is shown as the yellow dot points; and the AMS (IAP) is shown as the orange line. Atmospheric concentrations are displayed on the y-axis and time is displayed along the x-axis. The grey vertical lines represent midnight time points. The errors associated with the IC (UoY) are found in Fig. 3.11. Error values for the other instruments were unavailable.	153
Fig. 3.26.	Bar Charts presenting the weighted averages between the IC (UoY, blue), AMS (IAP, orange), AMS (CEH, grey) and IC (UoB, yellow) during the BWIN Campaign. The errors of measurements are shown for the IC (UoY), although the error values for the AMS (IAP and CEH) and IC (UoB) were unavailable.	154
Fig. 3.27.	Inter-instrument time-series comparison between the IC (UoY, blue) and IC (UoB, yellow) measurements (averaged to UoB filtering times, 24 hourly) for the major ions Cl ⁻ (top left), NO ₃ ⁻ (top right), SO ₄ ²⁻ (bottom left) and NH ₄ ⁺ (bottom right) during the BWIN campaign. The errors shown in the IC (UoY) time series demonstrate the SD across the concentrations averaged to the UoB filtering times. Atmospheric concentration is plotted on the y-axis, with time plotted on the x-axis. The grey vertical lines represent midnight time points.	154
Fig. 3.28.	Inter-instrument time-series comparison for the major ions Cl ⁻ (top left), NO ₃ ⁻ (top right), SO ₄ ²⁻ (bottom left) and NH ₄ ⁺ (bottom right) during the BSUM campaign. The IC (UoY) is shown as the blue dot points; the AMS (CEH) is shown as the grey line; and the IC (UoB) is shown as the yellow dot points; and the AMS (IAP) is shown as the orange line. Atmospheric concentrations are displayed on the y-axis and time is displayed along the x-axis. The grey vertical lines represent midnight time points. The errors associated with the IC (UoY) are found in Fig. 3.12. Error values for the other instruments were unavailable.	157

- Fig. 3.29. Bar Charts presenting the weighted averages between the IC (UoY, blue), AMS (IAP, orange), AMS (CEH, grey) and IC (UoB, yellow) during the BSUM Campaign. The errors of measurements are shown for the IC (UoY), although the error values for the AMS (IAP and CEH) and IC (UoB) were unavailable..... 158
- Fig. 3.30. Inter-instrument time-series comparison between the IC (UoY, blue) and IC (UoB, yellow) measurements (averaged to UoB filtering times, 24 hourly) for the major ions Cl^- (top left), NO_3^- (top right), SO_4^{2-} (bottom left) and NH_4^+ (bottom right) during the BWIN campaign. The errors shown in the IC (UoY) time series demonstrate the SD across the concentrations averaged to the UoB filtering times. The grey vertical lines represent midnight time points. Atmospheric concentration is plotted on the y-axis, with time plotted on the x-axis. 158
- Fig. 3.31. Time series of the $[\text{PM}_{10}]/[\text{PM}_{2.5}]$ % mass concentration obtained from available data during the APHH BWIN (A) and BSUM (B) campaigns. The black line shows the $[\text{PM}_{10}]/[\text{PM}_{2.5}]$ % (y-axis) as a function of time (x-axis). The horizontal red error bars show the sampling intervals for each filter sample; the dashed blue line demonstrates a 90% threshold; and the green cross points highlight the IC sampling times in which the $[\text{PM}_{10}]/[\text{PM}_{2.5}]$ mass concentration values were seen to be above 90% (blue horizontal dashed line). The grey vertical lines represent midnight time points. Errors from the AMS (IAP) and TEOM-FDMS were unavailable..... 165
- Fig. 3.32. Regression analysis of the Estimated Cl^- and SO_4^{2-} losses from filter samples against the pollutant metrics $[\text{PM}_{2.5}]$ and $[\text{CO}]$ during the BWIN campaign. The regression of Estimated $[\text{Cl}^-]$ Loss vs $[\text{PM}_{2.5}]$ (A) and $[\text{CO}]$ (B), as well as estimated $[\text{SO}_4^{2-}]$ Loss vs $[\text{PM}_{2.5}]$ (C) and $[\text{CO}]$ (D) are shown for samples where the average $\text{PM}_{10}/\text{PM}_{2.5} > 90\%$. The green regressions demonstrate Cl^- loss correlations and the red regression show the SO_4^{2-} loss correlations. The errors associated with $[\text{Cl}^-]$ and $[\text{SO}_4^{2-}]$ may be found in Fig. 3.11..... 166
- Fig. 3.33. Regression analysis of the Estimated $[\text{Cl}^-]$ Loss (A) and $[\text{SO}_4^{2-}]$ losses (B) from filter samples against the Σ [Monoterpenes] for filter samples where the average $[\text{PM}_{10}]/[\text{PM}_{2.5}] > 90\%$. The red data point in regression A is an anomaly. The errors associated with $[\text{Cl}^-]$ and $[\text{SO}_4^{2-}]$ may be found in Fig. 3.11..... 167
- Fig. 3.34. Linear regression analysis between the atmospheric concentration of benzene vs the Cl^- negative artefacts (black), with the omission of two potential anomalies (red). The errors associated with $[\text{Cl}^-]$ may be found in Fig. 3.11..... 167
- Fig. 3.35. Regression analysis of the Estimated $[\text{Cl}^-]$ Loss (A) and $[\text{SO}_4^{2-}]$ losses (B) from filter samples against the $[\text{O}_3]$ for filter samples where the average $[\text{PM}_{10}]/[\text{PM}_{2.5}] > 90\%$. The errors associated with $[\text{Cl}^-]$ and $[\text{SO}_4^{2-}]$ may be found in Fig. 3.12..... 168
- Fig. 3.36. Regression analysis of the Estimated $[\text{Cl}^-]$ Loss (A) and $[\text{SO}_4^{2-}]$ losses (B) from filter samples against the [Acrolein] measured during the campaign for filter samples where the average $[\text{PM}_{10}]/[\text{PM}_{2.5}] > 90\%$. The errors associated with $[\text{Cl}^-]$ and $[\text{SO}_4^{2-}]$ may be found in Fig. 3.12. 169
- Fig. 3.37. (A) Partisol time series of $[\text{PM}_{2.5}]$ taken by the UoB during the DPEM campaign where the time of sampling is shown on the x-axis and the $\text{PM}_{2.5}$ concentrations are recorded on the y-axis for IIT (green) and IGDTUW (orange). (B) Linear regression analysis for Partisol $[\text{PM}_{2.5}]$ demonstrating the lack of correlation between the IIT (x-axis) and IGDTUW (y-axis) measurements, for identical sampling times ($R^2 = 0.0008$). Partisol instrument error was unavailable..... 170
- Fig. 3.38. Partisol time series of $[\text{PM}_{2.5}]$ taken by the UoB during the DPOM campaign where the time of sampling is shown on the x-axis and the $\text{PM}_{2.5}$ concentrations are recorded on the y-axis for IIT (green) and IGDTUW (orange). Partisol instrument error was unavailable. 170
- Fig. 4.1. Map of Delhi representing the sampling sites of the reviewed studies (Table 4.1)..... 177
- Fig. 4.2. Map of Beijing representing the sampling sites of the reviewed studies (Table 4.2). 178
- Fig. 4.3. Change in $[\text{PM}_{2.5}]$ by time for the Delhi pre- (A) and post- (B) monsoon periods according to literature values. The shapes of the data points represent the type of site for which Urban (\times), Suburban (Δ), and Roadside (+) are included. The colours indicate atmospheric conditions including black (non-specific period) and red (Diwali period). The APHH average is shown as a blue data point. Time of sampling is shown along the x-axis. The associated SD for the reviewed studies may be found in the appendix tables. TEOM-FDMS error was unavailable..... 183
- Fig. 4.4. Change in $[\text{PM}_{2.5}]$ by time for the Beijing winter (A) and summer (B) periods according to literature values. The shapes of the data points represent the type of site for which Urban (\times), Suburban (Δ), Rural (\square) and mixed (O) are included. The colours indicate atmospheric conditions including black (non-specific period), red (haze period), light blue (pollution control period) and green (clean period). The APHH average is shown as a yellow data point. Time of sampling is shown along the x-axis. The associated SD for the reviewed studies may be found in the appendix tables. TEOM-FDMS error was unavailable..... 183

Fig. 4.5. The change in annual [PM _{2.5}] from 2009 to 2019 taken from US Embassy Network Data (Statista) ²⁸¹	184
Fig. 4.6. The change in annual [PM _{2.5}] from 2008 to 2013 taken from Network Data. Image is taken from Zhang et al., (2016) ⁴⁰⁶	184
Fig. 4.7. Historical Plots showing the change in [major ions] by time over the pre- and post-monsoon seasons in Delhi according to the literature. The shapes of the data points represent the type of site for which Urban (×), Suburban (Δ), and Roadside (+) are included. The colours indicate atmospheric conditions including black (non-specific period) and red (Diwali period). The APHH average is shown as a blue data point. Time of sampling is shown along the x-axis. The associated SD for the reviewed studies are found in the appendix tables and the APHH errors are found in chapter 3.....	186
Fig. 4.8. Emission Inventory of NO _x over India from 1970 - 2015 using EDGAR data (V5.0) ^{412,413} . The year is reported on the x-axis with the NO _x emissions across the whole of India reported on the y-axis.	188
Fig. 4.9. Historical Plots showing the change in [major ions] by time over the winter and summer seasons in Beijing according to the literature. The shapes of the data points represent the type of site for which Urban (×), Suburban (Δ), Rural (□) and mixed (O) are included. The colours indicate atmospheric conditions including black (non-specific period), red (haze period), light blue (pollution control period) and green (clean period). The APHH average is shown as a yellow data point. Time of sampling is shown along the x-axis. The associated SD for the reviewed studies are found in the appendix tables and the APHH errors are found in chapter 3.	190
Fig. 4.10. Timeline showing the change in PM _{2.5} particle composition as a function of time within the Delhi Summer (top) and Monsoon (bottom) seasons. The symbols next to the pie charts represent the type of site for which Urban (×), Suburban (Δ), and Roadside (+) are included. The symbol colours indicate atmospheric conditions including black (non-specific period) and red (Diwali period). The APHH average is highlighted (DPEM). Time of sampling is shown along the x-axis. The study code along with the specific sampling site and time are also presented above each pie chart. The species presented are coloured in the pie charts, as per the key shown in the top right.	192
Fig. 4.11. Timeline showing the change in PM _{2.5} particle composition as a function of time within the Delhi Post-Monsoon (top) and Winter (bottom) seasons. The symbols next to the pie charts represent the type of site for which Urban (×), Suburban (Δ), and Roadside (+) as well as (airplane) are included. The symbol colours indicate atmospheric conditions including black (non-specific period) and red (Diwali period). The APHH average is highlighted (DPOM). Time of sampling is shown along the x-axis. The study code along with the specific sampling site and time are also presented above each pie chart. The species presented are coloured in the pie charts, as per the key shown in the top right.....	195
Fig. 4.12. The change in [NO ₃ ⁻ %], [SO ₄ ²⁻ %], [K ⁺ %] and [known ions %] in PM _{2.5} as a function of time reported by reviewed studies (Delhi post-monsoon seasons). The shapes of the data points represent the type of site for which Urban (×), Suburban (Δ), and Roadside (+) are included. The colours indicate atmospheric conditions including black (non-specific period) and red (Diwali period). The APHH average is shown as a blue data point. Time of sampling is shown along the x-axis. The associated SD for the reviewed studies are found in the appendix tables and the APHH errors are found in chapter 3.	196
Fig. 4.13. Timeline showing the change in PM _{2.5} particle composition as a function of time within the Beijing Winter season. The symbols next to the pie charts represent the type of site for which Urban (×), Suburban (Δ), Rural (□) and mixed (O) are included. The colours indicate atmospheric conditions including black (non-specific period), red (haze period), light blue (pollution control period) and green (clean period). The APHH average is highlighted (BWIN). Time of sampling is shown along the x-axis. The study code along with the specific sampling site and time are also presented above each pie chart. The species presented are coloured in the pie charts, as per the key shown in the top right.	198
Fig. 4.14. The change in Cl ⁻ %, K ⁺ %, and NO ₃ ⁻ % by time, as well as Cl ⁻ % vs K ⁺ % (C) reported by reviewed studies (Beijing winter seasons). For plots A, B and C, the shapes of the data points represent the type of site for which Urban (×), Suburban (Δ), Rural (□) and mixed (O) are included. The colours indicate atmospheric conditions including black (non-specific period), red (haze period), light blue (pollution control period) and green (clean period). The APHH average is shown as a yellow data point. Time of sampling is shown along the x-axis. The associated SD for the reviewed studies are found in the appendix tables and the APHH errors are found in chapter 3.....	199
Fig. 4.15. Timeline showing the change in PM _{2.5} particle composition as a function of time within the Beijing Summer season. The symbols next to the pie charts represent the type of site for which Urban (×), Suburban (Δ), Rural (□) and mixed (O) are included. The colours indicate atmospheric conditions including black (non-specific period), red (haze period), light blue (pollution control period) and green (clean period). The APHH average is highlighted (BSUM). Time of sampling is shown along the x-axis.	

The study code along with the specific sampling site and time are also presented above each pie chart. The species presented are coloured in the pie charts, as per the key shown in the bottom left.201

Fig. 4.16. Change in NO_3^- %, SO_4^{2-} %, NH_4^+ % and known ions % by time reported by reviewed studies (Beijing summer seasons). The shapes of the data points represent the type of site for which Urban (\times), Suburban (Δ), Rural (\square) and mixed (O) are included. The colours indicate atmospheric conditions including black (non-specific period), red (haze period), light blue (pollution control period) and green (clean period). The APHH average is shown as a yellow data point. Time of sampling is shown along the x-axis. The associated SD for the reviewed studies are found in the appendix tables and the APHH errors are found in chapter 3.202

Fig. 5.1. Contour plots showing the $[\text{Cl}^-]$ in association with wind data averaged to the filter sampling times for the DPEM and DPOM, day and night-time periods. The $[\text{Cl}^-]$ is presented via a colouration scale (right) in these plots.210

Fig. 5.2 Map of Delhi showing the key potential Cl^- emitters consisting of Official Industrial Areas (Red); Waste Incineration Plants (Green); Landfill Sites (Brown); Gas Power Stations (Yellow); Coal Power Stations (Large Black); and Brick Kilns (Beige). Grey lines show major roads, light green patches show green spaces and blue colouration indicates a body of water.210

Fig. 5.3. NOAA HYSPLIT output for the DPEM campaign.211

Fig. 5.4. Contour Plot of $[\text{Cl}^-]$ over the total DPEM campaign. The $[\text{Cl}^-]$ is presented via a colouration scale (right) in these plots.211

Fig. 5.5. HYSPLIT for IGDTUW for between 23rd Oct 2018 - 6th Nov 2018.212

Fig. 5.6. HYSPLIT for IGDTUW for between 9th Oct 2018 – 23rd Oct 2018.212

Fig. 5.7. Contour plots showing the $[\text{Cl}^-]$ in association with wind data averaged to the filter sampling times for the BWIN and BSUM, day and night-time periods. The $[\text{Cl}^-]$ is presented via a colouration scale (right) in these plots.213

Fig. 5.8 Map of Beijing showing the key potential Cl^- emitters consisting of Waste Incineration Plants (Green); Landfill Sites (Brown); Gas Power Stations (Yellow); Coal Power Stations (Large Black); and Composting Sites (Purple). Grey lines show major roads, light green patches show green spaces and blue colouration indicates a body of water.214

Fig. 5.9. Time series of the $[\text{NO}_3^-]/[\text{SO}_4^{2-}]$ ratios during the DPEM, DPOM, BWIN and BSUM campaigns. The red error bars (x-axis) show the sampling times and the purple error bars (y-axis) show the calculated error for the $[\text{NO}_3^-]/[\text{SO}_4^{2-}]$ values. Time is shown along the x-axis with $[\text{NO}_3^-]/[\text{SO}_4^{2-}]$ shown up the y-axis. A blue dashed line is overlaid in each time series to demonstrate the $[\text{NO}_3^-]/[\text{SO}_4^{2-}] = 1.0$ threshold. The grey vertical lines represent midnight.217

Fig. 5.10. $[\text{NO}_3^-]/[\text{SO}_4^{2-}]$ averages (\pm SD) across the DPEM, DPOM, BWIN and BSUM campaigns. The orange, green and purple bars represent the day, night and total campaign periods, respectively, in Delhi. The yellow, red and dark blue bars represent the day, night and total campaign periods, respectively, in Beijing. A blue dashed line is overlaid in each time series to demonstrate the $[\text{NO}_3^-]/[\text{SO}_4^{2-}] = 1.0$ threshold.217

Fig. 5.11. Time series of NOR and SOR over the course of the Delhi pre-monsoon, post-monsoon, Beijing winter and summer campaigns. The blue error bars show the uncertainty of NOR and SOR in the y-axis and the red error bars demonstrate the length of sampling time. The time of sampling is shown in the x-axis. The y-error bars were calculated by propagating the errors of NO_3^- and SO_4^{2-} from the IC measurements (Chapter 3) with the error from the gas phase species (SO_2 3.12 % and NO_2 5.72 %).222

Fig. 5.12. 28th May 2018 - 1st Jun 2018 (lower SOR) back trajectories for IGDTUW.223

Fig. 5.13. 1st Jun 2018 - 5th Jun 2018 (higher SOR) back trajectories for IGDTUW.223

Fig. 5.14. NOR and SOR averages (\pm SD) across the DPEM, DPOM, BWIN and BSUM campaigns. The orange, green and purple bars represent the day, night and total campaign periods, respectively, in Delhi. The yellow, red and dark blue bars represent the day, night and total campaign periods, respectively, in Beijing. Black dashed lines are overlaid in each bar chart to demonstrate the 1.0 threshold as reported by the majority of the literature. A blue dashed line has been added to the SOR bar chart to show the 0.25 threshold as reported by Li et al., (2016)²⁰⁶.226

Fig. 5.15. Frequency distribution plots of the NOR (left) and SOR (right) over the DPEM, DPOM, BWIN and BSUM campaigns. The yellow distributions show the daytime values with the blue distributions representing the night-time data. The distribution density displayed is calculated by the kernel distribution function. The boxplot represents the inter quartile range and the white line within the boxplot represent the median atmospheric concentration for each ratio.227

Fig. 5.16. Mean RH % Across APHH Campaigns. Error ca. < 1%.234

Fig. 5.17. Mean Temperature Across APHH Campaigns. Error ca. < 1%.234

- Fig. 5.18. Molar Linear Regression Correlation of NH_4^+ with the $\Sigma [\text{Cl}^-] + [\text{NO}_3^-] + 2[\text{SO}_4^{2-}]$ for the day and night periods (A and C, respectively) for the BWIN campaign. The red dot point (C) and the circle points (D) represent an anomaly. Linear regression correlation of the individual ions with $[\text{NH}_4^+]$ is also shown for the BWIN campaign day and night-time periods (B and D, respectively). The red cross points represent NH_4^+ vs $2[\text{SO}_4^{2-}]$; the blue cross points represent NH_4^+ vs NO_3^- ; and the green cross points represent NH_4^+ vs Cl^- . The solid lines show the regression analysis for each relationship with the respective regression equation shown. The 1:1 molar equivalent ratio is also presented as a yellow dashed line in all charts. Errors associated with these measurements may be found in Chapter 3.243
- Fig. 5.19. Molar Regression Analysis of $[\text{NH}_4^+]$ vs $2[\text{SO}_4^{2-}]$, $[\text{NO}_3^-]$ and $[\text{Cl}^-]$ for the BSUM daytime hours. The 1:1 molar ratio is shown as a yellow dashed line. This is a separated-out version of Fig. 5.20B (for clarity). Errors associated with these measurements may be found in Chapter 3.245
- Fig. 5.20. Molar Linear Regression Correlation of NH_4^+ with the $\Sigma [\text{Cl}^-] + [\text{NO}_3^-] + 2[\text{SO}_4^{2-}]$ for the day and night periods (A and C, respectively) for the BSUM campaign. Linear regression correlation of the individual ions with $[\text{NH}_4^+]$ is also shown for the BSUM campaign day and night-time periods (B and D, respectively). The red cross points represent NH_4^+ vs $2[\text{SO}_4^{2-}]$; the blue cross points represent NH_4^+ vs NO_3^- ; and the green cross points represent NH_4^+ vs Cl^- . The solid lines show the regression analysis for each relationship with the respective regression equation shown. The 1:1 molar equivalent ratio is also presented as a yellow dashed line in all charts. Errors associated with these measurements may be found in Chapter 3.246
- Fig. 5.21. Molar Linear Regression Correlation of NH_4^+ with the $\Sigma [\text{Cl}^-] + [\text{NO}_3^-] + 2[\text{SO}_4^{2-}]$ for the day and night periods (A and C, respectively) for the DPEM campaign. Linear regression correlation of the individual ions with $[\text{NH}_4^+]$ is also shown for the DPEM campaign day and night-time periods (B and D, respectively). The red cross points represent NH_4^+ vs $2[\text{SO}_4^{2-}]$; the blue cross points represent NH_4^+ vs NO_3^- ; and the green cross points represent NH_4^+ vs Cl^- . The solid lines show the regression analysis for each relationship with the respective regression equation shown. The 1:1 molar equivalent ratio is also presented as a yellow dashed line in all charts. Errors associated with these measurements may be found in Chapter 3.249
- Fig. 5.22. Molar Linear Regression Correlation of NH_4^+ with the $\Sigma [\text{Cl}^-] + [\text{NO}_3^-] + 2[\text{SO}_4^{2-}]$ for the day and night periods (A and C, respectively) for the DPOM campaign. Linear regression correlation of the individual ions with $[\text{NH}_4^+]$ is also shown for the DPOM campaign day and night-time periods (B and D, respectively). The red cross points represent NH_4^+ vs $2[\text{SO}_4^{2-}]$; the blue cross points represent NH_4^+ vs NO_3^- ; and the green cross points represent NH_4^+ vs Cl^- . The solid lines show the regression analysis for each relationship with the respective regression equation shown. The 1:1 molar equivalent ratio is also presented as a yellow dashed line in all charts. Errors associated with these measurements may be found in Chapter 3.251
- Fig. 6.1. Calculating the concentration of organic nitrate using the AMS and PILS times series.258
- Fig. 6.2. Structures of the four Org- NO_3 compounds investigated for hydrolysis rates in this study.262
- Fig. 6.3. $[\text{NO}_3^-]$ (μmol) production as a function of time (in 25.4 ppm LiF) from various Org- NO_3 compounds synthesised by UEA. The error associated with these measurements was $\pm 1.95\%$. The error was calculated based on the IC instrument reproducibility of $[\text{NO}_3^-]$. The concentration of NO_3^- produced from Org- NO_3 hydrolysis (y-axis) is plotted against time of reaction (x-axis).264
- Fig. 6.4. Possible formation of carbocation via Org- NO_3 hydrolysis (compound 1).266
- Fig. 6.5. $[\text{NO}_2^-]$ (μmol) as a function of time (in 25.4 ppm LiF) from compound 4 synthesised by UEA. The error associated with these measurements was $\pm 4.78\%$. The error was calculated based on the IC instrument reproducibility of $[\text{NO}_2^-]$. The concentration of NO_2^- present (y-axis) is plotted against time of experiment (x-axis).268
- Fig. 6.6. Nitrite formation from the hydrolysis of Compound 4 through a possible elimination reaction.268
- Fig. 6.7. Pilot tests observing the light and temperature dependence on $[\text{NO}_3^-]$ (μmol) production as a function of time from compound 1 hydrolysis. The vertical grey lines correspond to 24-hour periods. The black data (1) corresponds to Org- NO_3 hydrolysis directly from the stock; the orange data points demonstrate the progress of Org- NO_3 hydrolysis after the sample had spent a night in the fridge; the blue data points (5) show the progress of Org- NO_3 hydrolysis after the sample solution had spent a weekend in the fridge. Group 3 (yellow) and Group 4 (grey) results are from a light and dark experiment, respectively. The error associated with these measurements was $\pm 1.95\%$. The error was calculated based on the IC instrument reproducibility of $[\text{NO}_3^-]$. The concentration of NO_3^- produced from Org- NO_3 hydrolysis (y-axis) is plotted against time of reaction (x-axis).269
- Fig. 6.8. Reduction in $[\text{NO}_3^-]$ for cooler temperatures and darker conditions. The black data (1) corresponds to Org- NO_3 hydrolysis directly from the stock; the orange data points (2) demonstrate the progress of Org- NO_3 hydrolysis after the sample had spent a night in the fridge; the yellow data points (3) show the

progress of Org-NO ₃ hydrolysis for an Org-NO ₃ sample which had been exposed to a bright light for 1 hour and the grey data points (4) show the progress of Org-NO ₃ hydrolysis from samples which had been wrapped in foil and placed into the fridge for an hour (at the same time as the light experiment). The error associated with these measurements was ±1.95 %. The error was calculated based on the IC instrument reproducibility of [NO ₃ ⁻].	270
Fig. 6.9. Direct comparison of rates of reactions and kinetic orders between Org-NO ₃ hydrolysis in 25.4 ppm LiF and 18.2 MΩ water for compounds 1-3. The error associated with these measurements was ±1.95 %. The error was calculated based on the IC instrument reproducibility of [NO ₃ ⁻]. The % [NO ₃ ⁻] molar yield (y-axis) is plotted against time (x-axis).	272
Fig. 6.10. Possible S _N ² substitution mechanism during Org-NO ₃ hydrolysis (mechanism A).	273
Fig. 6.11. Possible S _N ² nucleophilic substitution by OH ⁻ (mechanism B).	274
Fig. 6.12. Possible base catalysed β-hydride E ² elimination reaction for Org-NO ₃ hydrolysis (mechanism C).	275
Fig. 6.13. Acid catalysed reaction mechanism for the hydrolysis of compound 1 (mechanism D).	276
Fig. 6.14. Direct comparison of total % [NO ₃ ⁻] and % [NO ₂ ⁻] molar yield between Org-NO ₃ (compound) hydrolysis in 25.4 ppm LiF and 18.2 MΩ water. The error associated with the [NO ₃ ⁻] measurements was ±1.95 % and with the [NO ₂ ⁻] measurements was ±4.78 %. The error was calculated based on the IC instrument reproducibility of these species.	278
Fig. 6.15. Possible acid catalysed S _N ¹ hydrolysis pathway of compound 4 with OH ⁻ as the nucleophile producing NO ₃ ⁻ (mechanism E).	279
Fig. 6.16. Possible nucleophilic substitution reaction (S _N ²) reaction of compound 4 producing NO ₃ ⁻ (mechanism F).	279
Fig. 6.17. Possible acid catalysed elimination hydrolysis reaction (E ²) of compound 4 producing NO ₂ ⁻ (mechanism G).	280
Fig. 6.18. Possible base catalysed α-hydrogen elimination hydrolysis reaction (E ²) producing NO ₂ ⁻ (mechanism H).	280
Fig. 6.19. Time series for [NO ₃ ⁻] (A), [SO ₄ ²⁻] (B) and estimated [Org-NO ₃] (C) measured by the PILS-IC (cross points), as well as the AMS data (green time series) on the 17 th August. The injection of species into the chamber is shown as vertical lines across the x-axis which are summarised in the legend on the right. The error associated with the PILS-IC measurements are shown as error bars in the y-axis.	286
Fig. 6.20. Time series for [NO ₃ ⁻] (A), [SO ₄ ²⁻] (B) and estimated [Org-NO ₃] (C) measured by the PILS-IC (cross points), as well as the AMS data (green time series) on the 15 th August. The injection of species into the chamber is shown as vertical lines across the x-axis which are summarised in the legend on the right. The error associated with the PILS-IC measurements are shown as error bars in the y-axis.	288
Fig. 6.21. Time series for [NO ₃ ⁻] (A), [SO ₄ ²⁻] (B) and estimated [Org-NO ₃] (C) measured by the PILS-IC (cross points), as well as the AMS data (green time series) on the 16 th August. The injection of species into the chamber is shown as vertical lines across the x-axis which are summarised in the legend on the right. The error associated with the PILS-IC measurements are shown as error bars in the y-axis.	288
Fig. 6.22. The PILS-IC Org-NO ₃ time series plotted against AMS Org-NO ₃ and MPI NO _z concentrations for the 15 th Aug. The injection of species into the chamber is shown as vertical lines across the x-axis which are summarised in the legend on the right. The uncertainty in the PILS-IC [Org-NO ₃] can be found in Fig. 6.20C.	289
Fig. 6.23. The PILS-IC Org-NO ₃ plotted against isoprene, RH and the NO ₃ radical concentrations for the 15 th Aug. The injection of species into the chamber is shown as vertical lines across the x-axis which are summarised in the legend on the right. The uncertainty in the PILS-IC [Org-NO ₃] can be found in Fig. 6.20C.	290
Fig. 6.24. The PILS-IC Org-NO ₃ plotted against isoprene, RH and the NO ₃ radical and N ₂ O ₅ concentrations for the 16 th Aug. The injection of species into the chamber is shown as vertical lines across the x-axis which are summarised in the legend on the right. The uncertainty in the PILS-IC [Org-NO ₃] can be found in Fig. 6.21C.	291
Fig. 6.25. The PILS-IC Org-NO ₃ plotted against AMS Org-NO ₃ and MPI NO _z concentrations for the 16 th Aug. The injection of species into the chamber is shown as vertical lines across the x-axis which are summarised in the legend on the right. The uncertainty in the PILS-IC [Org-NO ₃] can be found in Fig. 6.21C.	292
Fig. 6.26. Time series for [NO ₃ ⁻] (A), [SO ₄ ²⁻] (B) and estimated [Org-NO ₃] (C) measured by the PILS-IC (cross points), as well as the AMS data (green time series) on the 18 th August. The injection of species into the chamber is shown as vertical lines across the x-axis which are summarised in the legend on the right. The error associated with the PILS-IC measurements are shown as error bars in the y-axis.	293

Fig. 6.27. Time series for [NO ₃ ⁻] (A), [SO ₄ ²⁻] (B) and estimated [Org-NO ₃] (C) measured by the PILS-IC (cross points), as well as the AMS data (green time series) on the 19 th August. The injection of species into the chamber is shown as vertical lines across the x-axis which are summarised in the legend on the right. The error associated with the PILS-IC measurements are shown as error bars in the y-axis.....	293
Fig. 6.28. Time series for [NO ₃ ⁻] (A), [SO ₄ ²⁻] (B) and estimated [Org-NO ₃] (C) measured by the PILS-IC (cross points), as well as the AMS data (green time series) on the 20 th August. The injection of species into the chamber is shown as vertical lines across the x-axis which are summarised in the legend on the right. The error associated with the PILS-IC measurements are shown as error bars in the y-axis.....	294
Fig. 6.29. Time series for [NO ₃ ⁻] (A), [SO ₄ ²⁻] (B) and estimated [Org-NO ₃] (C) measured by the PILS-IC (cross points), as well as the AMS data (green time series) on the 21 st August. The injection of species into the chamber is shown as vertical lines across the x-axis which are summarised in the legend on the right. The error associated with the PILS-IC measurements are shown as error bars in the y-axis.....	294
Fig. 6.30. Time series for [NO ₃ ⁻] (A), [SO ₄ ²⁻] (B) and estimated [Org-NO ₃] (C) measured by the PILS-IC (cross points), as well as the AMS data (green time series) on the 22 nd August. The injection of species into the chamber is shown as vertical lines across the x-axis which are summarised in the legend on the right. The error associated with the PILS-IC measurements are shown as error bars in the y-axis.....	295
Fig. 6.31. Time series for [NO ₃ ⁻] (A), [SO ₄ ²⁻] (B) and estimated [Org-NO ₃] (C) measured by the PILS-IC (cross points), as well as the AMS data (green time series) on the 23 rd August. The injection of species into the chamber is shown as vertical lines across the x-axis which are summarised in the legend on the right. The error associated with the PILS-IC measurements are shown as error bars in the y-axis.....	295
Fig. 6.32. The PILS-IC Org-NO ₃ plotted against isoprene and the NO ₃ radical concentrations for the 18 th Aug. The injection of species into the chamber is shown as vertical lines across the x-axis which are summarised in the legend on the right. The uncertainty in the PILS-IC [Org-NO ₃] can be found in Fig. 6.26C.	297
Fig. 6.33. The PILS-IC Org-NO ₃ plotted against isoprene, RH and the NO ₃ radical concentrations for the 21 st Aug. The injection of species into the chamber is shown as vertical lines across the x-axis which are summarised in the legend on the right. The uncertainty in the PILS-IC [Org-NO ₃] can be found in Fig. 6.29C.	298
Fig. 6.34. Ratios of Organic to Inorganic Nitrate in each NO ₃ ISOP Experiment as determined by PILS-IC for each experiment. The errors associated with these data can be found in sections 6.3.2.4.1 - 6.3.2.4.4.	299
Fig. 6.35. Average Isoprene, RH and NO ₃ Radical in each NO ₃ ISOP campaign Experiment.	300
Fig. 6.36. Time series comparison of the PILS-IC [NO ₃ ⁻] and [Org-NO ₃] as well as the AMS [NO ₃ ⁻] results from the experiment which was conducted on the 15 th August (see legend). The time during the experiment is given on the x-axis with the aerosol concentrations being displayed on the primary y-axis and the gas-phase concentrations displayed on the secondary y-axis. The injection of species into the smog chamber is shown as vertical lines along the x-axis which are summarised in the legend on the right. The error associated with the PILS-IC [NO ₃ ⁻] and [Org-NO ₃] can be found in Fig. 6.20A and Fig. 6.20C, respectively.	301
Fig. 7.1. Schematic of NDMA formation taken from Choi et al., (2020) ⁵⁴⁷	310
Fig. 7.2. Structures of the Nitrosamine species analysed in Beijing.	312
Fig. 7.3. GC × GC – NCD plot of the ON MegaMix Standard showing the distribution of different ON compounds classes. The 1D retention time (Rt ₁) is given on the x-axis and the 2D retention time (Rt ₂) is given on the y-axis. A key showing the ON chemical classifications for each species colour is shown in the legend on the right. The red boxes outline arbitrary slices (numbered) of the chromatogram for discussion later in this section.	317
Fig. 7.4. 2D GC × GC – NCD plot of ON MegaMix.	319
Fig. 7.5. Zoom in of section 2 (Fig. 7.3) in the MegaMix chromatogram (Fig. 7.4).	320
Fig. 7.6 . GC × GC – NCD Chromatogram of sample #88 representing the identification of nitrosamines using the Kovats Retention Index method (using nitroalkane mix from C ₂ - C ₁₂).	324
Fig. 7.7. Time series of NDMA, NMEA, N-tert-butylformamide + NDEA, Npyr, Nmor and Npip during a 7-day period during the Beijing APHH winter campaign. The black cross datapoints show the atmospheric nitrosamine concentrations in PM _{2.5} , with the uncertainty represented by the blue error bars in the y-axis (section 7.3.4). The red horizontal error bars demonstrate the time of sampling. The grey vertical lines show the time at 00:00.	326
Fig. 7.8. Time series of NDPA, NDBA, NDPhA, NNN, NAT and NAB during a 7-day period during the Beijing APHH winter campaign. The black cross datapoints show the atmospheric nitrosamine concentrations in PM _{2.5} , with the uncertainty represented by the blue error bars in the y-axis (section 7.3.4). The red horizontal error bars demonstrate the time of sampling. The grey vertical lines show the time at 00:00.	327

- Fig. 7.9. Time series of NNK during a 7-day period during the Beijing APHH winter campaign. The black cross datapoints show the atmospheric nitrosamine concentrations in PM_{2.5}, with the uncertainty represented by the blue error bars in the y-axis (section 7.3.4). The red horizontal error bars demonstrate the time of sampling. The grey vertical lines show the time at 00:00.328
- Fig. 7.10. [N-tert-butylformamide + NDEA] contour plot for the 7-day period analysed. The concentration of [N-tert-butylformamide + NDEA] (ng m⁻³) is given by the colour scale shown on the right.334
- Fig. 7.11. Cancer Risk factor Assessment of Beijing and London imposed by the nitrosamines within PM_{2.5} as a function of the Exposure Time (ET) for different age groups. The blue, orange and grey lines show the cancer risk imposed on the 0 to < 2, 2 to < 16 and 16 =< age brackets, against the amount of time an individual is exposed to (A) Beijing and (B) London [PM_{2.5}] (worst case scenarios). The vertical error bars demonstrate the uncertainty as calculated in section 7.3.8.341
- Fig. 7.12. Cancer Risk factor Assessment of Beijing imposed by the nitrosamines within PM_{2.5} (assuming no NDEA is present) as a function of the Exposure Time (ET) for different age groups. The blue, orange and grey lines show the cancer risk imposed on the 0 to < 2, 2 to < 16 and 16 =< age brackets, against the amount of time an individual is exposed to Beijing's [PM_{2.5}] (assuming no NDEA is present). The vertical error bars demonstrate the uncertainty as calculated as described in section 7.3.8.344
- Ap Fig. A. Map of India showing the distribution of ionic PM_{2.5} particle composition across India (Annual) from reviewed studies. A key denoting the segment species colours is shown in the top left corner. Red markers on the map of India show the different cities. Text shown above each study presents the details of each study. The species are presented as F⁻ (gold), CH₃SO₃⁻ (orange), Cl⁻ (green), NO₂⁻ (dark blue), Br⁻ (medium blue), NO₃⁻ (light blue), PO₄³⁻ (yellow), SO₄²⁻ (red), C₂O₄²⁻ (brown), Na⁺ (pink), NH₄⁺ (lilac), K⁺ (purple), Mg²⁺ (black), Ca²⁺ (grey) and other (amber) in the pie charts.391
- Ap Fig. B. Map of China showing the distribution of ionic PM_{2.5} particle composition across China (Spring) from reviewed studies. A key denoting the segment species colours is shown in the top left corner. Red markers on the map of India show the different cities. Text shown above each study presents the details of each study. The species are presented as F⁻ (gold), CH₃SO₃⁻ (orange), Cl⁻ (green), NO₂⁻ (dark blue), Br⁻ (medium blue), NO₃⁻ (light blue), PO₄³⁻ (yellow), SO₄²⁻ (red), C₂O₄²⁻ (brown), Na⁺ (pink), NH₄⁺ (lilac), K⁺ (purple), Mg²⁺ (black), Ca²⁺ (grey) and other (amber) in the pie charts.392
- Ap Fig. C. Map of China showing the distribution of ionic PM_{2.5} particle composition across China (Autumn) from reviewed studies. A key denoting the segment species colours is shown in the top left corner. Red markers on the map of India show the different cities. Text shown above each study presents the details of each study. The species are presented as F⁻ (gold), CH₃SO₃⁻ (orange), Cl⁻ (green), NO₂⁻ (dark blue), Br⁻ (medium blue), NO₃⁻ (light blue), PO₄³⁻ (yellow), SO₄²⁻ (red), C₂O₄²⁻ (brown), Na⁺ (pink), NH₄⁺ (lilac), K⁺ (purple), Mg²⁺ (black), Ca²⁺ (grey) and other (amber) in the pie charts.393
- Ap Fig. D. Map of China showing the distribution of ionic PM_{2.5} particle composition across China (Annual) from reviewed studies. A key denoting the segment species colours is shown in the top left corner. Red markers on the map of India show the different cities. Text shown above each study presents the details of each study. The species are presented as F⁻ (gold), CH₃SO₃⁻ (orange), Cl⁻ (green), NO₂⁻ (dark blue), Br⁻ (medium blue), NO₃⁻ (light blue), PO₄³⁻ (yellow), SO₄²⁻ (red), C₂O₄²⁻ (brown), Na⁺ (pink), NH₄⁺ (lilac), K⁺ (purple), Mg²⁺ (black), Ca²⁺ (grey) and other (amber) in the pie charts.394
- Ap Fig. E. Time series of Methanesulfonic acid measured by offline ion chromatography during the APHH Delhi pre-monsoon, Delhi Post-Monsoon, Beijing Winter and Beijing Summer campaigns. Ion concentrations are shown on the y-axes with time on the x-axes. The grey vertical lines represent midnight time points. The red error bars show the time of sampling and the blue error bars show the error of each concentration measurement in the y-axis.395
- Ap Fig. F. Time series of Nitrite measured by offline ion chromatography during the APHH Delhi pre-monsoon, Delhi Post-Monsoon, Beijing Winter and Beijing Summer campaigns. Ion concentrations are shown on the y-axes with time on the x-axes. The grey vertical lines represent midnight time points. The red error bars show the time of sampling and the blue error bars show the error of each concentration measurement in the y-axis. LOD for NO₂⁻ is 2.6 × 10⁻² ppm (BWIN), 9.2 × 10⁻² ppm (BSUM) and 2.7 × 10⁻¹ ppm for the Delhi campaigns.....396
- Ap Fig. G. Time series of Bromide measured by offline ion chromatography during the APHH Delhi pre-monsoon, Delhi Post-Monsoon, Beijing Winter and Beijing Summer campaigns. Ion concentrations are shown on the y-axes with time on the x-axes. The grey vertical lines represent midnight time points. The red error bars show the time of sampling and the blue error bars show the error of each concentration measurement in the y-axis. LOD for NO₂⁻ is 2.6 × 10⁻² ppm (BWIN), 9.2 × 10⁻² ppm (BSUM) and 2.7 × 10⁻¹ ppm for the Delhi campaigns.....397

Ap Fig. H. Time series of Phosphate measured by offline ion chromatography during the APHH Delhi pre-monsoon, Delhi Post-Monsoon, Beijing Winter and Beijing Summer campaigns. Ion concentrations are shown on the y-axes with time on the x-axes. The grey vertical lines represent midnight time points. The red error bars show the time of sampling and the blue error bars show the error of each concentration measurement in the y-axis.....	398
Ap Fig. I. Time series of Sodium measured by offline ion chromatography during the APHH Delhi pre-monsoon, Delhi Post-Monsoon, Beijing Winter and Beijing Summer campaigns. Ion concentrations are shown on the y-axes with time on the x-axes. The grey vertical lines represent midnight time points. The red error bars show the time of sampling and the blue error bars show the error of each concentration measurement in the y-axis.....	399
Ap Fig. J. Time series of Potassium measured by offline ion chromatography during the APHH Delhi pre-monsoon, Delhi Post-Monsoon, Beijing Winter and Beijing Summer campaigns. Ion concentrations are shown on the y-axes with time on the x-axes. The grey vertical lines represent midnight time points. The red error bars show the time of sampling and the blue error bars show the error of each concentration measurement in the y-axis.....	400
Ap Fig. K. Time series of Magnesium measured by offline ion chromatography during the APHH Delhi pre-monsoon, Delhi Post-Monsoon, Beijing Winter and Beijing Summer campaigns. Ion concentrations are shown on the y-axes with time on the x-axes. The grey vertical lines represent midnight time points. The red error bars show the time of sampling and the blue error bars show the error of each concentration measurement in the y-axis.....	401
Ap Fig. L. Time series of Calcium measured by offline ion chromatography during the APHH Delhi pre-monsoon, Delhi Post-Monsoon, Beijing Winter and Beijing Summer campaigns. Ion concentrations are shown on the y-axes with time on the x-axes. The grey vertical lines represent midnight time points. The red error bars show the time of sampling and the blue error bars show the error of each concentration measurement in the y-axis.....	402
Ap Fig. M. Time series of Fluoride measured by offline ion chromatography during the APHH Delhi pre-monsoon, Delhi Post-Monsoon, Beijing Winter and Beijing Summer campaigns. Ion concentrations are shown on the y-axes with time on the x-axes. The grey vertical lines represent midnight time points. The red error bars show the time of sampling and the blue error bars show the error of each concentration measurement in the y-axis.....	403
Ap Fig. N. Satellite image of the National Physical Laboratory of India (NPL) used for sampling site classification in chapter 4.	403
Ap Fig. O. Satellite image of the Indian Institute of Tropical Meteorology (IITM) used for sampling site classification in chapter 4.	404
Ap Fig. P. Satellite image of the School of Environmental Sciences, Jawaharlal Nehru University (JNU) used for sampling site classification in chapter 4.	404
Ap Fig. Q. Satellite image of the Mathura Rd. (Mat Rd.) used for sampling site classification in chapter 4.	404
Ap Fig. R. Satellite image of the Indira Gandhi International Airport (IGIA) used for sampling site classification in chapter 4.	405
Ap Fig. S. Satellite image of the Indira Gandhi Delhi Technical University for Women (IGDTUW) used for sampling site classification in chapter 4.	405
Ap Fig. T. Satellite image of the Beijing Normal University (BNU) used for sampling site classification in chapter 4.	405
Ap Fig. U. Satellite image of the Beihang University (BEI) used for sampling site classification in chapter 4.	406
Ap Fig. V. Satellite image of the Hei Shan Zhai (HSZ) used for sampling site classification in chapter 4.	406
Ap Fig. W. Satellite image of the Chinese Ecosystem Research Network (CERN) used for sampling site classification in chapter 4.	406
Ap Fig. X. Satellite image of the Chegongzhuang (CGZ) used for sampling site classification in chapter 4.	407
Ap Fig. Y. Satellite image of the Tsinghua University (THU) used for sampling site classification in chapter 4.	407
Ap Fig. Z. Satellite image of the Urban Site (US) used for sampling site classification in chapter 4.	407
Ap Fig. AA. Satellite image of the Capital Normal University (CNU) used for sampling site classification in chapter 4.	407
Ap Fig. BB. Satellite image of the Capital Steel Company (CSC) used for sampling site classification in chapter 4.	407
Ap Fig. CC. Satellite image of the Yihai Garden (YG) used for sampling site classification in chapter 4.	407

Ap Fig. DD. Satellite image of the Miyun (MY) used for sampling site classification in chapter 4.....	407
Ap Fig. EE. Satellite image of the Pinggu (PG) used for sampling site classification in chapter 4.	407
Ap Fig. FF. Satellite image of the Institute of Atmospheric Physics (IAP) used for sampling site classification in chapter 4.	407
Ap Fig. GG. Satellite image of the Peking University (PKU) used for sampling site classification in chapter 4.....	407
Ap Fig. HH. Satellite image of the Olympic Park (OLP) used for sampling site classification in chapter 4.	407
Ap Fig. II. Satellite image of the Ming Tombs (MT) used for sampling site classification in chapter 4.	407
Ap Fig. JJ. Satellite image of the Tongzhou (TZ) used for sampling site classification in chapter 4.	407
Ap Fig. KK. Satellite image of the Fangshan (FG) used for sampling site classification in chapter 4.	407
Ap Fig. LL. Satellite image of China Meteorological Administration (CMA) used for sampling site classification in chapter 4.	407
Ap Fig. MM. Satellite image of Institute of Geographic Sciences and Natural Resources Research (IGSNRR) used for sampling site classification in chapter 4.	407
Ap Fig. NN. Satellite image of the Chinese Research Academy of Environmental Sciences (CRAES) used for sampling site classification in chapter 4.	407
Ap Fig. OO. Satellite image of the Yuquan Campus, University of Chinese Academy of Sciences (YU CAS) used for sampling site classification in chapter 4.	407
Ap Fig. PP. Timeline showing the change in PM _{2.5} particle composition as a function of time (Delhi Annual Averages). The symbols next to the pie charts represent the type of site for which Urban (×) and Suburban (Δ) are included. The symbol colours indicate atmospheric conditions including black (non-specific period). Time of sampling is shown along the x-axis. The study code along with the specific sampling site and time are also presented above each pie chart. The species presented are coloured in the pie charts, as per the key shown in the top right.	407
Ap Fig. QQ. Timeline showing the change in PM _{2.5} particle composition as a function of time within the Beijing Spring (top) and Autumn (bottom) seasons. The symbols next to the pie charts represent the type of site for which Urban (×), Suburban (Δ), Rural (□) and mixed (O) are included. The colours indicate atmospheric conditions including black (non-specific period), red (haze period), light blue (pollution control period) and green (clean period). Time of sampling is shown along the x-axis. The study code along with the specific sampling site and time are also presented above each pie chart. The species presented are coloured in the pie charts, as per the key shown in the bottom right.	407
Ap Fig. RR. Timeline showing the change in PM _{2.5} particle composition as a function of time within Beijing (Annual Averages). The symbols next to the pie charts represent the type of site for which Urban (×), Suburban (Δ), Rural (□) and mixed (O) are included. The colours indicate atmospheric conditions including black (non-specific period), red (haze period), light blue (pollution control period) and green (clean period). Time of sampling is shown along the x-axis. The study code along with the specific sampling site and time are also presented above each pie chart. The species presented are coloured in the pie charts, as per the key shown in the top left.	407

Acknowledgements

I would like to express my sincere thanks, gratitude and appreciation to the most wonderful and fabulous PhD supervisor Professor Jacqueline F Hamilton, for her continuous advice, guidance, provision of opportunities as well as encouragement throughout my PhD studies. I have thoroughly enjoyed getting to work in Jacqui's Aerosol research group which I will sorely miss being a part of. I would also like to thank Professor Lucy J Carpenter for her supervision and guidance throughout my MChem and PhD, and whose 3rd year lecture course first sparked my fascination with Atmospheric Chemistry. It has been my privilege to have had these two incredibly inspirational women of science advise me during my research studies. I would also like to say a huge thank you to my co-supervisor Professor James D Lee for his advice during Thesis Advisory Panel meetings.

I would also like to express my sincere thanks and appreciation to all my colleagues in the Wolfson Atmospheric Chemistry Laboratories for being such great folk to work with. A special thank you goes to my friend and rugby team-mate Dr Martyn Ward for his teachings in the laboratories and for showing me how to fix several pieces of equipment. I would also like to especially thank my friend Will Drysdale for his assistance with R and for averaging numerous datasets to the HiVol filter times. In addition, I would like to thank Imogen Andrews, Pauline Maudet and Naomi Farren for their assistance in the manual labour of processing IC samples. I would also like to thank all who took part in the APHH and NO₃ISOP campaigns (especially in the collection of the University of York HiVol filter samples) for their collaboration.

I am so grateful to my parents Brigitta and Brian Swift whose love, provision, care and sacrifices have prepared me for my future. A very special thank you also to Robin Swift for providing the Indian UltraTech Cement (chapter 3) for this thesis. Furthermore, I would like to thank my fantastic science teachers, Mrs. Gloyns, Mr. Dell, Mrs. Darling, and Mr Stocks at Dartmouth Community College; as well as Mrs. Conibear and Dr Brown at Churston Ferrers Grammar School. A huge thank you is also expressed to all my fantastic teachers. In addition, I would like to thank my Auntie Rita and close friends Robyn Hickman, Angus Stevens, Philly Bowerman, Abigail Gibbs, Sam Cheetham, Dr Fliss McDowall, Becky Dorricott, Kurt Oliver, Ann Speakman, Simon Williams, Dr Victoria Awebajo, Emma Donnellan and Chris Roussel, for their superb encouragement over the years of my PhD.

I am incredibly grateful to my pastors and friends The Reverend Andy J Baker, The Reverend Greg C Downes and The Reverend Matthew J Porter, three great men of God who I have had the privilege of being taught and guided by throughout my time at university. Their prayers, love, encouragement, and spiritual guidance have given hope during the dark and stressful days during my studies, especially throughout the Covid-19 pandemic while finishing this PhD thesis. Thank you so much also to all those who have encouraged and prayed for me at St Michael Le Belfrey Church in York. Special thanks are given to my friends at Dynamic Prayer on a Tuesday morning. The hospitality shown to me by Matthew and Lauren Hudghton, as well as Temi over the years has been so

appreciated. I would also very much like to thank the community at Fore Street Methodist Church in Brixham, South Devon, for their love and prayers throughout my PhD. Thanks be to God. Amen.

Declaration

I declare that this thesis is a presentation of original work and I am the sole author. This work has not previously been presented for an award at this, or any other, University. All sources are acknowledged as References. Where campaign data has been provided by other institutions as part of collaborative work, this has been highlighted and acknowledged.

1 Introduction

1.1 Atmospheric Pollution

The chemistry of the atmosphere is an essential field of study, primarily for assessing the impact of species on radiative forcing and air quality. It is well known that most of the atmosphere is composed of O₂ and N₂ (*ca.* 99 %) although just over 1 % of the atmosphere (by mass) is comprised of thousands of different species (depending on region and time)¹. It is this small fraction of material which controls the vast majority of atmospheric chemistry¹. Therefore, the accurate identity and concentration of these trace species is fundamental to understanding the chemistry of the atmosphere and furthermore, the potential implications of the atmosphere's composition.

This very small fraction of the atmosphere is also the key driver for air pollution. Air pollution is known to be one the leading worldwide causes of preventable death and it has been estimated by the World Health Organisation (WHO) that 4.2 and 3.8 million deaths are caused by ambient outdoor and indoor air pollution per year². Furthermore, the WHO estimates that *ca.* 91 % of the world population inhabit areas where air pollution levels exceed WHO limits². CO, SO₂, NO_x, O₃ and Particulate Matter (PM) are known to be the dominant pollutants of concern with major health implications for humans when exposed to high levels. It has been suggested that for many air pollutants, no safe exposure concentrations exist³. CO has been reported to induce dizziness, headaches and nausea⁴; SO₂ has been shown to cause headaches among humans and stimulate anxiety, as well as invoke cardiovascular disease and induce breathing problems⁴; exposure to NO_x has been noted to affect the respiratory system by encouraging infections and shortness of breath, as well as impacting the blood, spleen and liver and being irritative⁴; O₃ has been reported to cause irritation and breathing problems as well as adversely affect the cardiovascular system⁴.

Finally, PM has been shown to affect the reproductive and central nervous systems in humans⁴; adversely affect the respiratory system^{4,5,3}, decreases lung function⁶ and aggravates asthma⁵; irritate the throat, nose and eyes⁴; and cause harmful effects on the cardiovascular system^{4,3,6} including non-fatal heart attacks and irregular heart beats⁵. In addition, the USA Environmental Protection Agency (EPA) suggest that PM causes premature death in humans who suffer from cardio-respiratory diseases⁵. PM also induces strokes as well as other severe conditions^{7,3}. In addition to these health effects, it has been noted that vulnerable groups (the elderly, those with underlying cardio-respiratory conditions and children) are most susceptible to the effects of PM⁶.

The WHO recommends that human exposure to [SO₂] should not exceed 500 $\mu\text{g m}^{-3}$ over 10 minutes or 20 $\mu\text{g m}^{-3}$ over 24 hours⁸; NO₂ should not exceed 200 $\mu\text{g m}^{-3}$ hour⁻¹ or 40 $\mu\text{g m}^{-3}$ per year⁸; O₃ should not exceed 100 $\mu\text{g m}^{-3}$ per 8 hour mean⁸; and the National Institute for Occupational Safety and Health Recommended Exposure Limit for CO is 35 ppm over an 8 hour time weighted average with a maximum exposure of 200 ppm⁹.

CO is known to be emitted anthropogenically by the incomplete combustion of fuels¹⁰ such as from biomass burning¹¹ and vehicular exhausts¹²; SO₂ is known to be dominantly emitted from power plants and industrial sources burning sulfurous fuel and is also be emitted form volcanoes^{13,4}; and NO_x is predominantly released by the burning of fossil fuels¹⁴ including vehicular exhaust emissions and power plants⁴. O₃ is an essential secondary material required at stratospheric levels protecting life at the earth's surface from harmful UV rays¹⁵, although is detrimental to human health when formed in the troposphere secondarily^{16,17,4}.

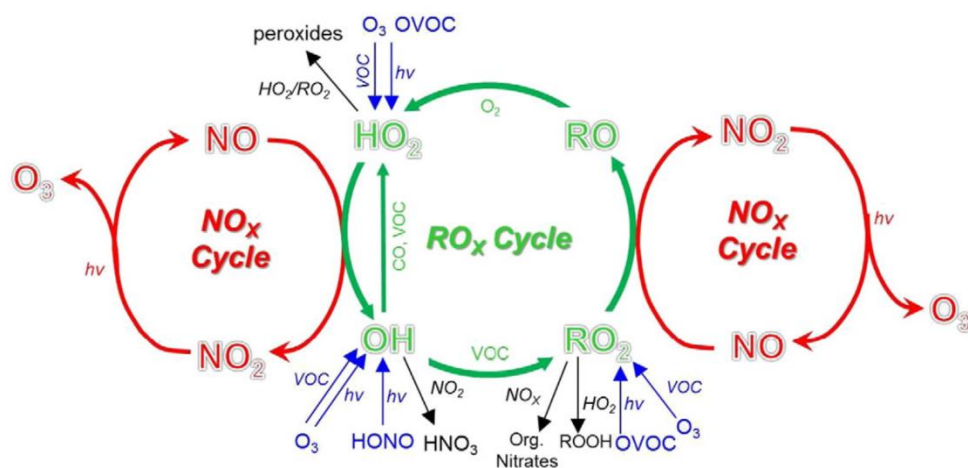


Fig. 1.1. NO_x and RO_x Cycles for O₃ production as depicted by Wang et al., (2017)²⁰.

O₃ is also significant in the troposphere as on photodissociation, the O(¹D) radical reacts with water vapour to produce OH, a dominant oxidising species in the atmosphere controlling the lifetime of many other species¹⁸. O₃ may also oxidise gaseous species on its own merit¹⁹. In the troposphere, O₃ is formed secondarily via the photolysis of NO₂ and Volatile Organic Compounds (VOCs), through the NO_x cycle as demonstrated in Fig. 1.1 by Wang et al., (2017)²⁰. PM is emitted naturally (e.g. sea salt and dust) or anthropogenically (e.g. vehicular emissions²¹, coal and biomass burning^{22,23}). It may also be secondarily formed in the atmosphere through coagulation and condensation of gaseous species^{24,25,26,27,28,29,30}. In addition, aerosol species serve as a surface for other atmospheric reactions²⁹.

PM is one of the major pollutants of concern for which the WHO estimated *ca.* 7 million attributable deaths annually³¹ (equivalent to over 10 % of the UK's population, as of 2021)³². PM is widely acknowledged to be the most important pollutant regarding health effects in humans⁶, and has been suggested to cause > 90 % of total air pollution related adverse health impacts (PM_{2.5})³. In addition to the severe health effects outlined, ambient PM is also known to cause significant environmental damage³³ including acid rain³⁴ contribution and decreasing the pH of water bodies; changing the diversity of ecosystems; adversely affecting agriculture and forests as well as causing acidification of soil bodies⁵. The knock-on effect of these human health and environmental impacts has caused significant impacts on economies^{6,35,36}. In addition and of much more recent significance, PM may

aid in the transport of infectious diseases including the Sars-Cov-2 virus (COVID-19)^{37,38,39,40,41,42,43}. Considering the combination of impacts of PM_{2.5} on society⁴⁴, it is evident why research into PM is vital and therefore this thesis focuses on the PM_{2.5} pollutant.

1.2 Atmospheric Aerosol and PM_{2.5}

Atmospheric aerosols are defined as suspended particles of solid, liquid or a mixture of both which are known to vary as a function of size and chemical composition^{28,45,29}. The variability in PM composition and size segregation is down to the complexity of contributing sources and secondary chemistry formation pathways which may change overtime as particles evolve and continue to uptake material²⁸. They are also described as continuously exchanging molecules with the gas phase which further constitutes to the complexity of composition²⁹ and physical characteristics such as density, hygroscopicity and optical properties²⁹. Aerosols exhibit varying lifetimes in the atmosphere ranging from a few days (PM₁₀) to weeks (PM_{2.5})²⁸. Loss of PM from the atmosphere may occur through the processes of dry or wet deposition^{34,46}. Furthermore, as an aerosol particle evolves and alters in size and chemical composition, the relative lifetime of a specific particle will also change³⁴.

PM is known to be made up of organic and inorganic constituents^{47,28} and may be segregated into different size fractions. PM₁₀, PM_{2.5}, PM₁ and PM_{0.1} denotes PM size fractions which are $\leq 10 \mu\text{m}$, $\leq 2.5 \mu\text{m}$, $\leq 1 \mu\text{m}$ and $\leq 0.1 \mu\text{m}$ in diameter, respectively^{48,49,50,51,52}. A depiction of the PM₁₀ and PM_{2.5} size ranges is shown in Fig. 1.2 (from the EPA⁴⁸) to aid the reader. Particles also vary in shape although it is thought that most aerosols are spherical and smooth⁵³. The WHO recommends that exposure limits to PM₁₀ should not exceed $50 \mu\text{g m}^{-3}$ (24 hour mean) or $20 \mu\text{g m}^{-3}$ (annual mean). PM_{2.5} however has been suggested not to exceed $25 \mu\text{g m}^{-3}$ (24 hour mean) or $10 \mu\text{g m}^{-3}$ (annual mean). The Indian National Ambient Air Quality Standard (NAAQS) is however $40 \mu\text{g m}^{-3}$ (annually)⁵⁴.

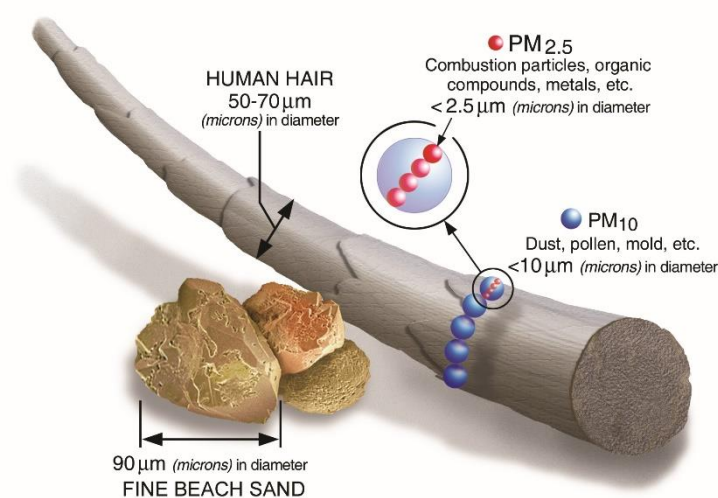


Fig. 1.2. Depictions of the PM₁₀ and PM_{2.5} size ranges compared to a grain of sand a strand of hair taken from the EPA⁴⁸.

1.2.1 Aerosol Effects on Climate

Briefly, atmospheric aerosols are known to affect radiative forcing^{28,30} and overall demonstrate a cooling effect on climate²⁹. Depending on particle composition, aerosols may either absorb or scatter solar radiation through the direct effect^{45,34}. Aerosols may also affect the characteristics of clouds (such as precipitation patterns and radiation reflectance) through the indirect effect⁴⁵. Certain aerosols are described as Cloud Condensation Nuclei (CCN)²⁹ and ice nuclei²⁸, and are essential in cloud formation mechanisms which contribute to the albedo effect of the planet. The extent of this is affected by the relative concentration and particle size of aerosol as a larger number of small particles will increase cloud droplet number for a specific air mass humidity and therefore cloud albedo^{28,55}. SO_4^{2-} is a particular constituent which is known to encourage nucleation. In addition, a larger number of small cloud droplets increases the lifetime of a cloud as water molecule coagulation and particle growth takes longer for smaller particle, before they are large enough to be precipitated (cloud lifetime effect)²⁸. This enhances the albedo effect of clouds^{28,56}.

Some constituents of aerosol such as Black Carbon (BC), some mineral dust and organic carbon species absorb solar radiation and induce a positive radiative forcing²⁸. This is because these constituents may alter cloud characteristics as to reduce the reflectance capability and albedo effect on the planet²⁸. As species absorb radiation, the surrounding air mass temperature increases resulting in evaporation of surrounding clouds. In addition, fewer solar rays may reach the surface of the earth, reducing surface temperatures and therefore convection currents which further reduces the potential for cloud formation (semi-direct effect)^{28,57}.

1.2.2 Particle Size and Deposition in the Respiratory Tract

The respiratory tract observes the second largest surface area to external materials (after the digestive system) with an estimated 150 m² internal surface area⁵¹ and 480 million alveoli⁵¹. The region of the respiratory tract in which PM deposits and comes into contact with has strong dependence on particle size^{51,58,59,52,60}. Larger particles (PM₁₀) may reach the bronchi⁵⁹; the PM_{2.5} fraction is small enough to penetrate deep into the lung and reach the alveoli in which it can bioaccumulate and induce oxidative stress and damage to the lung^{61,62,63,64,60,51}. Structural damage may lead to reduced lung function due to this⁶⁵. PM_{2.5} may even pass through into the blood stream and therefore around the body^{61,52,51} to effect other organs⁶⁶. It has been suggested that PM_{2.5} constitutes *ca.* 96 % of particles which enter the respiratory tract and are retained^{51,67,61}. PM_{2.5} are therefore one of the most damaging size fractions of PM to human health^{53,68} for which even very low exposure concentrations have been suggested to cause hazard to human health⁶¹. This has further been attributed to the fact that the toxicity of PM is inversely proportional to the particle size^{69,70}.

Depending on underlying health conditions, such as asthma, the flow and deposition of PM_{2.5} into the lungs may be altered, in which a higher PM_{2.5} deposition may occur due to the deformed airway tract^{53,71}. Deposition may also be altered as a function of breath flow rate in which previous studies have suggested that a smaller particle in conjunction with a faster breath flow rate may reduce the deposition potential of particles in the airway^{60,72}. Some inhaled PM_{2.5} may however be cleared by

the body in a variety of ways including through the mucociliary clearance mechanism (by mucus gel). These mechanisms and the biochemistry surrounding these pathways are fully explained by Wei and Tang., (2018)⁵¹.

1.2.3 Illnesses and Mechanisms Attributed to PM_{2.5} Exposure

The cardio-respiratory illnesses which surround PM_{2.5} have been well documented^{73,51,62,53} and have been associated with long-term PM_{2.5} exposure^{64,52,65,69}. In the worst cases, exposure to PM_{2.5} has been associated with pre-mature morbidity and mortality^{73,74,65,69}. Furthermore, PM_{2.5} exposure has also been linked to adverse effects on the human reproductive system⁷⁵, the central nervous system⁶⁸, as well as cancer⁷³ (notably respiratory cancers)^{66,62,69,59,65}. Other illnesses associated with PM_{2.5} exposure include pneumonia, reduction in lung function, asthma, emphysema, bronchitis, Chronic Obstructive Pulmonary Disease (COPD), provoking of birth defects, thrombosis, stroke, heart disease, adverse effects on the endocrine system, insulin resistance and diabetes^{66,64,76,53,61,52,65,76,45}. Several epidemiological studies have also been conducted and comprise significantly to the evidence of PM_{2.5} association with these adverse health effects as well as morbidity and mortality^{76,52,60,62,65,77,66} and an increased rate of short term effects such as hospitalisation associated with respiratory illnesses^{64,65,73}. It has been suggested that PM_{2.5} induces health effects via toxicological mechanisms such as oxidative stress^{62,74,52}, altered immunity, inflammation^{69,52,64,61} and mutagenicity/genotoxicity⁶¹.

1.2.3.1 Induced Oxidative Stress

Oxidative stress is a form of toxicity induced to the body in several manners prompting alterations in normal cell functions and cell death of those exposed to PM_{2.5}^{61,65,62}. It is essentially the imbalance between antioxidants and oxidising species (in excess)⁶². Oxidative stress is also understood to cause constriction of airways (vasoconstriction) from endothelial cell malfunction⁶¹. Numerous types of animal cell have been suggested to undergo damage as a result of oxidative stress from exposure to PM_{2.5}^{78,61,79,80}.

Oxidative stress is known to contribute to disease⁶⁵. PM_{2.5} may induce oxidative stress through the release of Reactive Oxygen Species (ROS)⁶⁵. ROS produced at the surface of particles, or may be produced from the particle as Transition Metals (TM), free radicals, organic and inorganic species^{65,62,74,76}. TM species have also been suggested to produce ROS at the particle surface via the Fenton reaction pathway^{50,81}. In addition, metabolically activated organic constituents from PM_{2.5} surfaces may go on to induce intracellular ROS formation⁶⁵. It has also been suggested that ROS may be formed from macrophages releasing ROS due to lung inflammation⁵⁰. Furthermore, ROS species produced from PM_{2.5} may directly react with antioxidant enzymes and cause DNA and RNA damage⁶². It is also thought that the production of ROS from PM_{2.5} may oxidise lung cells to cause significant injury⁷⁶. Some ROS produced by hydrophilic particle shave been reported to produce the OH radical in the body which is particularly damaging to DNA and may induce mutagenesis, teratogenesis and carcinogenesis if the damaged DNA is not repaired in good time⁷⁶. Other

biochemical mechanisms induce ROS production and therefore oxidative stress from exposure to PM_{2.5}, which are described by Li et al., (2018)⁶⁵.

1.2.3.2 Inflammation, Asthma and Infection

Inflammation of tissue by PM_{2.5} has been extensively studied^{61,82,83,84} and has been suggested to participate in the majority of adverse health effects in humans exposed to PM_{2.5}⁶¹. Respiratory inflammation may be caused by acute short-term exposure or long term PM_{2.5} exposure may induce prolonged inflammation which results in the infection of disease⁶⁵. In addition to observed nasal and lung inflammation by PM_{2.5} exposure^{85,61,86}, PM_{2.5} has also been reported to cause inflammation in the kidneys, heart, spleen and liver⁶¹. Exacerbation of chronic conditions which are specifically associated with inflammatory symptoms include autoimmune disease, cardiovascular disease and pulmonary hypertension, from PM_{2.5}⁶⁵. Further studies link the induction of inflammation with diabetes and insulin resistance, as well as heart disease⁷⁶. Increased inflammation induces morbidity and mortality through the induction of chronic respiratory illnesses⁶⁵ and may also induce cardiovascular stress⁵².

On exposure to PM_{2.5}, it has been suggested that muscles may contract to stimulate inflammation, encouraging disease and infection^{87,69}. Previous studies have shown that inflammation is provoked by the release of pro-inflammatory species in the body which increase with increasing time and concentration of PM_{2.5} exposure^{61,65}. Furthermore, PM_{2.5} may also increase intracellular Ca²⁺ concentrations. An imbalance of Ca²⁺ may also induce inflammation through imbalanced intracellular homeostasis of calcium, for which Ca²⁺ in too high concentrations within the cells may induce inflammation as well as cell impairment⁷⁶. A further description of the toxicological mechanisms of PM_{2.5} induced inflammation has been described previously^{76,61}.

Specifically, asthma is a common illness which is due to the inflammation of the lungs which causes respiratory tract walls to thicken, causing difficulties in breathing and asthmatic symptoms^{88,89,53,64} and is exacerbated by increase PM_{2.5} concentrations⁶⁵. Furthermore, acidic PM_{2.5} may lower the pH value in the deposited area which reduces the ability of haemoglobin to uptake oxygen⁵³. Exacerbation of asthma is also related to oxidative stress (section 1.2.3.1)⁶⁴. Finally, PM_{2.5} composition and concentration are directly related to respiratory inflammation and asthma pathogenesis⁶⁴. Finally, PM_{2.5} effects the lungs' immune system which in turn makes them much more vulnerable to infection⁶¹. PM_{2.5} may also reduce the possibility for bacterial removal from the bronchi (with bronchi mucus) and may also inhibit the normal function of the alveoli macrophages (used to destroy bacteria and other pathogens)⁶¹. Other studies also discuss the epidemiological relationship between PM_{2.5} exposure and bacterial infection in the lungs^{65,90}.

1.2.3.3 Cardiovascular disease

PM_{2.5} is known to reduce cardiovascular function, induce cardiovascular disease^{52,68} as well as cause death by cardiovascular illnesses caused and exacerbated by PM_{2.5}⁶¹. This may occur through the reduced effectiveness of the cardiac autonomic nervous system caused by exposure of humans to PM_{2.5}^{61,52}. This in turn reduces the variability of a person's heart rate which is linked to cardiovascular

mortality and morbidity^{61,52}. A potential mechanism to cardiovascular disease induction is by the destruction to the vascular endothelial cells by PM_{2.5}, which may cause death^{65,52}.

Exposure to PM_{2.5} has also been reported to affect the properties and flow of blood around the body^{50,91}. PM_{2.5} exposure may also increase the oxidation of low-density lipids in the blood stream which may contribute to plaque build-up in the blood vessels^{50,60}. Inflammation of the lungs (as described in section 1.2.3.2) may also increase the thickness of blood^{92,50} as well as release cytokine species⁶⁰. Production of blood clots from PM_{2.5} in the blood stream as well as the increased blood pressure produced via these different mechanisms may influence heart failure⁶⁰ and link PM_{2.5} to the incidence of strokes⁵². It has also been suggested that PM_{2.5} induced health effects are exacerbated by a high-fat diet⁷⁶.

1.2.3.4 Mutagenicity, Genotoxicity and Carcinogenicity

The presence of heavy metal compounds and organic compounds within PM_{2.5} has also demonstrated genotoxicity, mutagenicity and carcinogenicity to humans^{61,65}. Absorption of PM_{2.5} into cells has demonstrated to leach organic species which may stimulate the aryl hydrocarbon receptor and therefore increasing the metabolizing cytochrome P450 enzymes⁶¹. This in turn allows for the leached organic species to be metabolised by these enzymes producing reactive electrophilic metabolites which induce toxicity in the body⁶¹. In addition, PM_{2.5} has demonstrated mutagenicity through the Ames test and is known to damage DNA as well as slow down DNA repair and replicate damaged DNA inducing carcinogenesis^{61,76}. PM_{2.5} has been strongly related to lung cancer and the mortality and morbidity thereof⁶⁵. Furthermore, PM_{2.5} exposure to humans suffering from lung cancer may increase rate of death, according to epidemiological studies^{64,93,94}. In some cases a higher concentration of PM_{2.5} does not increase health risks in a linear relationship (at higher PM_{2.5} concentrations)^{73,95}. This is thought to be down to humans with underlying health conditions dying at lower PM_{2.5} concentrations⁷³. Further description of the mutagenic, genotoxic and carcinogenic mechanisms of PM_{2.5} to the body may be found in the work of Li et al., (2018)⁶⁵, Li et al., (2018)⁶⁴ and Feng et al., (2016)⁶¹.

In addition, as PM_{2.5} is smaller compared to other aerosol (PM₁₀) although observes a larger surface area to mass ratio^{61,76,64}. This therefore enables PM_{2.5} to absorb a greater proportion of toxic gaseous components compared to larger aerosol^{64,96}. Therefore, PM_{2.5} enables a higher concentration of toxic species to be carried deeper into the respiratory tract⁷⁶.

1.3 Chemical Composition of PM_{2.5}

PM_{2.5} consists of both organic and inorganic constituents, as well as free radicals⁶¹ and illness caused by PM_{2.5} is dependent on the particle composition in addition to PM_{2.5} concentration, size, surface area, solubility and origin^{69,62,76}. Some key species of anthropogenic PM_{2.5} include Polycyclic Aromatic Hydrocarbons (PAHs), metals, black carbon and ions such as nitrate and sulfate⁶⁴.

1.3.1 Inorganic Fraction

Inorganic constituents comprise a significant fraction of urban $PM_{2.5}$ ^{97,98,96}, often presenting the majority of the particle. Inorganic species within $PM_{2.5}$ are known to affect climate as they are constituents which scatter incident solar radiation⁹⁸; act as tracers for source apportionment purposes^{98,96}; and also change a particles' hygroscopicity^{96,99}, for which a larger fraction of ionic species encourages the absorption and retainment of water¹⁰⁰ due to the hydrophilicity of inorganic species¹⁰⁰.

The change in a particle's inorganic content and therefore hygroscopicity and hygroscopic growth is particularly significant. This is because the inorganic fraction and amount of water retained by a particle will affect the growth of a particle¹⁰⁰; influences the heterogenous reactions occurring within the particle⁹⁸; affects particle acidity¹⁰¹; affects the radiative forcing potential of a particle as well as degrades visibility^{99,96}. The toxicity of a particle may also be affected, as a higher hygroscopicity encourages more water to be present within the particle which in turn encourages the dissolution of toxic gases from the gas into the particle phase^{102,103}. The acidity of a particle may also affect the dissolution of metals within the aerosol and therefore acts as another means to toxic behaviour¹⁰⁴. Furthermore, the inorganic fraction also affects the lifetime of an aerosol¹⁰¹. Research into the inorganic fraction of $PM_{2.5}$ and their potential sources is therefore vital. Of these inorganic species, Cl^- , NO_3^- , SO_4^{2-} and NH_4^+ (as well as Na^+ in coastal areas) have been suggested to be the most dominant ions within fine aerosol^{99,26,105}.

1.3.1.1 Chloride

The presence of anthropogenic chloride in $PM_{2.5}$ is often through the exchange of primarily emitted hydrochloric acid¹⁰⁶. HCl is known to be emitted from a variety of sources including coal combustion^{107,108,109,110,111}, biomass burning^{108,110,111,25} (including torrefied biomass¹¹²), waste incineration^{113,114} (domestic and industrial)¹⁰⁷, industrial emissions¹¹⁰, flue gas from industrial municipal waste incineration¹¹⁵ (factories¹⁰⁷), steel work industries^{108,109}, the combustion of polyvinyl chloride^{108,115}, landfill sites¹¹⁶, metal processing factories, brick kilns, cooking¹¹⁷ and tobacco smoke. Fabric bleaching and fireworks¹¹⁸ are also known sources of anthropogenic chlorine. Emissions of chlorinated organic compounds such as polychlorinated biphenyls, dibenzo-p-dioxins and dibenzofurans may also come from waste combustion emissions¹¹⁹, and other organic chlorine compounds may be emitted from use as pesticides.

Industrial emissions are also thought to be a major contributor to chloride presence in $PM_{2.5}$ aerosol. A more specific industrial anthropogenic source for chlorine may include steel works, which has been previously mentioned in the literature¹²⁰. Other industrial activities that release chlorine may include chemical industries that use methyl chloride as either a solvent or a chemical feedstock in synthesis^{121,114}. (McCulloch et al., 1999)¹¹⁴ suggest that chloromethane may be used to produce resins, elastomers and silicone fluids, as well as antiknock agents for vehicles¹¹⁴. Chlorine may also be of domestic origin from cooking emissions¹²² or the use of cleaning products¹²³. A study by (Lee et al., 2001)¹²² suggested the detection of chloroform and methylene chloride from Chinese cuisine.

Chlorine isn't usually associated with vehicular emissions or oil refining processes, although Li et al., (2018)¹²⁴ suggests that organochloride compounds as well as inorganic salts may be found in crude oil, and that in Chinese refineries specifically, crude oil that has been desalted may have up to 3 mg L⁻¹ of salt. It has also been reported that organochloride compounds may be added to crude oil artificially during refining and transportation processes, which may in-turn produce HCl emissions¹²⁴. A range of organochloride compounds including 1,2-dichloropropane, 2-chloropropene and methylene chloride have been detected in Chinese naphtha samples¹²⁵. Inorganic chlorides in crude oil may also form HCl through hydrolysis during the refining processes¹²⁵.

It has been suggested in the literature that chlorine may also be associated with tobacco smoke. The presence of chlorine in tobacco leaves and smoke have been previously reported in several studies^{126,127,128}. (Häsänen et al., 1990)¹²⁶ conducted a study in which they analysed the chemical composition of nine different brands of cigarette and found that, on average, the tobacco emitted 68 µg of chloride in the particle phase as well as 90 µg of gaseous chlorine, per cigarette. A dominant organochloride compound emitted from cigarettes is thought to be methyl chloride¹²⁸. Other organochloride compounds may include vinyl chloride, tetrachloroethylene, methylene chloride and chloroform¹²⁶. The chlorine is thought to enter into the tobacco via the use of pesticides and (Fuqua et al., 1976)¹²⁷ reported that the concentrations of chlorine within the cured tobacco plant, increased proportionally to the concentration of chloride that was detected in the soil. Examples of such pesticides may include Dichlorodiphenyltrichloroethane (DDT) and Hexachlorocyclohexane (HCH) which are known to be Persistent Organic Pollutants (POPs) and despite their phasing out in 1983, may still be present in the Beijing suburbs¹²⁹. KCl and NH₄Cl are also known fertilizers¹³⁰ and therefore Cl⁻ may enter into the tobacco leaf in this manner also. The population of Beijing in 2017 was *ca.* 22 million, and it has been estimated that 40 % of global cigarettes are smoked in China¹³¹. Therefore, the contribution of chloride to PM_{2.5} from cigarette smoking may be significant in this thesis.

Non-combustion release of chlorine may include the evaporation of fertilizers and pesticides (see previous), however a much larger number of constituents of measured species may be associated with biogenic emissions from plants and soils^{132,133}. A possible explanation for this may be the production of organochloride compounds which a plant may produce biosynthetically^{132,133}. The source of biogenic chloride from soil may be explained by Keppler et al., (2000)¹³⁴ and the possible mechanism they deduced for methyl halide formation from soil is shown fully in Fig. 1.3. Keppler et al., (2000)¹³⁴ suggest that Fe³⁺ found in soil may oxidise organic matter to allow for halide ions in the soil to bind with alkyl groups and break down organic compounds, releasing organochloride substances, such as methylchloride. The mechanism shown in Fig. 1.3, is the expanded version from Keppler et al., (2000)¹³⁴.

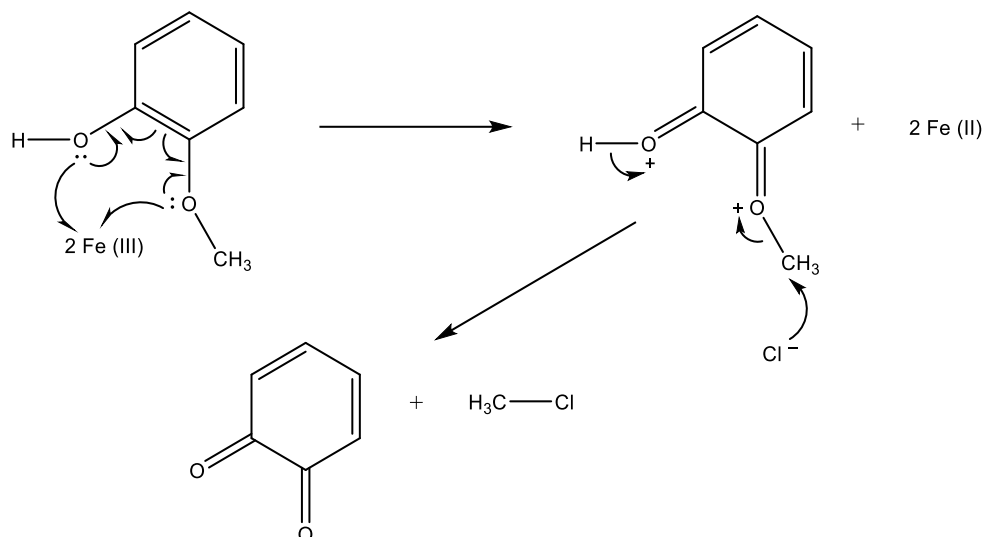
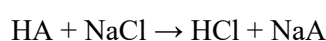


Fig. 1.3. Possible methylchloride formation mechanism based on the methylhalide formation mechanism from soil origin reported in Keppler (2000)¹³⁴.

Other non-combustion processes which have been suggested to result in Cl^- formation include the emissions of HCl from landfill sites and plant matter decay. Previous studies have also mentioned the release of organochlorides from plant matter decomposition^{135,134}. Chlorinated compounds known to be given off by landfill sites include chloroform, dichloromethane, vinyl chloride and trichloroethene¹¹⁶.

Naturally occurring Cl^- may also be present in the form of NaCl in sea spray aerosol in the vicinity of coastal sites¹³⁶. The presence chlorine in coal and biomass burning is likely from the accumulation of chlorine in plants and biological matters, for which different levels of chlorine are found as a function of geographical location (i.e. more chlorine may be found over land masses closer to coastal sites)¹³⁶.



Eq. 1.1. Chloride displacement from aerosol by atmospheric acids reacting with NaCl.

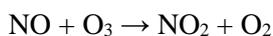
HCl may also be produced secondarily in the atmosphere from the reaction of acidic gases, such as HNO_3 and H_2SO_4 , with particulate phase salts such as NaCl, to produce HCl (Eq. 1.1)¹³⁷. (Laskin et al., 2012)¹³⁸ however also report the ability of weaker organic acids, such as methane sulfonic acid, to be able to displace chloride to produce gaseous HCl (Eq. 1.1), where A is the anionic constituent of the acid and HA is the acid.

Furthermore, a study conducted by (Chang et al., 2006)¹⁰⁶ suggest that chloride may be formed when Cl_2 released into the atmosphere is photolyzed producing chlorine radicals which can abstract hydrogens from hydrocarbons producing HCl.

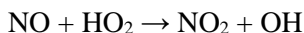
1.3.1.2 Nitrate

NO_3^- contributes substantially to urban $\text{PM}_{2.5}$ ^{139,140,141} and work by Xie et al., (2020)¹⁴² suggested that (in Beijing) particles which were high in NO_3^- under Relative Humidity (RH) 20 % – 50 % would absorb twice the quantity of water compared to aerosol which was high in SO_4^{2-} .

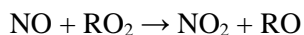
The conversion of NO_2 to NO_3^- directly influences atmospheric ozone and concentrations as well as NO_x ¹⁴³. NO_x is predominantly primarily emitted anthropogenically as NO from the result of N_2 and O_2 interacting at very high temperatures^{144,143}. NO is short lived (lifetime *ca.* < 1 day) in the atmosphere and may be oxidised to NO_2 ¹⁴³. NO may be oxidised by oxidising species such as O_3 , HO_2 , RO_2 and RCO_2 and shown in Eq. 1.2 - Eq. 1.5^{139,145,146,145}. Reactions Eq. 1.2 - Eq. 1.5 have been reported to be considerably faster compared to NO oxidation by O_2 ¹⁴⁵.



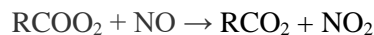
Eq. 1.2. NO oxidation to NO_2 by O_3 .



Eq. 1.3. NO oxidation to NO_2 by HO_2 .



Eq. 1.4. NO oxidation to NO_2 by RO_2 .



Eq. 1.5. NO oxidation to NO_2 by RCO_2 .

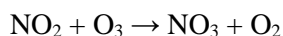
NO_2 may be oxidised further in the atmosphere by species such as OH, HO_2 , O_3 , H_2O_2 forming HNO_3 ^{143,140}. Major anthropogenic sources of NO_x include biomass burning^{139,140}, biofuel combustion¹⁴⁷ vehicle exhaust fumes^{148,143}, coal combustion^{148,147}, power plants and industries^{144,147}, fossil fuel combustion^{139,140,147}, waste^{139,140} and agricultural soils and activities^{139,148,140}. Natural NO_x emissions include wildfires, lightning and soil emissions¹⁴⁴. In addition to contributing to particle NO_3^- , NO_x emissions also induce adverse effects on human health directly, eutrophication, acid rain, tropospheric O_3 production^{149,143}.



Eq. 1.6. Major daytime NO_2 oxidation pathway forming HNO_3 .

Three major pathways¹³⁹ are involved in HNO_3 production from NO_2 . These include NO_2 oxidation by OH^{139,146,145} (Eq. 1.6); NO_3 production by NO_2 reaction with O_3 (Eq. 1.7)^{139,150} followed by the

NO₃ radical abstracting an H from a VOC^{139,146} (Eq. 1.8); and N₂O₅ formation followed by hydrolysis^{143,139}. The dominant daytime pathway is the oxidation of NO₂ by OH radicals, as shown in Eq. 1.6¹⁴³. This pathway however decreases as solar flux decreases¹⁵⁰.



Eq. 1.7. NO₃⁻ production via the reaction of NO₂ with O₃.



Eq. 1.8. H abstraction from a VOC by the NO₃ radical to produce HNO₃.

During night-time hours, OH concentrations decrease although HNO₃ from NO₃ and N₂O₅ chemistry increases¹⁴³. N₂O₅ chemistry also increases later in the afternoon due to an increase in NO₂ among already high O₃ in association with a decrease in solar flux and therefore N₂O₅ photolysis¹⁵⁰. A build-up of NO₃ may occur by Eq. 1.7 and a reduction in NO₃ photolysis¹³⁹. NO₃ may subsequently react with a VOC by abstracting an H to produce gaseous HNO₃¹³⁹.



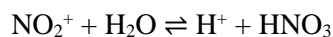
Eq. 1.9. Equilibrium of N₂O₅ from NO₃ and NO₂.



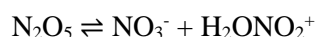
Eq. 1.10. Reaction of N₂O₅ with water (homogeneously or heterogeneously).



Eq. 1.11. N₂O₅ hydrolysis in aqueous aerosol.



Eq. 1.12. NO₂⁺ hydration forming HNO₃ in aqueous aerosol.



Eq. 1.13. N₂O₅ hydrolysis in aqueous aerosol forming NO₃⁻ and H₂ONO₂⁺.



Eq. 1.14. Hydrolysis of H_2ONO_2^+ forming NO_3^- .

During night-time hours, NO_3 may also react with NO_2 to produce N_2O_5 as shown in Eq. 1.9^{139,146,151}. N_2O_5 in particular may either re-dissociate back into NO_2 and NO_3 ; deposit on surfaces (with uptake coefficients of 0.001-0.05)¹⁵¹; or undergo hydrolysis on aerosol surfaces heterogeneously (or in the gas phase homogeneously) to produce HNO_3 ¹⁵¹. On N_2O_5 adsorption onto the aerosol surface, N_2O_5 may hydrolyse to produce HNO_3 as shown in Eq. 1.10^{139,146,145,152,141,153}, a process which may increase with increasing aerosol water content¹⁴¹. More detail into the N_2O_5 hydrolysis mechanism is given in the work of Chang et al., (2011)¹⁵⁴ who suggest Eq. 1.11 - Eq. 1.14.



Eq. 1.15. Ammonolysis of N_2O_5 as suggested by Sarker et al., (2020)¹⁵⁵.

The OH oxidation pathway is also dominant during the summer months¹³⁹ due to higher temperatures and solar flux, whereas due to the thermal instability of N_2O_5 , may make this pathway more prevalent¹³⁹. The OH pathway may however be present during winter from HONO dissociation¹⁴². Other possible HNO_3 formation pathways include Eq. 1.16 and Eq. 1.17¹⁴⁶.



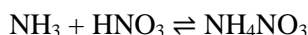
Eq. 1.16. HNO_3 formation from ClNO_3 .



Eq. 1.17. HNO_3 formation from NO_2 interaction with water.

For gaseous HNO_3 to convert into aerosol NO_3^- , it may either partition into the aerosol phase if enough water is present¹⁴¹ or may also be neutralised by either NH_3 ^{141,156,153} (the most abundant alkaline gas) or alkaline mineral aerosol species¹⁴³. Depending on whether the atmosphere is NH_3 rich or poor may also affect the NO_3^- formation pathway, which may favour N_2O_5 hydrolysis under NH_3 poor conditions¹⁵⁶ or HNO_3 uptake onto crustal species¹⁵³. Furthermore, aerosol acidity may

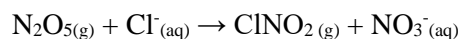
also affect which pathway is preferential for NO_3^- formation¹⁵⁶. In an ammonium rich atmosphere however, HNO_3 is neutralised by NH_3 through the reversible equilibrium shown in Eq. 1.18¹⁴³.



Eq. 1.18. HNO₃ neutralisation by NH₃.

The ability for HNO_3 and NH_4NO_3 to be able to partition into the aerosol phase is also down to meteorological conditions (lower temperatures and higher RH favour higher deposition into the aerosol)^{153,152,157,143}.

Pathways which do not require an alkaline species for NO_3^- formation within aerosol are those which occur heterogeneously on or within the aerosol. These NO_2 oxidation pathways within the aqueous phase may be catalysed by Transition Metal Ions (TMIs)¹⁴² from mineral dust¹⁵³. It has also been suggested that NO_3^- (aq) may also be formed from N_2O_5 abstraction of Cl^- from the particle phase to produce ClNO_2 and NO_3^- in the aqueous aerosol phase (Eq. 1.19)¹⁵⁸.



Eq. 1.19. Reaction of N₂O₅ with particle Cl⁻ to produce ClNO₂ and particle phase NO₃⁻.

1.3.1.3 Sulfate

Primary SO_4^{2-} may be emitted naturally from sources such as sea spray aerosol and from volcanic emissions¹⁵⁹. Dimethyl sulfide has also been established to convert into sulfate¹⁵⁹. Secondary production of SO_4^{2-} from SO_2 is however much more dominant in urban megacities. SO_2 is known to be emitted from combustion of coal and oil with a high sulfur content¹⁵⁹. Other sources of SO_2 include emissions from volcanoes, vehicular exhaust fumes, smelting activities, power plants, industrial activities, metal extraction from ore and the general burning of fuel with a high sulfur content^{160,161,147}.

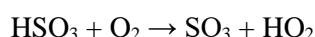
SO_4^{2-} in $\text{PM}_{2.5}$ is primarily formed through the oxidation of SO_2 via various mechanisms¹⁵⁹, through both homogenous (in the gas phase and in aerosol water) and heterogenous (oxidation of SO_2 at the particle surface, with water) reaction pathways although there is some disagreement between researchers as to the exact mechanisms^{162,163,164}. Specific SO_2 oxidants in SO_4^{2-} production include OH, H_2O_2 , O_3 , NO_x , HONO, ROOR', O_2 , N_2O_5 , $\text{CH}_3\text{COO}_2\text{NO}_2$, NO_3 , HO_2 , as well as criegee intermediates^{153,165,166,167,163,168,169,164}. It has however been identified that SO_2 gas phase oxidation by O_2 , HO_2 , N_2O_5 , NO_3 , $\text{CH}_3\text{COO}_2\text{NO}_2$, H_2O_2 and O_3 may be insignificant^{170,164}. Some of these species (such as O_3 and HONO) may however facilitate OH production and therefore indirectly oxidise SO_2 to SO_4^{2-} ¹⁵³. It has been suggested that on a global scale, the oxidation of SO_2 by OH (gas phase), as well as the oxidation of SO_2 (and the derived species in aqueous aerosol, $\text{SO}_2 \cdot \text{H}_2\text{O}$, HSO_3^- and SO_2^{3-}

) by O₃, H₂O₂ and O₂ (over TM catalysts in clouds) are the dominant SO₄²⁻ formation pathways^{170,171,172,153}. It is also acknowledged that the rate of SO₂ oxidation in the aqueous phase may be faster with and without a mineral oxide catalyst¹⁶³.

The major homogenous SO₂ gas-phase oxidation pathways is through the reaction of SO₂ with OH^{166,173,171,172,170,164}. A possible mechanism in the SO₂ oxidation by OH has been laid out by Calvert and Stockwell., (1983)¹⁷⁰ in Eq. 1.20 - Eq. 1.24.



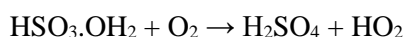
Eq. 1.20. Initiation of SO₂ oxidation by OH.



Eq. 1.21. Propagation reaction of HSO₃ with O₂.



Eq. 1.22. Propagation reaction of HSO₃ with H₂O.



Eq. 1.23. Propagation reaction of HSO₃·H₂O with O₂ forming H₂SO₄.

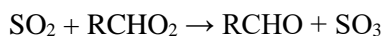


Eq. 1.24. Termination reaction of SO₃ and H₂O forming H₂SO₄.

In addition to SO₂ oxidation by OH, O(³P), criegee intermediates (O₃ + alkene reaction) and the methyldioxy radical may also a gas phase SO₂ oxidant. Another reaction scheme laid out by Calvert and Stockwell., (1983)¹⁷⁰ for these reaction pathways are shown in Eq. 1.25 - Eq. 1.29. Reactions Eq. 1.28 and Eq. 1.29 were however reported to be not as significant to H₂SO₄ production in the troposphere (based on qualitative rate data)¹⁷⁰.



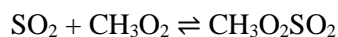
Eq. 1.25. Initiation of SO₂ oxidation by the O(³P) radical.



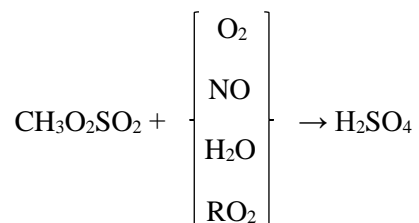
Eq. 1.26. Initiation reaction of SO₂ oxidation by a criegee intermediate.



Eq. 1.27. Termination reaction of SO₃ and H₂O forming H₂SO₄.



Eq. 1.28. Reversible initiation reaction of SO₂ oxidation with the methylendioxy radical.



Eq. 1.29. Possible H₂SO₄ production from CH₃O₂SO₂ oxidation.

Calvert and Stockwell., (1983)¹⁷⁰ noted that the SO₂ oxidation rate with these oxidising agents was significantly lower during night-time hours (0.1% h⁻¹) which was put down to their diminished concentrations by lack of solar activity. They also mention that the presence of night-time species, such as NO₃, may produce a very small amount of OH¹⁷⁰. O₃ may also increase at night and in the presence of unsaturated organics may produce criegee biradicals (Eq. 1.26 and Eq. 1.27)¹⁶⁴. This pathway is however thought to be even less significant than OH oxidation at night due to the inhibition of this pathway by water vapour¹⁶⁴. Some studies have however suggested that stabilised criegee intermediates are an important SO₂ oxidant^{166,174,175}.

Gas phase oxidation of SO₂ is however less prominent compared to the other pathways and aqueous phase SO₂ oxidation dominates in the troposphere¹⁶⁴. SO₄²⁻ is thought to be predominantly formed in the atmosphere through cloud droplets via the aqueous oxidation of SO₂ with dissolved oxidants (such as O₃ and H₂O₂) over metal catalysts (such as Fe or Mn)^{166,176}. It must however be highlighted that the generally low levels of H₂O within aerosol make aqueous phase SO₂ oxidation significantly less likely within aerosol compared to cloud droplets¹⁷¹. With high RH, SO₂ oxidation to SO₄²⁻ has been mentioned to occur predominantly via aqueous phase homogenous reaction^{153,166}. Heterogenous reactions at the particle surface (mineral dust and soot) are also significant, especially during haze events^{153,166}.

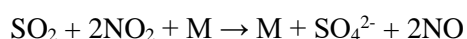
The heterogenous pathways are however strongly dependant on other factors such as liquid water content of a particle, inorganic ion concentrations as well as pH which all directly affect the rate of SO₂ oxidation¹⁵³. The heterogenous oxidation pathway of SO₂ on aerosol surfaces has been shown to be strongly dependant on TM presence¹⁷¹. A study by Shao et al., (2019)¹⁷¹ reported that in their study which focused on aerosol in Beijing, the heterogenous pathway was mostly governed by the

O₂ oxidising SO₂ over a TM catalyst for which the study observed 69 % and 67 % of the heterogenous oxidation during heavy polluted periods and clean periods, respectively. Shao et al., (2019)¹⁷¹ also reported 19 % of heterogeneous oxidation occurring over a TM catalyst with O₃ as the oxidant (for both the heavy polluted and clean periods). In addition, the composition and hygroscopicity of the aerosol affects the total water found at the aerosol surface. As hygroscopicity increase, this allows for a more efficient SO₂ heterogeneous reaction conversion SO₄²⁻¹⁷⁷.

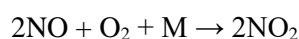
TM species enter aerosol through both anthropogenically (such as from construction activities) and form mineral dust^{153,171}. Mineral dust is known to be alkaline and the chemical composition of these aerosols affect SO₂ reactivity¹⁷⁸. For example, laboratory studies conducted have shown that SO₂ oxidation on the mineral dust surface may be slow (except if comprised of MgO and Fe₂O₃) in the absence of an oxidising agent such as O₃ or NO_x¹⁷⁷. Another example of this specificity is the sole capability of SO₂ to oxidise on a surface of CaO in the presence of O₂¹⁷⁷.

On absorption of SO₂ onto aerosol, sulfite (or bisulfite) is irreversibly¹⁶⁸ produced on the mineral surface (except SiO₂)¹⁶⁸ which can be oxidised (by NO₂ and O₃ at significant concentrations)^{166,162,168} in the aqueous phase in the presence of TM leached into the aerosol aqueous phase from mineral dust and anthropogenic matter^{171,178,176,169,168}. High NH₃ concentrations also encourage sulfite oxidation to sulfate by NO₂¹⁶². This leaching increases with lower pH in which TM species are more easily dissolved^{176,171,179}. Solubility of SO₂ is also affected by pH in which SO₂ solubility reduces with lower aerosol pH¹⁷¹. A study by Dong et al., (2020)¹⁵³ reported higher percentage fractions of SO₄²⁻ within aerosol, higher sulfur oxidation ratios (section 1.3.1.4) and higher atmospheric SO₄²⁻ concentration on sandy haze days. The authors attributed this to the catalytic properties and higher concentrations of TM within mineral dust with high O₃ concentrations and RH at 30 % - 70 %¹⁵³. A series of other studies have also attributed higher SO₄²⁻ formation and faster SO₂ oxidation to TM^{177,176,171,162,163,176,167}.

NO_x has also been reported to act as a catalyst in conjunction with mineral oxides, to oxidise SO₂ to SO₄²⁻ in the presence of O₂ (Eq. 1.30 and Eq. 1.31)¹⁷⁷. Therefore it has also been suggested that NO_x may enhance SO₂ oxidation in specific situations, such as in power plant plumes and sand storms¹⁷². Furthermore, it has been reported that aqueous NO₂ oxidation of SO₂ occurs preferentially on fine aerosol at high RH values (RH > 70 %), as well as at *ca.* pH 7¹⁶³.



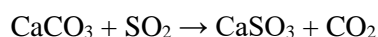
Eq. 1.30. Oxidation of SO₂ by NO₂ on the mineral oxide surface.



Eq. 1.31. NO₂ catalyst regeneration.

It is also known that TM solubility is affected by the aerosol evolution and changing pH as acidic species coagulate into the aerosol (such as gaseous H_2SO_4 and HNO_3)¹⁷⁶. Changes in particle acidity also change the preferential oxidation pathway of SO_2 ¹⁷² over the lifetime of an aerosol. For example, oxidation by O_3 is only substantial at higher pH levels, and therefore as SO_4^{2-} increases within a particle, this pathway is less favourable¹⁷².

Finally, lab studies^{168,180} have observed the direct reaction between SO_2 and CaCO_3 to produce SO_3 (which oxidises to SO_4^{2-}), as shown in Eq. 1.32. Depending on particle pH, the CaSO_3 may dissolve into Ca^{2+} and SO_3^{2-} , which could further oxidise in the aqueous phase to produce SO_4^{2-} .



Eq. 1.32. The direct reaction of gaseous SO_2 with solid CaCO_3 in the particle phase producing solid calcium sulfite.

The presence of dust may also photo-catalyse atmospheric OH formation¹⁶⁶ which contributes to the homogenous SO_4^{2-} formation pathway. This occurs from NO_2 conversion to HONO over a TiO_2 catalyst, which dissociates to OH^{181,182}. This process has however been reported to be dependent on RH^{183,166}. TiO_2 is also known to be a more efficient absorber of SO_2 into the particle compared to other metal oxides¹⁷⁸.

1.3.1.4 NOR and SOR

The secondary oxidation of NO_2 and SO_2 to form NO_3^- and SO_4^{2-} processes may be used to assess the extent of secondary formation of NO_3^- and SO_4^{2-} ^{184,185,186} by using the Nitrogen Oxidation Ratio (NOR) and Sulfur Oxidation Ratios (SOR) in equations Eq. 1.33 and Eq. 1.34, respectively (concentrations in moles).

$$\text{SOR} = \frac{[\text{SO}_4^{2-}]}{[\text{SO}_2] + [\text{SO}_4^{2-}]}$$

Eq. 1.33. Sulfur Oxidation Ratio (SOR).

$$\text{NOR} = \frac{[\text{NO}_3^-]}{[\text{NO}_2] + [\text{NO}_3^-]}$$

Eq. 1.34. Nitrogen Oxidation Ratio (NOR).

Numerous studies have applied the SOR and NOR to their datasets (Zhou et al., (2012)¹⁸⁷; Chen et al., (2015)¹⁸⁸; Wang et al., (2016)¹⁸⁹; Xu et al., (2019)¹⁹⁰; Zheng (2015)¹⁹¹; Zhang et al., (2016)¹⁹²; Ram (2012)¹⁹³; Wang (2006)¹⁹⁴; Chi et al., (2018)¹⁸⁴; Shao et al., (2019)¹⁷¹; Wang et al., (2016)¹⁹⁵; Sun et al., (2006)¹⁸⁵; Zhang (2016)¹⁹²; Wang (2019)¹⁹⁶; and Xu et al., (2017)¹⁸⁶. Other studies such as Khoder et al., (2002)¹⁹⁷; Hassan et al., (2013)¹⁴³ and Saxena et al., (2017)¹⁹⁸ calculate their SOR and NOR in terms of $\mu\text{g m}^{-3}$ as opposed moles, which is a much less common technique. Furthermore, Hu et al., (2014)¹⁹⁹, used a different calculation for NOR in their studies (Eq. 1.35).

$$NOR = \frac{[NO_3^-]}{[NO_y]}$$

Eq. 1.35. Alternative NOR Equation as used by Hu et al., (2014)¹⁹⁹.

Finally, Hu et al., (2014)¹⁹⁹ also suggest an ammonia conversion ratio, similar to Eq. 1.33 and Eq. 1.34 (replacing the gas with $[NH_3]$ and the ionic species with $[NH_4^+]$). Higher values of NOR and SOR suggest a higher extent of oxidation of NO_2 and SO_2 and therefore a larger proportion of the SO_4^{2-} and NO_3^- present would be suggested to originate from secondary oxidation processes^{200, 201, 192}. In this study, the SOR and NOR were calculated using Eq. 1.33 and Eq. 1.34, respectively in terms of moles as this was the most common technique used in studies.

It has been widely acknowledged that an SOR ratio of below 0.1 suggests the dominance of primarily emitted SO_4^{2-} (i.e. vehicle exhausts¹⁹⁵) whereas the SOR values larger than 0.1 indicate that secondary transformation of SO_2 to produce SO_4^{2-} in aerosol occurs^{202, 203, 185, 200, 192, 204, 195} and is the main source²⁰². Chatterjee et al., (2010)²⁰³, Sun et al., (2006)¹⁸⁵, Zhang et al., (2016)¹⁹², Chatterjee et al., (2012)²⁰⁴, Wang et al., (2016)¹⁹⁵ and Wang et al., (2005)²⁰⁰ specifically suggest that SOR values above 0.1 indicate the photochemical oxidation of SO_2 to produce SO_4^{2-} . The analogous case for NOR in which values below 0.1 imply primary sources and above 0.1 suggest the dominance of secondary formation of NO_3^- from NO_x has also been mentioned in the literature^{202, 205}. Different threshold values are however given in the work of Li et al., (2016)²⁰⁶ in which workers suggest that NOR and SOR values above 0.1 and 0.25, respectively, indicate the formation NO_3^- and SO_4^{2-} via the secondary pathways. Furthermore, Sun et al., (2006)¹⁸⁵ suggest that the larger the SOR and NOR values, the more secondary oxidation of SO_2 and NO_2 is occurring.

Numerous other studies however report positive correlations between temperatures and oxidation ratios^{203, 204, 194, 200}. Sun et al., (2006)¹⁸⁵, Wang et al., (2016)¹⁹⁵ and Wang et al., (2005)²⁰⁰ for example observe positive correlations between SOR and temperature²⁰⁷ (NH_4SO_4 is less volatile than NH_4NO_3) and suggest that (in these events) this is down to increased OH oxidation. Specifically, Zhou et al., (2012)¹⁸⁷ report an R^2 value of 0.76 for Temp vs SOR in Beijing in 2006. Wang et al., (2016)¹⁹⁵ however report no correlation between NOR vs Temp for any season in Beijing between Aug 2012 – Jul 2013.

Dependence of NOR and SOR as a function of RH has also been widely mentioned in the literature^{191, 208, 192, 186, 190, 185, 202, 188, 194, 187}. For example, Xu et al., (2017)¹⁸⁶ reported in their study that the NOR observed a strong positive correlation with RH at $RH < 60\%$ but stabilised at $RH > 60\%$. They also reported that the SOR was weakly affected by RH below 35 % RH with an average SOR of < 0.1 at $RH < 25\%$. It was also noted that an increase of 1% in SOR was observed between RH 25% - 35%. A dramatic increase was however reported in SOR for RH 80% – 90% (SOR of 0.49). Wang et al., (2019)¹⁹⁶ also reported a greater change in NOR and SOR (as well as $[NO_3^-]$ and $[SO_4^{2-}]$

) from an RH of 40% - 60% to 60% - 80%. Other examples include the works of Zhang et al., (2018)²⁰² who observed a dramatic rise in SOR levels for RH > 60% with a maximum SOR of 0.88 for RH 80% and saw an increase in NOR levels from 0.18 ± 0.06 for RH < 60 % to 0.21 ± 0.08 at RH > 60 %; and Zheng et al., (2015)¹⁹¹ who reported in their study that NOR and SOR levels were relatively unchanging for RH < 50%, although rose at RH > 50% and reached 0.28 and 0.34, respectively, for RH 70% - 80%. It has also been reported that the RH has a larger influence on the extent of SOR compared to NOR^{186,202}. Finally, RH is another reason why during haze and fog episodes the NOR and SOR also increase¹⁹³. The presence of haze-fog periods is often accompanied by much higher RH (RH > 90%¹⁸⁸) and therefore may also help explain the increases in NOR and SOR in the time series during haze-fog polluted periods, as described by Chen et al., (2015)¹⁸⁸, and suggests the dominance of the heterogenous aqueous reaction pathway²⁰².

1.3.1.5 Ammonium

It is widely acknowledged that NH₃ is the most abundant atmospheric alkaline gas^{209,210,26,211} and comprises a substantial fraction of total reactive nitrogen²¹². NH₃ transition to NH₄⁺ in the aerosol phase occurs via the neutralisation reaction of NH₃ with a range of acidic gases²⁶ and NH₄⁺ is known to comprise a substantial fraction of Secondary Inorganic Aerosol (SIA) in PM_{2.5}²¹². NH₃ and NH₄⁺ (NH_x) is also known to directly affect particle acidity²¹². A review by Behera et al., (2013)²¹² as well as studies by Shephard et al., (2020)²¹³, Van Damme et al., (2018)²¹⁴ and Clarisse et al., (2019)²¹⁵ indicated considerably higher NH₃ from India and China compared to other regions.

Agricultural emissions sources from livestock and fertilizer²¹⁶ use in particular is the main source of NH₃ emissions into the atmosphere^{217,218,209}. Animal husbandry produces urea (mammals)²¹⁸ uric acid (birds) as well as undigested proteins. The decomposition of urea and uric acid as described by Behera et al., (2013)²¹² is shown in Eq. 1.36 and Eq. 1.37, respectively. Behera et al., (2013)²¹² also describe how organic nitrogen species and NH₃ are also present in animal feces. Undigested proteins may therefore be present and these may decompose via bacterial decomposition, uricase and urease enzymes as stated by Behera et al., (2013)²¹².



Eq. 1.36. Decomposition of urea to produce gaseous NH₃²¹².



Eq. 1.37. Decomposition of uric acid to form gaseous NH₃²¹².

Other NH₃ emissions sources include combustion of fossil fuels²¹², biomass burning^{212,218,209}, human excreta²¹², soil emissions^{212,218}, crop residue compost²¹⁸, oceanic emissions^{212,209}, sewage²¹², waste disposal²¹⁸, vehicular exhaust emissions^{212,218}, industrial emissions^{212,218}, nitrogen fixing plants²¹⁸.

NH_x may also be transported from other regions by winds²¹². In addition, NH₃ emissions may be effected by season. For example, fertilizer application²¹⁹ and crop burning are seasonal activities²¹⁸. Different seasons also change in ambient temperature affecting the quantity of NH₃ which may evaporate²¹⁸, as well as soil conditions (e.g. pH)²¹⁹.

1.4 Overview of inorganic PM_{2.5} aerosol in India and China

A literature review has been conducted presenting the PM_{2.5} composition from a selection of studies in India and China. A total of 27 studies were reviewed across India for PM_{2.5} composition comparison (in the form of pie charts). These studies include (I1) Gautam et al., (2018)²²⁰; (I2) Kulshrestha et al., (2009)²²¹; (I3) Rengarajan et al. (2011)²²²; (I4) Rengarajan et al. (2011)²²³; (I5) Chatterjee et al., (2010)²⁰³; (I6) Deshmukh et al., (2010)²²⁴; (I7) Saxena et al., (2017)¹⁹⁸; (I8) Kumar et al., (2018)²²⁵; (I9) Pant et al., (2015)¹¹⁰; (I10) Deshmukh et al., (2011)²²⁶; (I11) Gawhane et al., (2017)²²⁷; (I12) Behera et al., (2016)²²⁸; (I13) Khare and Baruah., (2010)²²⁹; (I14) Behera et al., (2010)²³⁰; (I15) Khare et al., (2011)²³¹; (I16) Kumar et al., (2020)²³²; (I17) Kumar et al., (2016)²³³; (I18) Gawhane et al., (2019)²³⁴; (I19) Pipal et al., (2019)²³⁵; (I20) Bisht et al., (2015)²³⁶; (I21) Ghosh et al., (2014)²³⁷; (I22) Singh et al., (2018)²³⁸; (I23) Begam et al., (2017)¹⁰¹; (I24) Deshmukh et al., (2013)²³⁹; (I25) Verma et al., (2010)²⁴⁰; (I26) Sharma et al., (2014)²⁴¹; and (I27) Ram et al., (2011)²⁴².

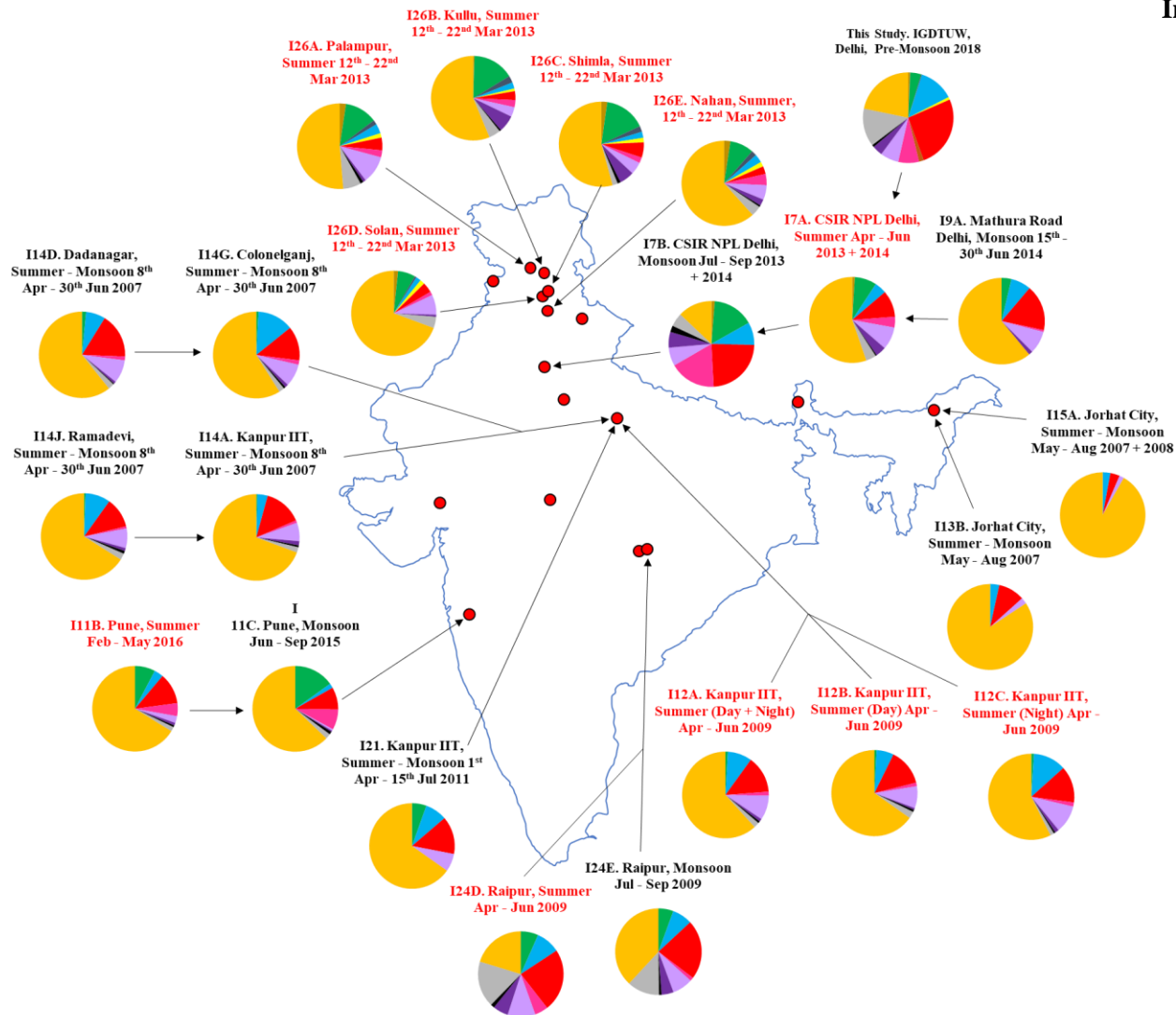
Similarly, a comprehensive selection of 17 studies were also reviewed across China. These studies include (C1) He et al., (2017)⁹⁶; (C2) Wang et al., (2006)²⁴³; (C3) Pathak et al., (2009)²⁴⁴; (C4) Zhu et al., (2015)²⁴⁵; (C5) Wang et al., (2016)²⁴⁶; (C6) Xu et al., (2017)²⁴⁷; (C7) Zhou et al., (2016)²⁴⁸; (C8) Hao et al., (2020)²⁴⁹; (C9) Ding et al., (2018)²⁵⁰; (C10) Chen et al., (2019)²⁵¹; (C11) Li et al., (2009)²⁵²; (C12) Chang et al., (2013)²⁵³; (C13) Lai et al., (2007)²⁵⁴; (C14) Zhang et al., (2018)²⁵⁵; (C15) Dai et al., (2013)²⁵⁶; (C16) Niu et al., (2016)²⁵⁷; and (C17) Zhang et al., (2013)²⁵⁸.

These data were produced into pie charts and the composition comparison and distribution of PM_{2.5} aerosol in India and China across the different seasons is shown in Fig. 1.4 - Fig. 1.7. The ions presented are F⁻ (gold), CH₃SO₃⁻ (orange), Cl⁻ (green), NO₂⁻ (dark blue), Br⁻ (medium blue), NO₃⁻ (light blue), PO₄³⁻ (yellow), SO₄²⁻ (red), C₂O₄²⁻ (brown), Na⁺ (pink), NH₄⁺ (lilac), K⁺ (purple), Mg²⁺ (black), Ca²⁺ (grey) and other (amber). Selected studies reviewed report multiple values for aerosol compositions under different atmospheric or sampling conditions. Therefore, each particle composition pie chart in Fig. 1.4 - Fig. 1.7 is associated with a code. The first letter of the code denotes the country (where I = India and C = China); the number is an arbitrary number given to a specific publication (mentioned in the previous two paragraphs); and the following letter denotes the specific set of conditions stated by the study. For example, study C1A is a study which was conducted in China by (C1) He et al., (2017)⁹⁶ and took place over the summer season (A). A full set of details of each study and sub-study (with codes) is given in the appendix, where Table A and E present the study specifications for the reviewed studies from other cities in India and China, respectively. Table B, C and D show the PM_{2.5} and major anion concentrations, minor anion concentrations, and cation concentrations for the reviewed studies in India, respectively. For the cities in China, Tables F, G

India Pre-Monsoon - Monsoon

Key

F^-
 $CH_3SO_3^-$
 Cl^-
 NO_2^-
 NO_3^-
 PO_4^{3-}
 SO_4^{2-}
 $C_2O_4^{2-}$
 Na^+
 NH_4^+
 K^+
 Mg^{2+}
 Ca^{2+}
 Other



Major Ions

Cl^-
 NO_3^-
 SO_4^{2-}
 Na^+
 NH_4^+
 Ca^{2+}

Fig. 1.4. Map of India showing the distribution of ionic $PM_{2.5}$ particle composition across India (Summer - Monsoon) from reviewed studies. A key denoting the segment species colours is shown in the top left corner with the major ions listed in the bottom right corner. Red markers on the map of India show the different cities. Studies presented in red text represent studies which solely took place over the summer period as opposed to summer-monsoon period (black text). Text shown above each study presents the details of each study.

India Post-Monsoon - Winter

Key

F^-
 $CH_3SO_3^-$
 Cl^-
 NO_2^-
 NO_3^-
 PO_4^{3-}
 SO_4^{2-}
 $C_2O_4^{2-}$
 Na^+
 NH_4^+
 K^+
 Mg^{2+}
 Ca^{2+}
 Other

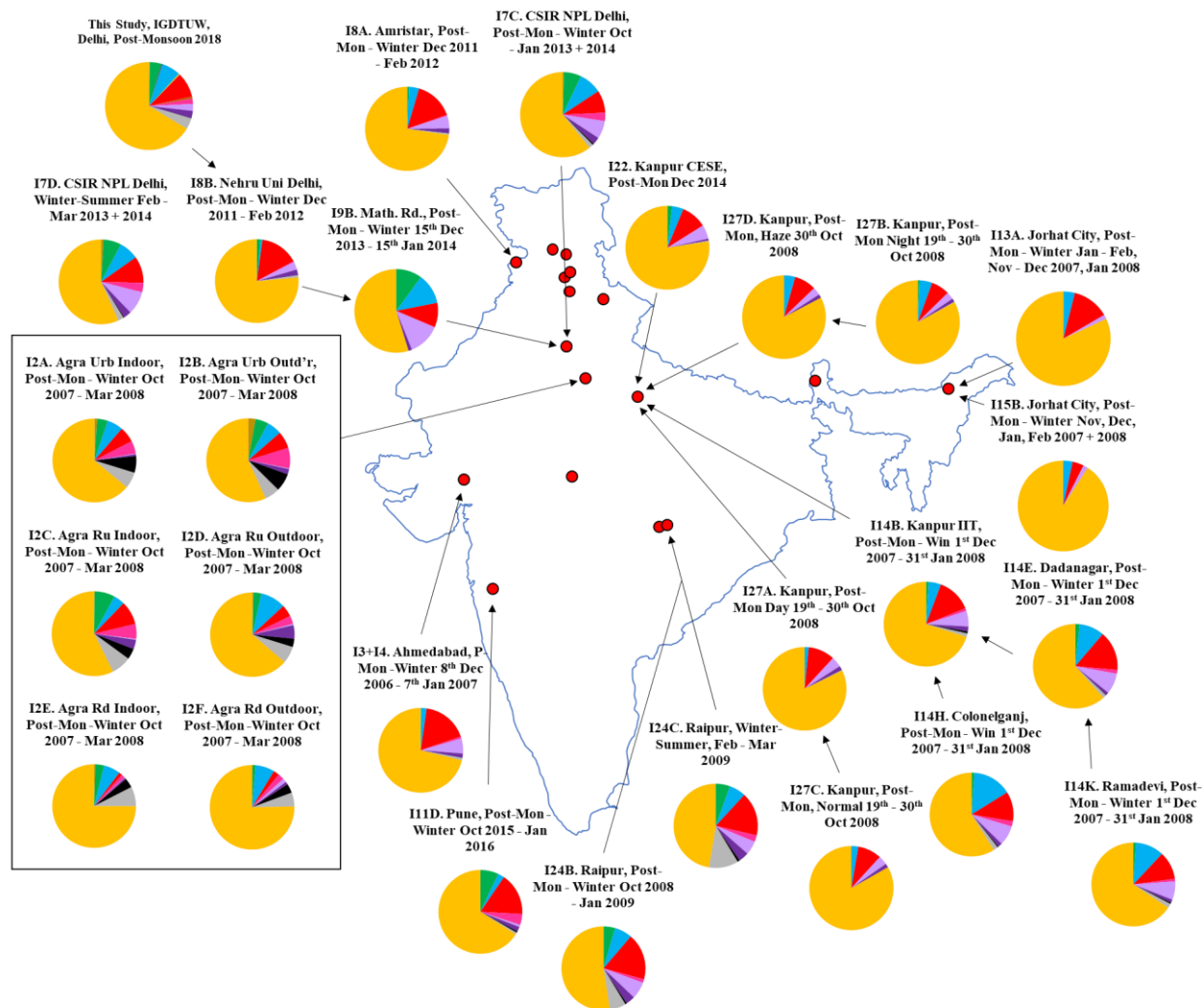
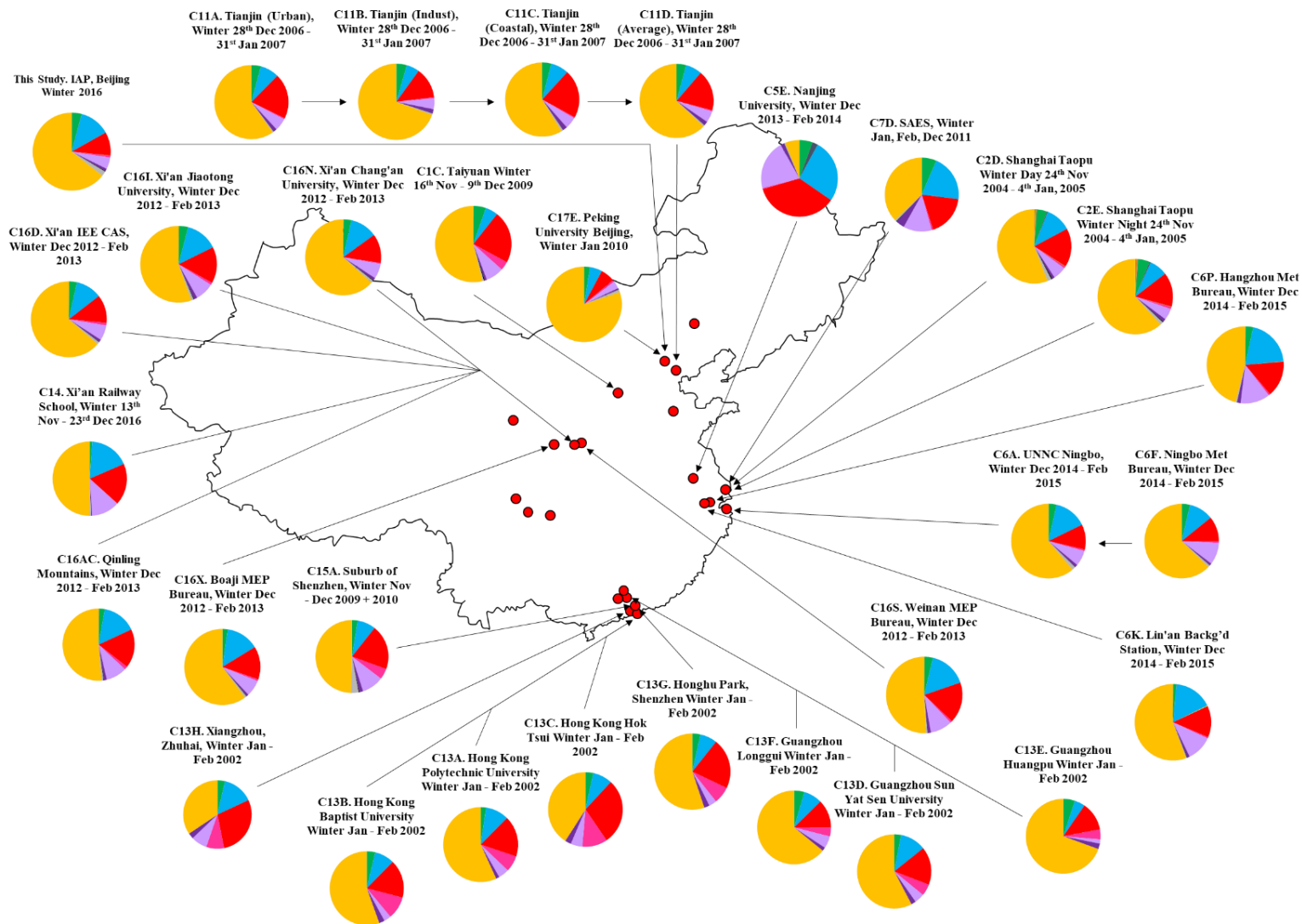


Fig. 1.5. Map of India showing the distribution of ionic $PM_{2.5}$ particle composition across India (Post - Monsoon - Winter) from reviewed studies. A key denoting the segment species colours is shown in the top left corner with the major ions listed in the bottom right corner. Red markers on the map of India show the different cities. Text shown above each study presents the details of each study.

China Winter

Key

- F^-
- $CH_3SO_3^-$
- Cl^-
- NO_2^-
- NO_3^-
- PO_4^{3-}
- SO_4^{2-}
- $C_2O_4^{2-}$
- Na^+
- NH_4^+
- K^+
- Mg^{2+}
- Ca^{2+}
- Other



Major Ions

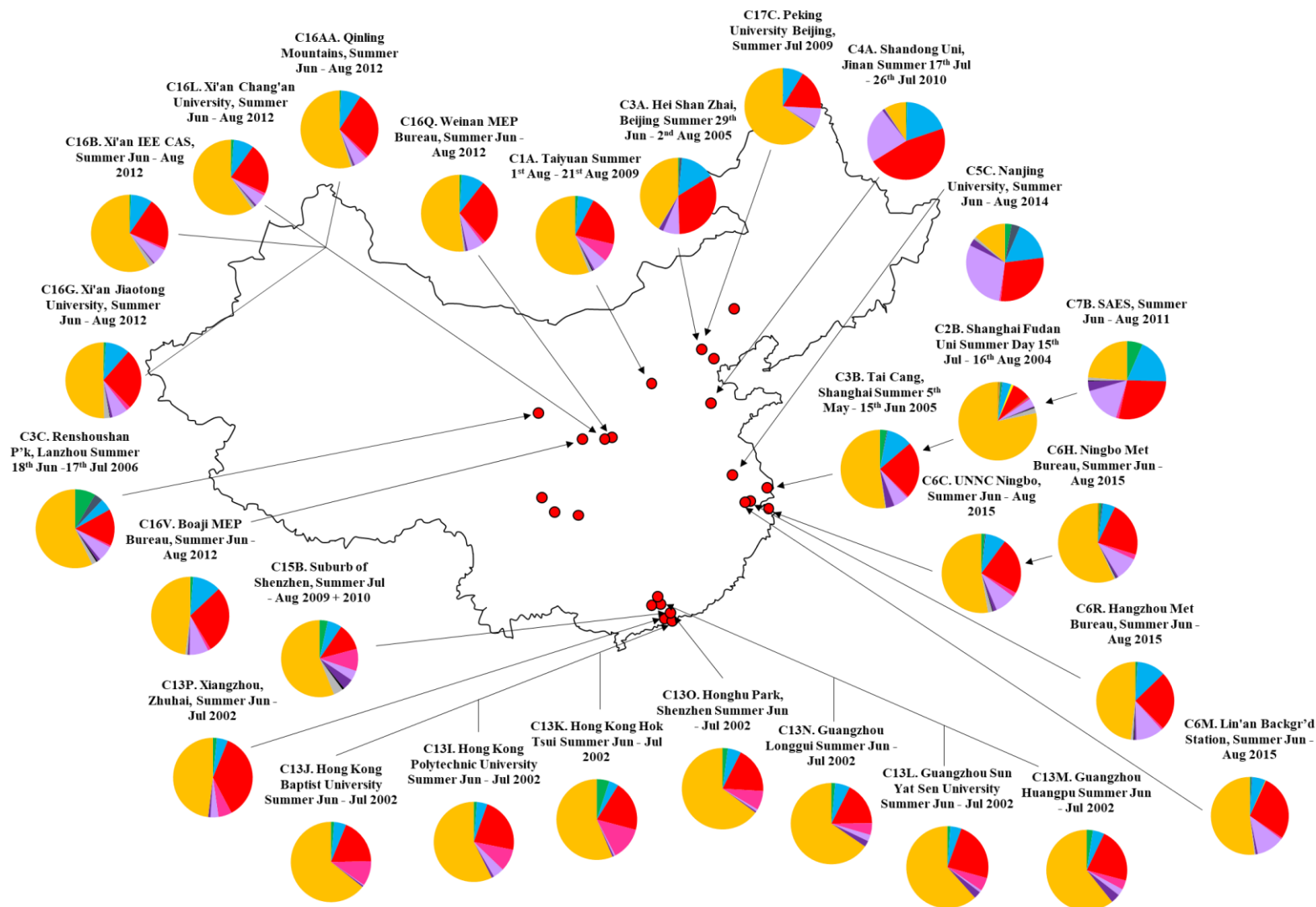
- Cl^-
- NO_3^-
- SO_4^{2-}
- Na^+
- NH_4^+

Fig. 1.6. Map of China showing the distribution of ionic $PM_{2.5}$ particle composition across China (Winter) from reviewed studies. A key denoting the segment species colours is shown in the top left corner with the major ions listed in the bottom right corner. Red markers on the map of China show the different cities. Text shown above each study presents the details of each study.

China Summer

Key

F^-
 $CH_3SO_3^-$
 Cl^-
 NO_2^-
 NO_3^-
 PO_4^{3-}
 SO_4^{2-}
 $C_2O_4^{2-}$
 Na^+
 NH_4^+
 K^+
 Mg^{2+}
 Ca^{2+}
 Other



Major Ions

NO_3^-
 SO_4^{2-}
 NH_4^+

Fig. 1.7. Map of China showing the distribution of ionic $PM_{2.5}$ particle composition across China (Summer) from reviewed studies. A key denoting the segment species colours is shown in the top left corner with the major ions listed in the bottom right corner. Red markers on the map of China show the different cities. Text shown above each study presents the details of each study.

and H present the PM_{2.5} and major anion concentrations, the minor anion concentrations, as well as the cation concentrations, respectively.

In this thesis, a focus is given on the pre- and post-monsoon seasons in Delhi as well as the winter and summer seasons in Beijing. Therefore, the following sections will discuss these particular seasons in India and China, respectively. *N.B.* A substantial proportion of the studies reviewed for the summer pre-monsoon seasons in India reported values which overlapped the summer and monsoon seasons. Therefore, Fig. 1.4 highlights the studies in red which were solely sampled over the summer season. Aerosol distribution reviews for India (Annual) as well as China (Spring, Autumn and Annual) are found in the appendix (Fig. A – Fig. D).

1.4.1 India Summer (Pre-Monsoon)

Fig. 1.4 shows the distribution of PM_{2.5} compositions from the reviewed studies during the pre-monsoon – monsoon periods. Most studies show *ca.* two thirds of unknown material and *ca.* one third as known ionic %. A particularly high known ionic % was found in Raipur in study I24D by Deshmukh et al., (2013)²³⁹ who sampled between Apr – Jun 2009 and suggested a ionic % of 79.7 %. The lowest summer ionic % was observed in Solan by Sharma et al., (2014)²⁴¹ who reported a ionic % fraction of 30.6 % between 12th – 22nd March 2013. Fig. 1.4 shows that the major ions in PM_{2.5} (generally) during the pre-monsoon period in India are Cl⁻, NO₃⁻, SO₄²⁻, NH₄⁺, Na⁺ and Ca²⁺.

Relatively large fractions of Cl⁻ were shown in numerous studies across India during the summer seasons. Cities that showed Cl⁻ contributions > 10 % included Palampur (12.3 %) in study I26A, Kullu (15.8 %) in I26B and Shimla (15.8 %) in the work by Sharma et al., (2014)²⁴¹. This is significant as each of these cities is located in the far north of India and are in close proximity to each other. Other relatively large fractions of Cl⁻ (> 5 %) have been observed in Delhi (8.27 %, D7A) by Saxena et al., (2017)¹⁹⁸ who sampled Apr – Jun (2013 - 2014); Pune (7.67 %, D11B) by Gawhane et al., (2017)²²⁷ who sampled between Feb – May in 2016; Raipur (6.63 %, D24D) by Deshmukh et al., (2013)²³⁹ who sampled between Apr – Jun 2009; Solan (6.60 %, D26D) and Nahan (9.03 %, D26E) by Sharma et al., (2014)²⁴¹ who sampled in these cities between 12th – 22th Mar 2013. Particularly low fractions of Cl⁻ were observed in Kanpur in which the overall day-night average Cl⁻ % as indicated by Behera et al., (2016)²²⁸ was 0.91 % (Apr - Jun 2009). Based on the studies reviewed, generally, higher Cl⁻ fractions in PM_{2.5} were generally seen in the north of India.

The distribution of NO₃⁻ was very variable across India with an average NO₃⁻ % fraction contribution of 5.31 % with standard deviation (SD) ± 3.46 %. For the summer seasons, an especially large NO₃⁻ fraction was observed by Behera et al., (2016)²²⁸ in Kanpur during the night-time hours of Apr – Jun 2009 observing 12.4 % (D12C). Another particularly large NO₃⁻ fraction was observed in Raipur between Apr – Jun 2009 by Deshmukh et al., (2013)²³⁹. Particularly low % contributions were found in the very north of India in the study by Sharma et al., (2014)²⁴¹. Workers measured NO₃⁻ in Palampur, Kullu, Shimla, Solan and Naham observing an average NO₃⁻ % fraction of 2.69 % (SD ± 0.69 %).

The maximum SO_4^{2-} % contribution observed between the reviewed studies was by Deshmukh et al., (2013)²³⁹ who suggested a SO_4^{2-} % 23.7 % in Raipur (Apr – Jun 2009). Other cities to observe > 10 % SO_4^{2-} include Delhi (10.0 %, I7A) by Saxena et al., (2017)¹⁹⁸; Pune (11.8 %, I11B) by Gawhane et al., (2017)²²⁷; and Kanpur (13.81 %, I12A) by Behera et al., (2016)²²⁸.

All of the NH_4^+ contributions between the summer studies were < 11 %, with an average across the reviewed studies of 7.41 % (SD \pm 2.84 %). In the very northern cities, which observed generally much lower contributions of NO_3^- and SO_4^{2-} , the NH_4^+ is variable. The maximum NH_4^+ contribution in the work by Sharma et al., (2014)²⁴¹ was 10.4 % (I26A) in Palampur and the minimum was 3.73 % in Kullu (I26B). This variability is likely down to differing agricultural and natural (dust) aerosol emissions between these cities. Out of all studies, the lowest NH_4^+ % contribution was 2.57 % in Pune between Feb – May 2016 (I11B) as indicated by Gawhane et al., (2017)²²⁷ which is most likely because Pune is a coastal city with a lesser amount of agricultural industry.

1.4.2 India Post-Monsoon – Winter

The $\text{PM}_{2.5}$ composition distribution across India for the Post-Monsoon – Winter period from the reviewed studies is shown in Fig. 1.5. Most of the studies conducted in other cities in India for this time of year combined averages for post-monsoon – winter and therefore for the sake of this review and for ease of analysis, the post-monsoon – winter period has been treated as one season.

Similar to the summer $\text{PM}_{2.5}$ compositions, the post-monsoon – winter $\text{PM}_{2.5}$ aerosol compositions also demonstrate *ca.* one third known ionic %. The average ionic % contribution was 31.2 % (SD \pm 11.49 %) across the reviewed studies. Some cities in Fig. 1.5 show a particularly low measured ionic fraction, such as Agra (24.7 %, I2F) measured by Kulshrestha et al., (2009)²²¹ who analysed the major anions and cations. The maximum ionic % fraction out of the studies was 52.6 % (I24C) as observed by Deshmukh et al., (2013)²³⁹ in Raipur (Feb – Mar 2009). Fig. 1.5 shows that the major ions in $\text{PM}_{2.5}$ (generally) during the post-monsoon period in India are Cl^- , NO_3^- , SO_4^{2-} , NH_4^+ , as well as Ca^{2+} in southern regions.

Generally, across the reviewed studies, Cl^- % were lower during the cooler months in Fig. 1.5 (average of 3.27 % (SD \pm 2.90 %)), compared to the warmer months shown in Fig. 1.4 (average of 7.71 %, SD \pm 5.44 %), by a factor of 2.36. In some cities however, such as Pune, the Cl^- % observed during the cooler months (7.04 %, I11D) was relatively similar to the warmer seasons (7.67 %, I11B) in the work of Gawhane et al., (2017)²²⁷. The maximum Cl^- % within $\text{PM}_{2.5}$ during the cooler seasons was seen in the work by Pant et al., (2015)¹¹⁰ who observed a Cl^- % of 10.0 % (I9B) in Delhi. The minimum Cl^- % was seen in the work by Ram et al., (2011)²⁴² who observed 0.04 % (I27A) in Kanpur during the day between 19th - 30th Oct 2008. Other cities which observed particularly high Cl^- % were Agra (7.78 %, I2C) by Kulshrestha et al., (2009)²²¹; Delhi (6.61 %, I7C) by Saxena et al., (2017)¹⁹⁸; and Raipur (5.52, I24C) by Deshmukh et al., (2013)²³⁹.

The SO_4^{2-} average across the cooler months (Fig. 1.5), was seen to be 10.3 % (SD \pm 4.66 %) which was very similar to the warmer months in Fig. 1.4 (average SO_4^{2-} % of 9.78 %, SD \pm 6.40 %). The

largest percentage contributions of SO_4^{2-} to $\text{PM}_{2.5}$ in the reviewed studies was found in Raipur by Deshmukh et al., (2013)²³⁹ who reported 17.9 % for study I24B between Oct 2008 – Jan 2009. Other cities to observe particularly high SO_4^{2-} % fraction contributions (< 15 %) include Ahmedabad (17.4 %, I3 + I4) by Rengarajan et al. (2011)²²² and Rengarajan et al. (2011)²²³; Amristar (15.0 %, I8A) by Kumar et al., (2018)²²⁵; Pune (16.3 %, I11D) by Gawhane et al., (2017)²²⁷; Dadanagar (15.1 %, I14E) by Behera et al., (2010)²³⁰; Raipur by Deshmukh et al., (2013)²³⁹ who observed 17.9 % (I24B, Oct 2008 – Jan 2009) and 16.8 % (I24C, Feb – Mar 2009). The minimum proportion of SO_4^{2-} was found in Agra by Kulshrestha et al., (2009)²²¹ who reported a percentage contribution of 1.27 % (I2E). Other particularly low SO_4^{2-} % values (< 2 %) were observed in Agra by the roadside between Oct 2007 – Mar 2008 (2.20 %, I2F) by Kulshrestha et al., (2009)²²¹ and Jorhat city (4.00 %, I15B) by Khare et al., (2011)²³¹.

The NH_4^+ fractions were found to be relatively variable across the different cities in the reviewed studies observing an average of 4.15 % (SD \pm 3.20 %). The minimum outdoor NH_4^+ % was observed in Agra between Oct 2007 – Mar 2008 by Kulshrestha et al., (2009)²²¹ who reported an average of 0.29 % NH_4^+ (I2B). The maximum NH_4^+ % out of the reviewed studies was observed in Delhi at 12.4 % by Pant et al., (2015)¹¹⁰ between 15th Dec 2013 – 15th Jan 2014. The average NH_4^+ % fraction across India during the cooler seasons (Fig. 1.5) was 4.15 % (SD \pm 3.20 %) which compares to the warmer seasons (Fig. 1.4) average of 7.41 % (SD \pm 2.84 %). This produces a factor difference between the seasons of 1.78.

1.4.3 China Winter

The winter season in China (Fig. 1.6) shows a substantial ionic % in most $\text{PM}_{2.5}$ compositions. The average known ionic % across the studies is 45.0 % (SD \pm 13.2 %). The maximum known ionic % was reported by Wang et al., (2016)²⁴⁶ who showed a value of 93.9 % (C5E) in Nanjing between Dec 2013 – Feb 2014. The smallest ionic % was evaluated by Zhang et al., (2013)²⁵⁸ who demonstrated a ionic % fraction of 19.7 % (C17E) in Beijing in Jan 2010. Substantial portions of measured ionic species were also found in Shanghai (C7D, 62.9 %) by Zhou et al., (2016)²⁴⁸; Hangzhou (C6P, 54.1 %) by Xu et al., (2017)²⁴⁷; Hong Kong Hok Tsui (C13C, 59.1 %) and Zhuhai (C13H, 65.6 %) by Lai et al., (2007)²⁵⁴. Fig. 1.6 shows that the major ions in $\text{PM}_{2.5}$ (generally) during the winter period in China are Cl^- , NO_3^- , SO_4^{2-} , NH_4^+ , as well as Na^+ in southern coastal regions.

Generally, a larger Cl^- % is seen in the northern cities of Taiyuan (C1C), Beijing (C17E) and Tianjin (C11) which average to 4.09 % (SD \pm 0.98 %). A similar average % fraction contribution is observed for the eastern cities of Shanghai (C2D, C2E, C7D), Nanjing (C5E), Ningbo (C6A, C6F), Lin'an (C6K) and Hangzhou (C6P) which average at 4.13 % (SD \pm 1.60 %). A lower average Cl^- % (3.51 %, SD \pm 0.89 %) was observed in the southern cities between Shenzhen (C13G, C15A), Xiangzhou Zhuhai (C13H), Hong Kong (C13A, C13B, C13C) and Guangzhou (C13D, C13E, C13F). The average Cl^- % observed in eastern cities between Nanjing (C5E), Shanghai (C7D, C2D, C2E), Hangzhou (C6P), Ningbo (C6A, C6F) and Lin'an (C6K) was 4.13 % (SD \pm 1.60 %). The average of Cl^- % contribution in the western cities of Weinan (C16S), Xi'an (C16N, C16I, C16D, C14, C16AC)

and Boaji (C16X) was 2.81 % (SD \pm 0.93 %). The maximum contribution of Cl⁻ to PM_{2.5} was found to be 6.48 % (C7D) in Shanghai observed by Zhou et al., (2016)²⁴⁸ during the winter months of 2011. The minimum Cl⁻ contribution across the reviewed studies was found to be 1.12 % (C14) in Xi'an between 13th Nov – 23rd Dec 2016, reported by Zhang et al., (2018)²⁵⁵.

The maximum NO₃⁻ % seen across the studies shown in Fig. 1.6 was 26.7 % (C5E) in Nanjing by Wang et al., (2016)²⁴⁶ who sampled between Dec 2013 – Feb 2014. A minimum of 4.52 % (C13E) in Guangzhou (Huangpu District) was recorded by Lai et al., (2007)²⁵⁴ between Jan – Feb 2002. The average NO₃⁻ % from the northern cities was 6.54 % (SD \pm 1.36 %); the average eastern value was 15.9 % (SD \pm 6.28 %); the average western value was 14.1 % (SD \pm 2.31 %); and the average southern value was 9.00 % (SD \pm 2.78%). The majority of the southern values for this average were however from Lai et al., (2007)²⁵⁴ from a campaign in 2002 and therefore this makes comparison challenging.

The maximum SO₄²⁻ % contribution to PM_{2.5} out of the reviewed studies (Fig. 1.6) was seen in Nanjing (35.9 %, C5E) by Wang et al., (2016)²⁴⁶. The minimum SO₄²⁻ % was 6.12 % observed in Beijing (C17E) by Zhang et al., (2013)²⁵⁸ who sampled in Jan 2010. The average SO₄²⁻ % between the northern cities was 16.7 % (SD \pm 6.10 %); eastern cities was 17.0 % (SD \pm 8.05 %); southern cities 19.4 % (SD \pm 6.04 %); and western cities 15.3 % (SD \pm 2.51 %). Therefore, generally the southern cities saw a higher fraction of SO₄²⁻ within aerosol of the reviewed studies. Particularly large fractions of SO₄²⁻ were observed in the south of China in studies C13H (28.8 %, Zhuhai) and C13C (28.6 %, Hong Kong Hok Tsui) by Lai et al., (2007)²⁵⁴.

NH₄⁺ fractions in PM_{2.5} out of the reviewed studies showed a maximum of 21.0 % in Nanjing (C5E) by Wang et al., (2016)²⁴⁶ and a minimum of 1.83 % in the Huangpu district of Guangzhou (C13E) as reported by Lai et al., (2007)²⁵⁴ producing a range of 19.1 % across studies (Fig. 1.6). The average NH₄⁺ contribution between the northern cities reviewed here was 5.17 % (SD \pm 1.42 %); between southern cities was 4.99 % (SD \pm 2.41 %); eastern cities 10.5 % (SD \pm 5.16 %); and western cities 8.38 % (SD \pm 2.09%). Therefore, despite study C13 by Lai et al., (2007)²⁵⁴ sampling in 2002 in southern cities, the most variable NH₄⁺ contributions to PM_{2.5} aerosol were seen in the eastern region.

1.4.4 China Summer

The studies that observed the largest fractions of known ionic % were C4A in Jinan (90.8%) by Zhu et al., (2015)²⁴⁵ who sampled between 17th – 26th Jul 2010; study C5C in Nanjing (86.4 %) by Wang et al., (2016)²⁴⁶ who sampled Jun – Aug 2014; and study C7B in Shanghai (76.2 %) by Zhou et al., (2016)²⁴⁸ between Jun – Aug 2011. Relatively large contributions of known ionic species (> 50 %) were also seen in study C3A (58.7 %) in Hei Shan Zhai (Beijing) by Pathak et al., (2009)²⁴⁴; study C6R (51.86 %) in Hangzhou by Xu et al., (2017)²⁴⁷; study C13P (51.94 %) in Xiangzhou Zhuhai by Lai et al., (2007)²⁵⁴; and study C16V (52.0 %) in Boaji by Niu et al., (2016)²⁵⁷. The minimum contribution of known ionic % to a study was found to be 21.7 % in study C2B by Wang et al.,

(2006)²⁴³ in Shanghai from sampling between 15th Jul – 16th Aug 2004. Fig. 1.7 shows that the major ions in PM_{2.5} (generally) during the summer period in China are NO₃⁻, SO₄²⁻, and NH₄⁺.

Out of the reviewed studies, Cl⁻ % were averaged in the northern cities Beijing (C3A, C17C), Taiyuan (C1A) and Jinan (C4A), giving an average of 0.60 % (SD ± 0.40 %); southern cities of Hong Kong (C13I, C13J, C13K), Guangzhou (C13L, C13M, C13N), Xiangzhou Zhuhai (C13P), as well as Shenzhen (C13O, C15B) giving an average of 2.22 % (SD ± 1.29 %); eastern cities of Nanjing (C5C), Shanghai (C2B, C3B, C7B), Ningbo (C6C, C6H), Hangzhou (C6R) and Lin'an (C6M) giving an average of 2.06 % (SD ± 2.02 %); and western cities of Weinan (C16Q), Xi'an (C16B, C16G, C16L, C16AA), Lanzhou (C3C) and Boaji (C16V) giving an average of 1.95 % (SD ± 2.88 %). The maximum Cl⁻ % fraction from the reviewed studies in Fig. 1.7 was reported to be 8.46 % (C3C) in Lanzhou sampled between 18th Jun - 17th Jul 2006 by Pathak et al., (2009)²⁴⁴ and the minimum Cl⁻ % fraction was observed in the work by Zhang et al., (2013)²⁵⁸ who calculated an average Cl⁻ contribution of 0.22 % (C17C) in Beijing (July 2009) by Zhang et al., (2013)²⁵⁸. The range was therefore 8.24 % across these studies. In addition, the average Cl⁻ % within PM_{2.5} across China in the studies in Fig. 1.7 was lower during the summer (average of 1.88 %, SD ± 1.92 %) compared to the winter (average of 3.62 %, SD ± 1.20 %) by a factor of 1.93.

The maximum NO₃⁻ contribution across the reviewed studies in China (summer) was 19.3 % seen in Jinan (C4A) by Zhu et al., (2015)²⁴⁵ who sampled between 17th Jul - 26th Jul 2010. The minimum was observed to be 3.61 % in Shanghai (C2B) by Wang et al., (2006)²⁴³ who sampled between 15th Jul - 16th Aug, 2004. This therefore gave a range of 15.7 % across the China studies in Fig. 1.7. The average NO₃⁻ % in the northern cities was 12.3 % (SD ± 5.82 %); southern cities was 4.85 % (SD ± 0.76 %); eastern cities was 10.07 % (SD ± 5.54 %); and western cities was 8.96 % (SD ± 2.13 %). Therefore, a larger contribution of NO₃⁻ within PM_{2.5} was observed in the northern and eastern cities out of the reviewed studies. The average NO₃⁻ across China for the summer campaign was 8.43 % (SD ± 4.49 %) compared to the winter season which demonstrated an average of 11.6 % (SD ± 5.21 %).

The northern average SO₄²⁻ contribution was 29.4 % (SD ± 13.3 %); southern average was 21.2 % (SD ± 6.69 %); eastern average was 23.2 % (SD ± 6.77 %); and western average was 24.1 % (SD ± 4.85 %). The average SO₄²⁻ across the reviewed studies was 23.7 % (SD ± 7.54 %) during the summer which is larger compared to the winter season (17.2 %, SD ± 6.00 %).

The maximum NH₄⁺ % out of the studies reviewed for the summer season in China was 29.9 % (C5C) in Nanjing reported by Wang et al., (2016)²⁴⁶ sampling in Jun – Aug 2014. The minimum seen between the studies is 0.32 % (C13J) in Hong Kong reported by Lai et al., (2007)²⁵⁴. The average NH₄⁺ % across all studies reviewed during the summer was 7.31 % (SD ± 6.56 %) across China and was therefore very variable. This variability is also observed within specific cities, such as in Shanghai (average of 8.48 %, SD ± 6.58 %). Some cities however showed a relatively constant contribution by NH₄⁺ with lower SD, such as Xi'an (average of 5.95 %, SD ± 0.79 %). This average

included both urban areas like the Xi'an High tech Zone (C16B) and the rural area of the Qing Ling Mountains site (C16AA). The average NH_4^+ % between northern cities was 10.9 % (SD \pm 8.21 %); southern cities was 2.21 % (SD \pm 1.59 %); eastern cities was 12.1 % (SD \pm 8.12 %); and western cities 6.40 % (SD \pm 0.91 %).

1.5 PM_{2.5} in Delhi and Beijing (and APHH)

According to World Population Review²⁵⁹, the estimated combined population of India and China comprises *ca.* 36 % of the world's population. PM_{2.5} pollution is known to be severe in these developing countries for which the megacities of Beijing and Delhi are the capitals. The current populations of Delhi and Beijing are 31,181,376 and 20,896,820 (in March 2021)²⁵⁹. Therefore, a significant number of inhabitants are ubiquitously exposed to seriously high levels of PM_{2.5} exposure. The understanding of particle composition and formation within these two megacities is therefore vital and has been explored in this thesis.

1.5.1 APHH Delhi and Beijing

The Air Pollution and Human Health (APHH) in Developing Megacities Programme was conducted in Delhi and Beijing over two seasons at in each city. The APHH Delhi project focused on emission flux although filter samples were also taken²⁶⁰. The aim of the project was to enhance the emissions inventory dataset and to suggest low-cost strategies which may be implemented to improve air quality²⁶⁰. This was a partnership between several UK and Indian research institutes²⁶⁰. The APHH Beijing campaign had the overarching objective to develop understanding of the source emissions, atmospheric chemistry and adverse effects on health of Beijing's atmosphere⁴⁴. A full list of participants and summary of this project can be found in Shi et al., (2019)⁴⁴.

1.5.2 Experimental Methods and Contribution of this Thesis to APHH

The work presented in this thesis focuses on the ionic constituents as well as some of the most carcinogenic organic compounds found in PM_{2.5}, Organic Nitrogen (ON) species. Filter collection was conducted during the Delhi pre-monsoon (DPEM), Delhi post-monsoon (DPOM), Beijing winter (BWIN) and Beijing summer (BSUM) campaigns using a High-Volume Sampler (HiVol) in the collection of ambient PM_{2.5} filter samples. Collected filter samples were sent back to the University of York in which they were analysed for their inorganic fraction and ON components, using Ion Chromatography (IC) and comprehensive Two-Dimensional Gas-Chromatography coupled to Nitrogen Chemiluminescence Detection (GC \times GC - NCD). Simulation experiments surrounding Organic Nitrate (Org-NO₃) formation, a key constituent to PM_{2.5} in an Asian urban megacity were also carried out using a Particle Into Liquid Sampler (PILS) at the Jülich Forschungszentrum. PILS is also a technique which has been used previously in ambient urban PM_{2.5} collection, although was not used for ambient aerosol collection in this thesis. A very brief description of the theory of operation of these species is outlined below.

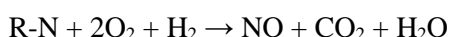
1.5.2.1 Ion Chromatography

Ion chromatography is a form of liquid chromatography based on the principle of ion exchange. The mobile phase is in the form of a salt solution (eluent) and the stationary phase is a column of fixed

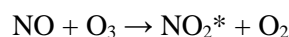
ions which are of the opposite charge to the analytes of interest. Different species being analysed observe different charge densities and therefore separation occurs based on electrostatic forces of attraction between the analytes and the column, which is specific to a particular species. Once separated by the column, analytes pass through to the suppressor. The suppressor acts to lower the background signal noise and increases the signal strength of the analyte of interest. This therefore allows lower Limit of Detection (LOD) levels of analytes. Finally, detectivity of sample analytes occurs based on conductivity. A further description of IC theory of operation may be found in “A Practical Guide to Ion Chromatography | An Introduction and Troubleshooting Manual”, by SeQuant²⁶¹.

1.5.2.2 GC × GC – NCD

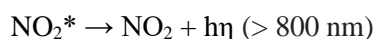
Separation in GC × GC – NCD is an orthogonal separation technique in which ON compounds are separated in the 1st dimension (separation by boiling point), followed by cryogenic modulation using liquid N₂ of species onto the 2nd dimension column (separation by polarity). Diagrams of the Orthogonal GC × GC system and NCD schematic are shown in Fig. 1.8 and Fig. 1.9, respectively.



Eq. 1.38. Burning of ON species to form NO.



Eq. 1.39. Reaction of NO₂ with O₃ producing excited state NO₂*.



Eq. 1.40. Relaxation of excited state NO₂* to NO₂, emitting red light.

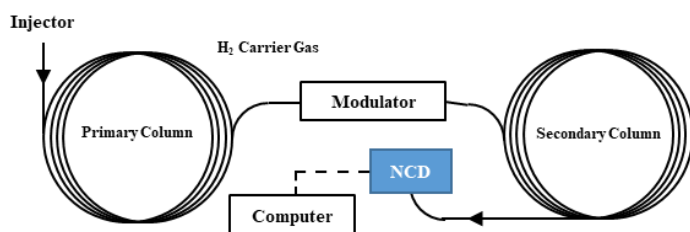


Fig. 1.8. Orthogonal GC × GC Schematic.

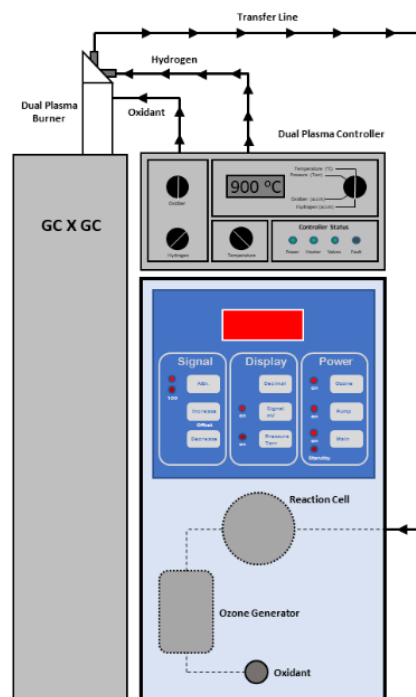


Fig. 1.9. NCD System Schematic.

When ON compounds resolve off the end of the second-dimension column, they are burned at 900 °C forming NO (Eq. 1.38)^{262,263}. NO subsequently flows through to the reaction cell. O₃ is continuously produced by a corona discharge and flows through to the reaction cell also²⁶³. In the reaction cell, NO reacts with O₃ to produce excited state NO₂* (Eq. 1.39)^{262,263}. NO₂* relaxes back to NO₂, releasing red light. The red light passes through a light filter (specific to NO₂* relaxation) before hitting the photomultiplier tube (Eq. 1.40)²⁶³. Photons hitting the photomultiplier tube causes

a cascade of electrons through the tube which hits an anode at the end of the tube causing an electric pulse to occur which is detectable^{262,264}.

1.5.2.3 PILS

Another method which could be used for ambient PM_{2.5} sample collection and which was used during smog chamber experiments as part of the NO₃ISOP campaign (Chapter 6) is PILS. A schematic of the BMI PILS system (taken from the BMI PILS manual)²⁶⁵ is shown in Fig. 1.10.

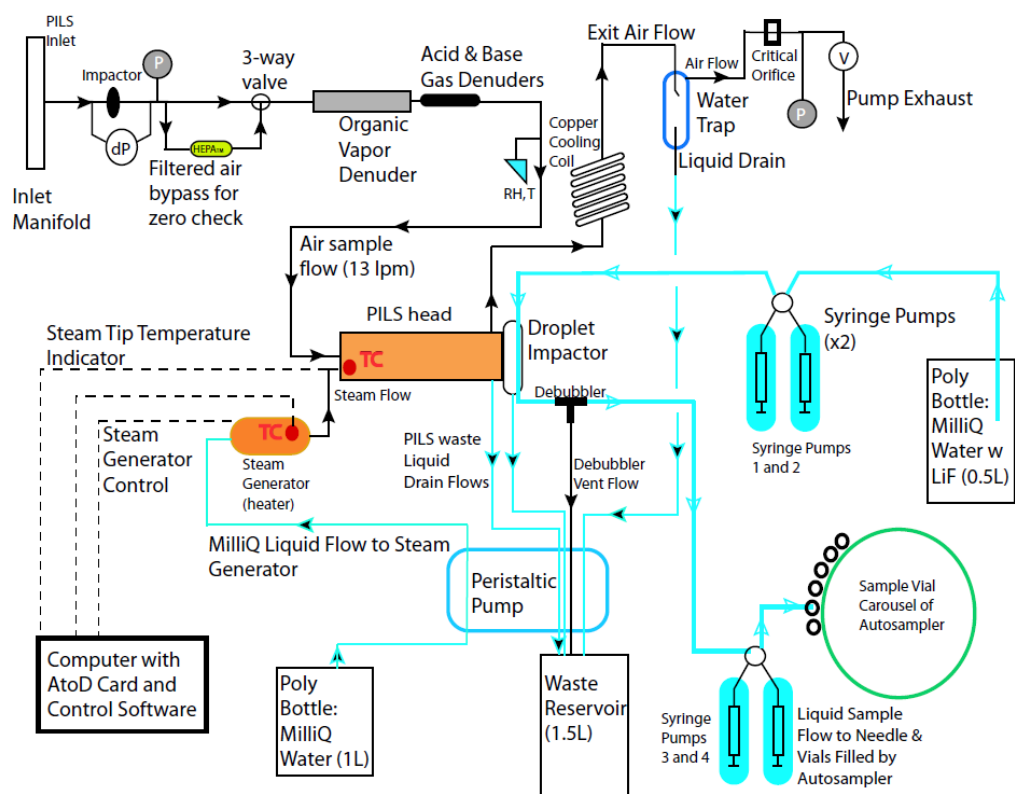


Fig. 1.10. Schematic of the BMI PILS System used during the NO₃ISOP Campaign (Chapter 6).

In Brief, aerosol enters the PILS system through the PILS inlet for which aerosol is then size segregated depending on the impactor specification (PM₁, PM_{2.5} etc.). Aerosols pass through acid and base denuders to remove any potentially interfering contaminant gaseous species. Aerosol then enter the PILS head. Simultaneously, 18.2 MΩ water from a reservoir in the PILS is pumped through tubing to the steam generator, for which steam also flows through to the PILS head. In the PILS head, super saturation of water occurs when the steam is presented with cooler air from the ambient aerosol air mass which causes fast adiabatic cooling of the steam. A supersaturated water environment in the PILS head allows for efficient coagulation of water onto the aerosol, causing the aerosol droplets to grow into a particle with a diameter of > 1 μm. At this size, aerosol may be effectively collected at the droplet impactor. A flow of LiF (added as an internal standard for the calculation of the dilution factor) solution is passed over the droplet impactor and washed the aerosol species into sample vials. A continuous flow of this system allows for offline collection of aerosol samples in water for a specific sampling period^{265,266}.

1.5.3 Aims and Hypotheses of PhD Thesis

The knowledge gaps within the literature, resulting aims and objectives of this PhD research as well as the hypotheses for this work are presented.

1.5.3.1 Literature Knowledge Gaps

To date, although Ion Chromatography is common-place in evaluating the ionic composition of PM_{2.5} aerosol in urban atmospheres, the critical analysis of the application of IC in this way (including sampling and extraction method as well as impact of instrument health and efficiency of IC analysis) has not to date been extensively evaluated and in conjunction the use of high frequency filter sampling for this technique (to avoid potential sampling artefacts) in an Asian megacity is also not currently available in the literature (to best knowledge). Furthermore, an inter-laboratory comparison for the use of IC had not yet been conducted until Xu et al., (2020)²⁶⁷ (for which work in this thesis contributes towards), which is vital for quality assurance of IC for ionic analysis within urban Asian megacity PM_{2.5} from filter samples.

Currently, despite Delhi being one of the most polluted megacities globally, there is relatively little literature surrounding ionic aerosol analysis on PM_{2.5} filter samples in Delhi and the literature available is very vague regarding exact sampling times, inclusion of error analysis, and reporting of exact sampling sites and conditions. A greater library of publications is available reporting the ionic PM_{2.5} fraction in Beijing, although no direct comparison has yet been conducted between Delhi and Beijing (two of the world's most polluted megacities) with regard to ionic composition of aerosol which gives an overview of the major formation pathways of PM_{2.5} in urban atmospheres. Furthermore, to date (and to best knowledge), no comparison has been conducted in the literature between IC and AMS techniques in conjunction with particle size data to investigate which size fractions ionic species may reside in, within PM_{2.5} in Delhi and Beijing's atmospheres. In addition, there is no mention in the literature (to best knowledge) regarding an evaluation of the key sources of error when comparing these two different analytical techniques for the major SIA.

Along with a lack of ionic PM_{2.5} concentration measurements conducted in Delhi, no historical reviews of ionic species concentrations or relative particle composition fractions of aerosol has yet been conducted in the literature to suggest which sources are either increasing or decreasing in PM_{2.5} contribution. Some historical work has been conducted in the work of Lang et al., (2017)²⁶⁸ in Beijing, although this is only includes data up to 2015. Furthermore, no comparison exists to date between the historical trends of two separate highly polluted Asian megacities. This information would be useful in identifying the general trends of species over the past 10 – 20 years in Delhi and Beijing, respectively, to identify which key species (and therefore their precursor gases) are pivotal in governing PM_{2.5} concentrations.

The specific formation of SIA from the most dominant pathway of acidic gas and NH₃ neutralisation in the atmosphere has been well documented in the literature. Up to now (to best knowledge), however, there is little discussion or direct comparison between Beijing and Delhi with regard to the

ammonium aerosol system and the dominant neutralisation reactions contributing to $[PM_{2.5}]$ in these extremely polluted megacities. There is also very little work conducted as yet investigating the role of weak acids in the possible formation of NH_4^+ in the aerosol phase.

NO_3^- and SO_4^{2-} are major SIA which comprise a considerable fraction of $PM_{2.5}$ by mass and are widely acknowledged to form from the neutralisation reaction between acidic gases (i.e. HNO_3 and H_2SO_4) with alkaline NH_3 . The formation of inorganic aerosol via an organic pathway (such as via the formation of organic nitrates) is however also a potentially significant formation route due to the abundance of BVOCs and precursor gases (NO_x and SO_x) in urban atmospheres, yet is a not much explored pathway. Total organic nitrate measurements (as well as hydrolysis measurements) are important as they are known to affect a particle's physical and chemical properties; make up a substantial fraction of organic aerosol^{269,270}; give an indication to a different formation pathway of NO_3^- in the aerosol phase; affect climate^{271,272}; as well as form a NO_x sink and reservoir^{273,272} (which inherently affects $[O_3]$)^{273,274} in an Asian megacity, for example. To date, there is no mention or evaluation in the literature of the use of PILS-IC to measure $\Sigma [Org-NO_3]$ which is a much simpler technique compared to conventional AMS. Relatively little work on the hydrolysis of primary Org- NO_3 species is also available from the literature (which predominantly focuses on tertiary Org- NO_3 species)^{275,274}. There is also no mention (to best knowledge) within the literature thus far of the use of IC to measure the kinetics of organic nitrate hydrolysis, which is a much less expensive (and much simpler) technique to run compared to conventional NMR (which is generally used in these sorts of studies)^{274,276}.

Despite the inorganic fraction composing the majority of $PM_{2.5}$ by mass and being an indicator of the major $PM_{2.5}$ formation sources, the particle toxicity is predominantly governed by the organic fraction, for which organic nitrogen species such as nitrosamines are known to be some of the most carcinogenic and mutagenic compounds found in $PM_{2.5}$ ²⁷⁷. Prior to this thesis, an estimation of the cancer risk from exposure to these highly toxic species in $PM_{2.5}$ had been conducted in London²⁷⁶, although no such study had yet been conducted in a highly polluted Asian megacity, such as Beijing (to best knowledge). In addition, this calculation has not yet been conducted with the use of high frequency filter sampling which avoids the production of filter artefacts and source apportionment has not yet been conducted of nitrosamines within Beijing which is essential to target a reduction in these species through policy initiatives resulting in a reduced burden on human health and state economies. Furthermore, nitrosamines are a single chemical group of highly toxic aerosol components, in which several other chemical classes of organic nitrogen species are known to induce acute toxicity in humans²⁷⁸. There is currently no mention in the literature of a library of suitable compounds for analysis on GC \times GC – NCD which is a highly sensitive and selective technique vital in the accurate measurement and analysis of these compound classes within urban $PM_{2.5}$ which would be very useful for future research projects.

1.5.3.2 Research Aims and Objectives

To address the current gaps in knowledge within the literature outlined in section 1.5.3.1, the aims of this thesis are outlined as follows:

1. To develop a suitable IC method and data manipulation procedure (with critical evaluation) for the analysis of ionic constituents within Asian megacity PM_{2.5} with high precision and accuracy using high frequency filter sampling.
2. To take part in an inter-laboratory comparison study to investigate the discrepancy in IC measurements across multiple laboratories worldwide for the same set of filter samples.
3. To use the IC method developed to conduct ionic species characterisation and quantification of PM_{2.5} filter samples collected as part of the APHH Delhi and Beijing campaigns including the reporting of exact sampling times, inclusion of error analysis, and reporting of exact sampling sites and conditions. A direct comparison of PM_{2.5} composition between two of the world's most polluted megacities (Delhi and Beijing) will also be analysed to assess the most prominent primary and secondary sources of PM_{2.5} in these cities.
4. To complete an intercomparison between the IC and AMS measurements in conjunction with particle size data for quality control purposes and to use this comparison to investigate under which conditions in an Asian megacity positive and negative ionic filter artefacts may arise from (using HiVol filter sampling). A critical assessment of the errors associated with each technique will also be evaluated.
5. To conduct an historical review of SIA mass and percentage fraction within PM_{2.5} to evaluate the most likely sources and species that contribute to PM_{2.5} as a function of time over the past 20 years (Beijing) and *ca.* 10 years (Delhi).
6. To assess the extent of secondary PM_{2.5} formation, the SIA correlations between NH₄⁺ and the acidic gas conjugate bases (Cl⁻, NO₃⁻, and SO₄²⁻) will be evaluated and compared in Delhi and Beijing. The role of weak acids in NH₃ neutralisation to form NH₄⁺ will also be investigated.
7. To investigate the formation of inorganic species via alternative pathways (such as via organic nitrates) from simulation chamber experiments (at atmospherically relevant concentrations) which focus on the reaction between isoprene and NO₃ radical (which are dominant species in highly polluted Asian megacities such as Delhi and Beijing). This will be done by developing a PILS-IC method which is much simpler compared to other AMS and GC techniques, to measure Σ[Org-NO₃] species from samples collected as part of the NO₃ISOP campaign at the Julich Forschungszentrum. This method will also be evaluated to give suggestions to future users who aim to quantify organic nitrate species using an offline technique.
8. To quantify the reaction kinetics of a selection of primary Org-NO₃ species to determine the extent of Org-NO₃ hydrolysis within aerosol to form NO₃⁻, by developing a much simpler and less expensive IC hydrolysis reaction kinetics experiment.

9. To obtain as many ON species commercially available as possible and test as to see whether these are suitable for GC × GC – NCD analysis and to produce a mixed standard from them.
10. To successfully characterise and quantify the nitrosamine concentrations within PM_{2.5} in Beijing and to use this to estimate the cancer risk to human health imposed by these species from exposure to PM_{2.5}.

1.5.3.3 Research Hypotheses

Based on the aims and objectives outlined in section 1.5.3.2, the relative research hypotheses for the research aims and objectives are given.

What were you trying to find out and what were you expecting to find out?

- A. Due to the reliability and frequent usage of IC in offline filter analysis of ionic species within PM_{2.5} in urban areas, it is hypothesised that good reproducibility will be observed between different labs worldwide.
- B. It is hypothesised that Delhi and Beijing will observe differences in their overall PM_{2.5} composition across the four different APHH campaigns due to large differences in temperatures, meteorology, cultures (and therefore emission sources – e.g. cooking styles and festivals), population density and land use. Due to much higher temperatures seen in Delhi, it is suspected that measurements in Delhi will show a significantly larger fraction of secondary inorganic aerosol species compared to the organic fraction, in relation to Beijing. It is also expected that Delhi will detect much greater ionic material concentrations compared to Beijing due to higher pollution levels^{279,280}.
- C. As IC and AMS are two very contrasting methods of measuring SIA in PM, it is hypothesised that these two measurements are unlikely to agree with one another in the first instance.
- D. In the historical analysis of SIA species as a function of time, it is expected that [SIA] will generally increase in Delhi although decrease in Beijing. This is because PM_{2.5} is known to have generally increased and decreased in Delhi and Beijing, respectively (in recent years)²⁸¹, and SIA is known to often be the most dominant fraction of PM_{2.5} in urban megacities.
- E. It is expected that as in most other urban environments, the production of SIA from the release of NH₃ and acidic gases will be dominant and that the strongest correlations (and gradients) of NH₄⁺ will be found with SO₄²⁻ > NO₃⁻ > Cl⁻ due to the NH₃ + H₂SO₄ neutralisation reaction being a non-reversible process and NH₄Cl being more volatile than NH₄NO₃²³⁰. It is also suspected that very high concentrations of acidic gases, particularly in Delhi, will result in a small influence of NH₃ neutralisation by weak acids.
- F. Despite atmospheric relevant concentrations being used for the measurement of Org-NO₃ species in PM₁ aerosol from chamber experiments, 15-minute sampling is expected to be sufficient for the measurement of NO₃⁻, SO₄²⁻ and F⁻ above detection limit of the PILS-IC system and a substantial fraction of Org-NO₃ is suspected to be detected on the reaction of the NO₃ radical with BVOCs in the chamber.

- G. It is also hypothesised that the hydrolysis of primary organic nitrates will be on the time scale of IC measurements (every 20 minutes) and that IC will be established to be an alternative and less expensive technique for these kinetic studies compared to NMR.
- H. It is expected that a considerable concentration of carcinogenic organic nitrogen species (specifically nitrosamines) are present in Beijing PM_{2.5} due to significantly high [NO_x] which is one of the major precursors. It is also expected that due to higher PM_{2.5} and NO_x pollution in Beijing compared to London that a greater concentration of nitrosamines will be detected in Beijing compared to previous studies conducted in London²⁷⁷. It is therefore also hypothesised that a greater cancer risk is imposed on the population of Beijing compared to London from PM_{2.5} exposure from these highly carcinogenic and mutagenic species.
- I. It is expected that the major sources of nitrosamine pollution in Beijing is from the Huaneng power plant (which has been recorded to have taken part in previous carbon capture initiatives)²⁸², as well as from the south of the IAP site where a substantial proportion of Beijing's industrial areas are located²⁸³.

1.5.4 Thesis Outline

The work presented in this thesis has been conducted to investigate and compare the overall bulk particle composition of PM_{2.5} within Asian megacities (such as Beijing and Delhi). The knowledge gained from this thesis enhances the understanding of the most prevalent ionic species in urban Asian megacity PM_{2.5} as well as the potential key PM_{2.5} formation pathways. It also gives an indication to the potential precursor sources which produce inorganic aerosol within an Asian megacity, using Delhi and Beijing as case studies. The inorganic particle composition has a direct influence on the particles physical and chemical properties, which may affect potential particle toxicity by controlling particle hygroscopicity.

Chapter 2: Experimental techniques used in the characterisation and quantification of major and minor ions within PM_{2.5} sampled during the APHH campaigns in Beijing and Delhi are presented along with method development. A critical evaluation is also given along with suggestions for future IC users to improve quality of data in within data manipulation steps.

Chapter 3: A comparison is conducted between the major ionic constituents measured in Delhi and Beijing regarding particle composition. Species concentrations are also compared between day and night-time hours in each city. Furthermore, an instrument comparison was conducted to critically assess the sampling and sample processing methods conducted between different institutions a part of the same campaign, to ensure accuracy in the quantified ionic concentrations.

Chapter 4: A comprehensive review of PM_{2.5} inorganic data from peer reviewed publications was collected to produce history plots to show the change in ionic species concentrations and contribution to PM_{2.5} since 2012 in Delhi and 1999 in Beijing. The ionic results calculated from this thesis (chapter 3) have been added to the trends of species in each city and are also compared to other studies that sampled over an identical sampling season.

Chapter 5: The major inorganic aerosol constituents are analysed for their most likely sources in each city. This was done using polar contour plots for HCl and due to the abundance of NO₂ and SO₂ in these megacities, the [NO₃⁻]/[SO₄²⁻] is used to evaluate emissions from mobile and stationary sources. The level of SO₂ and NO₂ oxidation within each city has also been assessed. An investigation was conducted into the neutralisation of these acidic gas species with gaseous NH₃.

Chapter 6: Experiments are presented which investigate the hydrolysis of primary organic nitrate constituents to compliment work conducted as part of the NO₃ISOP campaign based at the SAPHIR chamber (Jülich Forschungszentrum, Germany). A PILS-IC method was used to as part of this campaign to sample and estimate the concentrations of Org-NO₃ produced from the reaction of a variety of VOCs (predominantly isoprene) with the NO₃ radical. This gives insight into the formation of the inorganic NO₃⁻ constituents in the particle phase via an organic formation pathway.

Chapter 7: The inorganic fraction of PM_{2.5} directly affects the particles hygroscopicity and therefore the ability for a particle to absorb acidic gases. In this chapter, the concentration of some of the most harmful compounds (nitrosamines) have been characterised and quantified within PM_{2.5} samples during a polluted period during the APHH Beijing winter campaign. This data has been used to estimate the excess number of cancer cases due to exposure on Beijing's population to PM_{2.5}.

Chapter 8: Summary of conclusions and future work.

2 Ion Chromatography Theory of Operation and Method Development: Experimental Techniques, Method Development and Data Quality Assurance.

2.1 Introduction

The water soluble ionic contribution within PM_{2.5} may make up to 77 % of this size fraction^{267,190} and therefore comprises a substantial contribution. Ambient PM_{2.5} concentrations from field campaigns such as the Air Pollution and Human Health (APHH) Delhi and Beijing campaigns are critical in understanding the atmospheric chemistry occurring within polluted Asian megacities where PM_{2.5} concentrations are known to be exceptionally high²⁸⁴. Inorganic PM_{2.5} concentrations are required during large scale field campaigns for numerous purposes. Measurements allow for the indication of tracer species from known sources (such as K⁺ for biomass burning) which is required for understanding potential primary contribution to aerosol. Additionally, secondary aerosol species such as NO₃⁻ and SO₄²⁻ give an indication to the oxidation capacity of the atmosphere and to the relative contribution of mobile and stationary source of pollution through the NO₃⁻ / SO₄²⁻ ratio²⁵⁴. Furthermore, correlating tracer species with other gas-phase measurements from other instruments as part of the same campaign may give greater insight into the atmospheric chemistry occurring in these megacities.

In addition, PM_{2.5} measurements are required for atmospheric transport and forecasting models. Furthermore, the ions measured in this thesis in Delhi and Beijing may be used for the aerosol acidity (ISOROPPIA II) model which is critical in the accurate estimation of aerosol pH. Aerosol pH has great influence on the other chemistry occurring within aerosol and will give greater insight to others associated with the APHH campaigns into the relative chemistry occurring in the atmospheres of Beijing and Delhi. Moreover, this understanding may influence the successful discovery of future chemical mechanisms in aerosol (in conjunction with other model studies) which may contribute to the Master Chemical Mechanism²⁸⁵.

Numerous instrumental methods are available for online and offline inorganic aerosol measurements within PM_{2.5}. Online measurements constitute techniques such as Aerosol Mass Spectrometry (AMS) which has been commonly used in field campaigns investigating major ionic Secondary Inorganic Aerosol (SIA). AMS is however a very complicated set-up, measures PM₁ and has been known to observe issues regarding organic nitrate and sulfate measurements such as the degradation of these organic species at the AMS ionisation and vaporization stages, as well as the ambiguity which arises from using the NO⁺/NO₂⁺ ratio for organic nitrate quantification^{286,287}. Offline techniques involving filter sampling are also commonly used and include Inductively Coupled Plasma Mass Spectrometry (ICP-MS) and Ion Chromatography. Ion Chromatography has been widely used in the characterisation and quantification of inorganic Particulate Matter (PM) in both Delhi^{288,289,290,110} and

Beijing^{291,185,292,293}. It is also a much simpler and robust technique compared to other more complex instruments (such as AMS). In addition, Ion Chromatography (IC) instrumentation has been observed to measure inorganic ions reproducibly across 10 different laboratories across the world²⁶⁷, whereas no such comprehensive study for AMS has yet been conducted to date. Due to the reproducibility of IC measurements from filter samples confirmed in the work of Xu et al., (2020)²⁶⁷, inorganic PM_{2.5} measured from IC allows for a reliable indication of trends of measured ions during a campaign. Furthermore, the application of high-volume filter sampling (a novelty of this work) produces a comprehensive set of data for other more complex instruments to be able to compare their data to and IC may therefore also be a technique used for quality control purposes within other instruments. Therefore, the accurate identification and quantification of ionic species within PM_{2.5} aerosol is vital.

In this chapter, the experimental protocols surrounding the characterisation and quantification of the inorganic fraction within PM_{2.5} with Delhi and Beijing (chapters 3-5) has been described in detail. The experimental protocols for chapters 6 and 7 are described in the experimental sections of the respective chapters. The aim for this chapter is to define and evaluate the experimental protocol used in this thesis as well as explore and assess different quality control practices. The method development for ion atmospheric quantification has also been presented. Furthermore, this evaluation has been used to outline possible suggestions for improvement in the protocol for the benefit of future IC users investigating inorganic PM_{2.5} from filter samples. Finally, the contribution of the experimental protocol developed in this thesis is compared to 9 other laboratories who took part in a major IC inter-laboratory comparison study²⁶⁷.

2.2 Experimental and Method Development

2.2.1 Sample Collection

Quartz fibre filters (QMA, Whatman, UK) of size 203 mm × 254 mm were pre-conditioned in a furnace for 5 hours at 550 °C. These were then wrapped in aluminium foil until sampling. The HiVol sampler had been calibrated and thoroughly cleaned with blue tissue roll soaked with 18.2 MΩ Milli-Q (MQ) Deionised (DI) water before shipment to Beijing and Delhi for the start of the APHH campaigns. On a clean work surface in an air-conditioned lab, a clean pair of tweezers (while using gloves) were used to carefully remove the pre-conditioned QMA filters from their foil packaging and place them into the HiVol cassette. Travel blanks were however not conducted. A clean plastic bag was then used to transport the filter cassette from the lab to the HiVol sampler on the roof-top to avoid contact of the filter with the ambient air. This was especially necessary, for example, during high pollution events and during the Delhi post-monsoon period in which workmen were soldering the observation tower together for flux instrumentation on the path to the HiVol sampler. The sample filter pre-conditioning method, HiVol sampler specifications and collection methods were kept constant for both the Beijing and Delhi APHH campaigns.

For APHH Delhi, sampling was carried out at the Indira Gandhi Delhi Technical University for Women (IGDTUW) in Kashmere Gate, New Delhi, India (28°39'55.1"N 77°13'56.6"E, Fig. 2.1) as part of the Air Pollution and Human Health (APHH-Delhi) campaign. The site was located in a

predominantly residential and market district in close proximity to the Mahatma Gandhi Marg (route 44 highway) as well as the Yamuna river towards the north east of the city. The HiVol sampler which was located in a cage on the roof-top of the IGDTUW at a height of 8 m.



Fig. 2.1. Map of Delhi and the location of the Indira Gandhi Delhi technical University for Women indicated by the red star.

For APHH Beijing, PM_{2.5} samples were collected at the Institute of Atmospheric Physics (IAP) in Beijing, China (Fig. 2.2) as part of the Sources and Emissions of Air Pollutants in Beijing project (AIR-POLL). The sampling site was located in a mainly residential area between the 3rd (100 km north) and 4th (400 km east) ring road *ca.* 9 km from Beijing city centre to the north in the Huayuan road residential district.

A High-Volume air sampler (HiVol) (Ecotech 3000, Australia) at a flow rate of 80 m³h⁻¹ was used to collect PM_{2.5}. Day and night-time sampling hours were *ca.* 0.8:00 – 18:00 and 18:00-08:00, respectively in both Delhi and Beijing. Intensive sampling was carried out during the day at a filter change frequency of every 3 hours or 1 hour (as well as up to every half hour in Beijing) depending on predicted atmospheric PM_{2.5} atmospheric mass loadings (obtained from the USA embassy website's Air Quality Index tool, <http://aqicn.org/city/beijing/us-embassy/>). One filter change occurred for night-time hours. During sample collection, the filter cassette was carried back in plastic wrapping to an air-conditioned workstation where the filter was wrapped in aluminium foil, placed in a bag and into a freezer (-18 °C). The filter samples were then shipped back to the University of

York (UoY) in dry ice where they were analysed for their inorganic content. A summary of the start and end times of each sampling period, as well as the number of samples acquired, and the number of blocked filters reported are shown in Table 2.1. The quartz micro-fibre filter pieces (QMA, Whatman) had an area of 203 mm × 254 mm and were placed in a furnace at 550 °C for five hours prior to shipment, to decompose and volatilise any other species. These were then wrapped in tin foil and sent to Delhi and Beijing for sampling.

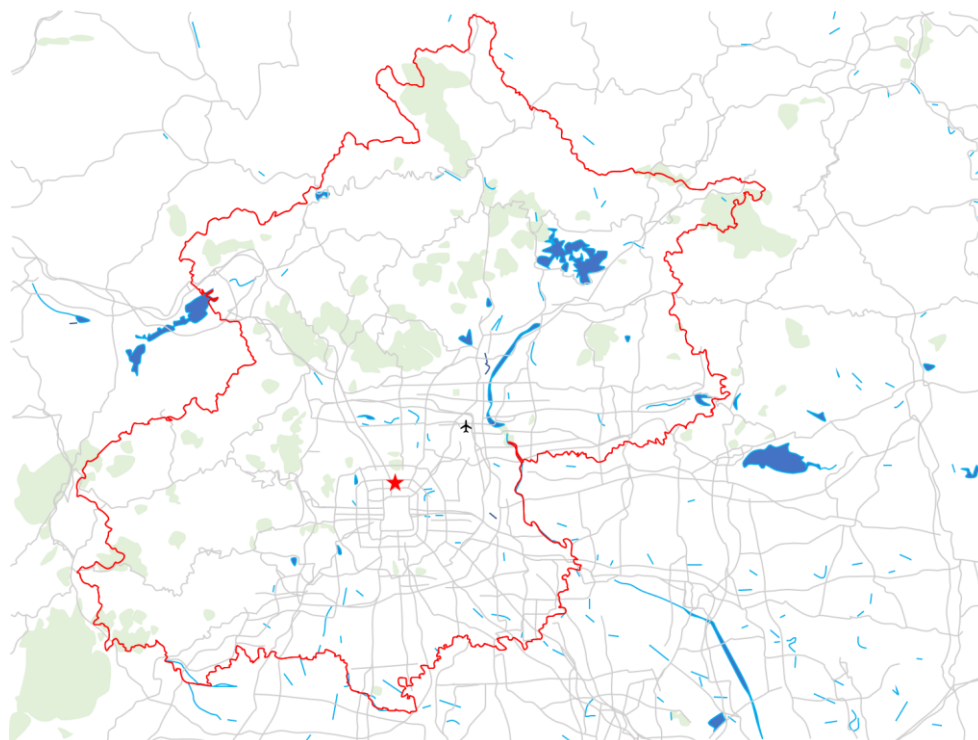


Fig. 2.2. Map of Beijing and the location of the Institute of Atmospheric Physics (Chinese Academy of Sciences) indicated by the red star.

Table 2.1. Table showing the campaign sampling start and end times, the number of filters and the number of blocked filters recorded for the Delhi pre- and post-monsoon campaigns and the Beijing winter and summer campaigns.

	Campaign	Start	End	No. filters	No. Blocked
Delhi	Pre-Monsoon	28 th May 2018; 08:30	5 th Jun 2018; 17:30	35	1
	Post-Monsoon	9 th Oct 2018; 14:54	6 th Nov 2018; 10:35	107	6
Beijing	Winter	9 th Nov 2016; 17:30	9 th Dec 2016; 17:30	127	3
	Summer	18 th May 2017; 13:00	25 th Jun 2017; 08:38	201	5

The HiVol sampler blocks when too much mass loading has built upon the QMA filter which restricts the air flow. If the air flow is restricted too much it automatically switches off. Blocked filters were therefore generally over-night filters with prolonged sampling times and produced gaps in the data time series (chapter 3). As the HiVol sampler was located on the roof top of the laboratories at both IGDTUW and IAP, frequent filter changes were only carried out during daytime hours due to safety

issues. Data was acquired from four field campaigns as part of the APHH project, over two seasons within the megacities of Beijing and Delhi. These campaigns have been referred to as Delhi pre-monsoon (DPEM), Delhi post-monsoon (DPOM), Beijing winter (BWIN) and Beijing summer (BSUM) in this study.

2.2.2 Comparison Data from APHH partners

The gas phase data of NO, NO₂, CO SO₂ and O₃, in chapter 3 was taken by the University of York²⁸³. The PM_{2.5} data was measured using a gravimetric method and a Tapered Element Oscillating Monitor - Filter Dynamics Measurement System (TEOM-FDMS) by the University of Birmingham (UoB) in the Delhi and Beijing campaigns, respectively (24-hour and 12-hour sampling was carried out, respectively). AMS measurements used for comparison purposes were measured by the Institute of Atmospheric physics (Beijing) and the Centre for Ecology and Hydrology (Beijing and Delhi). Further information on the gas-phase measurements may be found in Shi et al., (2019)⁴⁴ and Squires et al., (2020)²⁸³ for Beijing. Single Particle Soot Photometer (SP2) measurements referred to in chapter 5 were conducted by the University of Manchester (UoM) during the APHH Delhi campaign.

2.2.3 Filter Extraction

A flow chart presenting the experimental conducted for filter extraction for the Delhi and Beijing filter samples is presented in Eq. 2.3. For the Delhi and Beijing samples a 6.2 cm² and 5.7 cm² stencil was used, respectively. The only other difference is that Grenier bio-one (Germany) conical vials and Sarstedt (Germany) plastic vials were used for Beijing and Delhi samples, respectively.

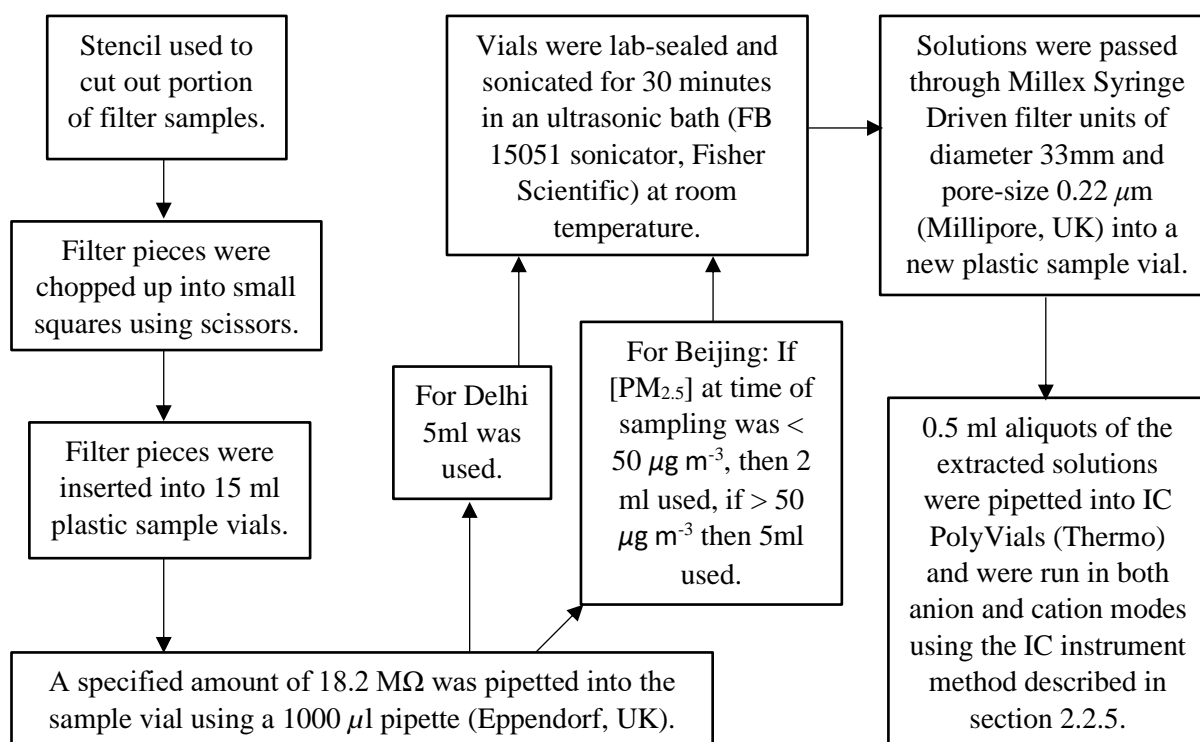


Fig. 2.3. Flow chart of general filter sample extraction protocol used in these IC analyses.

2.2.4 Calibration Standards

For anionic analysis (F^- , $CH_3SO_3^-$, Cl^- , NO_2^- , Br^- , NO_3^- , PO_4^{2-} , SO_4^{2-} and $C_2O_4^{2-}$), salt standard stock solutions of lithium fluoride (Fluorochem) (sonicated for 1 hour), methane sulfonic acid ($\geq 99.0\%$, Sigma), sodium chloride ($\geq 99.5\%$, Sigma), sodium nitrite (analytical reagent grade, Fisher Scientific), potassium bromide (99.5%, Fisons), sodium nitrate (analytical reagent grade, Fisher Scientific), sodium phosphate monobasic ($\geq 99.0\%$, Fluka), sodium sulfate anhydrous (99%, Alfa Aesar), and oxalic acid ($\geq 99.0\%$, Sigma). Lithium bromide ($>99\%$, Acros Organics) was used for the Beijing anion winter analysis.

For cationic analysis (Li^+ , Na^+ , NH_4^+ , K^+ , Mg^{2+} , and Ca^{2+}), salt standards of lithium fluoride (Fluorochem), sodium chloride ($\geq 99.5\%$, Sigma), ammonium chloride (Laboratory Reagent Grade, Fisher Scientific), potassium bromide (99.5%, Fisons) were individually made up in *ca.* 50 ml of 18.2 M Ω Milli-Q deionised water (ELGA LabWater purification system). Calcium carbonate ($>99\%$, Acros Organics) was dissolved in 0.1 M HNO_3 in water (0.1N), eluent concentrate for IC (Sigma, UK). A bought standard of Mg^{2+} for IC (1000 ppm Mg^{2+} , Supelco) was also used. For the Beijing data, the $NaNO_3$ and KNO_3 were used for Na^+ and K^+ respectively.

Separate mixed anion and cation standards were produced from these stocks and serial dilutions were carried out to produce a set of calibration mixed salt standards at 100 (Delhi), 50, 25, 10, 5, 2.5, 1, 0.5, 0.25, 0.1, 0.05, 0.01 ppm. Individual stock solutions were produced to *ca.* 500 ppm of each of the inorganic salts (for Beijing), and 10,000 ppm (for New Delhi). This was conducted by weighing out the salts and the amount of 18.2 M Ω MQ water on a five decimal place balance, assuming a density of 1 g ml $^{-1}$ for the density of water. These stocks were used to create the mixed standards for the IC calibrations.

2.2.5 Ion chromatographic analytical procedure

A Dionex ICS-1100 ion chromatography system was used coupled with a Dionex AS-DV autosampler. For anion analysis, an eluent of 8 mM Na_2CO_3 and 1 mM $NaHCO_3$ in 18.2 M Ω Milli-Q deionised water was produced as the mobile phase, with an isocratic flow of 1.00 ml min $^{-1}$. A Dionex IonPacTM RFICTM AG14A Guard column (4 \times 50 mm) (Thermo) and Dionex IonPacTM RFICTM AS14A Analytical column (4 \times 250 mm) (Thermo) were used. A Dionex AERS 500 4mm RFICTM (Thermo) electrolytically Regenerated Suppressor was used and set to a current of 45 mA. The cell temperature and the column oven temperature were set to 35 $^{\circ}C$. The data collection rate was 5 Hz over a run time of 18 minutes.

For cation analysis, a 20mM solution of methane sulfonic acid ($\geq 99.5\%$, Sigma) in 18.2 M Ω deionised water was produced as the mobile phase. The guard and analytical columns used were the Dionex IonPacTM RFICTM CG12A Guard (4 \times 50 mm) (Thermo) and Dionex IonPacTM RFICTM CS12A Analytical (4 \times 250 mm) (Thermo), respectively. A Dionex CDRS 600 4mm RFICTM (Thermo) dynamically regenerated suppressor was used and set to a current of 59 mA. The cell and column oven temperature were set to 30 $^{\circ}C$, with a data collection rate of 5 Hz over a 20 minute run.

500 μl of sample (for both modes) were loaded into Poly Vials (Thermo) and the delivery speed of the samples was set to 4.0 ml min^{-1} , with a delay volume of 75 μl and a flush factor of 2. The loading mode was set to Loop Mode. The software used for peak identification and concentration quantification was Chromeleon 7.1 (Thermo).

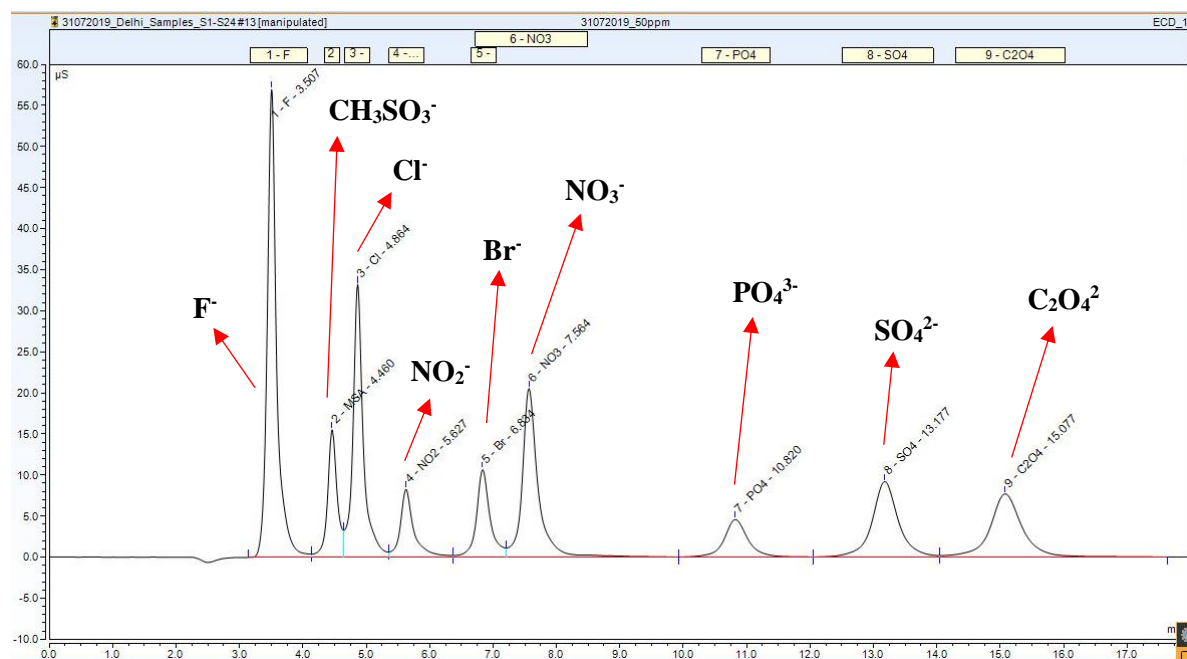


Fig. 2.4. Chromatogram of 50 ppm Salt Mix calibration standard for the Delhi Analysis in Anion Mode.

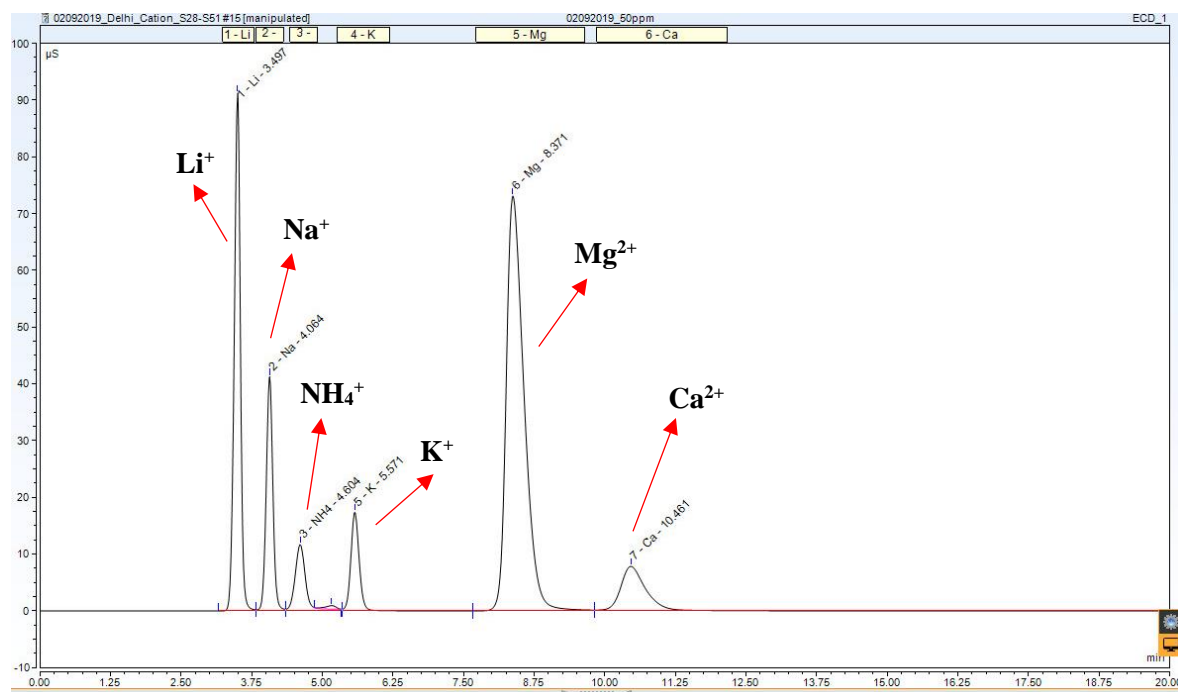


Fig. 2.5. Chromatogram of 50 ppm Salt Mix calibration standard for the Delhi Analysis in Cation Mode.

Example chromatograms of the calibration standards produced in section 2.2.4 are shown in Fig. 2.4 (50 ppm salts solution run in anion mode) and Fig. 2.5 (50 ppm solution of salt solution run in cation

mode). These chromatograms demonstrate that the ion chromatographic analytical method reported induces a good degree of separation. Although there is room for improvement, this was not needed for the scope of this work and was sufficient for PM_{2.5} aerosol IC analysis. Method development was however conducted in which quality control measures were introduced as to ensure an even higher degree of accuracy on the ion species quantification results reported in this thesis. These are described in section 2.2.6.

2.2.6 Quality Control

2.2.6.1 Calibration Correction

The salts bought-in from the supplier are not 100% pure, and during the synthesis of these salts in the manufacturing process, other ions may have leached into the final salt product (e.g. the calcium carbonate standard salt used for this thesis was 99+ % pure from Sigma Aldrich). Therefore, to correct for cross contamination, dilutions of 50 ppm of the individual salt standards were created and these were run separately to identify the instrument response contribution to the mixed anion and cation standards. To quantify the contaminant contribution to a particular peak, solutions which were a part of the mix were run three times consecutively on the IC. Fig. 2.6 shows an example chromatogram of NH₄⁺ in which a noticeable conductivity within the NH₄Cl salt contributes to the signals of the other cation peaks.

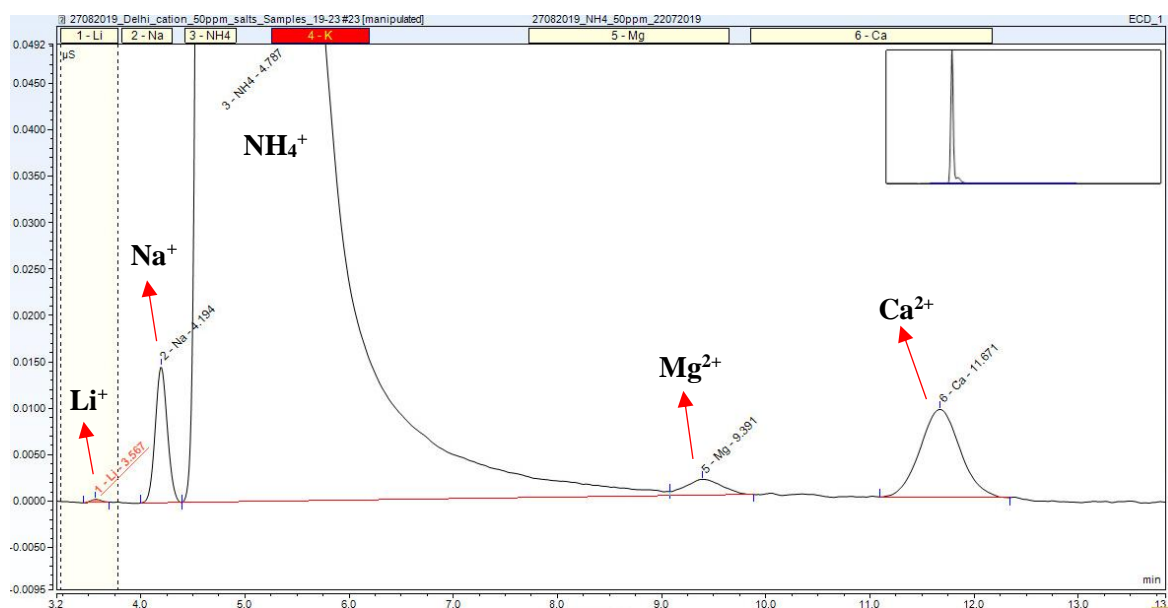


Fig. 2.6. 50ppm NH₄Cl IC Chromatogram demonstrating the contaminant ions present from the manufacturer.

The calibration peaks used in these analyses corresponded to 100 % (F⁻), 100 % (CH₃SO₃⁻), 99.5 % (Cl⁻), 96.8 % (NO₂⁻), 97.8 % (Br⁻), 97.4 % (NO₃⁻), 100 % (PO₄³⁻), 100 % (SO₄²⁻) and 100 % (C₂O₄²⁻). For the Beijing winter (BWIN) campaign a different salt mix calibration standard protocol was used with LiBr instead of KBr (LiBr was found to be challenging to weigh out due to its very ability to absorb water very quickly). For the BWIN anion mode, this correction step had not been developed and so calibration corrections were assumed at 100 %.

The cation mix standards salts for the Beijing analyses did not include LiF, however the Delhi mix did. Observing the LiF chromatograms, the cation suppressor has a much better Limit of Detection (LOD) associated with the cation mode analyses and therefore cross contamination from the LiF salt to the cation mode calibration was detected. For Beijing, the cation percentage contributions were 99.8 % (Na⁺), 99.7 % (NH₄⁺), 99.9 % (K⁺), 99.8 % (Mg²⁺) and 99.6 % (Ca²⁺), for cation analyses. For Delhi, the ion percentage contribution to actual peaks were 100 % (Li⁺), 99.4 % (Na⁺), 97.8 % (NH₄⁺), 99.5 % (K⁺), 99.8 % (Mg²⁺) and 99.6 % (Ca²⁺), for cation analyses. The measured peaks within calibrations were divided by these percentage values to gain the actual peak area for a corresponding ion.

A visual quality check of each calibration was conducted prior to concentration calculation using the Chromeleon 7.1 software. A new calibration was produced daily and was split into a low and high calibration using a quadratic fit with offset. The Chromeleon 7.1 software was used to semi-automate the calculation of sample solution concentrations.

2.2.6.2 Blank Correction

Blank analysis was conducted by completing the extraction protocol described in section 2.2.3 on blank pre-conditioned filter (6.2 cm² and 5.7 cm² for Delhi and Beijing analyses, respectively). Three blank repeats were conducted for the Delhi analyses. The blank concentration (*ppm*) results are presented in Table 2.2.

Four repeats of both the 2 ml and 5 ml extracts were conducted for the winter anion data. Two repeats were conducted for the winter cationic data set (year 2017). The filter extractions for the summer campaign were conducted a year later and the blank extractions were therefore repeated as to correct for the laboratory environment in which the filters were extracted in (year 2018). Three repeats were conducted in both 2 ml and 5 ml of 18.2 MΩ DI water. These three repeats were run on both anion and cation mode and the concentration values were used to correct the filter extracts from the summer campaign. For the Delhi analysis, 6 repeats were conducted for both anion and cation mode (year 2019).

In some cases, negative concentration values occurred due to blank concentration values exhibiting a larger concentration compared to the sample concentration calculated from the response of the instrument. This is problematic as it loses data points. This occurs because the blank concentrations are averaged across repeats (and therefore have an error associated with them) which means that if a response is calculated from an instrument and is close to the concentration of the blank filter response for that particular ion and filter, then the error margin overlaps and will result in the blank concentration being larger and therefore negative concentration being recorded. The blank concentrations required, were done with a maximum of 6 repeats which all originated from a single filter piece using a single calibration on IC analysis.

This may be due to a different proportion of ionic material in that specific filter piece in comparison to the 6 replicate blank extractions. The standard deviation (SD) of the replicate blanks is very good

Table 2.2. Blank concentrations for APHH IC analysis for extractions carried out between 2017 -2019 (ppm).

	Beijing 2017				Beijing 2018				Delhi 2019	
	2 ml		5 ml		2 ml		5 ml		5 ml	
	Avg.	%RSD	Avg.	%RSD	Avg.	%RSD	Avg.	%RSD	Avg.	%RSD
F⁻	-	-	-	-	-	-	-	-	<LOD	-
CH₃SO₃⁻	0.0632	115	<LOD	-	<LOD	-	<LOD	-	<LOD	-
Cl⁻	0.209	105	0.0797	106	0.116	27.6	0.0306	19.0	0.0363	-
NO₂⁻	0.0369	116	<LOD	-	<LOD	-	<LOD	-	<LOD	-
Br⁻	<LOD	-	<LOD	-	<LOD	-	<LOD	-	<LOD	-
NO₃⁻	0.109	13.4	0.0608	38.0	0.265	33.0	0.0522	20.6	0.0488	65.8
PO₄³⁻	6.00	23.7	2.40	32.3	3.26	5.11	1.74	2.74	2.32	5.38
SO₄²⁻	0.286	9.72	0.107	5.64	0.327	12.9	0.145	31.5	0.0916	18.3
C₂O₄²⁻	0.0298	123	0.0111	200	0.0761	173	<LOD	-	<LOD	-
Li⁺	-	-	-	-	-	-	-	-	0.00223	63.0
Na⁺	3.57	5.27	1.40	1.64	4.69	1.76	1.93	4.50	1.73	5.49
NH₄⁺	0.0850	6.49	0.0242	2.64	0.125	11.1	0.0523	6.81	0.123	38.0
K⁺	0.113	3.99	0.0370	11.1	0.162	3.03	0.163	112	0.0536	15.5
Mg²⁺	0.106	26.3	0.0399	17.7	0.0807	14.8	0.0311	20.1	0.0701	6.13
Ca²⁺	0.329	17.3	0.192	22.4	0.147	8.61	0.104	23.4	0.215	18.0

(Table 2.2), however these replicate extractions were all taken from a single pre-conditioned blank filter. It could be that (depending on the manufacturing process) the concentrations of specific ions are consistent in a section of a single piece of filter paper, but that the variance of filter ionic concentration changes throughout a pack of 25 sheets of Whatman QMA filter papers. Although testing this would be very expensive and wasteful, it may be suitable to re-assess the filter paper type before the next field campaign involving the HiVol sampler for filter samples which will end up being analysed using ion chromatography (as well as the other instruments that plan on using the filters). A Teflon filter may be an appropriate alternative. Other studies to have encountered contamination from commercial filters include Xu et al., (2020)²⁶⁷ who report Na^+ and PO_4^{3-} contamination from filters and suggest that filter washing might be an appropriate course of action to overcome contamination. Regarding the major ions Cl^- , NO_3^- , SO_4^{2-} and NH_4^+ , the LOD concentrations are sufficiently low for analysis of $\text{PM}_{2.5}$ samples in Delhi and Beijing. Although the %RSD is very high for Cl^- , $[\text{Cl}^-]$ values in ambient samples are up to two orders of magnitude above this. Regarding the minor ions which are of lower concentration in atmospheric ambient aerosol (such as Na^+ , Mg^{2+} , PO_4^{3-} and Ca^{2+}), Na^+ and PO_4^{3-} ions are of particular concern. If the focus of a study is on these ions, the QMA filters should be exchanged for another material (such as Teflon).

2.2.6.3 Recovery Correction

For the analysis of Delhi samples, the recoveries of individual ions from the filters were determined by cutting 6 pieces of Quartz Microfibre Filters QMA (Whatman, UK) using a circular biscuit cutter with an area of 6.2 cm^2 . These were pre-conditioned at $550 \text{ }^\circ\text{C}$ for *ca.* 5 hours in a furnace. For anion analysis, $100 \mu\text{l}$ of the 500 ppm standard mix was ubiquitously pipetted onto the blank filter pieces using a $200 \mu\text{l}$ Research Plus pipette (Eppendorf, UK). For cation analysis, $100 \mu\text{l}$ of 250 ppm standard mix was used. The filter piece was allowed to evaporate with gentle agitation until dry. The filter pieces were chopped-up into small squares using scissors and were transferred to a plastic sample vials (Sarstedt, Germany). 5 ml of $18.2 \text{ M}\Omega$ Milli-Q water (ELGA) was pipetted into the vials. The vials were lab-sealed and sonicated in an ultrasonic bath for 30 minutes at room temperature. The peak areas obtained for the anions were directly compared to a 10 ppm salt mix standard and the cation peak areas were compared to a 2.5 ppm salt mixed standard (responses averaged over three mixed standard runs), to assess the recovery of this extraction procedure. Six recovery tests were completed for both the anion and cation mixes.

A similar method was used for Beijing Recovery Analysis in which a hole punch with an area of 5.7 cm^2 was used. For anion analysis, a *ca.* 1000 ppm (of anions) mixed stock solution of each of NaCl , NaNO_2 , NaNO_3 , NaH_2PO_4 , NaSO_4 , $\text{C}_2\text{O}_4\text{H}$ and $\text{CH}_3\text{SO}_3\text{H}$ were produced. Recoveries were conducted in either 2 ml or 5 ml water to mimic sample extraction. For recoveries extracted in 2ml, 3 pieces of 5.7cm^2 blank pre-conditioned filter had $20 \mu\text{L}$ of the 1000 ppm mixture pipetted onto them. Three recoveries were also extracted in 5 ml DI water for which $50 \mu\text{L}$ of the anion mix was pipetted onto the filters. Samples were extracted in water for 60 minutes. Complete recovery for both these sets of recoveries would produce a final concentration value of 10 ppm anion mix which was

compared to a 10 ppm anion standard mix for direct comparison, for recovery analysis. For cation analysis, a similar protocol was taken although a mix of NaNO₃, NH₄Cl, KNO₃, CaCO₃ and Mg²⁺ (IC solution) was used. 40 μ l and 100 μ l of a 500 ppm cation mix was pipetted onto three filter pieces for the 2 ml and 5 ml recovery analyses, respectively. These were therefore also compared directly to a 10 ppm cation mixed standard for percentage recovery calculation.

Table 2.3. Recovery % correction values for the APHH Delhi (2019) and Beijing (2017) IC analysis.

Ion	Beijing (2 ml)		Beijing (5 ml)		Delhi (5 ml)	
	Average	%RSD	Average	%RSD	Average	%RSD
F ⁻	-	-	-	-	93.9	1.33
CH ₃ SO ₃ ⁻	99.2	1.86	99.4	0.829	95.2	2.63
Cl ⁻	97.7	1.93	98.8	0.868	96.0	2.15
NO ₂ ⁻	11.1	24.7	9.24	5.74	4.07	48.8
Br ⁻	-	-	-	-	89.3	1.21
NO ₃ ⁻	91.1	2.27	93.7	1.09	92.5	1.66
PO ₄ ³⁻	85.7	4.60	95.2	1.00	89.0	4.80
SO ₄ ²⁻	98.7	1.98	98.5	0.933	94.1	2.99
C ₂ O ₄ ²⁻	98.8	1.56	99.3	0.962	92.5	4.16
Li ⁺	-	-	-	-	97.8	0.374
Na ⁺	96.7	2.78	96.1	0.818	96.5	1.37
NH ₄ ⁺	91.2	0.573	90.5	0.953	93.9	0.472
K ⁺	94.9	1.39	94.6	0.398	95.2	0.633
Mg ²⁺	94.3	0.766	97.6	1.74	96.6	0.469
Ca ²⁺	63.1	5.73	76.9	2.09	56.4	7.79

Table 2.3 demonstrates that recovery results conducted in 2017 (Beijing 2 ml and 5 ml) as well as the recovery results conducted in 2019 (Delhi) present very good recovery for most ions as well as very good reproducibility. Very good reproducibility was also demonstrated for recoveries of most ions represented by low %RSD values in Table 2.3 for each set of analyses. Recovery analysis conducted in 2017 (Beijing 2ml and 5ml) however observed higher percentage recoveries generally. This was because a lower volume and higher concentration of ionic salt solution was pipetted onto the filter piece compared to the Delhi analysis (Delhi 5 ml). In using a lower volume, less solution make leak through the filter paper onto the foil work-station.

A relatively low recovery was however observed for Ca²⁺. Hall and Whitehead., (1970)²⁹⁴ suggested that Ca²⁺ may absorb onto plastic material from studies investigating calcium content in blood left in plastic autoanalyzer sample cups. Plastic is used throughout the IC analysis including for calibration standards. This may have an impact on the [Ca²⁺] within the plastic recovery sample vial, and although the calibration standards were also produced in plastic sample vials, calibration standards were present at much higher [Ca²⁺] concentrations. A much more likely reason for the lower Ca²⁺ recovery response is down to the use of quartz microfibre filters. Previous studies have suggested a much greater affinity of Ca²⁺ towards quartz material compared to other metallic cations^{295,296}. Work

by Wang et al., (2018)²⁹⁶ conducted a theoretical investigation into the interaction of aqueous Ca^{2+} and the oxygen atom on quartz (SiO_2) for the purposes of quartz activation with regards to mineral flotation and separation. Workers concluded that Ca^{2+} in the medium of aqua ligands ($\text{Ca}(\text{H}_2\text{O})_4$ and $\text{Ca}(\text{OH})(\text{H}_2\text{O})_3$) may effectively adsorb into an SiO_2 structure. This occurs via the electron donation of the aqua ligands surrounding Ca^{2+} to the oxygen of SiO_2 . Workers go on to mention that this occurs through a $\text{Ca}^{2+} 3^d \rightarrow \text{O} 2^p$ hybridised bond which induced an adsorption strength was closely related to Ca-O covalent bond formation. Hydrated Ca^{2+} is very likely to be the dominant form of Ca^{2+} within the aqueous cation mixed recovery solution and therefore may effectively adsorb into the porous QMA filter producing Ca-O interactions with the filter paper. This would in turn reduce the recovery concentration achieved of Ca^{2+} . Moreover, it may be argued that the method of recovery test used in this thesis may be inappropriate for Ca^{2+} . Aerosol samples collected from Beijing and Delhi were often dark brown and black from black carbon. If black carbon had covered the filter sufficiently enough, a lower surface area of the quartz filter piece would be presented to the aqueous solution and therefore less Ca^{2+} would be adsorbed into the filter piece during extraction. This is not representative of a pre-conditioned filter piece with almost pure ionic cation solution pipetted on.

Br^- recovery values were not calculated for the Beijing analysis, but were calculated for the Delhi extractions. These were then used for the APHH Beijing correction. Furthermore, the repeat of blank analyses between the sample batches was also necessary, as the conditions of the lab may have changed over the course of APHH sample analysis. The recovery test for NO_2^- was completed separately using the identical extraction method as with the anion standard mix. Three repeats of the NO_2^- recovery were completed, which was compared to a 10ppm NaNO_2 standard. The original result when conducting this recovery as part of the standard mix produced a recovery value of 4.07% (Table 2.3). When running the NO_2^- standard separately a recovery of 88.0% (4.2% %RSD) was obtained. It is suspected that the acids methane sulfonic acid and oxalic acid in the standard mix interact with the NO_2^- on the filter paper, producing HONO which volatilizes off during the water evaporation stage, dramatically reducing the amount of NO_2^- . Therefore, care should be taken when incorporating NO_2^- into mixed standards and for ambient sample mixtures.

2.2.6.4 Limit of Detection

The limit of detection (LOD) is defined as the lowest concentration at which a measurement (here a gaussian IC conductivity signal) may be reliably detected by a specific analytical method and is statistically different in comparison to the blank (with a confidence level of 99%)^{297,298}. The purpose of this parameter in analytical chemistry is to try and minimise the presence of false positive and false negative values in data sets²⁹⁸. The Limit of Quantification (LOQ) is defined as the lowest detection response possible before the reading should be treated as qualitative, with unknown uncertainty in the quantitative value²⁹⁸. The quantification level is specified as the standard deviation of signals from consecutive replicates multiplied by ten, and is method dependent²⁹⁷. There are several possible methods to calculate the LOD and LOQ^{299,298}, and no definite decision has been reached to date as to which method is best used^{297,298}.

The method of LOD and LOQ calculations used for the Delhi and Beijing IC analyses constituted running a calibration of mixed salt standards, followed by 10 replicates of a low concentration standard²⁹⁷. The exact concentrations of the ions in the replicates was calculated using the calibration, and the standard deviation of these 10 replicate concentrations was calculated and multiplied by three (to obtain LOD in Eq. 2.1) or 10 (to obtain LOQ in Eq. 2.2). The noise of the instrument can be measured over this sampling period and is reflected in the standard deviation of signal response over these replicates for each individual ion. Multiplying this standard deviation by three thus gives a signal response above which a signal can be identified as a peak.

$$LOD = StDev (10 \text{ replicates}) \times 3$$

Eq. 2.1. Calculation used to conduct LOD analysis for the APHH IC analysis.

$$LOQ = StDev (10 \text{ replicates}) \times 10$$

Eq. 2.2. Calculation used to conduct LOQ analysis for the APHH IC analysis.

The concentration of standard was chosen based on adequate response of the instrument for all species in the mixed standard at the time of LOD analysis and were different for anion and cation analyses. A fresh LOD calculation was conducted before the analysis of each campaign set of samples, as the state of the instrument and the relative response given may fluctuate over time.

In this work a 0.25 ppm salt mix was used for the 10 replicates in the anion LOD and LOQ analysis for the Beijing winter and summer campaigns. For the cation LOD and LOQ analyses for the Beijing campaign, detection limits were much lower and a 0.05 ppm salt standard was used as the replicate standard here. The Beijing winter cation LOD values were also taken for the summer analysis. Delhi analysis occurred a year after the Beijing work. LOD and LOQ samples were significantly higher for the Delhi analysis and a salt standard of 2.5 ppm was used for the replicates. The LOD and LOQ values established for the APHH Delhi and Beijing IC analyses are shown in Table 2.4 and Table 2.5, respectively. The percentage of samples taken for which ions were observed to be above LOD and LOQ are also presented.

The analysis of the Beijing winter filters, summer filters and Delhi filters were conducted in 2017, 2018 and 2019, respectively. Observing Table 2.4 and Table 2.5, generally for each ion, the LOD and LOQ values increase from BWIN < BSUM < DPEM + DPOM analyses. In some instances, LOD and LOQ values were very high (especially for Delhi). In some instances, LOD and LOQ are exceptionally high, such as for NO₃⁻ in Table 2.4 which demonstrates concentrations of 0.56 ppm

Table 2.4. LOD and LOQ concentrations (ppm) determined for the Delhi filter analysis in 2019 (with % of samples for each ion which where over the LOD and LOQ).

		F ⁻	CH ₃ SO ₃ ⁻	Cl ⁻	NO ₂ ⁻	Br ⁻	NO ₃ ⁻	PO ₄ ³⁻	SO ₄ ²⁻	C ₂ O ₄ ²⁻	Li ⁺	Na ⁺	NH ₄ ⁺	K ⁺	Mg ²⁺	Ca ²⁺
DPEM	LOD	0.17	0.19	0.15	0.27	0.29	0.56	0.31	0.23	0.30	8.9E-04	2.1E-03	3.5E-03	2.6E-03	6.3E-03	5.3E-03
	% > DL	100	2.9	100	8.8	2.9	100	100	100	100	61.8	100	100	100	100	100
	LOQ	0.58	0.62	0.50	0.91	0.96	1.86	1.1	0.75	1.0	3.0E-03	6.9E-03	1.2E-02	8.7E-03	2.1E-02	1.8E-02
	% > QL	17.7	0	100	0	0	100	100	100	26.5	8.8	100	100	100	100	100
DPOM	LOD	0.17	0.19	0.15	0.27	0.29	0.56	0.31	0.23	0.30	8.9E-04	2.1E-03	3.5E-03	2.6E-03	6.3E-03	5.3E-03
	% > DL	17.8	23.8	100	27.7	7.9	100	100	100	70.3	100	100	93.1	100	100	100
	LOQ	0.58	0.62	0.50	0.91	0.96	1.86	1.05	0.75	1.00	3.0E-03	6.9E-03	1.2E-02	8.7E-03	2.1E-02	1.8E-02
	% > QL	1.0	15.8	86.1	16.8	2.0	80.2	96.0	100	23.8	20.8	100	93.1	100	100	100

Table 2.5. LOD and LOQ concentrations (ppm) determined for the Beijing winter and summer filter analysis conducted in 2017 and 2018, respectively (with % of samples for each ion which where over the LOD and LOQ).

		F ⁻	CH ₃ SO ₃ ⁻	Cl ⁻	NO ₂ ⁻	Br ⁻	NO ₃ ⁻	PO ₄ ³⁻	SO ₄ ²⁻	C ₂ O ₄ ²⁻	Li ⁺	Na ⁺	NH ₄ ⁺	K ⁺	Mg ²⁺	Ca ²⁺
BWIN	LOD	-	0.054	0.056	0.026	0.056	0.044	0.081	0.047	0.066	-	5.1E-03	2.9E-03	4.2E-03	1.6E-03	1.5E-02
	% > DL	-	50.8	99.2	43.6	10.5	100	100	99.2	76.6	-	100	91.9	100	100	100
	LOQ	-	0.18	0.19	0.087	0.19	0.15	0.27	0.16	0.22	-	1.7E-02	9.8E-03	1.4E-02	5.5E-03	5.1E-02
	% > QL	-	20.2	96.8	21.8	0	98.4	100	99.2	25.8	-	100	91.9	100	100	100
BSUM	LOD	-	0.10	0.062	0.092	0.055	0.048	0.20	0.12	0.13	-	5.1E-03	2.9E-03	4.2E-03	1.6E-03	1.5E-02
	% > DL	-	47.5	99.5	14.3	8.2	100	100	100	93.4	-	99.5	96.9	100	100	99.5
	LOQ	-	0.34	0.21	0.31	0.18	0.16	0.65	0.40	0.43	-	1.7E-02	9.8E-03	1.4E-02	5.5E-03	5.1E-02
	% > QL	-	10.2	93.9	0	0	100	100	100	37.8	-	99.5	96.4	99.5	10	99.5

and 1.86 ppm, respectively. These are exceptionally high LOD and LOQ values and are problematic as they have the potential to lose detail within time-series calculations. Furthermore, on occasion very clear peaks were observed within samples which were officially < LOD and therefore improvements to the method of LOD and LOQ calculation must be applied in future. A pseudo LOD/2 value for each ion was used to replace readings <LOD. This considered the fact that although a sample concentration as not detected, it is likely that the species may still have been present in aerosol.

In evaluation of using this calculation method, a fundamental issue arises regarding relative peak response between ions in mixed standards. The LOD and LOQ calculations presented here rely on the lowest possible concentration of ion to be used. The mixed standards however observed varying responses for different ions (as seen in Fig. 2.4 and Fig. 2.5). For ions which demonstrated larger responses, the StDev values are inherently larger and therefore the LOD and LOQ values may be overestimated. In future salt mixes should be produced with calculated concentrations as to acquire a similar signal response for each peak, followed by dilution.

$$\frac{3 \times S_{y/x}}{\text{Slope}} = LOD$$

Eq. 2.3. LOD calculation using standard error of the calibration slope.

In addition, quality of data would be proved if the LOD and LOQ calculations were conducted more frequently. Conducting the method carried out here would be costly to conduct more frequently.

Other methods however exist which include using a calibration curve and the standard error of the slope^{298,299} as shown in Eq. 2.3. Where $S_{y/x}$ is the y -estimate standard error for a linear fit and the slope is the gradient. This method is however most suited to ions which demonstrate a linear fit calibration and most ions analysed on IC give a slight quadratic curve.

Very high LOD and LOQ values may also be down to column degradation. As the system is used and the column ages, the LOD values increase. This is most likely due to the wear of the instrument, particularly the degradation of the anion column. In addition to the 328 loaded Beijing PM samples and 142 Delhi filter samples, extensive use of the instrument was required for the NO3ISOP campaign at the SAPHIR smog chamber in Jülich (chapter 6). Even though the IC system had undergone the recommended cleaning procedure (Thermo Scientific IC Column Manual) in-between the Beijing and Delhi extractions, the PM samples from Beijing and Delhi are particularly heavily loaded with PM and it is therefore likely that column degradation of the IC system led to the decreased quality in LOD over time for this particular column²⁹⁷.

This degradation can also be witnessed in an MQ water blank baseline (Fig. 2.7). The black baseline is the response from the IC instrument of 18.2 MΩ MQ water back in 2017, and the blue line is the

MQ water baseline from 2019, around the time of the analysis of the Delhi samples. The blue baseline is much noisier and therefore delivers a reduced quality baseline than the original non-worn-out column before all the PM samples were put down it. The background is set to zero using the 'AutoZero' function on Chromeleon. The anion column and suppressor have recently been replaced for future work on the instrument. In evaluation of the work conducted during the NO3ISOP campaign which encountered huge difficulties with LOD values, replacement of the column (and perhaps suppressor) may have been useful for that particular campaign after the loaded Beijing filters had been run on the system.

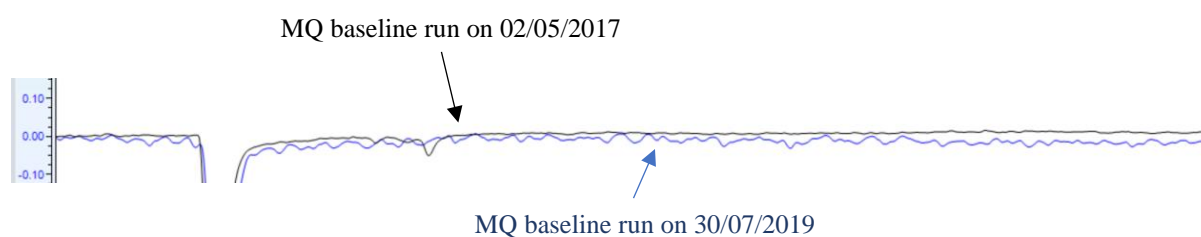


Fig. 2.7. Column degradation of IC overtime producing a noisier baseline.

The cation LOD values however remained consistently very low throughout. Table 2.4 and Table 2.5 shows that almost all of the cation data is above both LOD and LOQ across the campaigns. For the major anions (Cl^- , NO_3^- , PO_4^{2-} , SO_4^{2-}) that are generally at much higher concentration in these polluted megacities, the majority of samples are also above the LOD and LOQ. For the minor ions (F^- , CH_3SO_3^- , NO_2^- , Br^- , and $\text{C}_2\text{O}_4^{2-}$) however these higher LOD and LOQ results pose more issues and potentially mask interesting activity of these species in the time series. For example, the DPOM data demonstrated 17.8 % (F^-) and 7.9% (Br^-) of readings above the LOD which is very low.

In addition, some ions demonstrate 100% of measured values $>$ LOD, although a very low proportion of values $>$ LOQ. For example, in the DPEM data, F^- (DPEM) demonstrates an obvious diurnal pattern (Chapter 3) with peaks found during daytime hours and troughs at night which is consistent with an expected anthropogenic industrial source. Only 17.7% of these values however are above LOQ, despite the obvious trend seen. Despite the large LOQ for some ions, obvious diurnal patterns may still be observed and if all values below LOQ are not considered, significant loss of detail is lost in time series.

Another critique of the LOD and LOQ calculations in this study is that according to the Environmental Protection Agency (EPA), measuring the standard deviation across replicates of a calibration set standard officially gives the Instrument Detection Limit (IDL), and the actual detection limit should ideally involve the sonicated blank filter to account for matrix affects for the method detection limit. Therefore, to improve the LOD measurement in future, a pre-conditioned blank filter portion could be sonicated and filtered to produce a diluting solution which is consistent

(applying the matrix artefact) and used to produce the mixed standard. Although, as discussed in sections 2.2.6.2 and 2.2.6.3, the blank Whatman QMA filter may potentially demonstrate large variance in ionic loading in-between filters which would render this method inappropriate for the filters used in this study.

After all work was completed the anion column and suppressor were changed for the benefit of future users. Another set of LOD runs (using the same calculation method) was completed for the anion mode. Table 2.6 shows the LOD values using the old column and suppressor compared to the LOD values after these parts of the instrument were replaced. The improvement factor is also displayed.

Table 2.6. Table showing the anion LOD (ppm) values before and after replacement of the column and suppressor.

	F ⁻	CH ₃ SO ₃ ⁻	Cl ⁻	NO ₂ ⁻	Br ⁻	NO ₃ ⁻	PO ₄ ³⁻	SO ₄ ²⁻	C ₂ O ₄ ²⁻
LOD Before	0.17	0.19	0.15	0.27	0.29	0.56	0.31	0.23	0.30
LOD After	0.015	0.078	0.026	0.020	0.033	0.071	0.11	0.064	0.066
Factor	11.99	2.38	5.85	13.32	8.68	7.85	2.83	3.52	4.53

As shown in Table 2.6, on changing the anion suppressor, the LODs had vastly improved, changing by an order of magnitude for F⁻ and NO₂⁻, and changing by a factor of 5.85, 7.85, and 3.52 for Cl⁻, NO₃⁻, and SO₄²⁻, respectively.

2.2.7 Calculation Method Development

The method development of calculating the atmospheric concentrations of ionic species within PM_{2.5} is outlined in this section. Protocol schematics as to how the atmospheric ionic concentrations were calculated (in addition to quality control measures) are outlined for which an improvement and evaluation is discussed for the consecutive schemes. This section develops on previous methods which have been completed by workers at the University of York.

2.2.7.1 Iteration 1: Initial Atmospheric Concentration Calculation: (Initial Calculation)

Once calibration standards had been produced and run on the IC, the peaks were integrated using the Chromeleon 7 software. The peak areas were recorded and a simple linear regression was fitted for the calibration. The calibration was also forced through the origin in the assumption that no analyte would give no signal. In addition, some calibrations only involved three points (and one calibration for the Beijing winter cation dataset only involved two points in this calculation). The averaged blank peak area ($\mu\text{S}\cdot\text{min}$) was calculated and this was deducted from the sample peak area. The blank corrected peak area was passed through the calibration producing a solution concentration (ppm). This solution concentration was multiplied by the volume of water which had been used to extract the filter sample in, in order to calculate the mass of ionic species in μg (as $\text{ppm} = \mu\text{g ml}^{-1}$). This therefore gave the mass of ionic species which was present on the filter piece (μg).

The volume of air sampled was calculated by dividing the area of the filter piece segment by the area of the HiVol sampling cassette (the area of filter paper that was exposed to the air flow) and

multiplying this by $80 \text{ m}^3\text{h}^{-1}$ (the flow rate of the HiVol) and the time of sampling in hours. The mass of ionic species was then divided by the volume of air which had passed through the filter segment, to obtain the atmospheric concentration.

Recovery correction was completed as described in section 2.2.6.3. The instrument response average peak area ($\mu\text{S}\cdot\text{min}$) from these recoveries (three replicates) were averaged. The blank averages were then deducted from the recovery average. This peak area was then compared to the reference standard (average over three replicates) to calculate the percentage of material lost through the process (and therefore the recovery). The atmospheric concentration calculated was then divided by the recovery percentage to get the final atmospheric concentration of ionic species in $\text{PM}_{2.5}$.

2.2.7.2 Iteration 2: Atmospheric Concentration Calculation 2 (Improved Calculation)

On evaluation of calculation 1, there were several fundamental improvements that could be made. Firstly, it is incorrect to force the calibration equation through zero. This is to do with the LOD, and the fact that zero peak area may be present for situations in which an analyte may be present but simply at a lower concentration than the LOD. Therefore, this was rectified in calculation 2 and a constant was added to the linear regression.

The calibration used in iteration 1 was further inspected and it was noticed that the calibration gradient may change throughout the calibration range. To increase the accuracy of the procedure, each calibration was split at a pivot concentration. The pivot concentration was decided from visually inspecting the calibration linear squared regression coefficient results for the high and low ranges. The original non-split calibration run on IC on the 2nd May 2017 as shown in Fig. 2.8A had a gradient of $0.2028x$. The gradient of the high and low ranges were $0.2054x$ (Fig. 2.8B) and $0.1632x$ (Fig. 2.8C), respectively. Therefore, a relatively large percentage difference is observed in gradients which is directly applied to sample concentrations when these are calculated from the peak area response of the IC instrument.

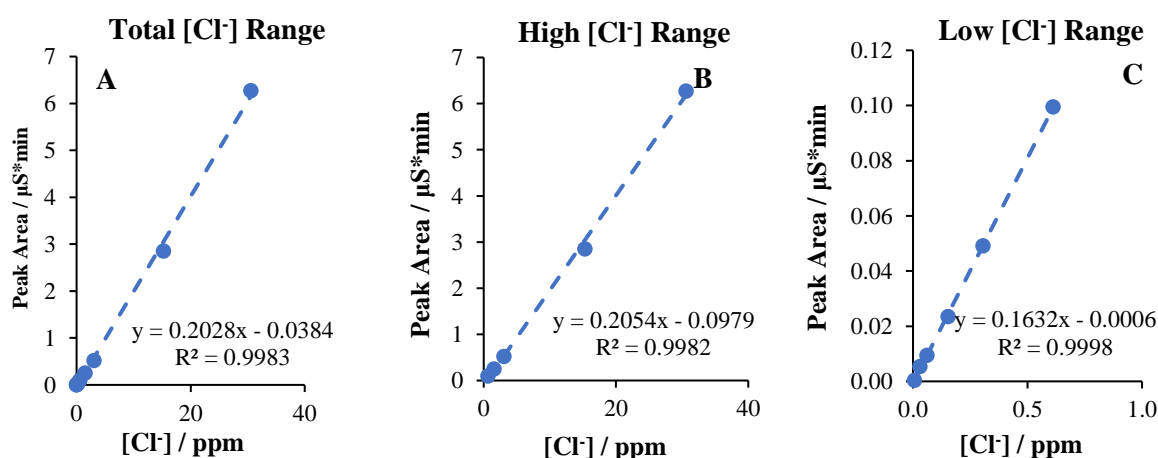


Fig. 2.8. Change in calibration gradient dependant on region of calibration concentrations chosen to demonstrate how the gradient changes at different sections of a calibration curve for IC analysis.

In calculation 1, there were also some calibrations which had only used three concentration points. These calibrations were spot check calibrations throughout a run to make sure that the calibration had not shifted but were used as calibration results in iteration 1 as they were closer to later samples. It was however decided that a three-point calibration for IC was inappropriate, as any anomaly within the calibration would skew the calibration greatly for numerous samples. Therefore, any three-point calibrations were discarded.

Another difference within iteration 2 compared to 1 is that the percentage recoveries of each species values were applied to the sample's blank corrected peak area, as opposed to the final atmospheric concentration. This was implemented as the recovery is directly associated with the solution of sample analyte as opposed to the final value. Moreover, the calculation of recovery analysis changed also. In iteration 2, each individual recovery repeat had the average blank peak area subtracted. These were then divided by the average peak area of the 3 repeats of the reference solution to give three recovery percentage values. These were then averaged for each ion. In addition, the cross-contamination correction as discussed in section 2.2.6.1 was also applied to the calibration concentrations.

In between producing calculation 2 and 3, an intercomparison was conducted between UoY and UoB to try and decipher the source of in poor comparability. UoY and UoB exchanged filter samples run one-another's samples on each other's IC instruments. On evaluation of this exercise, the importance of using a quadratic function in the calibration was highlighted along with comparing one another's samples through the means of a weighted average. After the inter-comparison and discussion with UoB, the final calculation procedure was produced for atmospheric PM_{2.5} ion concentration determination (iteration 3).

2.2.7.3 Iteration 3: Atmospheric Concentration Calculation 3

It was determined that the calibrations used in calculations 1 and 2 could be improved by applying a quadratic fit (with offset) to the calibrations, as opposed to using a linear regression (with offset). This is because the nature of IC analyses (for anion analyses) causes IC calibrations to observe a non-linear trend²⁶¹. The basis of this non-linearity occurs from the suppressor. Suppression of solutions during analysis causes the anions within the solution to convert to the respective acids (i.e. Cl⁻ converts to HCl). The anion is detected by the conductivity detector in the IC, whereas the acid is not. The mobile phase (IC eluent) is basic during anion analysis. At lower amounts of anion, less acid is produced from suppression, and therefore a larger proportion of the anion is detected within lower concentrated solutions. When anion species increase in concentrations, more acid is produced from suppression, and therefore the pH of the solution decreases. As this occurs, the acid produced is less susceptible to dissociation back into the anion (conjugate base anion), and therefore a lower percentage of anion is detected for higher concentration solutions. Therefore, this produces an expected calibration trend as shown in Fig. 2.9A for which a quadratic function should be fitted.

Many of the calibrations observed during the analysis of the Delhi and Beijing filter samples followed the expected calibration shape as seen in Fig. 2.9A. Some other calibrations however showed a positive quadratic (Fig. 2.9B). Observing the APHH IC calibrations at a closer level however, demonstrated that some calibrations show low coefficients for x^2 of quadratic regressions for which positive quadratics may be due to the uncertainty within the instrumental technique. In addition, although quadratic calibrations were implemented, many of the calibrations conducted were ultimately linear. Therefore, for iteration 3, the contamination correction, split calibration (after visual inspection and omission of any anomalies) and quadratic regression were all implemented.

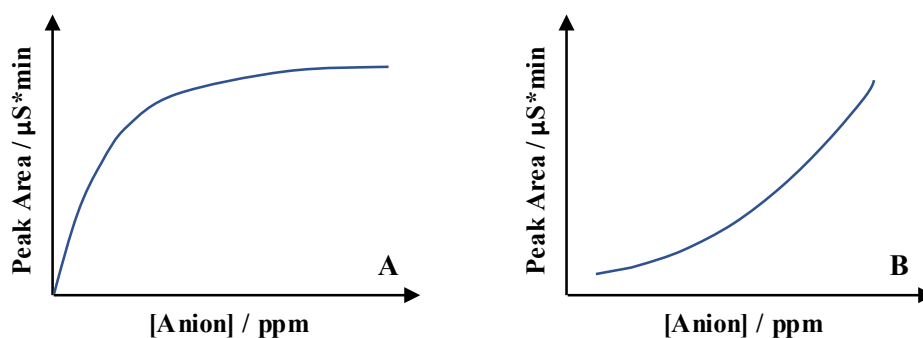


Fig. 2.9. Quadratic calibration shapes observed during the APHH IC analysis.

Another alteration in the calculation was the method of blank and recovery application. In calculations 1 and 2, the peak areas were averaged for blank analyses and this was subtracted from the peak areas of the sample for blank correction. The calculation of the recovery was also conducted by obtaining a peak area response from the instrument, subtracting the blank response ($\mu\text{S} \cdot \text{min}$) and comparing this response to the response of a reference solution. This was an inaccurate method, as the flux of the instrument may change over the course of weeks during data collection. This method was substituted by a much more accurate approach in which the blank runs and recoveries of species were calculated in terms of the concentrations of control solutions. The concentrations of species within the blanks, recovery run samples and reference samples were first calculated from an identical calibration. The average concentrations of the blanks were calculated and were deducted from the sample concentration for blank correction (in ppm). The recovery protocol involved averaging the concentrations of species within recovery runs, subtracting the average concentration of species from the blank analyses, and then comparing this value to the concentration of the reference standard (which was also put through the calibration).

The LOD was also calculated and implemented to further improve the data from iterations 1 and 2. After blank and recovery correction, the sample concentration was compared to the LOD. If the concentration was below the LOD value, then a pseudo value of $\text{LOD}/2$ was used as the sample solution concentration for a species for a specific sample.

2.2.7.4 Comparison and Evaluation of Calculation Methods

The work presented in this section was done in order to try and improve and develop the IC methods which had already been established at the UoY. The results from each iteration are shown in Fig. 2.10 for Cl^- , NO_3^- , SO_4^{2-} and NH_4^+ for the BWIN campaign (as an example). The time series shown in Fig. 2.10 are represented by calculation 1 (Pale Green), Calc 2 (Pale Orange), Calc 3 (Black) and the AMS (Blue). Calc 3 incorporates the best data practice and was the calculation used for the IC analysis between the Beijing and Delhi APHH Campaigns. The grey vertical lines shown in each time series also shows the times of midnight.

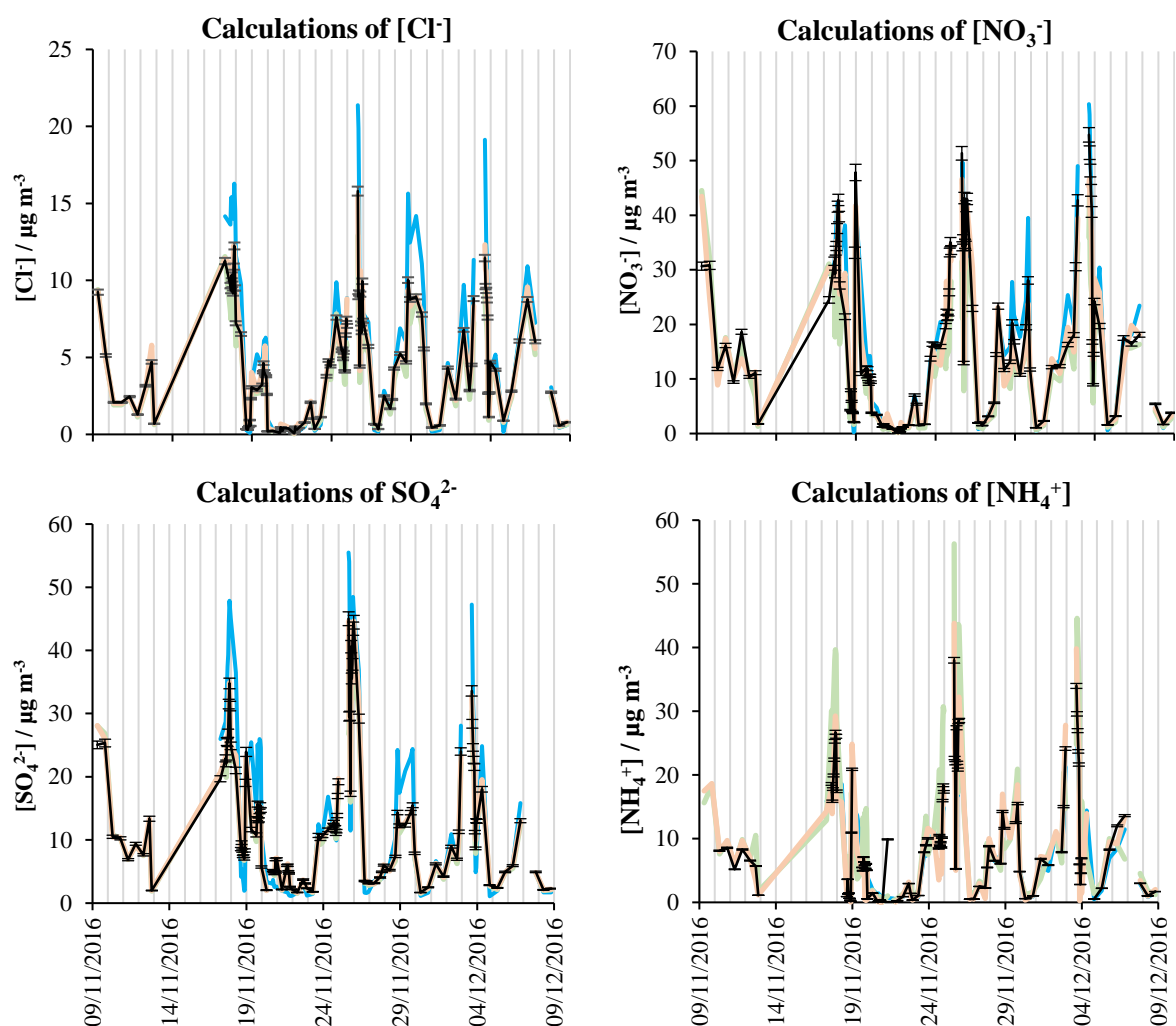


Fig. 2.10. Change and improvement in time series through iteration 1 (pale green), iteration 2 (pale orange), iteration 3 (black) and comparison of time series to the AMS (bright blue). The associated errors for iteration 3 are shown as black error bars in the y-axis. These errors are calculated using the calculation described in section 2.2.8. The grey vertical lines represent the time of 00:00 for the respective date shown on the x-axis.

Observing the time series of each species in Fig. 2.10, generally very little change is demonstrated between the three calculation iterations overall. The major differences between the IC and AMS time series occur during pollution episodes, and therefore the size, chemical composition and particle morphology is likely a cause of the difference, as the IC and AMS have different advantages and disadvantages in their measurement techniques. This is further explained in chapter 3.

A table comparing the R^2 linear regression correlation coefficients between each calculation and the AMS results, as well as showing the comparative average and SD values for each species is shown in Table 2.7. The three calculations were completed for the identical peak areas given by the IC instrument. Table 2.7 shows very good R^2 for this dataset between all three calculations and the AMS dataset. Very little improvement is seen across the three calculation iterations regarding the R^2 correlation coefficients in Cl^- , NO_3^- and NH_4^+ . For Cl^- , and NO_3^- , the R^2 correlation improves by 1 unit of R^2 from calc 1 to calc 2, and calc 2 to calc 3. The SO_4^{2-} R^2 does not change between calc 1 – calc 2 and decreases by 1 unit for the calc 3 iteration. The largest improvement for the linear regression correlation coefficients between the IC and AMS is seen for NH_4^+ , which improves from calc 1 ($R^2 = 0.80$) to calc 2 ($R^2 = 0.87$) to calc 3 ($R^2 = 0.93$). Therefore, by implementing the good practices of data analysis explained in this chapter, very little change occurs to the correlation between the IC and AMS for Cl^- , NO_3^- and SO_4^{2-} , although an improved change is noted between the calculations of the $[\text{NH}_4^+]$.

Table 2.7. Comparison of Weighted Averages ($\mu\text{g m}^{-3}$), StDevs ($\mu\text{g m}^{-3}$) as well as R^2 regression analysis between calculation iteration and the AMS.

		Calculation 1	Calculation 2	Calculation 3	AMS
Cl^-	Average	3.71	4.07	4.04	5.12
	StDev	3.07	3.83	3.64	5.44
	R^2	0.91	0.92	0.93	1.00
NO_3^-	Average	11.05	12.59	11.98	14.66
	StDev	11.19	13.59	14.92	15.85
	R^2	0.90	0.91	0.92	1.00
SO_4^{2-}	Average	9.08	9.54	9.23	11.82
	StDev	9.85	10.60	10.62	15.03
	R^2	0.89	0.89	0.88	1.00
NH_4^+	Average	7.62	7.71	6.01	7.39
	StDev	13.44	10.50	9.44	7.82
	R^2	0.80	0.87	0.93	1.00

$$\frac{\sum \text{Filter Time (hours)} \times \text{Concentration of ion } (\mu\text{g m}^{-3})}{\sum \text{Filter Time (hours)}}$$

Eq. 2.4. Weighted Average Calculation for Ionic Species.

Averages have also been shown in Table 2.7 between the different calculation improvements. AMS values were averaged to the filter times and the averages shown are weighted. This therefore corrects for the gaps in time in which the HiVol was not sampling (i.e during a filter change, when a filter blocked and the HiVol switched off automatically, or where data is missing etc.). The calculation used to establish the mean filter time - weighted averages is shown in Eq. 2.4.

For Cl⁻, NO₃⁻ and SO₄²⁻, averages of calculation 2 were the closest to the AMS and for NH₄⁺ iteration 1 was closest. This is unexpected although it is difficult to compare the improvements in averages with the AMS, predominantly because the AMS measures PM₁ (chapter 3) and because the difference in averages between calculations is so small. Therefore, calculation 3 which incorporates the best analytical practice out of the 3 iterations was used to calculate the ionic species concentrations within PM_{2.5} in Delhi and Beijing in this thesis.

Therefore, it may be concluded that although improvement is seen with respect to the R² values, this is minimal through the calculations. Therefore, the basic method (iteration 1) is therefore a good indication of the quantity of ionic PM_{2.5} species.

Finally, the contamination contribution calculation method as described in section 2.2.6.1 should be improved in future. Using peak area as a basis to calculating percentage contamination contribution has significant relative error associated with instrument response flux. The very low responses for ions (especially in anion mode) are far below detection limit and the overall contribution is very negligible. Moreover, whether this step is necessary is questionable.

2.2.8 Calculation of IC Errors

An appropriate calculation of errors was conducted for iteration 3 of the atmospheric concentration calculation of ionic species within PM_{2.5} from filter samples in an Asian megacity.

2.2.8.1 IC Sample Concentration Error

The error given by the IC instrument was measured by recording the %RSD of the calibration curve (calculated by the IC Chromeleon 7 software). It is known that the %RSD is equal to the SD (δA_1) divided by the mean (concentration value, A), multiplied by 100%, as shown in Eq. 2.5. This may be re-arranged to find the SD error associated with a specific concentration value (δA_1) as shown in Eq. 2.6.

$$\%RSD = \frac{\delta A_1}{[A]} \times 100$$

Eq. 2.5. Calculation of the %RSD, where δA_1 is the SD error associated with a specific IC solution concentration and [A] is the IC solution concentration.

$$\delta A_1 = \frac{\%RSD}{100} \times [A]$$

Eq. 2.6. Calculation of the Absolute Error of the Ion Concentration given by the IC using the %RSD value from the calibration curve as reported by the Chromeleon 7 Software, where δA_1 is the SD error associated with the concentration calculation of a specific IC sample; %RSD is the Relative SD associated with a specific sample; and [A] is the IC concentration in $\mu\text{g ml}^{-1}$ of a specific sample.

The %RSD was recorded for the High and Low calibration curves for each batch of samples (section 2.2.7). Depending on each individual IC solution concentration (associated with either the High or Low calibration %RSD error), the associated %RSD was selected and was multiplied by the

individual sample solution to work out calibration absolute error (SD, δA_1) for a specific sample, given in $\mu\text{g ml}^{-1}$. This is summarised in Eq. 2.6 where %RSD is the error of the calibration curve for a specific ion as reported by the Chromeleon 7 IC software; $[A]$ is the concentration of a specific ion within the aqueous IC samples solution calculated by the IC Chromeleon 7 Software; and δA_1 is the absolute SD error (in $\mu\text{g m}^{-1}$) of the calculated ion concentration value from the IC.

The reproducibility of the IC instrument across a batch of samples under a specific calibration was measured by recording the concentration response of a mixed standard solution of lowest concentration possible (separately for both anion and cation solution mixes) across 10 consecutive repeats. The SD (in $\mu\text{g ml}^{-1}$) was calculated for each ion across these ten repeats and was taken as the estimated absolute error of the instrument reproducibility. This error is referred to as δA_2 .

To propagate the calibration error (which also incorporates random error in pipetting of standard solutions) and the instrument reproducibility error (from the fluctuation of the IC instrument), the two sets of absolute errors (as SD) were added together, to give the total instrument (and therefore IC liquid sample concentration) error. This is summarised in Eq. 2.7 where δA_1 is the absolute calibration error; δA_2 is the absolute instrumental flux error; and δA is the combined IC sample concentration error.

$$\delta A = \delta A_1 + \delta A_2$$

Eq. 2.7. Summation of the calibration error (δA_1) and reproducibility error (δA_2) to give the total concentration error of ionic species from a calibration (δA).

2.2.9 Blank Subtraction Error

After calculating the sample concentration in iteration 3, blank correction is applied by subtraction of the blank concentration from the IC sample solution concentration as shown in Eq. 2.8, where B is the blank corrected value, A is the initial IC concentration and $BLNK$ is the average of the blank under a specific volume of water.

$$B = A - BLNK$$

Eq. 2.8. Blank subtraction step in which the concentration of ionic species from the blank extracted filter ($BLNK$) is subtracted from the ion concentration, (A), to produce the blank corrected concentration (B).

The error of the blank subtraction was calculated by calculating the concentration of ions from blank filter pieces (as described in section 2.2.6.2) and finding the SD across these repeats to give the absolute error of the blank in $\mu\text{g ml}^{-1}$. This SD is referred to as $\delta BLNK$ and is relative to 2 ml or 5 ml, depending on the volume of water a specific sample had been sonicated in.

The $\delta BLNK$ was propagated onto the initial IC sample concentration error (δA) to give the total propagated error for these two steps (δB) by using the addition rule of error propagation Eq. 2.9³⁰⁰.

$$\delta B = \sqrt{(\delta A)^2 + (\delta B L N K)^2}$$

Eq. 2.9. Propagated error of the IC concentration error (δA) and the blank concentration error ($\delta B L N K$) to give the total error of the blank corrected concentration (δB).

2.2.9.1 Recovery Correction Error

The blank corrected value calculated is then divided by the percentage recovery to obtain the blank and recovery corrected value of the IC sample solution, as summarised in Eq. 2.10, where C is the blank and recovery corrected concentration of IC sample solution, B is the blank corrected concentration and R is the percentage recovery (in the form of a decimal).

$$C = \frac{B}{R}$$

Eq. 2.10. Recovery correction stage of analysis where B is the blank corrected IC concentration, R is the recovery value (given as a decimal), and C is the recovery corrected IC concentration.

The error associated with the percentage recovery application was calculated by taking the SD across the percentage recovery results (as decimal values, section 2.2.6.3) and is referred to as δR . As the blank corrected IC concentration is divided by the recovery, Eq. 2.11 is used to propagate the error of the recovery application to the blank corrected solution concentration error, where C is the blank and recovery corrected value and δC is the propagated error for the blank and recovery corrected value, of the IC sample solution. Eq. 2.11 may also be rearranged to calculate δC (Eq. 2.12).

$$\frac{\delta C}{C} = \sqrt{\left(\frac{\delta B}{B}\right)^2 + \left(\frac{\delta R}{R}\right)^2}$$

Eq. 2.11. Propagated error of the blank correction error (δB) and the recovery corrected error δR to give the total error of blank and recovery correction (δC), where C is the blank and recovery corrected IC concentration, B is the blank corrected concentration and R is the recovery value.

$$\delta C = C \sqrt{\left(\frac{\delta B}{B}\right)^2 + \left(\frac{\delta R}{R}\right)^2}$$

Eq. 2.12. Rearrangement of Eq. 2.11

2.2.9.2 Mass of Ionic Species Error

On calculating the blank and recovery corrected concentration (C), the value is multiplied by the volume of water (Vol_{water}) used to sonicate the filter piece in, to calculate the mass of ionic species present on the filter piece. For Beijing this was 2 ml or 5 ml, and for Delhi this was 5 ml. This is summarised in Eq. 2.13.

$$D = Vol_{water} \times C$$

Eq. 2.13. Calculation of the mass of ionic species (D) from the multiplication of the volume of water (Vol_{water}) used for filter extraction for a specific sample and the corrected IC concentration value (C).

The uncertainty associated with the Vol_{water} was determined to be negligible. Therefore, to propagate the error at this step, the propagated blank and recovery corrected error (δC) is multiplied by the volume of water (Vol_{water}, a constant) to produce the absolute error associated with the calculated mass of ionic species (δD). This is summarised in Eq. 2.14.

$$\delta D = Vol_{water} \times \delta C$$

Eq. 2.14. Calculation of the absolute error of the mass of ionic species which was extracted from the filter piece by multiplying the volume of water (Vol_{water}) by the error associated with the corrected IC concentration value (δC).

2.2.9.3 Air Volume Error

The error associated with the air volume which passed through the filter piece in the HiVol sampler was calculated by recording the flow rate (given by the HiVol) and finding the SD across the measured flow rates ($\delta FlowRate$) from the available HiVol data. This gives the absolute error of the HiVol in m³ h⁻¹. The error is required to be corrected for the time of sampling associated with a specific filter, as well as the area of the filter piece sampled for IC analysis. Therefore, the overall error in the volume sampled which passed through the filter piece ($\delta AirVol$) may be summarised in Eq. 2.15, where Hrs is the number of hours sampled and % Area is the percentage surface area of the whole filter cassette surface area taken, for which the uncertainties were comparatively negligible. As the number of hours of sampling as well as the percentage of filter taken are constants, the rule for propagation of errors is taken for which $\delta FlowRate$ is multiplied by exact known constants, as shown in Eq. 2.15.

$$\delta AirVol = \delta FlowRate \times Hrs \times \% Area$$

Eq. 2.15. Calculation of the absolute error of the HiVol flow rate ($\delta AirVol$) by multiplying the absolute error associated with the HiVol flow rate ($\delta FlowRate$) by the time of sampling in hours (Hrs) and percentage of filter area taken (% Area) from the master filter piece, which are constants.

2.2.9.4 Final Atmospheric Concentration Error

The final atmospheric concentration value is calculated by dividing the mass of ionic species from the filter paper (D), by the volume of air sampled (AirVol), which produces the final atmospheric concentration of ionic species in PM_{2.5} for a specific sample (E). This is summarised in Eq. 2.16.

To propagate the errors, the multiplication and division rule is used and applied to the calculation of atmospheric ionic concentration calculation as shown in Eq. 2.17. δD is the propagated error in

calculating the mass of ionic species; δAirVol is the absolute error associated with the volume of air sampled and δE is the total propagated error associated with a specific atmospheric concentration of an ionic species.

$$E = \frac{D}{\text{AirVol}}$$

Eq. 2.16. Calculation of the atmospheric concentration of ionic species within $\text{PM}_{2.5}$ where D is the mass of ionic species determined from the filter, AirVol is the volume of air which passed through the filter piece, and E is the calculated atmospheric concentration of the ionic species.

$$\delta E = E \sqrt{\left(\frac{\delta D}{D}\right)^2 + \left(\frac{\delta \text{AirVol}}{\text{AirVol}}\right)^2}$$

Eq. 2.17. Calculation of error associated with the ionic concentration (δE), where (δD) is the error associated with the mass of ionic species and δAirvol is the error associated with the volume of air sampled.

In this thesis, these concentration errors associated with atmospheric concentrations are shown as error bars in the y-axis of associated charts.

2.2.10 Ionic $\text{PM}_{2.5}$ Ion Chromatography Inter-Laboratory Comparison Study

Developing on from the collaborative work conducted with UoB regarding the inter-instrument analysis of ionic constituents on the IC from offline filter sampling, an inter-laboratory IC study was conducted, led by the University of Birmingham. This study is now published and is entitled “An interlaboratory comparison of aerosol inorganic ion measurements by ion chromatography: implications for aerosol pH estimate” in *Atmospheric Measurement Techniques* by Xu et al, (2020)²⁶⁷.

2.2.10.1 Overview and Results

Despite the very wide use of IC analysis for ambient aerosol measurements in the literature, this is the first time that a blind inter-laboratory comparison study has been conducted for this technique. The study included 10 laboratories from the UK, China and Serbia including the University of York, Institute of Atmospheric Physics at the Chinese Academy of Sciences (CAS), Institute of Chemistry (CAS), Chongqing Institute of Green and Intelligent Technology (CAS), Beijing Normal University, the Ocean University of China, Nankai University, Zhejiang University, the University of Belgrade and the University of Birmingham. The purpose of this study was to observe whether different laboratories and instruments using varying extraction techniques would produce differing instrument responses (and therefore different ionic concentrations) for an identical set of ambient filter samples. This study also aimed to measure the uncertainty and reproducibility across the methods. An Aerosol Chemical Speciation Monitor (ACSM) was sampling on the same rooftop at IAP and was also used in the comparison.

The calculated concentrations from each instrument were then used to assess the impact of this variability between the labs and instruments on aerosol acidity estimation using the ion balance

approach and the ISORROPIA-II thermodynamic acidity model. In this study, the UoY is represented by Lab-9. The other laboratories are unknown. The study further provides an evaluation and suggests recommendations on ways in which IC analyses may be improved in future for the characterization and quantification of ionic species within ambient aerosol PM_{2.5}. The ions analysed in this study were F⁻, Cl⁻, NO₃⁻, SO₄²⁻, NH₄⁺, Na⁺, K⁺, Mg²⁺, Ca²⁺.

Anion and cation reference standard solutions, as well as 5 blank samples and 8 ambient aerosol filter samples were sent to each lab. The anion and cation reference standards (Sigma, UK) had been bought by the UoB and were diluted before being distributed (20 ml) to the individual laboratories. These were directly run on the IC instrument. These were also used by the UoB to conduct the recovery analysis of species from each institution. They calculated these by dividing the reported concentrations for each species given from each institution and dividing this by the concentration reported by the manufacturer.

Ambient PM_{2.5} filter samples were collected by UoB at IAP between 16th – 23rd Jan 2019 using a HiVol sampler (Tisch Environ, USA) at a flow rate of 1.13 m³ min⁻¹. Five field blank filter samples were also sent by UoB. These had been collected by placing pre-conditioned filter samples into the HiVol sampler at IAP with the flow rate turned off on the instrument. These filter samples (and blanks) were chopped up into 6cm² and 5 cm² pieces and sent to the 10 different laboratories. A further description of the ambient PM_{2.5} and blank filter collection is found in the work of Xu et al., (2020)²⁶⁷.

The method of filter extraction (presented in section 2.2.3) was used for lab-9 (this study, UoY) and extraction of a 6 cm² filter piece sent from UoB was completed into 10 ml of 18.2 MΩ water (30 minute sonication). The use of a shorter version of calculation 3 was also used, in which the quadratic calibration pivot was set at 2.5 ppm (salt concentration). Each of the anion and cation reference solutions (used for recovery correction) were run three times directly, and each of the blanks and ambient samples were run once. The blank correction and recovery correction stages of calculation were completed by the UoB. This was a blind analysis for which the concentrations for each ionic species were calculated and sent back to the UoB for collation and comparison.

The ionic atmospheric concentration results from each lab are shown in Fig. 2.11, in which lab 9 (UoY) is represented by a grey circle and line. Fig. 2.11 shows that Cl⁻, NO₃⁻, SO₄²⁻, NH₄⁺ and K⁺ in general show good agreement across all institutions. The study does however show more variability across the minor ions of F⁻, Mg²⁺ and Ca²⁺. The York (Lab-9, this thesis) results are largely in between the IC responses of the other laboratories.

To inspect the agreement between values more closely, error bars (red) have been displayed for the Lab-9 values (UoY, this thesis) which show ± 30 %. It can be seen that for Cl⁻, NH₄⁺, NO₃⁻, K⁺ and SO₄²⁻ that almost all values (apart from Lab-10 for NO₃⁻ and K⁺) reside within ± 30 % of the Lab-9

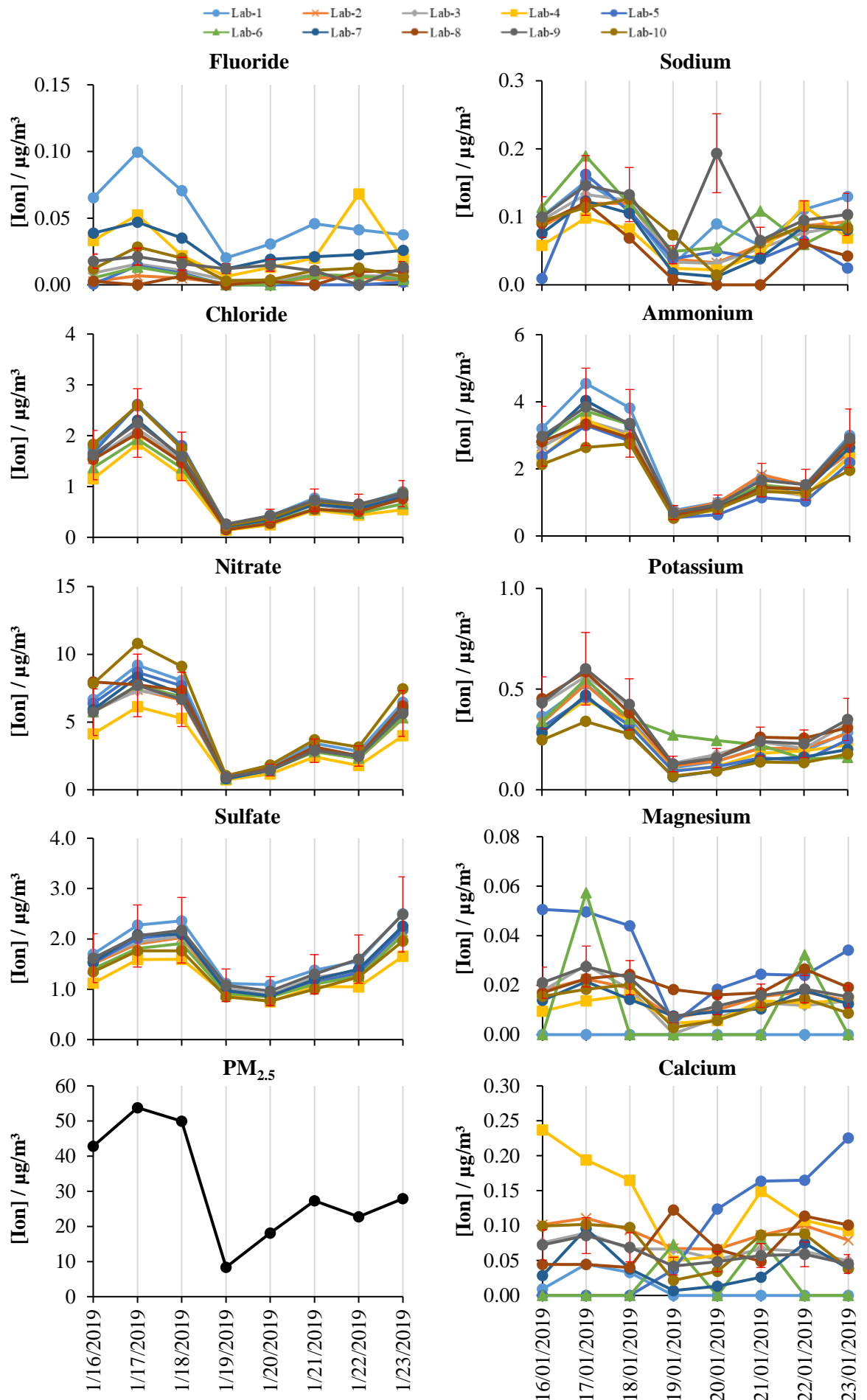


Fig. 2.11. Ionic Atmospheric Concentration Comparison Results from Xu et al., (2020)²⁶⁷. The results for each lab are shown via the key above the time series. The grey vertical lines represent the dates of sampling (shown on the bottom charts and are vertically identical). Red error bars have been added to the time series of Lab-9 (results from this thesis) to demonstrate the $\pm 30\%$ range.

values (from this thesis), with greater agreement between species found at lower concentration responses. For F^- , Na^+ , Mg^{2+} and Ca^{2+} however, there is significant disagreement between the institutions for which the majority of institutions do not fall within the Lab-9 values $\pm 30\%$. This is due to F^- , Na^+ , Mg^{2+} and Ca^{2+} exhibiting very low concentrations in which the absolute errors for each separate institution are likely much greater at these low levels. Therefore, for the major ions which make up the predominant fraction of $PM_{2.5}$, the reproducibility between the instruments is good. For the minor ions, this intercomparison could be completed again in future although with the absolute errors reported by each institution incorporated as well as to give a greater insight into the reproducibility between institutions.

Xu et al., (2020)²⁶⁷ concluded that most ions shown in Fig. 2.11 had good reproducibility between the 10 laboratories. Moreover, for the most important ions influencing aerosol acidity (Cl^- , NO_3^- , SO_4^{2-} , and NH_4^+) good consistency was observed between labs using a variety of instrument models and data analysis techniques. There was however greater variability between instruments demonstrated on the more polluted days. Furthermore, the minor ions (especially F^- , Mg^{2+} and Ca^{2+}) observed very large variability which was attributed to very low concentrations of these species within the $PM_{2.5}$ filter samples. Xu et al., (2020)²⁶⁷ also demonstrated that the anion/cation equivalence ratio as well as the ion balance were very poor estimation methods for acidity as very large variance was measured between the institutions. This was attributed to the variance in error between institutions and the inclusion of the minor ions such as Ca^{2+} , of which concentrations were very inconsistent between the laboratories. Acidity estimation using ISORROPIA II however demonstrated good agreement across all institutions. It was however suggested that the acidity estimation would be more greatly influenced by the variability in ionic measurements when $[NH_3]$ was low.

An issue arose during data analysis in which not all laboratories used the identical LOD calculation method. To rectify this, the LODs were calculated by Xu et al., (2020)²⁶⁷ taking the SD of the blank filter solution responses and multiplying these by 3. Xu et al., (2020)²⁶⁷ reported LOD values in $ng\ m^{-3}$ defining the lowest concentration of ionic species that could be present over a 24 hour filtering period at a flow rate of $1.13\ m^3\ min^{-1}$. For comparison purposes, the relative instrument LOD has been calculated back from $ng\ m^{-3}$ (from the values reported in table 3 in Xu et al., (2020)²⁶⁷) to the equivalent ppm concentration in a 10 ml solution. The LODs calculated by Xu et al., (2020)²⁶⁷ from each lab are reported in Table 2.8 in which Lab 9 (UoY) is shown in bold. Lab 9 shows no values for the F^- and Cl^- LOD values, as the quantities of these ions were too low in the blank sample and no SD could be calculated. As can be seen from Table 2.8, the results across the laboratories are very variable in which the UoY presents results which are in between the highest and lowest readings across all ions.

Observing the other LOD values in Table 2.8, most values are < 0.1 ppm. Particularly high LOD values were however seen by Lab-4 for the major ions, Cl⁻ and NO₃⁻ in Lab-5, as well as NO₃⁻ in Lab-10.

Table 2.8. Table of LODs (ppm) reported from 10 different laboratories for anion and cation species from Xu et al., (2020)²⁶⁷.

Lab	F ⁻	Cl ⁻	SO ₄ ²⁻	NO ₃ ⁻	Na ⁺	NH ₄ ⁺	K ⁺	Mg ²⁺	Ca ²⁺
Lab-1	0.01	0.07	0.03	0.02	0.07	0.04	0.05	0.01	0.04
Lab-2	8.9E-04	0.03	0.01	0.03	0.02	0.01	2.8E-03	0.02	0.13
Lab-3	4.6E-03	0.01	0.03	0.02	0.01	0.01	0*	0*	0.04
Lab-4	0.45	0.53	0.06	0.37	0.07	0.28	0.06	4.4E-03	0.21
Lab-5	0.01	0.23	0.09	0.27	0.13	0.13	0.02	0.02	0.11
Lab-6	NA	0.02	0.12	0*	0.08	0.11	NA	NA	NA
Lab-7	0.01	0.03	0.08	0.09	0*	0*	0.03	0.01	0.04
Lab-8	NA	0.08	0.06	NA	0.05	NA	NA	NA	0.06
Lab-9	NA	NA	0.08	0.05	0.03	0.02	0.01	5.4E-04	0.07
Lab-10	2.9E-03	0.05	0.05	0.24	0.12	0.08	0.19	0*	0.03

N.B. LODs which show 0* are from laboratories which reported a 0 LOD value.

A comparison was completed between the LOD values calculated in this thesis to the LODs calculated by Xu et al., (2020)²⁶⁷ which is presented in Table 2.9. For SO₄²⁻ and NO₃⁻, significantly lower LOD values were seen for UoB, whereas generally for the cations the UoY showed far lower detection limits. The much larger NO₃⁻ and SO₄²⁻ seen by UoY is most likely down to the degradation of the column (section 2.2.6.4). In addition, the much lower concentrations of solutions used by UoB (blank solution) compared to UoY generated much lower SD values for UoB. This therefore generates much lower LOD values. The disagreement seen in Table 2.9 also highlights the need for an official universal LOD calculation method.

Furthermore, an LOD could only be reported if a peak response was observed within the blank filter solution. In some instances where no peak was present, an 'NA' value was reported by Xu et al., (2020)²⁶⁷. A possible reason for the 'NA' values from some laboratories but not others is most likely down to the variability of ions within the blank filter and filter pack from the manufacturing stage (as discussed in section 2.2.6.2).

Table 2.9. Comparison of LOD (ppm) calculated in this work to the method by Xu et al., (2020)²⁶⁷.

LOD / ppm	F ⁻	Cl ⁻	SO ₄ ²⁻	NO ₃ ⁻	Na ⁺	NH ₄ ⁺	K ⁺	Mg ²⁺	Ca ²⁺
This Study	0.17	0.15	0.23	0.56	2.1E-03	3.5E-03	2.6E-03	6.3E-03	5.3E-03
Xu et al.,	-	-	0.08	0.05	0.03	0.02	0.01	5.4E-04	0.07
Factor	-	-	0.33	0.09	13.39	5.38	4.79	0.09	14.09

2.2.10.2 Specific Contribution of this work to the Intercomparison

The specific contribution of the work presented in this thesis to the publication “An interlaboratory comparison of aerosol inorganic ion measurements by ion chromatography: implications for aerosol pH estimate” by Xu et al., (2020)²⁶⁷ is the extraction of samples sent from the lead of this work (University of Birmingham) and the reporting of concentration results back to the project lead.

The project lead had sent one anion reference solution, one cation reference solution, in addition to 5 blank filter pieces and 8 ambient PM_{2.5} filter pieces, separately wrapped in foil. The blank and ambient PM_{2.5} samples taken by the University of Birmingham were collected as described in section 2.2.10.1 The filter pieces were extracted into 10 ml water (using the method described in chapter 2) and represented the method used by the laboratory at the University of York.

The calibration standards were self-made at the University of York as described in Chapter 2 and had not been sent from the project lead. Full calibrations were run on the IC instrument, followed by the reference solutions, extracted samples, as well as the filter blank pieces, for both anion and cation modes. The Lab’s ultrapure deionised water was also tested for contaminants. The reference solutions were ran 3 times, followed by each sample and blank, once. Quantitative solution concentration analysis of the separate sample reference solutions and blanks was conducted using calculation 3 (section 2.2.7.3).

The results of the concentration analysis of the reference solutions, ambient samples and blank filters, as well as the Lab’s ultrapure water for F⁻, Cl⁻, Br⁻, NO₂⁻, SO₄²⁻, NO₃⁻, PO₄³⁻, Li⁺, Na⁺, NH₄⁺, K⁺, Mg²⁺ and Ca²⁺ were finalised and sent back to the project lead. The project lead coagulated all the data from the separate institutions who conducted the same work but with their own separate instruments and methods. The lead then conducted further analysis in calculating the LODs of the instruments from each lab, by using the concentrations from the reported blank filter solutions. The results from this thesis are presented in Xu et al., (2020)²⁶⁷ as Lab 9.

2.2.10.3 Critiques Surrounding the IC Inter-Laboratory Comparison Study

Although the work conducted by Xu et al., (2020)²⁶⁷ is very informative and novel with respect to the worldwide inter-laboratory comparison of IC methods which was necessary, some areas of improvement for future analyses of this type are needed specifically in the area of quality control. Firstly, the sample sent by the University of Birmingham lead was damaged (Fig. 2.12) and as only a fraction of the entire filter piece was sent, it is unknown as to whether particulates were completely homogenous over the entire filter sample.



Fig. 2.12. Filter sample sent by the University of Birmingham for the IC inter-laboratory comparison study.

Further critiques are that different institutes were given different areas of filter paper to be extracted (either 5 cm² or 6 cm²) which is inconsistent. In future, each lab should be given the same surface area of filter sample. Furthermore, by close inspection of Fig. 2.12, the filter pieces were not cleanly cut.

Moreover, the LOD concentration calculations from each lab were all conducted by the project lead at the University of Birmingham. The LOD was calculated by taking the standard deviation of the blank concentration of each ion across the blank filter extractions and multiplying this by 3. For some instruments in the inter-comparison, some ions displayed no signal response as the concentration within the blank sample was below detection limit. Therefore, for some laboratories not all ions investigated have a reported LOD associated with them. This was the case for the LOD in this study, for which no LOD was reported for F⁻ or Cl⁻ for Lab 9 (the work from this thesis) in the work of Xu et al., (2020)²⁶⁷. A way to overcome this in future would be to send out a calibration standard of a very low concentration for each target ion, although a high enough concentration that all instruments give a signal response for all ions investigated. Furthermore, the blank and recovery correction stage was also conducted by the project lead which alters the full methods that would be used by participating laboratories in species concentration quantification.

2.2.11 Cement Analysis for Inter-Instrument Comparison

This experiment is specifically associated with the cement discussion and analysis presented in chapter 3. 0.05565g of UltraTech Cement (Mumbai, India), was weighed out into a plastic sample vial (Sarstedt). 13.65559 g of H₂O (18.2 MΩ) was added to this vial. The vial was lab-sealed and sonicated for 30 minutes. The resulting solution was shaken and passed through a Millex syringe-driven filter unit of diameter 33mm and pore-size 0.22 μm (Millipore). Three 0.5 ml aliquots of this solution were pipetted into IC Polyvials (Thermo), and the solution was run on the IC in anion mode, with a distilled water blank between each injection to prevent any carry over of material.

2.2.12 Validity of Measuring Nitrite on Filters

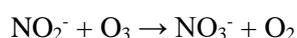
NO₂⁻ in the aerosol phase is known to be a reservoir for HONO^{301,302,303}, although little work investigating NO₂⁻ within particles has been done to date as NO₂⁻ is highly chemically unstable and is typically in very low concentration in the atmosphere^{301,304}. There has however recently been work by Wang et al., (2012)³⁰⁵, Wang et al., (2014)³⁰⁶ and Gao et al., (2011)³⁰⁷ which has indicated increased levels of NO₂⁻ within aerosol and therefore the accurate identification and quantification of NO₂⁻ within aerosol matrices is of atmospheric importance³⁰¹. Furthermore, HONO is known to dissociate to NO and OH in the presence of light³⁰², which are both key constituents in governing atmospheric chemistry. Therefore, the accurate measurement of NO₂⁻ within aerosol using filter samples would produce valuable datasets.

Very little is mentioned in the literature surrounding the validity of measuring nitrite on filters. There is however information in the literature surrounding NO₂⁻ formation and depletion as well as equilibrium with HONO³⁰¹, for which processes could be occurring on or within particles being sampled by HiVol onto filters. Specifically, Wang et al., (2015)³⁰¹ report that the particle NO₂⁻ and

gas phase HONO equilibrium may be controlled by various conditions such as RH, ambient temperature, acidity of particle surfaces and species concentrations within particles. These factors are all variables when filter sampling in a polluted Asian megacity for which an increased RH would favour the dissolution of HONO into the aerosol phase producing NO_2^- , and wet surface heterogeneous reactions of HONO are known to increase NO_2^- production^{308,309,301} producing positive NO_2^- artefacts; lower temperatures would encourage the condensation of HONO into the aqueous aerosol phase as well as trap NO_2^- within the particle; the relative concentrations of gas phase HONO and particulate NO_2^- evidently affect the equilibrium; and the higher the acidity of particles, the greater the interaction between NO_2^- and H^+ which goes on to produce HONO and depletes NO_2^- from the particle phase³⁰¹ causing negative NO_2^- filter artefacts. Another possible source of positive NO_2^- artefact formation during filter sampling may be down to the gas phase NO_2 reduction by hydrocarbons on sampled particle surfaces^{309,310,311}, as well as NO_2 gas phase reaction with dust particles^{312,313}. These multiple variables are all present during filter sampling and therefore the atmospheric conditions likely affect the proportion of positive and negative NO_2^- filter artefacts.

Although very little in the literature talks about the specific positive and negative NO_2^- artefacts surrounding filter sampling, the production of positive NO_2^- artefacts from the use of Particle into Liquid Sampler (PILS) sampling (chapter 6), has been mentioned previously^{314,266}. Orsini et al., (2003)²⁶⁶ however also suggest that even in the presence of acid and base gas denuders, any NO_x gas that may still pass through the denuders would contribute to the production of HONO which consequently dissolves within aqueous samples and forms NO_2^- , which is detected by IC²⁶⁶.

In particular, a possible significant source of negative NO_2^- artefacts may likely be due to the interaction of sampled NO_2^- with gas phase O_3 passing through the filter sampler. Poruthoor et al., (1995)³¹⁵ mention in their work that the interaction between particulate NO_2^- and gaseous O_3 passing through the their sampler is significant in NO_2^- degradation over prolonged filter sampling times. It is reported that NO_2^- may degrade in the presence of gaseous O_3 , through the reaction shown in Eq. 2.18³¹⁶.



Eq. 2.18. Reaction between filter based NO_2^- and O_3 producing NO_3^- and O_2 .

Furthermore, work by Koutrakis et al., (1993)³¹⁶ measured gaseous O_3 by filter sampling, in which they utilised nitrite coated filters to calculate the amount O_3 which had passed through their filters. They measured the atmospheric concentration of O_3 by quantifying the formation of NO_3^- . As the O_3 concentrations across the APHH campaigns was significant, reaching maximums of 194 ppbv, 352 ppbv, 36 ppbv and 182 ppbv for the DPEM, DPOM, BWIN and BSUM campaigns, respectively. It is therefore very likely that NO_2^- would have degraded somewhat during filter sampling across the APHH campaigns and that NO_3^- possibly obtained positive artefacts from this.

2.2.13 Evaluation and Validity of using a Quadratic fit for Calibrations

There are however some negative implications surrounding the use of quadratic fits for calibrations. These include the need for a greater number of data points; a greater error associated with the quadratic fit; considerably larger errors associated with outliers for which the calibration curve needs to be extrapolated; and that there is rarely a theoretical justification in having a quadratic curvature^{317,318,319}. Due to the role of the suppressor and the formation of acid from conjugate base species (as discussed previously in section 2.2.7.3, there is however a theoretical justification in this instance as to a negative quadratic fit due to the use of suppressor. There were however some calibrations which observed a positive quadratic curvature (Fig. 2.9B) for which it is suggested that the slight positive x^2 coefficient is most likely down to error in this technique. On reflection, it may have been more accurate to have used a linear calibration function. This is because conductivity should be a linear response and if needing to use a quadratic fit, this would suggest that the dynamic range used for the calibration is too large. Furthermore, in applying a quadratic fit to the calibration responses the calibration is forced into a polynomial model producing an artificially better fit for the calibration, despite the level of uncertainty in the calibration curve.

The use of a quadratic curvature may have also affected the data presented in this thesis by the reporting of a smaller error than is actually present. Furthermore, it is expected that for negative curvatures, the calibration for the IC will overestimate the actual concentration within the intermediate part of the curve, for which the adverse is true in the case of a positive quadratic curvature. To avoid the use of a quadratic calibration curve in future, it is recommended that samples are diluted to fit within the segment of the calibration which is linear at lower concentrations. The number of calibration points at these lower concentrations should also be increased to improve accuracy of calibration and solution concentration calculation.

2.2.14 Other Issues

Before the separate mixes (for anion and cation) were produced, the stock solutions were taken out of the fridge and left to warm up to room temperature (*ca.* 30 minutes). For solution preparation, 1000 μ l pipettes were used to make up the mixed standards. Therefore, allowing all solutions to warm up to room temperature avoided any errors in the measured quantities of ionic solutions and kept pipetted volumes consistent. This is because the volume of water expands with temperature as stock solutions are taken out of the fridge.

The mixed anion standard which included NO_2^- and NO_3^- only had a shelf life of *ca.* 3-4 days. This is because the NO_2^- and NO_3^- within solution partition with one-another in which NO_3^- converts to NO_2^- to a point of equilibrium as demonstrated in Fig. 2.13. In Fig. 2.13, the black chromatogram is a fresh mixed standard solution created and ran on 2nd May 2017 and the red line was the same standard ran on 30th May 2017. As can be seen the ration of peaks substantially changes over the course of *ca.* 1 month. Therefore, it is recommended for future users that a separate NO_2^- set of calibration standards is ran in conjunction with the main mixed anion standard mix. Separating NO_2^-

will also benefit the user with regards to needing to complete the NO_2^- recovery separately (as discussed in section 2.2.6.3).

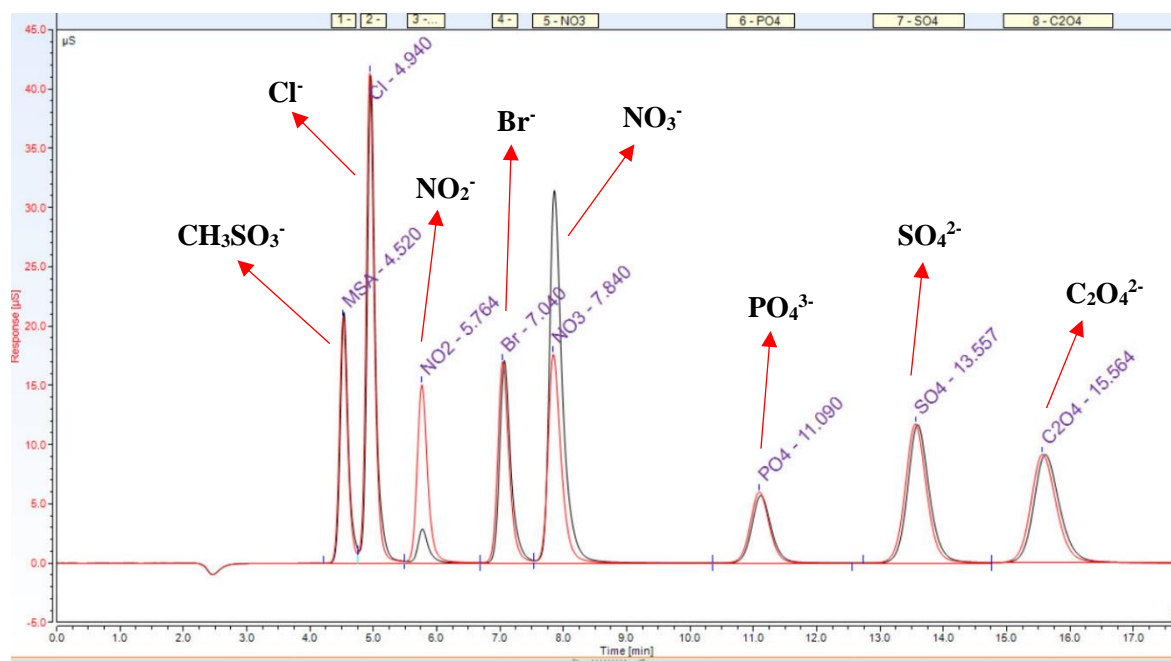


Fig. 2.13. IC Chromatogram representing NO_3^- to NO_2^- partitioning in a mixed standard over the course of ca. 1 month.

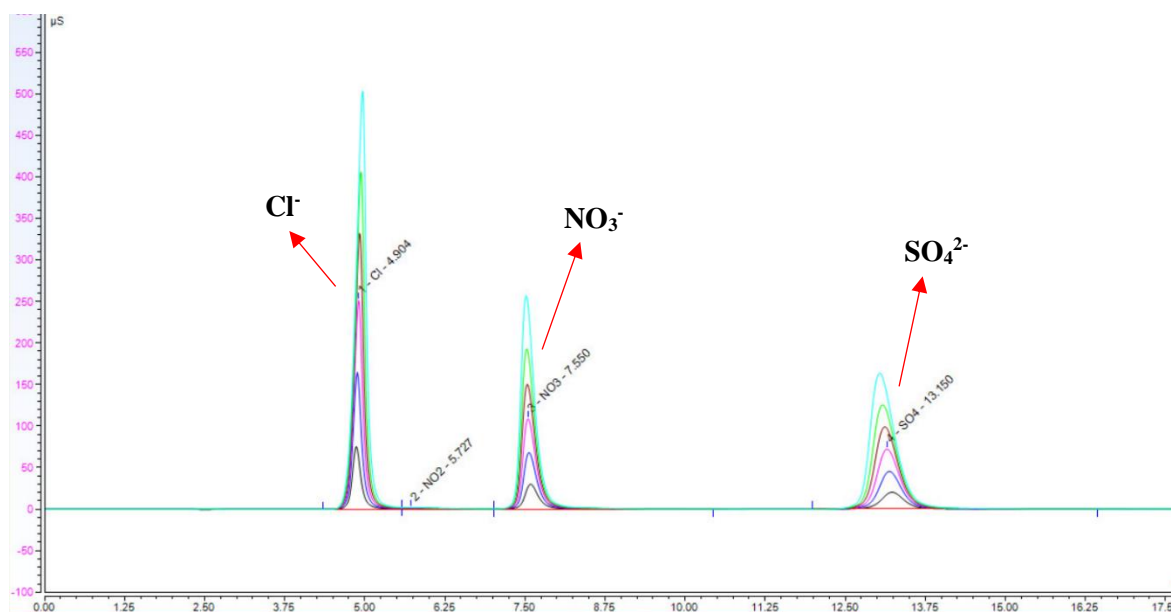


Fig. 2.14. NaCl , NaNO_3 and NO_2SO_4 mixed salt solution were ran on IC at 100 ppm (black), 200 ppm (dark blue), 300 ppm (pink), 400 ppm (brown), 500 ppm (green) and 650 ppm (light blue).

Finally, tests were completed to observe the maximum concentration of the major anions which would be expected to be seen in an Asian megacity. NaCl , NaNO_3 and NO_2SO_4 mixed salt solution were ran on IC at 100 ppm (black), 200 ppm (dark blue), 300 ppm (pink), 400 ppm (brown), 500 ppm (green) and 650 ppm (light blue), as shown in Fig. 2.14. Visually inspecting the chromatograms, the peaks start to skew to one side after ca. 200 ppm. Therefore, it is recommended that future users do not go above ca. 200 ppm of NaCl , NaNO_3 and Na_2SO_4 for an IC run.

2.3 Conclusions and Suggestions for Future IC Users

The experimental protocol for measuring ionic species in PM_{2.5} from filter samples collected during the APHH Delhi and Beijing campaigns has been described along with the developed methods for quantification. Separate quality control procedures have also been outlined and evaluated for their addition to accuracy in atmospheric measurements. For the benefit of future IC users measuring ionic species within PM_{2.5} from filter samples, suggestions and improvements to the methods used in this work are outlined.

Forming a mixed calibration standard from ionic stock solutions is essential for efficient calibration and quantification of IC solution concentration. It is recommended that ionic stock solutions are removed from the fridge and allowed to warm up for *ca.* 30 minutes before being pipetted for the purposes of producing fresh salt mix solutions. This is due to the volume of water being temperature dependant. Specifically, for anion mixed standards involving both NO₂⁻ and NO₃⁻ standards should either produce a fresh set of mixed standards *ca.* every 3 days or preferentially remove NO₂⁻ and produce a separate single salt calibration involving NO₂⁻ to be run in conjunction with the main salt mixed standard. This is due to the partitioning between NO₂⁻ and NO₃⁻ in solution. In addition, it is also recommended that salt solutions do not exceed *ca.* 200 ppm for NaCl, NaNO₂ and Na₂SO₄ to avoid skewing of the chromatographic peaks. Furthermore, running samples at too high ionic concentrations is likely destructive to the instrument. Further work needs to be conducted for other salt species to observe the maximum concentration suitable for the instrument. Finally, close inspection of separate 50 ppm salt solutions were inspected for the potential cross contamination of other ions within the salt stocks from the manufacturing process. In combining stock solutions for mixed standards production, the addition of minor conductivity from other ions should ideally be taken into account, although it was concluded that this step observed very little influence on the overall improvement or change in the dataset for the major ions.

When conducting blank comparison for filter analysis for ionic species within aerosol, it was concluded that Whatman QMA quartz filters are likely sufficient for the major ionic species (NH₄⁺, Cl⁻, NO₃⁻ and SO₄²⁻) although are not suitable for minor species such as PO₄³⁻. This is due to contamination of these ionic species found within the QMA filters and the ions leaching inconsistently during the sonication procedure. It was found that the concentrations of some ionic species such as PO₄³⁻ and Na⁺ are not evenly distributed throughout a filter or a pack of 25 filters. In the quantification of ionic species presented in this thesis, this resulted in negative concentration values which was down to the concentration of species (such as PO₄³⁻ and Na⁺) observing a large concentration within the sampled blank filter, compared to the filter piece used for sample analysis. This resulted in negative values being obtained, which were replaced with 'no data'. Although it is suspected that Whatman QMA filters are sufficient for Cl⁻, NO₃⁻, SO₄²⁻ and NH₄⁺ analysis, more work is required for contamination variability across filters to be ruled out completely. An alternative Teflon filter has been suggested to solve the contamination problem for future IC analyses.

Recovery analysis for the experimental protocol described in this chapter for IC correction demonstrated very good recovery results for most ions which observed Recovery values of > 90 %. PO_4^{3-} recovery values were > 85 %. NO_2^{2-} values demonstrated very low recovery values. This was attributed to the protocol involving the pipetting of a small volume of high concentration mixed anion (with NO_2^-) solution onto filter paper. It has been suspected that NO_2^- in the presence of other acids within the anion mix produced HONO which may volatilise off during the drying period of the filter piece. When the NO_2^- recovery was completed separately, a recovery of 88.0% (4.2% %RSD) was established. Ca^{2+} recovery values were also particularly low. This was attributed to the hydration of Ca^{2+} in aqueous solution forming the complexes ($\text{Ca}(\text{H}_2\text{O})_4$ and $\text{Ca}(\text{OH})(\text{H}_2\text{O})_3$). These complexes bind to the O in Si-O₂ of the quartz micro fibre filters used in this study. This results in a significantly lower recovery of Ca^{2+} within the filter samples. For accurate concentration calculation of Ca^{2+} , it is again suggested to future IC users that an alternative filter is used for sampling. Finally, slight improvement of recovery was observed when using higher concentrations of solutions and pipetting smaller volumes onto filters during the protocol. This is down to ion loss through the absorption of filter paper through the foil used underneath. It is therefore recommended that future users aim for *ca.* 1000 ppm anion and 500 ppm cation solutions and $\leq 100 \mu\text{l}$ pipetted onto a filter piece.

LOD calculation was conducted by running 10 replicates of a mixed standard salt solution 10 times and taking the standard deviation of the responses across the peak areas. It must however be emphasised that the lowest concentration possible should be used as described by the EPA which may require re-making of solution concentrations especially for the LOD and LOQ analyses. It was found in this work that if selected solution concentrations are too high, the LOD and LOQ become unrealistically high. Therefore, it is recommended for future users to prepare a special anion mix for the purposes of LOD analysis in which each ion is at the lowest possible for IC analysis. Another possibility may be to use a similar method to that of Xu et al., (2020)²⁶⁷, although the risk here lies in the uneven distribution of ions when analysing extracted filters and the investigator may risk not observing all ions.

Furthermore, the column and suppressor may also increase LOD values as they have been demonstrated in this work to degrade over time when presented with exceptionally high $\text{PM}_{2.5}$ filter samples. A total of 473 ambient $\text{PM}_{2.5}$ filters from Beijing and Delhi were extracted and ran on the IC from the start of this study. When replacing the anion and column suppressor at the end of this work, the LOD and LOQ values were re-calculated using the new instrument parts which provided exceptional improvement across the anions investigated. Cation LODs demonstrated generally much lower concentrations which is likely due to no acid being formed at the suppression stage. Anion improvements were by a factor of over an order of magnitude for species F^- and NO_2^- . Cl^- , NO_3^- , and SO_4^{2-} observed factor improvements of 5.85, 7.85 and 3.52, respectively. Owing the relatively rapid column and suppressor degradation for anion mode IC and to potential instrument flux, it is recommended that the LOD and LOQ measurements are much more frequently calculated compared to in this work. This may be completed either from the calibration curve of standards using Eq. 2.3,

or preferentially by using the EPA method on a more frequent basis. The disadvantage of doing this however is that IC PolyVials (Thermo) used for the Dionex system are expensive. Future work needs to be conducted to observe whether one EPA LOD and LOQ calculation per week is sufficient for sample analysis. Finally, this work has highlighted the need for an official universal LOD calculation.

The calculation for ionic species concentration within $PM_{2.5}$ was also developed to try and improve the accuracy of datasets. However, after implementing a number of work intensive good practices (i.e. the salt cross contamination step; splitting up the calibration into high and low; not passing the calibration equation through zero; more calibration points used; applying blanks and recoveries in terms of their concentrations as opposed to the instrument peak area; using a quadratic function; application of $LOD/2$ for samples $<LOD$ etc.) the overall improvement to the dataset was negligible. Finally, the IC method outlined in this protocol was used in an intercomparison study with IC instrumentation in 10 different laboratories around the world which was shown to generally be in good agreement with other laboratories. This may be found in the work of Xu et al., (2020)²⁶⁷, in which the contribution from this work is presented as Lab 9.

3 Atmospheric concentrations and characteristics of the major ions found in PM_{2.5} during the APHH Beijing and Delhi campaigns

3.1 Introduction

It has been widely reported that Delhi and Beijing have exceptionally high levels of outdoor particle pollution in recent years^{110,198,320,321} experiencing levels way beyond the World Health Organisation recommendations of $10 \mu\text{g m}^{-3}$ and $25 \mu\text{g m}^{-3}$ for the annual and 24-hourly means, respectively⁸. Numerous studies have suggested that the PM_{2.5} fraction of aerosol induces adverse health effects in humans, particularly targeting the lungs and cardiovascular system^{322,323,324,325}. PM_{2.5} is dominated by organic material (usually of secondary nature) or inorganic species for which tracers may be used in solving the potential source apportionment of this size fraction. Ionic species within PM_{2.5} predominantly make-up the bulk of the aerosol.

With a growing population in both Delhi and Beijing (currently at 30.26 and 20.46 million, respectively as of 2020, according to the world population review website)²⁵⁹ their rapid industrialisation and the ubiquitous exposure of the inhabitants to these toxic particles, means the characterisation and quantification of the inorganic fraction in these two megacities is vital. In addition, inorganic material within PM_{2.5} makes the aerosol have higher hydrophilicity and therefore enables the coagulation of water molecules and also enhances the accumulation of other gaseous toxins within the particle³²⁶. This therefore increases the risk of those exposed to PM_{2.5}.

In addition to health effects, the composition and amount of PM_{2.5} may affect radiative forcing of aerosol, and therefore climate³²⁷. Understanding the composition of the inorganic fraction within PM_{2.5} is also crucial in atmospheric models, for example in understanding the pH of aerosol using ISORROPIA^{328,329}. The pH of aerosol also has a direct link to other environmental catastrophes, including acid rain, which inherently effects economies.

The presence of ions such as NO_3^- , SO_4^{2-} , $\text{C}_2\text{O}_4^{2-}$ and the proportion of organic fraction may also give an indication of the amount of oxidation and secondary chemistry occurring in the atmosphere. Furthermore, the physical state of PM_{2.5} may also influence the fate of atmospheric gases such as NO_2 and SO_2 which may oxidise to HNO_3 and H_2SO_4 , respectively, and accumulate within aerosol (as to provide a sink for these gaseous species)^{145,164}. The rate at which processes like this occur depend on the availability of oxidants in the atmosphere³³⁰.

As part of the Air Pollution and Human Health (APHH) campaigns, ion chromatography analysis was completed to examine the inorganic fraction of PM_{2.5}, during four of the most comprehensive air quality measurement campaigns ever conducted within Delhi and Beijing using highly time resolved filter sampling. These campaigns took place during the Delhi Pre-Monsoon (DPEM), Delhi Post-Monsoon (DPOM), Beijing Winter (BWIN) and Beijing Summer (BSUM) seasons. Methane

Sulfonic Acid (CH_3SO_3^-), chloride (Cl^-), nitrite (NO_2^-), bromide (Br^-), nitrate (NO_3^-), phosphate (PO_4^{2-}), sulfate (SO_4^{2-}), oxalate ($\text{C}_2\text{O}_4^{2-}$), sodium (Na^+), ammonium (NH_4^+), potassium (K^+), magnesium (Mg^{2+}) and calcium (Ca^{2+}) were the ionic species measured in this study. Fluoride (F^-) was also included during the analysis of the Delhi samples. A brief analysis of the major gas-phase constituents NO , NO_2 , SO_2 and O_3 has also been completed to compare to the gas-phase chemistry and identify polluted periods.

An in-depth analysis has been constructed specifically for the most dominant ions of anthropogenic origin, including Cl^- , NO_3^- , SO_4^{2-} , NH_4^+ and $\text{C}_2\text{O}_4^{2-}$. In addition, this study for the first time provides a highly time-resolved inorganic time series for ions within $\text{PM}_{2.5}$, using off-line filter sampling coupled with ion chromatography, in Delhi as part of a much wider range of measurements. This study also provides an update to the very comprehensive set of studies^{331,332,292} which have been conducted on the composition of inorganic $\text{PM}_{2.5}$ within Beijing, using up to 30-minute filter sampling which allows for more detailed analysis and additional compositional information compared to Aerosol Mass Spectrometry (AMS). Minor ions such as NO_2^- , CH_3SO_3^- and Br^- are also included in this study which are not often reported in Ion Chromatography (IC) atmospheric analysis due to their low abundance.

An inter-instrument comparison has also been conducted assessing the responses of the University of York (UoY, this study) and the University of Birmingham IC (UoB) IC instruments; as well as the Institute of Atmospheric Physics (IAP) and Centre for Ecology and Hydrology (CEH) AMS instruments. This was conducted to identify the possible key sources of error which arise between instruments. IC analysis is also on occasion more dependable compared to AMS measurements such as in the separation and quantification of Hydroxymethanesulfonate (HMS) and SO_4^{2-} due to the potential interferences from other sulfur containing compounds using AMS³³³. In addition, vaporization and ionization AMS methods have been reported to breakdown organic nitrate and organic sulfate species leading to underestimation in these concentrations²⁸⁷. In addition, the AMS does not normally measure non-refractory³³⁴ species (e.g. mineral dust and sea salt) and therefore may potentially lead to an underestimation of ions within PM compared to IC methods. Inorganic $\text{PM}_{2.5}$ concentrations from IC were therefore critical for the benefit of other researchers who took part during the same campaign.

In this study, the major and minor atmospheric ions have been characterized and quantified to assess and compare the inorganic fraction of $\text{PM}_{2.5}$ in Delhi and Beijing (section 3.3.3). These species have been segregated into day and night-time atmospheric concentrations to help identify the different secondary chemical processes which may be occurring due to the presence of light in these atmospheres (section 3.3.4). A comparison of the weighted mean averages of each ionic species to the estimated daily concentration measurements of $\text{PM}_{2.5}$ (measured by UoB) produced an overall picture of $\text{PM}_{2.5}$ composition in each campaign and indicates whether the aerosol is of a more primary or secondary nature, depending on the type and proportion of each ion present (section 3.3.5).

3.2 Experimental

A full description of the IC experimental techniques carried out in Delhi and Beijing is described in Chapter 2.

3.3 Results and Discussion

3.3.1 Meteorological Conditions

Delhi experiences four main seasons throughout the year and are referred to as pre-monsoon/summer (Mar - May), monsoon (Jun – Sep), post-monsoon (Oct – Nov) and winter (Dec - Feb), whereas in Beijing, the seasons are designated as winter (Dec – Feb), spring (Mar – May), summer (Jun – Aug) and Autumn (Sep – Nov). The meteorological conditions associated with each of these sampling sites for the DPEM, DPOM, BWIN and BSUM campaigns are shown in sections 3.3.1.1 - 3.3.1.4). The temperature, Relative Humidity (RH) %, wind direction and wind speed data were measured by the UK Centre for Ecology and Hydrology (CEH) using high time resolution data. During the DPEM campaign, the tower that was used for the flux measurements had not been constructed until the autumn of 2018 during the DPOM campaign. Therefore, the DPEM wind speed and wind direction vectors had been taken from the Indira Gandhi International Airport (IGIA). Workers at CEH also reported an error of 30° with regard to the post-monsoon wind direction vectors. In Fig. 3.1 (Delhi) and Fig. 3.3 (Beijing), arbitrary colours are associated with the wind speeds shown in the top right hand of each wind rose plot. The scales on the right of each wind rose plots demonstrates the percentage frequency of winds associated with each wind vector.

3.3.1.1 Delhi Winds

During the DPEM period, wind data was used from 28th May 2018 08:30 until 5th Jun 2018 17:30 in hour increments (202 readings). Prevailing winds were observed from the E-SE direction and a maximum windspeed of 8.23 ms⁻¹ was recorded from the vector of 51.65° (NE-E). For the DPOM period, measurements were taken every half hour from 11th Oct 2018 14:30 until 6th Nov 2018 at 10:30. The prevailing winds during this campaign originated from the W-NW and the maximum wind speed measured was 6.26 ms⁻¹ which coincided with a direction vector of 70° (NE-E).

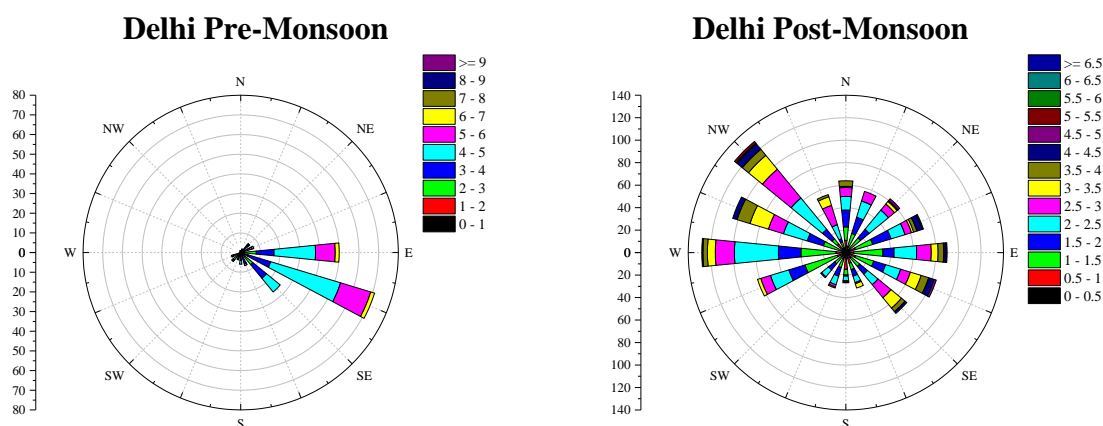


Fig. 3.1. Wind Rose Plots showing the overall wind speeds (legend, m s⁻¹) and wind directions across the APHH DPEM and DPOM campaigns.

3.3.1.2 Delhi Temperature and Relative Humidity

The data shown in Fig. 3.2 shows the time series for the temperature and RH% during the DPEM and DPOM campaigns. Meteorological data within the DPEM campaign was taken every half hour from 28th May 2018 at 17:00 until 5th Jun 2018 at 11:00 (371 readings) and during the post-monsoon campaign was taken from 11th Oct 2018 at 14:30 until 6th Nov 2018 at 10:30 (every half hour with 1041 readings), to match the timings of filter sampling. Data acquisition was every 1 minute in both Delhi campaigns.

The average temperature reading during the DPEM period was 34.0 °C, with a maximum reading of 43.4 °C and a minimum of 26.2 °C. The daytime average temperature was 36.7 °C (SD ± 3.3 °C, and the night-time average was 32.5 °C (SD ± 3.4 °C). During the DPOM campaign cooler temperatures were generally seen. An average temperature measurement of 24.7 °C was recorded over the course of the campaign, with a range of 17.8 °C – 34.1 °C. The maximum value recorded for the daytime was 34.1 °C which occurred on 17th Oct 2018 at 14:00, and the maximum night-time temperature was 30.9 °C which occurred on 17th Oct 2018 at 17:30.

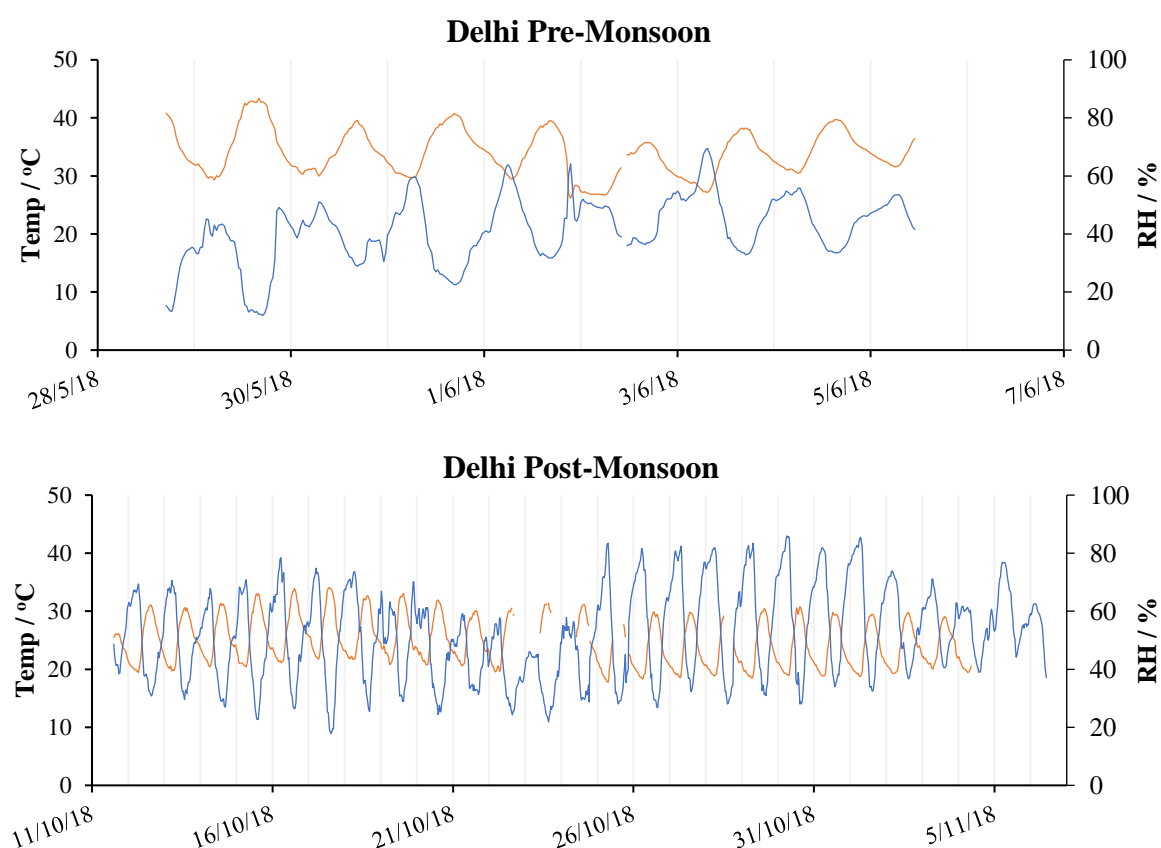


Fig. 3.2. Time series of Temperature (Orange) and Relative Humidity (Blue) across the APHH DPEM and DPOM campaigns. Error ca. < 1 %.

For the DPEM and DPOM campaigns, the RH ranged from 11.9 – 69.5 %, and 17.9 – 86.0 % respectively. RH% is generally lower during the day and higher at night. RH peaked in the early hours of the morning between ca. 06:00 – 08:00 and a diurnal cycle is seen. During DPEM, the

daytime average was 35.8 % (SD \pm 10.3 %) and the night-time average was 44.8 % (SD \pm 10.5 %). The DPOM day and night-time averages were 39.2 % (SD \pm 9.8 %) and 61.4 % (SD \pm 6.6 %), respectively. Therefore, the cooler temperatures during the autumn months generally allowed for a higher RH % during the night by *ca.* 20 %. The daytime values remain fairly similar.

3.3.1.3 Beijing Winds

Measurements were taken every 15 minutes during both BWIN and BSUM campaigns. During the winter period, measurements have been taken from 9th Nov 2016 at 17:30 – 9th Dec 2016 17:30 (2851 readings) and during the summer period from 18th May 2017 13:00 – 25th Jun 2017 08:30 (3564 readings) to coincide with filter sampling times. The prevailing winds in the Beijing campaign were seen to originate from the north of the city, whereas during the summer campaign prevailing winds were observed from the S-SW regions. The maximum wind speeds measured in winter and summer were 9.80 ms⁻¹ and 12.89 ms⁻¹, respectively. These corresponded to directional vectors of 302.19° (W-NW) and 69.38° (NE-E), respectively.

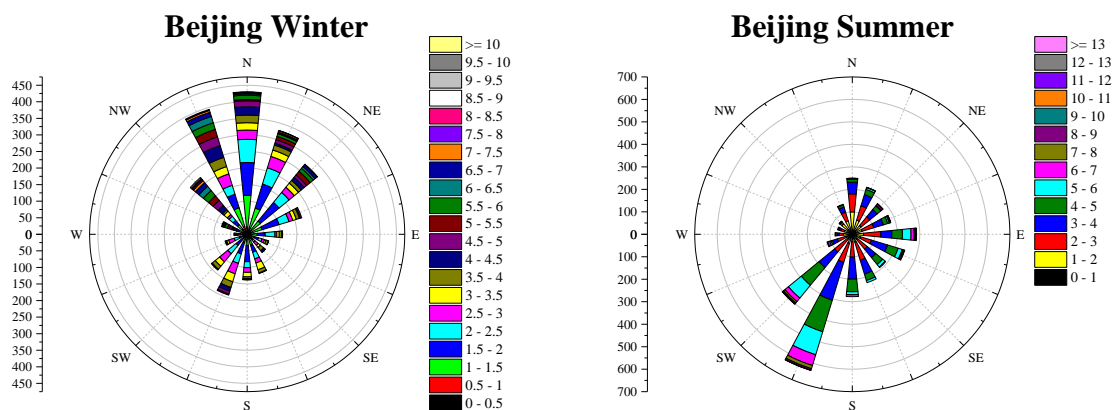


Fig. 3.3. Wind Rose Plots showing the overall wind speeds (legend, m s⁻¹) and wind directions across the APHH BWIN and BSUM campaigns.

3.3.1.4 Beijing Temperature and Relative Humidity

Temperature and RH% readings were taken every 15 minutes in Beijing from 9th Nov 2016 at 17:30 – 9th Dec 2016 at 17:30 (2875 readings) during the winter campaign and between 18th May 2017 at 13:00 until 25th Jun 2017 at 08:30 (3565 readings) as shown in Fig. 3.4.

The average temperature recorded during BWIN was 5.4 °C with a maximum of 16.7 °C (19th Nov 2016 at 13:45) and a minimum of -5.8 °C (22nd Nov 2016 at 07:15). Day and night-time temperature averages were 6.8 °C (SD \pm 3.8 °C) and 4.6 °C (SD \pm 3.6 °C).

During the summer campaign, an average temperature of 26.7 °C was recorded with a maximum of 39.8 °C and a minimum of 16.6 °C. The daytime maximum value was 39.8 °C and the minimum night-time value was 16.6 °C. The average day and night temperatures for the BSUM campaign were 29.0 °C (SD \pm 5.3 °C) and 25.2 °C (SD \pm 4.5 °C), respectively. Beijing was found to be generally cooler than Delhi, and the difference between the minimum Beijing winter campaign (-5.8 °C) and

maximum Delhi pre-monsoon campaign (43.4 °C) was 49.2 °C, allowing for a broad range of atmospheric conditions to be studied.

During the BWIN campaign, the RH% ranged from 7.5 – 98.0 %. The BSUM range was 13.6 % to 100 %. Similar to the Delhi campaigns, the BWIN and BSUM data show a clear diurnal profile with higher night-time RH% values. The BWIN day and night averages were 41.4 % (SD ± 21.0 %) and 54.9 % (SD ± 21.6 %), respectively. The minimum RH% was 7.5 % which is the lowest out of all campaigns. A significant drop to *ca.* 10 % is detected on 19th Nov at around midday. This coincides with a significant rise in temperatures. From the 19th Nov, temperatures gradually decrease until the 22nd Nov, for which a decrease is also observed in the RH%, although follows the decrease on the 21st to generally lower values. Particularly low values of RH% were observed on the 14th and 15th Nov of *ca.* 8 % and *ca.* 12 %, respectively.

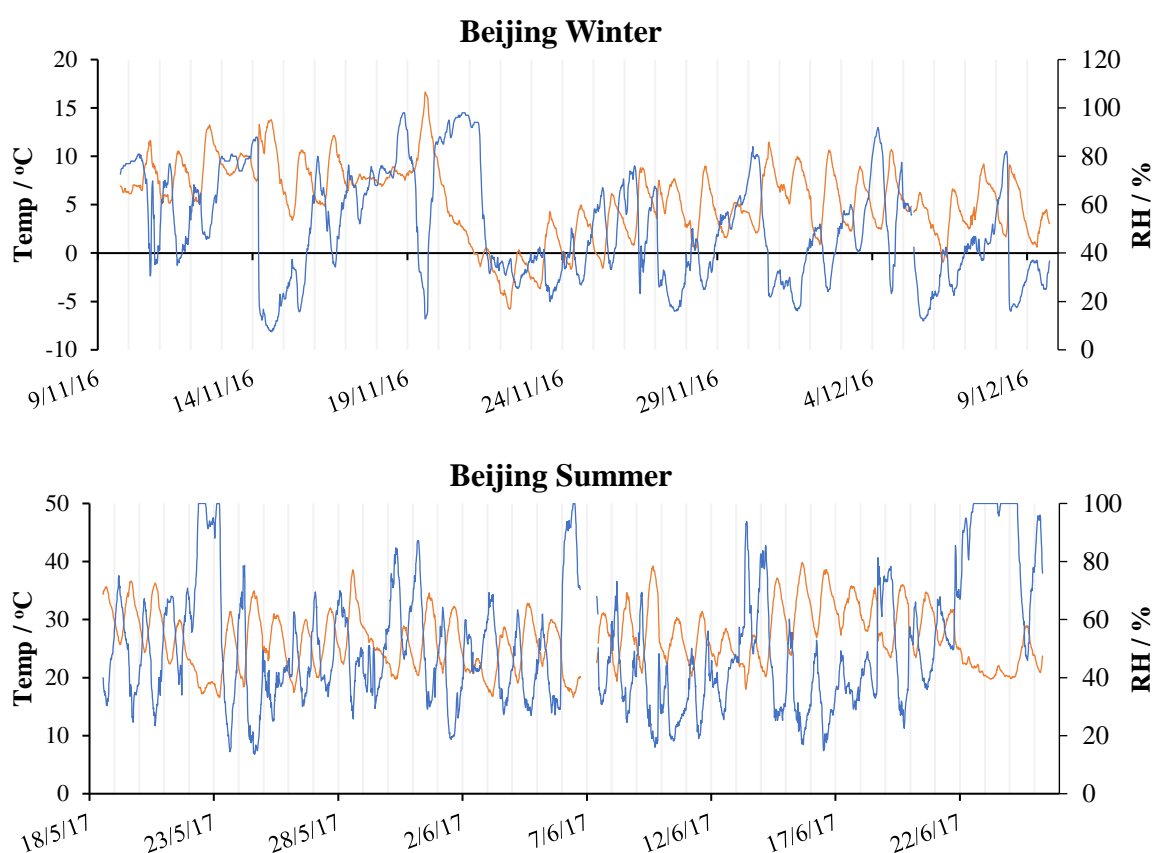


Fig. 3.4. Time series of Temperature (Orange) and Relative Humidity (Blue) across the APHH Beijing BWIN and BSUM campaigns. Error *ca.* < 1 %.

During the BSUM campaign, the day and night averages were 43.9 % (SD ± 22.7 %) and 55.2 % (SD ± 20.4 %), respectively. The average RH % measured across the entire BSUM campaign was 51.0 % (SD ± 22.0 %) which was similar to BWIN with RH 49.8 % (SD ± 22.3 %). The BSUM campaign observed an oscillation pattern in RH% from *ca.* 6th Jun 2017 until the end of the campaign (*ca.* 18 days). On some days instrument recorded a RH capped at 100 % RH% (21st – 22nd May; and 22nd – 23rd Jun), likely due to a precipitation event.

3.3.2 Gas and Particle Phase Composition in Delhi and Beijing

3.3.2.1 Time Series of Major Gas mixing ratios and Daily PM_{2.5} concentrations

The mixing ratio time series for NO, NO₂, CO, SO₂ and O₃, as well as the PM_{2.5} atmospheric concentrations during the APHH Delhi and Beijing campaigns are shown in Fig. 3.5 and Fig. 3.7, respectively. These plots have been used to determine the general air quality conditions throughout the four campaigns. The gas phase mixing ratios were measured by the UoY. The PM_{2.5} measurements were recorded by the UoB using an online Tapered Element Oscillating Monitor - Filter Dynamics Measurement System (TEOM-FDMS). The BWIN and BSUM mixing ratios are discussed in more detail by Squires et al., (2020)²⁸³.

Gas-phase measurements in Delhi were taken every minute and have been selected from the 28th May 2018 at 08:30 – 5th June 2018 at 17:30 (DPEM) and from 9th Oct 2018 at 14:54 – 6th Nov 2018 at 10:35 (DPOM). In the Beijing, measurements were recorded every 15 minutes and were selected from 9th Nov 2016 at 17:30 – 9th Dec 2016 at 17:30 and from 18th May 2017 13:00 – 25th Jun 2017 08:30, for the BWIN and BSUM campaigns, respectively. The grey vertical lines in each time series denotes the time of 00:00 on each day and the horizontal red lines in the PM_{2.5} time series display the UoB sampling times.

3.3.2.2 Delhi

During the DPEM period, very high levels of pollution were recorded towards the beginning of the campaign, especially in NO and CO. A maximum level of [NO] of 510 ppbv was reached on 29th May 2018 at 03:15. After this maximum, [NO] was much lower throughout the rest of the campaign. From the 30th May 2018 at 00:00 until the end of campaign, an average [NO] of 3 ppbv (SD ± 7 ppbv) was recorded. The [NO₂] generally rises in concentration later in the evening. The average day and night-time [NO₂] were 23 ppbv (SD ± 12 ppbv) and 36 ppbv (SD ± 20 ppbv), respectively. Similarly, [CO] usually peaks during the late evening and decreases towards mid-night. The maximum [CO] recorded was 5853 ppbv on 28th May 2018 at 22:42. Similar to [NO] and [CO], the highest values of [SO₂] were observed at the beginning of the campaign. In general, the concentrations of SO₂ are very low, with a median concentration across the campaign of 3 ppbv. Two very large spikes in [SO₂] are however observed on 4th Jun 2018 at 13:25 (1008 ppbv) and on 5th Jun 2018 at 17:29 (995 ppbv). These spikes are likely either due to an interference with the instrument or a sudden change in wind direction as a crematorium was located very near to the sampling site (corpse burning has been shown to emit SO₂)³³⁵. O₃ showed a rise in concentrations during the day (average of 75 ppbv, SD ± 26 ppbv), followed by a fall at night (average of 34 ppbv, SD ± 22 ppbv), in a diurnal cycle. The gases therefore indicate that the atmosphere was generally more oxidising during daytime periods compared to night-time hours.

In addition, 12-hourly PM_{2.5} data shows an overall decrease from the start of the campaign (54 μg m⁻³ at a midpoint of 29th May 2018 at 03:00) until midway through the campaign (mid-point of 1st Jun 2018 at 14:50) which also represents the campaign minimum of 13.00 μg m⁻³. A significant increase

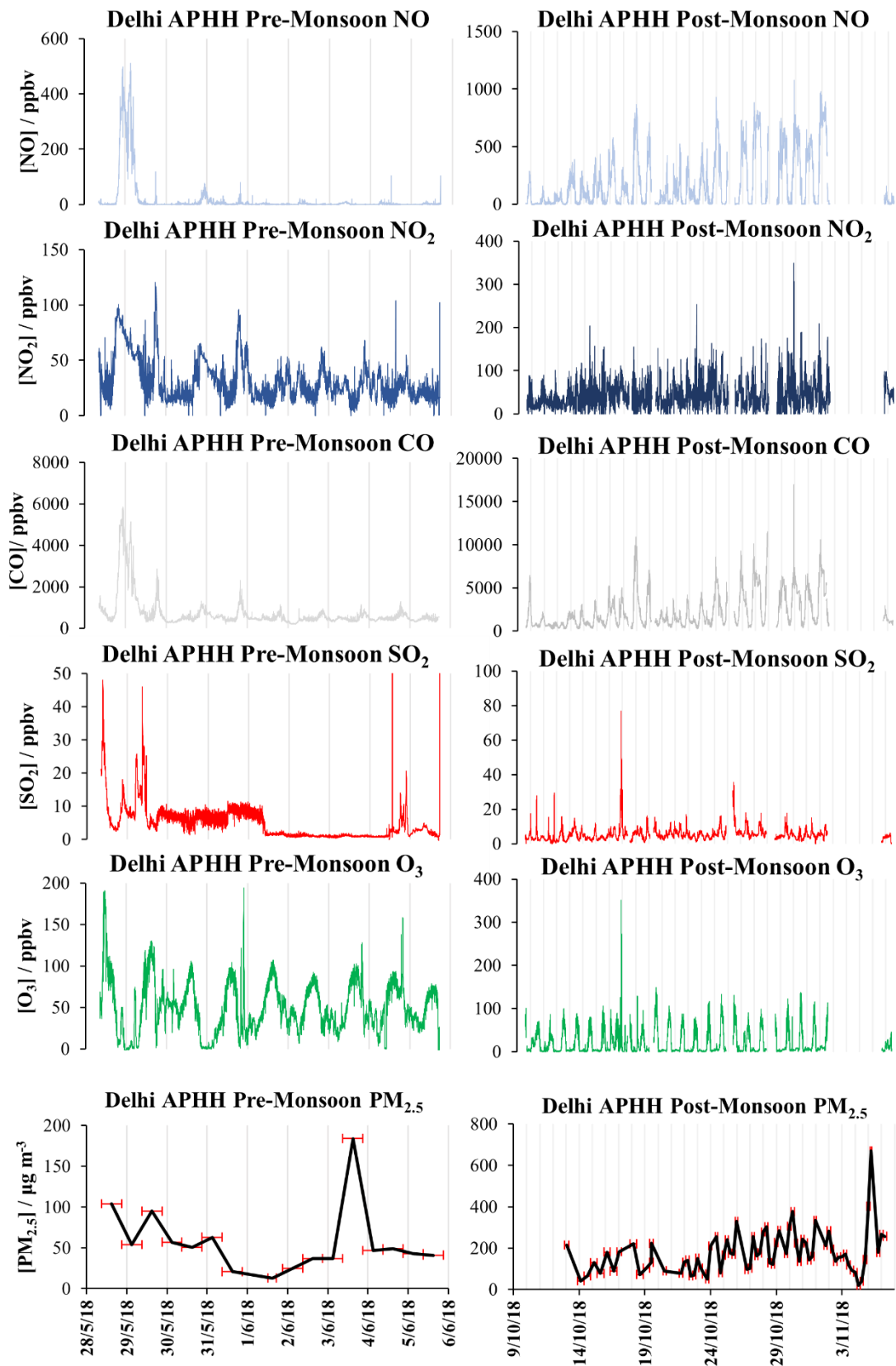


Fig. 3.5. Time series of the major gases and $[PM_{2.5}]$ measured during the APHH Delhi pre- and post-monsoon campaigns. The errors for the gas phase are NO (4.58 %), NO₂ (5.72 %), SO₂ (3.12 %), O₃ (4.04 %) and CO (9.14 %). TEOM-FDMS error was unavailable. Species concentrations are shown on the y-axes with time on the x-axes. The grey vertical lines represent midnight time points. The red error bars for $[PM_{2.5}]$ show the time of sampling. The x-axes are identical for each time series and are shown in the bottom chart ($[PM_{2.5}]$).

was seen in PM_{2.5} on 3rd Jun 2018 to 184 $\mu\text{g m}^{-3}$, although this is followed by a very gradual decrease in PM_{2.5} from 4th Jun 03:00 (47.00 $\mu\text{g m}^{-3}$) until the 5th Jun 15:00 (41.00 $\mu\text{g m}^{-3}$).

The DPOM period had much higher pollution levels compared to DPEM in all major gases and PM_{2.5}. NO concentrations peaked during night-time hours with much lower concentrations observed during daylight hours, in very clear diurnal cycles. The day and night-time averages were 18 ppbv (SD \pm 51 ppbv) and 268 ppbv (SD \pm 235 ppbv), respectively. A gradual increase in NO was also observed on the leadup to Diwali (7th Nov 2018). Opposite to NO, the NO₂ average was higher during the daytime (44 ppbv, SD \pm 28 ppbv), compared to night-time hours (40 ppbv, SD \pm 21 ppbv). The overall average NO₂ concentration was 42 ppbv which was *ca.* 35 % higher than in the DPEM (31 ppbv).

Similar to the DPEM period, CO mixing ratios rise in the very late hours of the day towards midnight and then drop significantly during morning hours. On top of this diurnal, a gradual increase in peak overnight CO concentrations is seen on the lead up to Diwali (as with NO). SO₂ concentrations are commonly higher at night and a particularly high peak occurs at a maximum of 77 ppbv in the evening on 16th Oct 2018 at 21:43. For O₃, a very clear diurnal is seen with the average day and night-time concentrations as 48 ppbv (SD \pm 30 ppbv) and 7 ppbv (SD \pm 17 ppbv), respectively. For NO, CO and O₃, very clear diurnal cycles are observed although O₃ demonstrates the opposite diurnal trend seen for NO and CO. This therefore indicates that oxidising species dropped during the DPOM night-time hours. This may be explained by a substantial drop in the boundary layer height during DPOM night-time hours (Fig. 3.6) causing very large increases in [NO_x] during night-time hours which starve the atmosphere of oxidising species resulting in higher [CO] and [NO], with significantly lower [O₃].

APHH Delhi Post-Monsoon Boundary Layer Height

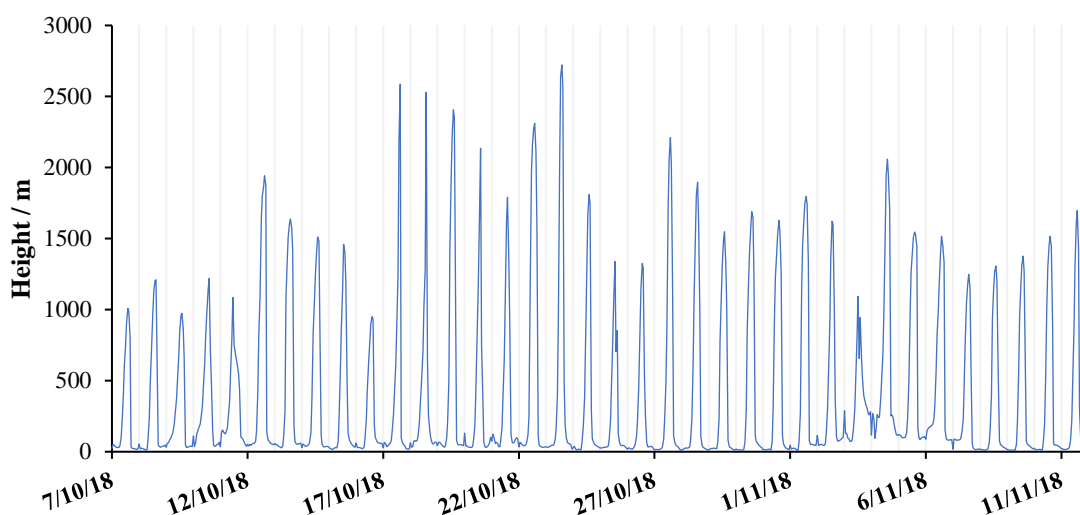


Fig. 3.6. Time series of the modelled boundary layer height (ECMWF)³³⁶ during the Delhi post-monsoon campaign.

Fig. 3.6 demonstrates the change in boundary layer height (m) as a function of time during the DPOM campaign. The data shown was modelled and taken from the European Centre for Medium-Range Weather Forecasts (ECMWF) database (using Lat 28.625, Lon 77.25 at 1 hour time resolution)³³⁶.

The contraction from day to night-time periods which very likely concentrated NO_x during the DPOM night-time hours was particularly strong. Boundary layer height is however known to contract generally under cooler temperatures, which accounts for the increase in the primary other pollutants during cooler periods across all campaigns.

PM_{2.5} concentrations showed very large variation (SD ± 103.46 μg m⁻³). The highest peak in this time series was found towards the end of the campaign (670 μg m⁻³). Finally, in the O₃ and SO₂ time series a spike is seen on the evening of the 16th Oct. These spikes were however suggested to be a potential interference with the instrument according to the UoY.

Therefore to summarise, the DPOM gas and particle phase concentrations indicated a more polluted atmosphere compared to the DPEM campaign. Substantially higher concentrations of PM_{2.5} are observed during the DPOM campaign compared to DPEM demonstrating much higher levels of combustion emissions during DPOM compared to DPEM. Furthermore, much higher levels of NO, NO₂, CO and SO₂ are also observed during the DPOM campaign, which are also associated with combustion emissions, likely down to the campaign taking place on the lead up to Diwali, increased regional agricultural burning and a decrease in boundary layer height at lower temperatures.

3.3.2.3 Beijing

During the BWIN campaign, the average NO mixing ratios were generally higher at night averaging 51 ppbv (SD ± 53 ppbv) compared to daytime hours 28 ppbv (SD ± 33 ppbv). The maximum NO concentration during the campaign was 264 ppbv sampled on the 7th Dec 2016 at 08:30. There was however a short period of *ca.* 2 days in the middle of the BWIN campaign (21st and 22nd Nov) in which values drop to near zero on two consecutive days. Observing Fig. 3.7, NO₂ concentrations generally rise throughout the day and peak at night. From the start of the campaign until the 20th Nov, NO₂ values vary significantly, with a mean of *ca.* 40 ppbv. NO₂ concentrations are also generally higher after the 25th Nov 2016, although frequently very low values are seen on 27th Nov, 1st Dec, 5th Dec and 8th Dec, for which values tend towards < 10 ppbv. The maximum value of 89 ppbv was recorded on 3rd Dec 2016 at 21:30 and the minimum value was 5 ppbv recorded on 8th Dec at 12:30. CO showed a relatively similar trend to NO₂, with mean mixing ratios of 967 ppbv (SD ± 695 ppbv) for daytime hours and 2970 ppbv (SD ± 2086 ppbv) for night-time hours, respectively.

These findings demonstrate that generally during the night-time hours, fewer oxidising species and a greater proportion of primary emissions were present. The maximum daytime [SO₂] measured during the BWIN campaign was 21 ppbv and the minimum values obtained was 0 ppbv (*ca.* two orders of magnitude smaller). The maximum and minimum observations during the BWIN night-time hours was 20 ppbv and 0 ppbv. SO₂ follows a very similar trend to NO, NO₂ and CO, showing multiple phases of relatively high SO₂ concentrations. Particularly high SO₂ values were measured on the 17th, 18th, 25th, 26th and 29th Nov which were > 25 ppbv.

The time series (CO, NO, NO₂, SO₂ and PM) indicate multiple large scale pollution episodes occurred over the course of the winter campaign. During the relatively clean periods, O₃ rises

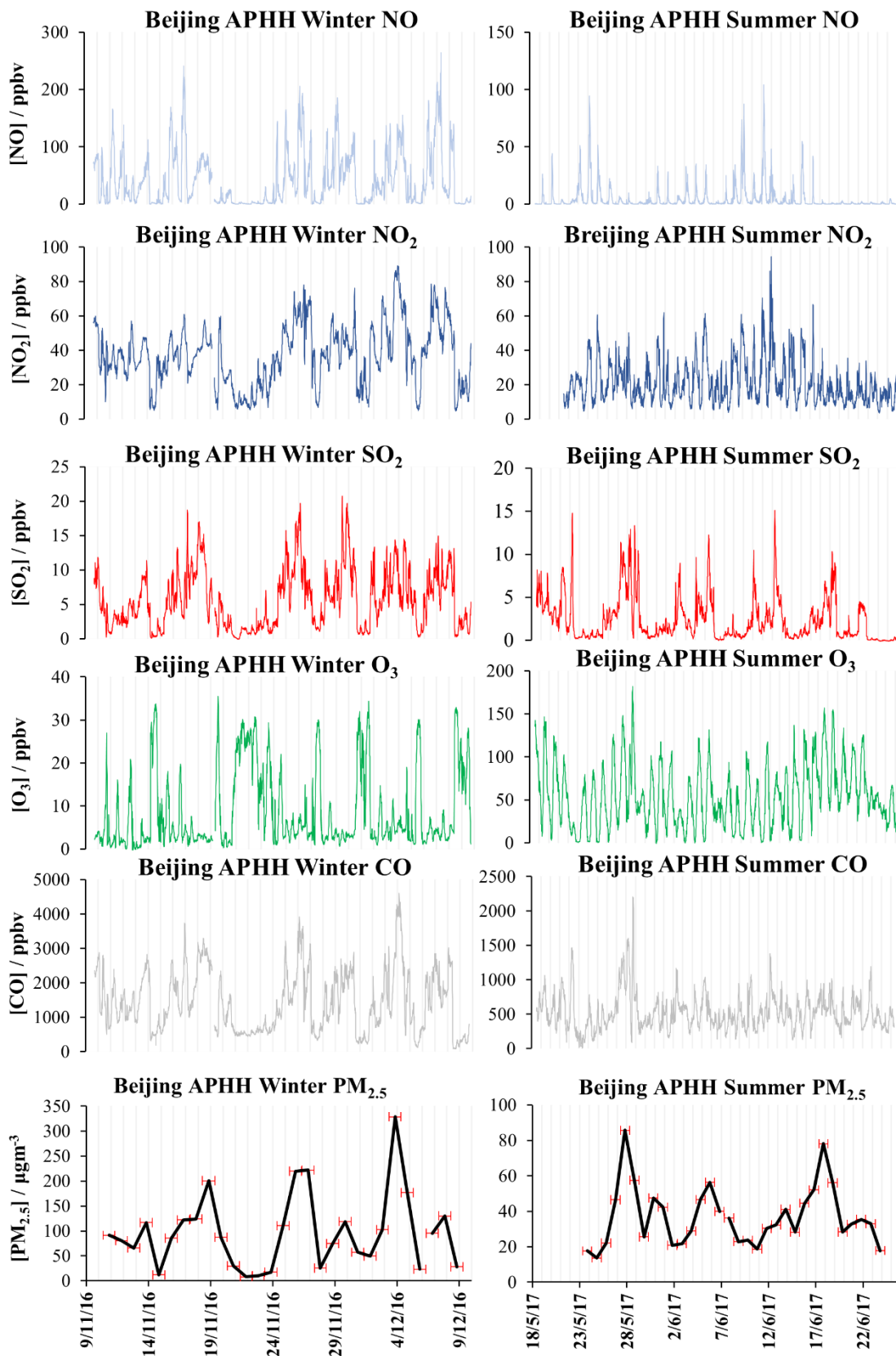


Fig. 3.7. Time series of the major gases and $\text{PM}_{2.5}$ measured during the APHH Beijing Winter and Summer campaigns. The errors for the gas phase are NO (4.58 %), NO_2 (5.72 %), SO_2 (3.12 %), O_3 (4.04 %) and CO (9.14 %). TEOM-FDMS error was unavailable. Species concentrations are shown on the y-axes with time on the x-axes. The grey vertical lines represent midnight time points. The red error bars for $[\text{PM}_{2.5}]$ show the time of sampling. The x-axes are identical for each time series and are shown in the bottom chart ($[\text{PM}_{2.5}]$).

significantly and is observed to have the inverse trend compared to the other major gases. This is expected due to NO titration of O₃ under polluted conditions. In addition, BWIN winter O₃ mixing ratios (9 ppbv) are on average much lower than in the other four campaigns and the BWIN campaign is also the only campaign in which a clear diurnal profile in the O₃ concentrations is not observed. This is due to the lack of ozone production under low solar intensity conditions and the high levels of NO and primary emissions indicated by high CO.

Six major peaks are seen in the TEOM-FDMS UoB BWIN PM_{2.5} data, which occur on 13th Nov (116.58 $\mu\text{g m}^{-3}$), 18th Nov (200.58 $\mu\text{g m}^{-3}$), 26th Nov (222.04 $\mu\text{g m}^{-3}$), 29th Nov (118.79 $\mu\text{g m}^{-3}$), 3rd Dec (328.67 $\mu\text{g m}^{-3}$, the maximum), and 7th Dec (129.87 $\mu\text{g m}^{-3}$). Troughs in the time series are observed on 14th Nov (12.12 $\mu\text{g m}^{-3}$), 21st Nov (8.13 $\mu\text{g m}^{-3}$), 27th Nov (25.50 $\mu\text{g m}^{-3}$), 1st Dec (49.50 $\mu\text{g m}^{-3}$), 5th Dec (23.08 $\mu\text{g m}^{-3}$) and 8th Dec (28.20 $\mu\text{g m}^{-3}$). PM_{2.5} generally follows the pattern of the pollution cycles in both campaigns with enhanced [PM_{2.5}] under more polluted conditions (similar to the gases).

During the BSUM campaign, NO has a very clear diurnal profile with high mixing ratios towards the beginning of the campaign on 24th May 2017 at 03:45 (94 ppbv). Further periods of elevated NO were observed on 9th Jun 2017 04:00 (88 ppbv) and 11th Jun 2017 at 05:00 (where the maximum of 104 ppbv was reached). Furthermore, very clear diurnal patterns are seen within the NO time series during periods of higher [NO]. NO₂ also demonstrates a very clear diurnal pattern with peaks occurring at night. The average day and night-time levels of NO₂ were 15 ppbv (SD \pm 8 ppbv) and 25 ppbv (SD \pm 13 ppbv), respectively. The campaign maximum was 95 ppbv and the minimum was 3 ppbv.

Increased daytime O₃ is down to greater solar activity and a substantial decline in NO. In addition, a mean [CO] of 527 ppbv (SD \pm 262 ppbv) was observed across the BSUM period reflecting the lower contribution of primary emitted species. Very clear diurnals were observed in O₃ showing peaks in concentrations during the daytime and troughs in concentrations over night-time hours. The daytime maximum was 182 ppbv (measured on 28th May at 17:15) and the minimum was 8 ppbv (measured on 22nd May at 08:45). The night-time maximum value was 178 ppbv (measured on 28th May at 17:30) and minimum was below the detection limit measured on 31st May at 04:15.

An SO₂ mean of 2 ppbv (SD \pm 3 ppbv) was observed over the course of the campaign. A particularly high SO₂ peak was also seen on 22nd May 2017 06:00 (15 ppbv) but does not correspond with an increase in any of the other major gases. Examining the PM_{2.5} time series in the BSUM period, five major pollution episodes are observed. In the PM_{2.5} data, these peak on 27th May (85.71 $\mu\text{g m}^{-3}$), 30th May (47.50 $\mu\text{g m}^{-3}$), 5th Jun (56.29 $\mu\text{g m}^{-3}$), 13th Jun (41.13 $\mu\text{g m}^{-3}$), and 17th Jun (78.13 $\mu\text{g m}^{-3}$). Very clear pollution cycles are mapped out in the PM_{2.5} time series, which is very clearly reflected in the time series of SO₂ and O₃ also (at close inspection).

3.3.2.4 Comparison of Gas Phase Species and PM_{2.5} in Beijing and Delhi

A summary table presenting PM_{2.5} statistics is shown in Table 3.1. These could not be split into day and night-time analyses as an average was measured *ca.* every 24 hours.

Table 3.1. TEOM-FDMS PM_{2.5} (UoB) statistical parameters for the APHH Delhi and Beijing campaigns ($\mu\text{g m}^{-3}$).

Campaign	μ	σ	Med	Max	Min	Range	P ₁₀	P ₉₀	N
Pre-Monsoon	59.18	41.26	48.00	184.00	13.00	171.00	23.00	99.50	16
Post-Monsoon	164.86	103.46	161.50	670.00	20.00	650.00	72.70	286.80	70
Winter	97.28	75.49	87.21	328.67	8.13	320.54	16.32	204.38	29
Summer	37.01	17.06	32.90	85.71	13.67	72.04	18.92	56.27	32

A summary of the mean gas and PM_{2.5} concentrations is shown in Fig. 3.8, for data in which the TEOM-FDMS (UoB) PM_{2.5} concentration sampling times overlapped with the HiVol (UoY) times. Fig. 3.8 shows the mean day, night and total NO (light blue), NO₂ (dark blue), SO₂ (red), O₃ (green), CO (grey) as well as average daily PM_{2.5} (black) concentrations measured over the course of the APHH Delhi and Beijing campaigns as bars. The concentrations of CO have been displayed on the secondary axes.

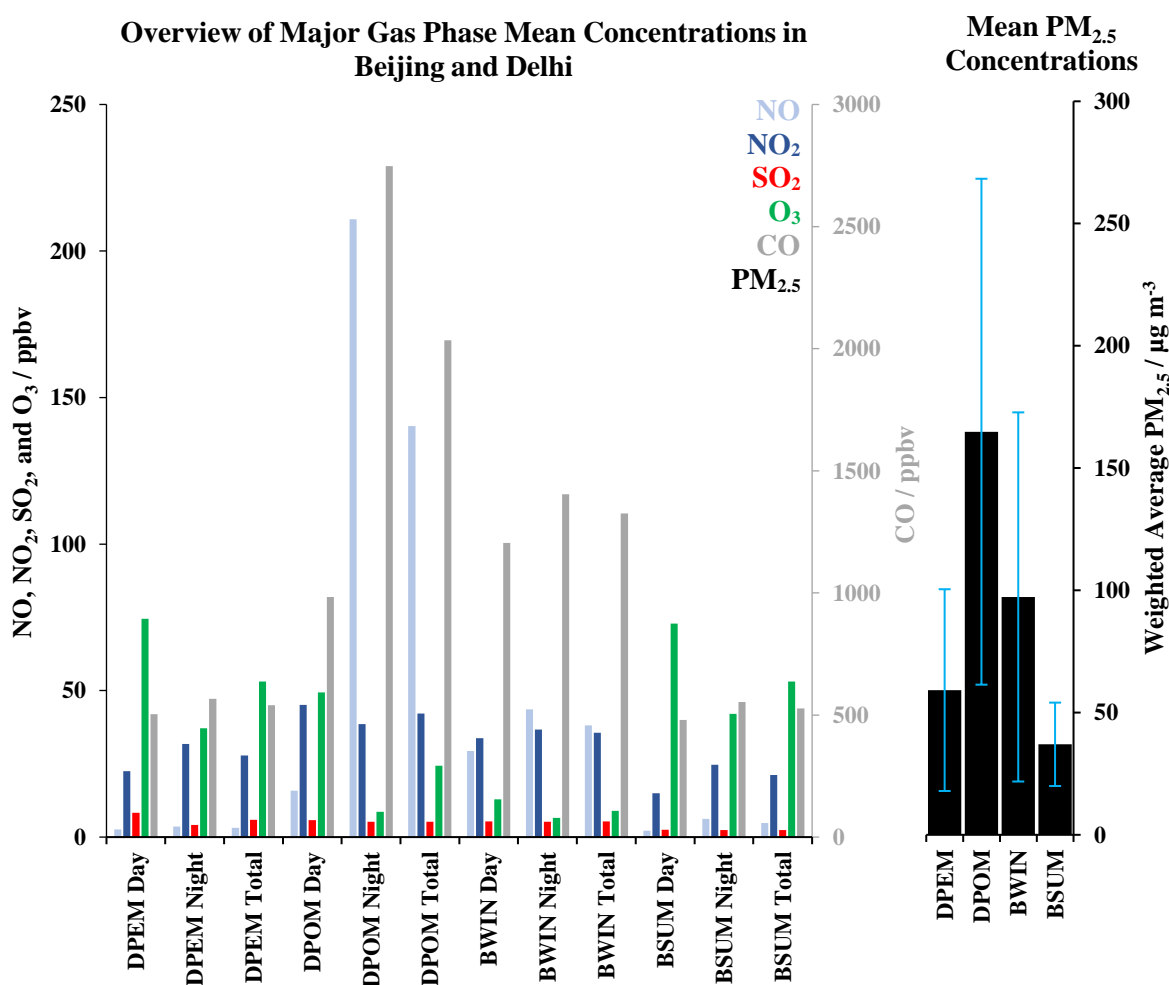


Fig. 3.8. Bar charts showing the mean major gas concentrations of NO (light blue), NO₂ (dark blue), SO₂ (red), O₃ (green), CO (grey) and PM_{2.5} (black) measured during the APHH DPEM, DPOM, BWIN and BSUM campaigns. The errors for the gas phase are NO (4.58%), NO₂ (5.72%), SO₂ (3.12%), O₃ (4.04%) and CO (9.14%). The error bars shown for [PM_{2.5}] values demonstrate the SD of the dataset.

Fig. 3.8 shows that the [NO] during the DPOM campaign was substantially higher compared the other APHH periods. This indicates considerably high NO_x emissions during the DPOM period. In each city, [NO] was higher during the cooler months (DPOM and BWIN) compared to the warmer months (DPEM and BSUM). This is reflective of the increased NO_x emissions from combustion during the Diwali periods (DPOM) and heating periods (BWIN). The DPEM and BWIN [NO] were very similar demonstrating 3 ppbv and 5 ppbv, respectively. In a similar manner, the [NO₂] were also slightly higher during cooler seasons in each season, reflective of NO_x combustion sources. The highest [NO₂] was seen during the DPOM period (42 ppbv) and the lower [NO₂] was observed for the BSUM period (21 ppbv). The [SO₂] was very similar between the DPEM, DPOM and BWIN campaigns demonstrating 6 ppbv, 5 ppbv and 5 ppbv, respectively. The BSUM [SO₂] was however *ca.* half of these values (2 ppbv). O₃ was higher during the warmer campaigns in each city, as would be expected from heightened solar flux. The DPEM and BSUM [O₃] were very similar, both demonstrating campaign means of 53 ppbv. The BWIN [O₃] was however *ca.* 3 times smaller compared to the DPOM campaign which may be explained by the substantially higher NO_x and VOC emissions during DPEM as well as much reduced BWIN temperatures. Finally, [CO] means were substantially higher compared to the other gaseous species. The DPOM campaign showed the highest [CO] at 2034 ppbv. The BWIN [CO] was also significant demonstrating a campaign mean of 1326 ppbv (*ca.* 65 % of the DPOM value). Like NO_x, [CO] showed lower values during the warmer seasons in each city. The DPEM and BSUM [CO] were very similar at 540 ppbv and 527 ppbv, respectively. Similar to NO_x, this is representative of higher primary combustion emissions observed during the DPOM and BWIN campaigns. For similar reasons, PM_{2.5} values were higher in the cooler months in both cities, although were considerably higher in Delhi than Beijing.

3.3.3 Time series of ionic species in PM_{2.5}

The time series of the major ions within PM_{2.5} measured during DPEM, DPOM, BWIN and BSUM campaigns are shown in Fig. 3.9 - Fig. 3.12. The ionic species data was produced by the author of this thesis whereas the gas-phase data from section 3.3.2 had been provided by colleagues at the UoY. The black line in each plot demonstrates the time series of each ion; the red error bar on the *x*-axis demonstrates the HiVol filter sampling time for each data point; and the grey vertical lines show 00:00 hours for each date indicated on the *x*-axis. Gaps in the time series are down to blocked filters or when no samples were collected. The other ions including F⁻ (Delhi), CH₃SO₃⁻, Cl⁻, NO₂⁻, PO₄³⁻, Na⁺, NH₄⁺, K⁺, Mg²⁺, and Ca²⁺ are shown at the end of this chapter.

3.3.3.1 Delhi Pre-Monsoon

Fig. 3.9 shows the time series of the major ions measured by IC over the course of DPEM. Cl⁻ had a maximum value of 5.54 μg m⁻³ during the late afternoon (midpoint of 16:02) on 31st May 2018 and a minimum value of 0.64 μg m⁻³ during overnight sampling (midpoint of 01:03) on 4th Jun 2018. The gap in all of the time series overnight between 28th - 29th May is due to a blocked filter which corresponds with an intense polluted period. Troughs in the Cl⁻ time series generally occur at night

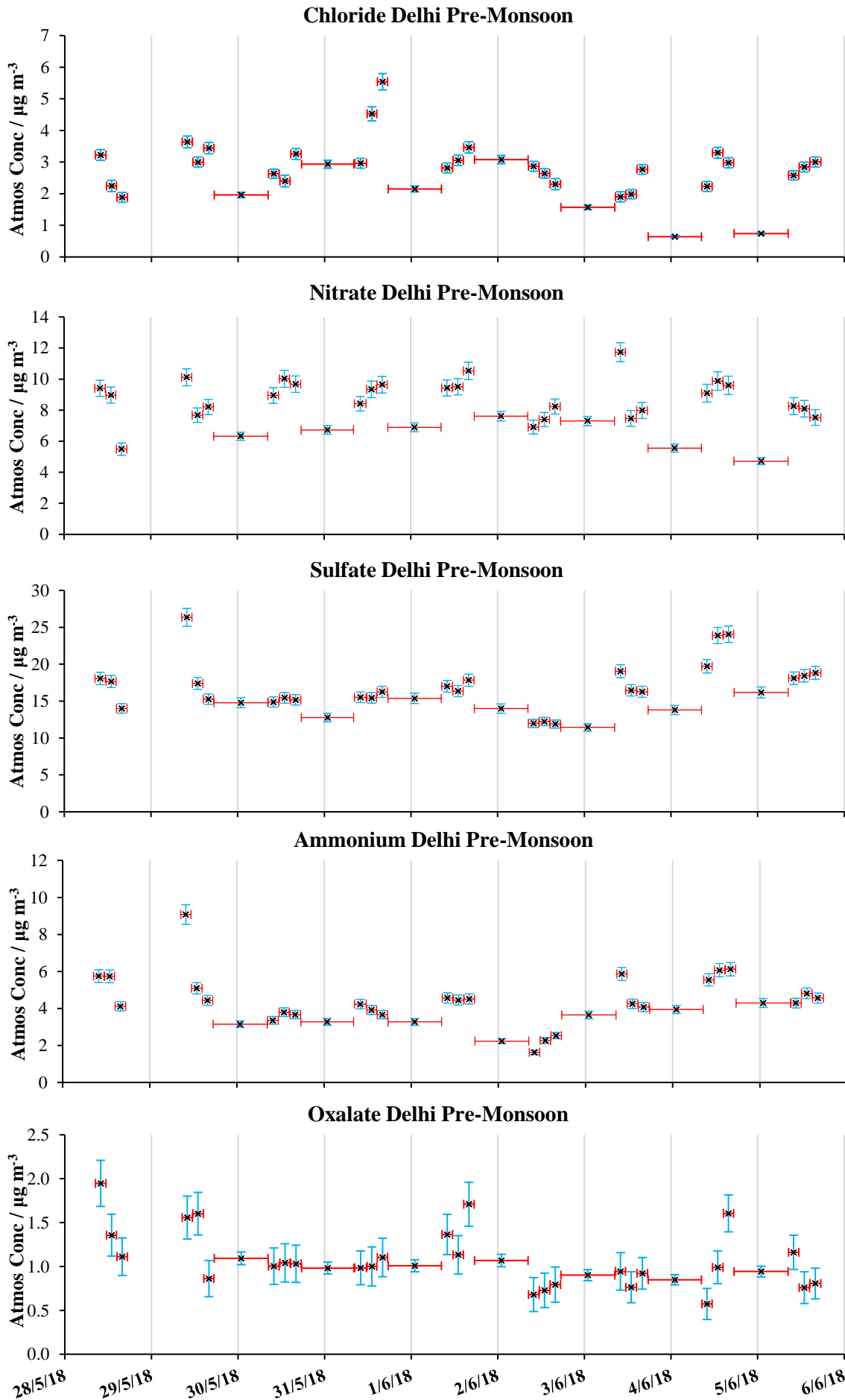


Fig. 3.9. Time series of the major ions measured by offline ion chromatography during the APHH Delhi pre-monsoon campaign. Ion concentrations are shown on the y-axes with time on the x-axes. The grey vertical lines represent midnight time points. The red error bars show the time of sampling and the blue error bars show the error of each concentration measurement in the y-axis. The x-axes are identical for each time series and are shown in the bottom chart (oxalate).

with higher concentrations observed during daytime hours. Generally, lower Cl^- concentrations are observed towards the end of the campaign. NO_3^- shows a very consistent diurnal pattern of rising concentrations during the day and decreases at night. The minimum $[\text{NO}_3^-]$ observed at night was $4.71 \mu\text{g m}^{-3}$ and the maximum daytime concentration was $11.73 \mu\text{g m}^{-3}$. Like Cl^- and the gas phase species (Fig. 3.5), NO_3^- follows the general pattern of higher concentrations during daylight hours. There are 2 days in the time series that deviate slightly from this general diurnal pattern on 29th May 2018 and on 3rd Jun 2018, with a small reduction in NO_3^- concentrations in the midday sample. The deviation on the 29th May could be down to temperature. The maximum temperature observed during the DPEM campaign (and therefore all APHH campaigns) was 43.4°C at 16:00 on 29th May.

The mid-point time for this filter was 12:56, for which the temperature at 13:00 was 42.2°C . The RH was also particularly low at this time (15.1 %). One of the major production pathways of particle phase NO_3^- is through the NH_3 and HNO_3 neutralisation reaction forming NH_4NO_3 (in equilibrium). NH_4NO_3 is known to be volatile under increased temperatures and therefore the trough observed on the 29th May is likely down to a significant loss of NH_4NO_3 due to significantly high temperatures. This is further discussed in chapter 5. The reason for the midday trough on the 3rd Jun is unclear.

The maximum $[\text{SO}_4^{2-}]$ was $26.36 \mu\text{g m}^{-3}$ observed at the beginning of the campaign and is likely the result of very high $[\text{SO}_2]$ on the 29th May. A very large drop in NO , with substantial concentrations of O_3 reaching *ca.* 130 ppbv (Fig. 3.5) were also seen on this date. This shows that on the 29th, a higher concentration of oxidising species was likely present along with high SO_2 . The time series for SO_4^{2-} was shown to be relatively unchanging during the first half of the campaign. The consistency in SO_4^{2-} concentration is similar to the relatively stable time series observed in SO_2 (Fig. 3.5), for which not much deviation is observed until 3rd June 2018 at 00:56. The SD for SO_4^{2-} across this stable period (30th May 2018 00:53 – 2nd June 2018 0:58) was $1.28 \mu\text{g m}^{-3}$ (range of $5.06 \mu\text{g m}^{-3}$), compared to an overall SD of $3.38 \mu\text{g m}^{-3}$ (range of $14.92 \mu\text{g m}^{-3}$) across the campaign. A drop in SO_2 is observed after this stable period at around 1st June 2018 at 01:00, which is also reflected in a drop in SO_4^{2-} between 1st June 2018 at 15:59 ($17.84 \mu\text{g m}^{-3}$) – 3rd June 2018 at 00:56 ($11.43 \mu\text{g m}^{-3}$). Therefore, the SO_4^{2-} concentration reduction follows the drop in SO_2 mixing ratios with a time lag of *ca.* > half a day. The two SO_4^{2-} peaks observed towards the very end of the campaign on 3rd June 2018 at 10:00 and 4th June 2018 at 15:56 may be associated with the two very large peaks observed in SO_2 earlier in the day on these two dates and would be consistent with a time lag of SO_2 to SO_4^{2-} conversion. The relationship between SO_2 and SO_4^{2-} therefore demonstrates the dependence of SO_2 for SO_4^{2-} production.

Furthermore, the SO_4^{2-} trend follows that of NH_4^+ very closely and therefore gives further evidence to the oxidation of SO_2 followed by NH_3 neutralisation. Finally, SO_4^{2-} forms a substantial fraction of $\text{PM}_{2.5}$ in this study, and on 29th May 2018 at 09:56, SO_4^{2-} concentrations were $26.36 \mu\text{g m}^{-3}$, thus SO_4^{2-} concentrations alone were higher than the World Health Organisation (WHO) limits of $25 \mu\text{g m}^{-3}$ for $\text{PM}_{2.5}$.

Similarly, to SO_4^{2-} , NH_4^+ shows a large drop on the 29th May when exiting the particularly polluted period as shown in Fig. 3.5 (especially NO , CO and SO_2) for which acidic acids are likely present. A drop is seen on 29th in all anions which are conjugate bases to atmospheric acid gases. A diurnal profile is observed with generally higher concentrations during the day. NH_4^+ also shows a stable concentration period between 30th May 2018 at 00:53 and 2nd June 2018 at 00:58. Over this period the SD is $0.66 \mu\text{g m}^{-3}$ which compared to an SD of $1.38 \mu\text{g m}^{-3}$ across the whole dataset.

$\text{C}_2\text{O}_4^{2-}$ demonstrates the lowest concentrations between these major ions. The maximum and minimum values of $\text{C}_2\text{O}_4^{2-}$ were found to be $1.95 \mu\text{g m}^{-3}$ and $0.57 \mu\text{g m}^{-3}$ respectively (range of $1.37 \mu\text{g m}^{-3}$). There are however obvious troughs followed by peaks during daytime hours on 1st June and 3rd June, both at *ca.* 13:00. These features are also reflected in the time series of NH_4^+ , SO_4^{2-} and NO_3^- (for 1st June) and NO_3^- (3rd June) which indicates that oxalic acid may have been formed and neutralised with NH_4^+ during the DPEM period.

Overall, all ions observe a decrease from *ca.* midday on 29th May until early evening representing a change from a particularly polluted period to cleaner atmospheric conditions.

3.3.3.2 Delhi Post-Monsoon

The DPOM campaign was conducted during the run-up to Diwali during the autumn of 2018 and the major ion time series are shown in Fig. 3.10. A particularly high Cl^- episode occurred on the 16th Oct, with the campaign maximum of $29.74 \mu\text{g m}^{-3}$. Directly after, concentrations drop rapidly to $9.28 \mu\text{g m}^{-3}$ on 16th Oct at 12:08. Another Cl^- rise occurred to $20.70 \mu\text{g m}^{-3}$ on 16th Oct at 13:09 and therefore demonstrates rapidly switching Cl^- on this day. This may have been due to a sudden change in wind direction or a very localised HCl source. A minimum value of $0.60 \mu\text{g m}^{-3}$ was observed on 11th Oct at 10:48. Generally, the time series seems to demonstrate a build-up of Cl^- during the day followed by a gradual decline towards night-time hours.

The NO_3^- trend is opposite to that observed in the DPEM dataset as peaks occur more often during daytime hours compared to night. The maximum daytime $[\text{NO}_3^-]$ was $47.95 \mu\text{g m}^{-3}$ on 30th Oct at 10:36. The minimum $[\text{NO}_3^-]$ was $3.11 \mu\text{g m}^{-3}$ observed during the late afternoon at 16:51 on 11th Oct. This produced a large range of $44.84 \mu\text{g m}^{-3}$. Some similarities are also seen in the overall trends of NO_3^- with NH_4^+ and further investigation into possible HNO_3 neutralisation with NH_3 during the DPOM campaign is described in chapter 5.

Unlike in the pre-monsoon which exhibited clear examples of an increase in SO_4^{2-} concentrations in the particle phase following a rise in gas phase SO_2 , this is less obvious in the post-monsoon dataset. The maximum and minimum daytime concentrations observed were $26.75 \mu\text{g m}^{-3}$ and $6.98 \mu\text{g m}^{-3}$, respectively. For the night-time period these means were $22.24 \mu\text{g m}^{-3}$ and $5.88 \mu\text{g m}^{-3}$, respectively. Furthermore, unlike the DPEM campaign, no significant similarity is observed between the NH_4^+ and SO_4^{2-} .

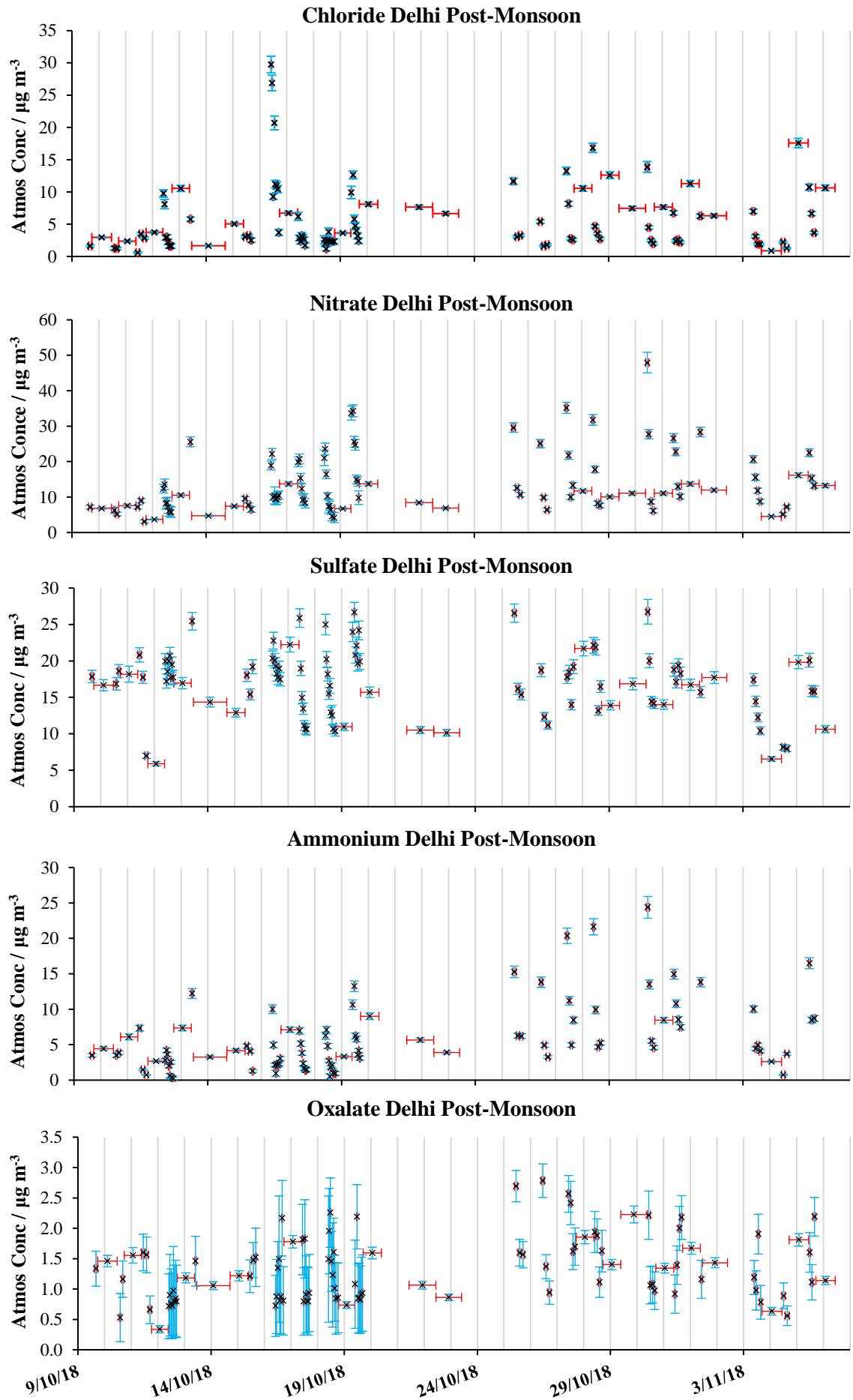


Fig. 3.10. Time series of the major ions measured by offline ion chromatography during the APHH Delhi post-monsoon campaign. Ion concentrations are shown on the y-axes with time on the x-axes. The grey vertical lines represent midnight time points. The red error bars show the time of sampling and the blue error bars show the error of each concentration measurement in the y-axis. The x-axes are identical for each time series and are shown in the bottom chart (oxalate).

The maximum daytime NH_4^+ concentration was measured on 30th Oct at 10:36 ($24.37 \mu\text{g m}^{-3}$) and the minimum was observed on 12th Oct at 16:55 ($0.20 \mu\text{g m}^{-3}$). Visually inspecting Fig. 3.10, $[\text{NH}_4^+]$ generally increases on the lead-up to Diwali. NH_3 is known to be emitted by numerous sources including biomass burning, fossil fuel combustion, and agriculture, fertilizer usage²¹², vehicle emissions as well as industrial emissions^{337,212}. These are all activities which are likely to increase on the lead up to Diwali, increasing NH_3 and therefore neutralisation to NH_4^+ . In addition, Gradual increases are also seen in the $\text{PM}_{2.5}$ and CO during this period (Fig. 3.5). In addition, the lead up to Diwali is likely to increase the concentrations of acidic gases, which increases NH_3 neutralisation and therefore NH_4^+ production in the particle phase. Another possible reason for NH_4^+ build up may be due to the relatively low windspeeds during the DPOM campaign as shown in Fig. 3.1. This would allow for the build-up of both NH_3 and NH_4^+ .

For $\text{C}_2\text{O}_4^{2-}$, the maximum day and night concentrations were $2.78 \mu\text{g m}^{-3}$ and $1.85 \mu\text{g m}^{-3}$ and minimum were $0.53 \mu\text{g m}^{-3}$ and $0.34 \mu\text{g m}^{-3}$, respectively. $[\text{C}_2\text{O}_4^{2-}]$ were generally higher during the day compared to the night-time hours. Deviations from this general trend do however occur. For example, a trough ($0.53 \mu\text{g m}^{-3}$) is seen at 13:59 (10th Oct) and on 28th Oct at 14:11 ($1.11 \mu\text{g m}^{-3}$). The trough on 10th Oct seems substantial although this is due to much lower $[\text{C}_2\text{O}_4^{2-}]$ compared to the other ions (which also observe a decrease here). The trough on the 28th of Oct is considerable and in agreement with large decreases in all other major ions shown in Fig. 3.10. This is however in disagreement with the $\text{PM}_{2.5}$ trend which only observes a slight decrease from $129 \mu\text{g m}^{-3}$ (28th Oct 12:00) to $122 \mu\text{g m}^{-3}$ (28th Oct 18:00). Therefore, this trough may not be explained by a decrease in $\text{PM}_{2.5}$ alone. Another three consecutive days that show troughs in daylight hours and do not show this general pattern are also seen on 30th Oct at 15:56 ($0.97 \mu\text{g m}^{-3}$), 31st Oct at 10:08 ($0.92 \mu\text{g m}^{-3}$) and 1st Nov 10:01 ($1.16 \mu\text{g m}^{-3}$).

Comparing the major ions cumulatively, the large peak in $\text{PM}_{2.5}$ detected at the end of the campaign (5th Nov at 04:40, $670 \mu\text{g m}^{-3}$) is not reflected in a larger concentration on the 5th Nov in any of the major ions. Diwali was celebrated on the 7th Nov in 2018 and therefore this large $\text{PM}_{2.5}$ peak was detected two days prior. As Secondary Inorganic Aerosol (SIA) species form a substantial fraction of inorganic $\text{PM}_{2.5}$ this may indicate that $\text{PM}_{2.5}$ present in the days close to Diwali is predominantly organic based. In addition, a much stronger overall increase in major or minor ion concentrations over the course of the campaign is not seen, despite the lead up to Diwali. This suggests that inorganic ions do not play a key role in the very high $\text{PM}_{2.5}$ levels seen in Delhi during the start of November.

3.3.3.3 Beijing Winter

From the $\text{PM}_{2.5}$ and the major gases time series (Fig. 3.7), six major pollution periods were observed and are reflected in the time series on the major ions. The Cl^- daytime maximum and minimum readings were $15.80 \mu\text{g m}^{-3}$ and $0.07 \mu\text{g m}^{-3}$ respectively. The night-time maximum and minimum values were found to be $11.26 \mu\text{g m}^{-3}$ and $0.23 \mu\text{g m}^{-3}$. Peaks were detected during day (e.g. 18th Nov at 15:05, $12.24 \mu\text{g m}^{-3}$) and night periods (e.g. 1st – 2nd Dec, $4.33 \mu\text{g m}^{-3}$ and 2nd – 3rd Dec, $6.79 \mu\text{g m}^{-3}$).

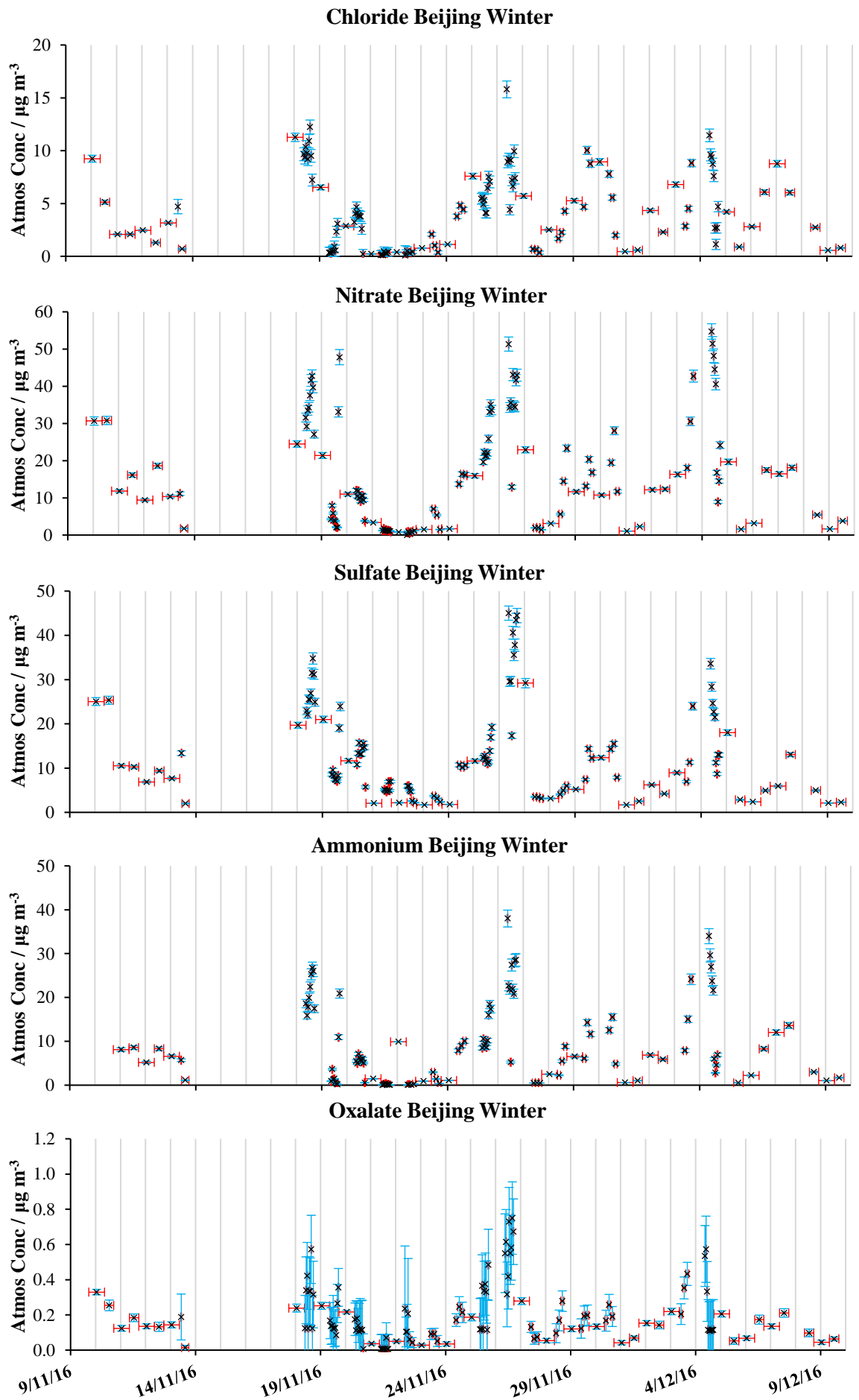


Fig. 3.11. Time series of the major ions measured by offline ion chromatography during the APHH Beijing Winter campaign. Ion concentrations are shown on the y-axes with time on the x-axes. The grey vertical lines represent midnight time points. The red error bars show the time of sampling and the blue error bars show the error of each concentration measurement in the y-axis. The x-axes are identical for each time series and are shown in the bottom chart (oxalate).

m^{-3}). A low concentration and stable period was seen between the 21st and 22nd Nov averaging at $0.48 \mu\text{g m}^{-3}$ ($\text{SD} \pm 0.14 \mu\text{g m}^{-3}$). Dissimilar to the Delhi $\text{PM}_{2.5}$ readings, the Cl^- during BWIN follow the $\text{PM}_{2.5}$ pollution cycles (Fig. 3.7) well. This is due to suspected high HCl emissions from combustion sources such as biomass and coal during the cooler winter heating season. In addition, the very cool temperatures promote partitioning of Cl^- into the particle phase.

The daytime maximum and minimum $[\text{NO}_3^-]$ were $54.72 \mu\text{g m}^{-3}$ and $0.06 \mu\text{g m}^{-3}$, respectively. For the night-time hours, these were $30.66 \mu\text{g m}^{-3}$ and $0.81 \mu\text{g m}^{-3}$, respectively. Most peaks in NO_3^- were observed during the day. The maximum $[\text{NO}_3^-]$ was $54.72 \mu\text{g m}^{-3}$ on 4th Dec at 08:58, which occurred consecutively after a blocked Hivol filter sample (indicated by the break in time series in Fig. 3.11) indicating high SIA $\text{PM}_{2.5}$. The $[\text{NO}_3^-]$ at this time was over twice the WHO $\text{PM}_{2.5}$ $25 \mu\text{g m}^{-3}$ limit (24 hour). An over-night filter between the 3rd and 4th Dec was also blocked due to very high $\text{PM}_{2.5}$ (on inspection of the gas and $\text{PM}_{2.5}$ data in Fig. 3.7 shows a particularly polluted period here). Between 19th Nov 15:05 and 17:05, a large increase is observed in NO_3^- from $2.05 \mu\text{g m}^{-3}$ to $47.83 \mu\text{g m}^{-3}$. Increases between these two samples are also seen in the other major ions, although the largest increase is by far associated with NO_3^- .

Inspecting the gas data (Fig. 3.7), shows that the large increase in NO_3^- occurs at around the same time at which a dramatic decrease in O_3 occurs (after a large spike in O_3) with a rise in concentration of NO_2 and CO . NO is also shown to be at a minimum on this day. Therefore, on the 19th Nov it seems as though a burst of oxidising species was created although was quickly titrated away. The large spike in NO_3^- is likely due to a rapid NO_x oxidation on this day producing HNO_3 . This is accompanied by a significant increase in NH_4^+ which may indicate the formation of particle phase NH_4NO_3 . Another possibility for the drastic change in $[\text{NO}_3^-]$ on this day may be a wind direction change.

Rapidly changing concentrations are observed in all the major ions on 26th Nov, although the variability in NO_3^- is greatest with a SD of $10.62 \mu\text{g m}^{-3}$, compared to SO_4^{2-} ($\text{SD} \pm 9.11 \mu\text{g m}^{-3}$), Cl^- ($\text{SD} \pm 3.14 \mu\text{g m}^{-3}$) NH_4^+ ($\text{SD} \pm 8.81 \mu\text{g m}^{-3}$) and $\text{C}_2\text{O}_4^{2-}$ ($\text{SD} \pm 0.14 \mu\text{g m}^{-3}$). This period is therefore likely due to rapid changes in wind directions. Similar to Cl^- , NO_3^- follows a very close pattern to the BWIN $\text{PM}_{2.5}$ time series (Fig. 3.7) which indicates that NO_3^- and similar formation processes to NO_3^- has a substantial influence on $[\text{PM}_{2.5}]$ during the BWIN campaign. This is further explored in chapter 5.

A general diurnal pattern of SO_4^{2-} build-up during night-time hours followed by loss during the day is seen in Fig. 3.11. The SO_4^{2-} trend approximately followed the trend of SO_2 (Fig. 3.7) as with the DPEM campaign. In the SO_2 time series a large peak is observed on 26th Nov, on the same day that the maximum SO_4^{2-} concentration of $45.02 \mu\text{g m}^{-3}$ appears. The maximum and minimum $[\text{SO}_4^{2-}]$ were $45.02 \mu\text{g m}^{-3}$ and $2.00 \mu\text{g m}^{-3}$ for the daytime as well as $29.20 \mu\text{g m}^{-3}$ and $1.68 \mu\text{g m}^{-3}$ for the night-time, respectively. Similarly to Cl^- , the campaign maximum concentration of SO_4^{2-} occurs

during the second pollution period ($45.02 \mu\text{g m}^{-3}$), although the maximum $[\text{PM}_{2.5}]$ was observed on 3rd Dec at 20:02 ($328.67 \mu\text{g m}^{-3}$).

The maximum $[\text{NH}_4^+]$ was recorded on 26th Nov at 09:07 ($38.00 \mu\text{g m}^{-3}$) and the minimum was $0.01 \mu\text{g m}^{-3}$ (21st Nov 10:00). Considering NH_4^+ is known to be closely related to Cl^- , NO_3^- and SO_4^{2-} , on the 22nd Nov a rise in NH_4^+ to $9.89 \mu\text{g m}^{-3}$ at 01:03 occurs and is not mimicked in either Cl^- , NO_3^- or SO_4^{2-} . The rise in NH_4^+ could therefore be from a transported air mass or NH_3 neutralisation from an acidic gas which has not been measured. NH_4^+ generally follows a similar pattern to the other major ions (Fig. 3.11) and $\text{PM}_{2.5}$ (Fig. 3.7) showing the six main pollution periods. The campaign daytime maximum and minimum $[\text{NH}_4^+]$ were $38.01 \mu\text{g m}^{-3}$ and $0.01 \mu\text{g m}^{-3}$, respectively. For the night-time period, these values were $12.01 \mu\text{g m}^{-3}$ and $0.59 \mu\text{g m}^{-3}$, respectively.

Despite the low $[\text{C}_2\text{O}_4^{2-}]$, the major periods of pollution throughout the campaign can be seen in the time series. The general diurnal pattern consists of a rising during the day and a decrease during the night. There are some exceptions here, such as peaks during the night observed between 1st – 3rd Dec (although a gradual increase in concentrations is generally seen here). In addition to the variability seen on 26th Nov in $\text{C}_2\text{O}_4^{2-}$ (as with the other ions), two other periods of great variability not seen in the other major ions but in $\text{C}_2\text{O}_4^{2-}$ were observed on the 19th and 25th Nov. The %RSD for the 19th, 25th, and 26th for $\text{C}_2\text{O}_4^{2-}$ during daytime hours was 52.94 %, 53.85 % and 21.21 %, respectively. The daytime maximum and minimum $[\text{C}_2\text{O}_4^{2-}]$ were $0.75 \mu\text{g m}^{-3}$ and $0.01 \mu\text{g m}^{-3}$, respectively. For the night-time hours, these values were $0.33 \mu\text{g m}^{-3}$ and $0.03 \mu\text{g m}^{-3}$, respectively.

3.3.3.4 Beijing Summer

Fig. 3.12 shows the time series of the major ions during the BSUM campaign. Analogous to all other campaigns, Cl^- tends to increase during the early hours and decreases towards mid-night. In the BSUM campaign, an exception is found on 26th May at 01:06 in which a rise is seen at night to $1.52 \mu\text{g m}^{-3}$ (the second highest value for BSUM). The peak shown on 2nd Jun at 10:00 ($1.57 \mu\text{g m}^{-3}$) is also particularly high, within a region of relatively low concentration. The average wind direction from the 26th May at 01:06 was 175.28° and on the 2nd Jun 10:00 was 104.97° . With respect to IAP, these winds had come directly from a composting site (*ca.* 30 km away) on 26th May 01:06 and a landfill site *ca.* 15 km away on 2nd Jun 10:00 (map shown in chapter 5). In addition, the trend of Cl^- tends to rise towards the latter half of the campaign (from *ca.* 10th June). Concentrations are also much more variable after this point until the end of the campaign with a SD of $0.76 \mu\text{g m}^{-3}$ (mean of $0.46 \mu\text{g m}^{-3}$), in comparison to before this point with a SD of $0.29 \mu\text{g m}^{-3}$ (mean of $0.41 \mu\text{g m}^{-3}$). The very fluctuating trend on the 20th and 21st Jun is indicative of rapidly changing wind directions.

Similarly, $[\text{NO}_3^-]$ tends to be higher during the day, although exceptions with peaks during night periods are seen, such as on the 21st May 01:10 and 28th May at 00:57. NO_2 measurements had not caused this rise on the 21st May. On 28th May, no significant increases are observed in either Cl^- or SO_4^{2-} and therefore it is unlikely that an increase in NH_3 had occurred (NH_4^+ was not recorded at this specific time). There were also no obvious deviations in the gas time series which were able to

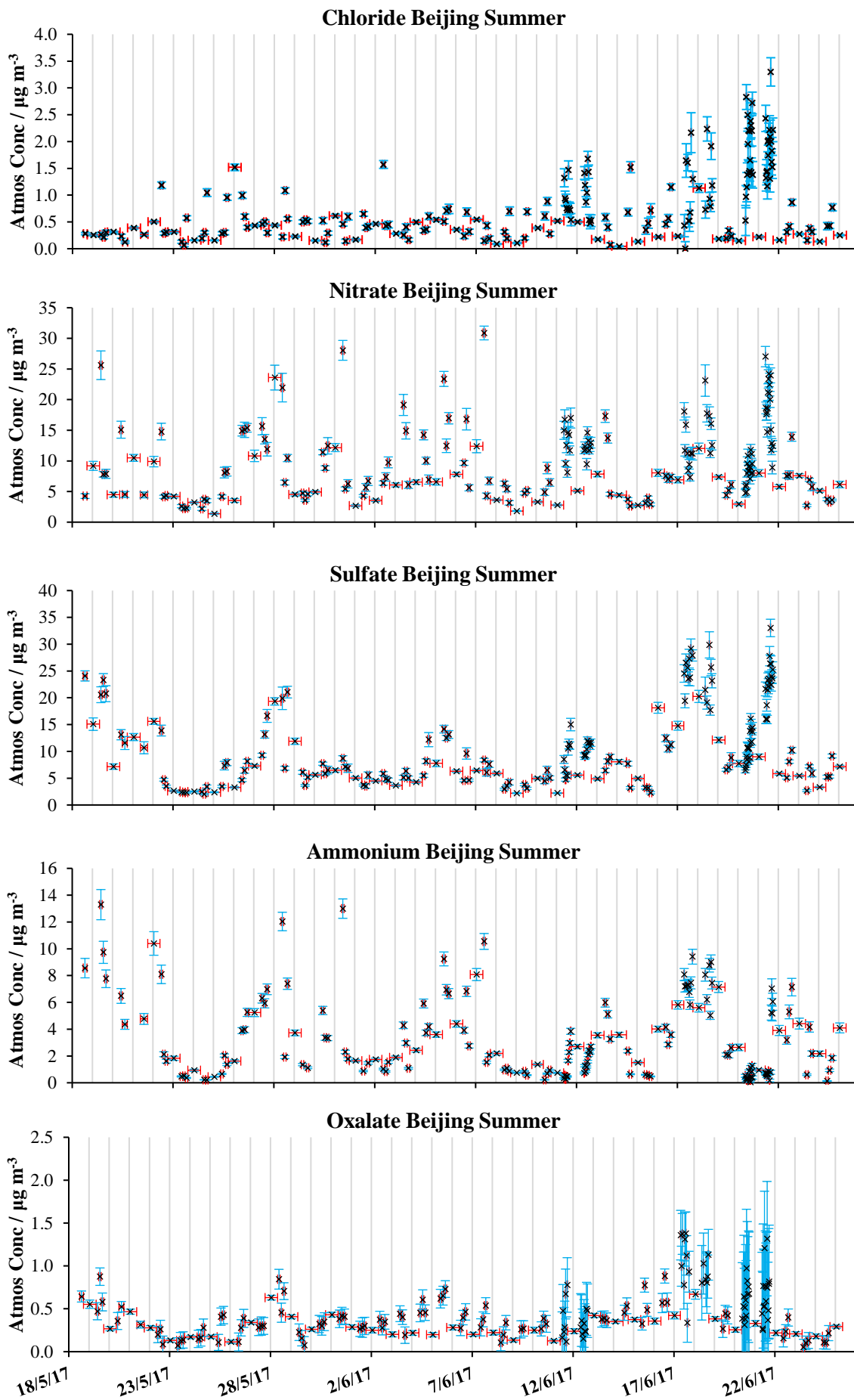


Fig. 3.12. Time series of the major ions measured by offline ion chromatography during the APHH Beijing Summer campaign. Ion concentrations are shown on the y-axes with time on the x-axes. The grey vertical lines represent midnight time points. The red error bars show the time of sampling and the blue error bars show the error of each concentration measurement in the y-axis. The x-axes are identical for each time series and are shown in the bottom chart (oxalate).

explain a possible increased oxidation of NO_2 (section 3.3.2). The increase in NO_3^- at this specific time may therefore have been from another pathway such as from a primary emission source. The maximum and minimum $[\text{NO}_3^-]$ were $30.88 \mu\text{g m}^{-3}$ and $1.38 \mu\text{g m}^{-3}$, respectively. On the 31st May at 09:55, a dramatic increase in concentration occurs producing a peak of $28.05 \mu\text{g m}^{-3}$ which is parallel to a peak in the NH_4^+ time series. A peak at this time is however not seen in either Cl^- nor SO_4^{2-} and is likely due to HNO_3 and NH_3 neutralisation forming NH_4NO_3 . This also occurs on 7th Jun 10:02.

The $[\text{SO}_4^{2-}]$ maximum daytime concentration was measured as $33.03 \mu\text{g m}^{-3}$, which was *ca.* 60 % higher than the maximum recorded for night-time samples of $20.25 \mu\text{g m}^{-3}$. The minimum day and night-time concentrations were $2.02 \mu\text{g m}^{-3}$ and $2.21 \mu\text{g m}^{-3}$, respectively. The SO_4^{2-} trend follows the cycle in SO_2 concentrations relatively well (Fig. 3.7). Increases and decreases in SO_2 and SO_4^{2-} occur together on multiple days, such as on the 22nd and 28th of May (Fig. 3.7 and Fig. 3.12). Even though a similar trend is seen, the relative concentrations of SO_2 and SO_4^{2-} for specific times of increase and decrease are inconsistent. For example, the peaks in the SO_4^{2-} on the 17th, 18th and 21st June are above the 90th percentile for SO_4^{2-} , although the rise in SO_2 is not larger than previous SO_2 events. This may therefore demonstrate the dependence on oxidation capability of the atmosphere as opposed to $[\text{SO}_2]$ on H_2SO_4 formation.

NH_4^+ also follows the same pollution cycles seen in the other major ions and gases (Fig. 3.7 and Fig. 3.12). The maximum day and night-time concentrations were relatively similar at $13.29 \mu\text{g m}^{-3}$ and $10.40 \mu\text{g m}^{-3}$, respectively. The minimum $[\text{NH}_4^+]$ for the day and night-time periods were $0.04 \mu\text{g m}^{-3}$ and $0.44 \mu\text{g m}^{-3}$, respectively.

Like NH_4^+ , $\text{C}_2\text{O}_4^{2-}$ also follows the pollution cycles seen in the other ions, for which peaks are observed on the 28th May, 5th Jun, 11th Jun, 17th Jun and 20th - 21st Jun. The $\text{C}_2\text{O}_4^{2-}$ concentrations remain below $1 \mu\text{g m}^{-3}$ up until 17th June, when a maximum value of $1.38 \mu\text{g m}^{-3}$ is reached. These values are much less variable in concentration compared to the other major ions due to the much lower concentrations and represent a standard deviation of $0.28 \mu\text{g m}^{-3}$. The %RSD over the campaign for $[\text{C}_2\text{O}_4^{2-}]$ was however relatively large at 85 %.

3.3.4 Average Inorganic $\text{PM}_{2.5}$ Concentrations Comparison in Delhi and Beijing

The average day and night concentrations of ionic species within $\text{PM}_{2.5}$ are compared in this section to assess the relative concentrations of species and whether the influence of daylight has a considerable effect on these concentrations. A comparison also shows how the relative ionic species concentrations changes between cities and seasons. Typically, the mean is used for direct comparison between species although as seen in the time series of section 3.3.3, the atmospheric ion concentrations may be very variable with few very high or low concentration values with the potential to skew mean values. Therefore, using solely, the mean for ionic concentration comparison is insufficient. Violin plots are a way to display the full distribution of data and have been used here.

3.3.4.1 Building a Violin Plot

The visualisation of atmospheric data using a violin plot is particularly important as it gives an indication as to whether the data has multiple normal distributions within the dataset, and if so, which sub-distribution density is the most dominant. It also gives the user an indication as to which average would be the most suitable to report. This section therefore explores the importance of displaying the data distribution as opposed to simply reporting the mean of atmospheric concentrations or displaying simple boxplots.

Violin plots are formed of a typical box plot with the distribution density surrounding each box plot allowing the data distribution to be much better visualized and outliers to be obvious. For example, it can be seen in Fig. 3.13 that very few high data points of Cl^- may cause the mean to be skewed slightly higher in the Beijing summer data set, which would not be obvious in a box plot. The median is also represented as opposed to the mean as the median is not skewed. In determining the data distribution, the continuous atmospheric concentration data is required to be sorted into bins, forming a histogram. An example of this has been shown for the DPOM Cl^- campaign data as shown in Fig. 3.13A. Depending on the bin size, some ions may demonstrate two different distributions, such as the chloride DPOM data in Fig. 3.13A and Fig. 3.13B. When the data is distributed into smaller bin ranges in a histogram, more detailed information about the data set is revealed (Fig. 3.13B). For example, in the chloride DPOM data set, transferring from a bin range of $5 \mu\text{g m}^{-3}$ (Fig. 3.13A) to $1 \mu\text{g m}^{-3}$ (Fig. 3.13B) reveals a multimodal distribution function. In this example, the chloride data could be described as three overlapping normal distributions, with means at *ca.* $2.5 \mu\text{g m}^{-3}$, $6 \mu\text{g m}^{-3}$ and $10.5 \mu\text{g m}^{-3}$.

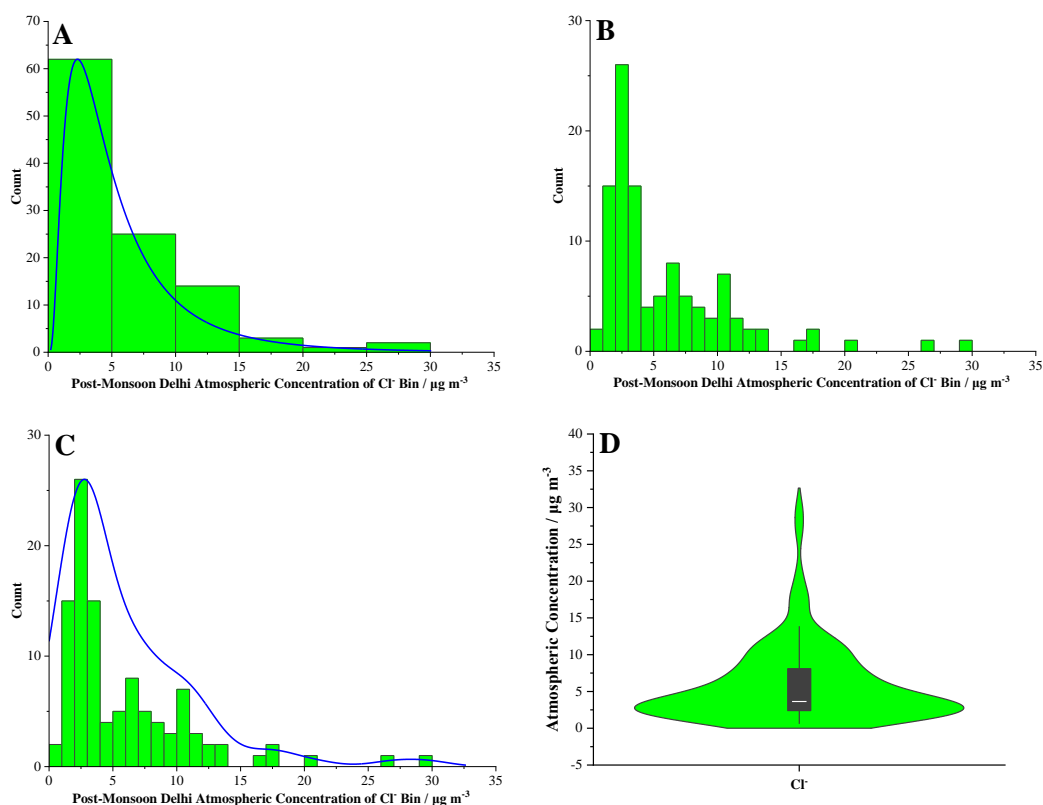


Fig. 3.13. Build-up of a violin plot. (A) Data segregated into large bin size; (B) Data segregated into smaller bin sizes; (C) Data segregated into smaller bin sizes with kernel distribution overlay; (D) Final violin with box plot.

A multimodal distribution function suggests that the data may possess multiple statistical parameters in sub-set groups and therefore indicates the presence of different atmospheric environments, for example, a very polluted versus a cleaner period during a campaign, or possibly daytime and night-time averages. Non-normality would be expected in atmospheric data sets because of the numerous contributing factors affecting atmospheric concentrations, such as range of sources of primary pollutants, secondary reactions, and changes in meteorology. It was therefore most appropriate to apply a kernel distribution function, as this calculates a smoothing of the distribution of the data set (Fig. 3.13C). The distribution function therefore includes the characteristics of a log type curve (Fig. 3.13A) with deviations towards the centres of sub-groups normally distributed (Fig. 3.13D). The width of the distribution density demonstrates the relative frequency of values at specific atmospheric concentrations (Fig. 3.13D). In data sets where a lot of values are close to zero, the kernel density curve may extend into the negative range where no data points are present. This is because the kernel distribution fitted is a continuous function without a boundary, although best demonstrates the shape of the data and has been chosen as the best fit for the violin plots in the APHH ionic data. These data show a range of distribution functions.

3.3.4.2 Delhi and Beijing Day and Night Concentration Comparison

For Delhi, the mean ionic concentrations are represented in Fig. 3.14. The day and night averages were calculated by omitting 24-hour and blocked filter samples (DPOM). The 24-hour filters were however included in calculating the mean over the total campaign periods. The heights of the bars represent the mean values across the daytime (orange), night-time (green) and total campaign (purple) periods. The lighter shaded bars represent the DPEM period and the darker shaded bars represent the DPOM period. In conjunction, violin plots for the anions and cations measured during the APHH Delhi campaigns are also shown in Fig. 3.15. The day and night-time data are presented as yellow and blue violins, respectively for which the area represents the distribution density. A black box plot is presented within each violin which demonstrates the interquartile range and a white line within each box presents the median. Ions of generally higher and lower concentration are shown in plots for each campaign on the left and right, respectively (Fig. 3.14). Li^+ has been omitted from these violin plots as very few data points were observed to be above the LOD. For ease of comparison, the statistical parameters (mean, median etc.) in this thesis were calculated assuming normal distribution, although the statistics of these concentrations may be far more exploited in future as to increase the accuracy of reported values and error analysis.

Fig. 3.16 represents bar charts visually evaluating the mean ionic species concentrations within $\text{PM}_{2.5}$ sampled during the APHH Beijing winter and summer campaigns. The daytime is represented by yellow bars; night is represented by red bars; and dark blue bars represent the total campaign average values. The lighter bars represent the BWIN campaign and the darker bars present the BSUM campaign. The violin plots in Fig. 3.17 were formed in the same manner as for Delhi in section 3.3.4.2.

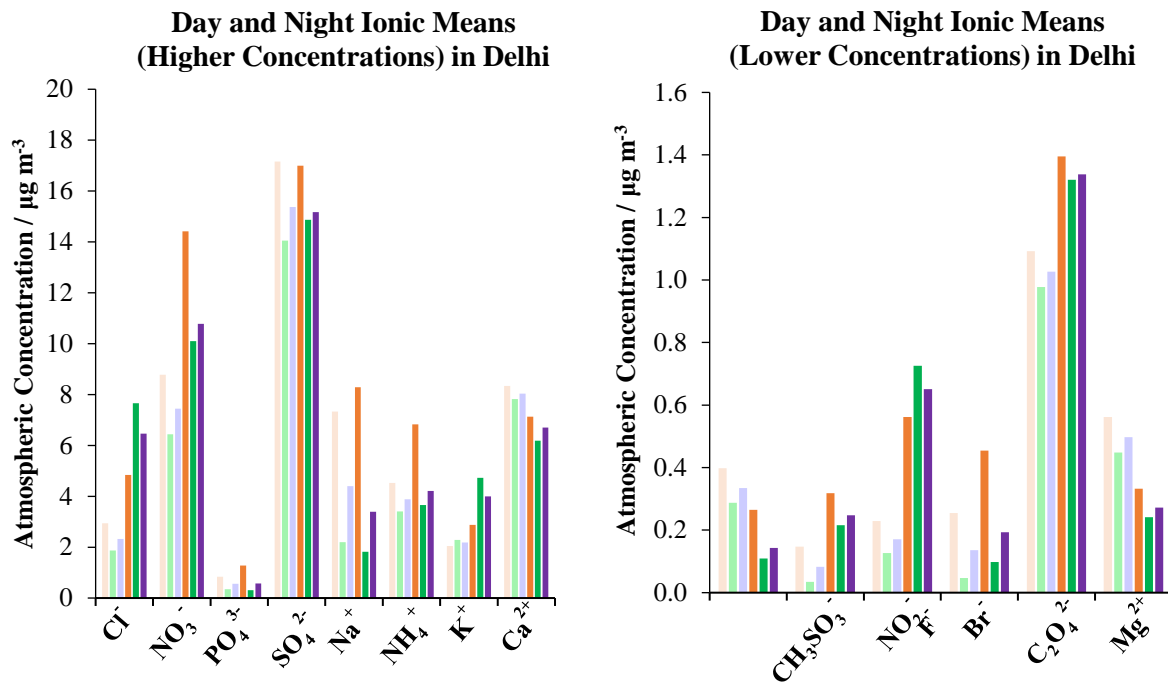


Fig. 3.14. Bar Charts representing Day and Night Ionic $PM_{2.5}$ data in Delhi. The orange bars represent the daytime mean, the green bars represent night-time mean, and the purple bars represent the total campaign mean. The lighter 3 bars (3 bars to the left of each species) represent the DPDM campaign, and the darker bars represent the DPOM campaign. The associated errors for these data may be found in Fig. 3.9 - Fig. 3.10.

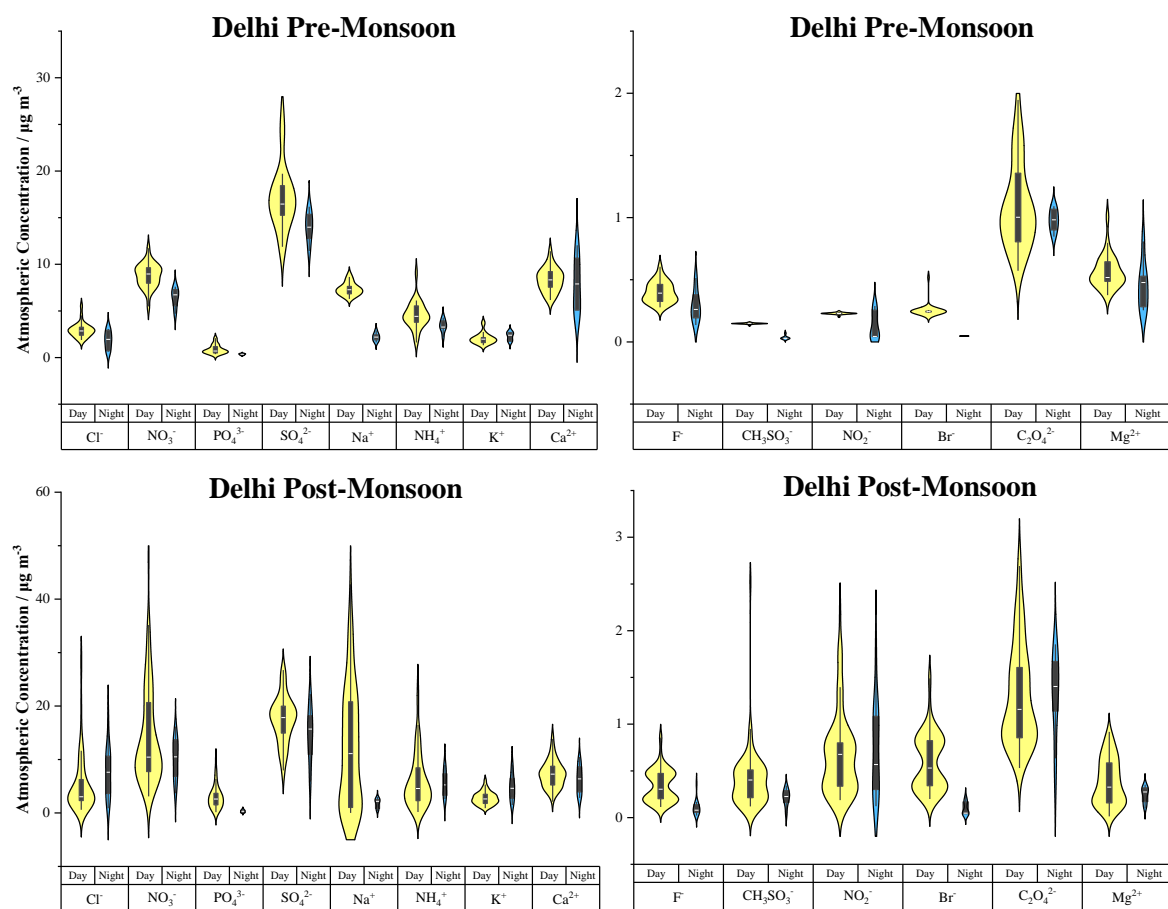


Fig. 3.15. Violin Plots demonstrating Day (yellow distribution) and Night (blue distribution) ionic $PM_{2.5}$ distribution data in Delhi. The distribution density displayed is calculated by the kernel distribution function. The boxplot represents the inter quartile range and the white line within the boxplot represent the median atmospheric concentration for each species (labelled along the bottom axis). High concentration ions are shown on the left and low concentration ions to the right. The pre-monsoon data is presented on the top and the post-monsoon data is shown on the bottom.

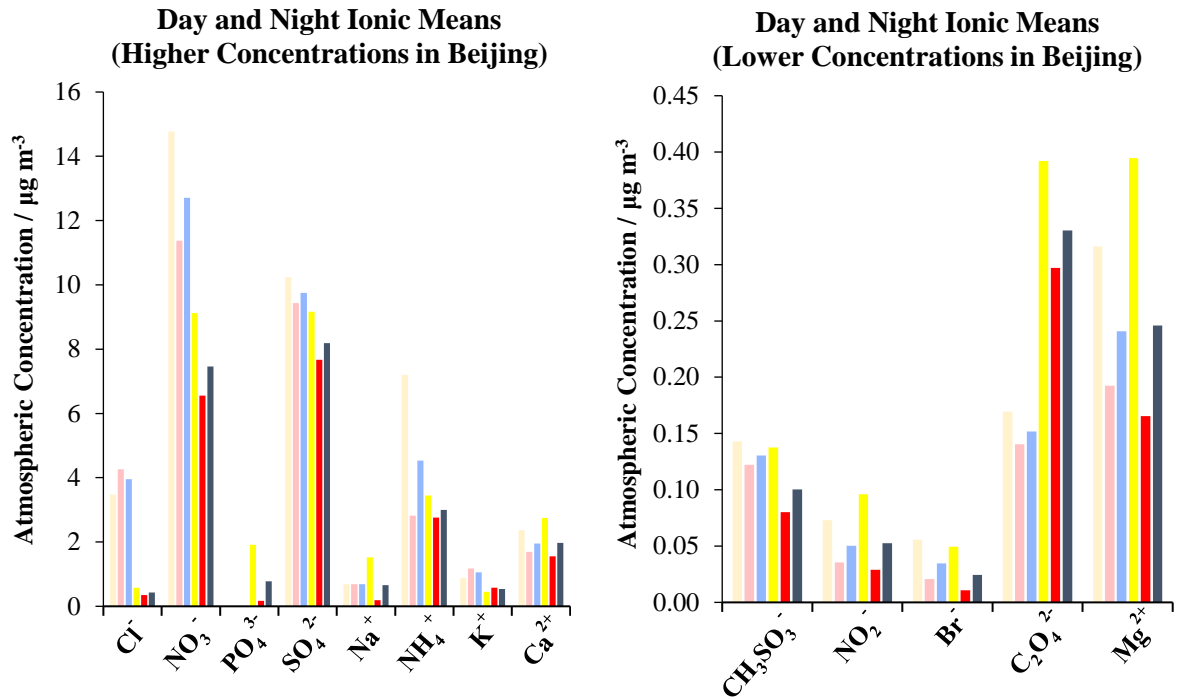


Fig. 3.16. Bar Charts representing Day and Night ionic $PM_{2.5}$ data in Beijing. The yellow bars represent the daytime mean, the red bars represent the night-time mean, and the blue bars represent the total campaign mean. The lighter 3 bars (3 bars to the left of each species) represent the BWIN campaign, and the darker bars represent the BSUM campaign. The associated errors for these data may be found in Fig. 3.11 - Fig. 3.12.

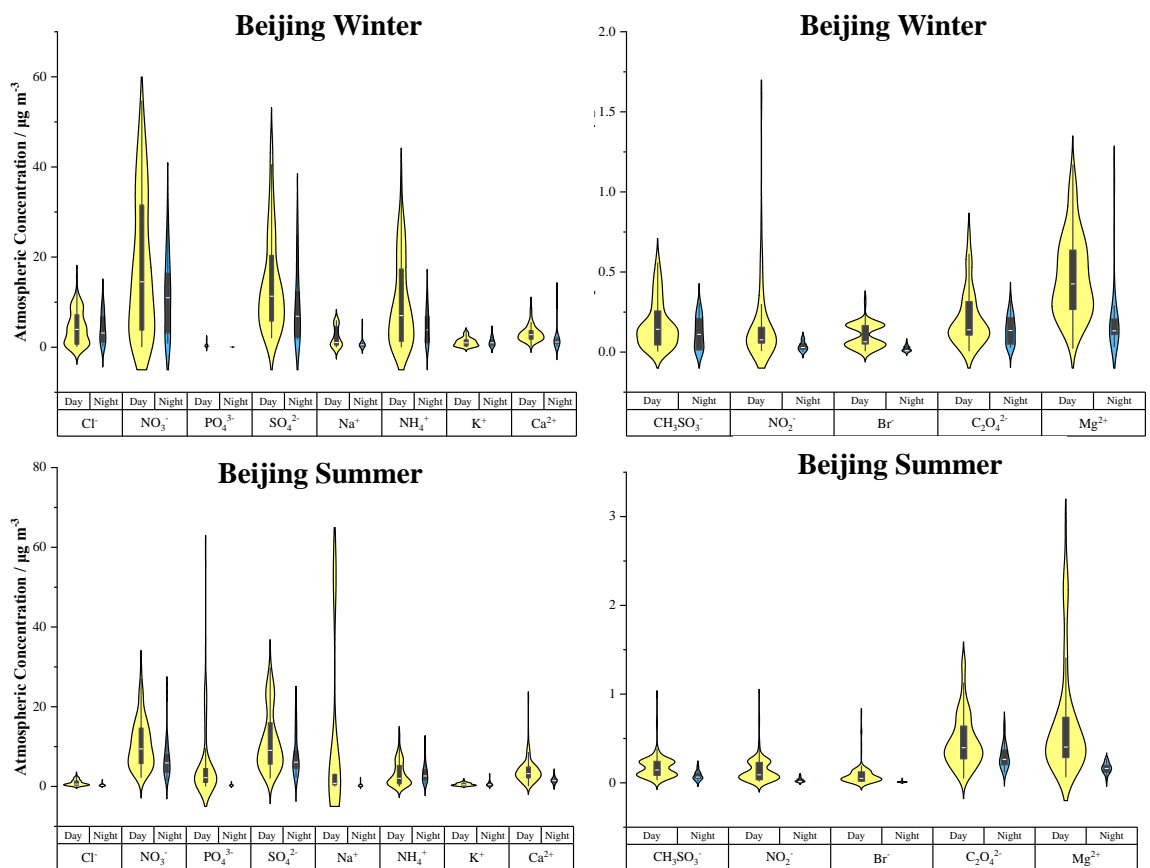


Fig. 3.17. Violin Plots demonstrating Day (yellow distribution) and Night (blue distribution) ionic $PM_{2.5}$ distribution data in Beijing. The distribution density displayed is calculated by the kernel distribution function. The boxplot represents the inter quartile range and the white line within the boxplot represent the median atmospheric concentration for each species (labelled along the bottom axis). High concentration ions are shown on the left and low concentration ions to the right. The winter campaign is presented on the top and the summer campaign is shown on the bottom.

3.3.4.3 Chloride

The mean Cl^- ion concentrations obtained across the four campaigns are shown in Table 3.2, Fig. 3.14 (Delhi) and Fig. 3.16 (Beijing). The distributions of Cl^- measurements are shown in the violin plots in Fig. 3.15 (Delhi) and Fig. 3.17 (Beijing). The highest total mean concentrations were found during the DPOM period, followed by the BWIN > DPEM > BSUM campaigns.

Table 3.2. Day, Night, Day/Night and Total campaign [Cl^-] means ($\mu\text{g m}^{-3}$).

Cl^-	DPEM	DPOM	BWIN	BSUM
Day	2.94	4.84	3.47	0.58
Night	1.86	7.66	4.26	0.35
Day/Night	1.58	0.63	0.81	1.68
Total	2.32	6.46	3.95	0.43

The mean [Cl^-] are larger during the DPEM day compared to night-time hours, with most of the values normally distributed surrounding the median during both day and night-time hours. The higher daytime compared to night-time Cl^- infers greater HCl emissions from daytime anthropogenic activities such as steel pickling. In contrast during the DPOM campaign, night-time [Cl^-] is higher compared to daytime hours. Fig. 3.15 demonstrates that the night-time data is widely distributed across the range of $0.89 \mu\text{g m}^{-3}$ – $17.58 \mu\text{g m}^{-3}$, whereas a few Cl^- values greatly skew the mean to a higher concentration for the daytime values. The exceptionally high [Cl^-] observed during the DPOM night-time period is most likely down to the contraction of the boundary layer in conjunction with an enhancement of HCl emissions on the run-up to Diwali from combustion activities.

The BWIN daytime mean was slightly lower compared to the night-time average, although the daytime range was slightly larger compared to night-time hours and multimodal character was seen. The marginally larger [Cl^-] during night-time hours is most likely down to even cooler temperatures as well as increased humidity. The fact that Cl^- changes very little during the night-time hours suggests that HCl sources do not increase substantially at night. To compare, the BSUM Cl^- daytime mean was larger compared to night-time hours, in which the distributions were normally distributed around the median values of $0.63 \mu\text{g m}^{-3}$ and $0.26 \mu\text{g m}^{-3}$, respectively. The higher Cl^- seen during the day is most likely down to an increase in [NH_3] within the atmosphere from significantly higher daytime temperatures causing evaporation from agricultural sources and soil. An increase in atmospheric ammonia allows for more Cl^- in the particle phase from more neutralisation with HCl.

The BWIN mean day [Cl^-] was significantly larger than the BSUM day. This is most likely down to the significantly reduced temperatures keeping Cl^- within the particle phase bound to NH_4^+ and increased primary emissions in winter. The distribution of Cl^- across daytime datapoints during BWIN are relatively evenly distributed across the range, whereas for the BSUM campaign a very small range was observed across very low concentrations, for which all values are observed within a

very collected normal distribution. In both cities, larger $[Cl^-]$ were observed during daytime hours in the warmer months, mostly likely as a result of HCl production from secondary reactions of Cl radicals.

3.3.4.4 Nitrate

The day, night and total means for $[NO_3^-]$ across the APHH campaigns is shown in Table 3.3, Fig. 3.14 (Delhi) and Fig. 3.16 (Beijing). The distributions of NO_3^- data are shown in the violin plots in Fig. 3.15 (Delhi) and Fig. 3.17 (Beijing). The highest total mean NO_3^- was recorded during the BWIN campaign, followed by DPOM. The DPEM and BSUM campaign mean $[NO_3^-]$ values were almost the same.

Table 3.3. Day, Night, Day/Night and Total campaign $[NO_3^-]$ means ($\mu g m^{-3}$).

NO_3^-	DPEM	DPOM	BWIN	BSUM
Day	8.78	14.42	14.77	9.12
Night	6.44	10.10	11.38	6.56
Day/Night	1.36	1.43	1.30	1.39
Total	7.44	10.77	12.71	7.46

During the DPEM campaign, higher $[NO_3^-]$ were observed during daytime hours with a relatively uniformly distributed set of $[NO_3^-]$ measurements. The night-time $[NO_3^-]$ were also evenly distributed although exhibited a smaller range of $4.71 \mu g m^{-3} - 7.61 \mu g m^{-3}$. The larger daytime $[NO_3^-]$ suggests increased NO_2 oxidation compared to night-time hours. This may be explained by a higher proportion of oxidising species found during daytime hours as well as higher NO_2 concentrations from anthropogenic activities such as traffic emissions. Likewise, the DPOM daytime average is also higher compared to the night due to increased NO_2 oxidation. The daytime distribution of the NO_3^- measurements however demonstrated a few particularly high $[NO_3^-]$ values which skewed the mean to higher $[NO_3^-]$. NO_x is known to be exceptionally high during the DPOM campaign due to the campaign taking place on the lead up to Diwali which exhibits a large increase in biomass burning. These few particularly high daytime $[NO_3^-]$ may be due to an episode of particularly high NO_2 from increased atmospheric oxidants. During both the day and night-time hours however, Fig. 3.15 shows that the majority of the data distribution surrounds the medians of $10.46 \mu g m^{-3}$ and $10.52 \mu g m^{-3}$, respectively.

In addition, considering the large increase in NO_x during the DPOM campaign, the DPOM campaign mean $[NO_3^-]$ is not significantly higher. A much higher $[NO]$ may reduce the concentrations of oxidant species (such as OH) which are able to oxidise NO_2 to HNO_3 . In addition, the formation of organic nitrate species from NO_3 radical oxidation at night, which could dissociate in aerosol to form NO_3^- (chapter 6), is reduced due to reduced NO_3 production in the presence of exceedingly high NO and very low O_3 (Fig. 3.8).

The BWIN daytime $[\text{NO}_3^-]$ showed a higher mean, a multimodal distribution and a range of $0.06 \mu\text{g m}^{-3} - 54.72 \mu\text{g m}^{-3}$. A possible reason for the multimodal distribution may be due to NO_3^- observing two means for measurements during haze and non-haze periods. The presence of haze is known to increase the heterogenous oxidation of NO_2 to NO_3^- within the aerosol as well as the gas phase oxidation of NO_2 by OH which significantly increases $[\text{NO}_3^-]$. This compares to a lower mean during night-time hours, which also showed a single normal distribution around the median and a smaller range of $0.81 \mu\text{g m}^{-3} - 30.66 \mu\text{g m}^{-3}$. Likewise to each campaign, the daytime NO_3^- is larger than the night-time mean, although the daytime $[\text{NO}_3^-]$ observes a log-normal distribution density surrounding a median of $9.45 \mu\text{g m}^{-3}$. In contrast, the BSUM night-time $[\text{NO}_3^-]$ mean of $6.56 \mu\text{g m}^{-3}$ was skewed by few particularly high NO_3^- values. These especially high NO_3^- may have originated from a change in wind direction or substantially lower wind speeds allowing for the build-up of NO_2 and NO_3^- in the particle phase.

What is common throughout each campaign is that the NO_3^- average is always higher during the daytime. The predominant reason for this is likely down to the increased photooxidation of NO_2 producing HNO_3 which may either dissolve into humid aerosol particles, neutralise NH_3 forming NH_4NO_3 or react with basic dust material incorporating NO_3^- into the particle phase. This is further evidenced by the larger daytime $[\text{O}_3]$ compared to night-time $[\text{O}_3]$ observed in each campaign (Fig. 3.8). The day/night ratio of NO_3^- is also relatively similar between each campaign. Table 3.3 also demonstrates a temperature dependence on $[\text{NO}_3^-]$. Higher NO_3^- were seen during the cooler months compared to the warmer months in each city. This is down to the volatility of NH_4NO_3 (the dominant form of particle NO_3^-).

3.3.4.5 Sulfate

The mean day and night $[\text{SO}_4^{2-}]$ are shown in Table 3.4. These results are graphically represented as bar charts in Fig. 3.14 (Delhi) and Fig. 3.16 (Beijing). The distribution of SO_4^{2-} data are shown in the form of violin plots in Fig. 3.15 (Delhi) and Fig. 3.17 (Beijing). The highest total campaign average $[\text{SO}_4^{2-}]$ was observed during the DPEM campaign, followed by the DPOM > BWIN > BSUM.

Table 3.4. Day, Night, Day/Night and Total campaign $[\text{SO}_4^{2-}]$ means ($\mu\text{g m}^{-3}$).

SO_4^{2-}	DPEM	DPOM	BWIN	BSUM
Day	17.15	17.00	10.24	9.16
Night	14.05	14.86	9.43	7.66
Day/Night	1.22	1.14	1.09	1.19
Total	15.38	15.17	9.75	8.19

The mean $[\text{SO}_4^{2-}]$ for the DPEM daytime was higher compared to night-time hours, for which the daytime values demonstrated multimodal distribution around two means of *ca.* $17 \mu\text{g m}^{-3}$ and *ca.* $25 \mu\text{g m}^{-3}$. The reason for the bimodal character in the DPEM daytime SO_4^{2-} values is due to the significant rise in daytime $[\text{SO}_4^{2-}]$ after the second of Jun 2018 (Fig. 3.9) which has been attributed

to a substantial change in prevailing wind direction (chapter 5). Chapter 5 also discusses how the sulfur oxidation ratio is generally considerably larger after this date also. This compares to normally distributed data surrounding the night-time median which observed a significantly smaller range of $11.43 \mu\text{g m}^{-3} - 16.18 \mu\text{g m}^{-3}$. This smaller range reflects the lesser influence of SO_2 photooxidation occurring at night. The DPOM day and night-time averages were very similar to the DPEM values, although the daytime DPOM SO_4^{2-} was normally distributed around the median. The night-time SO_4^{2-} data was log normally distributed, with a few SO_4^{2-} values skewing the mean to a lower value. This infers that on few occasions, the night-time SO_4^{2-} was particularly low which were likely due to significantly higher night-time primary VOC and NO_x emissions (during night-time celebrations on the lead up to Diwali) acting as a sink for night-time oxidants, in addition to less photooxidation occurring at night.

The BWIN day-time mean was normally distributed and was also slightly higher compared to night-time hours. The night-time mean was however significantly skewed by few particularly high SO_4^{2-} values which made the median 73 % the value of the mean. Similar to Cl^- , this is due to less evaporation of $(\text{NH}_4)_2\text{SO}_4$ and NH_4HSO_4 from the particle phase during even cooler night-time hours. The difference is however only marginal as the substantially cooler winter-time temperatures keep SO_4^{2-} locked in the particle phase and much reduced solar flux compared to the other campaigns decreases daytime photooxidation of SO_2 . The small difference is also likely down to the very similar day and night-time dominant SO_2 source being the coal combusting Huaneng Thermal Power plant operating is very close proximity to IAP. Although the BSUM daytime SO_4^{2-} mean was higher compared to the night-time average, the BSUM $[\text{SO}_4^{2-}]$ contrasts the BWIN distribution by having bimodal character with distribution density surrounding two separate means of $5 \mu\text{g m}^{-3}$ and $25 \mu\text{g m}^{-3}$. This suggests that SO_4^{2-} produced under two significantly different pathways or atmospheric conditions. A possible explanation may be due to SO_4^{2-} entering the particle phase from both primary (dust) and secondary (photooxidation pathways). To compare, although the BSUM night-time value was slightly lower compared to daytime values, Fig. 3.17 shows that the night-time mean of was significantly skewed by few especially high SO_4^{2-} values, potentially due to a change in wind direction transporting dust.

Similar to the $[\text{NO}_3^-]$ data in section 3.3.4.4, the daytime values are consistently higher compared to night-time averages across the campaigns. This is attributed to a higher level of SO_2 oxidation occurring during daytime hours causing higher H_2SO_4 concentrations as well as greater NH_4^+ occurring during daytime hours. Comparing cities, Delhi observed substantially higher SO_4^{2-} compared to Beijing in general. This infers much greater SO_2 concentrations within Delhi compared to Beijing which is most likely down to the three coal fired power plants in relatively close proximity to Indira Gandhi Delhi Technical University for Women (IGDTUW) (Badarpur, Faridabad and Dadri), as well as the likely higher sulfur content in diesel fuel in Delhi compared to Beijing³³⁸.

3.3.4.6 Ammonium

Table 3.5 presents the day, night and total campaign averages of $[\text{NH}_4^+]$ across the APHH campaigns. These values are also visually presented in Fig. 3.14 (Delhi) and Fig. 3.16 (Beijing). The data distribution densities are presented in the form of violin plots in Fig. 3.15 (Delhi) and Fig. 3.17 (Beijing). Comparing the total campaign means of BSUM ($3.00 \mu\text{g m}^{-3}$) < DPEM ($3.88 \mu\text{g m}^{-3}$) < DPOM ($4.20 \mu\text{g m}^{-3}$) < BWIN ($4.54 \mu\text{g m}^{-3}$).

Table 3.5. Day, Night, Day/Night and Total campaign $[\text{NH}_4^+]$ means ($\mu\text{g m}^{-3}$).

NH_4^+	DPEM	DPOM	BWIN	BSUM
Day	4.52	6.82	7.20	3.44
Night	3.40	3.65	2.82	2.76
Day/Night	1.33	1.87	2.55	1.25
Total	3.88	4.20	4.54	3.00

The DPEM daytime $[\text{NH}_4^+]$ mean was larger than for the night-time period, with the daytime values log-normally distributed around the median. The daytime mean is also skewed to a higher value by the particularly high $[\text{NH}_4^+]$ found on 29th May 2018 at 09:56 (Fig. 3.9). This is accompanied by higher concentrations in the other major anions and therefore may be due to a particular increase in acidic gases on the 29th May from anthropogenic sources such as coal combustion. Like DPEM, the daytime DPOM $[\text{NH}_4^+]$ mean is higher during the day, with a clear log-normal distribution shown. The NH_4^+ mean was lower with a smaller range of $2.61 \mu\text{g m}^{-3} - 9.01 \mu\text{g m}^{-3}$ for the night-time compared to daytime values. This is therefore indicative of lower $[\text{NH}_3]$ and more consistent neutralisation of the acidic gases during the night-time period. This is representative of the much-increased night-time DPOM NO_x acting as a sink for oxidising species (Fig. 3.8). In addition, the DPOM campaign shows a much greater Day/Night ratio of NH_4^+ compared to the DPEM campaign. This is due to the higher DPEM daytime temperatures causing NO_3 loss from the aerosol.

This is also reflected in the BWIN $[\text{NH}_4^+]$ which showed the highest campaign mean $[\text{NH}_4^+]$ as well as the highest Day/Night ratio which may be explained by the considerably lower BWIN temperatures. The BWIN daytime mean is higher with the data distribution exhibiting multimodal character around the means of $5 \mu\text{g m}^{-3}$ and $20 \mu\text{g m}^{-3}$. As cooler temperature and lower solar flux decrease the atmospheric photooxidation potential of NO_2 and SO_2 , the considerable increase in NH_4^+ may therefore be down to HCl neutralisation. This is because HCl is an acidic gas which was likely in high concentrations, emitted directly from coal burning from the Huaneng power station. The significantly lower NH_4^+ during the night-time may indicate substantial particle dry or wet deposition. Like the BWIN campaign, the BSUM campaign showed higher daytime $[\text{NH}_4^+]$, although a significantly lower Day/Night NH_4^+ ratio. The daytime BSUM NH_4^+ also showed multimodal distribution around means of *ca.* $1 \mu\text{g m}^{-3}$ as well as *ca.* $3 \mu\text{g m}^{-3}$, which may be representative of NH_4^+ in aerosol during haze (higher concentrations) and non-haze (lower concentrations) periods, as SIA is known to form readily during haze events. To compare to the BSUM night NH_4^+ , the mean

was lower although showed a very similar range to daytime values of $0.44 \mu\text{g m}^{-3} - 10.40 \mu\text{g m}^{-3}$, for which the data was normally distributed. The fact that the day/night concentrations of NO_3^- are very similar may be indicative of very similar levels of day and night-time NH_4^+ neutralisation.

To summarise, similar to the other SIA, the daytime mean $[\text{NH}_4^+]$ are consistently higher compared to the night-time values across the APHH campaigns. This is as a result of higher photooxidation of NO_2 and SO_2 producing acidic gases which neutralises NH_3 to form NH_4^+ in the particle phase. This is likely down to the fact that generally, higher NH_3 may be present during the daytime, as warmer temperatures increases soil temperatures resulting in soil ammonification causing higher atmospheric $[\text{NH}_3]$ ³³⁹. NH_3 is also volatilised from fertilizer use, animal husbandry and manure^{212,340}, for which higher daytime temperatures would encourage NH_3 evaporation. The higher daytime NH_4^+ is also due to increased acidic acid gas concentrations from increased anthropogenic HCl emissions, as well as NO_2 and SO_2 photooxidation.

In addition, $[\text{NH}_4^+]$ were lower during the warmer campaigns in each city, due to increased NO_3^- evaporation from the particle phase. During the cooler campaigns (DPOM and BWIN), the day and night difference is significantly larger than the warmer campaigns. This is likely down to increased NH_3 released from biomass burning and fossil fuel combustion for heat²¹². The highest $[\text{NH}_4^+]$ in BWIN was likely down to the much cooler temperatures keeping NH_4^+ locked in the particle phase (analogous to NO_3^- and SO_4^{2-}). The lowest total NH_4^+ mean during the BSUM period is most likely down to higher temperatures and generally lower NH_3 emissions in Beijing compared to Delhi.

3.3.4.7 Oxalate

The day, night and total campaign averages of $[\text{C}_2\text{O}_4^{2-}]$ are shown in Table 3.6, Fig. 3.14 (Delhi) and Fig. 3.16 (Beijing). The distributions of these $\text{C}_2\text{O}_4^{2-}$ datasets are presented in the violin plots in Fig. 3.15 (Delhi) and Fig. 3.17 (Beijing).

Table 3.6. Day, Night, Day/Night and Total campaign $[\text{C}_2\text{O}_4^{2-}]$ means ($\mu\text{g m}^{-3}$).

$\text{C}_2\text{O}_4^{2-}$	DPEM	DPOM	BWIN	BSUM
Day	1.09	1.40	0.17	0.39
Night	0.98	1.32	0.14	0.30
Day/Night	1.12	1.06	1.21	1.32
Total	1.03	1.34	0.15	0.33

In each campaign, the daytime mean is higher than for the night-time periods. This is down to an increase in the production of oxalic acid from the photooxidation of VOCs. The DPEM daytime and night-time values are very similar, although the daytime range ($0.57 \mu\text{g m}^{-3} - 1.95 \mu\text{g m}^{-3}$) is considerably larger than for the night. This is most likely down to much fewer filter samples taken during the night-time periods compared to the day-time hours. For the DPOM period, Table 3.6 shows that the daytime mean is higher than the night. Inspecting Fig. 3.15 however shows that the night-time median is higher than that for the DPOM daytime period and that few particularly low

$C_2O_4^{2-}$ values may have skewed the mean to lower values. Taking the median as the average would suggest higher $[C_2O_4^{2-}]$ at night. This could be down to a reduction of $C_2O_4^{2-}$ evaporation from the aerosol phase under cooler night-time temperatures and higher RH%.

The BWIN daytime $[C_2O_4^{2-}]$ mean was very close to the night-time concentration indicating that the atmospheric concentration of oxalic acid was likely very similar during the day and night periods. The BWIN daytime mean is however slightly higher due to the long-normal distribution shown reaching a max $[C_2O_4^{2-}]$ of $0.75 \mu\text{g m}^{-3}$ compared to the normal distribution shown by the night-time value displaying a range of $0.03 \mu\text{g m}^{-3} - 0.33 \mu\text{g m}^{-3}$. This shows that higher oxalic acid was produced during the daytime compared to night-time hours which is reflective of higher daytime anthropogenic VOC emissions, increased solar flux and temperatures. Likewise, the BSUM campaign had a higher daytime mean $[C_2O_4^{2-}]$, although demonstrated a multimodal distribution function, with most of the distribution density lying around the lowest mode of *ca.* $0.3 \mu\text{g m}^{-3}$. In comparison, the night-time hours demonstrated a log normal distribution, in which few particularly high $[C_2O_4^{2-}]$ concentrations skewed the mean up. Most of the night-time distribution density surrounded the median of $0.27 \mu\text{g m}^{-3}$. Similar to the BWIN campaign, higher VOC emissions and an increase in photooxidation are likely the main cause for the increased $C_2O_4^{2-}$. During the BSUM campaign, increased NH_3 release from the surface from higher temperatures may also be contributing to increased $C_2O_4^{2-}$ from neutralisation of NH_3 with oxalic acid.

Comparing cities, Delhi observes significantly higher $C_2O_4^{2-}$ compared to Beijing. $C_2O_4^{2-}$ is derived from oxalic acid which is an oxidised species originating from several potential hydrocarbons³⁴¹. The higher temperature in Delhi and much higher proportion of primary VOC emissions increases the amount of oxidisable VOC emissions forming $C_2O_4H_2$, in Delhi compared to Beijing. Although the DPOM campaign was cooler than the DPEM period, the DPOM mean may be slightly larger due to higher general VOC emissions and significantly higher $[\text{PM}_{2.5}]$, on the lead up to Diwali.

3.3.4.8 Other Ions

The minor ions F^- (Delhi), CH_3SO_3^- , NO_2^- , and Br^- show multimodal distribution patterns in both Delhi and Beijing campaigns (Fig. 3.15, Fig. 3.17). Much stronger multimodal distribution is seen especially in the DPOM data, although within these data for the ions F^- , CH_3SO_3^- , NO_2^- , and Br^- , 17.8 %, 23.8 %, 27.7%, and 7.9 % respectively of these data are above LOD for which other data is given a pseudo LOD/2 (Chapter 2) value. Therefore, these multimodal distributions in these cases are more a reflection of the distributions of sampling times and demonstrate very similar trends.

3.3.5 Composition of $\text{PM}_{2.5}$ in Delhi and Beijing during the APHH Campaigns

In order to compare the mean inorganic ion contribution to the total particle mass, the $\text{PM}_{2.5}$ mass concentrations measured by the TEOM-FDMS (UoB) were averaged to the same filter times. This was used to produce pie charts showing the relative contribution of the inorganic ions to $\text{PM}_{2.5}$ particle composition (Fig. 3.18). The average mass loading measured was $59.2 \mu\text{g m}^{-3}$, $164.9 \mu\text{g m}^{-3}$, $97.3 \mu\text{g m}^{-3}$ and $37.0 \mu\text{g m}^{-3}$ for the DPEM, DPOM, BWIN and BSUM campaigns, respectively. The $\text{PM}_{2.5}$ data taken from the TEOM-FDMS (UoB) was 24-hourly, and therefore day and night pie

charts were not possible. As shown in Fig. 3.18, the inorganic fraction of PM_{2.5} in both cities over both seasons makes a substantial contribution to the mass loading. The PM_{2.5} ions included are F⁻ (gold), CH₃SO₃⁻ (orange), Cl⁻ (green), NO₂⁻ (dark blue), Br⁻ (medium blue), NO₃⁻ (light blue), PO₄³⁻ (yellow), SO₄²⁻ (red), C₂O₄²⁻ (brown), Na⁺ (pink), NH₄⁺ (lilac), K⁺ (purple), Mg²⁺ (black), Ca²⁺ (grey) and other (amber). The pie charts for the warmer months in each city are shown on the left and the cooler months are shown on the right (Fig. 3.18).

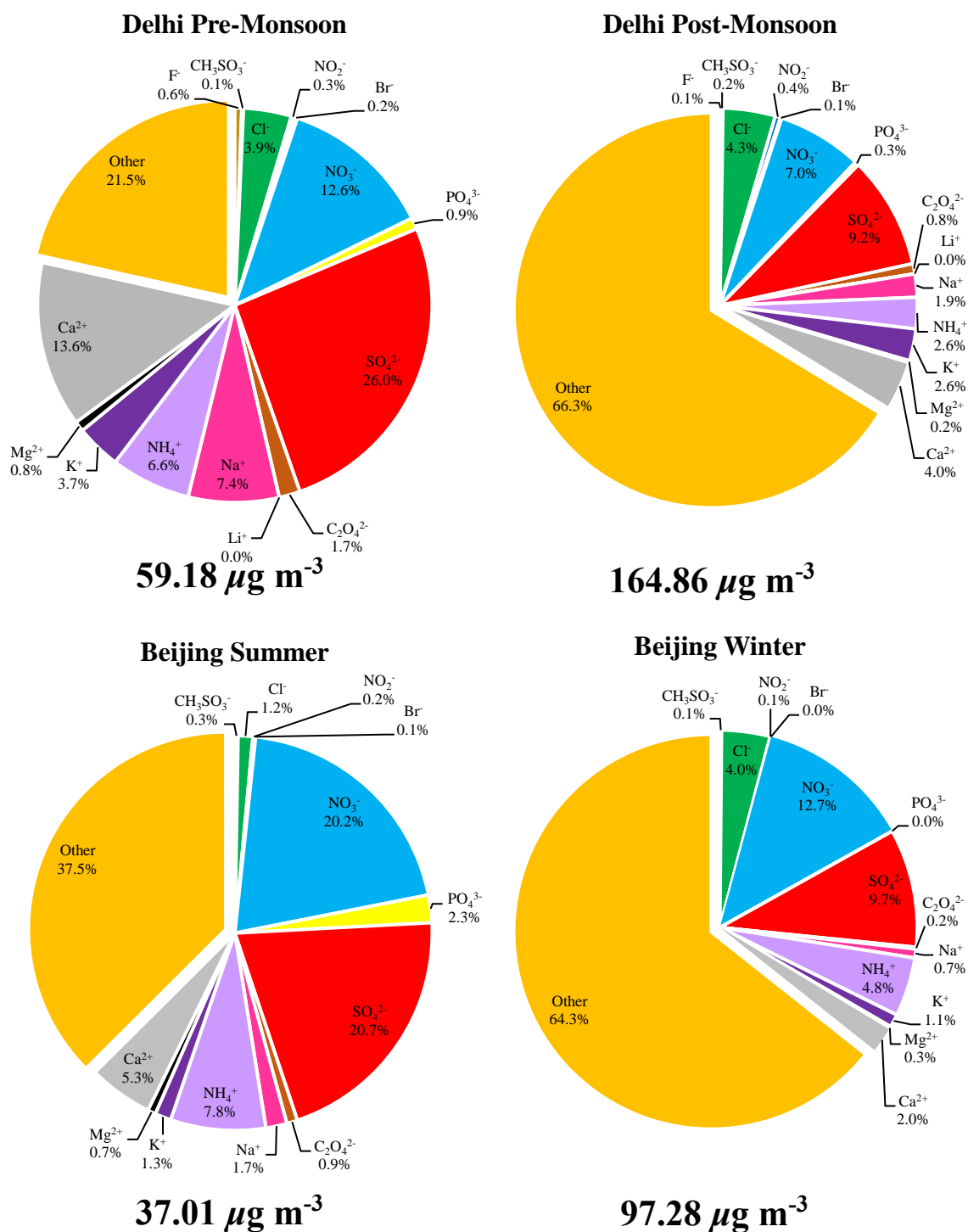


Fig. 3.18. Pie charts representing the averaged composition of PM_{2.5} aerosol during the APHH Delhi pre- (top left) and post-monsoon (top right), and Beijing winter (bottom right) and summer (bottom left) campaigns. The species are presented as F⁻ (gold), CH₃SO₃⁻ (orange), Cl⁻ (green), NO₂⁻ (dark blue), Br⁻ (medium blue), NO₃⁻ (light blue), PO₄³⁻ (yellow), SO₄²⁻ (red), C₂O₄²⁻ (brown), Na⁺ (pink), NH₄⁺ (lilac), K⁺ (purple), Mg²⁺ (black), Ca²⁺ (grey) and other (amber). Percentage contributions are also labelled underneath each species in each pie chart. The average [PM_{2.5}] from a TEOM-FDMS (UoB) is also given underneath each pie chart for the respective campaign.

In both cities, higher PM_{2.5} was observed during the cooler months (DPOM and BWIN). Ionic material made up a great proportion of the total PM_{2.5} mass during the warmer months (DPEM and BSUM). As discussed, higher levels of combustion during DPOM (Diwali) and BWIN (for heating) occur in conjunction with a shallower boundary layer, decreased temperature and increased RH, causing higher PM_{2.5} during the cooler seasons in each city. Slightly lower wind speeds were also observed during the cooler months in Delhi and Beijing which may contribute to the accumulation of PM_{2.5} also.

The total percentage of known ionic material in PM_{2.5} in each campaign were DPEM (78.5 %), DPOM (33.7 %), BWIN (35.7 %) and BSUM (62.5 %). Therefore, the largest proportion of known ionic material was observed during the DPEM campaign. The campaign with the largest proportion of unmeasured composition was the DPOM campaign (66.3 %) and this is expected to be dominated by organic material. Therefore, during the warmer seasons in each city, a higher fraction of inorganic aerosol species may strongly influence the hygroscopicity of particles^{342,343,344}. During the cooler seasons the hygroscopicity may be lowered due to increased fraction of organic species to the aerosol.

Closer inspection of the DPEM pie chart indicates that a substantial proportion of PM_{2.5} (45.2 %) was made up of SIA (NH₄⁺, NO₃⁻ and SO₄²⁻). As discussed in previous sections, the much higher temperatures and increased solar flux during the DPEM campaign increases the oxidation potential which is also evidence by the fact that 45.2 % of the DPEM PM_{2.5} consists of SIA. Due to the hot weather and dusty arid climate, another substantial proportion of the DPEM PM_{2.5} consists of cations which are strongly related to natural dust sources. This fraction ($\Sigma [\text{Na}^+ + \text{Mg}^{2+} + \text{Ca}^{2+}]$ %) contributes 21.8 % of the total PM_{2.5}. The Cl⁻ and K⁺ proportions are also relatively similar demonstrating 3.9 % and 3.7 % of DPEM PM_{2.5}, respectively.

The DPOM aerosol was dominated by the 'other' fraction (presumably mostly organic). This fraction was *ca.* three time higher compared to the DPEM campaign and comprised 66.3 % of the average aerosol composition. Work conducted by Cash et al., (in review, 2020)³⁴⁵ reported an organic fraction in aerosol of 68 % during the same APHH DPOM sampling period, using an AMS with size selective inlet PM₁. The AMS and IC organic fractions are therefore in very good agreement with each-other. Cash et al., (in review, 2020)³⁴⁵ also show through a Positive Matrix Factorisation (PMF) technique, that the dominant sources of organics during the DPOM campaign are from traffic, cooking and solid fuel burning (e.g. biomass).

Due to the much higher [NO] during the DPOM campaign, it may be suggested that this fraction was likely comprised of substantial primary non-oxidised organic species most likely from traffic, cooking and biomass sources³⁴⁵. The SIA fraction of DPOM PM_{2.5} is significantly lower at $\Sigma [\text{NH}_4^+ + \text{NO}_3^- + \text{SO}_4^{2-}] = 18.8$ % and contributes the lowest fraction out of all the APHH campaigns. Similarly, this is due to the lack of oxidative species during the DPOM period. The Cl⁻ fraction increases slightly from the DPEM season and although the K⁺ fraction decreases the [K⁺] mean was substantially higher during the DPOM campaign compared to DPEM due to increased biomass

burning and fireworks from Diwali celebrations. The increased Cl^- compared to decreased K^+ may be due to Cl^- originating from other sources for which K^+ is not a tracer, such as municipal waste burning³⁴⁶ and plastic burning³⁴⁷. The natural dust tracers of $\Sigma [\text{Na}^+ + \text{Mg}^{2+} + \text{Ca}^{2+}] = 6.1\%$. This is a decrease by *ca.* third as the $\text{PM}_{2.5}$ increases by *ca.* a factor of 3 indicating that the natural dust contribution to aerosol may have been similar during the DPOM campaign although was likely diluted by primary non-oxygenated organic species.

The ‘other’ fraction within the BWIN aerosol dominates and is very similar to the DPOM fraction. Considering the composition of gases (section 3.3.2.4 and Fig. 3.8), the much lower $[\text{NO}]$ during BWIN compared to DPOM could suggest this fraction comprises more Secondary Organic Aerosol (SOA) species compared to primary non-oxidated organics more likely present in the DPOM. Regarding SIA however, a larger fraction was observed during BWIN ($\Sigma [\text{NH}_4^+ + \text{NO}_3^- + \text{SO}_4^{2-}] = 27.2\%$) compared to DPOM, which is down to the much lower temperatures observed during the BWIN campaign which increases NH_4Cl , NH_4NO_3 , NH_4HSO_4 and $(\text{NH}_4)_2\text{SO}_4$ partitioning to the particle phase. The Cl^- fraction was similar to DPEM and DPOM and was *ca.* 4 times larger than BWIN K^+ which is likely down to a greater proportion of coal combustion compared to biomass burning. The contribution of natural dust was estimated to be low as $\Sigma [\text{Na}^+ + \text{Mg}^{2+} + \text{Ca}^{2+}] = 3\%$. This is likely as Beijing is much further north and less arid compared to Delhi and the cooler temperatures likely inhibit dust suspension. In addition, Beijing generally observed higher wind speeds (Fig. 3.3) compared to Delhi (Fig. 3.1) which encourages dust transportation from further afield.

To further evidence that the ‘other’ fraction is most likely organic during the DPOM and BWIN campaigns, the AMS PM_1 organic fraction results were calculated as a percentage of $\text{PM}_{2.5}$ mass concentration and was compared to the pie charts in Fig. 3.18. Table 3.7 presents the mass of organic species measured by the AMS in PM_1 , the average $[\text{PM}_{2.5}]$ across the campaigns from data which overlapped with the sampling times; and the AMS organic fraction as a percentage of the $\text{PM}_{2.5}$ reported by the TEOM-FDMS (UoB). This value is then compared to the ‘other’ fraction reported from IC measurements as depicted in Fig. 3.18. The estimated unknown is the $[\text{IC } \text{PM}_{2.5} \text{ Other } \%] - [\% \text{ Known Org in } \text{PM}_{2.5} / \mu\text{g m}^{-3}]$. To calculate the values in Table 3.7, the AMS data from CEH and IAP were averaged to the HiVol filter times. N is the number of data points that were available.

Table 3.7 shows that a substantial fraction of the ‘other’ fraction measured during the DPOM and BWIN campaigns was organic. Particularly during the DPOM campaign, the AMS organic fraction was very close to the estimated ‘other’ fraction calculated from the IC which shows that most of the ‘other’ fraction during the DPOM campaign was organic. The 6.5 % of unknown fraction is also likely to be organic within the $\text{PM}_{2.5} > x > \text{PM}_1$ particle sizes. Based on the IAP and CEH AMS organic results from the AMS, the BWIN $\text{PM}_{2.5}$ also comprised of a considerable fraction of organic, although a larger proportion of $\text{PM}_{2.5}$ is unknown during this campaign. Future work needs to be

completed to assess this unknown fraction. Future work comprises seeking the different AMS factors for primary and secondary organic species within each of these campaigns.

Table 3.7. Comparison of the IC 'other' fraction to the AMS PM₁ organic fraction.

Measurement	AMS (CEH)		AMS (IAP)
	DPOM	BWIN	BWIN
<i>N</i>	74	32	114
Average AMS Organic PM ₁ / $\mu\text{g m}^{-3}$	98.5	35.1	30.0
TEOM-FDMS (UoB) [PM _{2.5}] / $\mu\text{g m}^{-3}$	164.9	97.3	97.3
% Known Org in PM _{2.5} / $\mu\text{g m}^{-3}$	59.8	36.1	30.9
IC PM _{2.5} Other %	66.3	64.3	64.3
Estimated Unknown %	6.5	28.2	33.4

During the BSUM campaign, PM_{2.5} was dominated by the inorganic ions, with the 'other' fraction contributing 37.5 %. Based on the gas compositions and higher temperatures this other fraction was likely predominantly SOA. This is consistent with the AMS results, where almost 80 % of PM₁ on average was classified as oxidised organic aerosol. C₂O₄²⁻ was also observed to comprise a higher fraction compared to the winter campaign due to higher oxidation levels. A high proportion of SIA ($\Sigma [\text{NH}_4^+ + \text{NO}_3^- + \text{SO}_4^{2-}] = 48.7 \%$) was observed, which is very similar to the DPEM fraction. This is due to much higher temperatures and solar flux in both cities causing more oxidation of NO₂ and SO₂. The Cl⁻ fraction was much lower compared to BWIN and was similar to BSUM K⁺. This is most likely down to the closure of the Huaneng between the BWIN and BSUM campaigns.

In summary, the warmer months in both cities observed a higher fraction of known ionic material whereas the cooler months showed a considerable 'other' fraction which was most likely predominantly organic. This is based on comparison to AMS results from CEH and IAP, as well as the DPOM campaign taking place on the lead up to Diwali as well as the BWIN campaign taking place during the heating season. The cooler seasons enforce a lower boundary layer which allows for the accumulation of organics into the aerosol phase during these heavily polluted periods. Based on the mixing ratios gas phase data, it is suspected that the much-increased NO seen during the DPOM campaign most likely makes the DPOM organic fraction comprise mostly of primary VOCs. In contrast, the BWIN campaign demonstrated much lower NO which is hypothesised to make the organic fraction during BWIN comprise of a higher proportion of SOA. In contrast, the DPEM displayed almost half of the aerosol composition as SIA which was attributed to much increased temperatures and a higher solar flux causing oxidation of NO₂ and SO₂ to acidic gases which neutralise NH₃. The very high temperatures also made the DPEM campaign observe the highest contribution from mineral dust species. The BSUM campaign also demonstrated a significantly high known ionic fraction which was considerably larger than the DPOM and BWIN campaigns. Because of this, the aerosol during the warmer seasons were more hygroscopic compared to the cooler

seasons. This may be indicative of a higher absorption capability of the warmer seasons aerosol to absorb toxic gases from the atmosphere.

3.3.6 Inter-Instrumental Comparison of Inorganic Species

An inter-instrument comparison of the major inorganic species was conducted between the IC (UoY) (data presented in this chapter), the IC (UoB) and the AMS (CEH) (as well as the IAP AMS for BWIN and BSUM). Time series; bar charts of day, night and total campaign averages; as well as linear regression analysis between identical measurements across different instruments from the separate institutions were conducted in order to establish an inter-instrument comparison as well as the reproducibility of the IC (UoY) measurements.

In the time series for the campaigns presented in this section (3.3.6), the grey and orange line time-series represent the much higher time resolution AMS measurements from CEH and IAP, respectively. The blue and yellow point markers represent the average filter sample readings using IC from UoY and UoB, respectively. The bar charts take identical colouration with the bar heights representing the weighted average values for overlapping sampling times between instruments. Error analysis was possible for the IC (UoY) data, although was not for the other instruments and institutions as the data was not available. This error was calculated by finding the average species error associated with a campaign and calculating the percentage error. This percentage error was subsequently applied to the IC (UoY) bar charts shown in this section. *N.B.* the error is not identical to the SD in the following discussions.

3.3.6.1 Delhi Pre-Monsoon

A set of time series for Cl^- , NO_3^- , SO_4^{2-} and NH_4^+ across the DPEM campaign showing the inter-comparison between the IC (UoY) and the AMS (CEH) instruments is shown in Fig. 3.19, with point markers showing the mid-points of sampling times, without averaging of data. During this campaign, the UoY samples were taken *ca.* every 3 hours with an overnight filter sample lasting *ca.* 14 hours. The AMS (CEH) sampling time was every 2 minutes using online AMS. *N.B.* The UoB sampled a few weeks prior to UoY and CEH. Therefore, no IC (UoB) data is seen in the time series in Fig. 3.19 although for comparison across the same season, the IC (UoB) has been added to the bar chart in Fig. 3.20.

The Cl^- (UoY) measurements (blue) were generally higher in concentration compared to the AMS (CEH). As shown in Fig. 3.20, the daytime IC (UoY) average was around 7 times higher ($2.94 \mu\text{g m}^{-3}$) compared to the AMS (CEH) data ($0.43 \mu\text{g m}^{-3}$). The night-time IC (UoY) average was 2.38 times larger than the AMS (CEH) during the night periods, presenting a smaller difference between the instruments compared to the daytime averages. A possible reason for this may be down to the different sizes measured during the day and night-periods. The AMS (CEH) instrument was only able to measure up to PM_{10} , whereas the HiVol used for the IC (UoY) samples had a size selective inlet of $\text{PM}_{2.5}$. Therefore, the greater $[\text{Cl}^-]$ seen may be due to the size of particles measured, which may have observed a larger proportion of larger particles during the daytime with larger $[\text{Cl}^-]$. Scanning Mobility Particle Sizer (SMPS) data is needed to justify this hypothesis. Furthermore,

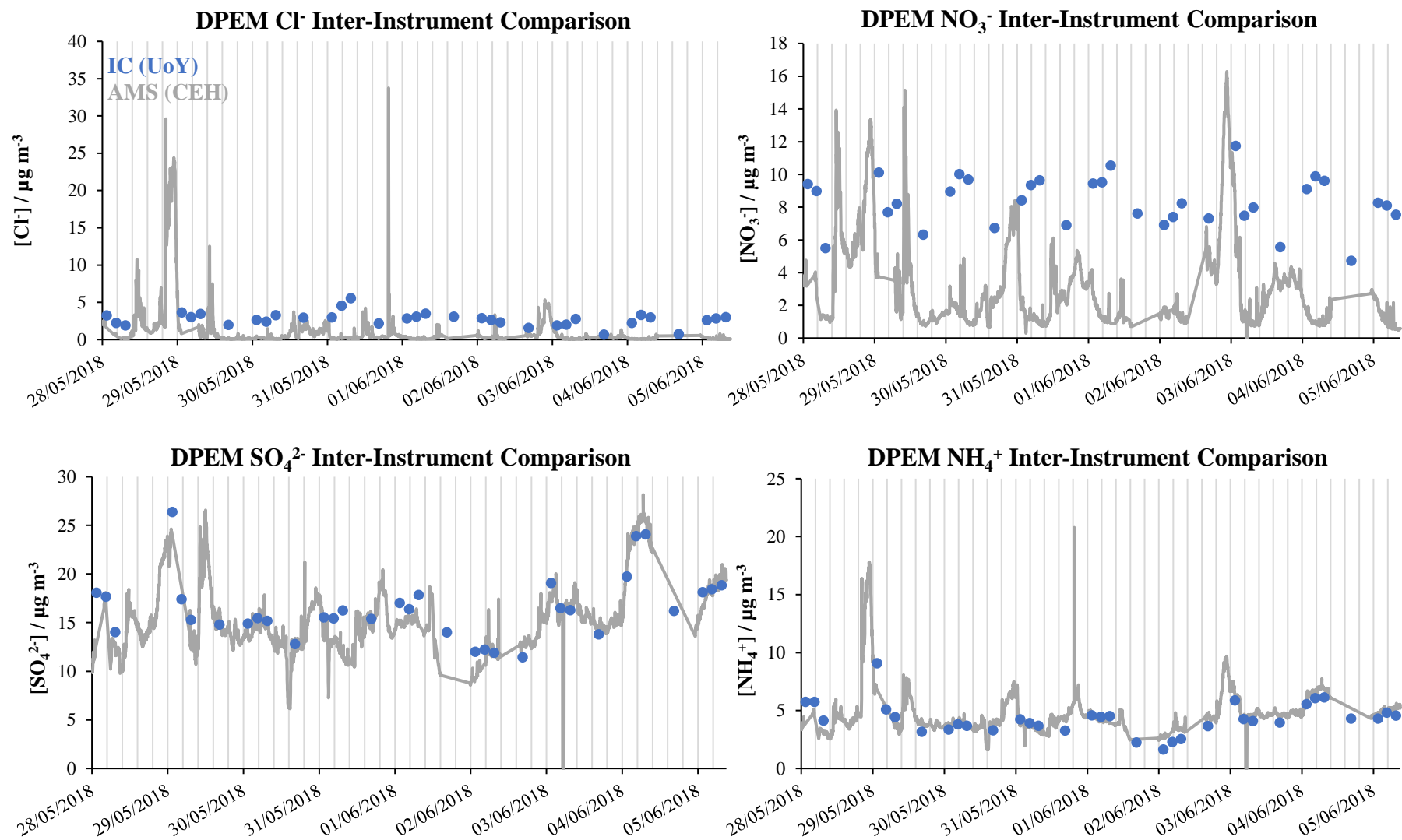


Fig. 3.19. Inter-instrument time-series comparison for the major ions Cl^- (top left), NO_3^- (top right), SO_4^{2-} (bottom left) and NH_4^+ (bottom right) during the DPEM campaign. The IC (UoY) is shown as the blue dot points and the AMS (CEH) is shown as the grey line. Atmospheric concentrations are displayed on the y-axis and time is displayed along the x-axis. The grey vertical lines represent midnight time points. The errors associated with the IC (UoY) are found in Fig. 3.9. Error values for the other instruments were unavailable.

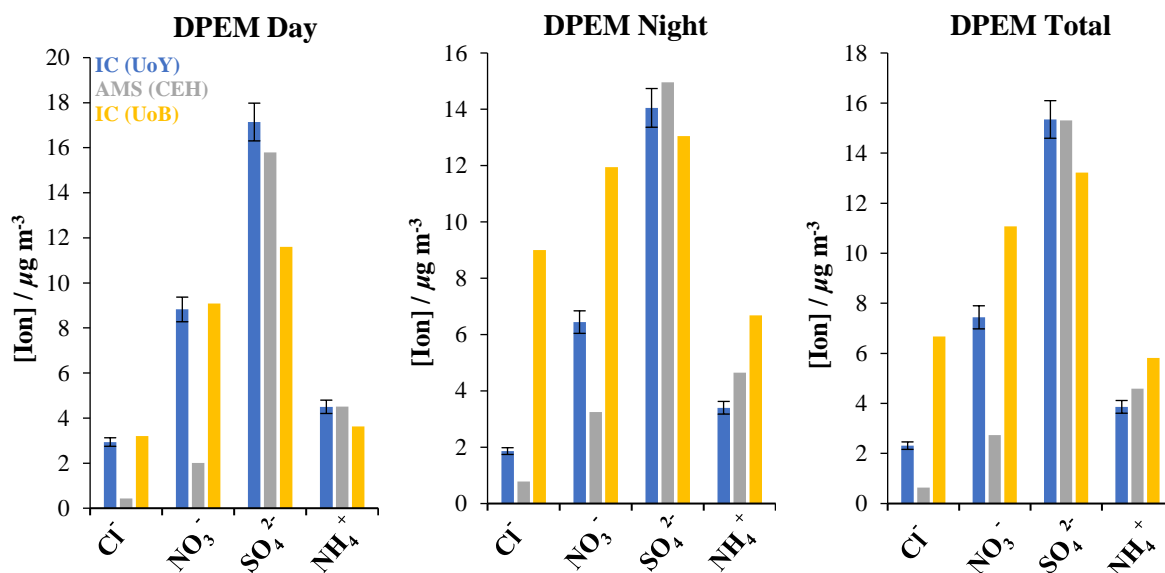


Fig. 3.20. Bar Charts presenting the weighted averages between the IC (UoY, blue) and AMS (CEH, grey) during the DPEM campaign, as well as IC (UoB, yellow) during the same season. The errors of measurements are shown for the IC (UoY), although the error values for the AMS (CEH) and IC (UoB) were unavailable.

Table 3.8. R^2 regression coefficients of the IC (UoY) vs the AMS (CEH) and IC (UoB) DPEM datasets.

R^2	Day				Night				Total			
Grp.	Cl^-	NO_3^-	SO_4^{2-}	NH_4^+	Cl^-	NO_3^-	SO_4^{2-}	NH_4^+	Cl^-	NO_3^-	SO_4^{2-}	NH_4^+
CEH	0.02	0.22	0.80	0.70	0.02	0.08	0.64	0.58	0.00	0.01	0.74	0.59
UoB	-	-	-	-	-	-	-	-	-	-	-	-

observing the R^2 correlation between the IC (UoY) and AMS (CEH) results (Table 3.8) demonstrates a daytime $R^2 = 0.02$, and night-time $R^2 = 0.02$, with no correlation seen. Therefore, the difference in concentration was unlikely a calibration issue between the instruments.

Although the HiVol (UoB) filter sampling took place a few weeks previous to the HiVol (UoY) sampling and AMS (CEH) sampling, the daytime averages measured by the IC (UoB) was also shown in Fig. 3.20 and was in good agreement with the IC (UoY) measurement ($2.94 \mu\text{g m}^{-3}$). The night-time IC (UoY) average [Cl^-] of $1.86 \mu\text{g m}^{-3}$ was however much smaller than the IC (UoB) average of $9.01 \mu\text{g m}^{-3}$, by a factor of 4.84, which may be down to the different sampling periods.

The IC (UoY) [NO_3^-] measurements were much larger than the AMS (CEH) as shown in both Fig. 3.19 and Fig. 3.20. For the total campaign averages, IC (UoY) measurements were around 3 times larger than the AMS (CEH). A larger difference was also observed during the daytime similar to Cl^- , the linear regression analysis showed almost no correlation between the IC (UoY) and AMS (CEH) measurements during the campaign. It is possible that the larger values of NO_3^- measured by the IC (UoY) compared to the AMS (CEH) may be down to the presence of Organic Nitrate (Org- NO_3) compounds. Org- NO_3 compounds are known to be destroyed by the vaporizer during sampling using AMS²⁸⁷ hydrolysis although are also known to undergo hydrolysis to produce NO_3^- in the aqueous phase^{275,348,349,276} (chapter 6). If this was however predominant, a larger difference would be expected between the night-time IC and AMS results compared to the daytime. The IC (UoB) average values

have also been shown in Fig. 3.20 in order to assess the comparability during the same season. Very good agreement was observed during the daytime for which the IC measurements (UoY and UoB) observed averages of $8.82 \mu\text{g m}^{-3}$ and $9.09 \mu\text{g m}^{-3}$, respectively.

For SO_4^{2-} , the time series in Fig. 3.19 shows a very good agreement between the IC (UoY) and AMS (CEH) instruments, for which the overall campaign averages for the IC (UoY) and AMS (CEH) were $15.34 \mu\text{g m}^{-3}$ and $15.30 \mu\text{g m}^{-3}$, respectively. A very strong correlation was also observed during the daytime ($R^2 = 0.80$), compared to the night-time period ($R^2 = 0.64$).

Very good agreement was also seen between the IC (UoY) and the AMS (CEH) for the NH_4^+ time series in Fig. 3.19. The averages show that the majority of this agreement originates from daytime values which observed averages of $4.50 \mu\text{g m}^{-3}$ ($\text{SD} \pm 1.46 \mu\text{g m}^{-3}$) and $4.51 \mu\text{g m}^{-3}$ ($\text{SD} \pm 1.23 \mu\text{g m}^{-3}$), for the IC (UoY) and AMS (CEH), respectively. A substantial difference is observed between the night-time IC (UoY) and AMS (CEH) averages of $3.40 \mu\text{g m}^{-3}$ ($\text{SD} \pm 0.66 \mu\text{g m}^{-3}$) and $4.65 \mu\text{g m}^{-3}$ ($\text{SD} \pm 0.68 \mu\text{g m}^{-3}$), respectively, for which the respective averages do not fall within the other instrument's SD. The linear regression correlation coefficient was also lower between the two instruments for the night-time period ($R^2 = 0.58$) compared to the daytime ($R^2 = 0.70$). A possible reason for the higher AMS (CEH) value within PM_1 compared to the average $\text{PM}_{2.5}$ IC (UoY) [NH_4^+] is likely down to the sampling times. AMS (CEH) values were taken every 2 minutes (2-minute average) whereas the night-time IC (UoY) values were averaged from single filters sampled for *ca.* 14 hours each night. As the average DPEM night-time temperature was 32.3°C and is significantly high, this may have encouraged the volatilisation of NH_3 into the gas from the $\text{PM}_{2.5}$ sampled onto the filter during the *ca.* 14 hours sampling time.

3.3.6.2 Delhi Post-Monsoon

An inter-instrumental comparison of time-series is shown in Fig. 3.21, for Cl^- , NO_3^- , SO_4^{2-} , and NH_4^+ during the DPOM campaign. The frequency of the samples from this study (IC, UoY) were taken every hour, three hours or over-night. The HiVol (UoB) samples were taken *ca.* every 12 hours for day and night analysis, and the AMS (CEH) samples were taken as online measurements every 5 minutes. The day, night and total campaign averages are shown in Fig. 3.22 and represent the averages of where sampling times had overlapped.

Observing the time series in Fig. 3.21, the IC (UoY) and IC (UoB) [Cl^-] readings both have a similar trend to the time series of the AMS (CEH). Comparing the averages over the whole campaign, good agreement is observed between the three instruments with the IC (UoY), IC (UoB) and AMS (CEH), demonstrating averages of $6.75 \mu\text{g m}^{-3}$, $6.45 \mu\text{g m}^{-3}$ (within IC (UoY) error) and $5.97 \mu\text{g m}^{-3}$, respectively. There were however discrepancies seen between instrumental averages between the day and night-time periods. During daytime periods, the AMS (CEH) ($3.26 \mu\text{g m}^{-3}$) and IC (UoB) ($3.19 \mu\text{g m}^{-3}$) means were very similar although in disagreement with the IC (UoY) ($5.87 \mu\text{g m}^{-3}$, $\text{SD} \pm 6.56 \mu\text{g m}^{-3}$). The AMS (CEH) and IC (UoB) values did however lie within 1 SD of the IC (UoY) values. The R^2 results of the IC (UoY) vs the IC (UoB) were calculated by averaging the IC (UoY)

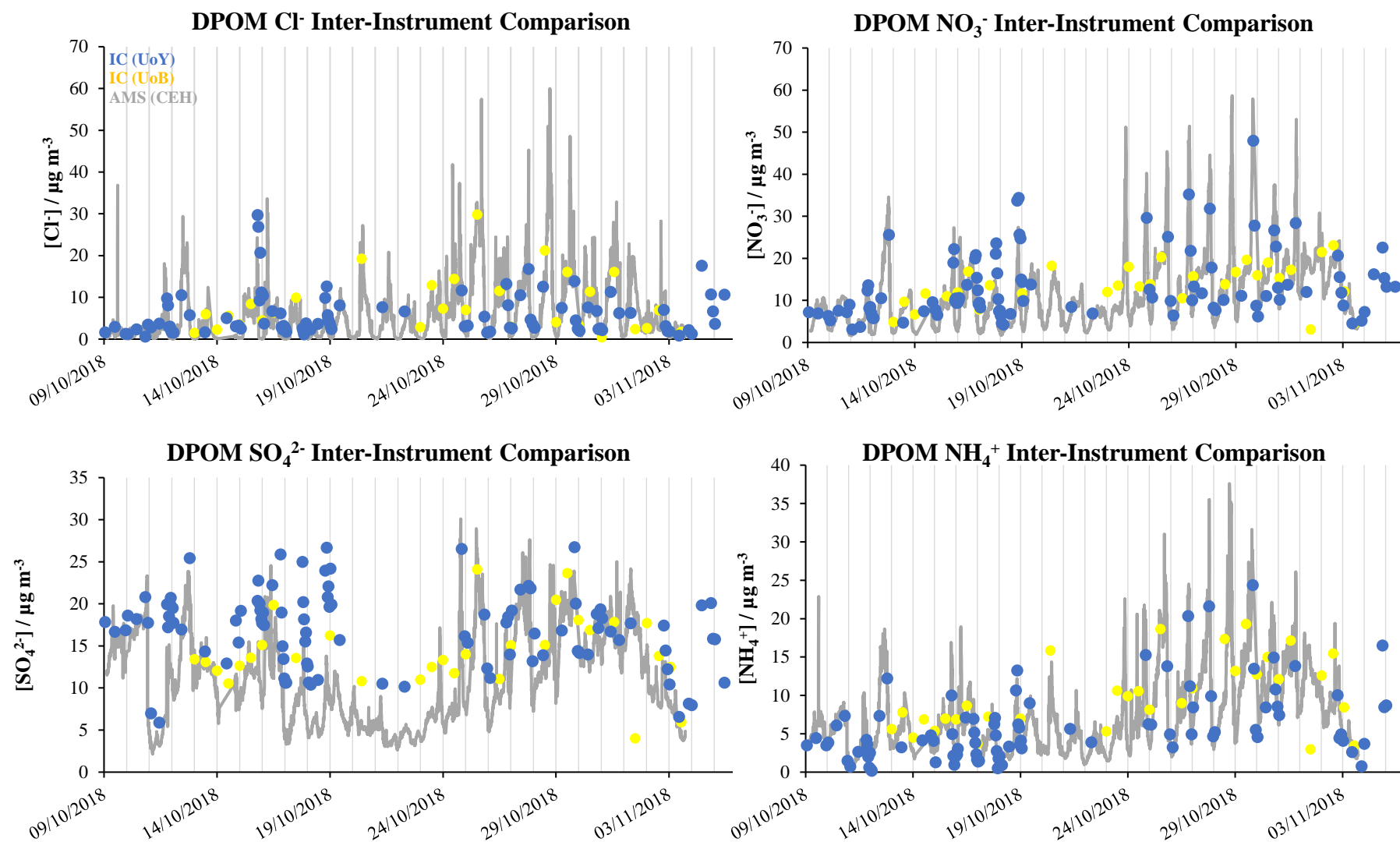


Fig. 3.21. Inter-instrument time-series comparison for the major ions Cl^- (top left), NO_3^- (top right), SO_4^{2-} (bottom left) and NH_4^+ (bottom right) during the DPOM campaign. The IC (UoY) is shown as the blue dot points; the AMS (CEH) is shown as the grey line; and the IC (UoB) is shown as the yellow dot points. Atmospheric concentrations are displayed on the y-axis and time is displayed along the x-axis. The grey vertical lines represent midnight time points. The errors associated with the IC (UoY) are found in Fig. 3.10. Error values for the other instruments were unavailable.

data to the IC (UoB) time-series times (Table. 3.9). The R^2 results of IC (UoY) vs AMS (CEH) were established by averaging the 5 minute AMS data to the IC (UoY) filter sampling times (Table. 3.9). Inspecting the linear regression analysis, the day-time correlation between IC (UoY) vs the IC (UoB) and AMS (CEH) demonstrated R^2 values of 0.20 and 0.40, respectively, which was poor. A possible reason for the increase in Cl^- during the IC (UoY) daytime measurements compared to the AMS (CEH) measurements may be due to positive artefacts such as the deposition of gaseous HCl onto the surfaces of particles sampled by the HiVol as no denuders were installed on the HiVol. This may be further evidenced by the relative R^2 values attained between NH_4^+ and Cl^- within the IC (UoY) data during the day and night times, which were $R^2 = 0.1$ and $R^2 = 0.6$. A much-reduced R^2 value during the daytime suggests that Cl^- was not present in the form of NH_4Cl and therefore entered the aerosol via a different mechanism to the neutralisation process via NH_3 (such as from HCl adsorption onto filtered $\text{PM}_{2.5}$). The reason for the lower IC (UoB) $[\text{Cl}^-]$ compared to IC (UoY) may be down to post-sample treatment. The HiVol filters obtained by the UoB were left exposed in a warm room (*ca.* 25 °C) to allow for the excess H_2O to evaporate off before sample analysis. This may however have caused evaporation of NH_4Cl .

During the night-time hours however, very good agreement is seen between the IC (UoY) and the AMS (CEH) averages, with averages of $7.24 \mu\text{g m}^{-3}$ ($\text{SD} \pm 4.26 \mu\text{g m}^{-3}$) and $7.51 \mu\text{g m}^{-3}$ ($\text{SD} \pm 6.44 \mu\text{g m}^{-3}$), respectively (Fig. 3.22, Cl^-). The IC (UoB) values however averaged at $10.75 \mu\text{g m}^{-3}$ ($\text{SD} \pm 7.28 \mu\text{g m}^{-3}$) which was substantially larger, although the average did lie within 1 SD of the IC (UoY) values. During night-time hours however, much-improved R^2 correlations were observed of $R^2 = 0.92$ and $R^2 = 0.74$, between IC (UoY) vs IC (UoB) and AMS (CEH), respectively. This is likely down to the much similar sampling times between IC (UoY) and IC (UoB) which were *ca.* 14 hours and *ca.* 12 hours, respectively. It may also indicate that the majority of the Cl^- during the night-time hours was within the PM_1 fraction based on the similarity of averages between the IC (UoY) and AMS (CEH).

The IC (UoY) and IC (UoB) generally follow the AMS (CEH) results very well for NO_3^- (Fig. 3.21). The total campaign average $[\text{NO}_3^-]$ observed very good agreement between all instruments. The IC (UoY), IC (UoB) and AMS (CEH) averages were $12.23 \mu\text{g m}^{-3}$, $12.89 \mu\text{g m}^{-3}$ and $12.09 \mu\text{g m}^{-3}$, respectively. Similar to $[\text{Cl}^-]$, the daytime IC (UoY) $[\text{NO}_3^-]$ mean was considerably higher than the AMS (CEH) or IC (UoB) measurements. The NH_4^+ vs NO_3^- correlation for IC (UoY) was $R^2 = 0.76$, suggesting the substantial presence of NH_4NO_3 . The average daytime temperature during DPOM was 28.8 °C. NH_4NO_3 is known to be volatile and therefore the much longer filter sampling times during the daytime (*ca.* 12 hours for UoB), may have allowed for the volatilisation of NH_4NO_3 from the UoB filter samples during sampling, resulting in lower $[\text{NO}_3^-]$ for the IC (UoB) measurements compared to the IC (UoY). Furthermore, the IC (UoY) may be larger compared to the AMS (CEH) due to the HiVol sampling $\text{PM}_{2.5}$ and AMS (CEH) measuring PM_1 .

The night-time averages of $[\text{NO}_3^-]$ between IC (UoY), IC (UoB), and the AMS (CEH) were $9.98 \mu\text{g m}^{-3}$, ($\text{SD} \pm 3.61 \mu\text{g m}^{-3}$), $14.12 \mu\text{g m}^{-3}$, ($\text{SD} \pm 5.29 \mu\text{g m}^{-3}$), and $11.43 \mu\text{g m}^{-3}$ ($\text{SD} \pm 5.89 \mu\text{g m}^{-3}$), respectively. Therefore, the relation between the IC (UoY) and IC (UoB) averages is inverted compared to the daytime values. Therefore, most instruments were in one-another's SD.

The IC (UoY) time series for SO_4^{2-} (Fig. 3.21) had a very similar trend to the IC (UoB) although a positive offset was seen between the IC measurements and the AMS (CEH) measurements. The total campaign average $[\text{SO}_4^{2-}]$ between the IC (UoY) ($15.52 \mu\text{g m}^{-3}$) and IC (UoB) ($14.48 \mu\text{g m}^{-3}$) were similar (although the IC (UoB) was not within the IC (UoY) error). These averages were both substantially higher than the AMS (CEH) $[\text{SO}_4^{2-}]$ average of $11.61 \mu\text{g m}^{-3}$. It is hypothesised that the difference between the AMS and IC results (from UoY and UoB) is down to the influence of cement from a building site *ca.* 50 meters away from the sampler towards the NNW-N of the sampler location, which was active during the DPOM campaign but was not in use during the DPEM campaign. As the HiVol samplers sampled $\text{PM}_{2.5}$ (UoY and UoB) and the AMS sampled PM_1 , it is proposed that larger primary cement particles are the result of the increases SO_4^{2-} detection within the IC (UoY and UoB) measurements compared to the AMS (CEH) readings.

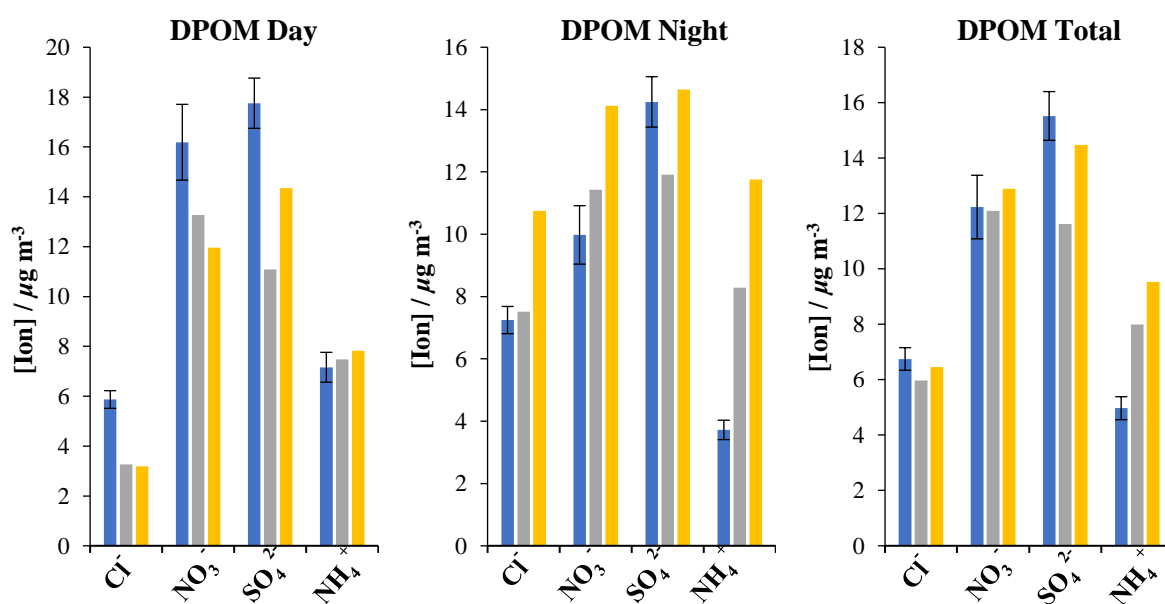


Fig. 3.22. Bar Charts presenting the weighted averages between the IC (UoY, blue), AMS (CEH, grey) and IC (UoB, yellow) during the DPOM Campaign. The errors of measurements are shown for the IC (UoY), although the error values for the AMS (CEH) and IC (UoB) were unavailable.

Table 3.9. R^2 regression coefficients of the IC (UoY) vs the AMS (CEH) and IC (UoB) for the DPOM datasets.

R^2	Day				Night				Total			
Grp.	Cl ⁻	NO ₃ ⁻	SO ₄ ²⁻	NH ₄ ⁺	Cl ⁻	NO ₃ ⁻	SO ₄ ²⁻	NH ₄ ⁺	Cl ⁻	NO ₃ ⁻	SO ₄ ²⁻	NH ₄ ⁺
CEH	0.40	0.79	0.48	0.91	0.74	0.68	0.74	0.69	0.40	0.73	0.44	0.90
UoB	0.20	0.48	0.41	0.78	0.92	0.82	0.84	0.87	0.45	0.19	0.57	0.64

A qualitative assessment of anions within UltraTech [largest Indian manufacturer of white and grey cement, as well as ready mixed concrete] cement (Mumbai, India) was conducted (see experimental,

Chapter 2). Three duplicates produced reproducible results which are shown in the chromatograms in Fig. 3.23. The most prominent anionic constituent was qualitatively observed to be SO_4^{2-} within the cement IC sample. According to the UltraTech test report³⁵⁰ supplied by Normet³⁵¹, SO_4^{2-} is not mentioned to be present although SO_3 is. Therefore, it is most likely that the SO_4^{2-} observed in the chromatograms was due to the reaction between SO_3 and H_2O within the cement IC sample, forming H_2SO_4 (Eq. 3.1) which dissociates to SO_4^{2-} in 18.2 M Ω water.



Eq. 3.1. Hydration of SO_3 forming H_2SO_4 .

The average day, night and total RH % for the DPOM period were 39.2 %, 61.4 % and 52.0 %, respectively. These are relatively high values and may have encouraged the SO_3 within $\text{PM}_{2.5}$ to hydrate to H_2SO_4 forming the extra SO_4^{2-} present within the UoY and UoB IC samples. Another possibility may be that the HiVol samplers (UoY and UoB) had sampled SO_3 and then extraction into water caused formation of $[\text{SO}_4^{2-}]$, which would not be measured by AMS (independent of particle size). The interference of cement may also explain the reduced correlation between the IC (UoY) and AMS (CEH) during the DPOM daytime ($R^2 = 0.48$) compared to the DPOM night-time period ($R^2 = 0.74$), as less agitation of building site surfaces would occur during the night-time.

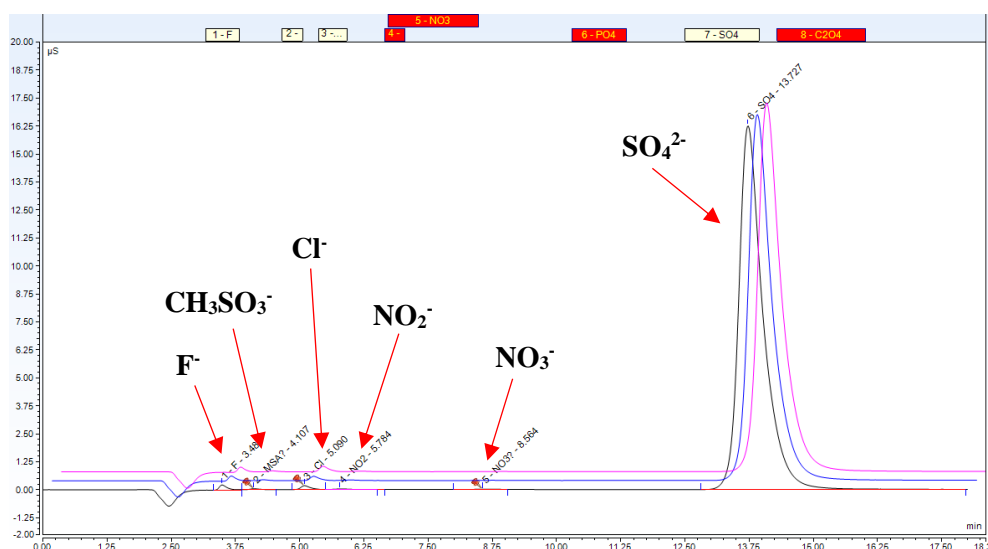


Fig. 3.23. Screen shot of replicate IC Chromatograms of UltraTech Cement displaying very high SO_4^{2-} response (large peak) with the incorporation of much lower concentration ions. The x-axis is time and the y-axis is peak area ($\mu\text{S} \cdot \text{min}$).

The presence of cement may also explain the significantly low $R^2 = 0.24$ between NH_4^+ vs SO_4^{2-} within the IC (UoY) DPOM daytime dataset which compares to a better correlation at night ($R^2 = 0.49$). Furthermore, the relative $[\text{SO}_4^{2-}]$ difference between the daytime IC (UoY) and AMS (CEH)

averages was $6.67 \mu\text{g m}^{-3}$, and at night was $2.34 \mu\text{g m}^{-3}$. The closer night-time averages may indicate less SO_4^{2-} from cement sources as the construction was carried out during the daytime.

CaO , MgO , Na_2O , K_2O , as well as Cl^- [at much lower concentration] were also reported to be present in the UltraTech cement³⁵⁰. Other sources suggest that PO_4^{3-} could also be present in construction materials³⁵². Therefore, further evidence for the cement interference may be seen by analysing the diurnal profiles of the other ions linked to construction materials and which may be expected to be detected in cement (Fig. 3.24). Fig. 3.24 was produced by grouping data points to the nearest hour and averaging these. The beige lines shown in Fig. 3.24 represent the \pm SD values.

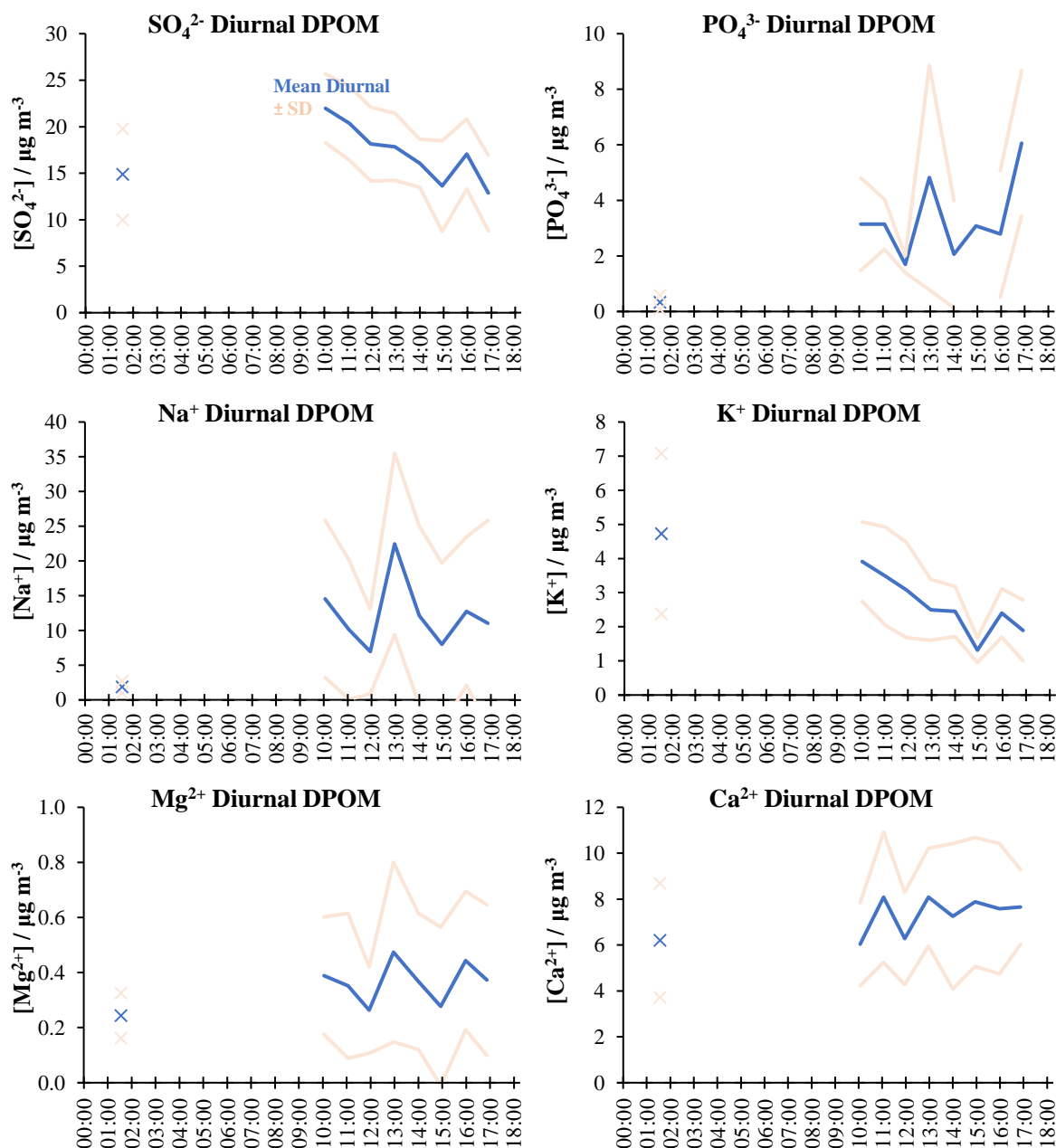


Fig. 3.24. Diurnal profiles of other ions which may exist in cement. The blue time series shows the average diurnal averaged across the available data and the beige lines on each side demonstrate the \pm SD of these values. Atmospheric concentration of ionic species is on the y-axis, with time of day on the x-axis. The crosses represent a single measurement for midnight.

Within the profiles of Na^+ , Mg^{2+} , PO_4^{3-} , and Ca^{2+} , a substantial drop is seen at *ca.* 12:00 which corresponds to lunchtime in which manual labour work could have ceased, reducing the agitation of cement particles and therefore reducing atmospheric cement $\text{PM}_{2.5}$ loading during this hour. No substantial drop is observed in the K^+ or SO_4^{2-} but this is easily explained by the abundance of biomass burning occurring on the lead up to Diwali which is a significant source of K^+ , and SO_4^{2-} is majorly produced from numerous sources. This is however very tenuous and further work is required to confirm this.

Despite the common cement influence, during daytime hours, the IC (UoY) average ($17.76 \mu\text{g m}^{-3}$) was substantially higher than the IC (UoB) ($14.48 \mu\text{g m}^{-3}$) and AMS (CEH) ($11.61 \mu\text{g m}^{-3}$). This was most likely due to either the impact of sampling times or HiVol locations, as the UoY and UoB samplers were located on different roofs. The night-time IC (UoY) ($14.25 \mu\text{g m}^{-3}$) and IC (UoB) ($14.64 \mu\text{g m}^{-3}$) values were much similar and observed a much stronger correlation coefficient of $R^2 = 0.84$. This is due to much similar sampling times and sampling of $\text{PM}_{2.5}$ compared to PM_1 (AMS).

For NH_4^+ , the IC (UoY) and IC (UoB) values overlap the AMS (CEH) time series very well in Fig. 3.21, despite the varying sampling times of each instrumentation technique. Very good agreement is observed between the three instruments for the daytime samples which observed averages of $7.16 \mu\text{g m}^{-3}$, $7.83 \mu\text{g m}^{-3}$ and $7.48 \mu\text{g m}^{-3}$ for the IC (UoY), IC (UoB) and AMS (CEH), respectively. Linear regression correlation also had $R^2 = 0.91$ between the IC (UoY) and AMS (CEH) and $R^2 = 0.78$ for the IC (UoY) vs IC (UoB). Large disagreement in $[\text{NH}_4^+]$ was however seen during the night-time for which averages of $3.72 \mu\text{g m}^{-3}$, $11.76 \mu\text{g m}^{-3}$ and $8.29 \mu\text{g m}^{-3}$ were established for the IC (UoY), IC (UoB) and AMS (CEH), respectively. Therefore, the disagreement between the instrument averages over the total campaign (Fig. 3.22) is largely driven by the night-time values. The night-time linear regression correlation coefficients were however strong, observing $R^2 = 0.69$ between the IC (UoY) and AMS (CEH) and $R^2 = 0.87$ between the IC (UoY) and IC (UoB).

3.3.6.3 Beijing Winter

The time-series between two sets of IC measurements from the IC (UoY) (blue) and IC (UoB) (yellow), as well as two sets of AMS measurements from IAP (orange) and CEH (grey) are shown in Fig. 3.25, for Cl^- , NO_3^- , SO_4^{2-} , and NH_4^+ during the BWIN campaign. The York samples were taken every 1 or 3 hours during the daytime with an overnight filter of *ca.* 14 hours; the HiVol (UoB) samples were taken every 24 hours (with filter changes at *ca.* 08:00); the AMS measurements from IAP were hourly averaged and the AMS (CEH) measurements were taken inconsistently from between every *ca.* 2 minutes to *ca.* 35 minutes throughout the campaign. Comparing the IC (UoY) samples to the AMS samples, the general pattern of concentrations across the species observed is $\text{IC (UoY)} < \text{AMS (IAP)} < \text{AMS (CEH)}$. Also, generally much stronger linear regression correlation coefficients between instruments are established during the BWIN campaign compared to the other three APHH campaigns.

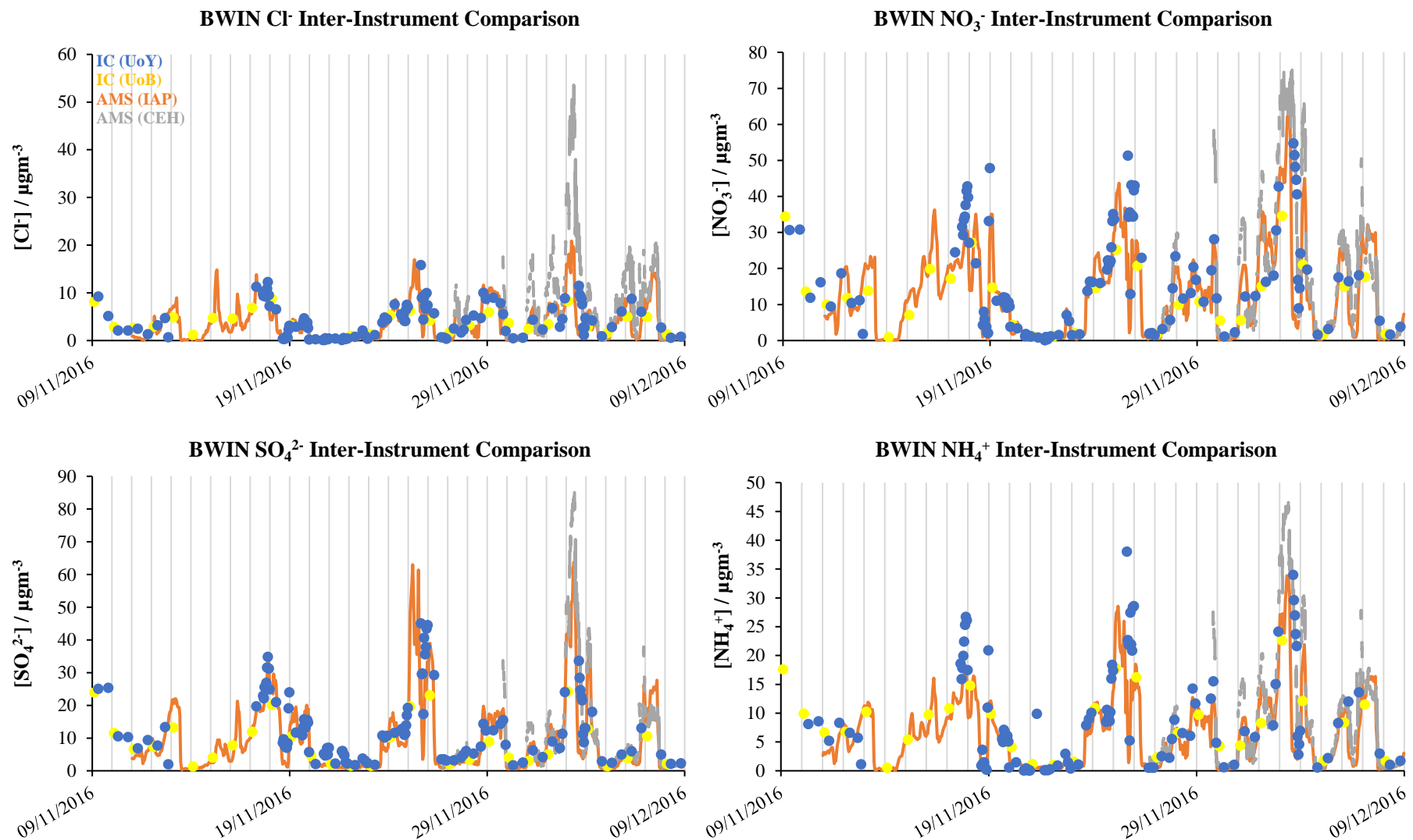


Fig. 3.25. Inter-instrument time-series comparison for the major ions Cl⁻ (top left), NO₃⁻ (top right), SO₄²⁻ (bottom left) and NH₄⁺ (bottom right) during the BWIN campaign. The IC (UoY) is shown as the blue dot points; the AMS (CEH) is shown as the grey line; the IC (UoB) is shown as the yellow dot points; and the AMS (IAP) is shown as the orange line. Atmospheric concentrations are displayed on the y-axis and time is displayed along the x-axis. The grey vertical lines represent midnight time points. The errors associated with the IC (UoY) are found in Fig. 3.11. Error values for the other instruments were unavailable.

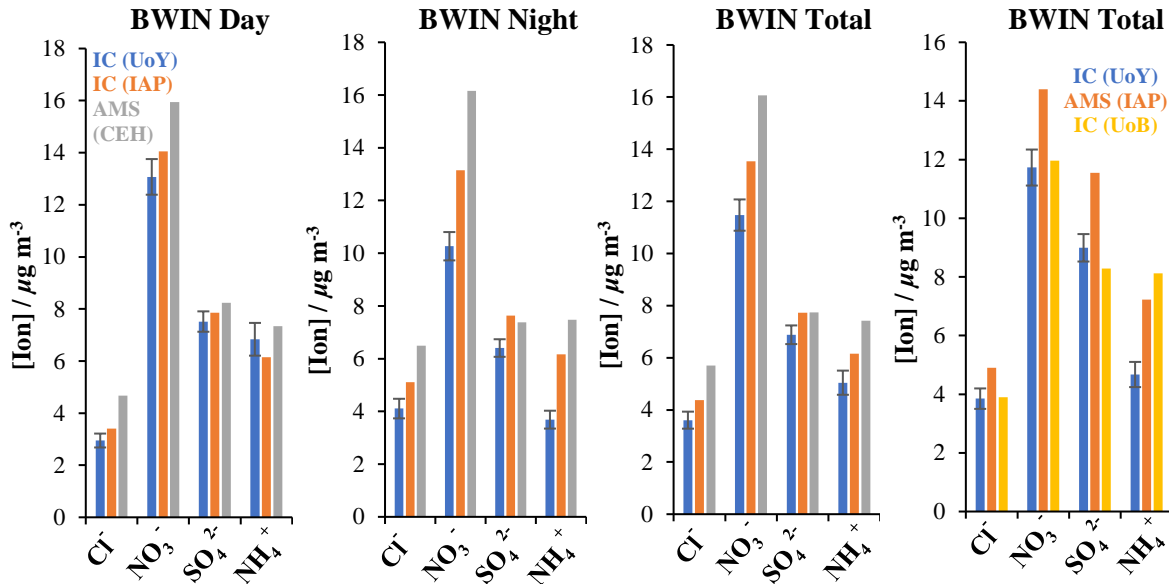


Fig. 3.26. Bar Charts presenting the weighted averages between the IC (UoY, blue), AMS (IAP, orange), AMS (CEH, grey) and IC (UoB, yellow) during the BWIN Campaign. The errors of measurements are shown for the IC (UoY), although the error values for the AMS (IAP and CEH) and IC (UoB) were unavailable.

Table 3.10. R^2 regression coefficients of the IC (UoY) vs the AMS (CEH) and IC (UoB) for the BWIN datasets.

R^2	Day				Night				Total			
Grp.	Cl ⁻	NO ₃ ⁻	SO ₄ ²⁻	NH ₄ ⁺	Cl ⁻	NO ₃ ⁻	SO ₄ ²⁻	NH ₄ ⁺	Cl ⁻	NO ₃ ⁻	SO ₄ ²⁻	NH ₄ ⁺
IAP	0.96	0.97	0.94	0.98	0.98	0.94	1.00	0.95	0.93	0.92	0.88	0.93
CEH	0.94	0.90	0.89	0.94	0.89	0.83	0.97	0.67	0.93	0.88	0.89	0.93
UoB	-	-	-	-	-	-	-	-	0.64	0.94	0.78	0.56

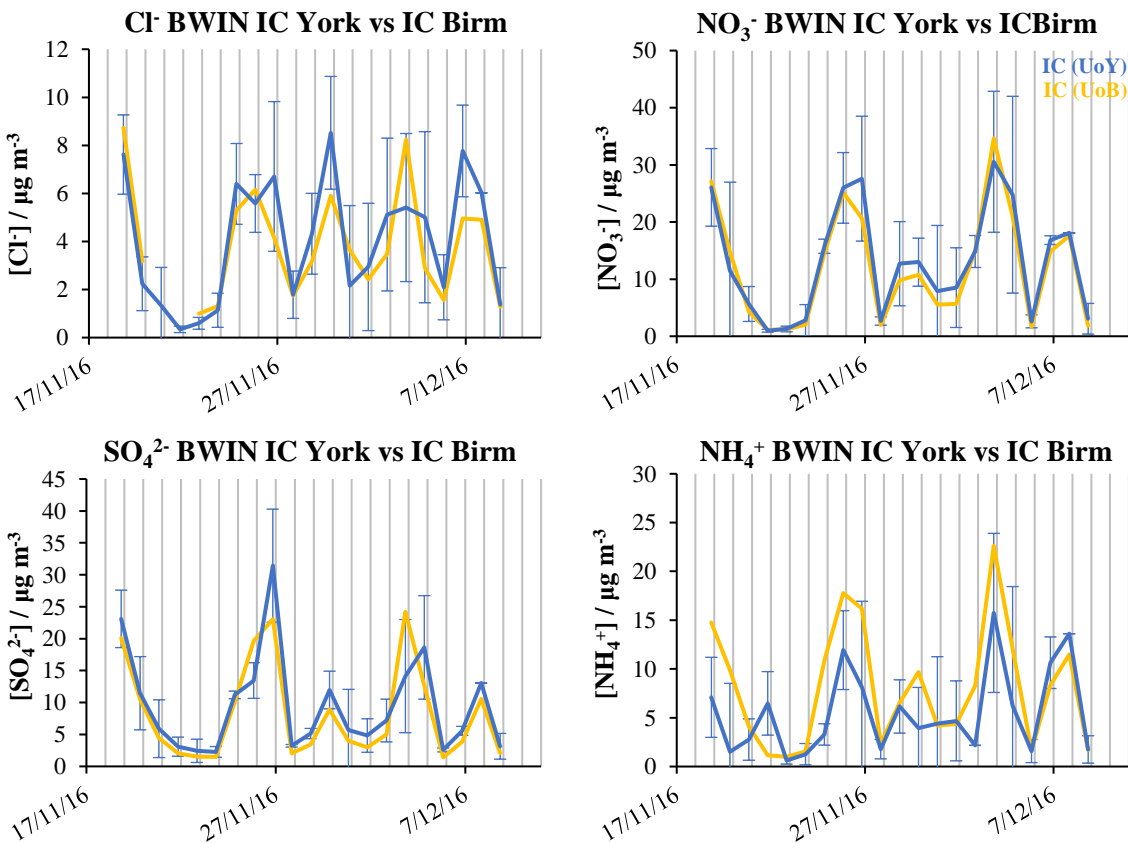


Fig. 3.27. Inter-instrument time-series comparison between the IC (UoY, blue) and IC (UoB, yellow) measurements (averaged to UoB filtering times, 24 hourly) for the major ions Cl⁻ (top left), NO₃⁻ (top right), SO₄²⁻ (bottom left) and NH₄⁺ (bottom right) during the BWIN campaign. The errors shown in the IC (UoY) time series demonstrate the SD across the concentrations averaged to the UoB filtering times. Atmospheric concentration is plotted on the y-axis, with time plotted on the x-axis. The grey vertical lines represent midnight time points.

Comparing instruments for Cl^- , the time series in Fig. 3.25 shows that generally all instruments follow the same overall trend. The main discrepancy is observed within the AMS (CEH) data which shows particularly high values on 4th Dec 2016 that do not align with the other instruments. Fig. 3.26 shows the day, night, and total campaign averages comparing the IC (UoY), AMS (IAP) and AMS (CEH) averages. The daytime averages were similar and a larger difference was seen between the instruments at night time. During both the day and night- time sampling, the AMS (IAP and CEH) averages were within 1 SD of the averages (IC) reported in this thesis (UoY). Over the entire campaign, the linear regression correlation was also very strong between IC (UoY) vs AMS (IAP) ($R^2 = 0.93$), and IC (UoY) vs AMS (CEH) ($R^2 = 0.93$) where sampling overlapped. Therefore, the differences in averages between these three institutions may be down to a calibration issue.

When the UoY filter times were averaged to the UoB 24-hour sampling times, weaker correlation was observed between the two IC methods, for which the correlation coefficient was calculated as $R^2 = 0.64$. The reason for this is likely down to the loss of detail in sampling over 24- hours. In doing this, less samples are attained over the entire sampling period, and therefore single data points may skew the correlation coefficient. When comparing the total campaign averages, the IC (UoB) and IC (UoY) are in very good agreement. Furthermore, inspecting Fig. 3.27 which demonstrates a time-series of the IC (UoB) and IC (UoY) measurements (averaged to UoB filter times), very good agreement is generally seen between the two instruments for Cl^- analysis, apart from three substantial discrepancies on 29th Nov, 3rd Dec, and 6th Dec, where difference of *ca.* $3 \mu\text{g m}^{-3}$ are seen.

$[\text{NO}_3^-]$ measurements between the different instruments had very good agreement as shown in Fig. 3.25. Particularly precise agreement is seen between the two IC techniques between UoY and UoB for the total campaign average. The correlation coefficient between the IC (UoY) and IC (UoB) data was also excellent. The campaign average AMS (IAP) data was larger than the IC (UoY) and IC (UoB) most likely due to NO_3^- loss through NH_4NO_3 evaporation during filter sampling for both the UoY and UoB datasets as a higher flow rate is associated with HiVol sampling compared to AMS analysis. NO_3^- volatilisation may also be the reason for the larger discrepancy between the IC (UoY), AMS (IAP) and AMS (CEH) NO_3^- averages during the night-time hours compared to the daytime values as significantly longer sampling times are associated with the HiVol (UoY) compared to the AMS instruments at night.

The $[\text{SO}_4^{2-}]$ were very similar between the IC (UoY), AMS (IAP) and AMS (CEH) when averaging AMS data to the UoY filter times. When averaging data to the UoB filter times, the IC (UoY) and IC (UoB) SO_4^{2-} averages were similar although the AMS (IAP) average was significantly larger. In addition, very good linear regression correlation coefficients were observed between the IC (UoY) and IC (UoB) ($R^2 = 0.78$) measurements with a comparison shown in Fig. 3.27. The regression analysis between the IC (UoY) and the two AMS instruments also indicated a strong correlation, with $R^2 = 0.88$ (AMS, IAP) and $R^2 = 0.89$ (AMS, CEH) over the BWIN period.

Fig. 3.26 demonstrates lower $[\text{NH}_4^+]$ measured from the UoY IC. The IC (UoY), AMS (IAP) and IC (UoB) total campaign averages were $4.67 \mu\text{g m}^{-3}$ ($\text{SD} \pm 9.45 \mu\text{g m}^{-3}$), $7.22 \mu\text{g m}^{-3}$ ($\text{SD} \pm 7.83 \mu\text{g m}^{-3}$) and $8.12 \mu\text{g m}^{-3}$ ($\text{SD} \pm 6.16 \mu\text{g m}^{-3}$), respectively. Therefore, the IC (UoY) average determined was around half the value determined by IC (UoB) and AMS (IAP). The correlation coefficient between the IC (UoY) and IC (UoB) was also $R^2 = 0.56$, which was generally lower compared to the other ions. However, when averaging the AMS (IAP) and AMS (CEH) data to the IC (UoY) sampling times, much better agreement is observed. The correlation coefficients of the IC (UoY) vs AMS (IAP) and IC (UoY) vs AMS (CEH) were both $R^2 = 0.93$. Therefore, the lower IC (UoY) value may be down to a calibration issue.

Similar to $[\text{SO}_4^{2-}]$, better agreement was seen between $[\text{NH}_4^+]$ averages between the IC (UoY), AMS (IAP) and AMS (CEH) instruments during the daytime compared to night-time hours (Fig. 3.26). The daytime correlation coefficients were also very high between IC (UoY) and AMS (IAP) ($R^2 = 0.98$) and IC (UoY) vs AMS (CEH) ($R^2 = 0.94$). Much larger deviations in the agreement are seen during the night-time samples. The correlation coefficient between the IC (UoY) and AMS (IAP) was still very high ($R^2 = 0.95$), however, a reduced correlation regression was observed between the IC (UoY) and AMS (CEH) ($R^2 = 0.67$) values.

3.3.6.4 Beijing Summer

The BSUM inter-instrument comparison time-series for the IC (UoY, blue) and IC (UoB, yellow), and AMS (IAP, orange) and AMS (CEH, grey) measurements are shown in Fig. 3.28. During this campaign, the HiVol (UoY) sampled every half hour, hour, 3 hours or over-night (*ca.* 14 hours); the HiVol (UoB) sampled every 24 hours; the AMS (CEH) sampled every hour; and the AMS (IAP) sampled every 5 minutes.

The $[\text{Cl}^-]$ measured during the BSUM campaign are very low in all instruments. Inspecting the time series, the IC (UoY), IC (UoB) and AMS (IAP) are all in good agreement with one another during the first half of the campaign (until *ca.* 11th Jun 2017). CEH is also in good agreement, although observes three major peaks in $[\text{Cl}^-]$ on 26th May, 31st May, and 5th Jun 2017. During the latter half of the campaign (from *ca.* 11th Jun until the 21st Jun 2017), the IC (UoY) measurements increasingly deviate from the general trend seen in the other instruments until the 21st Jun 2017. These increased Cl^- concentrations correspond to much more frequent sampling times (up to 30-minute sampling). This is down to less $\text{PM}_{2.5}$ accumulating on the filter and therefore a Cl^- signal very close to the LOD. Propagating through the atmospheric concentration calculation, a shorter filter sampling time may cause an artificially large $[\text{Cl}^-]$. Overall, it is difficult to assess the relative agreement between instruments during this campaign, as the results of $[\text{Cl}^-]$ are generally much lower and the relative SD for each instrument is inherently much higher.

The IC (UoY) and AMS (CEH) averages are in closer agreement compared with the AMS (IAP), although, this agreement is down to the average result of the particularly high values observed at the beginning of the campaign for the AMS (CEH) and at the end of the campaign for the IC (UoY)

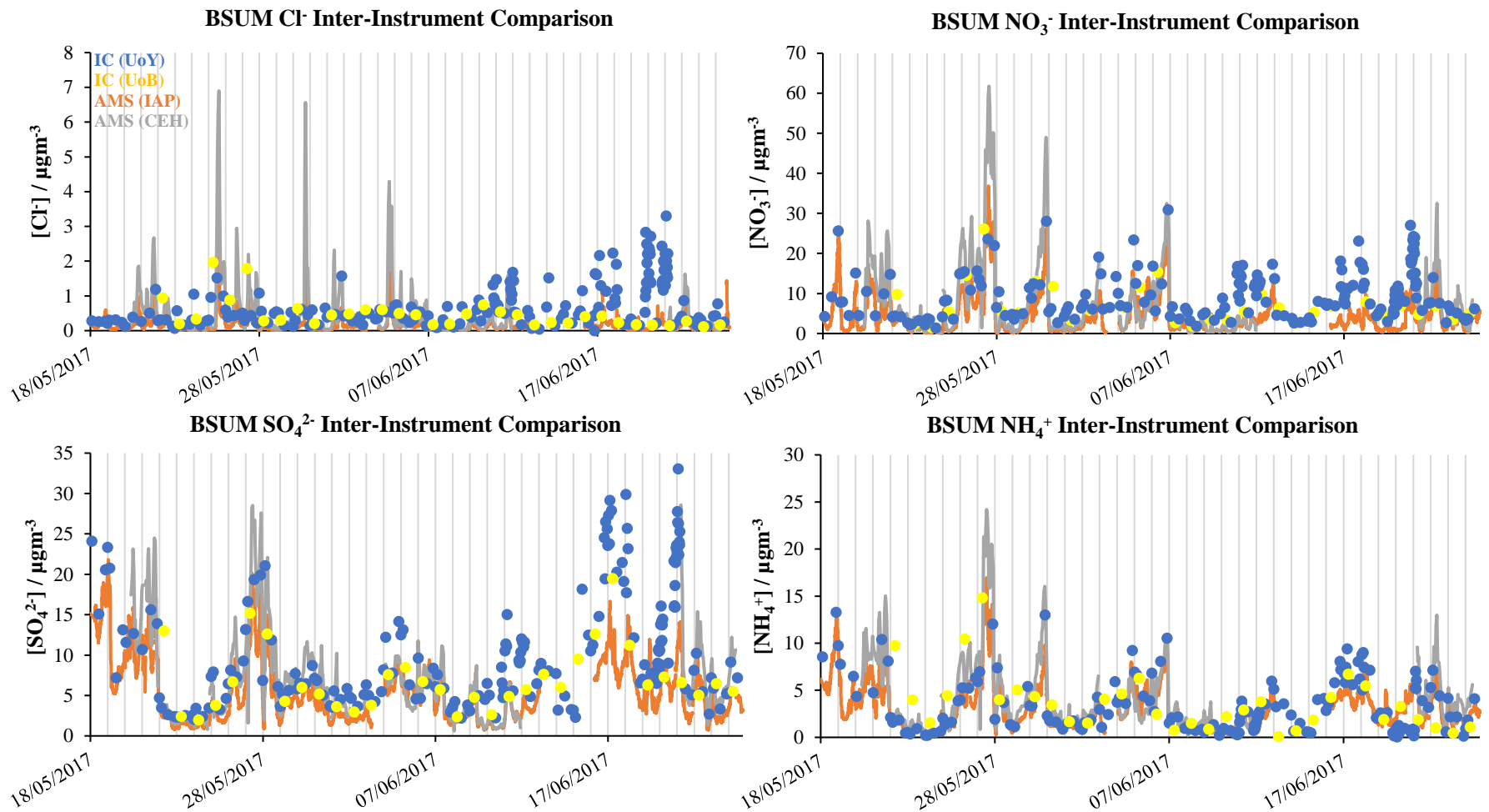


Fig. 3.28. Inter-instrument time-series comparison for the major ions Cl^- (top left), NO_3^- (top right), SO_4^{2-} (bottom left) and NH_4^+ (bottom right) during the BSUM campaign. The IC (UoY) is shown as the blue dot points; the AMS (CEH) is shown as the grey line; and the IC (UoB) is shown as the yellow dot points; and the AMS (IAP) is shown as the orange line. Atmospheric concentrations are displayed on the y-axis and time is displayed along the x-axis. The grey vertical lines represent midnight time points. The errors associated with the IC (UoY) are found in Fig. 3.12. Error values for the other instruments were unavailable.

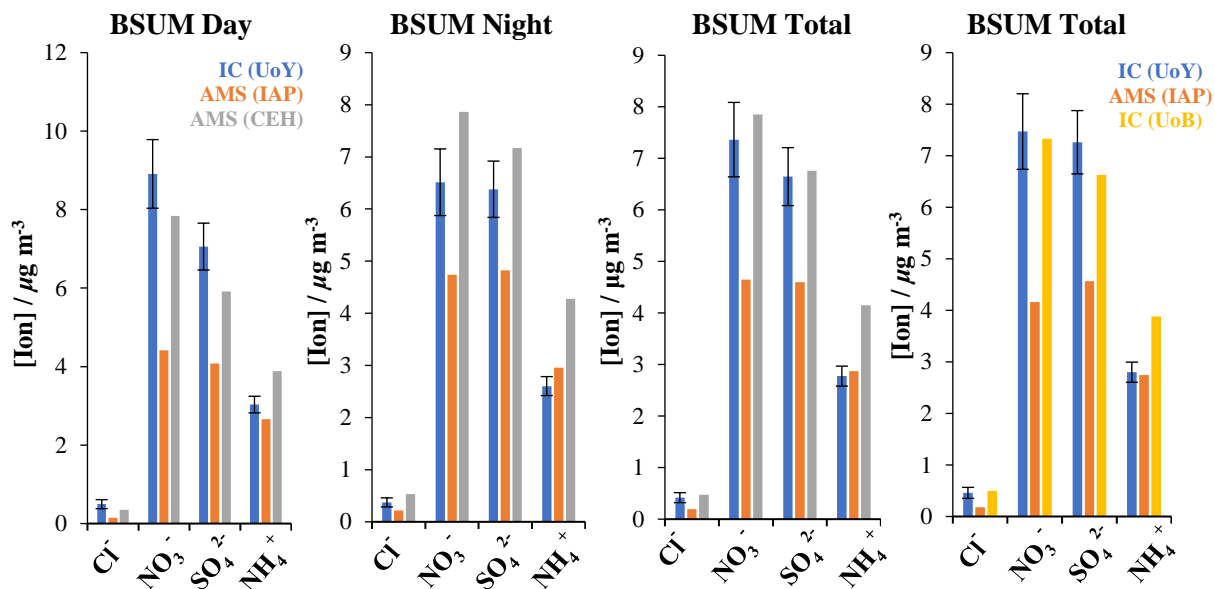


Fig. 3.29. Bar Charts presenting the weighted averages between the IC (UoY, blue), AMS (IAP, orange), AMS (CEH, grey) and IC (UoB, yellow) during the BSUM Campaign. The errors of measurements are shown for the IC (UoY), although the error values for the AMS (IAP and CEH) and IC (UoB) were unavailable.

Table 3.11. R^2 regression coefficients of the IC (UoY) vs AMS (CEH and IAP) and IC (UoB), BSUM datasets.

R^2	Day				Night				Total			
Grp.	Cl ⁻	NO ₃ ⁻	SO ₄ ²⁻	NH ₄ ⁺	Cl ⁻	NO ₃ ⁻	SO ₄ ²⁻	NH ₄ ⁺	Cl ⁻	NO ₃ ⁻	SO ₄ ²⁻	NH ₄ ⁺
IAP	0.04	0.71	0.65	0.90	0.80	0.96	0.94	0.93	0.00	0.50	0.72	0.66
CEH	0.01	0.50	0.49	0.74	0.84	0.95	0.91	0.86	0.08	0.53	0.56	0.74
UoB	-	-	-	-	-	-	-	-	0.25	0.79	0.78	0.05

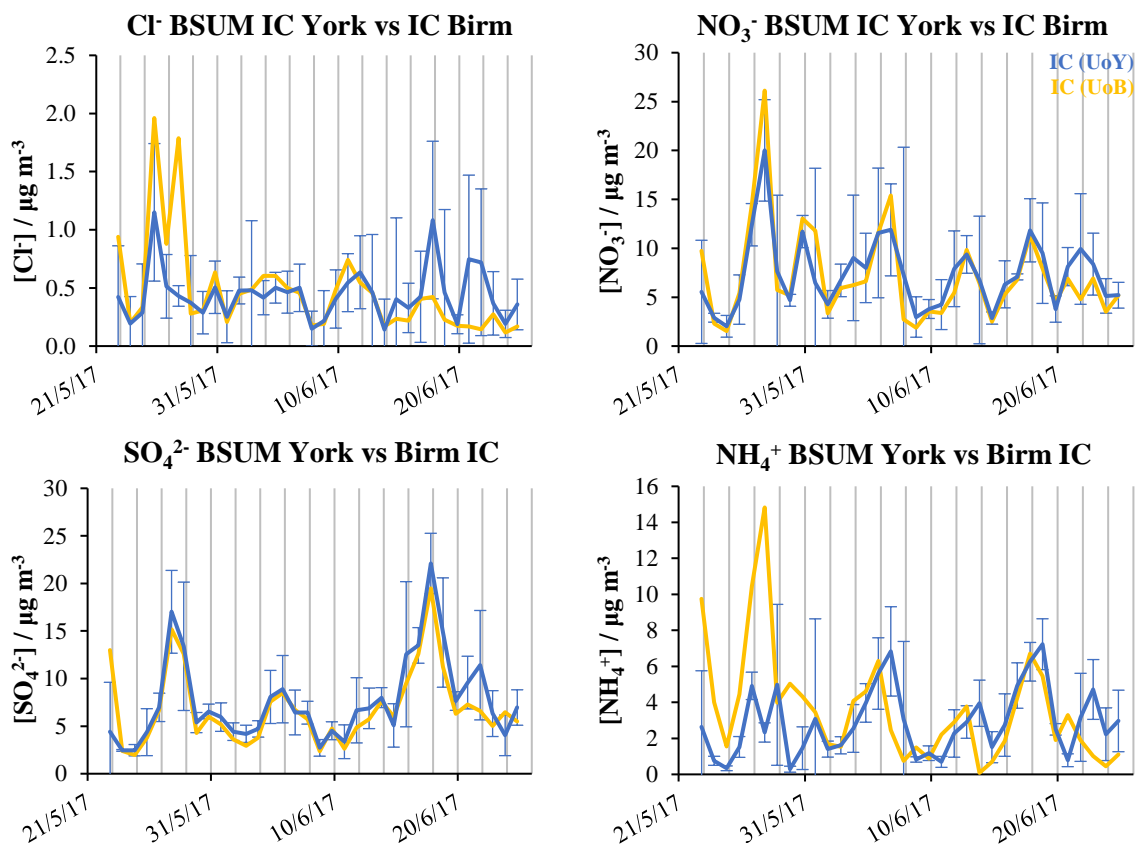


Fig. 3.30. Inter-instrument time-series comparison between the IC (UoY, blue) and IC (UoB, yellow) measurements (averaged to UoB filtering times, 24 hourly) for the major ions Cl⁻ (top left), NO₃⁻ (top right), SO₄²⁻ (bottom left) and NH₄⁺ (bottom right) during the BWIN campaign. The errors shown in the IC (UoY) time series demonstrate the SD across the concentrations averaged to the UoB filtering times. The grey vertical lines represent midnight time points. Atmospheric concentration is plotted on the y-axis, with time plotted on the x-axis.

(Fig. 3.28). Regression analysis also indicates very poor agreement between the IC (UoY) and the AMS (CEH, $R^2 = 0.08$). Furthermore, almost no correlation at all is seen between the IC (UoY) and the AMS (IAP) data sets ($R^2 = 0.00$, to 2 d.p.). The campaign averages comparing the IC (UoY) and IC (UoB) over identical sampling times were in very good agreement. The correlation coefficient observed between these two datasets was however low ($R^2 = 0.25$). Fig. 3.28 demonstrates that this poor agreement originates from deviations between the instruments before 28th May and after 16th Jun. Between these two days however, the Cl⁻ time-series agree very well with each other.

The NO₃⁻ time-series showed good agreement between all instruments throughout the campaign, although the IC (UoY) demonstrates higher values than the AMS (IAP) between the 10th – 22nd Jun 2017 (Fig. 3.28). During this period, the trend still however shows some correlation ($R^2 = 0.47$) between the two instruments. Generally, the IC (UoY) and AMS (CEH) NO₃⁻ values were closer in agreement compared to the IC (UoY) vs AMS (IAP) (Fig. 3.29).

Averaging the UoY data to the UoB 24-hour sampling times observes very good agreement between the two IC datasets, as shown in Fig 3.29 with averages of $7.47 \mu\text{g m}^{-3}$ and $7.33 \mu\text{g m}^{-3}$, respectively. A much lower average was however seen within the AMS (IAP) dataset ($4.16 \mu\text{g m}^{-3}$, $\text{SD} \pm 3.91 \mu\text{g m}^{-3}$). This is most likely due to the larger sampling size of the HiVol (UoY and UoB) methods (PM_{2.5}) compared to the AMS (IAP, PM₁). During the summer in Beijing, dust may flow in from the northwest. Strong acids such as HNO₃ are known to be able to react with basic dust species to produce compounds such as NaNO₃, therefore producing a formation pathway of NO₃⁻ in the aerosol without the need for NH₃ neutralization. These particles are less likely to be PM₁ and therefore may be why a higher NO₃⁻ was observed by filter sampling compared to AMS. When the IC (UoY) data is averaged to the IC (UoB) data, very good agreement is observed within the time series (Fig. 3.30).

For SO₄²⁻, very good agreement was seen between the IC (UoY) and AMS (CEH) averages for total campaign analysis, presenting averages of $6.65 \mu\text{g m}^{-3}$ and $6.76 \mu\text{g m}^{-3}$, respectively, with a correlation coefficient of $R^2 = 0.56$. A much stronger correlation coefficient was observed between the IC (UoY) and AMS (IAP) ($R^2 = 0.72$), however the average AMS (IAP) [SO₄²⁻] over these sampling times was much lower ($4.60 \mu\text{g m}^{-3}$) which may therefore be down to a calibration issue. There was however very good agreement between the two IC techniques over the campaign (Fig. 3.29 and Fig. 3.30).

Regarding NH₄⁺, all instruments show a similar temporal evolution (Fig. 3.28). The campaign average measured by IC (UoY) is in much better agreement with the AMS (IAP) compared to CEH (Fig. 3.29). The agreement between IC (UoY) and AMS (IAP) was seen in the total campaign average, for which the CEH data was higher.

3.3.6.5 Summary of Inter-Instrument Comparison

To summarise the inter-instrument comparison, overall the IC (UoY) measurements are in relatively good agreement with the other instruments across the APHH campaigns. There were however some discrepancies which were highlighted in both trends and campaign average values of ions. In comparing the IC and AMS instruments, the main discrepancies have been attributed to the different aerosol size fractions sampled ($PM_{2.5}$ and PM_1 , respectively). Different size distributions of aerosol during day and night-time periods likely caused different extents of disagreement. In addition, a potential local pollution plume of a specific primary SO_4^{2-} cement source during the DPOM campaign is thought to be the reason for the difference in SO_4^{2-} averages between IC and AMS, with larger cement particles causing a higher IC (UoY) SO_4^{2-} value. In studies where the concentration averages were however very similar, this gave an indication that the majority of a species concentration may be residing in the PM_1 fraction. Furthermore, specific discrepancies in NO_3^- may be down to the presence of Org- NO_3 species, as these are destroyed by the AMS vaporizer²⁸⁷ whereas would hydrolyse in water for IC analysis.

Differences in average concentrations between instruments was also attributed to the location of samplers as well as the length of sampling time, in which the AMS samples much more frequently compared to the offline filter samplers. In addition, The HiVol (UoB) filter sampling periods were significantly longer than those of the UoY. Possible reasons for discrepancies include the loss of volatile ammonium salts for longer filter sampling times for the IC methods. Possible positive artefacts include the potential for acidic gases and NH_3 in the atmosphere to pass through the HiVol and deposit on the filter piece. These positive and negative artefacts²¹² are significant for much longer sampling periods. Particularly good agreement was however seen during the BWIN campaign between the IC (UoY) and the IC (UoB) methods which was most likely down to a lack of either positive or negative artefacts from the much-reduced ambient temperatures. Other inter-instrumental discrepancies in which similar trends were found (good R^2 values) in conjunction with significant differences in average concentrations was put down to possible calibration issues between the instruments. In the IC (UoY) data where sampling was very frequent (up to 30 mins in BSUM), an overestimation of ionic species may have occurred. Other reasons for the discrepancies between instruments include post filter sample treatment by the UoB and the relative flow rate of samplers.

3.3.6.6 Summary of Expectations vs Observations between Sampling Methods

Furthermore, the responses from each instrument were sometimes unexpected regarding the system in which it is known that the IC and AMS instruments function. To summarise, it would generally be expected that higher concentrations across all ions would be measured by the IC instrument compared to the AMS, as the IC measures $PM_{2.5}$ whereas the AMS measures PM_1 . Furthermore, the AMS sampling frequency was every 2 minutes, whereas the IC sampling times were on the scale of hours, for which positive inorganic artefacts may be expected from the deposition of acidic gases and NH_3 onto sampled $PM_{2.5}$, and negative artefacts would be expected for where ambient

temperatures are high enough to encourage the volatilisation of ammonium salts. In addition, the extent of artefact formation across the ions would be expected to be higher for the 12- and 24-hour daytime filter samples (UoB), compared to the 0.5 – 3 hour filter samples (UoY).

Furthermore, another possible reason for NO_3^- to be measured higher for offline filter measurements for IC (compared to AMS), may be from the ability of IC to measure organic nitrate species as inorganic NO_3^- from the hydrolysis of organic nitrate compounds. AMS instruments sometimes incur difficulties in measuring organic nitrate species (further discussed in chapter 6) due to the decomposition of these species at the vaporizer stage of the AMS instrument, for example²⁸⁷. Moreover, differences are expected to occur between IC (UoY) samples and IC (UoB) samples due to different sampling locations causing discrepancies in measurements (in Delhi); varying methods of post filter treatments as well as the differing flow rates between samplers ($80 \text{ m}^3 \text{ h}^{-1}$ for UoY and $1.1 \text{ m}^3 \text{ h}^{-1}$ for UoB).

3.3.6.6.1 Delhi Pre-Monsoon

Therefore, for DPEM (Fig. 3.20), the higher Cl^- and NO_3^- averages across the campaign for the IC (UoY) compared to the AMS (CEH) are expected (Fig. 3.20) due to the HiVol measuring a higher size fraction and because of the potential of HNO_3 as well as HCl gases producing positive artefacts. For NO_3^- specifically, the possibility of positive artefact formation from the sampling of organic-nitrates also leads to the expected higher NO_3^- response from the HiVol IC method, although it is likely that this contribution is negligible. Overall, the SO_4^{2-} concentration between the IC (UoY) and AMS (CEH) were very similar which would be unexpected due to the sampling of different size fractions, although this may be down to the majority of the SO_4^{2-} within $\text{PM}_{2.5}$ residing in the PM_{10} mass fraction. Finally, the NH_4^+ IC concentrations were generally lower during DPEM for the IC (UoY) method, which is surprising, although the difference is minimal and may be down to the volatilisation of ammonium salts across the significantly longer (*ca.* 14 hour) night-time filter sampling causing negative NH_4^+ artefacts to form.

3.3.6.6.2 Delhi Post-Monsoon

Similarly to the DPEM campaign (Fig. 3.22), the DPOM campaign observed higher Cl^- and NO_3^- daytime values for the IC (UoY) method compared to the AMS method (CEH), which is expected due to sampling size. The lower daytime IC (UoB) averages are likely down to the increased HiVol filtering times (UoB) causing negative artefacts to occur during the heat of the day (average DPOM temp of $25.0 \text{ }^\circ\text{C}$). The IC (UoY) measurements are in close agreement with the AMS (CEH results) during the night for Cl^- although the IC (UoY) [NO_3^-] was lower which is unexpected as the HiVol samples a greater size range. A potential reason for this may be down to negative artefact formation on the IC (UoY) Hivol filter sample as oxidants are known to be minimal during the DPOM night-period and the average temperature was $22.4 \text{ }^\circ\text{C}$. Therefore, the equilibrium of NH_4NO_3 and NH_4Cl would be encouraged to the side of $\text{NH}_3 + \text{HNO}_3$ and HCl , respectively, causing partitioning out of the aerosol phase from filter samples for these species over the long night-time filter sampling period

(ca. 14 hours). The night-time IC (UoB) Cl^- and NO_3^- values were significantly higher, although the HiVol (UoB) sampler was sampling at a different location within the IAP sampling site.

Comparing the IC (UoY) and AMS (CEH), both the day and night-time DPOM averages saw higher SO_4^{2-} for IC measurements, which adheres to the greater sampling size measured by the HiVol. The daytime difference is also larger compared to the night, which abides by the greater oxidation of SO_2 during the day forming more H_2SO_4 and potentially greater SO_4^{2-} positive artefacts during filter sampling, or more ammonium sulfate salts within the $\text{PM}_1 - \text{PM}_{2.5}$ range. In addition, the daytime $\text{PM}_{2.5}$ likely had primary SO_4^{2-} from cement embedded within particles, which would also give rise to an expected higher SO_4^{2-} from the IC (UoY). The relationship between the IC and AMS for the DPOM $[\text{NH}_4^+]$ was however largely unexpected as the IC (UoY) value was significantly lower compared to the AMS (CEH). This therefore indicates the presence of negative NH_4^+ artefacts exhibited by the HiVol and IC (UoY) during night-time hours.

3.3.6.6.3 Beijing Winter

For the BWIN campaign (Fig. 3.26), significantly lower temperatures would anticipate greater locking of ammonium salts within PM, and therefore a lack of negative artefacts from IC filter samples, which is the case. Unexpectedly however, the results show significantly higher ion averages for the AMS results (both IAP and CEH), compared to the IC measurements (UoY), with a greater discrepancy observed during the night-time hours. The lower concentrations across the ions reported by the IC compared to the AMS methods may therefore be down to the different flow rates of sampling between the methods, as well as frequency of sampling. For Cl^- , NO_3^- and SO_4^{2-} , very good agreement is seen between the two IC methods. This is expected as the very low temperatures likely lead to a lesser extent of positive and negative artefacts to occur, despite differing sampling times. For NH_4^+ , the IC (UoY) value reside between both AMS methods during the daytime, although with a much lower NH_4^+ average reported during night-time hours which is unexpected and indicates the presence of negative artefacts of NH_4^+ occurring in the IC method (UoY) at night.

3.3.6.6.4 Beijing Summer

For the BSUM campaign (Fig. 3.29), mean $[\text{Cl}^-]$ values across all instruments were significantly lower compared to the other species due to the volatility of NH_4Cl during warmer temperatures and therefore the difference between methods is negligible. For NO_3^- , SO_4^{2-} and NH_4^+ , the two AMS signals are in significant disagreement with each other. The much higher IC (UoY) values compared to the AMS (IAP) is however expected as this reflects the different sampling sizes. Comparing the IC (UoY) averages for NO_3^- and SO_4^{2-} to the AMS (CEH) averages shows that the daytime AMS values are lower and that the night-time AMS average is higher. This could reflect higher HNO_3 and H_2SO_4 daytime values producing positive NO_3^- and SO_4^{2-} filter artefacts, respectively, along with negative night-time artefacts caused by a lack of atmospheric oxidation in conjunction with considerably longer filtering times and high temperatures (average BSUM night temperature of 25.2 °C).

For the NH_4^+ averages, the IC (UoY) measurements are significantly lower compared to the AMS (CEH) which is surprising, although would further evidence the presence of negative filter artefacts from the loss of ammonium salts from the higher summer temperatures present in Beijing along with longer sampling times on the HiVol. Finally, the Cl^- , NO_3^- and SO_4^{2-} averages between both IC methods are very similar which is expected. For NH_4^+ however, the IC (UoB) was significantly higher compared to the IC (UoY) and AMS (IAP) values which is unexpected. The filter methods (for both IC (UoY) and IC (UoB)) are also likely to have gained positive artefacts during the summer for NO_3^- and SO_4^{2-} (compared to the AMS (IAP)) in which higher temperatures and more sunlight leads to more oxidation of NO_2 and SO_2 producing higher concentrations of HNO_3 and H_2SO_4 respectively. These strong acids also react with basic dust species producing Cl^- , NO_3^- and SO_4^{2-} which are seen in the higher size fraction for IC ($\text{PM}_1 - \text{PM}_{2.5}$), but not for the lower AMS sizes (PM_1)¹⁴³.

3.3.7 Further analysis of the AMS and IC Comparison

Due to AMS (PM_1) and IC ($\text{PM}_{2.5}$) measuring different size fractions, more in-depth analysis is required to accurately compare these techniques. Comparing the major inorganic concentration measurements between these two techniques also allows for more in-depth study of the quality of inorganic filter sampling using a HiVol sampler within a polluted Asian megacity. In order to accurately compare species concentrations between the AMS and IC techniques, samples were selected where the majority of $\text{PM}_{2.5}$ mass was comprised of PM_1 ($\text{PM}_1/\text{PM}_{2.5} > 0.9$) as to validate the comparison. Ideally, HCl , HNO_3 , H_2SO_4 as well as NH_3 gas phase concentrations would also be used to estimate the maximum contribution of Cl^- , NO_3^- , SO_4^{2-} and NH_4^+ to the IC signal via positive artefact formation to filter samples across the sampling time. This data was however not available for any of the APHH campaigns in Beijing or Delhi, or was insufficient to complete any meaningful correction analysis.

3.3.7.1 Artefacts

Filter based $\text{PM}_{2.5}$ sampling is a simple technique which is also relatively low-cost (compared to other online techniques), for which methods are also well established³⁵³. Disadvantages however include the relatively long sampling times compared to online methods (hours compared to minutes, respectively)³⁵³. Filter sampling is also labour intensive³⁵³ and is disfavoured during night-time hours; production of positive and negative artefacts during sampling on filters also frequently occurs³⁵³. Positive artefacts may arise from the accumulation of NH_3 and acidic gaseous species (inorganic and organic)³⁵⁴ onto collected particles on the filter paper during sampling, whereas negative artefacts are associated with sample evaporation from filter pieces during sampling^{353,355}.

Potential methods to remove positive artefacts include the use of gas denuders which has been widely reported³⁵⁴. It has however also been reported that the use of denuders may cause the production of negative artefacts. On removing gases from the analysed air masses, the gas-particle phase equilibrium is shifted to the gas phase which in turn removes species from the collected aerosol phase causing negative artefacts to occur^{353,354,356,357,358,353}. This issue may however be overcome by the

installation of back-up filters^{353,354}. Negative artefacts due to losses may also be offset by increased water content of aerosols^{354,359}. Other factors which may affect the production of artefacts include filter face velocity³⁶⁰, upstream gas and particle phase concentrations being sampled³⁶¹, gas-particle phase equilibrium constants for specific species³⁵⁶, particle acidity³⁵⁸, inter-particle interactions³⁵⁸ and the relative pressures on either side of the filter piece^{354,356}. Furthermore, negative artefacts of volatile species may arise during sample storage and filter piece treatment^{354,362,363}. Specifically, the work of Witz et al., (1990)³⁶², Tsai and Perng (1998)³⁶³ as well as Liu et al., (2014)³⁵⁴ report the substantial evaporation loss of Cl^- , NO_3^- and NH_4^+ from filter samples (through NH_4Cl and NH_4NO_3 dissociation)³⁵⁸, as negative artefacts, during both sampling and storage. It has also been reported by Kim et al., (2015)³⁵³ that temperature is much more influential than RH with regard to volatile inorganic species evaporation, from filter samples.

To best knowledge, there has been no mention of artefact formation as a result of filter exposure to other major and trace gas phase pollutants (such as O_3) in a polluted Asian megacity. Therefore, based on the work conducted in section 3.3.6 thus far, further analysis has been conducted to accurately indicate under which other atmospheric conditions potential filter artifacts arise when filtering $\text{PM}_{2.5}$ using a HiVol sampler in an Asian megacity.

No denuders or back-up filters had been applied during sampling over any of the APHH campaigns, although by comparing the IC and AMS signals during times where PM_1 comprised the majority of $\text{PM}_{2.5}$ allows for a valid comparison between an online high resolution AMS technique against offline filter sampling and would indicate where artefacts from filter sampling may occur. Initially, the concentrations of PM_1 and $\text{PM}_{2.5}$ for each data point were gathered to discern where the PM_1 mass fraction comprised the majority of the $\text{PM}_{2.5}$ mass fraction. By comparing the concentrations of the major inorganic species over these particular filter sampling times gives an indication as to under which conditions artifacts may arise.

3.3.7.2 Beijing

To indicate the conditions under which major ion losses occurred during filter sampling throughout the APHH BWIN and BSUM campaigns, aerosol size distribution data was required. For the Beijing campaigns, SMPS data was only recorded in the size range of 14.6 nm – 615 nm (0.0146 μm – 0.615 μm) and was therefore unsuitable for the comparison of PM_1 to $\text{PM}_{2.5}$ concentrations. Alternatively, the $\text{PM}_1/\text{PM}_{2.5}$ mass ratio was determined by comparing the concentrations of PM_1 from the AMS and $\text{PM}_{2.5}$ from a TEOM-FDMS.

PM_1 data was obtained from the Institute of Atmospheric Physics from AMS measurements^{364,365}. This high resolution AMS PM_1 data was averaged to the IC filter times (York) for samples presented in this thesis to find the average PM_1 reading for when both instruments were sampling. The high time resolution $\text{PM}_{2.5}$ TEOM-FDMS measurements taken at IAP were also averaged to the IC (UoY) filter times.

To figure out which filter samples were associated with the PM_1 mass fraction dominating the $PM_{2.5}$ samples, the $PM_1/PM_{2.5}$ percentage mass (for where data was available) was calculated and is presented in Fig. 3.31. The error associated with the TEOM-FDMS was not measured during either of the Beijing APHH campaigns and therefore the propagated absolute error of $PM_1/PM_{2.5}$ percentage mass could not be calculated in Fig. 3.31. In Fig. 3.31, the black points demonstrate the $PM_1/PM_{2.5}$ mass percentage, the red horizontal lines demonstrate the filter sampling time for each data point. The green points demonstrate the samples which are associated with $PM_1/PM_{2.5} > 90\%$; and the blue dashed line demonstrates where $PM_1/PM_{2.5} = 90\%$. For IC samples associated with sampling times in which the average $PM_1/PM_{2.5} > 90\%$, this has been high-lighted in Fig. 3.31 (green points).

Where $PM_1/PM_{2.5} > 90\%$, it may be assumed that PM_1 comprises the dominant fraction of $PM_{2.5}$ measured by the HiVol. These were the samples which were specifically selected to complete the further AMS vs IC comparison with.

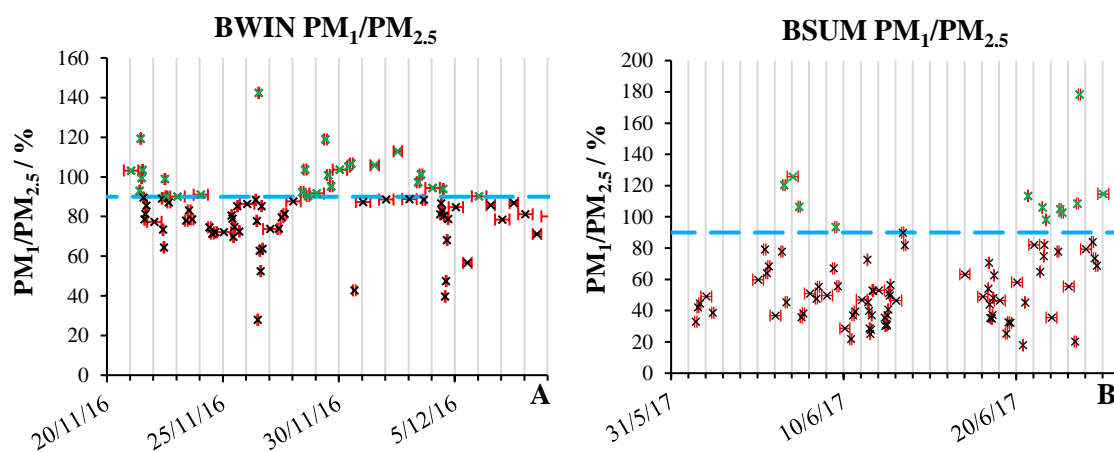


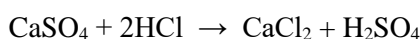
Fig. 3.31. Time series of the $[PM_1]/[PM_{2.5}]$ % mass concentration obtained from available data during the APHH BWIN (A) and BSUM (B) campaigns. The black line shows the $[PM_1]/[PM_{2.5}]$ % (y-axis) as a function of time (x-axis). The horizontal red error bars show the sampling intervals for each filter sample; the dashed blue line demonstrates a 90% threshold; and the green cross points highlight the IC sampling times in which the $[PM_1]/[PM_{2.5}]$ mass concentration values were seen to be above 90% (blue horizontal dashed line). The grey vertical lines represent midnight time points. Errors from the AMS (IAP) and TEOM-FDMS were unavailable.

The high resolution AMS data from IAP used in this comparison was averaged to the IC filter times to allow for direct comparison of the selected samples. The AMS concentration was deducted from the IC measurement for each inorganic ion from the selected data to indicate the presence of artefacts. If the IC-AMS concentration value for an ion is positive, this would suggest that a higher concentration was measured by the IC and therefore indicates the presence of a potential positive artefact from filter sampling. If IC-AMS is negative, this is indicative of a potential negative sampling artefact from filter sampling. These artefact values (the estimated loss of ionic species) were compared to the library of gas phase data as part of the APHH BWIN and BSUM campaigns (for where $PM_1/PM_{2.5} > 90\%$).

3.3.7.2.1 Beijing Winter

For the BWIN campaign a total of 28 filter samples met the criteria of $PM_{10}/PM_{2.5} > 90\%$. Positive correlations between the estimated loss of Cl^- and SO_4^{2-} against $[PM_{2.5}]$ and $[CO]$ were found which indicated an increase in negative artefacts for Cl^- and SO_4^{2-} as the general level of pollution increases. Fig. 3.32 shows the linear regression analysis between the estimated loss of Cl^- with $[PM_{2.5}]$ (Fig. 3.32A) and $[CO]$ (Fig. 3.32B), as well as the regression relationship between the estimated loss of SO_4^{2-} vs $[PM_{2.5}]$ (Fig. 3.32C) and $[CO]$ (Fig. 3.32D). As filter losses are associated with increased $[PM_{2.5}]$ and $[CO]$, it is inferred that negative Cl^- and SO_4^{2-} artefacts are associated with a general increase in pollution.

A possible contributing explanation for these negative artefacts may be due to inter-particle interactions³⁵⁸. If pollution increases, it is most likely that particle acidity also increases causing the displacement of Cl^- and SO_4^{2-} from mineral sources (i.e. $CaSO_4$).



Eq. 3.2. Reaction of $CaSO_4$ with HCl to produce $CaCl_2$ and H_2SO_4 .

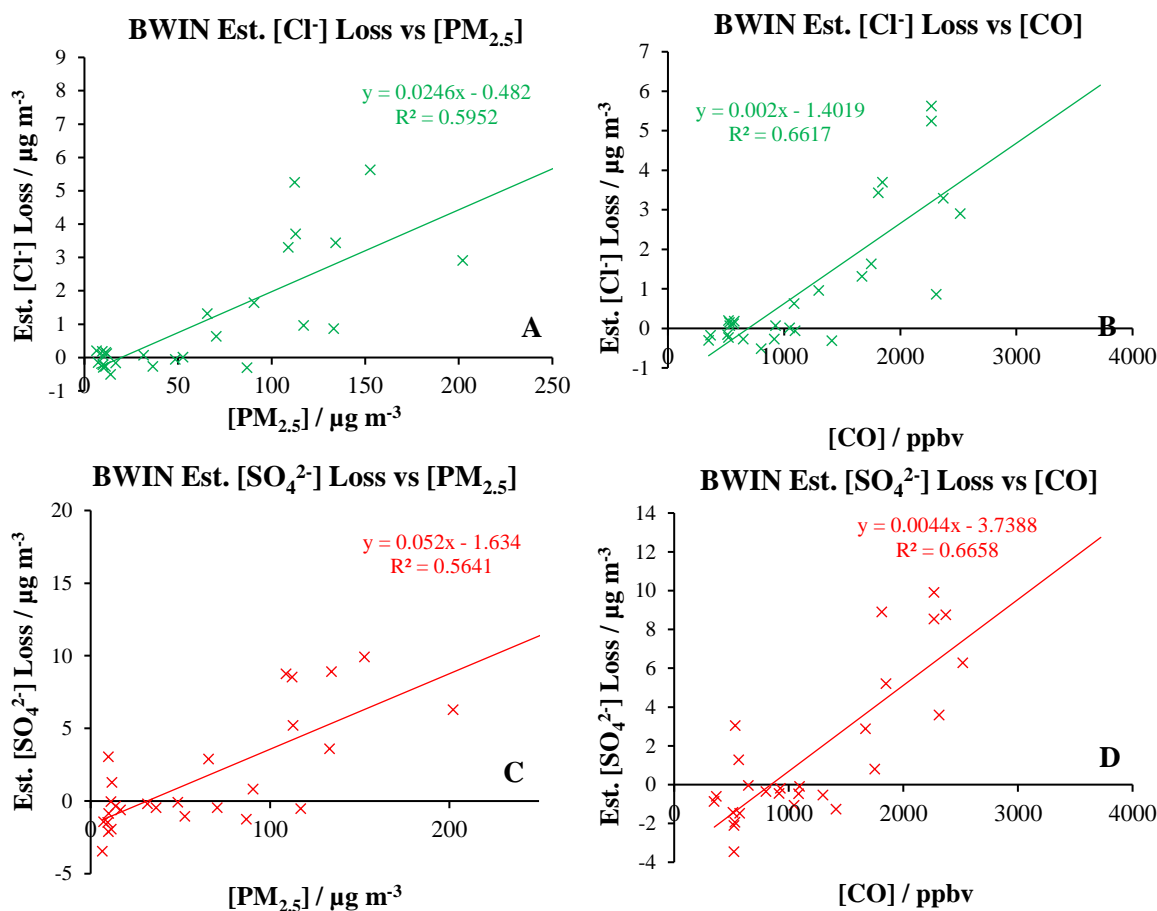


Fig. 3.32. Regression analysis of the Estimated Cl^- and SO_4^{2-} losses from filter samples against the pollutant metrics $[PM_{2.5}]$ and $[CO]$ during the BWIN campaign. The regression of Estimated $[Cl^-]$ Loss vs $[PM_{2.5}]$ (A) and $[CO]$ (B), as well as estimated $[SO_4^{2-}]$ Loss vs $[PM_{2.5}]$ (C) and $[CO]$ (D) are shown for samples where the average $PM_{10}/PM_{2.5} > 90\%$. The green regressions demonstrate Cl^- loss correlations and the red regression show the SO_4^{2-} loss correlations. The errors associated with $[Cl^-]$ and $[SO_4^{2-}]$ may be found in Fig. 3.11.

An example is given in Eq. 3.2, for which the H_2SO_4 product is not bound to an NH_4^+ and therefore may partition into the gas phase, causing a loss of SO_4^{2-} from the filter. This would increase the extent of negative artefact formation within major inorganic aerosols^{358,143}, although considerably more work is required to confirm this hypothesis.

An increase in negative artefact formation for Cl^- and SO_4^{2-} was also positively correlated with selected primary organic species. An example of this is given in Fig. 3.33 which represents the linear regression analysis between the Σ [Monoterpenes] vs the estimated $[\text{Cl}^-]$ (Fig. 3.33A) and $[\text{SO}_4^{2-}]$ (Fig. 3.33B) loss. During the BWIN campaign, a strong positive correlation is found between Cl^- and SO_4^{2-} negative artefacts vs Σ [Monoterpenes] of $R^2 = 0.83$ and $R^2 = 0.61$, respectively. The red data point in Fig. 3.33A represents a potential anomaly and was removed from coefficient analysis.

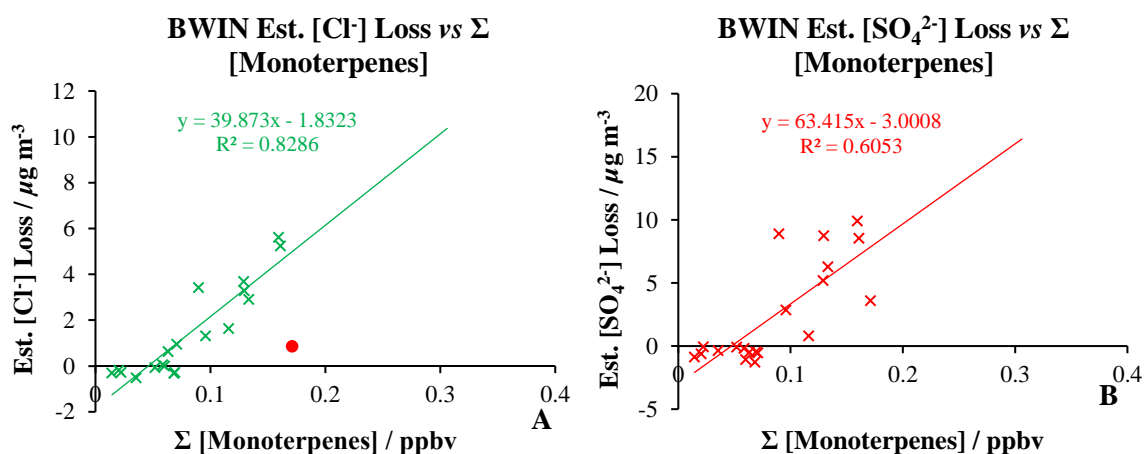


Fig. 3.33. Regression analysis of the Estimated $[\text{Cl}^-]$ Loss (A) and $[\text{SO}_4^{2-}]$ losses (B) from filter samples against the Σ [Monoterpenes] for filter samples where the average $[\text{PM}_{10}]/[\text{PM}_{2.5}] > 90\%$. The red data point in regression A is an anomaly. The errors associated with $[\text{Cl}^-]$ and $[\text{SO}_4^{2-}]$ may be found in Fig. 3.11.

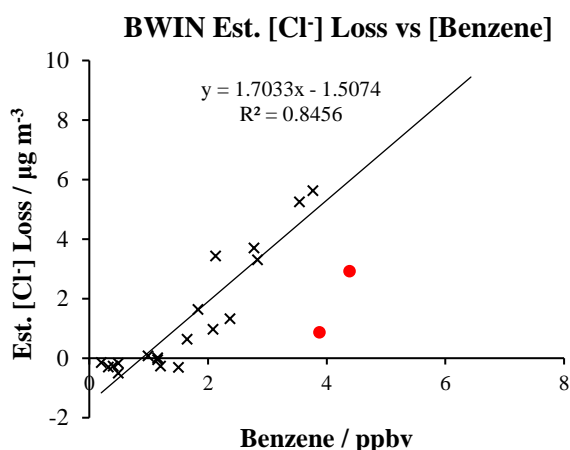


Fig. 3.34. Linear regression analysis between the atmospheric concentration of benzene vs the Cl^- negative artefacts (black), with the omission of two potential anomalies (red). The errors associated with $[\text{Cl}^-]$ may be found in Fig. 3.11.

In addition to positive regressions observed between Cl^- and SO_4^{2-} vs Σ [Monoterpenes], benzene demonstrated positive correlations of $R^2 = 0.63$ vs both Cl^- and SO_4^{2-} losses; isoprene demonstrated $R^2 = 0.64$ and $R^2 = 0.61$ for Cl^- and SO_4^{2-} losses, respectively; ethene demonstrated $R^2 = 0.72$ and $R^2 =$

= 0.62 for Cl^- and SO_4^{2-} losses, respectively; and acetonitrile demonstrated $R^2 = 0.52$ and $R^2 = 0.56$ for Cl^- and SO_4^{2-} , respectively. All gradients are positive for these reported regressions. Furthermore, when two potential anomalies are removed from the regression (red points, Fig. 3.34) of Est. $[\text{Cl}^-]$ loss vs benzene, the R^2 regression coefficient improves to $R^2 = 0.85$, as shown in Fig. 3.34.

Therefore, it is evident that during the winter season in Beijing an increase in $\text{PM}_{2.5}$, $[\text{CO}]$, as well as a selection of primary non-oxygenated organic compounds (such as benzene) causes an increase in the estimated negative artefact production for Cl^- and SO_4^{2-} during filter sampling. Estimated NO_3^- and NH_4^+ negative artefacts were also analysed by regression analysis, although no significant regressions were observed for these species.

A possible explanation for the increase in negative artefacts from Cl^- and SO_4^{2-} vs primary non-oxygenated organic compounds may be due to $\text{PM}_{2.5}$ and CO having positive correlations with Cl^- and SO_4^{2-} which inherently causes a positive correlation between $[\text{PM}_{2.5}]$ and $[\text{CO}]$ vs [primary organics], as $[\text{PM}_{2.5}]$ and $[\text{CO}]$ are correlated with primary organic species such as benzene ($R^2 = 0.79$ and $R^2 = 0.73$, respectively). Another possible explanation could be down to the partitioning between Cl^- and SO_4^{2-} with HCl and H_2SO_4 , respectively, within the aerosol phase on the filter sample during sampling. It is known that HCl and H_2SO_4 react with unsaturated organic species through an addition reaction^{366,367}, which could produce a sink for Cl^- and SO_4^{2-} from the aerosol phase, respectively, as primary unsaturated organic species pass through the HiVol. Significantly more work however needs to be conducted to confirm this hypothesis, which constitutes to future work.

3.3.7.2.2 Beijing Summer

An identical calculation was conducted for the investigation between the negative artefacts between the major inorganic species vs the other gas phase components measured as part of the APHH BSUM campaign. Similarly to BWIN, the AMS and gas-phase data were averaged to the IC filter times of the data presented in this thesis for which an R^2 correlation was produced for each species against the major inorganic concentrations for filter samples where $\text{PM}_1/\text{PM}_{2.5} > 90\%$.

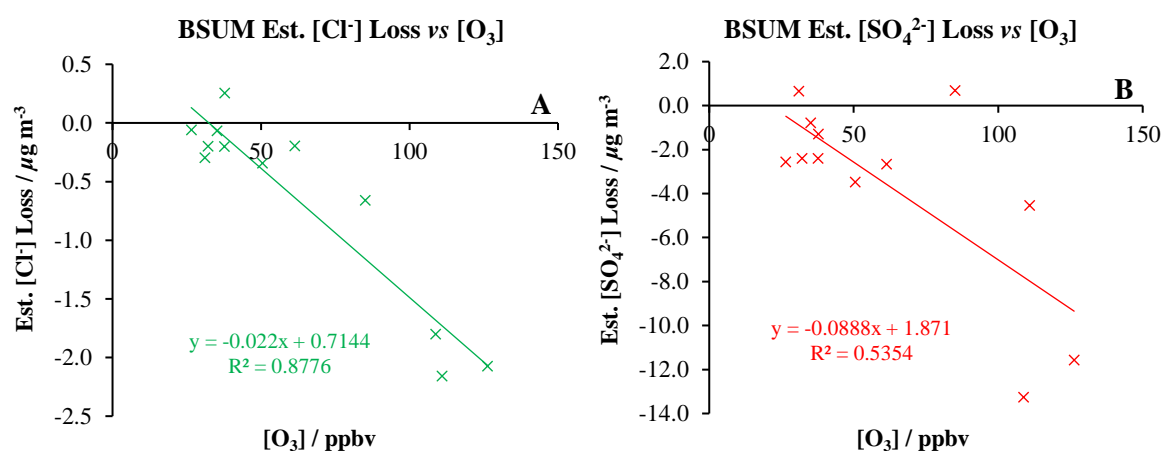


Fig. 3.35. Regression analysis of the Estimated $[\text{Cl}^-]$ Loss (A) and $[\text{SO}_4^{2-}]$ losses (B) from filter samples against the $[\text{O}_3]$ for filter samples where the average $[\text{PM}_1]/[\text{PM}_{2.5}] > 90\%$. The errors associated with $[\text{Cl}^-]$ and $[\text{SO}_4^{2-}]$ may be found in Fig. 3.12.

Significantly fewer filter samples compared to the BWIN campaign were associated with $PM_1/PM_{2.5} > 90\%$ (Fig. 3.31B), for which 12 samples altogether met this criterion, and as a result much fewer correlations were seen for the BSUM campaign compared to BWIN.

A particular gas-phase species which showed a considerable correlation against both Cl^- and SO_4^{2-} negative artefacts was O_3 (Fig. 3.35). A negative correlation was demonstrated for both Cl^- and SO_4^{2-} , indicating that as O_3 concentrations increase, so do the incorporation of positive artefacts of Cl^- and SO_4^{2-} .

A potential explanation for this may be due to the relative level of oxidising species available in the atmosphere. When O_3 is high, this is representative of a high oxidative species loading in the atmosphere. With a high concentration of oxidising species, a higher proportion of NO_2 and SO_2 may be oxidised into HNO_3 and H_2SO_4 , respectively. As a result, it would be sensible to assume that an increase in NH_3 neutralisation would occur, reducing the residual $[NH_3]$. As a result of this, HCl and H_2SO_4 are more likely end up in excess and at high enough concentrations will form positive artefacts on $PM_{2.5}$, on sampling filters.

No other significant correlations were found, apart from between Cl^- and SO_4^{2-} losses vs $[Acrolein]$ as shown in Fig. 3.36. In conjunction with the O_3 correlations (Fig. 3.35), the likely reason for an increase in positive artefacts with increasing acrolein concentrations may be due to increasing oxidative species concentrations, as well as increasing propene oxidation to acrolein, for which HCl and H_2SO_4 would be in increasing in excess of NH_3 (as previously).

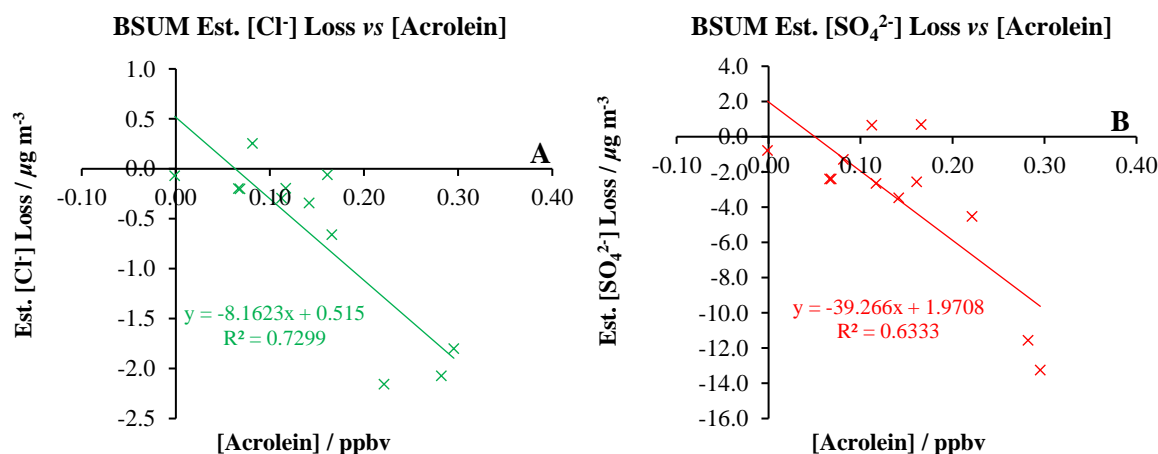


Fig. 3.36. Regression analysis of the Estimated $[Cl^-]$ Loss (A) and $[SO_4^{2-}]$ losses (B) from filter samples against the $[Acrolein]$ measured during the campaign for filter samples where the average $[PM_1]/[PM_{2.5}] > 90\%$. The errors associated with $[Cl^-]$ and $[SO_4^{2-}]$ may be found in Fig. 3.12.

3.3.7.2.3 Delhi

To indicate the conditions under which major ion losses occurred during filter sampling throughout the APHH DPEM and DPOM campaigns, aerosol size distribution data was required. For the Delhi campaigns, SMPS data was only available in the size range 15 nm – 660 nm ($0.015\ \mu m - 0.660\ \mu m$) and was therefore unsuitable for the comparison of PM_1 to $PM_{2.5}$ concentrations. Alternatively, the

PM₁/PM_{2.5} mass ratio was determined by comparing the concentrations of PM₁ from the AMS and PM_{2.5} from a TEOM-FDMS.

High resolution PM_{2.5} data are required for the comprehensive comparison between the IC and AMS instruments. TEOM-FDMS data was available at a resolution of every 1 hour although was only available from the Indian Institute of technology (IIT), a site which was 2 km to the south-west of IGDTUW. A Partisol sampler was however also available at both sites which gave a daily reading of PM_{2.5}. Therefore, to indicate whether the TEOM-FDMS data was similar enough (and therefore could be used for this analysis), the Partisol data between both IIT and IGDTUW were compared.

A comparison between the 24-hour Partisol data for IGDTUW and IIT for the times which overlap with the filtering times for IC analysis are shown in Fig. 3.37A for the DPEM campaign. The regression analysis for the PM_{2.5} masses is also shown in Fig. 3.37B.

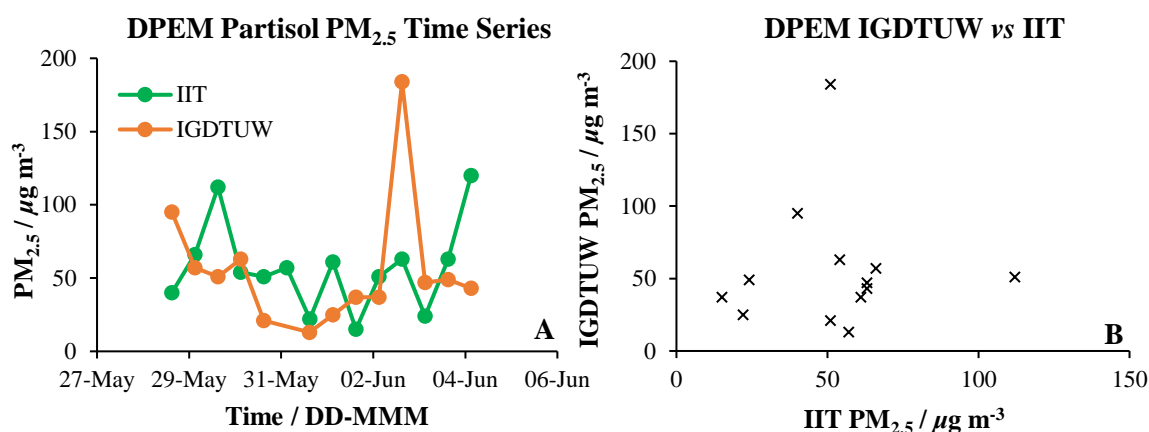


Fig. 3.37. (A) Partisol time series of [PM_{2.5}] taken by the UoB during the DPEM campaign where the time of sampling is shown on the x-axis and the PM_{2.5} concentrations are recorded on the y-axis for IIT (green) and IGDTUW (orange). (B) Linear regression analysis for Partisol [PM_{2.5}] demonstrating the lack of correlation between the IIT (x-axis) and IGDTUW (y-axis) measurements, for identical sampling times ($R^2 = 0.0008$). Partisol instrument error was unavailable.

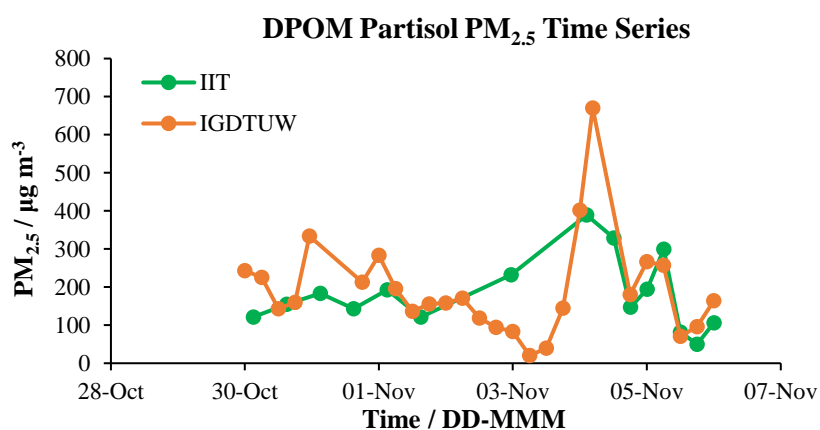


Fig. 3.38. Partisol time series of [PM_{2.5}] taken by the UoB during the DPOM campaign where the time of sampling is shown on the x-axis and the PM_{2.5} concentrations are recorded on the y-axis for IIT (green) and IGDTUW (orange). Partisol instrument error was unavailable.

As can be seen in Fig. 3.37, the Partisol PM_{2.5} data between IGDTUW vs IIT do not agree ($R^2 = 0.0008$, Fig. 3.37) and therefore it would be inappropriate to assume that the PM_{2.5} concentrations were similar enough between the two sites to allow for the high resolution TEOM-FDMS data (from IIT) to be used for the IC vs AMS comparison in this section, for the DPEM campaign. Therefore, IC vs AMS comparison was not possible for the DPEM campaign.

A similar analysis was conducted for the DPOM period for the comparison between IIT and IGDTUW for the Partisol PM_{2.5} measurements. Unlike for the DPEM campaign, the timings of these measurements at the two sites were not consistent with each other and therefore linear regression correlation analysis for [PM_{2.5}] from each site was not possible for the DPOM campaign. The time series for comparison was however still conducted and is shown in Fig. 3.38.

Fig. 3.38 was subsequently used to select the timings where the [PM_{2.5}] values were in close agreement. Six data points were selected although these were far between one another and only cover two full days as well as a half day (5th Nov) and half night (3rd November). This is out of *ca.* 28 full days of filter sampling. In addition to the lack of data availability, the exact Partisol sampling times did not match up closely between the two sites (regarding time of day). Furthermore, for the time periods where the data agreed, there was some missing data in the TEOM-FDMS dataset, further reducing the amount of data available for the inter-comparison between the AMS and IC measurements. Therefore, it was not possible to conduct an accurate comparison between the IC and AMS data sets for the DPOM campaign, due to the lack of data availability of [PM_{2.5}] particle size data.

Although it has been attempted to draw conclusions from the data on the losses of ions from filters and conditions where this is negligible and conditions where it is an important factor, realistically insufficient [PM_{2.5}] size distribution data was available for any meaningful analysis or conclusive arguments for the DPEM or DPOM campaigns.

3.4 Conclusion

An evaluation of the major gases and PM_{2.5} concentrations was conducted across the DPEM, DPOM, BWIN and BSUM campaigns to give a background into the general atmospheric conditions at time of sampling. These data provided by UoY and UoB (IC) demonstrated higher atmospheric ionic concentrations during the cooler DPOM ($54.11 \mu\text{g m}^{-3}$, campaign average) and BWIN ($35.26 \mu\text{g m}^{-3}$, campaign average) seasons compared to the DPEM ($46.45 \mu\text{g m}^{-3}$, campaign average) and BSUM ($23.12 \mu\text{g m}^{-3}$, campaign average) seasons. Increased pollution concentrations were seen during night-time hours as a result of lower temperatures, higher RH and a shallower boundary layer. Higher levels of pollution were also associated with the Diwali period and increased regional agricultural burning in Delhi (DPOM) and the heating season during winter in Beijing (BWIN). It was demonstrated by the gas-phase data that higher temperatures and longer daylight hours increasing solar flux likely increased the oxidative capacity of the atmosphere leading to an increase in oxidative

products during these periods. This is reflected in the relative O₃ concentrations across the day and night periods of the four campaigns. DPOM had very high [NO] (campaign maximum of 1076 ppbv) which quenched the oxidation capacity of the atmosphere significantly. The DPOM campaign also observed a very low boundary layer height at night (reaching down to *ca.* 15 m), leading to a less dilute atmospheric mixture.

The average [PM_{2.5}] concentrations were 59.18 μg m⁻³, 164.86 μg m⁻³, 97.28 μg m⁻³, 37.01 μg m⁻³ measured by the TEOM-FDMS (UoB) for the DPEM, DPOM, BWIN and BSUM campaigns, respectively. The higher level of atmospheric oxidation capacity observed within the gas phase constituents is reflected in the higher day and lower night concentrations of NH₄⁺, NO₃⁻ and SO₄²⁻ across the four campaigns. Cl⁻ behaved differently, with larger average concentrations during night in the winter seasons (DPOM and BWIN) and during the day in the summer seasons (DPEM and BSUM). This was attributed to greater combustion sources (such as biomass and waste burning) releasing Cl⁻ during late October in Delhi and for heating (coal combustion) during much cooler temperatures observed in Beijing (-5.8– 16.6 °C during BWIN).

In Delhi, the higher temperatures during the DPEM campaign (34.0 °C) as well as longer daytime hours increases solar flux and the presence of oxidative species. This is demonstrated in the larger SIA fraction observed within the DPEM PM_{2.5} fraction (Σ [NH₄⁺ + NO₃⁻ + SO₄²⁻] = 45.2 %). In addition, the DPEM PM_{2.5} also consisted of a significantly high fraction of mineral dust species (Σ [Na⁺ + Mg²⁺ + Ca²⁺] %) = 21.8 % which is reflective of Delhi's dusty soil and semi-arid climate over the summer seasons³⁶⁸. A lower SIA fraction was observed in the DPOM PM_{2.5} for which Σ [NH₄⁺ + NO₃⁻ + SO₄²⁻] = 18.8 %. This was attributed to a possible lower level of oxidation occurring due to higher NO_x present compared to other campaigns, a result of the combination of a large decrease in nocturnal boundary layer, Diwali celebrations and very high anthropogenic emissions in Delhi. In addition, high temperatures (DPOM average of 24.7 °C) could also increase the volatilisation of ammonium salts from the particle phase during DPOM.

In Beijing, the SIA (Σ [NH₄⁺ + NO₃⁻ + SO₄²⁻] = 27.2 %) during the BWIN campaign was lower than summer as a result of decreased photochemistry and increased organic emissions from other sources, although the absolute concentrations were much higher than summer. Lower NH₄⁺, NO₃⁻ and SO₄²⁻ atmospheric concentrations were observed during the BSUM campaign (campaign averages of 3.00 μg m⁻³, 7.46 μg m⁻³ and 8.19 μg m⁻³, respectively), although these made up a considerably larger fraction of aerosol (Σ [NH₄⁺ + NO₃⁻ + SO₄²⁻] = 48.7 %). This was reflected in the meteorology and gas-phase pollutants, which showed that the higher temperatures and increased solar flux, leading to production of OH radicals and O₃, which enhanced NO₂ and SO₂ oxidation to HNO₃ and H₂SO₄.

This chapter provides sufficient evidence that the inorganic fraction of PM_{2.5} in Beijing and Delhi during the APHH campaigns makes up a substantial portion of aerosol. The total percentage of known ionic material in PM_{2.5} during the APHH Delhi and Beijing campaign was DPEM (78.5 %),

DPOM (33.7 %), BWIN (35.7 %) and BSUM (62.5 %). During the warmer seasons in each city, a higher fraction of the total PM mass is made up of inorganic aerosol species (also generally seen within the literature for Beijing and Delhi, chapter 4), which may strongly influence the hygroscopicity and pH of particles. Thus, PM_{2.5} concentration and composition are heavily reliant of the inorganic species. This fraction in turn is strongly dependant on the types and quantity of gaseous emissions as well as the level of photooxidation occurring in the atmosphere.

An inter-instrument comparison was also conducted between the IC (UoY), IC (UoB), AMS (IAP) and the AMS (CEH) instruments for the major ions, in which the changes in agreement over the day and night-time periods was also assessed. The most likely reasons for disagreement between the IC and AMS methods was due to sampling of different size fractions (PM_{2.5} vs. PM₁). Differences between the two IC methods was thought to be primarily down to differing sampling times in which artefacts may develop on filters that are sampled for longer periods of time. There were some instances where better agreement was observed between the IC (UoY) and AMS measurements compared to the IC (UoB), potentially as a result of the longer UoB sampling times. This therefore indicates the more frequent sampling should be considered in future campaigns. In addition, blocked filters were observed during the high-intensive sampling which would have resulted in more loss of data if longer sampling periods had been taken. This intercomparison shows that filter collection, followed by extraction and IC, is a suitable and accurate method to obtain time resolved inorganic ion concentrations where it is not possible to deploy the more expensive and labour intensive AMS. This could be particularly useful for longer term sampling or in remote locations, if an automated filter sampling system is used.

In addition to the sampling of different size fractions, significantly different sampling frequencies, as well as the production of artefacts, other causes of discrepancy between the IC and AMS measurements in a field campaign setting include the data availability which overlaps between the two instruments as well as the inclusion of a meteorological impact on the transport of alkaline dust from distant regions (increasing acidic gas neutralisation in the PM_{2.5}-PM₁ size fraction). In addition to the uncertainties surrounding the field campaign experiences, the conclusions of chapter 2 had highlighted possible sources of error surrounding IC measurements once offline filters had been brought back to the laboratory, including the partitioning of NO₂⁻ and NO₃⁻ within IC samples; very variable blank contaminant concentrations of ions extracted from blank filters; the age of the instrument and the degradation level of the instrumental parts (column, suppressor etc.); as well as the lack of agreement between IC instrument from different laboratories (in some cases). Combining the experiences of field and lab work as well as their associated uncertainties, the instrument inter-comparison between the IC and AMS instruments is highly not recommended when sampling different size fractions.

Novel to this work, it was found that negative filter artefacts in [Cl⁻] and [SO₄²⁻] occur when primary pollution increases (i.e. [PM_{2.5}], [CO], [primary non-oxygenated organic compounds]), during the

BWIN campaign. This has been attributed to possible inter-particle interactions on the filter paper displacing anions from dust aerosol to reproduce the acidic gas. Another hypothesis produced from this correlation is that unsaturated primary organic species passing through the HiVol may react with acidic species within the aerosol as to remove them from the filter piece during sampling. During the BSUM campaign, positive filter artefacts were also seen with increasing $[O_3]$ and [acrolein] which has been attributed to an increase in acidic gas formation resulting in a decrease in residual $[NH_3]$, causing acidic gases such as H_2SO_4 and HCl to be able to composite and accumulate on the filtered aerosol surface. More work is however required to confirm these hypothesis. These conclusions however highlight to future investigators who use HiVol filter sampling that an increase in primary pollutants could cause the presence of negative artefacts and increase in $[O_3]$ may increase the proportion of positive artefacts. for SO_4^{2-} and Cl^- . Insufficient data was however available for the DPEM and DPOM campaigns to make any conclusive arguments or hypothesis.

Finally, the IC method developed extends the range of species that were observed in these two locations beyond the standard NH_4^+ , NO_3^- , SO_4^{2-} , Cl^- inorganic suite measured by AMS. A comprehensive dataset for ions within $PM_{2.5}$ during the APHH campaigns in Delhi and Beijing has successfully been produced and has been published on the Centre for Environmental Data Analysis database (CEDA)³⁶⁹ for Delhi³⁷⁰ and Beijing³⁷¹. These datasets are therefore now also available for other researchers to use in future modelling studies (such as ISORROPIA^{328,329}).

For interest of the reader, the time series for the other minor ions including $CH_3SO_3^-$, NO_2^- , Br^- , PO_4^{3-} , Na^+ , K^+ , Mg^{2+} and Ca^{2+} (as well as F^- for Delhi) are presented in the appendix in Fig. E – Fig. M.

4 Concentration and Composition of PM_{2.5} Comparison to Previous Studies in Delhi and Beijing

4.1 Introduction

To further investigate the role of ionic species in urban Asian megacity PM_{2.5} (particularly in Delhi and Beijing), an in-depth literature review has been conducted and compared to the results presented in chapter 3. In addition, ionic concentrations and calculated % fraction contributions to PM_{2.5} have been plotted against time for each study. By investigating particle composition and ionic species concentration as a function of time, an overview of the change in Secondary Inorganic Aerosol (SIA, i.e. NO₃⁻, SO₄²⁻ and NH₄⁺)¹⁵⁷, source contributions to PM_{2.5}, the direction of concentration trends, as well as how the inorganic fraction of PM_{2.5} has changed has been evaluated. This in turn gives an indication as to which species (and therefore potential emission sources) are generally increasing or decreasing over time in Delhi and Beijing. Using particle composition as a marker of potential sources and assessing the relative concentrations of species and their fraction contribution may assist in identifying which emission controls should be put in place and which sources should be prioritised for mitigation strategies.

Continuous measurements are conducted of key pollutants such as NO_x, SO₂, O₃, and CO as well as PM_{2.5} in Asian megacities such as Delhi and Beijing, as well as many other major cities worldwide²⁷⁹. Although the online continuous measurement of these major pollutants is useful, the continuous analysis of more detailed pollution such as the composition of PM_{2.5} is still lacking. This is because the analysis of species such as those which comprise SIA involve either much more technical offline manual labour using wet chemical techniques such as ion chromatography^{110,320} or mass spectrometry^{372,291}. Online techniques are also available such as Aerosol Mass Spectrometry (AMS) or Aerosol Chemical Speciation Monitor (ACSM), although this technique is expensive to maintain; endures very high capital costs (not feasible to place at multiple sampling sites within a city if a developing country); is often only capable of measuring only few ions; and more complex techniques such as AMS are known to encounter problems such as inaccuracies in organic nitrate measurements (as these may decompose at the vaporizer stage)²⁸⁷. AMS instruments are also known to disagree with one another frequently.

Little has been attempted to assess the concentration and composition of SIA within PM_{2.5} as a function of time, making this a lacking research area. In Beijing specifically, previous work by Lang et al., (2017)²⁶⁸ has been carried out to assess the change in PM_{2.5} and major ionic species of NO₃⁻ and SO₄²⁻ in Beijing between the years 2000 – 2015. Lang et al., (2017)²⁶⁸ estimate that the fraction of SIA in Beijing between the years of 2000 and 2015 had increased by 0.7 % year⁻¹ and that since 2009 (in Beijing), the majority of PM_{2.5} is made up of inorganic constituents. In addition, Sun et al.,

(2020)³⁷³ observe a general increase in NO_3^- and NH_4^+ fractions of $\text{PM}_{2.5}$ from AMS measurements taken around the time of the Chinese New Year holiday period (2012 - 2020). To best knowledge, no such other study has yet been conducted in Delhi (one of the worlds most polluted megacities). Based on the style of study conducted by Lang et al., (2017)²⁶⁸ who assessed the change in $\text{PM}_{2.5}$ from reviewed literature over the course of 15 years in Beijing, a similar and updated analysis has been conducted for both Beijing and Delhi in this work observing the change in $[\text{PM}_{2.5}]$, [ions], as well as the % fraction of individual ions to $\text{PM}_{2.5}$ as a function of time. A greater number of ionic species have been investigated compared to the work of Lang et al., (2017)²⁶⁸ and the gap of studies between 2015 until 2020 has also been filled and accounted for in Beijing. Furthermore, the comprehensive review of studies has been separated into seasons as well as atmospheric conditions (such as clean, haze or pollution control periods) and sites (such as a rural sites) based on the description of previous works reviewed.

The results of the Air Pollution and Human Health (APHH) campaigns for the Delhi pre-monsoon (DPEM), Delhi post-monsoon (DPOM), Beijing winter (BWIN) and Beijing summer (BSUM) (chapter 3) were integrated into these analyses to assess where the work of chapter 3 fits into the consensus of changing ionic mass trends and $\text{PM}_{2.5}$ composition. Therefore, this chapter aims to give a greater insight into the change in SIA species mass concentrations and SIA $\text{PM}_{2.5}$ compositions as a function of time in Delhi and Beijing. Furthermore, the trends established may allow for future predictions to be made regarding ionic $\text{PM}_{2.5}$ mass fractions and composition within these two megacities.

4.2 Experimental

The ionic atmospheric concentration values represented in this chapter from the DPEM, DPOM, BWIN and BSUM APHH campaigns are associated with the experimental described in chapter 2 and the results reported in chapter 3. A comprehensive comparison study was conducted between the data presented in this chapter and numerous similar previous studies which had been performed in Delhi and Beijing, evaluating the ionic species concentrations within $\text{PM}_{2.5}$, within these two megacities.

4.2.1 Studies Reviewed for Delhi and Beijing

The data in this chapter was compared and reviewed against 14 studies which were carried out in Delhi and 30 studies which had been conducted in Beijing. These studies were numbered, and in Delhi include the work of study No. (D1) Saraswati et al., (2019)³⁷⁴; (D2) Chandra et al., (2019)³⁷⁵; (D3) Bisht et al., (2015)³⁷⁶; (D4) Tiwari et al., (2009)²⁸⁸; (D5) Gadi et al., (2001)²⁹⁰; (D6) Sharma et al., (2017)³⁷⁷; (D7) Saxena et al., (2017)¹⁹⁸; (D8) Kumar et al., (2018)²²⁵; (D9) Pant et al., (2015)¹¹⁰; (D10) Sharma et al., (2016)³⁷⁸; (D11) Ali et al., (2019)³⁷⁹; (D12) Shivani et al., (2019)²⁸⁹; (D13) Acharja et al., (2020)³⁸⁰; and (D14) Jain et al., (2020)³⁸¹. *N.B* study no. 5 was conducted analysing PM_2 and was eventually omitted from the comparison.

Fig. 4.1 shows the geographical location of the different sampling sites within Delhi that were used across the reviewed studies in this chapter. The red star shown in Fig. 4.1 shows the location of IGDTUW (F). Table 4.1 also displays the list of sampling sites used in Delhi with acronyms (labelled in Fig. 4.1). These are referred to in the following sections.

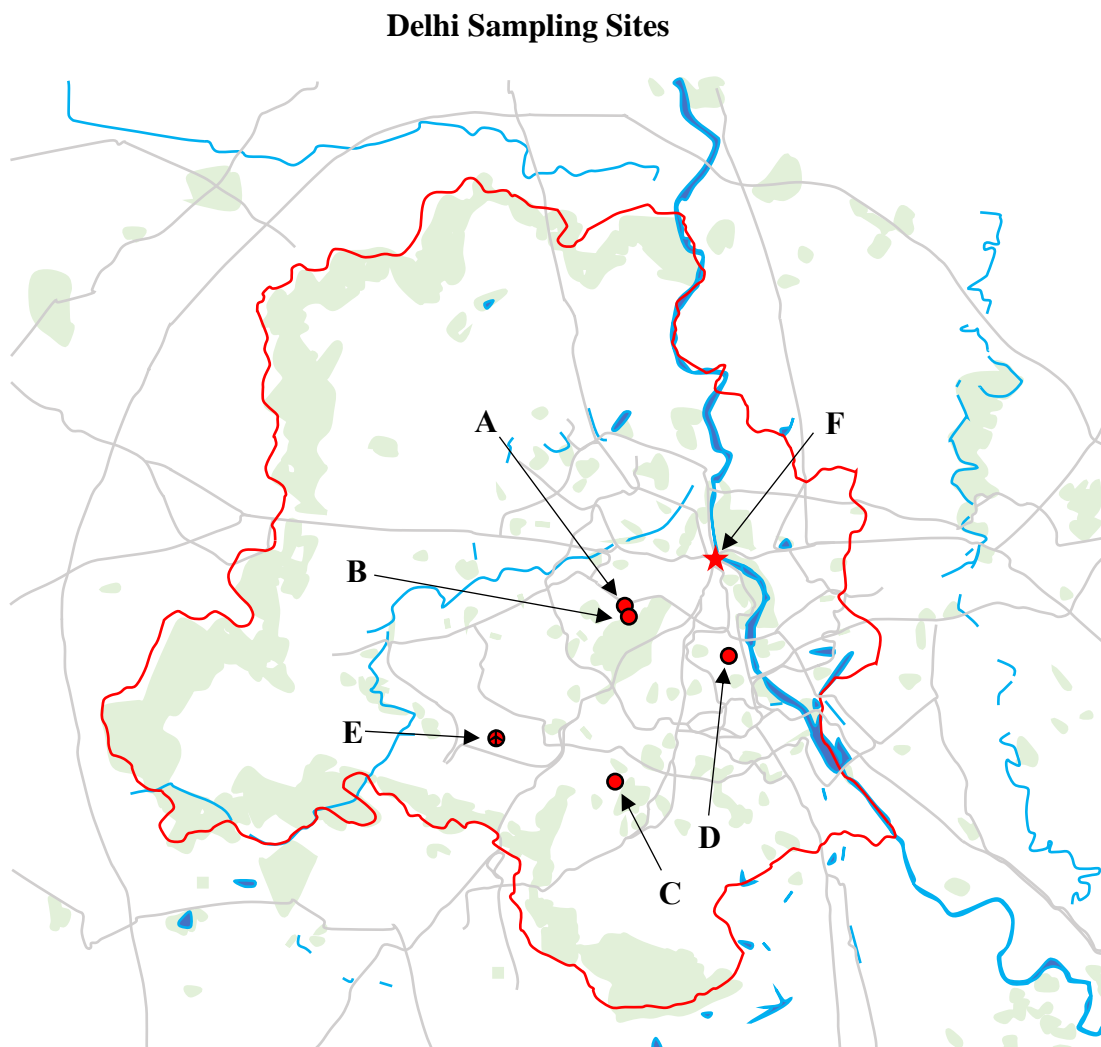


Fig. 4.1. Map of Delhi representing the sampling sites of the reviewed studies (Table 4.1).

Table 4.1. Sampling sites reported by the reviewed studies in Delhi.

No.	Site	Abbrev.
A	National Physical Laboratory of India	NPL
B	Indian Institute of Tropical Meteorology New Delhi Branch	IITM
C	School of Environmental Science, Jawaharlal Nehru University	JNU
D	Mathura Road (50 metres away)	Mat Rd.
E	Near T3, Indira Gandhi International Airport, Delhi	IGIA
F	Indira Gandhi Delhi Technical University for Women	IGDTUW

Beijing Sampling Sites

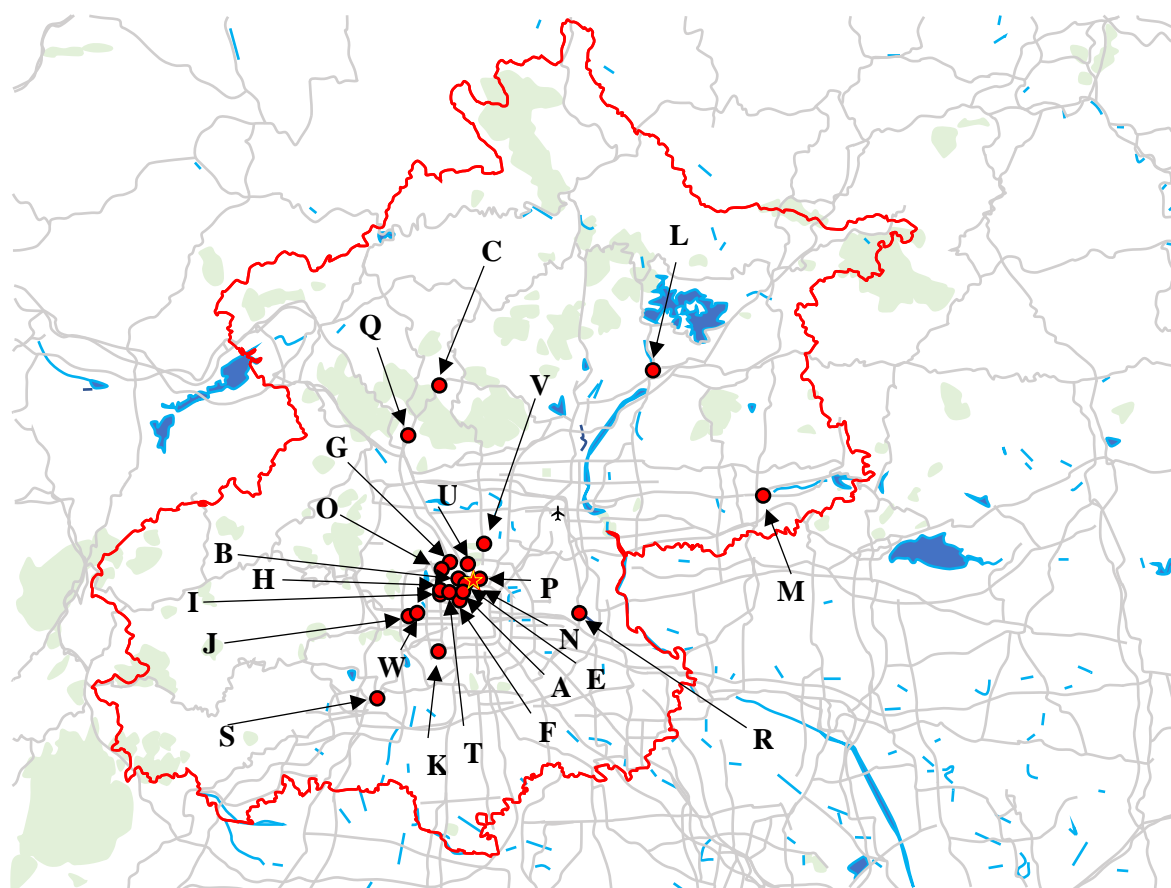


Fig. 4.2. Map of Beijing representing the sampling sites of the reviewed studies (Table 4.2).

In Beijing, the results in this chapter were compared to the work of study No. (B1) Sun et al., (2006)¹⁸⁵; (B2) Wang et al., (2015)³⁸²; (B3) Pathak et al., (2011)³⁸³; (B4) Dao et al., (2014)³⁸⁴; (B5) Cheng et al., (2014)²⁹²; (B6) Yao et al., (2002)³⁸⁵; (B7) Yu et al., (2004)²⁹³; (B8) Liu et al., (2014)³⁸⁶; (B9) Yang et al., (2016)³⁸⁷; (B10) Li et al., (2019)³⁸⁸; (B11) Duan et al., (2006)³⁸⁹; (B12) Wang et al., (2005)²⁰⁰; (B13) Shen et al., (2017)²⁹¹; (B14) Song et al., (2007)³⁹⁰; (B15) Zhang et al., (2018)³⁹¹; (B16) Hu et al., (2014)¹⁹⁹; (B17) Han et al., (2016)³⁹²; (B18) He et al., (2001)³⁹³; (B19) Zhang et al., (2013)²⁵⁸; (B20) Shao et al., (2018)³⁹⁴; (B21) Han et al., (2016)³⁹⁵; (B22) Sun et al., (2004)³⁹⁶; (B23) Zhou et al., (2012)¹⁸⁷; (B24) Zhang et al., (2016)¹⁹²; (B25) Gao et al., (2016)³⁹⁷; (B26) Li et al., (2013)³⁹⁸; (B27) Pathak et al., (2009)²⁴⁴; (B28) Wu and Wang., (2007)³⁹⁹; (B29) Okuda et al., (2011)⁴⁰⁰; and (B30) Xu et al., (2019)¹⁹⁰.

Fig. 4.2 also shows the geographical location of the different sampling sites Beijing that were used. The yellow star shown in Fig. 4.2 shows the location IAP. Table 4.2 also displays the list of sampling sites used in Beijing, with acronyms. Letters associated with each sampling site in Beijing and are referred to in the following sections.

Table 4.2. Sampling sites reported by the reviewed studies in Beijing.

No.	Site	Abbrev.
A	Beijing Normal University	BNU
B	Beihang University Beijing	BEI
C	Hei Shan Zhai, a rural mountainous site near Beijing (40°21'N, 116°18'E)	HSZ
D	Downtown Beijing (Not clear exactly where)	DOW
E	Chinese Ecosystem Research Network Atmospheric Sub-Centre	CERN
F	Chegongzhuang	CGZ
G	Tsinghua University	THU
H	Urban Site (116°18'10"8E, 39°56'50"7N)	US
I	Capital Normal University (39°58'N, 116°22'E)	CNU
J	Capital Steel Company (Assumed Location - Study Not Clear)	CSC
K	Yihai Garden	YG
L	Miyun	MY
M	Pinggu	PG
N	Institute of Atmospheric Physics	IAP
O	Peking University	PKU
P	Olympic Park	OLP
Q	Ming Tombs	MT
R	Tongzhou	TZ
S	Fangshan	FG
T	China Meteorological Administration (39°56'N, 116°24'E)	CMA
U	Institute of Geographic Sciences and Natural Resources Research	IGSNRR
V	Chinese Research Academy of Environmental Sciences	CRAES
W	Yuquan Campus, University of Chinese Academy of Sciences	YU CAS

4.2.2 Heights and Types of Sampling Sites

The sites displayed in Fig. 4.1 and Table 4.1 for Delhi were inspected using google maps⁴⁰¹ as to indicate whether the sampling location was either an urban, suburban, roadside or airport site.

Table 4.3. Table showing the sampling site region classification as depicted on google maps, sampling site height above sea level (S.L) and ground level (G.L) for each publication reviewed, as reported by the specific study, for Delhi.

Study	Site	Class	Height > S.L	Height > G.L
D1	NPL	Urban	218 m	NR
D2	NPL	Urban	283 m	15 m
D3	IITM	Suburban	217 m	15 m
D4	IITM	Suburban	NR	15 m
D5	NPL	Urban	NR	12 m
D6	NPL	Urban	218 m	NR
D7	NPL	Urban	218 m	10 m
D8	JNU	Suburban	265 m*	Roof Top
D9	Mat Rd.	Roadside	215 m*	2 m
D10	NPL	Urban	218 m	10 m
D11	IGIA	Airport	237 m	NR
D12	IGDTUW	Urban	220 m*	6 m
D13	IGIA	Airport	237 m	10 m
D14	NPL	Urban	216 m	10 m
Thesis	IGDTUW	Urban	220 m*	8 m

Table 4.4. Table showing the sampling site region classification as depicted on google maps, sampling site height above sea level (S.L) and ground level (G.L) for each publication reviewed, as reported by the specific study, for Beijing.

Study	Site	Class	Height > S.L	Height > G.L
B1	BNU	Urban	54 m*	40 m
B2	BEI	Urban	57 m*	NR
B3	HSZ	Rural	280 m	NR
B4	DOW	NA	NR	NR
B5	CERN	Urban	55 m*	11 m
B6	CGZ	Urban	55 m*	4.5 m
B6	THU	Suburban	55 m*	4.5 m
B7	Unknown	Unknown	NR	NR
B8	US	Urban	55 m*	30 m
B9	BNU	Urban	54 m*	20 m
B10	CNU	Urban	58 m*	Two Stories
B11	CGZ	Urban	55 m*	4.5 m
B11	THU	Suburban	55 m*	4.5 m
B12	BNU	Urban	54 m*	40 m
B12	CSC	Industrial	70 m*	4 m
B12	YG	Suburban/Residential	48 m*	40 m
B12	MY	Rural	217 m*	NR
B12	PG	Rural	42 m*	NR
B13	IAP	Urban	65 m*	10 m
B14	PKU	Urban	57 m*	5 Stories
B14	OLP	Urban	47 m*	Ground
B14	MT	Rural	104 m*	NR
B14	TZ	Urban	26 m*	10 Stories
B14	CSC	Industrial	70 m*	4 Stories
B14	FG	Urban	769 m*	Ground
B15	BNU	Urban	54 m*	35 m
B16	CMA	Urban	58 m*	35 m
B17	IGSNRR	Urban	50 m*	24 m
B18	CGZ	Urban	55 m*	4.5 m
B18	THU	Suburban	55 m*	4.5 m
B19	PKU	Urban	57 m*	26 m
B20	BNU	Urban	54 m*	NR
B21	CRAES	Urban	44 m*	Roof Top
B22	BNU	Urban	54 m*	40 m
B22	CSC	Industrial	70 m*	4 m
B22	YG	Suburban/Residential	48 m*	40 m
B23	IAP	Urban	65 m*	2 Stories
B24	YU CAS	Urban	65 m*	24 m
B25	CRAES	Urban	44 m	2 m
B26	IAP	Urban	65 m*	2 Stories
B27	HSZ	Rural	280 m	5 m
B28	HSZ	Rural	280 m	NR
B29	IGSNRR	Urban	50 m*	NR
B30	THU	Suburban	57 m	Three Stories
Thesis	IAP	Urban	10 m	10 m (Lab Roof Top)

N.B. Non reported values (from publications) are presented as (NR) and an * indicates an estimate using an online elevation finder tool⁴⁰².

These sampling site classifications have been reported for each site for Delhi, in Table 4.3. The corresponding satellite images are given as evidence in the appendix (Fig. N – Fig. S). The heights of each sampling site, both above sea level (> S.L) and above ground level (> G.L), reported by each study are also shown in Table 4.3 for Delhi. In many instances, identical sampling sites were used between studies, although each separate study reported a unique height at which their sampler was located.

Similarly for Beijing, the sampling site region classifications (Urban, Suburban, Suburban/Residential, Rural and industrial) of those represented in Fig. 4.2 and Table 4.2 were classified based on the use of google maps⁴⁰³, for which evidence is given in the appendix from Fig. T – Fig. OO. The sampling heights for each publication within each site are also presented in Table 4.4.

4.2.3 Full Review Compilation

Compilation tables of the reviewed studies for Delhi, Beijing are shown in the appendix. A table of study specifications and sampling details, PM_{2.5}, anion and cation concentrations are reported. Tables I and L present the reviewed study specifications and sampling conditions for Delhi and Beijing, respectively. Column 1 in these tables denotes a code which is associated with a measurement within a study. The first letter indicates the city (D = Delhi and B = Beijing) and the number which follows is an arbitrary number (order of having been reviewed) associated with a single publication. In many of these studies, PM_{2.5} was analysed under different atmospheric conditions and sampling times (i.e. day-night sampling, different seasons, haze or clean-periods, different sampling site types etc.) and therefore were subcategorised. This is denoted by another letter after the study number. For example, study D1B is a study that focuses on Delhi; is the publication by Saraswati et al., (2019)³⁷⁴ (D1); under the second specific set of conditions reported by the publication (B) which in this case is summer sampling (Mar - Jun). For Delhi, table J presents the PM_{2.5} and anion concentrations and table K presents the cation concentrations for each study. For Beijing, table M presents the PM_{2.5} and major anion concentrations; table N presents the minor anion concentrations; and table O presents cation concentrations of the reviewed studies.

4.3 Results and Discussion

4.3.1 History of Major Ionic Species in Delhi and Beijing

The averages of ionic species found in PM_{2.5} in Delhi and Beijing were plotted against their campaign mid-points to produce historical plots depicting how the concentrations of ionic species within PM_{2.5} has changed over the last *ca.* 10 years (Delhi) and *ca.* 20 years (Beijing). Historical plots for the major ions and PM_{2.5} for the Delhi pre-monsoon, post-monsoon as well as the Beijing winter and summer seasons have been shown for PM_{2.5}, Cl⁻, NO₃⁻, SO₄²⁻, and NH₄⁺ in Fig. 4.7 - Fig. 4.9. A much more comprehensive dataset was available for Beijing compared to Delhi. The studies conducted in Beijing also reach further back in time, having been measured since the millennium (as opposed to 2012 in Delhi).

4.3.1.1 Delhi

Most of the works conducted in Delhi were very ambiguous regarding sampling times. Specific dates were mostly not given and many studies reported concentrations for a season across multiple years. For the Delhi analyses (Fig. 4.3 and Fig. 4.7), the datapoints demonstrate the assumed averaged mid-point for a study's entire sampling period, representing a single time for each reported average concentration. The cross points represent urban sampling sites and the plus symbol represents a roadside site. The light blue dot points represent the DPEM and DPOM mean concentrations for each ionic species (chapter 3). In addition, the red cross points shown in the Delhi post-monsoon historical plot represents the Diwali specific study (D12) by Shivani et al., (2019)²⁸⁹. The black datapoints have not been specified by the publications and are described as 'non-specified'.

4.3.1.2 Beijing

Similar to Delhi, historical plots have also been conducted for Beijing in which most studies gave specific dates. In the cases where no specific dates were given, an assumed mid-point was assigned (i.e. the middle of a month). The mid-points of each study were plotted against the concentrations reported to show how the average concentration of individual ions (and PM_{2.5}) has changed over the course of the past *ca.* 20 years in Beijing. In Fig. 4.4 and Fig. 4.9 (Beijing), the black datapoints represent studies for which no specific conditions were given. These points have been defined as 'non-specific' or 'non-specified' studies in the following sections. Red datapoints represent measurements which were specifically described to have taken place during a haze period; and green datapoints represent averages from samples taken during clean periods. Pollution control measures were also described by Han et al., (2016)³⁹² (study B17) and Okuda et al., (2011)⁴⁰⁰ (B29), shown as light blue datapoints (Beijing summer seasons). The large yellow point in the Beijing historical plots represents the ionic mean concentration for the BWIN and BSUM campaigns (chapter 3). The symbols represent Urban (×), Suburban (Δ), Rural (□) and mixed (O) sampling sites.

4.3.1.3 Historical change in [PM_{2.5}] in Delhi and Beijing

Fig. 4.3 shows that the Delhi pre-monsoon periods showed a significant drop in [PM_{2.5}] from 2012 – 2015 with a strong negative correlation (*vs* time) coefficient. The addition of the APHH average shows a levelling off of concentrations in PM_{2.5} from around 2014 until 2018. The Delhi post-monsoon seasons show a very similar trend, although the [PM_{2.5}] are significantly larger. The plots shown in Fig. 4.3 therefore indicate a general decrease in [PM_{2.5}] in Delhi across both these seasons from 2012, although the small decrease observed from 2013 onwards suggests that improvements in [PM_{2.5}] were small from 2013 – 2018. A decrease in PM_{2.5} in Delhi was also reported by the Centre for Science and Environment (CSE)⁴⁰⁴, Delhi between 2012 and 2018. In addition, the PM_{2.5} concentrations observed during the Diwali period are significantly higher compared to the other PM_{2.5} averages. In 2018, the DPEM [PM_{2.5}] and DPOM [PM_{2.5}] were still considerably high at 59.18 μg m⁻³ and 164.86 μg m⁻³, respectively. These values were therefore 2.37 and 6.59 times larger than the World Health Organisation (WHO) 24-hour mean exposure limit of 25 μg m⁻³.

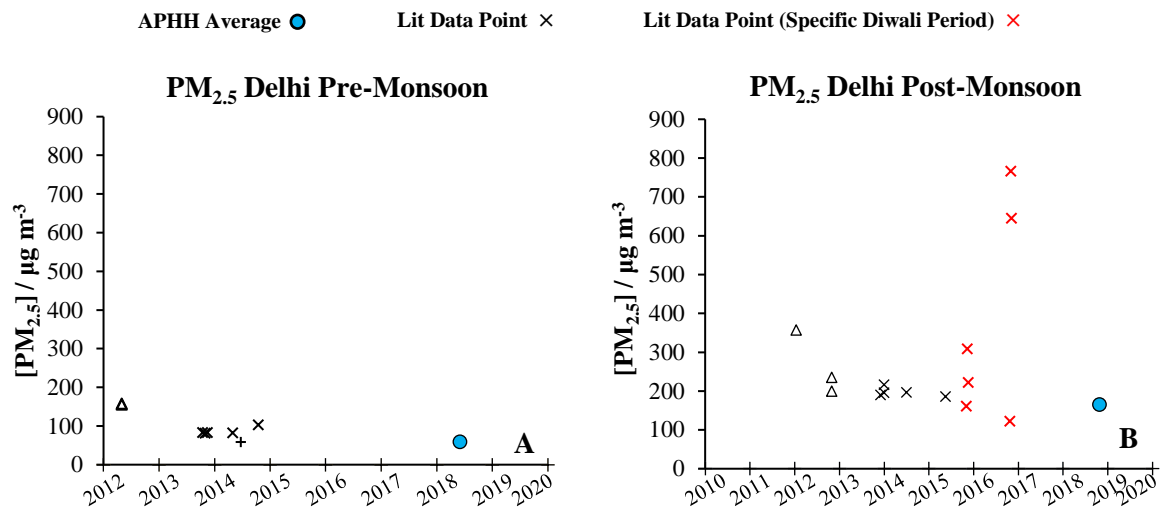


Fig. 4.3. Change in $[PM_{2.5}]$ by time for the Delhi pre- (A) and post- (B) monsoon periods according to literature values. The shapes of the data points represent the type of site for which Urban (\times), Suburban (Δ), and Roadside ($+$) are included. The colours indicate atmospheric conditions including black (non-specific period) and red (Diwali period). The APHH average is shown as a blue data point. Time of sampling is shown along the x-axis. The associated SD for the reviewed studies may be found in the appendix tables. TEOM-FDMS error was unavailable.

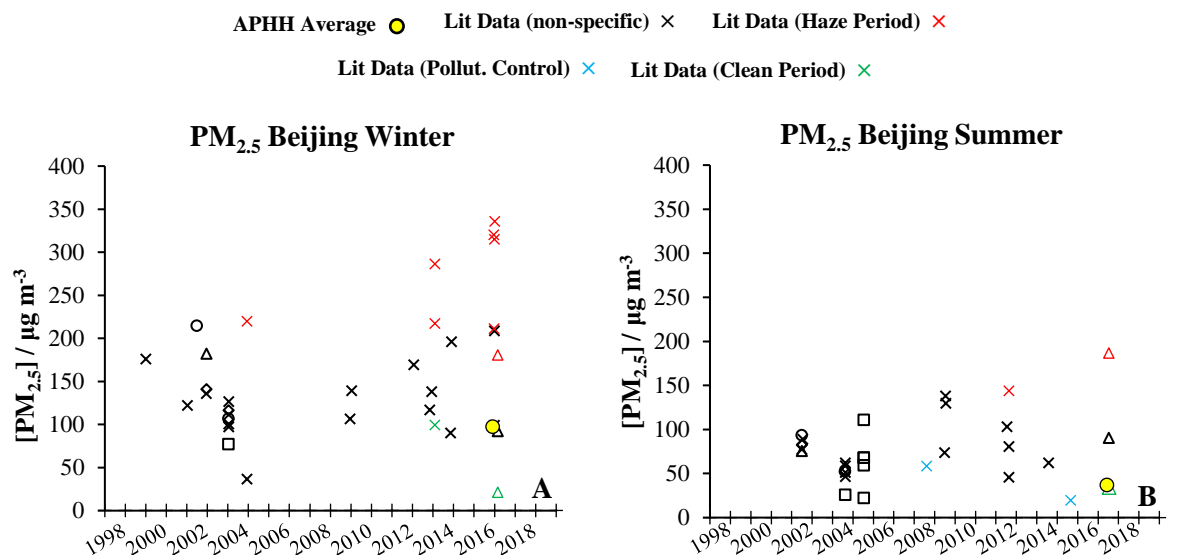


Fig. 4.4. Change in $[PM_{2.5}]$ by time for the Beijing winter (A) and summer (B) periods according to literature values. The shapes of the data points represent the type of site for which Urban (\times), Suburban (Δ), Rural (\square) and mixed (O) are included. The colours indicate atmospheric conditions including black (non-specific period), red (haze period), light blue (pollution control period) and green (clean period). The APHH average is shown as a yellow data point. Time of sampling is shown along the x-axis. The associated SD for the reviewed studies may be found in the appendix tables. TEOM-FDMS error was unavailable.

To compare Beijing, neither the winter or summer seasons showed a trend and the literature values are widely scattered across the last 20 years. The BWIN and BSUM $[PM_{2.5}]$ were among the lower concentrations reported in Fig. 4.4, although were still 3.89 and 1.48 times larger than the WHO 24-hour exposure limit. The BWIN $[PM_{2.5}]$ of $97.28 \mu\text{g m}^{-3}$ was in very good agreement with the work of Shao et al., (2018)³⁹⁴ who reported an average $[PM_{2.5}]$ of $98.97 \mu\text{g m}^{-3}$ during a non-specific period between 15th Dec 2016 – 15th Jan 2017 (just after the BWIN campaign). The BSUM $[PM_{2.5}]$ was in close agreement with the work of Xu et al., (2019)¹⁹⁰ who sampled during clean periods between 1st May - 30th Sep 2017 (overlapping BSUM) and reported an average of $34.11 \mu\text{g m}^{-3}$. A review study

by Lang et al., (2017)²⁶⁸ suggests that a decreasing trend in annual $[PM_{2.5}]$ concentrations has been observed in Beijing from the year 2000 – 2015 although they report a linear correlation coefficient of concentration vs time of $R = 0.53$, ($R^2 = 0.2809$). This is not seen in Fig. 4.4 for either the BWIN or BSUM periods.

The $PM_{2.5}$ data shown in Fig. 4.4 is data purely taken from publications which focus on inorganic aerosol composition. Network data is however continuously running in both cities. Network data for Beijing which sampled from 2009 – 2019 available from Statista²⁸¹ (one site within network, US Embassy) is shown in Fig. 4.5. Fig. 4.6 also shows the change in $PM_{2.5}$ concentrations from 2008 – 2013, measured by the USA Embassy⁴⁰⁵ and reported by Zhang et al., (2016)⁴⁰⁶.

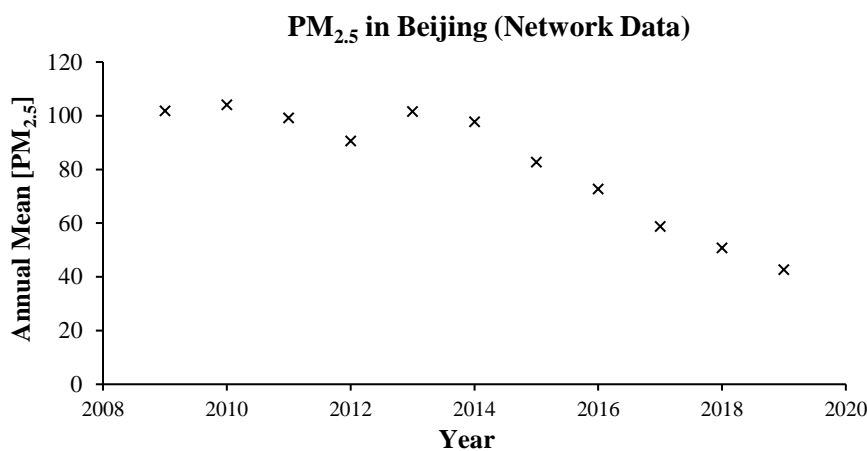


Fig. 4.5. The change in annual $[PM_{2.5}]$ from 2009 to 2019 taken from US Embassy Network Data (Statista)²⁸¹.

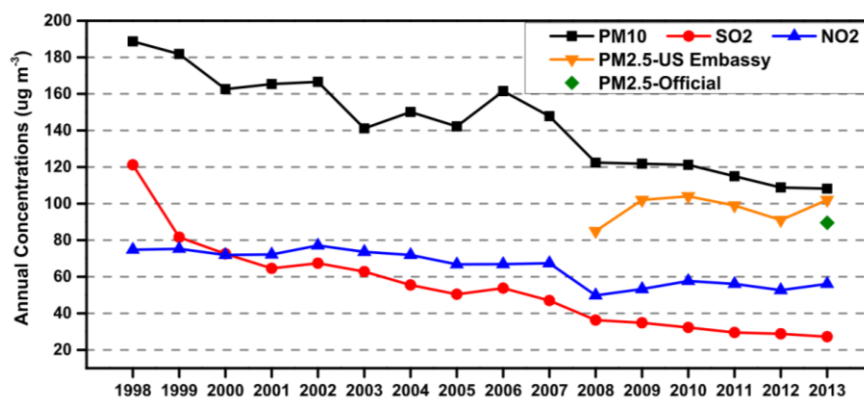


Fig. 4.6. The change in annual $[PM_{2.5}]$ from 2008 to 2013 taken from Network Data. Image is taken from Zhang et al., (2016)⁴⁰⁶.

Both Fig. 4.5 and Fig. 4.6 show a rise and fall in $[PM_{2.5}]$ between 2008 and 2013. Fig. 4.5 shows that from 2013 to 2018, a general decrease in $[PM_{2.5}]$ is observed which is in line with the work of Lang

et al., (2017)²⁶⁸ although does not agree with the scatter shown in Fig. 4.4 due to the selective concentrations of PM_{2.5} taken from publications which measured the inorganic fraction.

The PM_{2.5} network data for Delhi has been requested from the USA Embassy and comparison of Fig. 4.3 to the network data from the USA Embassy in Delhi constitutes to future work.

4.3.1.4 Historical [ion] change in Delhi

The historical plots for Cl⁻, NO₃⁻, SO₄²⁻ and NH₄⁺ in Delhi are shown in Fig. 4.7. During the Delhi pre-monsoon seasons there is no obvious trend between the previous studies in the [Cl⁻] vs time. The DPEM Cl⁻ mean (2.32 μg m⁻³) is also much lower compared to most other studies, although the DPEM mean was very close in concentration to the average of 2.14 μg m⁻³ reported by Pant et al., (2015)¹¹⁰ who sampled in 2014 between 15th – 30th Jun 2014 (site D, Fig. 4.1). Post monsoon seasons in Fig 4.5B show increasing [Cl⁻] vs time since Jan 2012 with a relatively strong positive correlation coefficient (vs time). This infers that an increase in [HCl] most likely occurred between 2012 – 2015 which would indicate a rise in anthropogenic emissions from sources such as biomass burning, steel pickling and coal burning. In addition, the population of Delhi had increased from 23.5 m – 25.9 m between 2012 and 2015 (by *ca.* 10 %) ²⁵⁹. A higher population requires more coal combustion across the city for heat and electricity, which would result in higher HCl emissions due to the proximity of three major coal power plants to Delhi. In comparison to previous works however, the DPOM average [Cl⁻] measured in this study (blue dot, 6.46 μg m⁻³) was lower compared to the most recent studies, likely due to the fact that sampling stopped prior to the most intense pollution around Diwali. What is striking about Fig. 4.7B is that on Diwali in 2017, Shivani et al., (2019)²⁸⁹ reported a [Cl⁻] of 29.34 μg m⁻³. This was 4.54 times higher than the DPOM average and was also sampled at IGDTUW (site F, Fig. 4.1).

The change in [NO₃] vs time for the Delhi pre-monsoon seasons shows a moderate negative correlation between 2012-2015, although care needs to be taken due to the low number of data points. NO_x was reported to have increased between 2012 and 2016 in Delhi⁴⁰⁷ and therefore this may account for this decrease, if an increase in NO had decreased the concentrations of the oxidative species. The DPEM [NO₃⁻] was however higher than most other studies. This could therefore indicate that NO₃⁻ may be rising again, but since only 1 week of data was collected this requires further study. In addition, the minimum [NO₃⁻] of 3.3 μg m⁻³ as reported by Saraswati et al., (2019)³⁷⁴ who sampled at NPL (site A, Fig. 4.1) between Mar – Jun in 2013 – 2015 is of particular interest. This is because this data point potentially is affected by NO₃⁻ volatilisation under long filtering times as discussed in chapter 3. Saraswati et al., (2019)³⁷⁴ describe that sampling was carried out every 24 hours using a flow rate of 1 m³h⁻¹. The filters are described to have been placed in a desiccator for 24 hours after sample collection (20 °C ± 1 °C, RH% 40 ± 2 °C).

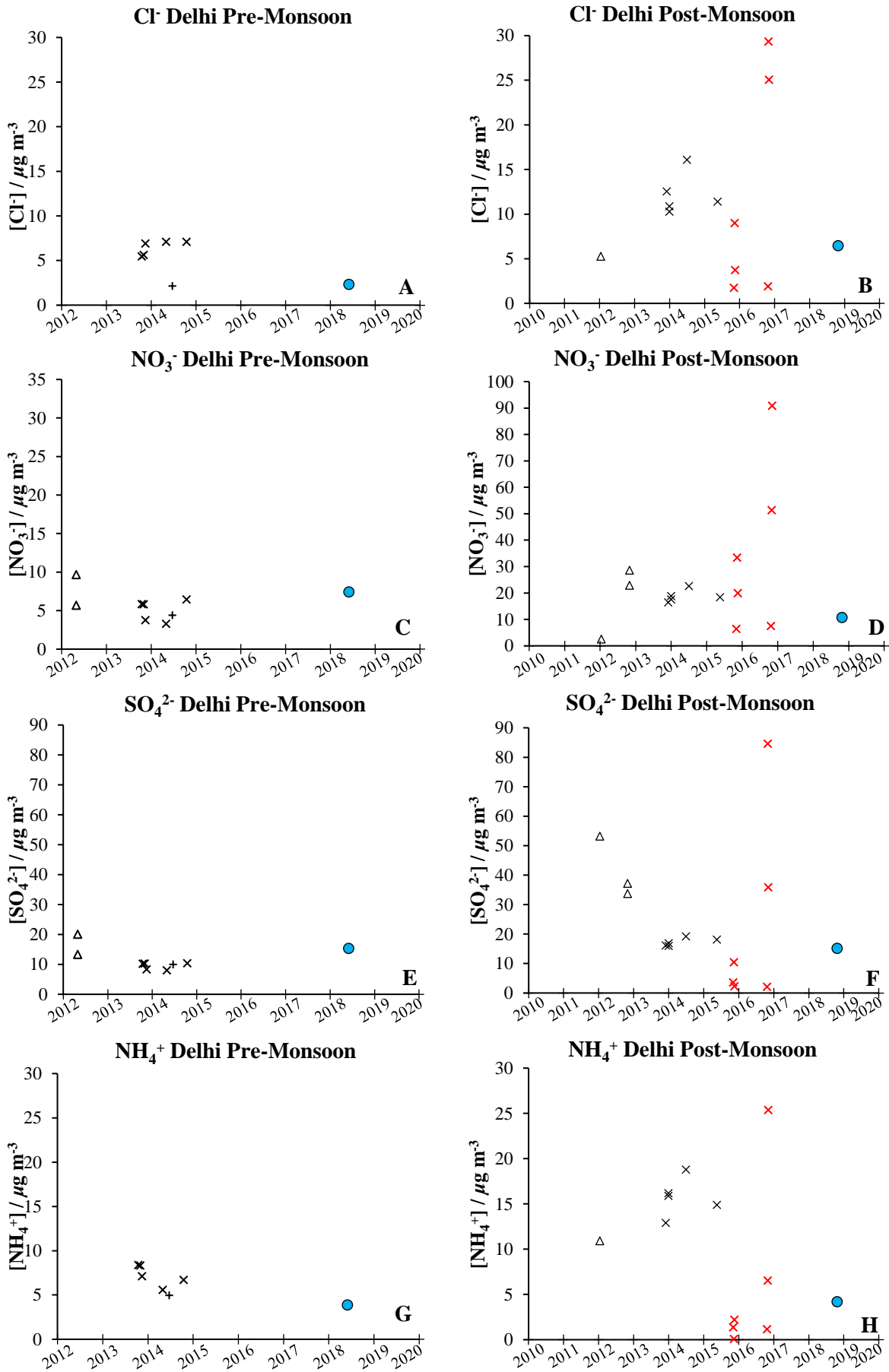


Fig. 4.7. Historical Plots showing the change in [major ions] by time over the pre- and post-monsoon seasons in Delhi according to the literature. The shapes of the data points represent the type of site for which Urban (x), Suburban (Δ), and Roadside (+) are included. The colours indicate atmospheric conditions including black (non-specific period) and red (Diwali period). The APHH average is shown as a blue data point. Time of sampling is shown along the x-axis. The associated SD for the reviewed studies are found in the appendix tables and the APHH errors are found in chapter 3.

Sample collection also took place during the summer in Delhi, where the study reports a maximum temperature of *ca.* 45 °C. Under these conditions, it is likely that a substantial proportion of NO_3^- may have been lost from the aerosol phase on the filter²¹². The Delhi post-monsoon seasons showed a weak correlation in $[\text{NO}_3^-]$ vs time (Fig. 4.7D), for which the DPOM average of $10.77 \mu\text{g m}^{-3}$ sits in line if this trend was extrapolated to 2018. As with the DPEM campaign, this could be down to an increase in NO_x ⁴⁰⁷ although more gas-phase data is required to confirm this. What may be surprising however is the particularly low $[\text{NO}_3^-]$ reported by Shivani et al., (2019)²⁸⁹ over the Diwali period in 2016 and 2017, as well as the low DPOM $[\text{NO}_3^-]$ considering the much increased pollution expected on the lead up to Diwali. As has been shown in chapter 3 however is that leading up to Diwali (2018), a much higher NO concentration is observed which was attributed to very high NO_x and VOC emissions and therefore low oxidant species concentrations to form HNO_3 .

The $[\text{SO}_4^{2-}]$ vs time showed a strong negative trend over the sampling period with a strong correlation observed during both the pre-monsoon and post-monsoon seasons. The $d[\text{SO}_4^{2-}]/dt$ from the gradient was $-0.0089x$ and $-0.0304x$ corresponding to $-3.27 \mu\text{g m}^{-3} \text{ year}^{-1}$ and $-11.10 \mu\text{g m}^{-3} \text{ year}^{-1}$, respectively. A decrease in SO_4^{2-} could potentially be explained by the reduction of sulfur within diesel fuel from 350 ppm in 2012 to 50 ppm in 2017 across India³³⁸. A study by Suneja et al., (2020)⁴⁰⁸ however measured $[\text{SO}_2]$ across Delhi from 2011 to 2018 and described a slight increase. If $[\text{SO}_2]$ increases and SO_4^{2-} decreases, a possible explanation could be due to a decrease in oxidative species available (as suggested for the pre-monsoon NO_3^- analysis). The APHH DPEM and DPOM values however do not follow the trends in Fig. 4.7E and Fig. 4.7F, respectively. In the pre-monsoon historical plot the APHH $[\text{SO}_4^{2-}]$ average reported in this study was generally higher than all other reviewed studies. This is the same aerosol campaign which reported the highest NO_3^- and was taken during the daytime. Therefore, the higher NO_3^- and SO_4^{2-} reported by Bisht et al., (2015)³⁷⁶ is likely down to the selective sampling during daytime hours which would lead to higher oxidation of NO_2 and SO_2 . For the post-monsoon, the $[\text{SO}_4^{2-}]$ concentrations follow the same trend as $[\text{PM}_{2.5}]$ in which the DPOM $[\text{SO}_4^{2-}]$ indicates a levelling off.

The $[\text{NH}_4^+]$ showed a negative trend and the measurements in this thesis may again suggest species levelling off between 2015 – 2018. This indicates that over time, lower NH_4^+ is found in the aerosol which may either be down to a lower concentration in acidic gases, NH_3 , or higher temperatures causing NH_4^+ loss from the aerosol. Maximum pre-monsoon temperatures have seen little change since 2012⁴⁰⁹ and $[\text{NH}_3]$ have been demonstrated to increase annually in the work of Sharma et al., (2017)⁴⁰⁷ (between 2008 - 2016). The reason for the decrease may most likely therefore be due to a reduction in H_2SO_4 , HNO_3 and NH_3 neutralisation, as was suspected for the decrease in the NO_3^- and SO_4^{2-} trends also, due to possible higher annual NO_x ⁴⁰⁷. The DPOM campaign however showed an increase in $[\text{NH}_4^+]$. As an increase was also seen in Cl^- and NO_3^- for this campaign, this may therefore indicate a likely increase in the amount of biomass burning occurring over time. Another possibility may be down to an increase in NH_3 ⁴⁰⁷, such as from cattle as a 4.6 % increase was recorded over

India in the total livestock from 2012 - 2019 according to the Indian Government website⁴¹⁰. The DPOM [NH₄⁺] mean however does not agree with the increasing trend although it shows similar [NH₄⁺] to the low concentrations seen by Shivani et al., (2019)²⁸⁹ (red cross points, Fig. 4.7H). This is most likely down to the other studies sampling over a greater sampling period (multiple months) compared to the work of Shivani et al., (2019)²⁸⁹ who sampled particularly over Diwali period and the APHH campaign for which sampling was just under a month on the lead up to Diwali. A potential explanation for this may be that very high NO and primary VOC emissions present during Diwali may reduce the oxidant species concentrations significantly (chapter 3). This in turn would reduce NO₂ and SO₂ oxidation to HNO₃ and H₂SO₄ which are significant in NH₃ neutralisation and transition to the particle phase. Another possible reason for the lower NH₄⁺ may be down to the other sampling sites (Fig. 4.1) being further away from the city centre and may possibly be more impacted by agricultural emissions. The work by Shivani et al., (2019)²⁸⁹ and work conducted for this thesis are the only two studies which were conducted at IGDTUW.

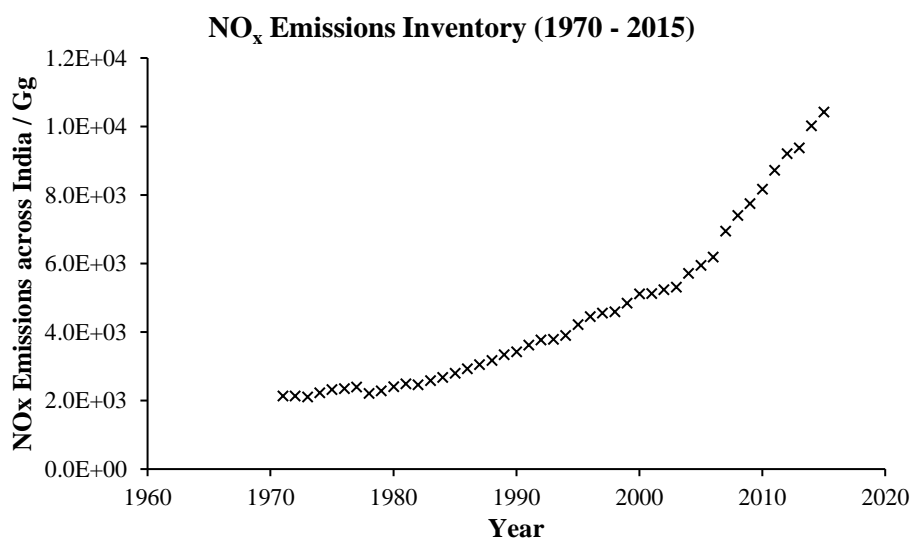


Fig. 4.8. Emission Inventory of NO_x over India from 1970 - 2015 using EDGAR data (V5.0)^{412,413}. The year is reported on the x-axis with the NO_x emissions across the whole of India reported on the y-axis.

To summarise, the change in [SIA] as a function of time showed a negative correlation for NO₃⁻ and SO₄²⁻ between 2012 – 2015. This has been attributed to a possible decrease in oxidative species as a potential result of increased NO_x⁴⁰⁷ and therefore decreased atmospheric oxidation species concentrations, causing less NO₂ and SO₂ oxidation forming less HNO₃ and H₂SO₄ to neutralise NH₃. The increase in NO_x may be evidenced by an increase in NO₂ concentrations observed over Delhi by Vohra et al., (2020)⁴¹¹ who show an increase in NO₂ emissions from OMI satellite data in their study across the years 2005 - 2019. Emission inventory data was also available from the Emissions Database for Global Atmospheric Research (EDGAR, V5.0)^{412,413} and demonstrates that NO_x emissions have been increasing since the 1970's (Fig. 4.8) across India.

The change in $[\text{NO}_3^-]$ and $[\text{SO}_4^{2-}]$ as a function of time follows the same negative trend as the Delhi pre-monsoon $\text{PM}_{2.5}$ (Fig. 4.3B). This may be down to the fact that $\text{PM}_{2.5}$ during pre-monsoon seasons in Delhi has a substantial contribution of SIA as shown in chapter 3. No trend was seen in the change in $[\text{Cl}^-]$ as a function of time (Fig. 4.7A) for the pre-monsoon seasons as HCl is not required to be oxidised before neutralising NH_3 . For the post-monsoon periods, increases were seen in Cl^- and NH_4^+ between 2012 and 2015 which suggests a possible increase in solid fuel burning such as coal combustion or biomass burning. $[\text{NO}_3^-]$ and $[\text{SO}_4^{2-}]$ however showed a general decrease which may be down to lower levels of oxidant species or sulfur in diesel fuel (for SO_4^{2-}). Particularly low ion concentrations were seen in the DPOM campaign as well as the work of Shivani et al., (2019)²⁸⁹ which was attributed to short sampling periods in very close proximity to Diwali compared to the other studies which sampled over multiple months. The lack of literature values available for the pre- and post-monsoon periods however makes trend analysis challenging and longer-term studies of aerosol composition are required.

4.3.1.5 Historical [ion] change in Beijing

Fig. 4.9 shows the change in [major ions] as a function of time for the Beijing winter and summer seasons. Like the $[\text{PM}_{2.5}]$ trend, each ion shows a great deal of scatter. The Beijing winter $[\text{Cl}^-]$ across the literature was very variable, ranging from $0.76 \mu\text{g m}^{-3}$ – $7.36 \mu\text{g m}^{-3}$ with a %RSD of 46.13 % (for the non-specified values, black cross points in Fig. 4.9, incl. BWIN). Fig 4.4 does however show that the study by Shao et al., (2018)³⁹⁴ who sampled at BNU (site A, Fig. 4.2) between 15th Dec 2016 – 15th Jan 2017 observed a $[\text{Cl}^-]$ concentration of $4.07 \mu\text{g m}^{-3}$ which was very close to the BWIN $[\text{Cl}^-]$ mean of $3.95 \mu\text{g m}^{-3}$. Furthermore, the campaign by Shao et al., (2018)³⁹⁴ took place over a month (*ca.* the same length as BWIN) and most likely observed a mixture of clean and haze periods, like the BWIN campaign. Over the summer periods (Fig. 4.9B), most values are much smaller than the winter values, with recent years generally having low values. The most recent BSUM mean $[\text{Cl}^-]$ was at the lower end of the values in the literature.

There is a large amount of scatter seen in the $[\text{NO}_3^-]$ trend for the winter and summer seasons in Beijing. To compare the BWIN $[\text{NO}_3^-]$ to the other studies over the winter of 2016 – 2017, Fig. 4.9C shows that the BWIN $[\text{NO}_3^-]$ lies within the range of the other studies during this period. Fig. 4.9C also shows that the haze period NO_3^- concentrations over this specific winter had higher NO_3^- concentrations. The clean period $[\text{NO}_3^-]$ of $7.46 \mu\text{g m}^{-3}$ for between 7th Feb - 15th March 2017 sampled by Xu et al., (2019)¹⁹⁰ was also lower than the BWIN $[\text{NO}_3^-]$ which is expected. For BSUM, relatively few other studies were conducted over the summer of 2017, although the work of Xu et al., (2019)¹⁹⁰ who report a $[\text{NO}_3^-]$ of $32.37 \mu\text{g m}^{-3}$ during a haze period; $17.9 \mu\text{g m}^{-3}$ during a slightly polluted period; and $6.06 \mu\text{g m}^{-3}$ during the clean period. It is interesting that the BSUM mean of NO_3^- is in much closer agreement with the clean period mean compared to the slightly polluted or haze period means reported by Xu et al., (2019)¹⁹⁰. For the Beijing winter and summer seasons, again no obvious trend was observed for $[\text{NH}_4^+]$ over time.

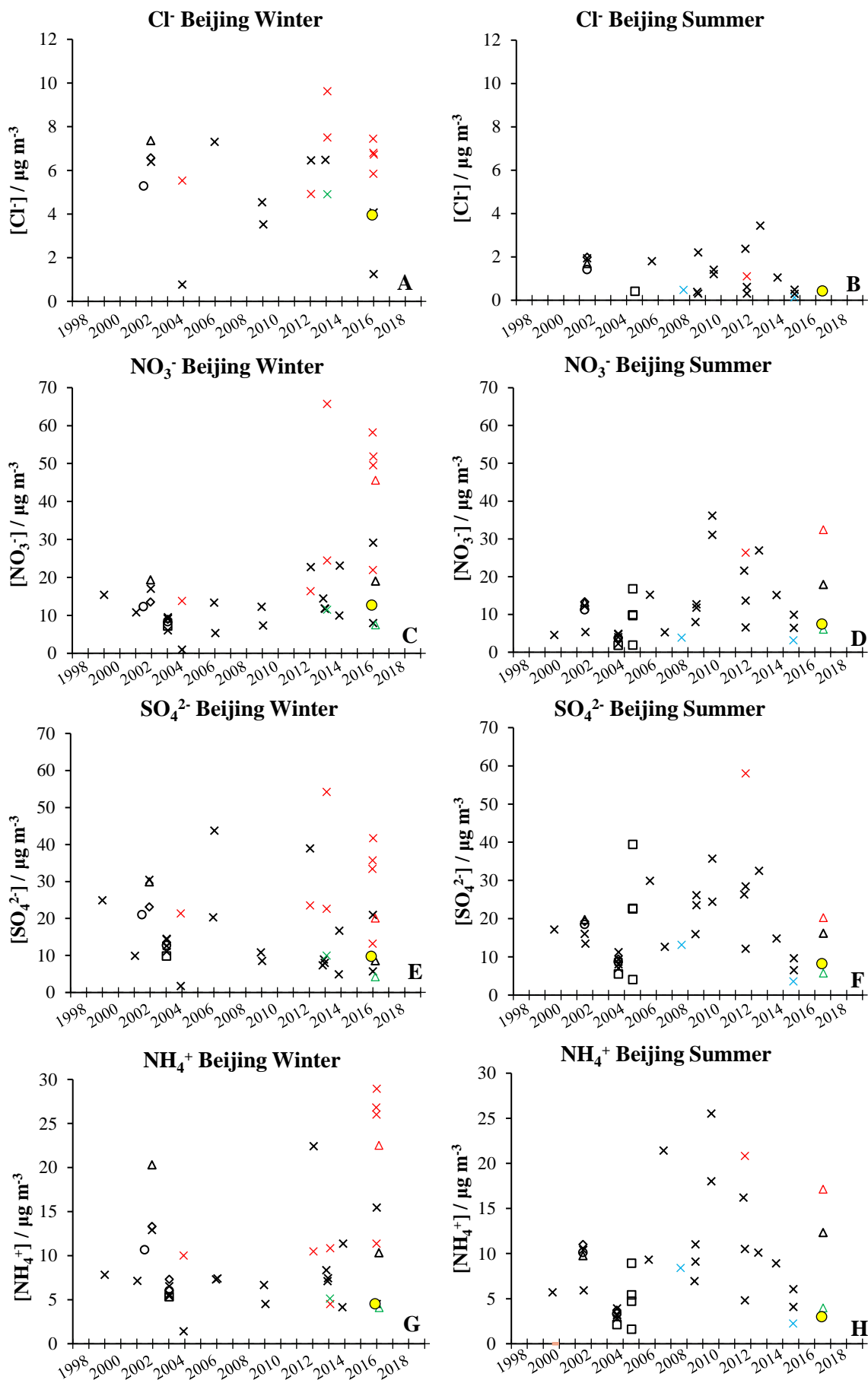


Fig. 4.9. Historical Plots showing the change in [major ions] by time over the winter and summer seasons in Beijing according to the literature. The shapes of the data points represent the type of site for which Urban (x), Suburban (Δ), Rural (\square) and mixed (O) are included. The colours indicate atmospheric conditions including black (non-specific period), red (haze period), light blue (pollution control period) and green (clean period). The APHH average is shown as a yellow data point. Time of sampling is shown along the x-axis. The associated SD for the reviewed studies are found in the appendix tables and the APHH errors are found in chapter 3.

During the APHH BWIN campaign, $[\text{NH}_4^+]$ was $4.54 \mu\text{g m}^{-3}$ which was in very good agreement with the work of Shao et al., (2018)³⁹⁴ who measured just after the BWIN campaign and reported a $[\text{NH}_4^+]$ of $4.5 \mu\text{g m}^{-3}$. Another study that was in very close agreement to BWIN was that of Xu et al., (2019)¹⁹⁰ who reported $4.09 \mu\text{g m}^{-3}$ for the clean periods between 7th Feb - 15th March 2017. The BSUM $[\text{NH}_4^+]$ average was $3.00 \mu\text{g m}^{-3}$ which was very close in concentration to the clean period in the work by Xu et al., (2019)¹⁹⁰ who reported an $[\text{NH}_4^+]$ average of $3.96 \mu\text{g m}^{-3}$. In summary, no significant reductions or increases were seen for the major inorganic ions in $\text{PM}_{2.5}$ for either the winter or summer seasons in Beijing, although the means of the major ions were frequently in good agreement with other works under similar conditions.

4.3.2 Particle Composition Comparison of $\text{PM}_{2.5}$ in Delhi and Beijing (Timelines)

By identifying the change in inorganic $\text{PM}_{2.5}$ species composition, the key ions which affect $\text{PM}_{2.5}$ hygroscopicity, growth, particle size, number and ultimately $\text{PM}_{2.5}$ concentrations over time may be identified. In addition, a comparison has been conducted between the APHH campaigns (chapter 3) and % fraction contribution values calculated from other studies in the literature. The change in $\text{PM}_{2.5}$ particle composition as a function of time was performed using the reviewed studies to produce timelines showing aerosol evolution across the pre- and post-monsoon seasons as well as the winter and summer seasons in Delhi and Beijing, respectively. The studies included in this review are labelled identically to the studies listed in section 4.2.1. Composition timelines for each season are shown in Fig. 4.10 (Delhi pre-monsoon), Fig. 4.11 (Delhi post-monsoon), Fig. 4.13 (Beijing winter) and Fig. 4.15 (Beijing summer).

To produce the pie charts shown in this section, the reported average atmospheric concentrations of each individual ion was taken as a percentage of the average $\text{PM}_{2.5}$ reported from each publication. The colours of segments for species within the pie charts are identical to those represented in chapter 3. The date mid-points taken for study campaigns were calculated in the same way as previously for Delhi and Beijing (section 4.3.1). In most of the reviewed studies, the ‘other’ fraction may be assumed to be predominantly organic however it should be noted that very few studies reviewed measured only a selection of ions (some studies only measure 3 ions) resulting in the ‘other’ fraction being a combination of organic and non-measured ionic species. Therefore, the trends in the ‘known ions %’ and ‘other’ fractions should be taken with some caution, although SIA often does make up the dominant inorganic fraction. The pie charts for the APHH DPEM, DPOM, BWIN and BSUM (chapter 3) campaigns have also been added to these timelines for comparison.

4.3.2.1 Delhi Pre-Monsoon

The change in $\text{PM}_{2.5}$ composition as a function of time for studies reviewed over the pre-monsoon seasons in Delhi are shown in Fig. 4.10. The top half of the timeline represents the pre-monsoon seasons and the bottom half presents the monsoon seasons across the studies (for interest of the reader). The symbols adjacent to the pie charts resemble the sampling site and conditions, as previously described in section 4.3.1.1

Delhi Pre-monsoon

Delhi Pre- Monsoon and Monsoon PM_{2.5} Composition Timeline

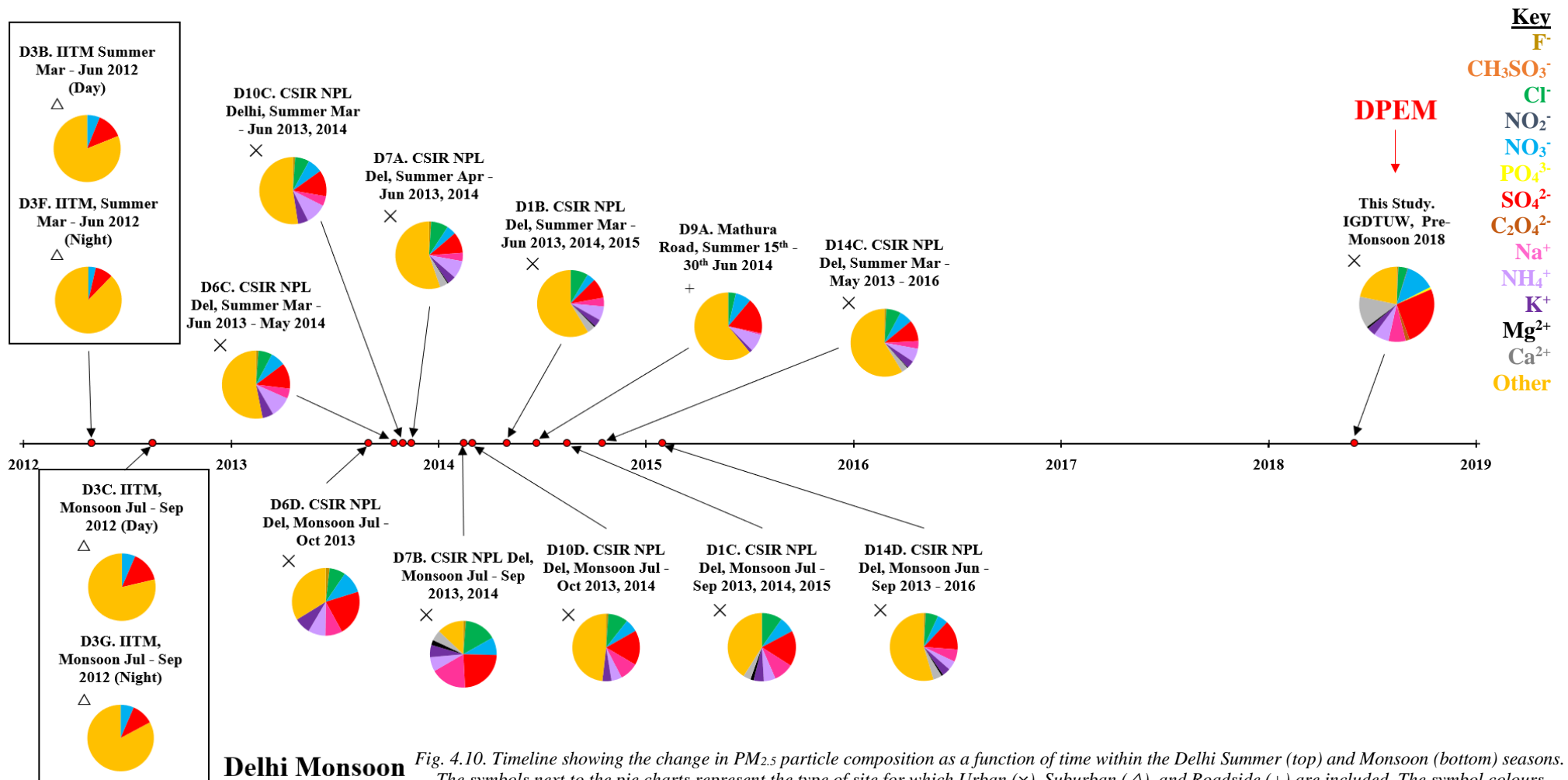


Fig. 4.10. Timeline showing the change in PM_{2.5} particle composition as a function of time within the Delhi Summer (top) and Monsoon (bottom) seasons. The symbols next to the pie charts represent the type of site for which Urban (\times), Suburban (Δ), and Roadside ($+$) are included. The symbol colours indicate atmospheric conditions including black (non-specific period) and red (Diwali period). The APHH average is highlighted (DPEM). Time of sampling is shown along the x-axis. The study code along with the specific sampling site and time are also presented above each pie chart. The species presented are coloured in the pie charts, as per the key shown in the top right.

The average known ions % fraction seen during the APHH DPEM (78.48 %) was much larger compared to the other studies reviewed during this season in Delhi. The average known ions % fraction (excl. study D3 as no cations were reported, as well as DPEM) was 43.44 % (SD \pm 3.44 %). Therefore the DPEM average was significantly higher compared to the average across the other publications. The maximum known ions % fraction (excl. DPEM) was 47.53 % reported by Sharma et al., (2016)³⁷⁸ (10C). The minimum known ions % fraction between the reviewed studies (excl. DPEM or D3) was 38.99 % reported by Pant et al., (2015)¹¹⁰ (9A). Generally, the DPEM proportion of known ions % is more representative of the monsoon studies where the average (excl. D3) was 61.90 % (SD \pm 16.09 %).

The maximum Cl⁻ % fraction in this review was 8.56 % reported by Saraswati et al., (2019)³⁷⁴ in study D1B and was 2.18 times larger than the DPEM average of 3.93 %. The minimum Cl⁻ % was observed to be 3.68 % (D9A) reported by Pant et al., (2015)¹¹⁰ which was 0.25 % smaller than the DPEM value. The average across the Delhi pre-monsoon reviewed studies (excl. DPEM) was 6.81 % (SD \pm 1.74 %) which was therefore *ca.* twice larger than the DPEM average.

The maximum NO₃⁻ % between reviewed studies was 7.51 % (D9A) reported by Pant et al., (2015)¹¹⁰. The minimum NO₃⁻ % was found in study D3F (3.66 %) reported by Bisht et al., (2015)³⁷⁶. The APHH DPEM NO₃⁻ % fraction (12.58 %) was found to be higher than all other studies, although only 8 other studies were available for review here. The average NO₃⁻ across the reviewed studies (excl. DPEM) was 5.77 % (SD \pm 1.51 %) and therefore the DPEM average was around twice as large.

The APHH DPEM SO₄²⁻ % shows a much larger fraction (25.98 %) compared to the average SO₄²⁻ contribution across all studies (excl. DPEM) of 11.62 %. The maximum SO₄²⁻ % fraction within the reviewed studies was 17.13 % in study D9A and the minimum was 8.57 % in study D3F. The range of SO₄²⁻ % fraction across all studies (incl. DPEM) was 17.42 %. The average SO₄²⁻ % fraction across all reviewed studies (excl. DPEM) was 11.62 % (SD \pm 2.70 %), for which the DPEM average was *ca.* twice larger.

The maximum NH₄⁺ % contribution between the reviewed studies was 10.20 % (D10C) reported by Sharma et al., (2016)³⁷⁸. The minimum NH₄⁺ % was 6.51 % (D14C) reported by Jain et al., (2020)³⁸¹ and was found to be very close in NH₄⁺ % the DPEM study (6.56 %). The average NH₄⁺ % across all studies reviewed (excl. DPEM) was 8.42 % (SD \pm 1.56 %) and therefore was relatively close to the DPEM average NH₄⁺ % contribution.

Most of the ions represented in the pie charts in Fig. 4.10 do not represent any trend regarding the % fraction composition within PM_{2.5}. This is mostly down to relatively few studies conducted within the literature. For interest of the reader, the annual change in PM_{2.5} composition in Delhi is presented in the appendix (Fig. PP).

4.3.2.2 Delhi Post-Monsoon

The change in composition of PM_{2.5} across the reviewed studies as a function of time for the Delhi post-monsoon and winter seasons are shown in Fig. 4.11. The pie charts shown on the upper half of the timeline are the studies which were taken during post-monsoon periods (some bridged into winter months), and the pie charts on the bottom of the timeline show the compositions of PM_{2.5} during the winter periods. The symbols adjacent to the pie charts resemble the sampling site and conditions, as previously described in section 4.3.1.1. In addition, the airplane symbols indicate measurements which were taken at the IGIA (airport) outside of the city centre away from most other sampling sites (Fig. 4.1).

The maximum known ions % was reported as 47.92 % in study D1A³⁷⁴. The minimum known ions % out of the reviewed studies was 12.85 % in study D12A²⁸⁹. The measured known ions % fraction for the APHH DPOM campaign was 33.72 % which was relatively similar to the average across all studies (excl. D3 and DPOM) of 30.39 $\mu\text{g m}^{-3}$.

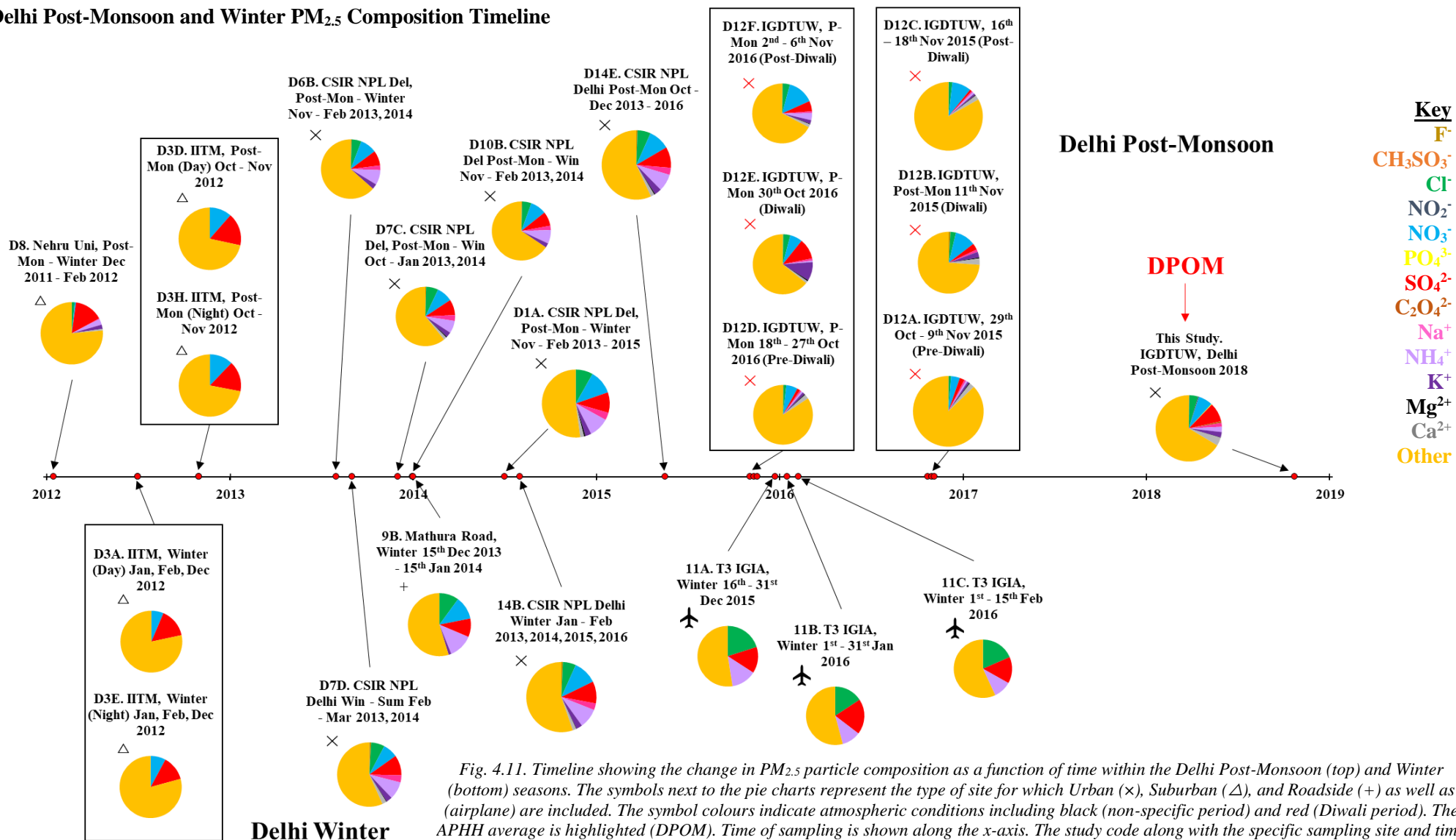
The maximum Cl⁻ % out of studies reviewed in Fig. 4.11 was 8.18 % by Saraswati et al., (2019)³⁷⁴ in study D1A. The minimum Cl⁻ % was 1.09 % which was measured during the pre-Diwali period (29th Oct, 3rd, 5th, and 9th Nov 2015) by Shivani et al., (2019)²⁸⁹ at IGDTUW (D12A). This is surprising as Diwali is the Hindu festival is expected to have much greater biomass burning and firework displays which are known to be sources of Cl⁻^{414,415,118}. The DPOM Cl⁻ % fraction is most similar to study D12E (Diwali 30th October in 2016)²⁸⁹ with an average Cl⁻ % fraction of 3.83 % at IGDTUW. The average Cl⁻ % contribution across all the reviewed studies (excl. DPOM) was 3.97 % (SD \pm 2.31 %) for which the DPOM average of 4.28 % Cl⁻ was within 1 SD.

Kumar et al., (2018)²²⁵ reported a value of 0.70 % NO₃⁻ within PM_{2.5} (study D8) which was the minimum out of all reported. The maximum % NO₃⁻ was 14.09 % (D12F) measured by Shivani et al., (2019)²⁸⁹ during the Post-Diwali days in 2016. The DPOM average (6.97 %) was within one SD of the mean (μ 8.78 $\mu\text{g m}^{-3}$, SD \pm 3.50 $\mu\text{g m}^{-3}$) of the [NO₃⁻] values from reviewed studies (excl. DPOM). The DPOM average also lied closest to study D12E (6.71 %) by Shivani et al., (2019)²⁸⁹.

The maximum SO₄²⁻ % contribution out of all studies reviewed (excl. DPOM) was 16.91 % measured in study D3D³⁷⁶. The minimum SO₄²⁻ % was 1.03 % by Shivani et al., (2019)²⁸⁹ (D12C) measured during the post-Diwali period in 2015 (16th and 18th Nov) at IGDTUW. The average SO₄²⁻ % fraction between all reviewed studies (excl. DPOM) was 8.33 % (SD \pm 5.19 %) and therefore the DPOM % SO₄²⁻ (9.23 %) was within the average plus 1 SD.

The reviewed study in closest agreement to the DPOM average by % fraction was that of D14E by Jain et al., (2020)³⁸¹ who reported a value of 9.73 %. The maximum NH₄⁺ % fraction was 9.55 % (D1A) reported by Saraswati et al., (2019)³⁷⁴. The minimum NH₄⁺ contribution out of the studies in Fig. 4.11 was 0.03 % (D12B) as reported by Shivani et al., (2019)²⁸⁹ from samples taken on Diwali

Delhi Post-Monsoon and Winter PM_{2.5} Composition Timeline



in 2015 (11th Nov). The average NH_4^+ % contribution across all reviewed studies (excl. DPOM) was 4.22 % (SD \pm 3.54 %).

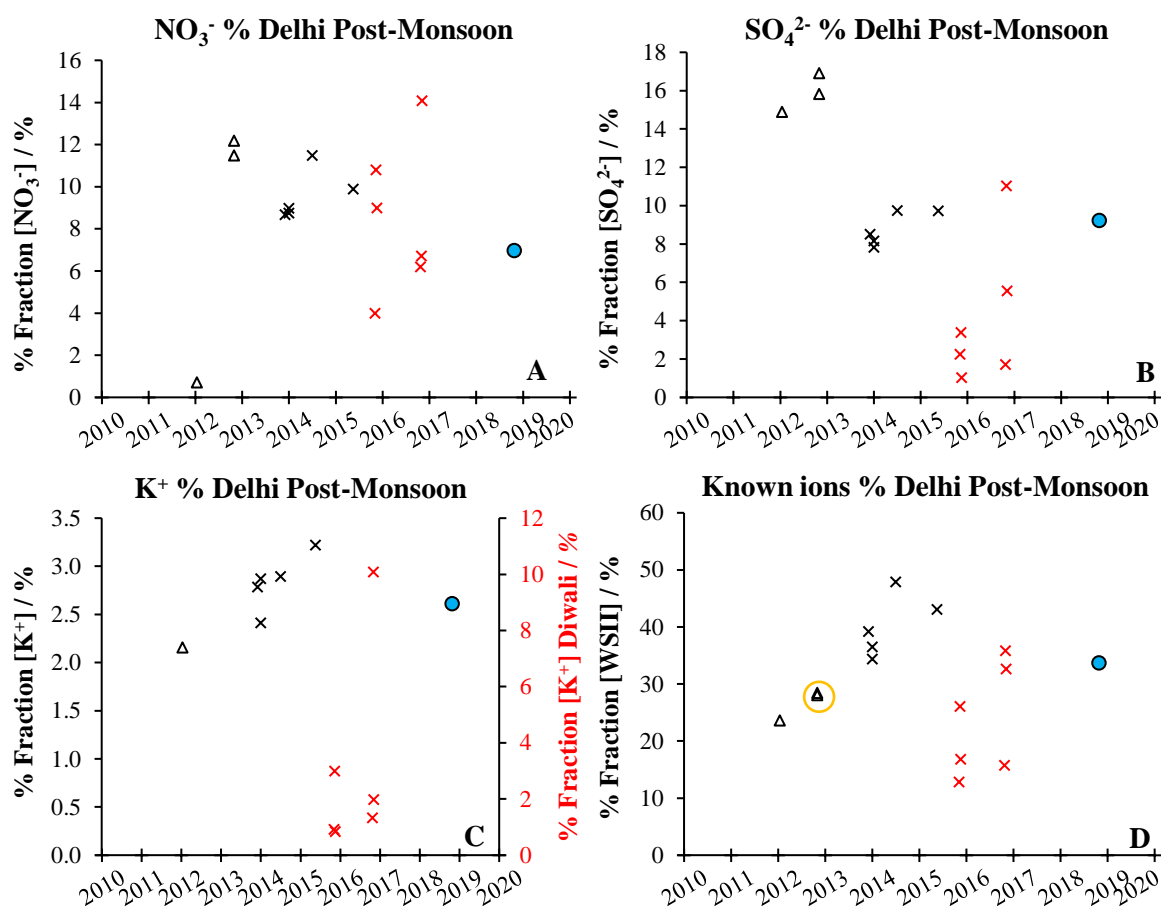


Fig. 4.12. The change in $[\text{NO}_3^- \text{ %}]$, $[\text{SO}_4^{2-} \text{ %}]$, $[\text{K}^+ \text{ %}]$ and $[\text{known ions } \text{ %}]$ in $\text{PM}_{2.5}$ as a function of time reported by reviewed studies (Delhi post-monsoon seasons). The shapes of the data points represent the type of site for which Urban (\times), Suburban (Δ), and Roadside ($+$) are included. The colours indicate atmospheric conditions including black (non-specific period) and red (Diwali period). The APHH average is shown as a blue data point. Time of sampling is shown along the x-axis. The associated SD for the reviewed studies are found in the appendix tables and the APHH errors are found in chapter 3.

Further analysis of the known ions % vs time for the Delhi post-monsoon periods is shown in Fig. 4.12, which displays the historical trends of known ions % over time. The only ions to show distinct trends in known ions % vs time were NO_3^- (Fig. 4.12A), SO_4^{2-} (Fig. 4.12B), K^+ (Fig. 4.12C) and known ions % (Fig. 4.12D). For clarity, the Diwali points by Shivani et al., (2019)²⁸⁹ have been removed. A strong negative correlation of $[\text{NO}_3^-]$ and $[\text{SO}_4^{2-}]$ vs time for between 2012 – 2018 may be observed which may be down to a reduction in oxidative species as mentioned previously (section 4.3.1.4). These trends are in agreement with the negative trends of $[\text{NO}_3^-]$ and $[\text{SO}_4^{2-}]$ concentrations vs time displayed in Fig. 4.7D and Fig. 4.7F, respectively (section 4.3.1.4). An interesting positive trend was also seen for the K^+ % vs time over the reviewed period. This may be attributed to a potential increase in biomass and coal combustion due to increasing population.

Of particular interest is the increase in known ions % (Fig. 4.12D) over time, demonstrating that the inorganic fraction is contributing to a larger fraction of the $\text{PM}_{2.5}$ mass (study D3 which only

measured NO_3^- and SO_4^{2-} has been highlighted by a yellow circle). This is significant because as the inorganic fraction increases, so does the hygroscopicity of the aerosol (and therefore its physical and chemical properties), inducing changes in climate affects, health exposure risk etc. As the hygroscopicity increases, this may lead to a higher proportion of toxic gaseous constituents being absorbed by the aerosol, increasing particle toxicity. During the DPOM campaign and the Diwali period sampling by Shivani et al., (2019)²⁸⁹, known ions % do not follow this trend. This may be explained by severely increased primary VOC pollution levels occurring over the Diwali period which dominate the aerosol, reducing known ions % fraction, which is reflected in the other ions also.

4.3.2.3 Beijing Winter

The change in $\text{PM}_{2.5}$ composition as a function of time using available literature studies of ion measurements in Beijing during the winter seasons is shown in Fig. 4.13. The symbols adjacent to the pie charts resemble the sampling site and conditions, as previously described in section 4.3.1.2. The time points are the calculated mid-points from studies (analogous to section 4.3.1). The composition of $\text{PM}_{2.5}$ during the APHH BWIN campaign is also shown. For clarity, the $\text{PM}_{2.5}$ particle composition from the APHH BWIN campaign has a red arrow pointing to it in Fig. 4.13.

The maximum known ions % in the reviewed studies was seen in the work of Xu et al., (2019)¹⁹⁰ (B30D) who reported 75.29 % and the minimum was 19.22 % (B1B) reported by Sun et al., (2006)¹⁸⁵. This therefore resulted in a wide range of 56.07 % across the literature in Fig. 4.13. Across all studies (excl. BWIN) the average known ions % fraction contribution to $\text{PM}_{2.5}$ was 33.36 % ($\text{SD} \pm 12.65$ %). The BWIN campaign had an average known ions % of 35.67, which was therefore very close to this mean.

The maximum Cl^- % observed in Fig. 4.13 was 4.93 % in study B10A by Li et al., (2019)³⁸⁸. The minimum Cl^- % was seen by Shao et al., (2018)³⁹⁴ in study B20E who reported 1.25 %. The average Cl^- contribution over the non-specified studies was 3.25 % ($\text{SD} \pm 1.31$ %) which compares to the average between the haze periods of 2.65 % ($\text{SD} \pm 0.57$ %) and shows that between the studies reviewed here (Fig. 4.13) the haze periods generally have a lower fraction of Cl^- compared to the non-specified periods. This is likely because during haze periods higher levels of oxidation occur and therefore the $\text{PM}_{2.5}$ is more likely to demonstrate a higher proportion of secondary oxidised ions such as NO_3^- and SO_4^{2-} , compared to ions that come from a non-oxidative source, such as Cl^- . This is also likely the reason why the BWIN Cl^- (3.96 %) had a considerably higher fraction compared to the haze Cl^- fractions in the work of Shao et al., (2018)³⁹⁴ and Xu et al., (2019)¹⁹⁰. The average Cl^- % fraction across all studies (excl. BWIN) was 3.07 % ($\text{SD} \pm 1.11$ %), for which the BWIN Cl^- % was within the mean plus 1 SD.

The maximum NO_3^- % fraction was 35.59 % by Xu et al., (2019)¹⁹⁰ (B30D) which took place during a clean period, just after the APHH BWIN campaign. The lowest NO_3^- % contribution to $\text{PM}_{2.5}$ was

Beijing Winter PM_{2.5} Composition Timeline

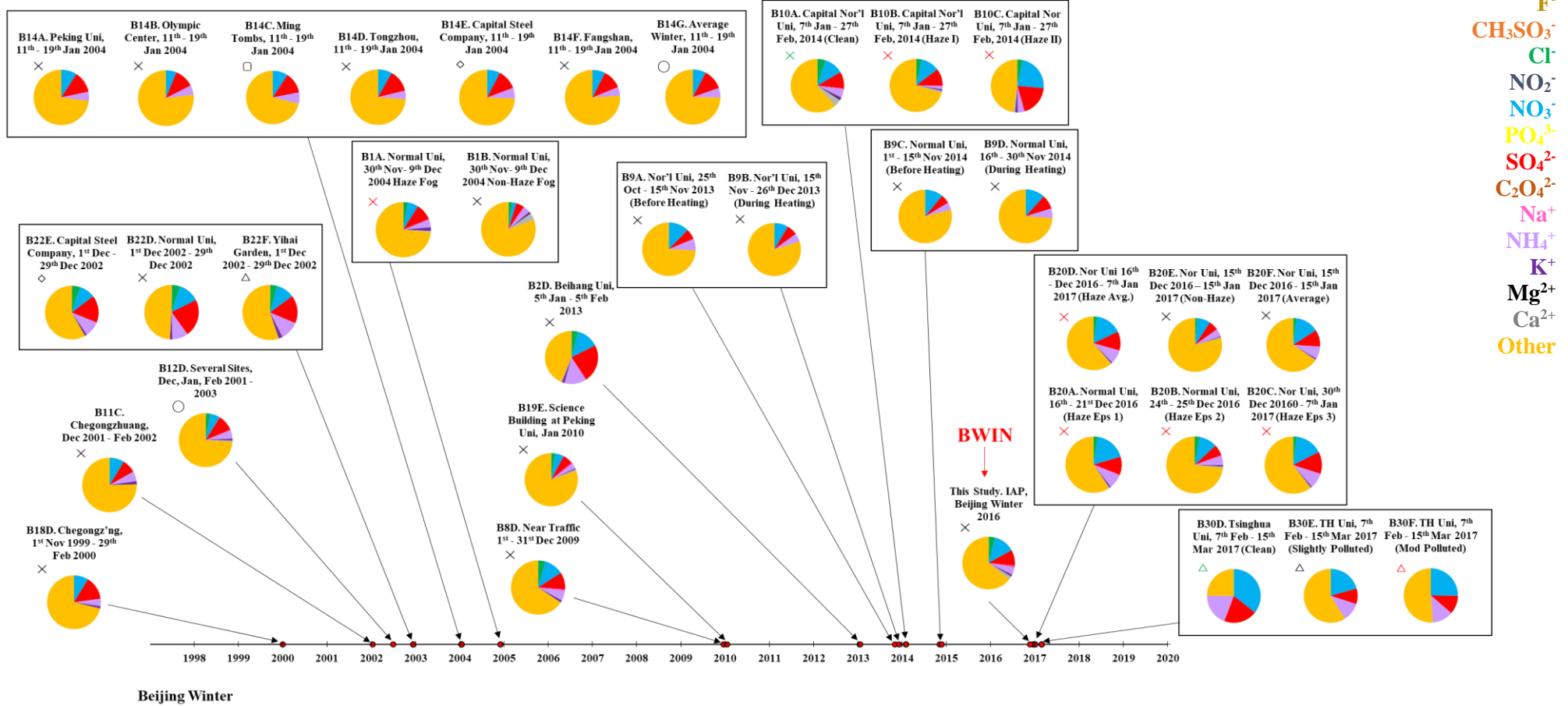


Fig. 4.13. Timeline showing the change in PM_{2.5} particle composition as a function of time within the Beijing Winter season. The symbols next to the pie charts represent the type of site for which Urban (x), Suburban (Δ), Rural (□) and mixed (O) are included. The colours indicate atmospheric conditions including black (non-specific period), red (haze period), light blue (pollution control period) and green (clean period). The APHH average is highlighted (BWIN). Time of sampling is shown along the x-axis. The study code along with the specific sampling site and time are also presented above each pie chart. The species presented are coloured in the pie charts, as per the key shown in the top right.

seen by Sun et al., (2006)¹⁸⁵ in study B1B who reported 2.56 %. The average NO_3^- % over all reviewed studies (excl. BWIN) was 11.86 % (SD \pm 6.48 %) and the BWIN NO_3^- % fraction (12.70 %) was therefore within 1 SD of this.

The maximum SO_4^{2-} % was 23.00 %³⁸² and the minimum was 4.66 %¹⁸⁵. Furthermore, the BWIN SO_4^{2-} average of 9.71 % was very close to the mean value across all studies (excl. BWIN) of 11.42 % (SD \pm 4.64 %).

The maximum NH_4^+ % contribution was 19.51 %¹⁹⁰ and the minimum was 2.07 %³⁸⁸. The BWIN NH_4^+ average of 4.84 % was relatively close to most other studies, for which an average of 6.93 % (SD \pm 3.45 %) was calculated across all publications presented (excl. BWIN). Specifically, the BWIN NH_4^+ % was very close to the values by Shao et al., (2018)³⁹⁴ who reported 4.55 % (non-specific period) as well as 5.37 % (haze periods).

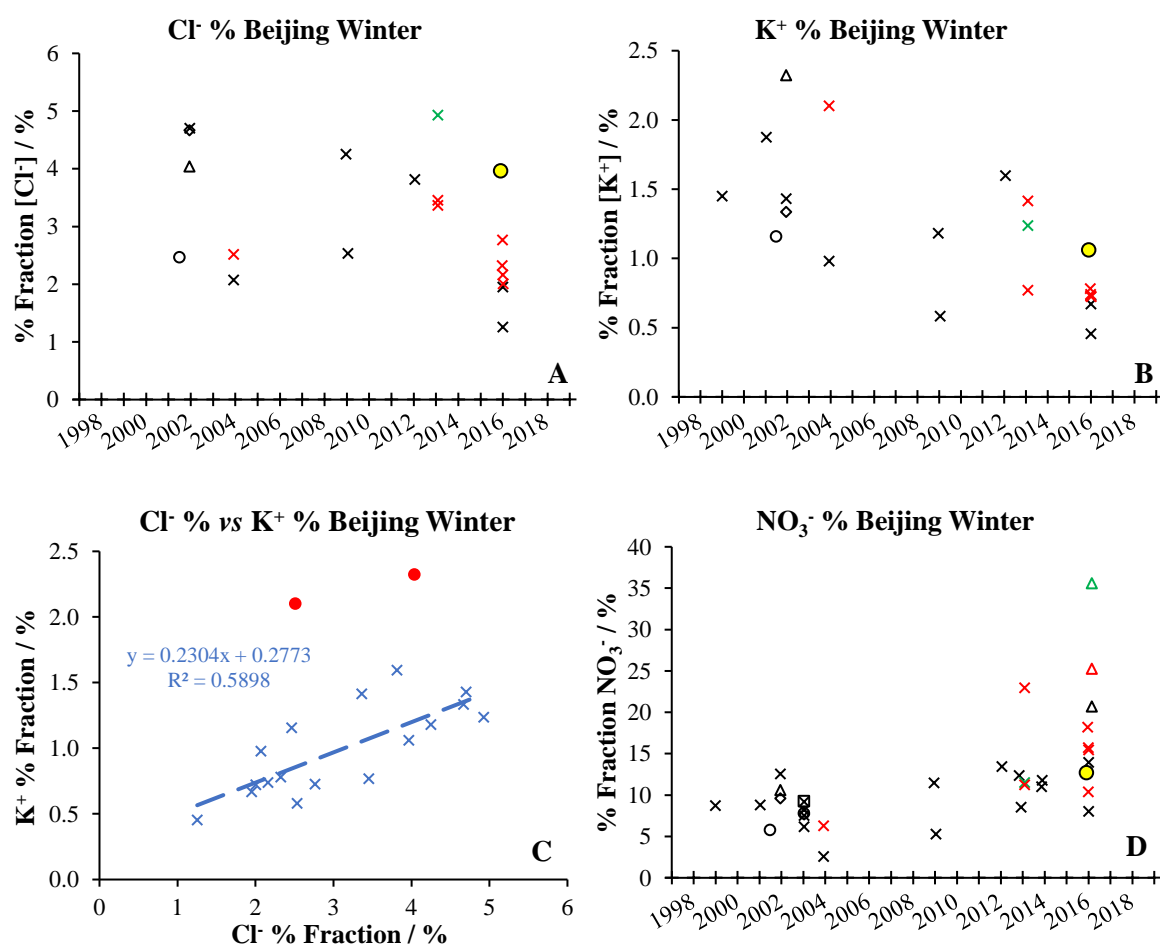


Fig. 4.14. The change in Cl^- %, K^+ %, and NO_3^- % by time, as well as Cl^- % vs K^+ % (C) reported by reviewed studies (Beijing winter seasons). For plots A, B and C, the shapes of the data points represent the type of site for which Urban (\times), Suburban (Δ), Rural (\square) and mixed (O) are included. The colours indicate atmospheric conditions including black (non-specific period), red (haze period), light blue (pollution control period) and green (clean period). The APHH average is shown as a yellow data point. Time of sampling is shown along the x-axis. The associated SD for the reviewed studies are found in the appendix tables and the APHH errors are found in chapter 3.

When investigating the change in ionic fraction as a function of time, the only species that showed significant correlations over time were Cl^- % ($R^2 = 0.46$) and K^+ % ($R^2 = 0.44$), which both observed negative trends (Fig. 4.14A and Fig. 4.14B, respectively). A significant correlation is also observed between the literature values of Cl^- % vs K^+ % fraction shown in Fig. 4.14C. When two anomalies are removed (shown as red dots in Fig. 4.14C), the linear regression coefficient improves to $R^2 = 0.59$. Therefore, over the past *ca.* 20 years during the Beijing winter season, the fraction of $\text{PM}_{2.5}$ from K^+ and Cl^- , or potentially even KCl , has decreased. Similar sources for Cl^- and K^+ include biomass and coal combustion. A recent study by Sun et al., (2020)³⁷³ also observed a general decrease in the Cl^- % fraction contribution, within PM over the years 2013 – 2020 between Jan – Mar (by 4 – 6 %). This is therefore consistent with the review of studies completed in this section (Fig. 4.13).

Sun et al., (2020)³⁷³ also report increases in NO_3^- % from 2013-2015 until 2018 – 2020 by 8-10 % from AMS data across the Chinese New Year period as well as a non-heating period. The annual increase in NO_3^- was seen for each sampling season. In the literature review conducted in this thesis, a very weak positive correlation is observed between NO_3^- % vs time (Fig. 4.14D). Furthermore, Sun et al., (2020)³⁷³ also observed a slight increase in NH_4^+ between 2012 and 2020, although no correlation ($R^2 = 0.0051$) was observed between the reviewed studies in this thesis for NH_4^+ % vs time. The other species observed no trends of interest in this analysis. The known ions % as a function of time showed no significant trend in the studies reviewed. This appears to disagree with the work of Lang et al., (2017)²⁶⁸ who indicate that in Beijing between 2000 – 2015, the SIA fraction (annual average) increases by 0.7 % year⁻¹.

4.3.2.4 Beijing Summer

Fig. 4.15 shows the change in $\text{PM}_{2.5}$ composition as a function of time during the summer seasons in Beijing. The symbols adjacent to the pie charts resemble the sampling site and conditions, as previously described in section 4.3.1.2. The APHH BSUM campaign is also included, which overlapped the sampling period of Xu et al., (2019)¹⁹⁰.

The known ions % fraction of the BSUM campaign was 62.53 % and was within range of the maximum reported in study B14I (78.91 %) and the minimum in study B24B (23.57 %). The average known ions % over all the reviewed studies (excl. BSUM) was 52.38 % ($\text{SD} \pm 14.01$ %) for which the BSUM known ions % was ~1.2 times larger.

The maximum Cl^- % over the summer seasons was 2.50 % (B22A). The minimum Cl^- % was 0.22 % (B19C) which resulted in a range across the review of 2.28 %. The BSUM Cl^- % was 1.20 % which lies within the range of the reviewed values. The average Cl^- % across all reviewed studies (excl. BUSM) was 1.24 % ($\text{SD} \pm 0.79$ %) and therefore for was very close to the BSUM average.

The maximum NO_3^- % out of the studies reviewed was 24.42 % (B25A). The minimum NO_3^- % was 2.56 % (B29A), producing a range of 21.86 %. The average NO_3^- % across all reviewed studies (excl. BSUM) that reported NO_3^- was 12.66 % ($\text{SD} \pm 5.47$ %) and therefore the BSUM NO_3^- % (20.21 %)

Beijing Summer PM_{2.5} Composition Timeline

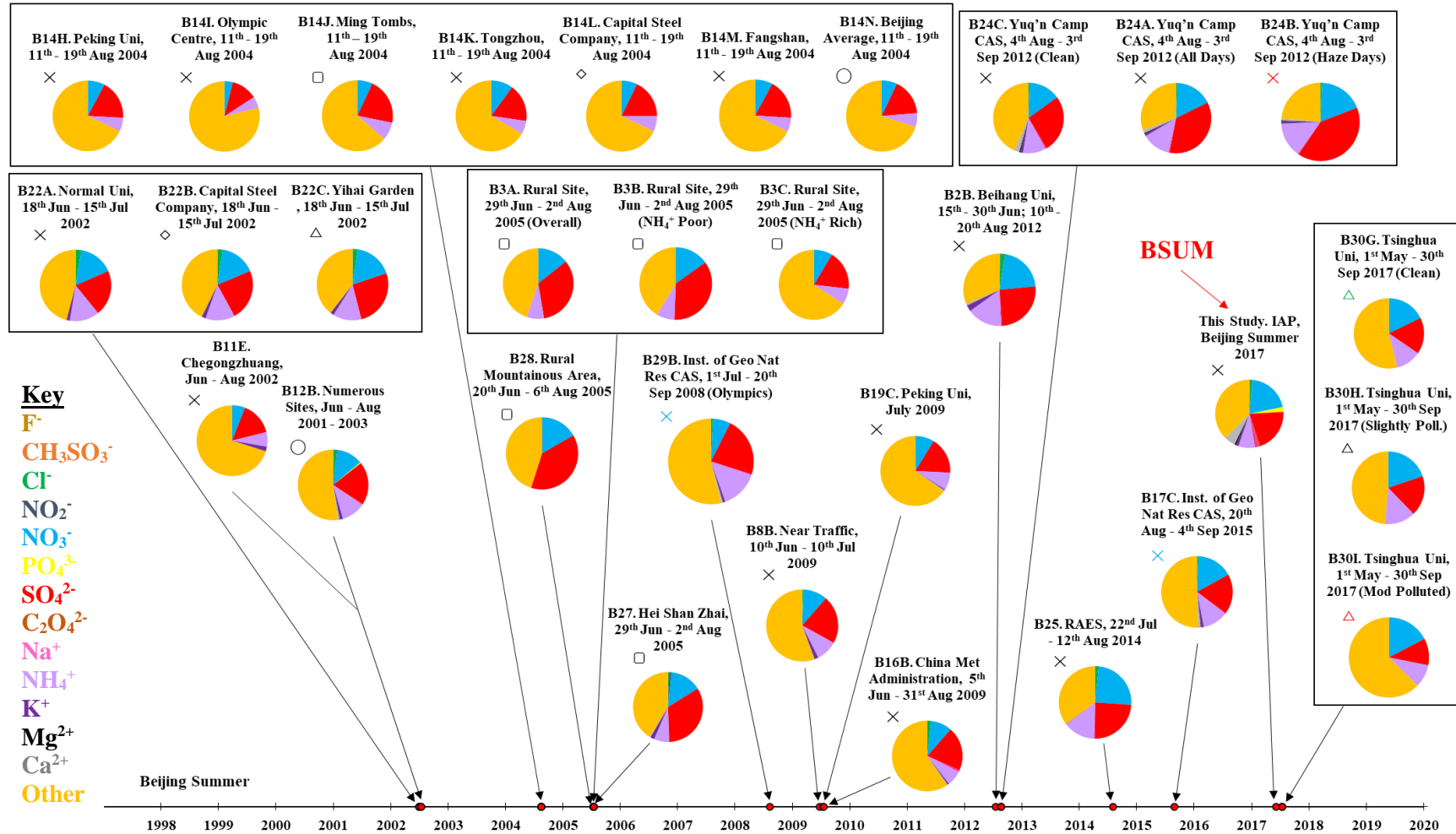


Fig. 4.15. Timeline showing the change in PM_{2.5} particle composition as a function of time within the Beijing Summer season. The symbols next to the pie charts represent the type of site for which Urban (x), Suburban (Δ), Rural (□) and mixed (O) are included. The colours indicate atmospheric conditions including black (non-specific period), red (haze period), light blue (pollution control period) and green (clean period). The APHH average is highlighted (BSUM). Time of sampling is shown along the x-axis. The study code along with the specific sampling site and time are also presented above each pie chart. The species presented are coloured in the pie charts, as per the key shown in the bottom left.

was significantly larger than this average. In comparison to other measurements, during the same summer, very good agreement was seen with the work of Xu et al., (2019)¹⁹⁰ who reported an average NO_3^- % of 19.86 % for 1st May - 30th Sep 2017 at THU (slightly polluted period).

The study that showed the maximum SO_4^{2-} % was B24B by Zhang et al., (2016)¹⁹² who reported 40.33 %. The minimum SO_4^{2-} % was reported by Xu et al., (2019)¹⁹⁰ in study B30I (10.82 %). Both the maximum and minimum SO_4^{2-} % reported here were classified as haze periods and the APHH BSUM average of 20.71 % sits within this range. Comparing to the work of Xu et al., (2019)¹⁹⁰ who reported a SO_4^{2-} % of 17.90 % over the summer of 2017 also, the BSUM average is good agreement. The average SO_4^{2-} % across all reviewed studies (excl. BSUM) was 23.17 % (SD \pm 8.08 %) and therefore the BSUM average was very close to this mean.

The maximum NH_4^+ % was 15.68 % by Wang et al., (2015)³⁸² (B2B). The smallest NH_4^+ % was 5.27 % (14I) in the work of Song et al., (2007)³⁹⁰. The APHH BSUM NH_4^+ % contribution (7.80 %) value was the lowest observed out of the 2017 values, for which the closest other study was B30G (clean period) by Xu et al., (2019)¹⁹⁰ who reported 11.61 %. The average NH_4^+ % across all reviewed studies (excl. BSUM) in Fig. 4.15 was 9.96 % (SD \pm 3.25 %) and therefore the BSUM NH_4^+ % average was relatively close.

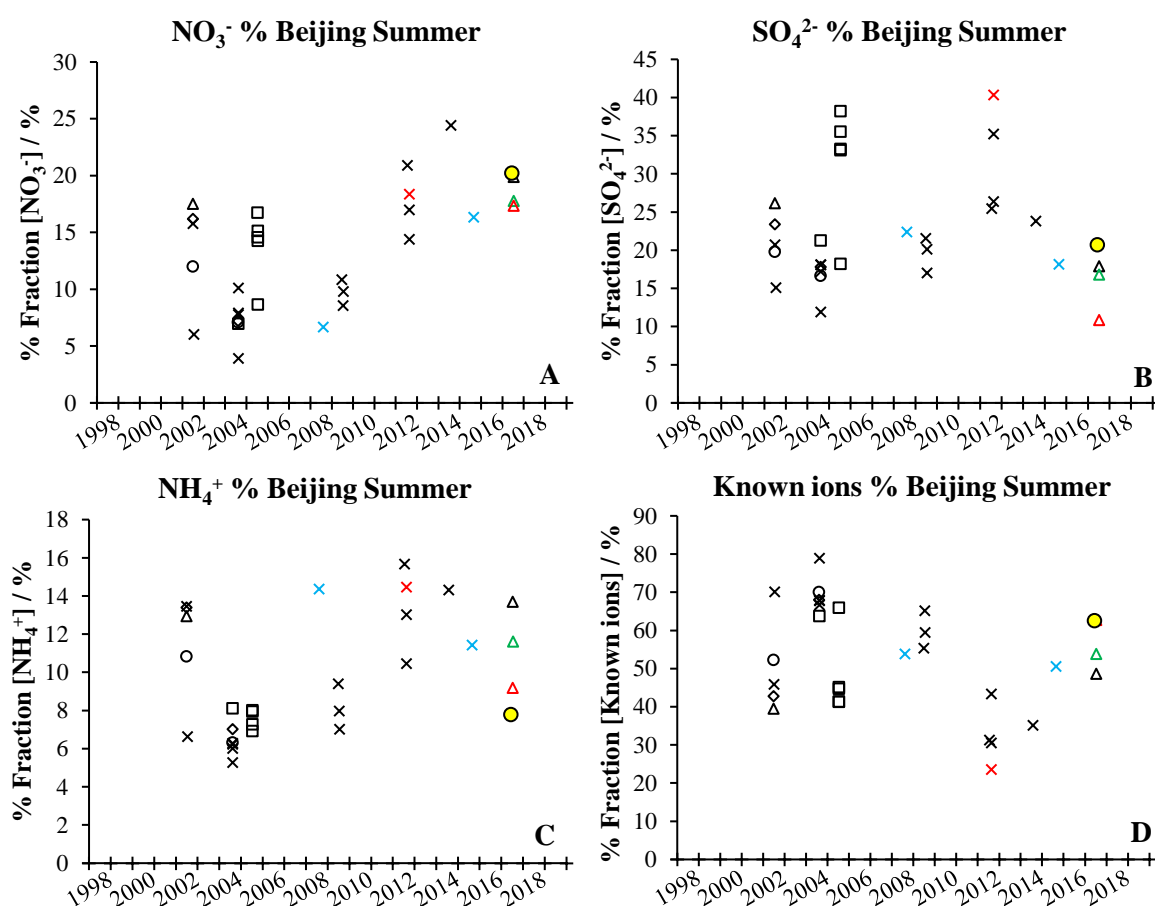


Fig. 4.16. Change in NO_3^- %, SO_4^{2-} %, NH_4^+ % and known ions % by time reported by reviewed studies (Beijing summer seasons). The shapes of the data points represent the type of site for which Urban (x), Suburban (Δ), Rural (\square) and mixed (O) are included. The colours indicate atmospheric conditions including black (non-specific period), red (haze period), light blue (pollution control period) and green (clean period). The APHH average is shown as a yellow data point. Time of sampling is shown along the x-axis. The associated SD for the reviewed studies are found in the appendix tables and the APHH errors are found in chapter 3.

Fig. 4.16 shows the change in [ion %] by time for NO_3^- , SO_4^{2-} , NH_4^+ , and overall ions. Considering the difficulty of this analyses and the numerous uncertainties which may arise, a weak positive correlation was observed for NO_3^- % vs time trend (Fig. 4.16A). It is however very difficult to depict a trend in the SIA species due to the extent of scatter in the data. The known ions % was also seen to decrease over the past two decades, although the most recent data is observed above the trendline. Therefore, much longer-term data is required for definite conclusions. The positive correlation in NO_3^- could be down to an increase in oxidation and atmospheric oxidation capacity, which may be reflected in the increasing in ozone concentrations observed in the Beijing-Tianjin-Hebei region in recent years^{416,417}. This is however speculative due to the very weak positive correlation observed in NO_3^- as well as the almost no correlation seen in SO_4^{2-} or NH_4^+ as a function of time. Finally, the change in $\text{PM}_{2.5}$ composition for the Beijing spring and autumn seasons (Fig. QQ) as well as the annual change (Fig. RR) is shown in the appendix for the interest of the reader.

4.3.3 Comparison Challenges

Particles were seen to be very variable in mass concentration and composition of the major ions (Cl^- , NO_3^- , SO_4^{2-} and NH_4^+) across the reviewed studies in both Delhi and Beijing for all four seasons. Finding spatio-temporal variation in mass concentrations and % compositional data within the available studies was very challenging. This is down to numerous factors including; the very varying meteorology which has a direct impact on $\text{PM}_{2.5}$ levels and partitioning into the aerosol phase; the different sampling times between studies within seasons; the different locations of sampling; and different sampling times at locations. Using this dataset was very challenging.

Furthermore, no specific dates of sampling are given in the majority of the studies reviewed in Delhi. In addition, the work by Bisht et al., (2015)³⁷⁶ is the only study in this review that splits their data into day and night. Many studies conducted in Delhi are very ambiguous regarding sampling timings. In some cases, studies reported average concentrations from overlapping seasons making it very difficult to accurately assign studies to their respective seasons. For example, the work by Saxena et al., (2017)¹⁹⁸ describe Delhi as experiencing four seasons of summer (Apr – Jun); monsoon (Jul – Sep); winter (Oct – Jan); and spring (Feb – Mar) which is inconsistent with other works such as Bisht et al., (2015)³⁷⁶ that describe the seasons in Delhi as winter (Dec – Feb); Summer (Mar – Jun); Monsoon (Jul – Sep); and post-monsoon (Oct – Nov). Other studies such as study D6 by Sharma et al., (2017)³⁷⁷ only describe 3 seasons which are the summer (pre-monsoon) season as Mar – Jun; the monsoon season as Jul – Oct; and the winter season as Nov - Feb. This brings difficulty for the accurate comparison between studies.

Furthermore, the differences in sampling duration make comparison difficult. For example, the average values obtained during the APHH DPOM campaign is likely to be skewed more greatly by the high concentrations at the end of November, compared to study D14 by Jain et al., (2020)³⁸¹ which sampled over a greater sampling period (Oct - Dec). Some studies such as study D9¹¹⁰ describe only winter (15th Dec 2013 - 15th Jan 2014) and summer (15th - 30th Jun 2014), for which only a very small window of time is sampled compared to most other studies. This is also true for the APHH

DPEM campaign that only sampled for one week (28th May – 5th Jun 2018). In addition, despite the work by Shivani et al., (2019)²⁸⁹ being segregated as the Diwali period, many other studies average their post-monsoon seasons across many months which incorporate non-Diwali and Diwali periods together.

Other studies take the averages of seasons over numerous years which is unsuitable for comparison in these analyses. These studies include Saraswati et al., (2019)³⁷⁴, Sharma et al., (2017)³⁷⁷, Saxena et al., (2017)¹⁹⁸ and Sharma et al., (2016)³⁷⁸. As an example, the work by Saraswati et al., (2019)³⁷⁴ report average values of PM_{2.5} and ionic species during the seasons of winter (Nov – Feb), summer (Mar – Jun), and monsoon (Jul – Sep) between Jan 2013 and Dec 2015.

In addition, sampling sites in Delhi were also very diverse and spread out across the city (Fig. 4.1). In different locations, different emission sources dominate and therefore this has the potential to skew the means of results. Moreover, very few studies have been conducted in Delhi compared to Beijing also making this task very challenging. A two year gap also occurs between the last work shown by Shivani et al., (2019)²⁸⁹ and the APHH DPEM and DPOM studies and generally very few studies were available in the literature.

A much more comprehensive set of studies was available for the Beijing review and the studies were conducted over a much longer period (*ca.* past 20 years). Another advantage in the Beijing dataset is that most studies gave exact dates of sampling. Furthermore, some studies reported ion concentrations although no PM_{2.5} concentrations. Although long term data helps to build an understanding of the change in concentrations of species as a function of time, the accuracy of data reported (and instrumentation used) for the older studies will not be to the same quality as for the more recent studies, potentially affecting the historical plots and overall comparisons.

Further difficulties arose in the Beijing review in assigning whether a study was conducted strictly during a haze period, clean period, non-specific period or whether the sampling site was strictly rural. Whether a study was defined as a haze period was subjective between studies making comparison ambiguous. For example, the work by Zhang et al., (2016)¹⁹² suggests that a haze period is when the visibility is no more than 10 km with RH % <90%, which was a method also used by Wu et al., (2007)⁴¹⁸. The work by Xu et al., (2019)¹⁹⁰ 2019 however segregates the data into clean periods (PM_{2.5} ≤ 75 μg m⁻³); moderately polluted periods (75 μg m⁻³ ≤ PM_{2.5} ≤ 115 μg m⁻³); and moderately polluted periods (PM_{2.5} 115 μg m⁻³); and the work by Shen et al., (2017)²⁹¹ describes haze as visibility < 10 km, but haze events as occurring on days in which the visibility is constantly < 5 km over a 6 hour period (also seen in the work by Sun et al., (2006)¹⁸⁵). In other studies, such as Li et al., (2019)³⁸⁸, no definition of haze is given. Furthermore, the some studies may have occurred over haze episodes which were not declared and individual studies that are non-specific may have had varying amounts of haze.

The description of some sampling sites was also very ambiguous. For example, for study B12D by Wang et al., (2005)²⁰⁰, these values were taken as an average between BNU, CSC, YG, MY and PG

which mixes both urban and rural sampling sites (Fig. 4.2). Therefore, this mixes city centre and rural sites. Finally, it should also be noted that the description of specific details in some studies may make comparison challenging. For example, in study B10C³⁸⁸, the site is described as Capital Normal University, (39°58'N, 116°22'E). There is however a confliction here as the coordinates do not agree with the location of CNU in Beijing.

In both Delhi and Beijing further complications arise from comparing the known ions % fractions. Not all studies measured the same ions although most did measure the major ions (Cl^- , NO_3^- , SO_4^{2-} and NH_4^+) which make up the largest contribution of inorganic species to $\text{PM}_{2.5}$ in all studies. For example, in Delhi study D3 by Bisht et al., (2015)³⁷⁶ only ions NO_3^- and SO_4^{2-} were measured and therefore assuming that the rest of the $\text{PM}_{2.5}$ was made up of just organic material would be false. For better understanding of the change in % fraction and mass concentration as a function of time, more data is needed under more consistent segregation variables where possible to be able to establish the change of mass concentration and % fraction of ions as a function of time.

4.4 Conclusion

In summary, this chapter explores the literature of inorganic $\text{PM}_{2.5}$ and compares the mass and % fraction contribution to $\text{PM}_{2.5}$ of individual species to the APHH results presented in chapter 3. This literature data (as well as APHH data) was plotted against time in the attempt to observe a change in concentrations and evolution of $\text{PM}_{2.5}$ within Beijing and Delhi. For most species, no mass or % fraction correlations were observed against time. Completing analyses of the change in species concentration and fraction contribution to $\text{PM}_{2.5}$ is very challenging. The main uncertainties revolve around different sampling times within seasons and sampling durations; different locations of sampling; quality of publication analyses; as well as literature availability. The age of instrumentation and scientific techniques have also vastly improved in the past 20 years and therefore earlier studies are associated with more error. It is recommended that this sort of analysis is not completed for any other city.

The analysis showed that over the Delhi pre-monsoon seasons, SIA showed decreases as a function of time which matched the pre-monsoon overall trend in $\text{PM}_{2.5}$. The decrease in SIA (and therefore $\text{PM}_{2.5}$) was attributed to the hypothesis that acidic gases had decreased over time due to fewer atmospheric oxidative species which may be caused by an increase in NO_x . This is also suspected to be the reason for the decrease in $[\text{NO}_3^-]$ and $[\text{SO}_4^{2-}]$ for the post-monsoon seasons also. In addition, a decrease in $[\text{SO}_4^{2-}]$ over time during both seasons could have been down to a reduction of sulfur in fuel. During the post-monsoon period, the $[\text{Cl}^-]$, and $[\text{NH}_4^+]$ showed increases over 3 years, which suggests an increase in anthropogenic activities that emit the precursors to these species such as biomass and coal burning. In contrast, no correlations (with time) were seen for either of the Beijing campaigns for the major ion concentrations, although the APHH average concentrations were in good agreement with other studies.

For the Delhi post-monsoon season data, a decrease in NO_3^- % and SO_4^{2-} % was seen which indicated a reduction in SIA contribution to the $\text{PM}_{2.5}$ over this time-period. K^+ % increased during post-monsoon seasons which indicated a potential rise in biomass or coal burning contribution to $\text{PM}_{2.5}$ over the 3 years reviewed. Winter seasons in Beijing showed a reduction in the Cl^- % and K^+ % with time, as well as a strong positive relationship for Cl^- % vs K^+ % indicating that these species came from the same sources (most likely biomass and coal burning emission contribution to $\text{PM}_{2.5}$ during the Beijing winter seasons over the past *ca.* 20 years).

A possible increase in NO_3^- % contribution to $\text{PM}_{2.5}$ was seen in the summer seasons in Beijing which could be down to the general increasing ozone concentrations found in the Beijing-Tianjin-Hebei region. Although very few significant trends were observed in this chapter, a comprehensive set of data was obtained for the APHH Delhi and Beijing campaigns. To investigate the inorganic fraction of $\text{PM}_{2.5}$ in within Asian megacities further, chapter 5 explores the sources and chemistry surrounding the major ions during APHH Delhi and Beijing.

5 Investigation and Interpretation of the inorganic PM_{2.5} species concentrations and compositions within Delhi and Beijing: Implications and Comparisons on the Ammonium Aerosol system

5.1 Introduction

PM_{2.5} pollution is widely acknowledged to induce adverse effects on climate, visibility and human health^{26,326}. Specifically, Secondary Inorganic Aerosol (SIA) is known to comprise between 20-60% of PM_{2.5} and therefore makes up a substantial fraction of this pollutant^{26,388,326}. SIA constitutes NH₄⁺, Cl⁻, NO₃⁻ and SO₄²⁻ and the formation of these species is a direct contributor to [PM_{2.5}]^{419,26}. Consequently, the understanding of the formation pathways of these constituents within PM_{2.5} in Asian Megacities with dangerously high levels of [PM_{2.5}] is a vital area of research. The formation of these species is principally affected by the relative levels of gaseous HCl, HNO₃, H₂SO₄ and NH₃. The acidic gases neutralise NH₃ (the most abundant basic gas) forming ammonium salts in the particle phase^{326,26,420}. The products of these reactions are NH₄Cl and NH₄NO₃ (in reversible equilibrium)^{421,422} as well as NH₄HSO₄ followed by (NH₄)₂SO₄ on full H₂SO₄ neutralization^{422,330,26} (non-reversible)^{423,327}. It is widely accepted in the literature that H₂SO₄ will react preferentially with NH₃, followed by HNO₃ and HCl if excess NH₃ is available for neutralization^{327,421,26}. In addition, it is known that HNO₃ may react with other basic materials such as crustal species, minerals and sea-salt to produce NO₃⁻, and that H₂SO₄ (and (NH₄)₂SO₄) may react with basic carbonates such as MgCO₃ and CaCO₃, producing SO₄²⁻^{424,425,426,427}. In particular, the oxidation of NO₂ and reaction with NH₃ to produce NH₄NO₃ may affect the relative [NO₂] gas and therefore the NO_x / O₃ cycle. Furthermore, the oxidation of SO₂ to SO₄²⁻ directly impacts the radiative forcing potential of aerosol³³⁰ and SO₄²⁻ is known to act as Cloud Condensation Nuclei (CCN) which directly impacts the earth's albedo⁴²⁸. Therefore, the interaction of HCl, HNO₃ and H₂SO₄ with NH₃ may have great influence on air quality and climate and the understanding of this NH₄⁺ aerosol system is therefore an essential area of research.

The aims of this chapter include investigating the most likely routes of Cl⁻, NO₃⁻, SO₄²⁻ and NH₄⁺ into PM_{2.5} aerosol during the APHH Delhi Pre- and Post-Monsoon campaigns, as well as the Beijing winter and summer campaigns as to identify the most up to date sources of these species within polluted Asian megacities. This will be conducted by identifying the most likely pollution sources of Cl⁻ into PM_{2.5} by producing polar plots in conjunction with meteorological data; using indicator metrics such as the NOR, SOR and [NO₃⁻]/[SO₄²⁻] to confirm whether the majority of PM_{2.5} sampled in these megacities is from a primary or a secondary source; identifying whether other routes of major ion introduction into aerosol such as from acidic gas (HCl, HNO₃ and H₂SO₄) reaction with alkaline dust is a significant pathway of formation; exploring the potential pathways of formation of NO₃⁻ and SO₄²⁻ in more detail by correlating the determined NOR and SOR data with data from partners

during the APHH campaigns, such as temperature, RH, oxidant concentrations (i.e. HONO), particle diameter etc.; confirming that the formation of NH_4^+ is primarily from acid-base neutralisation reaction with acidic gases by conducting linear squared regression; and identifying whether weak acids contribute significantly to NH_3 neutralisation and NH_4^+ formation. In addition, this chapter also aims to evaluate the equilibrium conditions of the ammonium and acidic gas aerosol system in two highly polluted Asian megacities (Delhi and Beijing) which will give an indication as to whether NH_4^+ or the acidic gases should be reduced to aid depletion of $\text{PM}_{2.5}$ loading within two of the worlds most polluted megacities.

Therefore, to complete the objectives of this chapter, $[\text{Cl}^-]$ IC data was obtained from the APHH campaigns (chapter 3) in conjunction with meteorological data to try and observe the major sources of HCl within Delhi and Beijing. As NO_2 and SO_2 are generally at higher concentrations compared to HCl in an urban atmosphere with many more potential sources, the extent to which these species were oxidised to HNO_3 and H_2SO_4 has been quantified using the Nitrogen Oxidation Ratio (NOR) and the Sulfur Oxidation Ratio (SOR), respectively. These ratios have been applied in numerous studies including Lin et al., (2006)⁴²⁹, Kadowaki et al., (1986)⁴³⁰, Khoder et al., (2002)¹⁹⁷ and Hassan et al., (2013)¹⁴³. Furthermore, $[\text{NO}_3^-]/[\text{SO}_4^{2-}]$ was used to assess the relative contribution of mobile and stationary sources to $\text{PM}_{2.5}$. Following this, the secondary chemistry to SIA formation through relative levels of gaseous neutralization of these species under each set of atmospheric conditions has been investigated using linear regression analysis between NH_4^+ and the conjugate bases outlined.

By identifying the significant HCl point sources, NO_x and SO_2 oxidation levels and the regression correlations between NH_4^+ , Cl^- , NO_3^- and SO_4^{2-} (as well as effects of meteorology), an indication will be given as to which anthropogenic activities and gases in particular may have the greatest effect on the reduction of SIA within $\text{PM}_{2.5}$ (and therefore relative $[\text{PM}_{2.5}]$ within different seasons in Delhi and Beijing). Furthermore, an insight will be given to this vital ammonium system within two extremely polluted megacities and whether the level of pollution affects this system in anyway; an understanding which is also crucial for future atmospheric models. A particular novelty of this chapter is the investigation in the ammonium particle system by use of highly time resolved ambient $\text{PM}_{2.5}$ filter samples.

5.2 Experimental

The data represented in this chapter are associated with the experimental described in chapter 3.

5.3 Results and Discussion

5.3.1 Chloride

5.3.1.1 Non-Sea Salt Chloride

In some instances in the analysis of inorganic ion species researchers calculate the sea-salt contribution of specific ions in a similar fashion to the calculation laid out by Farren et al., (2019)⁴³¹. This is so that any contribution from sea salt may be eliminated and corrected for, leaving the anthropogenic contribution of ionic species (such as Cl^-) to $\text{PM}_{2.5}$. This was deemed unnecessary in

this study as Beijing and Delhi are *ca.* 150 km and over 1000 km from the coast, respectively. In addition, Tiwari et al., (2009)²⁸⁸ state that a poor correlation between Na^+ and Cl^- implies Cl^- measured from non-sea salt sources. The Cl^- vs Na^+ correlation coefficient values obtained from the Delhi pre-monsoon (DPEM), Delhi post-monsoon (DPOM), Beijing winter (BWIN) and Beijing summer (BSUM) campaigns were 0.38, 0.03, 0.06 and 0.26 respectively (over entire campaigns). The night-time hours during the DPEM campaign did observe a correlation coefficient of 0.68 between these species, however this involved only 7 samples. In addition, Na^+ and Cl^- may also both originate from coal and biomass burning⁴³² (which are two much more likely sources of Cl^- and Na^+ in Delhi). Therefore, these calculations have not been completed for any ions in the four APHH campaigns presented in this chapter.

5.3.1.2 Major Chloride Sources

Analyses were completed to evaluate the major Cl^- sources in Delhi and Beijing for the day and night-time periods. This was conducted by retrieving the wind data associated with sampling times of filters and conducting polar contour plots in association with filter sample Cl^- concentrations. The polar contour plots were created using wind data collected by the Indira Gandhi International Airport (IGIA) (for DPEM) and the Centre of Hydrology and Meteorology (for DPOM, BWIN, and BSUM). In each contour plot, the *y*-axes represent the wind speed in ms^{-1} ; the *x*-axes show the wind direction vector; and the *z*-axes represent the relative concentration of Cl^- in $\mu\text{g m}^{-3}$ for which the relative colouration on the contour plot is defined by the colour gradient shown in the colour bar. To assess the most likely Cl^- sources during the day and night-time period in each campaign, the contour plots have been compared to maps of Delhi and Beijing representing the major likely Cl^- emission points sources.

5.3.1.3 Delhi

Fig. 5.1 shows the $[\text{Cl}^-]$ contour plots during the DPEM and DPOM day and night-time sampling periods. This is compared to the map of Delhi in Fig. 5.2 highlighting some of the most likely HCl emission sources.

The major industrial areas are found predominantly towards the north-west of Delhi^{108,109}, with three found towards the east (Friends Colony Shahdara Industrial Site, Jhilmil Colony Industrial Area and Patparganj Industrial Area) and two found towards the south-east-south of the IGDTUW sampling site, (Okhla Industrial Area and Mohan Cooperative Industrial Estate). A major power station (Badarpur Thermal Power Station) is also found towards the south-east-south of the city. A cluster of brick kilns is seen towards the north-west of the city just outside the Delhi perimeter. Three official waste incineration plants are located in the north-west (Narela-Bawana), the east-south-east (Ghazipur), and the south-east-south (Timarpur Okhla Waste Management Company Limited) of IGDTUW. Three official landfill sites are also located towards the northwest (Bhalswa), east-south-east (Ghazipur) and south-east-south (Okhla). Due to the proximity, the contribution of Cl^- to $\text{PM}_{2.5}$ measured during the APHH DPEM and DPOM campaigns may be heavily influenced by industrial areas such as the Flatted Factory Complex, Jhandewalan.

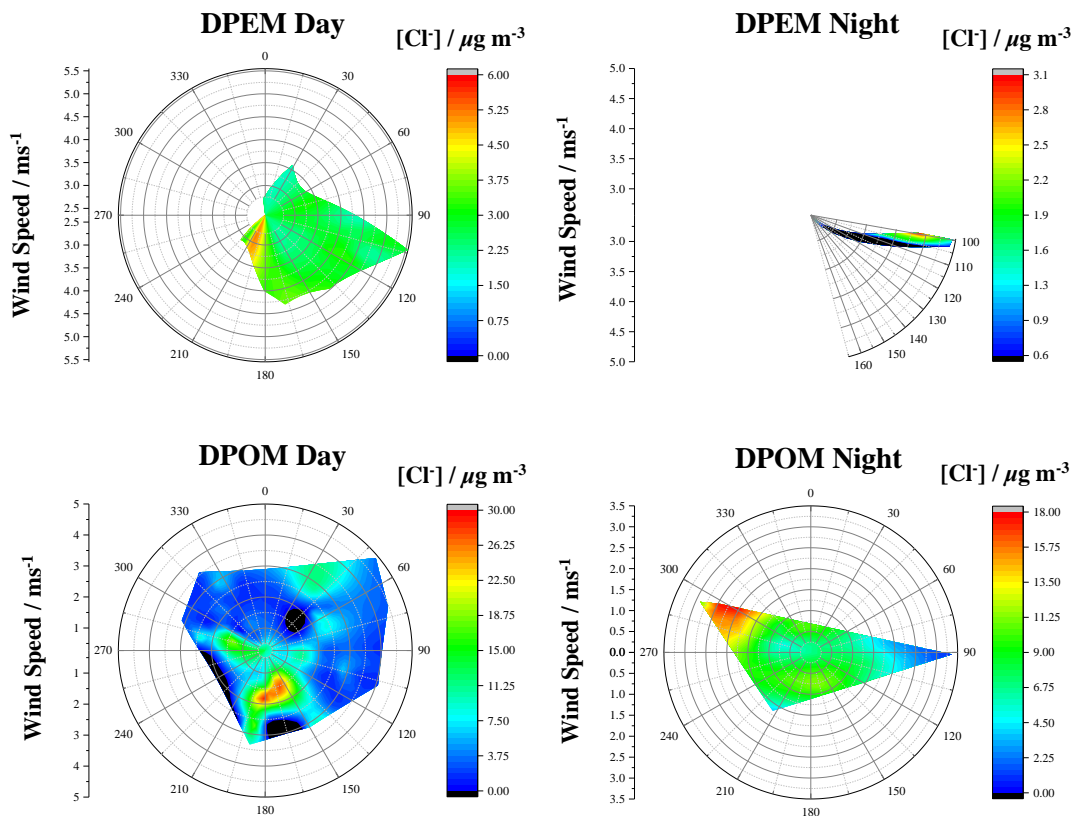


Fig. 5.1. Contour plots showing the [Cl⁻] in association with wind data averaged to the filter sampling times for the DPEM and DPOM, day and night-time periods. The [Cl⁻] is presented via a colouration scale (right) in these plots.

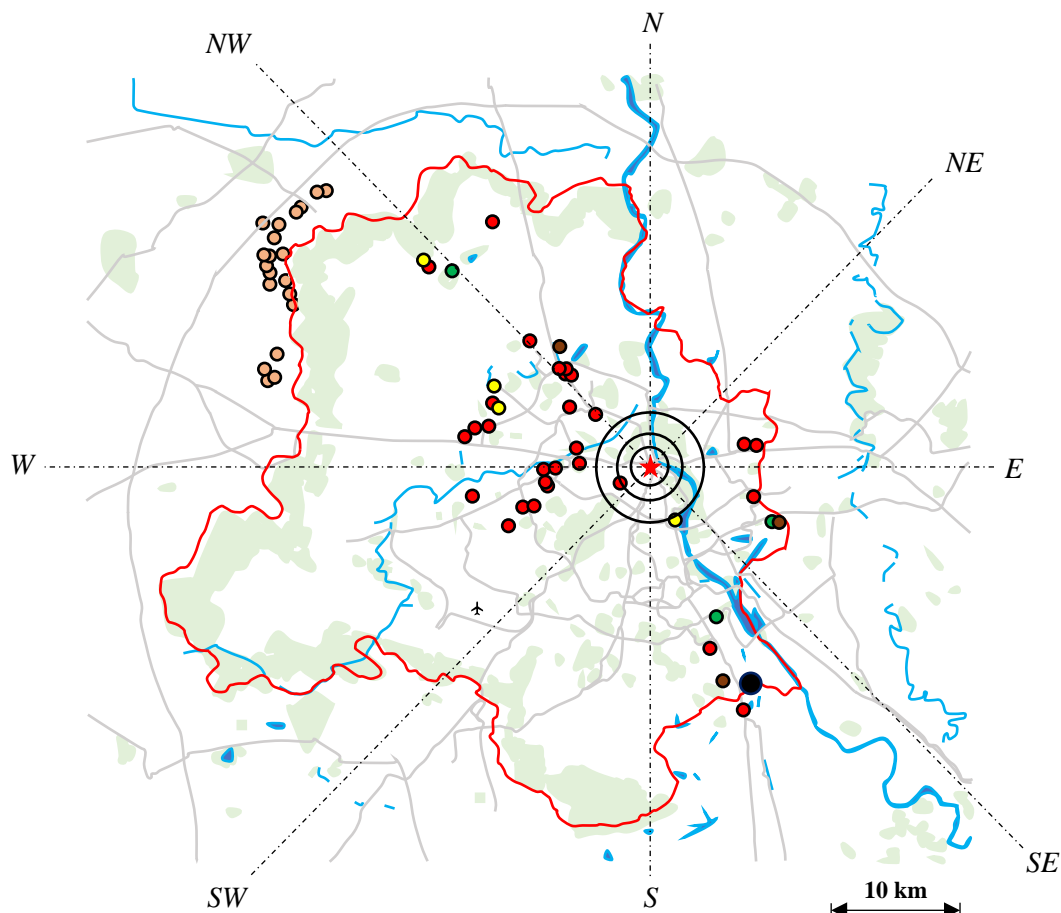


Fig. 5.2 Map of Delhi showing the key potential Cl⁻ emitters consisting of Official Industrial Areas (Red); Waste Incineration Plants (Green); Landfill Sites (Brown); Gas Power Stations (Yellow); Coal Power Stations (Large Black); and Brick Kilns (Beige). Grey lines show major roads, light green patches show green spaces and blue colouration indicates a body of water.

5.3.1.4 Delhi Pre-Monsoon

During the daytime (27 filter samples), these winds do not directly line up with any potential Cl^- sources marked in Fig. 5.2, although the industrial areas of Mayapuri Industrial Area Phase I, Mayapuri Industrial Area Phase II and Naraina Industrial Area Phase I are found towards the W-SW direction. The night-time Ion Chromatography (IC) data was associated with 7 filter samples and the limited data makes source apportionment suggestion challenging. To better understand the possible sources during the DPEM campaign, back trajectory analysis was conducted using the NOAA HYSPLIT model^{433,434,435} in conjunction with the relatively little data obtained during the DPEM campaign (specially for the night-time period). The results for the HYSPLIT analysis are shown in Fig. 5.3 and are compared to the DPEM total hours contour plot.

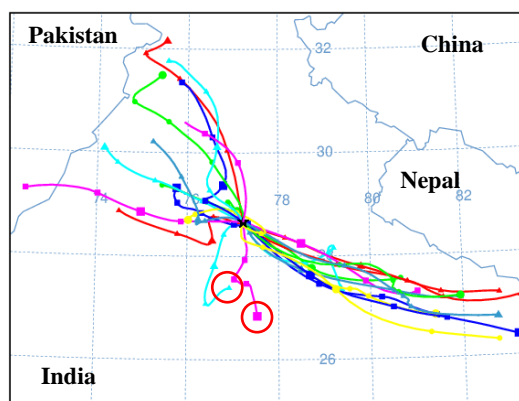


Fig. 5.3. NOAA HYSPLIT output for the DPEM campaign.

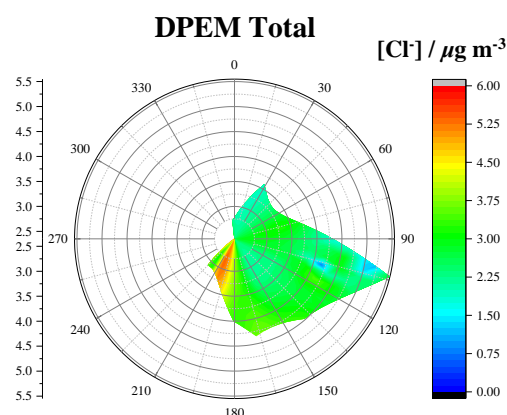


Fig. 5.4. Contour Plot of $[\text{Cl}^-]$ over the total DPEM campaign. The $[\text{Cl}^-]$ is presented via a colouration scale (right) in these plots.

The HYSPLIT model was run for back trajectory analysis from IGDTUW (black star at 28.6653°N , 77.2324°E) for the DPEM campaign. The meteorology dataset used for these trajectories was GDAS (1 degree, global, 2006-present). The end of the HiVol sampling during the DPEM campaign was 5th Jun 2018 at 12:30 (UTC) in which a new trajectory was started every 12 hours for a duration of 24 hours. The labelled intervals represent 6 hours periods. The colours of each trajectory are arbitrary. This is compared to the polar contour plot of the DPEM campaign over the total campaign period (day and night).

As can be seen in Fig. 5.3, most air masses originated from the NW and E-SE directions. The winds from the NW pass over many Cl^- emissions sources (industrial sites and brick kilns, Fig. 5.2) and air masses from the E-SE pass over an industrial site (Patparganj Industrial Area), a waste incineration plant (Ghazipur) and a land-fill site (Ghazipur). These sites may therefore have contributed to the Cl^- found in the detected DPEM $\text{PM}_{2.5}$.

It is however noticed that the highest overall DPEM $[\text{Cl}^-]$ emissions (Fig. 5.4) originate from the S-SW direction. Only two trajectories were detected by the HYSPLIT model which enter IGDTUW from the south and south west directions. These have been circled in Fig. 5.3. The back trajectories

show that these air masses may have passed over the coal power plant (Badarpur Thermal Power Station), two industrial sites (Okhla Industrial Area and Mohan Cooperative Industrial Estate) as well as a land fill site towards the south east of Delhi (Landfill Okhla). The wind speeds observed during the DPEM campaign were however very low at $< 6 \text{ ms}^{-1}$, which may indicate that the Cl^- more likely originated from much more localised sources. Most of the DPEM total contour plot observes a green colouration which indicates that most of the area surrounding IGDTUW was associated with concentrations surrounding $ca. 3.00 \mu\text{g m}^{-3}$. This indicates a ubiquitous and baseline $[\text{Cl}^-]$ emissions detected around IGDTUW. This is down to the abundant presence in Delhi of illegal, informal and much minor metal processing factories, e-waste recycling units, medical waste units, plastic processing units, and others³⁴⁷ which are all activities which use HCl^{347} .

5.3.1.5 Delhi Post-Monsoon

The contour plot for the DPOM daytime (Fig. 5.1) shows that a significant contribution of Cl^- came from the south of IGDTUW, with air masses reaching $> 25 \mu\text{g m}^{-3}$ (for 77 filter samples). No obvious Cl^- emission point sources are found directly below IGDTUW although a coal power plant, two industrial sites, a waste incineration and a landfill site are found towards the SE which may be contributing to Cl^- concentrations. To investigate this further, the NOAA HYSPLIT model was run a second time for the DPOM campaign and is represented in Fig. 5.6 and Fig. 5.5. The model was run using the same conditions as for the DPEM campaign (Fig. 5.3), although was run for 9th Oct 2018 – 23rd Oct 2018 (Fig. 5.6) and 23rd Oct 2018 – 6th Nov 2018 (Fig. 5.5), as the HYSPLIT mode is only capable of representing 24 back trajectories at once.

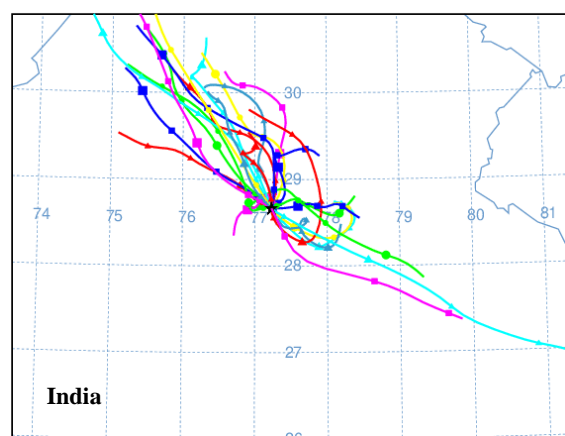


Fig. 5.6. HYSPLIT for IGDTUW for between 9th Oct 2018 – 23rd Oct 2018.

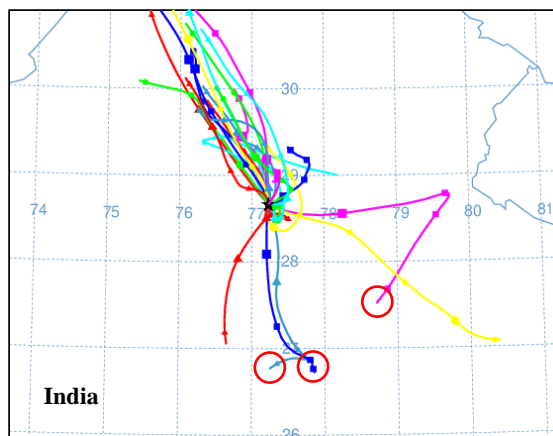


Fig. 5.5. HYSPLIT for IGDTUW for between 23rd Oct 2018 - 6th Nov 2018.

Fig. 5.5 shows instances in which air masses from the south originated from the direction of the power plant (highlighted by red circles). Three DPOM filter samples observed $[\text{Cl}^-] > 20 \mu\text{g m}^{-3}$ (red and yellow shading in the DPOM day contour plot in Fig. 5.1) which were associated with wind vectors 160, 182, and 190. Comparing these data to Fig. 5.5, it is probably that these very high Cl^- concentrations most likely originated from the coal power plant as well as the of other HCl emitters

mentioned which surround it. In addition to this, relatively high concentrations were also seen to be observed from the NW direction, with $[Cl^-]$ ranging from between $10 \mu\text{g m}^{-3}$ – $20 \mu\text{g m}^{-3}$. In addition, Fig. 5.6 and Fig. 5.5 demonstrate that prevailing winds also occurred from this direction. Therefore, during the daytime it may be suggested that a substantial emission of Cl^- originates from the majority of Delhi's major industrial sites, the cluster of brick kilns, as well as the waste incineration site (Bawana) situated towards the NW of Delhi. For the DPOM night-time periods (13 filter samples), Fig. 5.1 shows that the predominant Cl^- emission sources originate from the NW. Closer inspection of Fig. 5.1 shows that relatively similar Cl^- concentrations originate from the NW compared to daytime values, although that generally lower $[Cl^-]$ were observed from other directions. Gani et al., (2019)¹⁰⁸ and Jaiprakash., (2017)¹⁰⁹ also mention the release of HCl from industrial sources originating from the northwest of Delhi.

5.3.1.6 Beijing

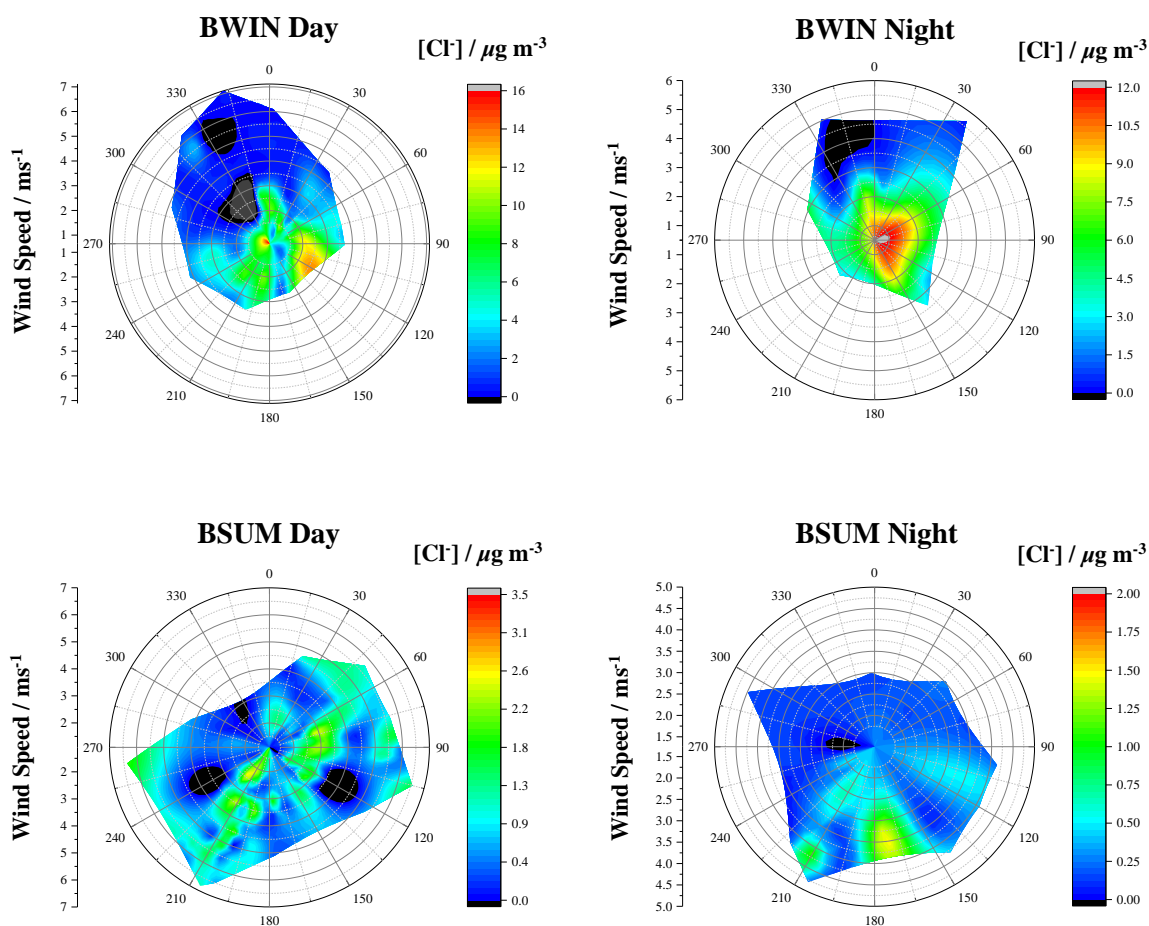


Fig. 5.7. Contour plots showing the $[Cl^-]$ in association with wind data averaged to the filter sampling times for the BWIN and BSUM, day and night-time periods. The $[Cl^-]$ is presented via a colouration scale (right) in these plots.

The contour plots (Fig. 5.7) were produced in the same manner as for the Delhi APHH campaigns. The map of Beijing in Fig. 5.8 also shows the potential major emission point sources of HCl in Beijing. The waste incinerators, landfill and composting sites were located using a study by Wang and Wang (2013)⁴³⁶. The exact locations of the other sites were found using Google Maps⁴⁰³. The

locations shown in Fig. 5.8 include waste incineration plants (green); landfill sites (brown); gas power stations (yellow); coal power station (black); and composting sites (purple). It was unclear from available sources where the major industrial areas were located in Beijing.

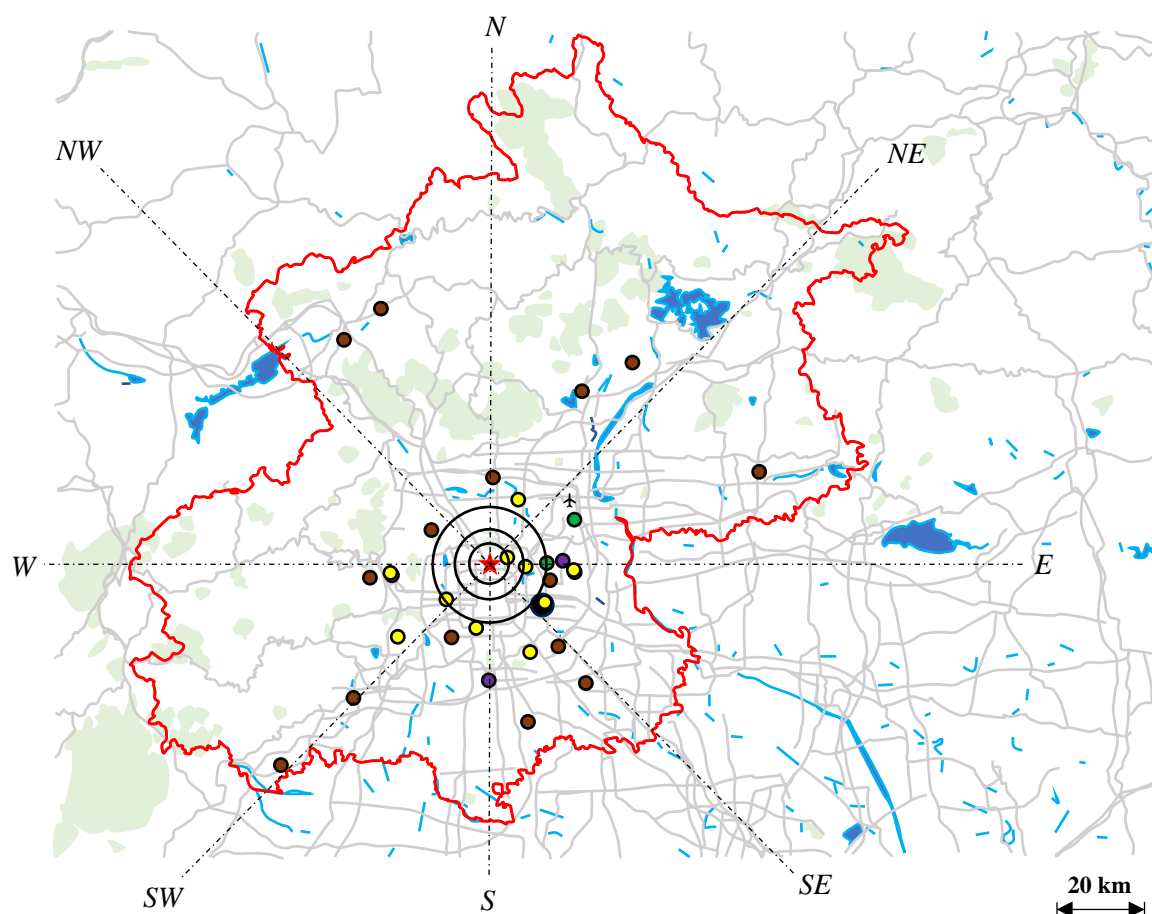


Fig. 5.8 Map of Beijing showing the key potential Cl^- emitters consisting of Waste Incineration Plants (Green); Landfill Sites (Brown); Gas Power Stations (Yellow); Coal Power Stations (Large Black); and Composting Sites (Purple). Grey lines show major roads, light green patches show green spaces and blue colouration indicates a body of water.

5.3.1.7 Beijing Winter

Fig. 5.7 demonstrates that during the BWIN daytime hours (100 filter samples), observed the highest concentrations of Cl^- originating from the SW direction ($> 12 \mu\text{g m}^{-3} [\text{Cl}^-]$). This is most likely due to the presence of the last remaining coal power plant in Beijing (the Huaneng thermal power station) which was located *ca.* 16.5 km away from the IAP sampling site (Fig. 5.8). Coal is known to be a dominant emitter of HCl and therefore the Huaneng power station is a very likely source to the very high $[\text{Cl}^-]$ observed. Fig. 5.7 also demonstrates that relatively high Cl^- concentrations (*ca.* $8 \mu\text{g m}^{-3}$) were also observed to originate from the N and S-SW. Fig. 5.8 shows that these higher Cl^- may be from landfill sites. Furthermore, Fig. 5.7 also shows a particularly high concentration of Cl^- very close to the centre of the BWIN daytime contour plot. This signifies a very high localised Cl^- source which most likely would have been from HCl release from localised sources such as smoking¹²⁶, cooking, dishwasher detergent used, as well as use of cleaning products⁴³⁷.

During BWIN night-time hours (23 filter samples), Fig. 5.7 demonstrates that high Cl^- originated from the E, SE and S directions. Similar to daytime value, this is most likely down to the coal power plant in very close proximity to IAP. In addition, it is known that an industrial area is situated to the south of IAP which may be emitting HCl emissions²⁸³. A much lower intensity in the BWIN contour plot is observed towards the N and W directions. These vectors line up with landfill sites for which less evaporation of HCl from non-combustion sources is likely down to the BWIN campaign temperatures (average temperature was 5.01 °C).

5.3.1.8 Beijing Summer

The BSUM campaign observed significantly lower $[\text{Cl}^-]$ values compared to the BWIN or Delhi campaigns. This therefore produced a more intermittent contour plot for the BSUM daytime hours in Fig. 5.7 (158 filter samples). At closer inspection of Fig. 5.7, lighter green patches are observed towards the SW as well as the E and NE. This could be due to the presence of landfill sites in the SW; as well as the presence of a landfill, composting and waste incineration sites in the E and NE. This is however speculative and the inconsistent shading of the BSUM daytime contour plot is most likely down to the very low Cl^- concentrations and the errors associated with NH_4Cl evaporation and dissociation from the aerosol into the gas phase. This occurs more prominently during times of higher temperatures (average BSUM daytime temperature of 28.8 °C).

For the BSUM night-time hours (37 filter samples), even lower $[\text{Cl}^-]$ is observed although a very clear dominance is seen from the S and SW directions. This would be in line with a composting site to the S as well as landfill sites to the SW. It is also in line with the industrial region found to the south of IAP²⁸³. No dominance of Cl^- is observed towards the SW during day or night-time hours (as was during BWIN) as the Huaneng power plant closed between the BWIN and BSUM campaigns.

5.3.1.9 Challenges in Cl^- source identification

There are many more sources of Cl^- present than those outlined in Fig. 5.2 and Fig. 5.8 for Delhi (especially)³⁴⁷ and Beijing, respectively. In particular, biomass burning and is a major source of Cl^- ^{121,438,112}, and fire-works^{118,439} were known to occur ubiquitously across Delhi during the DPOM campaign during the lead-up to Diwali. Other possible sources (not identified as major points sources) of Cl^- may include localised sources in the vicinity of IGDTUW and IAP such as smoking^{440,127,121,126}, cooking^{122,437,441} and cleaning^{437,437}. Another source of Cl^- may originate from the reaction of HCl with basic dust particles and some Cl^- (where higher wind speeds are observed) may have originated from other regions through long range transport)^{143,442,443}.

Particular difficulties in identifying a comprehensive set of Cl^- point sources in Delhi arises from the numerous illegal and unauthorized industries which are spread across the city (such as steel works)^{444,347}. In Beijing, particular challenges arose in information availability of the specific locations of industries.

Finally, the meteorological measurements and meteorology contribute to the uncertainty in these data. The wind measurements were taken much more frequently in each campaign compared to the

relatively much longer filtering times. To produce the contour plots shown in Fig. 5.1 and Fig. 5.7, the wind direction and speed data needed to be averaged to the filter times. Issues arise in the calculation of wind direction averages using vectors as detail is lost in very quick changes in wind direction. Furthermore, the mean wind vector calculated may be incorrectly averaged to a wind direction which was not present. Temperature also has a large influence on the volatility of particle phase Cl⁻ due to the volatility of NH₄Cl^{426,422,421,327} and it should be emphasised that a lower Cl⁻ concentration does not equate to reduced HCl sources.

5.3.2 Nitrate and Sulfate

5.3.2.1 [NO₃⁻]/[SO₄²⁻] Ratio

The [NO₃⁻] / [SO₄²⁻] mass ratio can be used to indicate the comparative magnitude of contribution of stationary and mobile sources to PM_{2.5}^{188,445,192,202,195,395,446}, as traffic emissions are substantial sources of NO₂ (oxidising to NO₃⁻) and fossil fuel combustion (namely coal combustion) contributes considerably to SO₂ emissions (oxidising to SO₄²⁻)⁴⁴⁶. The ratio of [NO₂] / [SO₂] has also been used in previous studies^{445,192}. A larger value of [NO₃⁻] / [SO₄²⁻] would suggest that mobile sources are of a greater influence^{188,202,395}. Huang et al., (2016)⁴⁴⁶ report that [NO₃⁻] / [SO₄²⁻] > 1.0 indicates that mobile emission sources are more substantial to PM_{2.5} composition than stationary sources. The [NO₃⁻] / [SO₄²⁻] = 1.0 threshold is shown as a blue dashed line in Fig. 5.9 and Fig. 5.10.

To calculate the error associated with the [NO₃⁻]/[SO₄²⁻] mass ratio results shown in Fig. 5.9 for the DPEM, DPOM, BWIN and BSUM campaigns, the division rule for error propagation³⁰⁰ is taken (shown in Eq. 5.1) where [NO₃⁻]/[SO₄²⁻] is equal to Q. Eq. 5.2 shows the rearrangement in the calculation of the absolute error of Q. These errors are presented as purple error bars on the time series shown in Fig. 5.9.

$$\left(\frac{\delta Q}{Q}\right)^2 = \left(\frac{\delta[NO_3^-]}{[NO_3^-]}\right)^2 + \left(\frac{\delta[SO_4^{2-}]}{[SO_4^{2-}]}\right)^2$$

Eq. 5.1. Division rule for propagation of error used to calculate the associated error of [NO₃⁻]/[SO₄²⁻] values across the APHH campaigns. Q is the [NO₃⁻]/[SO₄²⁻] and δQ is the total propagated error.

$$\delta Q = Q \sqrt{\left(\frac{\delta[NO_3^-]}{[NO_3^-]}\right)^2 + \left(\frac{\delta[SO_4^{2-}]}{[SO_4^{2-}]}\right)^2}$$

Eq. 5.2. Rearrangement of the [NO₃⁻]/[SO₄²⁻] propagated error (δQ).

A summary of the analysis conducted with [NO₃⁻] / [SO₄²⁻] including the time series of this ratio during each of the APHH campaigns is shown in Fig. 5.9 and a comparison of the day, night and total campaign averages is shown in Fig. 5.10. In Fig. 5.10, orange, green and purple bars represent the day, night and total average [NO₃⁻]/[SO₄²⁻], respectively for the Delhi campaigns. The block and

hashed-coloured bars are associated with the DPEM and DPOM campaigns, respectively. Yellow, red and dark blue bars present the day, night and total average $[\text{NO}_3^-]/[\text{SO}_4^{2-}]$, respectively for the Beijing campaigns. The block and hashed coloured bars present the BWIN and BSUM campaigns, respectively.

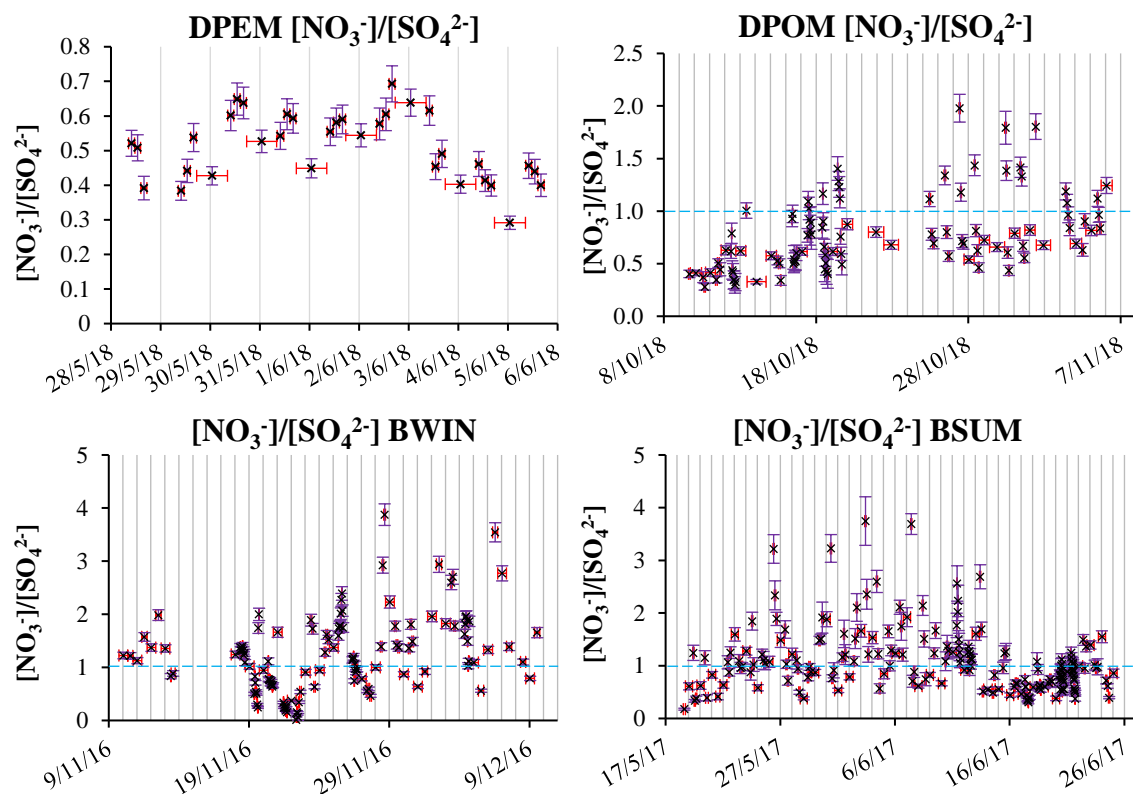


Fig. 5.9. Time series of the $[\text{NO}_3^-]/[\text{SO}_4^{2-}]$ ratios during the DPEM, DPOM, BWIN and BSUM campaigns. The red error bars (x-axis) show the sampling times and the purple error bars (y-axis) show the calculated error for the $[\text{NO}_3^-]/[\text{SO}_4^{2-}]$ values. Time is shown along the x-axis with $[\text{NO}_3^-]/[\text{SO}_4^{2-}]$ shown up the y-axis. A blue dashed line is overlaid in each time series to demonstrate the $[\text{NO}_3^-]/[\text{SO}_4^{2-}] = 1.0$ threshold. The grey vertical lines represent midnight.

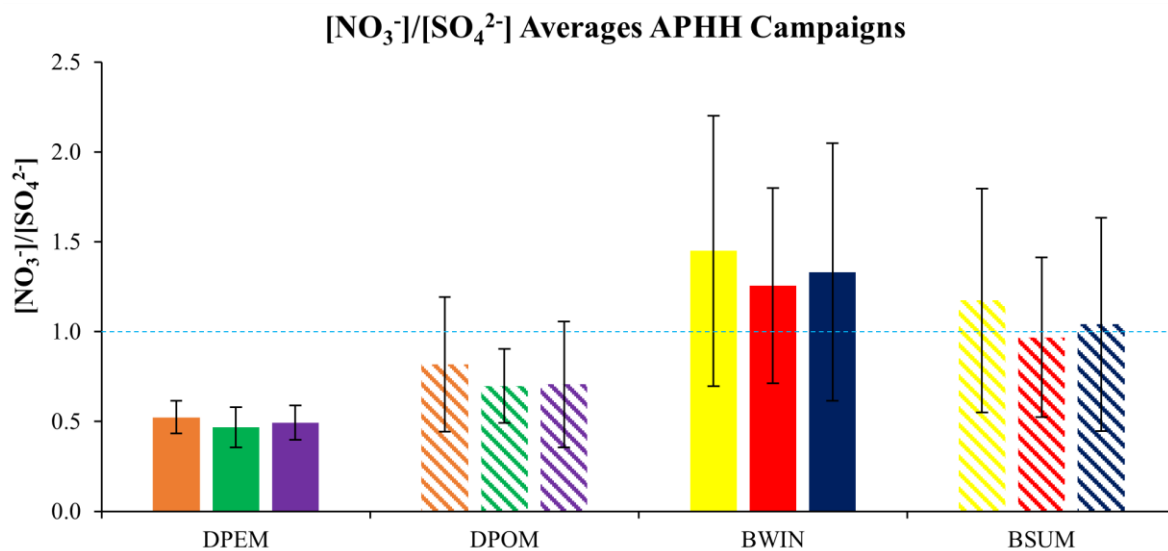


Fig. 5.10. $[\text{NO}_3^-]/[\text{SO}_4^{2-}]$ averages (\pm SD) across the DPEM, DPOM, BWIN and BSUM campaigns. The orange, green and purple bars represent the day, night and total campaign periods, respectively, in Delhi. The yellow, red and dark blue bars represent the day, night and total campaign periods, respectively, in Beijing. A blue dashed line is overlaid in each time series to demonstrate the $[\text{NO}_3^-]/[\text{SO}_4^{2-}] = 1.0$ threshold.

The DPEM and DPOM campaigns demonstrate $[\text{NO}_3^-] / [\text{SO}_4^{2-}] < 1.0$, and the BWIN and BSUM show $[\text{NO}_3^-] / [\text{SO}_4^{2-}] > 1.0$ (except for the BSUM night which has a ratio of slightly < 1). Therefore, using the $[\text{NO}_3^-] / [\text{SO}_4^{2-}]$ analyses and based on this very basic metric, on average the stationary emissions in Delhi and the mobile sources in Beijing contribute more to the $\text{PM}_{2.5}$ pollution in these megacities during the respective campaigns.

5.3.2.2 $[\text{NO}_3^-]/[\text{SO}_4^{2-}]$ Ratio Comparison between Delhi and Beijing

Analysing the $[\text{NO}_3^-]/[\text{SO}_4^{2-}]$ times series for the DPEM campaign shows a very clear diurnal profile in which $[\text{NO}_3^-]/[\text{SO}_4^{2-}]$ is higher during daylight hours and lower at night. The time series of DPOM, BWIN and BSUM also show this diurnal pattern for $[\text{NO}_3^-]/[\text{SO}_4^{2-}]$, although reach much higher $[\text{NO}_3^-]/[\text{SO}_4^{2-}]$ ratios. It should however be noted that only 8 days of data were collected for DPEM. This therefore suggests that in each campaign, the mobile source contribution to $\text{PM}_{2.5}$ is larger compared to the stationary phase during the daytime compared to the night. The daytime average is larger by a factor of 1.11 (DPEM), 1.17 (DPOM), 1.16 (BWIN), and 1.21 (BSUM). Therefore, the greatest day to night difference was found during the BSUM campaign. This is due to mobile vehicle emission sources releasing NO_2 (traffic) being much greater than the release of SO_2 (predominantly stationary sources) in the change from the heating (BWIN) to the non-heating (BSUM) seasons in Beijing.

Fig. 5.10 shows that the average $[\text{NO}_3^-]/[\text{SO}_4^{2-}]$ within Beijing was overall larger compared to Delhi. The lower ratios of $[\text{NO}_3^-]/[\text{SO}_4^{2-}]$ within Delhi compared to Beijing may be due to different fuel composition for vehicles. According to the UN environment programme³³⁸, in 2018 sulphur levels in diesel were 50 ppm in India and 10 ppm in China (also for 2017). In addition, Delhi observes greater use of coal power stations. In addition to the Badarpur Thermal power station, another two coal fired power stations are observed just outside the city perimeter towards the SW. These are the NTPC power stations in Dadri ($28^\circ35'54''\text{N } 77^\circ36'34''\text{E}$) and Faridabad ($28.374^\circ\text{N } 77.307^\circ\text{E}$). In addition, Delhi is known to have many unofficial industries ubiquitously spread over the city and therefore may have a larger industry to vehicle emission inventory ratio compared to Beijing³⁴⁷. For example, industries such as metal extraction and treatment (i.e. steel works) are known to be emitters of SO_2 gas⁴⁴⁷. In addition, China has reported to have implemented the GB13223-2011 emission standards in 2012 and the Ultra - Low Emissions standards (ULE) in 2014 in order reduce emissions from power plants contributing to poor air quality⁴⁴⁸.

The DPOM overall average $[\text{NO}_3^-]/[\text{SO}_4^{2-}]$ was larger compared to the DPEM campaign by 1.45 times. This was likely due to the lead up to Diwali where a general increase in the ratio is seen towards the end of the DPOM time series (Fig. 5.9). Diwali is the Hindu festival of lights and therefore an increased amount of traffic experienced⁴⁴⁹ from population relocation to see family etc. may be the cause of the higher $[\text{NO}_3^-]/[\text{SO}_4^{2-}]$ during the DPOM campaign, through NO_x release. Furthermore, the post-monsoon period is also the start of the crop burning season^{450,451} and the higher $[\text{NO}_3^-]/[\text{SO}_4^{2-}]$ may be due to increased NO_x emissions from regional sources.

The overall $[\text{NO}_3^-]/[\text{SO}_4^{2-}]$ average of the BWIN campaign was larger than the BSUM campaign by 1.29 times. This is surprising as Beijing closed its last remaining coal fired power plant between the BWIN and BSUM campaigns¹⁹². This power plant was *ca.* 16.5 km away from the IAP site and therefore emissions should have had great influence. With no coal burning emissions from the coal power plant in proximity to IAP occurring during the summer campaign, the amount SO_2 released should have reduced, and therefore the $[\text{NO}_3^-] / [\text{SO}_4^{2-}]$ would have been expected to increase. This could be down to changes in wind direction, or the chemistry involved in producing these ions from NO_x and SO_2 . Furthermore, Beijing is known to require the desulfurization of coal⁴⁵². In addition, it is likely that the BWIN average $[\text{NO}_3^-]/[\text{SO}_4^{2-}]$ is larger than BSUM due to the heating period (BWIN) for which a much greater level of domestic heating occurs through biomass burning which is a significant source of NO_x ⁴⁵³. Although domestic biomass burning is banned within the city, it could be occurring within the region. Furthermore, average $[\text{NO}_3^-]/[\text{SO}_4^{2-}]$ values may also be larger during the cooler seasons due to the volatile nature of NH_4NO_3 .

Although not much work has been conducted in Delhi surrounding the $[\text{NO}_3^-]/[\text{SO}_4^{2-}]$ ratios, numerous studies have been conducted in Beijing such as the work of Huang et al., (2016)⁴⁴⁶ (although using the $\text{PM}_{2.5}$ mass fraction). Huang et al., (2016)⁴⁴⁶ report $[\text{NO}_3^-]/[\text{SO}_4^{2-}]$ values of 1.1 and 1.0 for the clean and haze periods, respectively, during the summer in Beijing. They also report values of 1.1 and 1.2 for the clean and haze periods for the winter season⁴⁴⁶, respectively. These values are relatively similar with the work presented in this thesis, for which the BWIN and BSUM campaigns observed overall $[\text{NO}_3^-]/[\text{SO}_4^{2-}]$ ratios of 1.33 and 1.04, respectively. The reason for the similarity between winter and summer has been proposed by previous works to be down to a rise in $[\text{SO}_2]$ during the heating season in the winter months, and a rise in the photochemical activity during the summer months, leading to winter and summer observing lower values compared to the autumn and spring seasons⁴⁴⁶.

Table 5.1. $[\text{NO}_3^-]/[\text{SO}_4^{2-}]$ ratios reported by other studies in Beijing from $\text{PM}_{2.5}$ measurements.

Author	Site	Sampling Time	Ratio	Notes
Zhang et al., (2016) ¹⁹²	YU CAS	4 th Aug 2012 - 3 rd Sep 2012	0.51	Haze Days
Zhang et al., (2016) ¹⁹²	YU CAS	4 th Aug 2012 - 3 rd Sep 2012	0.53	Non-Haze Days
Han et al., (2015) ⁴⁵⁴	PKU	18 th Aug - 8 th Sep 2006	0.79	Non-Haze Days
Han et al., (2015) ⁴⁵⁴	PKU	18 th Aug - 8 th Sep 2006	0.63	Haze Days
Wang et al., (2006) ¹⁹⁴	BNU	Spring 2001 - 2004	0.96	Clear Period
Wang et al., (2006) ¹⁹⁴	BNU	Spring 2001 - 2004	0.89	Haze Period
Wang et al., (2006) ¹⁹⁴	BNU	Spring 2001 - 2004	0.3	Dust Period
Zhao et al., (2013) ⁴⁵⁵	Beijing	6 th April 2009 - 8 th Feb 2010	1.07	Annual Average
Zhang et al., (2018) ²⁰²	BMRI	10 th Feb to 19 th Mar 2015	1.43	-
Han et al., (2016) ³⁹⁵	CRAES	Jan 2013	0.68	-
Wang et al., (2016) ¹⁹⁵	YF	Nov 2012 - Jul 2013	1.12	Annual Average
Wang et al., (2016) ¹⁹⁵	FG	Aug 2012 - Jul 2013	1.08	Annual Average
Wang et al., (2016) ¹⁹⁵	CGZ	Aug 2012 - Jul 2013	1.25	Annual Average
Wang et al., (2016) ¹⁹⁵	DL	Aug 2012 - Jul 2013	1.01	Annual Average

To compare, a selection of $[\text{NO}_3^-]/[\text{SO}_4^{2-}]$ from other studies have been presented in Table 5.1. The site codes are identical to those reported as previously in chapter 4, although with the addition of BMRI (Beijing Municipal Research Institute of Environmental Protection); YF (Yufa); and DL (Dingling). No specific sampling site was reported of Beijing in the work of Zhao et al., (2013)⁴⁵⁵.

Work by Zhang et al., (2018)²⁰² briefly reviews $[\text{NO}_3^-]/[\text{SO}_4^{2-}]$ ratios and demonstrates an increasing trend (in winter) from 1999 - 2015 (table 3 in Zhang et al., (2018)²⁰²). The last data point in their time series reported a ratio of 1.53 from sampling in Feb 2015. They suggest that the increasing trend indicates the increasing fraction of mobile source contribution to $\text{PM}_{2.5}$ (i.e. vehicle emissions)²⁰². Other studies have also mentioned the increase fraction contribution to $\text{PM}_{2.5}$ from mobile emission sources^{395,200,195}. The values reported in this thesis (1.33 for BWIN) do not follow the increasing trend from reviewed studies found by Zhang et al., (2018)²⁰², although the BWIN average is in relatively good agreement with the general values reported in the studies reviewed by Zhang et al., (2018)²⁰². The other values in Table 5.1 are very variable depending on time, sampling site and atmospheric conditions and it is difficult to directly compare the results from the BWIN and BSUM campaigns to the other reported values.

Linear regression analysis was also conducted between the $[\text{NO}_3^-]/[\text{SO}_4^{2-}]$ and the other variables measured during the four APHH campaigns. An interesting correlation was observed during the daytime hours of the BWIN campaign of $[\text{NO}_3^-] / [\text{SO}_4^{2-}]$ with mean particle diameter (Dia). Mean particle diameter data was measured by the University of Manchester (UoM) using a Single Particle Soot Photometer (SP2) instrument (200 nm–720 nm), as described in Liu et al., (2010)⁴⁵⁶ in which an $R^2 = 0.76$, positive correlation was observed. This indicates that as the particle size increases, the relative amount of particulate $[\text{NO}_3^-]$ also increases, suggesting that mobile sources may have a greater contribution to larger PM, within the $\text{PM}_{2.5}$ size range.

Finally, correlation analysis was also conducted between $[\text{NO}_3^-]$ and $[\text{SO}_4^{2-}]$ concentrations for the BWIN and BSUM campaigns. Over the total campaign periods, regression coefficients of $R^2 = 0.77$ and $R^2 = 0.35$ were calculated for the BWIN and BSUM campaigns, respectively. This correlation is in close agreement with the work of Duan et al., (2020)⁴⁵⁷ who reported a strong correlation of $R^2 = 0.6$ between $[\text{NO}_3^-]$ and $[\text{SO}_4^{2-}]$ during the winter period (4th Dec 2015 – 6th Feb 2016), and no obvious correlation during the summer period in Beijing (1st Jul – 19th Aug 2015). Duan et al., (2020)⁴⁵⁷ workers did however investigate PM_1 as opposed to $\text{PM}_{2.5}$ in their study. This is surprising as NO_3^- and SO_4^{2-} are both known to be oxidation products and more oxidation would have been expected in summer.

In summary, generally higher $[\text{NO}_3^-] / [\text{SO}_4^{2-}]$ in Beijing compared to Delhi would suggest a higher contribution of mobile sources to $\text{PM}_{2.5}$ in Beijing compared to Delhi. This is however a very basic indication. Although the $[\text{NO}_3^-]/[\text{SO}_4^{2-}]$ gives a very basic indication that $\text{PM}_{2.5}$ in Beijing may have a higher contribution from mobile sources compared to Delhi, this calculation maintains many uncertainties. The main uncertainties include comparing two cities with different legislation on fuel

use and the relative fuel sulfur content and generally dirtier fuels burned in Delhi will affect the $[\text{NO}_3^-]/[\text{SO}_4^{2-}]$ ratio. The relative temperature differences between each city and season also make comparison difficult. This is because NO_3^- and SO_4^{2-} are predominantly found in aerosol bound with NH_4^+ . NH_4HSO_4 , $(\text{NH}_4)_2\text{SO}_4$ and NH_4NO_3 may volatilise back into the gas phase at higher temperatures for which NH_4NO_3 may dissociate back into HNO_3 and NH_3 . There may also be uncertainties surrounding the efficiency of NO_2 and SO_2 oxidation, as the climates and meteorology observed between the four APHH campaigns are very variable.

5.3.2.3 SOR and NOR in Delhi and Beijing

The extent of oxidation of NO_2 and SO_2 to form NO_3^- and SO_4^{2-} may be measured using the NOR and SOR, as described in the thesis introduction (chapter 1). Time series of the SOR and NOR were conducted for all four campaigns, and these are shown in Fig. 5.11. The dates and ratios are shown on the x -axes and y -axes, respectively. Grey vertical lines demonstrate hour 00:00 for each date and the red error bars represent filter sampling times.

To calculate the error of SOR, the error of SO_2 (F) from the gas-phase data taken by Squires et al., (2020)²⁸³ was 3.12 % (to 2σ). This was converted to the absolute error in ppbv (δF_1) when multiplied by the SO_2 concentrations. The reproducibility error of the SO_2 instrument was reported as 0.03 ppbv (δF_2). The absolute total instrumental error for the gas phase instrumentation was therefore $\delta F_1 + \delta F_2$, which is abbreviated as δF . δF was converted from ppbv to mol m^{-3} for the purposes of the SOR calculation. The error of SO_4^{2-} , (δG , where G is IC $[\text{SO}_4^{2-}]$), was previously calculated and is described in chapter 2. This error was also converted into mol m^{-3} . In the SOR calculation, the denominator comprises of $[\text{SO}_2] + [\text{SO}_4^{2-}]$ which is referred to as H in this calculation. Therefore, the addition rule of propagation is taken and is shown in Eq. 5.3, where δH (propagated error of the SOR denominator) is the propagated error of δF and δG .

$$\delta H = \sqrt{(\delta F)^2 + (\delta G)^2}$$

Eq. 5.3. Addition rule of propagation to calculate the total error of the denominator for the SOR calculation. δF is the error of SO_2 , δG is the error of SO_4^{2-} , and δH is the propagated error of these two variables.

The SOR is the ratio of G/H, and therefore the division rule is required to propagate the error of the SOR (I), as shown in Eq. 5.4 which is re-arranged to make the total SOR error (δI) the subject in Eq. 5.5.

$$\left(\frac{\delta I}{I}\right)^2 = \left(\frac{\delta G}{G}\right)^2 + \left(\frac{\delta H}{H}\right)^2$$

Eq. 5.4. Division rule for propagation of error used to calculate the associated error of SOR values across the APHH campaigns. I is the SOR and δI is the total propagated error for SOR.

$$\delta I = I \sqrt{\left(\frac{\delta G}{G}\right)^2 + \left(\frac{\delta H}{H}\right)^2}$$

Eq. 5.5. Rearrangement of the SOR propagated error (δI).

An analogous calculation was completed for NOR, for which the instrument uncertainty (2σ) for NO_2 was 5.72 % and the reproducibility error was 0.04 ppbv, as reported by Squires et al., (2020)²⁸³. These errors are shown in Fig. 5.11 as blue error bars in the y-axis.

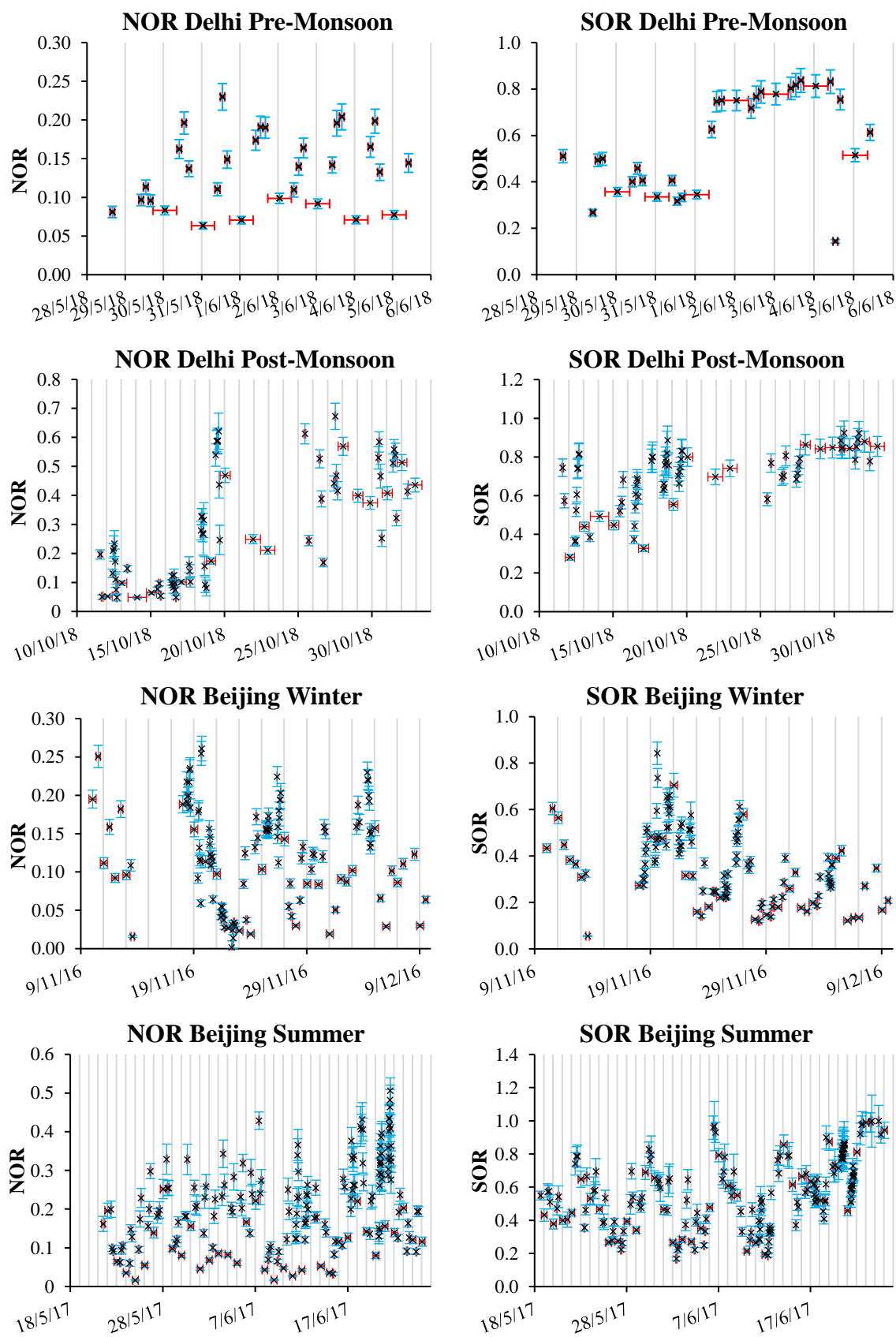


Fig. 5.11. Time series of NOR and SOR over the course of the Delhi pre-monsoon, post-monsoon, Beijing winter and summer campaigns. The blue error bars show the uncertainty of NOR and SOR in the y-axis and the red error bars demonstrate the length of sampling time. The time of sampling is shown in the x-axis. The y-error bars were calculated by propagating the errors of NO_3^- and SO_4^{2-} from the IC measurements (Chapter 3) with the error from the gas phase species (SO_2 3.12 % and NO_2 5.72 %).

5.3.2.4 Delhi Pre-Monsoon

A very clear diurnal pattern is seen in the times series of NOR during the DPEM campaign (Fig. 5.11), with peaks shown during the daytime and troughs shown at night (similar pattern to O₃, Chapter 3). The average daytime NOR was 0.15, and at night was 0.08. The median NOR was found to be 0.14 with a campaign maximum of 0.23 (31st May 2018 at 13:07) and a minimum of 0.06 (31st May 2018 at 00:52) giving a range of 0.17.

The SOR (Fig. 5.11) shows a less clear diurnal trend with lower ratios generally seen during the beginning of the campaign. It is clear from Fig. 5.11 that the SOR values switch from a low to high regime from 28th May 2018 – 1st Jun 2018 and 1st Jun 2018 - 5th Jun 2018. The average SOR before 1st Jun 2018 was 0.37 and the average SOR value from 1st Jun 2018 at 10:00 – 4th Jun 2018 at 09:58 was 0.78. A very low value was observed on the 4th June and was caused by a large increase in local SO₂ concentrations (chapter 3). The NOAA HYSPLIT model was run again for IGDTUW for 28th May 2018 – 1st Jun 2018 (Fig. 5.12) and 1st Jun 2018 - 5th Jun 2018 (Fig. 5.13) using the same conditions as previously described, although a new trajectory was calculated every 6 hours.

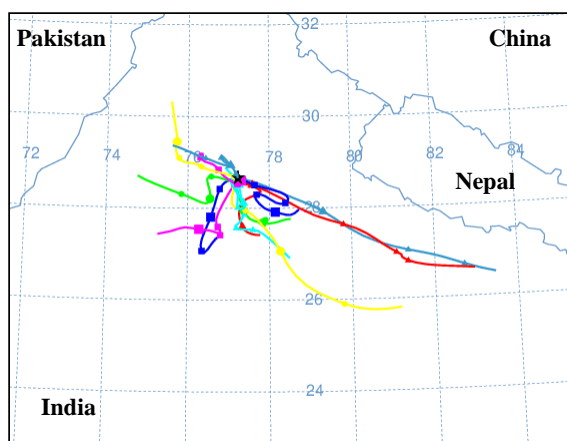


Fig. 5.12. 28th May 2018 - 1st Jun 2018 (lower SOR) back trajectories for IGDTUW.

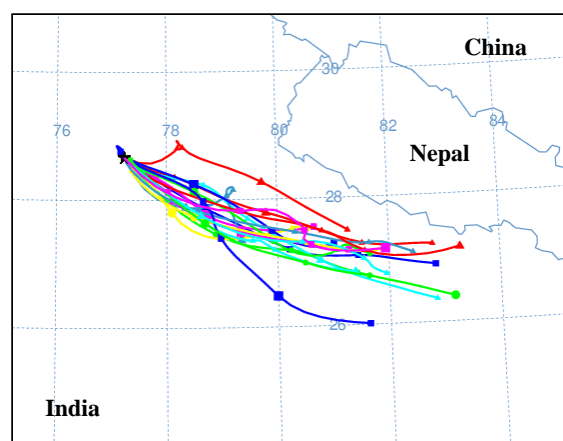


Fig. 5.13. 1st Jun 2018 - 5th Jun 2018 (higher SOR) back trajectories for IGDTUW.

The change in average SOR is most likely down to the very large change in air mass observed before and after the pivot date of 1st Jun 2018. Before the 1st Jun, lower SOR are associated with air masses which originated from multiple direction, generally originating from the south of IGDTUW. After the 1st Jun, prevailing winds are observed from the SE.

Most air masses in Fig. 5.12 meander around Delhi and the surrounding region whereas the back trajectories in Fig. 5.13 follow much straighter trajectory paths. This is significant as air parcels circulating Delhi are much more likely to observe reduced oxidising species concentrations as these are likely to have been lots from reaction with high primary VOC concentrations towards the centre of Delhi. Furthermore, the air masses from after the 1st Jun directly over the Badarpur thermal power station. As discussed, coal combustion emissions are a significant source of SO₂ emissions, especially in India where sulfur levels in coal may be very high^{458,459}. In addition, a reduction in SO₂

concentrations observed after the 1st Jun (chapter 3). This reflects the increased oxidation of SO₂ to SO₄²⁻ by the time the air parcels reach the HiVol from the power plant.

5.3.2.5 Delhi Post-Monsoon

During the DPOM campaign, the NOR values were relatively stable from the start of sampling up until 17th Oct 2018 (Fig. 5.11). From this date until the end of the campaign the time series of NOR varies greatly. The average from the 11th Oct at 13:51 – 17th Oct 16:34 was 0.08 and the average from the 18th Oct at 09:44 – 1st Nov 2018 at 22:16 was 0.38.

A gradual increase is seen in the SOR time series throughout the campaign. Applying a linear regression to the time series observes a gradient of 0.0149 SOR day⁻¹ ($R^2 = 0.40$). The variance of data is also seen to decrease gradually over the course of the campaign closer to Diwali celebrations. As NO₂ concentrations were seen to increase on the lead up to Diwali (chapter 3), a potential reason for this could be down to the oxidation of SO₂ by NO₂ as mentioned in the work of Wang et al., (2020)²⁴ who describe rapid SO₂ oxidation by NO₂ within Beijing haze. In addition, a possible mechanism is given by Yang et al., (2019)⁴⁶⁰. Other studies have also mentioned NO₂ to be a significant oxidant of SO₂ within urban regions^{461,462,177,163}.

Like the NOR time series, the average SOR observed from 11th Oct at 13:51 – 17th Oct 16:34 was 0.46 and from 18th Oct 09:44 – 1st Nov 22:16 2018 was 0.79. Unlike the DPEM campaign, the increase in NOR and SOR towards the latter half of the campaign is unlikely down to a change in wind direction, as the DPOM prevailing winds are from the NW with very relatively few trajectories originating from other directions (as seen in Fig. 5.5 and Fig. 5.6).

The general increase in NOR and SOR during the DPOM campaign is therefore more likely to be down to general changes in atmospheric conditions. Furthermore, the lower average and higher variability of SOR at the start of the campaign is likely down to the influence of the primary cement contribution with changing wind direction (as described in chapter 3).

5.3.2.6 Beijing Winter

The NOR cycles shown in Fig. 5.11 follow the same pollution cycles as seen in the NO₂ gas-phase time series (chapter 3) for the BWIN campaign, with four dominant pollution episodes. The peaks of these NOR cycles are observed to be on the 19th Nov, 26th Nov, 30th Nov and 4th Dec (Fig. 5.11). The day, night and total mean concentrations were 0.12, 0.09 and 0.10, respectively. The SOR times series also mirrors the large-scale pollution cycles of the campaign. However, the SOR values generally decrease from the peak on the 19th Nov until the end of the campaign.

It has been widely acknowledged that SOR and NOR may be affected by haze, fog and pollution episodes^{184,193,171,202,185,192,194,186,191}. Other studies which report larger SOR and NOR values during more polluted periods (and therefore agree with the time series shown in Fig. 5.11) include the work of Chi et al., (2018)¹⁸⁴ who observed that the NOR and SOR were larger during pollution episodes compared to clean periods; Shao et al., (2019)¹⁷¹ who reported an increase in SOR average ratios from 0.09 (clean periods) to 0.32 (haze periods), during the winter season in Beijing; and Zhang et

al., (2018)²⁰² who reported an increase in SOR values during polluted periods (in spring 2015, in Beijing) from 0.24 (clean period average) to 0.33 (haze period average). Finally, the work by Zhang et al., (2018)²⁰² was 0.13 ± 0.08 (clean periods) which increased to 0.18 ± 0.06 during pollution events (for NOR).

A reason for the increase in NOR and SOR during the pollution cycles is likely due to an increase in the NO_3^- and SO_4^{2-} production through the heterogenous oxidation pathway^{184,193,186}. Furthermore, Zhang et al., (2018)²⁰² also suggest that the reason for increased SOR during haze episodes is due to the catalysis of SO_2 by transition metals within aerosol during haze events through increased oxidation of SO_2 in the aqueous phase. Additionally, Wang et al., (2006)¹⁹⁴ reported higher NOR and SOR during haze periods and suggested in their study that larger values in haze events could be as a result of high $[\text{O}_3]$ and high Relative Humidity (RH) aiding NO_2 and SO_2 oxidation (heterogenous) and reducing NH_4NO_3 evaporation.

Finally, although the NOR and SOR time series follow the general pollution pattern seen in the gas and particle phases in Chapter 3 (BWIN), this is less obvious in the other APHH campaigns. A reason for this may be down to the NOR and SOR being dominated by non-heterogenous oxidation pathways instead; larger primary NO_3^- and SO_4^- contributions; or that the NOR and SOR are an over simplification of the NO_2 and SO_2 oxidation processes (a study by Wang et al., (2019)²⁰¹ aims to rectify this by incorporating a correction factor to correct for the over-estimation in NOR and SOR by primary sources, in their model estimations).

5.3.2.7 Beijing Summer

The average NOR value for the BSUM campaign was 0.14 which was 1.4 times higher compared to the BWIN campaign (0.10) and showed a greater overall variance. Peaks in NOR are generally observed during the day with troughs seen at night which can be explained by the higher $[\text{OH}]$ during daytime hours from increased solar flux causing gas-phase oxidation to HNO_3 followed by neutralization with NH_3 to produce NH_3NO_3 . Unlike in winter, the NOR BSUM time series does not show an obvious link to the trend of the large-scale gas and particle pollution cycles.

In contrast, the SOR time series shows a more distinct cycle of SOR. The peaks of these cycles in SOR are observed on the 22nd May, 30th May, 3rd Jun, 6th Jun and 18th Jun 2017 which reflect the pollution cycles of the SO_2 time series for BSUM (chapter 3), although the SOR cycles seem to observe a delay of 1-2 days after the SO_2 peaks. This may give an indication that the rate of SO_2 oxidation during the BSUM campaign was between 1-2 days. Further investigation is however needed to clarify this. The SOR values are also generally higher during the day compared to the night-time periods which is also likely due to higher gas phase SO_2 oxidation OH.

5.3.2.8 NOR and SOR (Inter-Campaign) Average Comparisons

A summary of the mean NOR and SOR values (\pm SD) for the day, night and total campaign for the DPEM, DPOM, BWIN and BSUM is shown in Fig. 5.14. In evaluating the campaign averages, the blocked filters were omitted. For the day and night averages, whole day filter samples were also

omitted. Fig. 5.14 was produced in the same manner as Fig. 5.10. As presented in the thesis introduction (chapter 1), NOR and SOR values > 0.1 indicates a predominance of secondary NO_3^- and SO_4^{2-} species^{202,205,202,203,185,200,192,204,195}. Based on this previous literature, dashed black lines have been applied to the 0.1 level of both the NOR and SOR bar charts (Fig. 5.14). For SOR, the study by Li et al., (2016)²⁰⁶ indicates that the threshold should be classed at a level of 0.25 which is presented by the blue dashed line (Fig. 5.14).

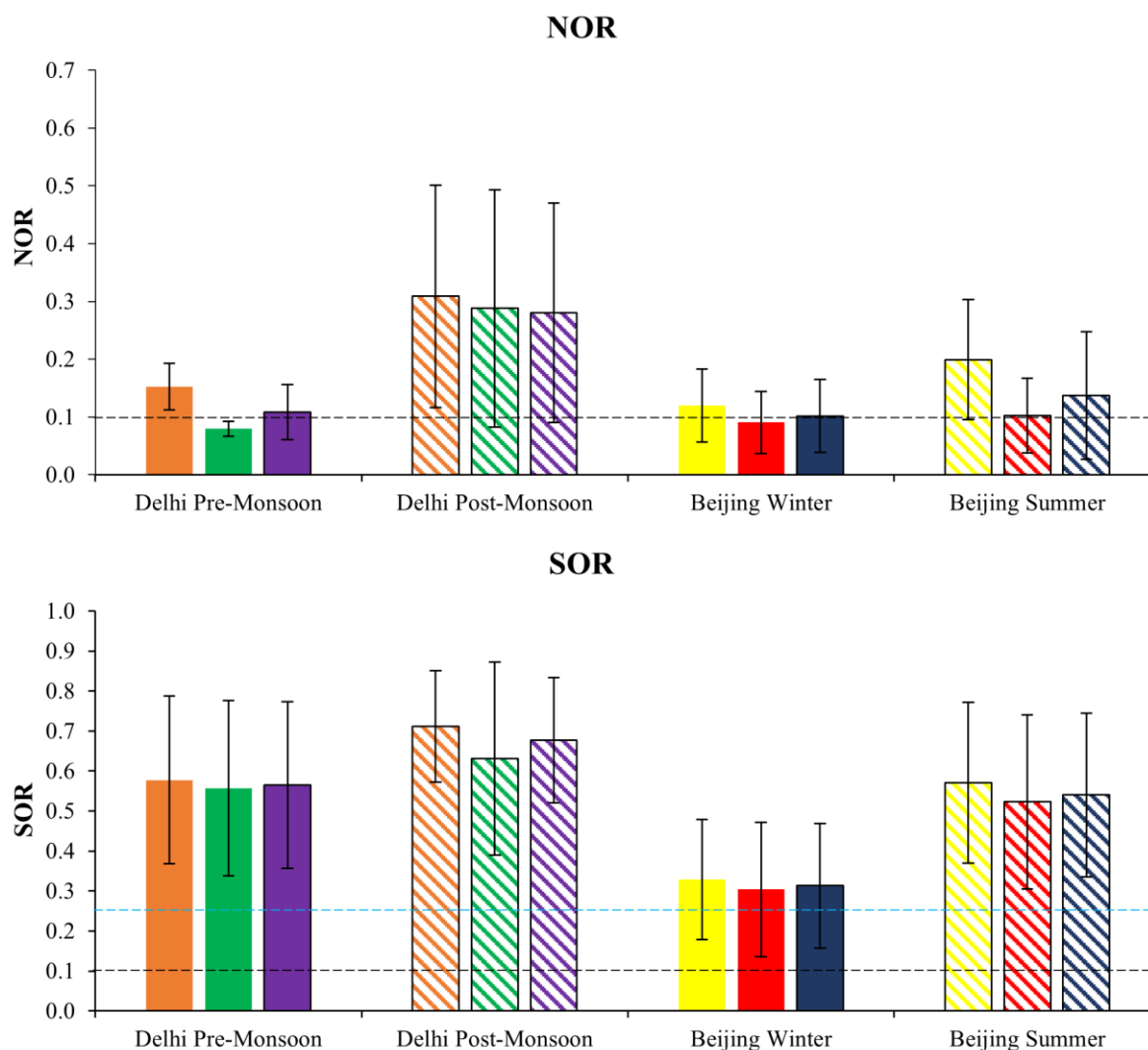


Fig. 5.14. NOR and SOR averages (\pm SD) across the DPEM, DPOM, BWIN and BSUM campaigns. The orange, green and purple bars represent the day, night and total campaign periods, respectively, in Delhi. The yellow, red and dark blue bars represent the day, night and total campaign periods, respectively, in Beijing. Black dashed lines are overlayed in each bar chart to demonstrate the 1.0 threshold as reported by the majority of the literature. A blue dashed line has been added to the SOR bar chart to show the 0.25 threshold as reported by Li et al., (2016)²⁰⁶.

For the NOR values, the daytime values in all campaigns are shown to be above the 0.1 threshold, although the night-time averages are < 0.1 during the DPEM and BWIN campaign night-time periods. The night-time BSUM NOR value was very close to 0.1 although the DPOM average night NOR was significantly > 0.1 . This indicates that during daytime hours, the NO_3^- is predominantly from secondary formation whereas at night, primarily emitted NO_3^- dominates the detected $[\text{NO}_3^-]$ during the DPEM and BWIN campaigns. A potential primary NO_3^- emission source could be dust,

although is more likely from direct release of NH_4NO_3 used in agricultural areas for which emissions would be independent of $[\text{NO}_x]$. For daytime hours during the DPEM and BWIN campaigns, the average NOR values are much closer to the 0.1 threshold (Fig. 5.14) compared to the DPOM and BSUM campaigns. As the DPOM and BSUM campaigns demonstrated larger NOR values, greater influence of secondary NO_2 photooxidation is likely to be the sources of measured NO_3^- in these periods.

Fig. 5.14 shows that for SOR, all reported averages in this study are above the 0.1 threshold (and the 0.25 threshold reported by Li et al., (2016)²⁰⁶). Therefore, the SO_4^{2-} within $\text{PM}_{2.5}$ measured in Delhi and Beijing in this study is predominantly from secondary formation. These results are in agreement with previous studies conducted. Zhang et al., (2016)¹⁹² sampled $\text{PM}_{2.5}$ aerosol in Beijing between 4th Aug 2012 – 3rd Sep 2012 and also reported SOR values on each sampling day to be > 0.1 (concluding that secondary formation processes were a dominant contributor to SO_4^{2-}). In addition, the work by Zhou et al., (2012)¹⁸⁷ reported that 94 % of their values indicated $\text{SOR} > 0.1$ (over four seasons in 2006, with values reaching up to 0.9 (0.4 annual mean), concluding the dominance of secondary SO_4^{2-} formation. The daytime averages for all measurement periods appear larger compared to the night-time averages across all campaign periods in Fig. 5.14. To further inspect the data, frequency distribution plots have been produced and are shown in Fig. 5.15. In addition, the number of data points used to calculate the NOR and SOR are also presented in Table 5.2.

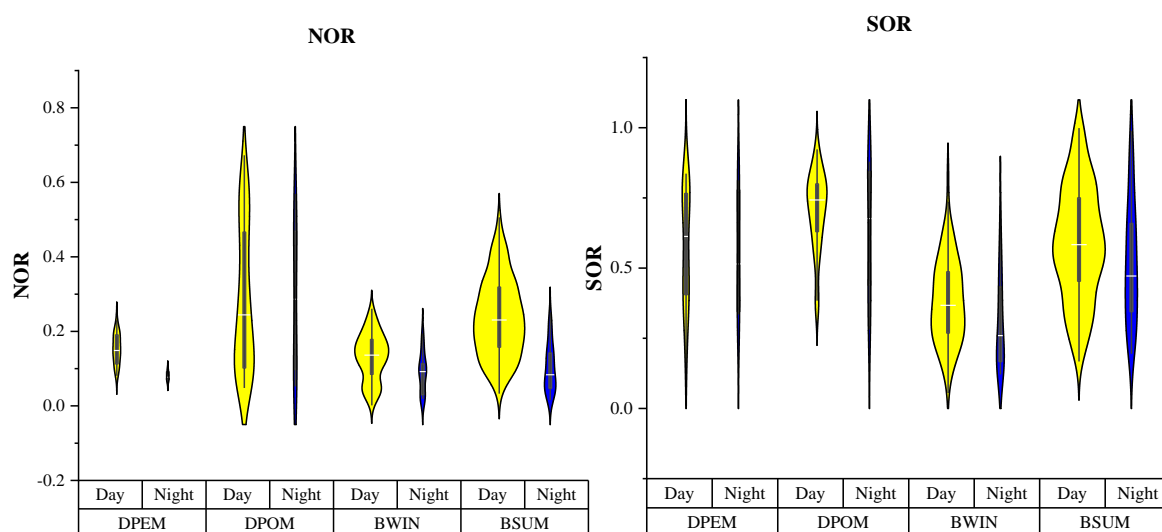


Fig. 5.15. Frequency distribution plots of the NOR (left) and SOR (right) over the DPEM, DPOM, BWIN and BSUM campaigns. The yellow distributions show the daytime values with the blue distributions representing the night-time data. The distribution density displayed is calculated by the kernel distribution function. The boxplot represents the inter quartile range and the white line within the boxplot represent the median atmospheric concentration for each ratio.

As can be seen in Fig. 5.15, a larger distribution density surrounds higher values in the NOR and SOR distributions during the daytime periods for the BWIN and BSUM campaigns. This may be explained by increased photochemical oxidation by the OH radical. OH may also be produced by HONO photolysis ($<30\%$ of daily $[\text{OH}]$ with highest HONO photolysis occurring early morning²⁰²), as well as from O_3 ²⁰².

Table 5.2. Number of data points used to calculate the NOR and SOR values across the APHH campaigns.

	<i>N</i>	DPEM	DPOM	BWIN	BSUM
NOR	Day	23	59	101	152
	Night	7	10	23	34
SOR	Day	23	59	100	156
	Night	7	10	23	36

With higher solar radiation during daytime hours, a larger [OH] is expected and would therefore increase the photochemical gas-phase oxidation occurring on NO₂ and SO₂. This is in line with the work of Wang et al., (2019)¹⁹⁶ who reported in their study that the oxidative potential of the atmosphere increased as [OH] increased, enhancing SO₂ oxidation to SO₄²⁻ through photochemical processing. In addition, Zhang et al., (2018)²⁰² reported in their study that NO₃⁻ was predominantly formed by heterogenous and photochemical oxidation during daytime hours, but that heterogenous NO₂ oxidation was predominant over night-time hours. Table 5.2 however shows that there are significantly more data points associated with the daytime periods compared to the night-time in Beijing. Therefore, these arguments should be taken with caution.

The DPEM NOR daytime distribution appears to reside at larger values compared to the night-time period (Fig. 5.15), whereas for the DPOM NOR and the DPEM and DPOM SOR datasets (Fig. 5.15), the night-time periods seem very evenly distributed. Inspecting Table 5.2 however, it is evident that too few night-time samples are available to make any definite conclusions in Delhi for the day and night-time comparisons.

Fig. 5.14 demonstrates that the ambient temperature also has a significant effect on NOR and SOR values. This is predominantly seen when comparing the two Beijing campaigns (Fig. 5.14 and Fig. 5.15) for which the mean values for NOR and SOR of the BSUM campaign are larger than for BWIN during the daytime periods when there is a higher solar flux (reflected in Fig. 5.15). This relationship between the Beijing summer and winter oxidation ratios was also observed in the work of Wang et al., (2016)¹⁹⁵ who reported that during the warmer seasons (spring and summer) the SO₂ to SO₄²⁻ conversion was predominantly via gas-phase photochemical oxidation pathway. During the cooler seasons (autumn and winter) however, Wang et al., (2016)¹⁹⁵ described that both a slow gas-phase photochemical oxidation reaction and a heterogeneous pathway were key in SO₂ oxidation to SO₄²⁻. As gas phase photochemical oxidation via OH is known to be strongly affected by temperature^{200,207,203}, this helps explain the elevated NOR and SOR during the Beijing summer season. Numerous other studies also suggest that increased temperatures and solar intensity facilitate photochemical oxidation^{196,199,204,187,195}.

The NOR and SOR relationship with temperature was however the opposite in Delhi, in which NOR and SOR values were larger during the DPOM campaign compared to the DPEM campaign (Fig. 5.14). This is in agreement with the work by Saxena et al., (2017)¹⁹⁸ who also observed larger NOR and SOR values during the winter months in Delhi (2013-2014). This relationship is unexpected, as

much higher temperatures were observed during the DPEM campaign and the DPOM campaign was found to observe very high [NO] and primary [VOC] which act as a sink for oxidants (chapter 3). It is therefore surprising that during the DPEM campaign a smaller NOR and SOR were calculated (compared to DPOM) as it would be expected that fewer oxidants available for photochemical gas phase oxidation would reduce NOR and SOR. A potential reason for the greater NOR and SOR values seen during the DPOM campaign is likely due to sampling taking place on the lead up to Diwali. During this period, much higher levels of NO and NO₂ were present which are precursors of the NO₃ radical which is known to react readily with organics to form organic nitrates (chapter 6). Organic nitrate species may dissociate in the particle phase to produce NO₃⁻ (chapter 6). It must however be emphasised that significantly fewer samples were available for analysis in Delhi compared to Beijing (Table 5.2) and that this argument should be taken with caution. Furthermore, the DPOM campaign has significantly more samples compared to the DPEM campaign.

For comparison, a set of reviewed studies is shown for India in Table 5.3. The studies reviewed included Saxena et al., (2017)¹⁹⁸ (IOX1); Ram et al., (2012)¹⁹³ (IOX2); Chatterjee et al., (2010)²⁰³ (IOX3); and Chatterjee et al., (2012)²⁰⁴ (IOX4). Only one study was available for comparison in Delhi (to best knowledge) and therefore NOR and SOR values from different cities across India have also been reported for comparison in Table 5.3.

Table 5.3. Review of NOR and SOR across other studies in Delhi

Study	Site	Time	NOR	± SD	SOR	± SD
IOX1A	Delhi	Jan 2013 - Dec 2014; Apr - Jun	0.15	0.05	0.39	0.08
IOX1B	Delhi	Jan 2013 - Dec 2014; Jul - Sep	0.12	0.1	0.31	0.09
IOX1C	Delhi	Jan 2013 - Dec 2014; Oct - Jan	0.31	0.17	0.56	0.18
IOX1D	Delhi	Jan 2013 - Dec 2014; Feb - Mar	0.22	0.09	0.41	0.09
IOX1E	Delhi	Jan 2013 - Dec 2014	0.22	0.14	0.43	0.15
IOX2A	Allahabad	Dec 2004	0.25	0.08	0.39	0.05
IOX2B	Allahabad	Dec 2004	0.20	0.04	0.45	0.12
IOX2C	Allahabad	Dec 2004	0.33	0.11	0.52	0.15
IOX2D	Hisar	Dec 2004	0.23	0.15	-	-
IOX2E	Hisar	Dec 2004	0.30	0.04	-	-
IOX2F	Hisar	Dec 2004	0.39	0.08	-	-
IOX3	Darjeeling	Jan - Dec 2005	-	-	0.11	0.07
IOX4	Kolkata	Jan - Dec 2006	-	-	0.11	0.06

The total DPEM NOR value in this study was 0.11 which was in relatively good agreement with the work by Saxena et al., (2017)¹⁹⁸ who reported a pre-monsoon NOR average of 0.15. The average DPOM NOR was 0.31 which was also in very good agreement with the work of Saxena et al., (2017)¹⁹⁸ who reported a post-monsoon average of 0.31. The SOR values however showed less agreement and were higher during the APHH campaigns compared to the work of Saxena et al., (2017)¹⁹⁸. The DPEM SOR campaign average was 0.56 which was significantly larger than the 0.39 average reported by Saxena et al., (2017)¹⁹⁸ during the pre-monsoon season. The DPOM SOR

campaign average was 0.68 which was larger than the post-monsoon average of 0.56 demonstrated by Saxena et al., (2017)¹⁹⁸.

Table 5.4. Review of NOR and SOR across other studies in Beijing.

Study	Site	Time	NOR	± SD	SOR	± SD
BOX1A	IAP	19 th Jul - 31 st Aug 2006	0.17	-	0.70	-
BOX1B	IAP	23 rd Oct - 13 th Nov	0.15	-	0.40	-
BOX1C	IAP	6 th Dec - 29 th Dec	0.1	-	0.2	-
BOX1D	IAP	16 th Mar - 6 th Apr 2006	0.14	-	0.30	-
BOX1E	IAP	16 th Mar - 29 th Dec 2006	0.14	-	0.40	-
BOX2A	BMRI	10 th Feb - 19 th Mar 2015 (Average)	0.17	0.08	0.27	0.2
BOX2B	BMRI	10 th Feb - 19 th Mar 2015 (Clean)	0.13	0.08	0.24	0.09
BOX2C	BMRI	10 th Feb - 19 th Mar 2015 (Poll. Eps.)	0.18	0.06	0.33	0.23
BOX3A	UCAS	Oct 2014 - Jan 2015 (Non-Polluted)	0.09	0.05	-	-
BOX3B	UCAS	Oct 2014 - Jan 2015 (Polluted)	0.31	0.1	-	-
BOX4A	DL	Aug 2012 - Jul 2013	0.269	-	0.433	-
BOX4B	CGZ	Aug 2012 - Jul 2013	0.186	-	0.383	-
BOX4C	FG	Aug 2012 - Jul 2013	0.223	-	0.438	-
BOX4D	YF	Nov 2012 - Jul 2013	0.305	-	0.46	-
BOX5A	BNU	30 th Nov - 9 th Dec 2004 (Haze Fog Sth)	0.22	-	0.38	-
BOX5B	BNU	30 th Nov - 9 th Dec 2004 (Haze Fog Wst)	0.13	-	0.14	-
BOX5C	BNU	30 th Nov - 9 th Dec 2004 (No Haze Fog)	0.04	-	0.06	-
BOX6A	MBEJ	2001 - 2003	0.05	-	0.12	-
BOX6B	MBEJ	2001 - 2003	0.08	-	0.39	-
BOX6C	MBEJ	2001 - 2003	0.04	-	0.19	-
BOX6D	MBEJ	2001 - 2003	0.05	-	0.07	-
BOX6E	MBEJ	20 th Mar 2002 (Dust Storm)	0	-	0.08	-
BOX7A	THU	1 st - 31 st Jan 2013 (RH < 50 %)	< 0.2	-	< 0.2	-
BOX7B	THU	1 st - 31 st Jan 2013 (RH 70 - 80 %)	0.28	-	0.34	-
BOX8A	BJ	14 th - 23 rd Jan 2010 (Haze)	0.51	-	0.29	-
BOX8B	BJ	14 th - 23 rd Jan 2010 (Non-Haze)	0.28	-	0.16	-
BOX9	YU CAS	4 th Aug - 3 rd Sep 2012	0.2	-	0.63	-
BOX10A	BNU	2001 - 2004 (Dust)	0.09	-	0.25	-
BOX10B	BNU	2001 - 2004 (Haze)	0.22	-	0.24	-
BOX10C	BNU	2001 - 2004 (Clear)	0.13	-	0.15	-
BOX11A	WBJ	22 nd - 27 th Oct 2014	0.15	-	0.51	-
BOX11B	WBJ	23 rd - 28 th Oct 2017	0.24	-	0.55	-
BOX12A	WBJ	2013	0.16	0.12	0.26	0.19
BOX12B	WBJ	2014	0.13	0.1	0.28	0.21
BOX12C	WBJ	2015	0.12	0.08	0.38	0.23
BOX12D	WBJ	2016	0.14	0.11	0.41	0.24
BOX12E	WBJ	2017	0.12	0.08	0.42	0.2
BOX13A	CMA	5 th Jun - 30 th Nov 2009	0.625	0.219	0.584	0.29
BOX13B	CMA	5 th Jun - 31 st Aug 2009	0.691	0.217	0.702	0.322
BOX13C	CMA	1 st Sep - 30 th Nov 2009	0.577	0.207	0.471	0.211
BOX14A	THU	1 st - 31 st Oct 2014 (Overall)	0.1	-	0.25	-
BOX14B	THU	1 st - 31 st Oct 2014 (Clean)	0.07	-	0.16	-
BOX14C	THU	1 st - 31 st Oct 2014 (Polluted)	0.15	-	-	-
BOX14D	THU	1 st - 31 st Oct 2014 (Heavily Polluted)	0.14	-	0.41	-

As a comparison, a review of SOR and NOR was also conducted for the available literature in Beijing shown in Table 5.4. *N.B.* site codes are identical as previously mentioned, with the addition of UCAS (University of the Chinese Academy of Sciences); MBEJ (multiple sites across Beijing); BJ (Beijing in which exact sampling locations were not reported); and WBJ (a western urban district of Beijing). The studies reviewed for Beijing include Zhou et al., (2012)¹⁸⁷ (BOX1); Zhang et al., (2018)²⁰² (BOX2); He et al., (2018)⁴⁶³ (BOX3); Wang et al., (2016)¹⁹⁵ (BOX4); Sun et al., (2006)¹⁸⁵ (BOX5); Wang et al., (2005)²⁰⁰ (BOX6); Zheng et al., (2015)¹⁹¹ (BOX7); Zhao et al., (2013)⁴⁶⁴ (BOX8); Zhang et al., (2016)¹⁹² (BOX9); Wang et al., (2006)¹⁹⁴ (BOX10); Wang et al., (2019)²⁰¹ (BOX11); Wang et al., (2019)¹⁹⁶ (BOX12); Hu et al., (2014)¹⁹⁹ and Xu et al., (2017)¹⁸⁶ (BOX14).

Comparing the NOR values to other studies in Beijing however, Sun et al., (2006)¹⁸⁵ report winter NOR averages of 0.22, 0.13 and 0.04 for haze-fog (southerly), haze-fog (westerly) and non-haze-fog periods (in 2004). The BWIN total NOR average of 0.10 is therefore in good agreement with the haze-fog (westerly) NOR reported by Sun et al., (2006)¹⁸⁵. Furthermore, work by Zhou et al., (2012)¹⁸⁷ also reported an NOR value of 0.1 during the winter season in 2006 which agrees very closely to the BWIN average observed. More recent winter NOR values were not available (to best knowledge).

The most likely explanation to NOR values very close to the 0.1 threshold in each study presented is most likely down to significantly cooler temperatures and reduced solar flux in Beijing during the winter seasons inhibiting NO₂ homogeneous gas-phase oxidation to NO₃⁻. The temperature may also inhibit the rate of aqueous phase NO₂ oxidation.

For BSUM, the total campaign average NOR was 0.14. This was shown to be in good agreement with the work by Meng et al., (2017)⁴⁶⁵ who reported an average NOR of 0.13 during the summer of 2009. In addition, a study by Zhou et al., (2012)¹⁸⁷ reported an NOR average of 0.17 which was also in relatively good agreement with the BSUM average, despite the study having sampled over the summer of 2006. Slightly higher NOR values were reported by Zhang et al., (2016)¹⁹² who reported an NOR average of 0.2 for the summer of 2012; and by Hu et al., (2014)¹⁹⁹ who reported an NOR of 0.22 for the summer of 2009. Generally, considering the uncertainties of the NOR and SOR calculation, the BSUM NOR average showed good agreement to previous studies. A particularly low NOR was calculated by Wang et al., (2005)²⁰⁰ who reported an average 0.08 across sampling sites for the summers between 2001 – 2003. This campaign was however *ca.* 14 years prior to the BSUM campaign and workers also sampled mostly at rural locations in which lower [NO_x] would be expected.

The BWIN SOR campaign average of 0.31 was generally higher than the other studies reviewed (Table 5.4), although was in relatively close agreement with the work by Sun et al., (2006)¹⁸⁵ who reported a winter SOR average of 0.38 for the haze-fog (southerly) periods during the winter in Beijing in 2004. For the BSUM campaign, an SOR average of 0.54 was calculated which was in closest agreement with Meng et al., (2017)⁴⁶⁵ who reported a summer SOR of 0.52 in 2009. Relatively good agreement was also observed with the work of Zhang et al., (2016)¹⁹² who reported

an SOR of 0.63 for the summer of 2012. Other studies however observed significantly lower and higher values as demonstrated in Table 5.4.

Realistically, it is very difficult to compare the NOR and SOR values to the previous literature presented in Table 5.3 and Table 5.4, as the sampling times, atmospheric conditions and sampling sites are very variable in between studies. Furthermore, the NOR and SOR do not take into account the lifetimes of species under specific atmospheric conditions and these parameters are very simple. Table 5.3 and Table 5.4 do however demonstrate that the APHH NOR and SOR values shown in Fig. 5.14 are in the proximate range that would be expected for each of these parameters. The NOR and SOR values in Fig. 5.14 would ideally be compared to much more recent studies in both Delhi and Beijing, although the reviewed studies in Table 5.3 and Table 5.4 was the extent of the literature available.

The knowledge of the relative NOR and SOR between campaigns is useful, although greater detail about the dominant NO_3^- and SO_4^{2-} formation mechanisms for day and night-time periods in heavily polluted urban atmospheres such as Delhi and Beijing may be useful for future models.

5.3.2.9 NOR and SOR Correlations

It is known that NO_2 and SO_2 can oxidise through different pathways. NOR and SOR time series data were used to perform linear regression analysis to try and indicate which other species and conditions measured during the campaigns may have had an influence on the oxidative pathways. This may therefore suggest which oxidation mechanisms could have occurred producing NO_3^- and SO_4^{2-} in Delhi and Beijing (over the four campaigns for day and night). The temperature, RH, $[\text{O}_3]$, $[\text{HONO}]$, $[\text{NO}_2]$, $[\text{SO}_2]$ and particle size were averaged to the IC filter times of this study to conduct linear regression analysis between species concentrations and conditions with NOR and SOR. Day and night-time analysis were also conducted for which any whole day filters were omitted. Blocked filters were also omitted from these analyses. Table 5.5 shows the linear regression correlation coefficient results of NOR and SOR for the day, night and total campaigns for the DPEM, DPOM, BWIN and BSUM periods against these variables. Regressions detected > 0.5 are bolded in red; > 0.7 bolded in yellow; > 0.9 bolded in green. Underlined and italic values represent negative gradients.

5.3.2.10 Temperature

The DPEM night-time period is the only dataset which shows any substantial correlation of NOR with temperature ($R^2 > 0.5$). This correlation is negative and therefore suggests the decrease in NOR as temperature increases. A reason for this may be due to the evaporation of NO_3^- from the particle phase (NH_4NO_3), as NO_3^- in $\text{PM}_{2.5}$ is predominantly found as NH_4NO_3 . Therefore, as $\text{NOR} = \frac{[\text{NO}_3^-]}{([\text{NO}_2] + [\text{NO}_3^-])}$, evaporation of NO_3^- from the particle phase would observe a seemingly lower NOR value^{193,466}. This argument was also proposed by Sun et al., (2006)¹⁸⁵ in their work. There was however no other significant correlation with any other time-period. Work by Zhang et al., (2018)²⁰² and Liu et al., (2015)¹⁵⁶ also report no correlation between temperature and SOR, during pollution episodes, and therefore the lack of correlation in the DPEM, DPOM, BWIN and BSUM campaigns

Table 5.5. Linear Correlation Coefficient values between NOR and SOR against other Key Oxidation Variables. Values in Red, Amber and Green are $R^2 > 0.5$, 0.7 and 0.9 , respectively. Within these values, those underlined demonstrated negative gradients. The number of data points used for correlation calculation are also given for each value (N).

R^2			N	Temp	N	RH	N	O ₃	N	HONO	N	NO ₂	N	SO ₂	N	Dia	N	NH ₄ ⁺	N	NO ₃ ⁻	N	SO ₄ ²⁻
SOR	DPEM	Day	23	0.11	23	0.12	23	0.02	13	0.03	23	0.09	23	<u>0.59</u>	-	-	23	0.07	23	0.02	23	0.07
		Night	7	0.42	7	0.71	7	0.09	5	0.17	7	0.25	7	<u>0.98</u>	-	-	7	0.00	7	0.01	7	0.18
		Total	30	0.08	30	0.10	30	0.00	18	0.09	30	0.10	30	<u>0.55</u>	-	-	30	0.04	30	0.00	30	0.05
	DPOM	Day	59	0.04	59	0.06	59	0.01	0	-	59	0.01	59	0.11	-	-	59	0.00	59	0.02	59	0.11
		Night	10	0.34	10	0.53	10	0.13	0	-	10	0.03	10	0.15	-	-	7	0.40	10	0.28	10	0.08
		Total	74	0.02	74	0.02	74	0.02	0	-	74	0.01	74	0.09	-	-	69	0.00	74	0.00	74	0.02
	BWIN	Day	90	0.04	100	0.04	100	0.07	62	0.03	100	0.10	100	0.25	19	0.25	97	0.00	100	0.01	100	0.05
		Night	21	0.13	23	0.44	23	0.01	18	0.05	23	0.04	23	0.11	8	0.38	14	0.00	23	0.10	23	0.23
		Total	111	0.06	123	0.06	123	0.07	80	0.03	123	0.08	123	0.20	27	0.08	111	0.00	123	0.00	123	0.09
	BSUM	Day	156	0.00	156	0.29	156	0.01	99	0.09	150	0.19	156	0.50	-	-	147	0.00	156	0.04	156	0.01
		Night	36	0.00	36	0.41	36	0.01	30	0.05	33	0.18	36	0.47	-	-	30	0.12	36	0.00	36	0.01
		Total	192	0.00	192	0.25	192	0.02	129	0.04	183	0.19	192	0.47	-	-	177	0.00	192	0.02	192	0.01
NOR	DPEM	Day	23	0.01	23	0.09	23	0.02	13	0.18	23	<u>0.72</u>	23	0.01	-	-	23	0.02	23	0.14	23	0.00
		Night	7	<u>0.54</u>	7	0.14	7	0.24	5	<u>0.56</u>	7	0.36	7	0.31	-	-	7	0.23	7	0.21	7	0.04
		Total	30	0.08	30	0.02	30	0.29	18	0.25	30	<u>0.74</u>	30	0.01	-	-	30	0.01	30	0.40	30	0.05
	DPOM	Day	59	0.08	59	0.10	59	0.28	0	-	59	0.00	59	0.40	-	-	59	0.48	59	0.49	59	0.12
		Night	10	0.29	10	0.59	10	0.06	0	-	10	0.11	10	0.09	-	-	7	0.51	10	0.37	10	0.16
		Total	74	0.04	74	0.07	74	0.17	0	-	74	0.00	74	0.29	-	-	69	0.46	74	0.43	74	0.12
	BWIN	Day	90	0.10	101	0.11	101	0.38	62	0.42	101	0.47	101	0.43	20	0.82	98	0.65	101	0.74	100	0.56
		Night	21	0.27	23	0.53	23	0.27	18	0.51	23	0.24	23	0.27	8	0.27	14	0.31	23	0.88	23	0.77
		Total	111	0.15	124	0.12	124	0.27	80	0.30	124	0.40	124	0.40	28	0.57	112	0.63	124	0.75	123	0.60
	BSUM	Day	152	0.10	152	0.00	152	0.41	101	0.12	152	0.17	150	0.05	-	-	143	0.09	152	0.00	152	0.00
		Night	34	0.00	34	0.18	34	0.34	30	0.19	34	0.39	33	0.08	-	-	31	0.60	34	0.72	34	0.41
		Total	186	0.16	186	0.00	186	0.50	131	0.25	186	0.31	183	0.06	-	-	174	0.08	186	0.04	186	0.06

between NOR and SOR with temperature may be down to other overriding variables affecting NOR and SOR.

5.3.2.11 Relative humidity

Table 5.5 shows that significant positive correlations with RH are only seen during the night-time periods during the DPOM ($R^2 = 0.59$) and BWIN ($R^2 = 0.53$) campaigns for NOR and the DPEM ($R^2 = 0.71$), DPOM ($R^2 = 0.53$), BWIN ($R^2 = 0.44$) and BSUM ($R^2 = 0.41$) campaigns for SOR. In addition, RH levels observed during the night-time hours were consistently higher throughout the campaigns compared to the daytime hours (Fig. 5.16) and temperatures were consistently lower at night also (Fig. 5.17). There is therefore significance between the RH % and the NOR and SOR values in Delhi and Beijing. For the particularly high correlation coefficients of NOR and SOR vs RH %, it is hypothesised that aqueous homogenous or heterogenous oxidation pathways were the dominant oxidation mechanisms during these periods for SO_2 and NO_2 , respectively.

To explain this correlation, a higher RH causes a larger uptake of water molecules onto pre-existing particles producing more aqueous aerosol, enhancing the ability of NO_2 and SO_2 to dissolve into the particle and undergo heterogenous and aqueous phase oxidation (transition metal catalysed)¹⁸⁶. In addition, coagulation of water onto pre-existing particles also dilutes the components in the particles, preventing saturation of atmospheric gases (i.e. SO_2 and NO_2 etc.) within the liquid phase and therefore increases dissolved $[\text{NO}_2]$, $[\text{HNO}_3]$, $[\text{SO}_2]$ and $[\text{H}_2\text{SO}_4]$. Furthermore, with increased RH, NH_4NO_3 and $(\text{NH}_4)_2\text{SO}_4$ and NH_4HSO_4 evaporation may decrease^{194,187}.

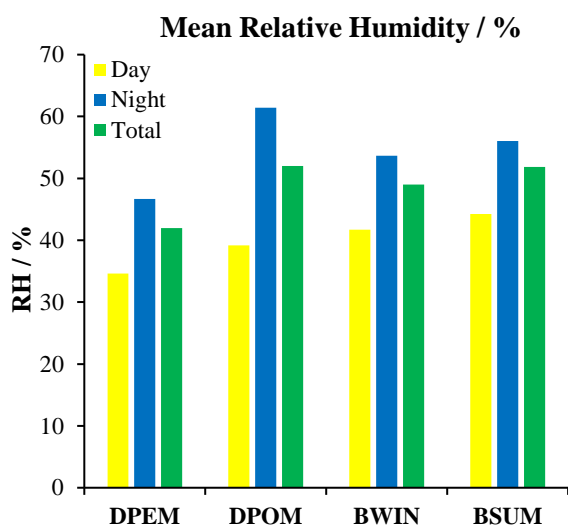


Fig. 5.16. Mean RH % Across APHH Campaigns. Error ca. < 1%.

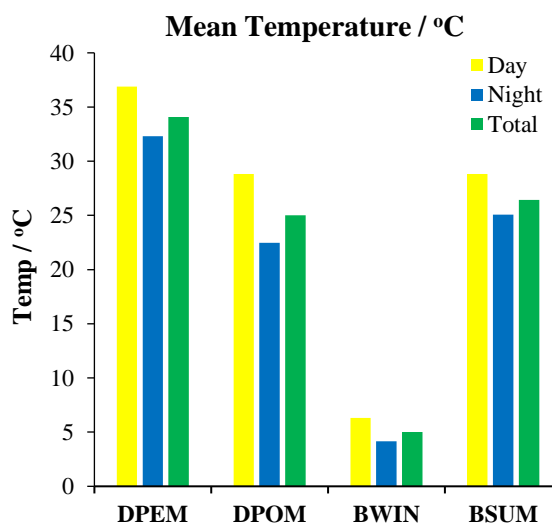


Fig. 5.17. Mean Temperature Across APHH Campaigns. Error ca. < 1%.

These arguments are in line with the work of Zhang et al., (2018)²⁰² who observed a relationship between RH and NOR in Beijing during the night (because of higher RH levels) and who concluded that this was due to a greater influence of the heterogenous pathway of NO_2 oxidation. Zhang et al., (2018)²⁰² also report an R^2 value of 0.58 for SOR vs RH and indicated the predominance of the aqueous pathway occurring for SO_2 oxidation in Beijing from 10th Feb – 19th Mar 2015.

Little literature is available of NOR and SOR vs RH correlation for comparison with Delhi however work by Saxena et al., (2017)¹⁹⁸ did evaluate in their study that cooler conditions with a relatively higher RH encouraged NO_3^- and SO_4^{2-} formation and that specifically, SO_4^{2-} was most likely to be produced in winter via the aqueous heterogenous pathway by oxidation with H_2O_2 and O_3 .

Several studies have observed very good correlations of NOR and SOR vs RH in Beijing. To compare the Beijing winter season, Sun et al., (2006)¹⁸⁵ reported significant correlation of NOR and SOR with RH reporting R values of 0.88 and 0.96, respectively (R^2 0.77 and 0.92, respectively) for their study in Beijing from 30th Nov – 9th Dec 2004 which were much larger compared to the APHH BWIN campaign correlations shown in this study. Chi et al., (2018)¹⁸⁴ report NOR and SOR vs RH correlation values of R 0.79 and 0.67, respectively (R^2 0.62 and 0.45) and also concluded the presence of the aqueous oxidation pathway for NO_3^- and SO_4^{2-} production, during haze events in Beijing between 26th Nov 2016 – 12th Jan 2017. Furthermore, work by Wang et al., (2016)¹⁹⁵ observed a stronger correlation between SOR and RH during the autumn and winter (cooler seasons) and a greater positive correlation between RH and NOR over the winter, spring and autumn periods which led the authors to conclude that heterogeneous (and slow photochemical oxidation) occurred during these seasons in Beijing for SOR and NOR. Work by Duan et al., (2020)⁴⁵⁷ indicated that SOR vs RH represented an exponential relationship during the winter season in Beijing in 2015 and concluded that SOR was dependant on RH and that heterogenous SOR pathways were key (authors also noted that the homogeneous pathway was still present during this period from a good correlation observed between SOR vs [oxidant]). In contrast however, Zhou et al., (2012)¹⁸⁷ stated that in winter there was much lower RH and therefore suggested that the SO_4^{2-} was more likely to originate from homogeneous gas-phase processes. Duan et al., (2020)⁴⁵⁷ also reported that the NOR was less dependent on RH during the winter for which NOR was dominated by the photochemical pathway (higher correlation of NOR vs [oxidants]).

The fact that little correlation was observed between NOR and SOR vs RH during the BSUM campaign is likely down to the warmer weather and larger solar flux causing a preference for the photochemical gas-phase oxidation pathway as opposed to the heterogenous reaction. This argument would be in line with the work by Duan et al., (2020)⁴⁵⁷ who observed no correlation between SOR vs RH but who reported a positive correlation for SOR vs [oxidants] instead. Workers also report that the measured NOR was impartial of the RH (and [oxidant]), and suggested that the increased [NO_3^-] levels in summer measured in their study during high RH periods is likely down to the presence of readily soluble NH_4NO_3 , as well as N_2O_5 hydrolysis (chapter 1)⁴⁵⁷. The lack of correlation during BSUM is however in disagreement with the work of Zhang et al (2016)¹⁹² who demonstrated positive correlations of R 0.68 and 0.71 for NOR and SOR respectively ($R^2 = 0.46$ and 0.50, respectively) in Beijing from 4th Aug – 3rd Sep 2012 and concluded considerable presence of the aqueous pathway occurring. Zhou et al., (2012)¹⁸⁷ also mention that the higher RH in summer may augment the heterogenous oxidation pathway in Beijing¹⁸⁷, although this is not seen in the R^2 correlations of the

BSUM (Table 5.5) campaign for neither NOR or SOR and may simply be due to atmospheric conditions prioritising other oxidation pathways.

It must however be highlighted that relatively little regression is observed for NOR vs RH during the DPEM ($R^2 = 0.14$) and BSUM ($R^2 = 0.18$) night-time periods. For DPEM, this may be down to the relatively lower RH% (Fig. 5.16) and higher temperatures (Fig. 5.17) observed at night compared to the other campaigns. For BSUM however, the night-time temperatures are relatively like DPOM and the RH% is high compared to BWIN. This could therefore indicate that during the night-time periods of the DPEM and BSUM seasons, NO_2 may not preferentially be aqueous based. In addition, no daytime NOR or SOR trends observe a significant correlation with RH which may also indicate the predominance of other oxidation mechanisms.

Overall, it may be suggested that in cases where strong correlation regression is observed (predominantly at night) between NOR and SOR vs RH, the heterogenous or aqueous phase oxidation mechanism may be occurring. For NOR during the DPEM and BSUM night-time periods, as well as the daytime periods in each campaign, this is however not the case. Further investigation is therefore required and may be conducted by comparing the NOR and SOR correlations with the potential precursors measured during the campaign.

5.3.2.12 Concentrations of precursor oxidants

Table 5.5 shows that the only correlation of oxidation with O_3 was from NOR vs O_3 exhibited during the BSUM campaign. This was also seen in the work of Zhang et al., (2018)²⁰² who reported a correlation of $[\text{O}_3]$ with NOR values during the daytime in Beijing during the winter – spring period (10th Feb – 19th Mar 2015) and concluded that NO_3^- was predominantly produced via gas-phase processing. In addition, NOR also observed a regression correlation with HONO. Table 5.5 displayed a positive correlation ($R^2 = 0.51$) for the BWIN night-time period which indicates the heterogenous production of HONO from NO_2 oxidation.

No other significant correlations are observed in Table 5.5 with O_3 or HONO. This is likely down to O_3 and HONO being relatively minor oxidants to the oxidation of NO_2 and SO_2 , although these were the oxidising species which were available at the time of analyses. In addition, large uncertainties residing in the NOR and SOR calculation (section 5.3.2.14). Future work comprises investigating into the correlations of NOR and SOR with other oxidant species.

5.3.2.13 Particle Size and Surface Area

Mean particle diameter data was only available for the BWIN campaign (UoM). Table 5.5 shows that a strong positive correlation was observed between NOR and particle diameter during the daytime hours ($R^2 = 0.82$), although very little positive correlation was observed at night ($R^2 = 0.27$). Based on the work of Rattigan et al., (2001)⁴⁶⁷, it could be suggested that the NOR mechanism during the BWIN daytime is more likely to occur via the heterogenous metal catalysed oxidation of NO_2 with O_2 and O_3 , whereas the BWIN night may observe a different oxidation mechanism (such as via H_2O). This is evidenced by NOR also observing some correlation with O_3 ($R^2 = 0.38$) and NO_2 (0.47).

Furthermore, the increased availability for particle surface area (i.e. mineral dust) for the heterogeneous oxidation on increasing particle diameter would increase the oxidation rate¹⁹¹ (a low regression ($R^2 = 0.11$) was observed for NOR vs RH for the daytime BWIN which makes this pathway unlikely to be homogenous or aqueous heterogeneous).

No significant correlation was however observed between particle diameter vs SOR (Table 5.5), although previous studies have implied that SOR may be affected by particle size¹⁹¹. Work by Rattigan et al., (2001)⁴⁶⁷ have suggested that this could be down to the changing pH of particles as a function of drop size which affects the rate of SO₂ oxidation in the aqueous phase through metal catalysed oxidation via O₂ and O₃ (pH > 6). Furthermore, work by Xu et al., (2017)¹⁸⁶ also reported that NOR and SOR levels were raised in their work as a function of PM_{2.5} concentrations (and therefore higher particle surface area), most likely via heterogeneous processes. The reason why NOR has good correlation with particle size but SOR does not (in BWIN) is likely down to differing mechanisms and warrants further future study.

5.3.2.14 Uncertainties in [NO₃⁻]/[SO₄²⁻], NOR and SOR

Although a basic indication may be given of the proportion of mobile and stationary emission sources to PM_{2.5} composition, there are several flaws which arise using the [NO₃⁻]/[SO₄²⁻], NOR and SOR analyses. Firstly, the ratio calculation assumes that all the NO₃⁻ and SO₄²⁻ originate from a secondary nature. Even though most of the NO₃⁻ and SO₄²⁻ in these two megacities may be assumed to be from secondary oxidation, a substantial amount of primary SO₄²⁻, for example, was observed as cement dust from a building site next to the IGDTUW sampling site in Delhi (chapter 3). Both Delhi and Beijing may also experience dust intrusion which also carries primary NO₃⁻ and SO₄²⁻. Furthermore, an example of primary NO₃⁻ emission would be from the volatilisation of NH₄NO₃ which could partition onto PM_{2.5} and dissociate into NH₃ and HNO₃. Another area of uncertainty is from the release of SO₂ (and a very small fraction of SO₄²⁻) from mobile emission sources, such as from diesel powered vehicles⁴⁴⁷. On the other hand, some dominant sources of NO₃⁻ such as biomass burning are also stationary (explaining the augmented [NO₃⁻] / [SO₄²⁻] ratios observed during the winter compared to the summer in Beijing). Finally, other variables affect whether NO₃⁻ may be found in the gas or particle phase, such as RH¹⁹⁵.

The NOR and SOR calculations are a very basic metric which incorporate numerous assumptions and purely consider the concentration of precursors and products without consideration of other variables such as lifetimes etc. For NOR particularly, numerous studies mention the formation of NO₃⁻ by N₂O₅ hydrolysis which would also produce error in the NOR^{193,202,195,199,24,186} as well as the [NO₃⁻]/[SO₄²⁻] equation. N₂O₅ data was not available at the time of these analyses, and so correction regarding N₂O₅ hydrolysis to [NO₃⁻] constitutes to future work. Further error may alter the NOR if warmer temperatures allow for the evaporation of NH₄NO₃ back into the gas phase as NH₃ and HNO₃. (NH₄)₂SO₄ and NH₄HSO₄ are known to be significantly less volatile²⁶. It has also been suggested in the literature that transportation of NO₃⁻ and SO₄²⁻ from other regions may also skew the NOR and SOR results¹⁹⁶.

Additionally, improved methods of correlation analysis (instead of R^2 linear regression) have been reviewed by Mikkonen et al., (2019)⁴⁶⁸, who state that orthogonal regression is a more accurate regression analysis (in general). Finally, the DPEM campaign only acquired a weeks-worth of data, and therefore the regression analyses (Table 5.5) and average values (Fig. 5.14) should be taken with caution. Much fewer studies were also conducted in Delhi compared to Beijing, and therefore comparison of the Delhi correlation regressions with the literature was challenging, and most comparisons in these sections surround work in Beijing.

In essence, NOR and SOR calculations are over-simplified for the purposes of evaluating the relative levels of NO_2 and SO_2 oxidation and primary and secondary NO_3^- and SO_4^{2-} proportions, although are used abundantly in inorganic $\text{PM}_{2.5}$ literature studies. Work by Wang et al., (2019)²⁰¹ however suggest an alternate equation by incorporating their modelling results in order correct for the over-estimation of NOR and SOR.

To further evaluate the use of NOR and SOR as indicator metrics of atmospheric NO_2 and SO_2 oxidation, it is useful to compare these metrics to other basic indicator metrics regarding their usefulness. As such, a very similar metric to the NOR and SOR is the ammonium conversion ratio (which NOR and SOR may be compared to), shown in Eq. 5.6, as used by Meng et al., (2018)⁴⁶⁹.

$$\text{NHR} = \frac{\text{NH}_4^+}{\text{NH}_4^+ + \text{NH}_3}$$

Eq. 5.6. Ammonium Conversion Ratio

The main disadvantages in using these indicator metrics surround the very broad assumptions associated with the contributing variables, that the ions originate solely from NO_2 and SO_2 oxidation (for NOR and SOR, respectively), or NH_3 neutralisation (NHR). This may not be the case in instances where aerosol has travelled from more arid and dusty regions, in which species such as SO_4^{2-} may be found already bound with a cation such as calcium or magnesium (in naturally occurring CaSO_4 and MgSO_4 , for example), or in cases where these ions may enter the aerosol from primary sources (i.e. SO_4^{2-} from cement, chapter 3), for example. For NHR however, there are fewer pathways to NH_3 neutralisation compared to NO_2 or SO_2 oxidation, increasing the accuracy of the NHR compared to NOR, SOR and $[\text{NO}_3^-]/[\text{SO}_4^{2-}]$ indicator metrics.

In addition, even when NO_3^- , SO_4^{2-} and NH_4^+ have been formed from neutralisation processes, the equations do not consider the age of the aerosol, where the aerosol originated from and how far it may have travelled. Therefore, the metrics may be influenced from oxidation and neutralisation processes which had not occurred at that sampling site. In addition, these calculations ignore the fact that the precursor gases (NO_2 , SO_2 and NH_3) may contribute to the formation of NO_3^- , SO_4^{2-} and

NH₄⁺, respectively, within PM_{2.5-10}, such as from the neutralisation of HNO₃ and H₂SO₄ with basic dust species¹⁴³.

A further source of error for the use of these metrics in this thesis specifically, is the use of filter sampling data which is prone to the presence of positive and negative artefacts^{470,354}. Furthermore, using filter-based measurements limits the number of data points which can contribute to the NOR and SOR. Further detail is also lost in the instances when the HiVol is not sampling. These criticisms may also be applied to the [NO₃⁻]/[SO₄²⁻] ratio described in section 5.3.2.1. This further increases the uncertainty surrounding these basic indicator metrics when using offline filter sampling data.

Another criticism of each of these metrics is that they are not used consistently across the literature. For example, Meng et al., (2018)⁴⁶⁹ and Liu et al., (2015)¹⁵⁶ use molar quantities in calculating NOR and SOR, whereas Hassan et al., (2013)¹⁴³ and Khoder., (2002)¹⁹⁷ conduct the calculation using the atmospheric mass concentration. Hassan et al., (2013)¹⁴³ and Khoder., (2002)¹⁹⁷ also include the gas phase NO₃⁻ in their calculation, which doesn't exist. This also affects the ability to be able to compare results to other studies, in some cases.

Moreover, these indicator metrics only give a basic indication of the relative level of oxidation, neutralisation and very basic source apportionment (mobile or stationary) and may be used to evidence what may already be known or expected (e.g. NOR and SOR are higher during higher temperatures and higher solar flux and that the majority of these major ionic species are from secondary processes). The usefulness of these metrics is therefore questionable. Basic metrics such as NOR, SOR, NHR and [NO₃⁻]/[SO₄²⁻] could however be used to test for any unexpected surprises in the data.

Another indicator metric which may be used is the ion balance, which gives a suggestion as to the state of particle acidity based on the relative molar quantities of anions and cations. The ion balance (also known as strong acidity) as described in Farren et al., (2019)⁴³¹ is given in Eq. 5.7.

$$\text{Ion Balance} = \Sigma \text{ Anions (Moles)} - \Sigma \text{ Cations (Moles)}$$

Eq. 5.7. Ion balance equation to calculate particle acidity.

A higher positive number indicates the greater excess of anionic species and therefore a greater acidity associated with the particles. Similar to NOR and SOR however, this metric is very basic and is susceptible to errors from filter sample data from potential intrusion of positive and negative artefacts. Furthermore, the estimation of acidity from ion balance is influenced highly by the number of ions which are considered. Xu e al., (2020)²⁶⁷ compared three different methods of ion balance using data from 10 different laboratories around the world. Ion balance method 1 incorporated NO₃⁻, SO₄²⁻ and NH₄⁺; method two incorporated the addition of Cl⁻, Na⁺ and K⁺; and method 3 further

incorporated Mg^{2+} and Ca^{2+} , as described by the authors. They found that method 1 showed best agreement between the laboratories. Similar to NOR and SOR, this very basic metric does not compare to much more sophisticated and improved methods of aerosol analysis which give indications to the gas-aerosol phase equilibrium and acidity, such as the E-AIM⁴⁷¹ and ISORROPIA II³²⁹ thermodynamic aerosol models.

To conclude, NOR and SOR are very basic metrics, similar to $[\text{NO}_3^-]/[\text{SO}_4^{2-}]$ and ion balance (for acidity) and should be used with caution, with a preference to using more sophisticated aerosol analytical models such as the E-AIM⁴⁷¹ and ISORROPIA II³²⁹ thermodynamic models. Furthermore, there is very little mention in the literature surrounding the issues associated with NOR, SOR and $[\text{NO}_3^-]/[\text{SO}_4^{2-}]$ in particular. The NOR and SOR are however very simple to use and may be a very quick method to identify the relative oxidation of NO_2 and SO_2 in the atmosphere when comparing between samples, although mostly these metrics will simply confirm what is already known in this regard.

In summary, an insight has been given into the potential oxidation levels and mechanisms occurring for NO_2 and SO_2 during the campaigns (where enough data was available). Although not enough data was available for reliable NO_2 and SO_2 oxidation mechanistic interpretation in this study, this type of analysis may be useful in future for modelling purposes. In addition, a knowledge of the key possible oxidation mechanisms occurring is a useful basis for understanding ammonium neutralisation and therefore SIA formation (section 5.3.3). It was found that a greater proportion of stationary and mobile sources likely contributed to $\text{PM}_{2.5}$ in Delhi and Beijing, respectively. In both cities, an increase of $[\text{NO}_3^-]/[\text{SO}_4^{2-}]$ demonstrated an increased contribution to $\text{PM}_{2.5}$ from mobile source during daytime hours which is attributed to higher traffic emissions during the day. The BSUM NOR and SOR values were higher than the BWIN values due to higher temperatures and increased solar flux during summer periods. The DPOM SOR was higher than the DPEM campaign which is suspected to be due to the much-increased NO_x emissions and the oxidation of SO_2 by NO_2 . NOR and SOR were higher during the day across all campaigns due to an increase in solar flux and temperatures. The SOR values also indicate that across all campaigns, SO_4^{2-} is predominantly from secondary oxidation of SO_2 . The NOR values indicate that across the campaigns, secondary formation is the prominent pathway for NO_3^- formation although the DPEM and BWIN night-time periods may have had a significant contribution from primary sources.

To correctly assess the particle acidity and solve particle composition explicitly, thermodynamic models such as E-AIM⁴⁷¹ or ISORROPIA II³²⁹ can be used. These models have not been applied to the data presented in this thesis, due to the lack of gas phase (H_2SO_4 , HNO_3 , HCl and NH_3) data which was not available from the APHH campaigns conducted in Delhi or Beijing, which is essential for the accurate running of these models. Alternatively, an estimation of the equilibrium composition has been conducted using the ion balance⁴³¹ method (using correlation regression analysis, section 5.3.3) which although is a basic method (as discussed) gives a good indication of the ammonium salt

equilibrium with HCl, HNO₃ and H₂SO₄ when NH₄⁺, Cl⁻, NO₃⁻ and SO₄²⁻ are the only species used. As NH₄⁺, Cl⁻, NO₃⁻ and SO₄²⁻ make up the predominant fraction of the inorganic fraction within Asian megacity PM_{2.5}, the ion balance method was deemed suitable in this instance. *N.B.* It must however be emphasised that the ion balance method gives an indication of the aerosol acidity from the point of the inorganic species and does not take into account any organic acids.

5.3.3 Ammonium and Particle Acidity

SIA is widely acknowledged to form a predominant part of urban aerosol in which the dominant SIA formation into the particle phase is known to occur via the neutralisation of acidic gases with NH₃ (section 5.1). It is known that NH₃ neutralises preferentially with H₂SO₄ > HNO₃ > HCl and therefore it is expected that NH₄⁺ should be found predominantly in the form of NH₄HSO₄ + (NH₄)₂SO₄ > NH₄NO₃ > NH₄Cl in these heavily polluted megacities. Molar correlation regression analysis was conducted during the day and night-time periods over all four APHH campaigns to investigate the pathway of NH₄⁺ into the particle phase and which acids would predominantly neutralise NH₃ in these megacities. This was completed to give a greater insight into SIA formation within these highly polluted megacities as well as the equilibrium positions of the reactions of NH₃. This analysis may also be helpful in future atmospheric models involving SIA.

To further enhance the understanding of aerosol formation within these polluted Asian megacities from ammonia and acidic gas neutralisation forming PM_{2.5}, the equilibrium conditions of these reversible reactions are investigated in this section. This has been explored by conducting molar regression analyses between NH₄⁺ vs the major conjugate bases Cl⁻, NO₃⁻ and SO₄²⁻.

The day and night-time [NH₄⁺] have been plotted against the Σ [Cl⁻] + [NO₃⁻] + 2[SO₄²⁻] to evaluate the extent of NH₄⁺ neutralisation for the DPEM, DPOM, BWIN and BSUM campaigns. Correlation plots are also shown for NH₄⁺ vs 2[SO₄²⁻] (red); NH₄⁺ vs NO₃⁻ (blue) and NH₄⁺ vs Cl⁻ (green) in this section. The yellow dashed line on each plot represents the 1:1 equimolar ratio. Trend lines have been passed through each regression as a solid line, for which the regression equations and R² coefficients are displayed. *N.B.* 2[SO₄²⁻] is plotted against [NH₄⁺] as complete neutralisation of NH₃ with H₂SO₄ results in the production of (NH₄)₂SO₄.

5.3.3.1 Beijing Winter Day

Fig. 5.18 demonstrates that the BWIN daytime correlation of NH₄⁺ vs Σ [Cl⁻] + [NO₃⁻] + 2[SO₄²⁻] gradient is 1.025 with an R² = 0.9712. This indicates the full neutralisation of NH₃ from the major acidic gases. The correlation coefficient was also R² = 0.9712 demonstrating a high level of certainty in this regression analysis. In addition to this, strong correlation regression coefficients were seen between NH₄⁺ and the separate anions, individually. This therefore confirms that the dominant formation route of NH₄⁺ into the aerosol phase is through acidic gas neutralisation reactions. At closer inspection the daytime correlation coefficients observed very strong positive correlations for all conjugate bases, due to reduced temperatures keeping the NH₄⁺ equilibria within the particle phase.

Fig. 5.18B however shows that the NH_4^+ vs $2[\text{SO}_4^{2-}]$ gradient ($0.3894x$) is lower compared to the NH_4^+ vs NO_3^- gradient ($0.4541x$). This implies that NH_3 was in excess of H_2SO_4 and that the equilibrium of ammonium sulfate formation was likely dominant towards the products side, although this reaction was limited by the concentration of H_2SO_4 . Furthermore, the molar ratio of $[\text{NH}_4^+] / [\text{SO}_4^{2-}] = 3.75$ was considerably above 1.5 suggesting that the form of NH_4^+ was likely $(\text{NH}_4)_2\text{SO}_4$. Regarding the relative vapour pressures of the ammonium salts, the residual NH_3 is able to react with HNO_3 which explains the strong correlation as well as gradient of $0.4541x$ observed. The NH_4^+ vs NO_3^- gradient was significantly steeper compared to that of Cl^- and $2[\text{SO}_4^{2-}]$ suggesting that the dominant species neutralising NH_3 is HNO_3 , as opposed to H_2SO_4 which would be expected. As this gradient is larger compared to the NH_4^+ vs $2[\text{SO}_4^{2-}]$ correlation, this may indicate that a higher concentration of HNO_3 (compared to H_2SO_4) was available in the atmosphere to neutralise NH_3 .

The presence of a high R^2 correlation coefficient for the NH_4^+ vs Cl^- regression also indicates the presence of the $\text{NH}_3 + \text{HCl}$ neutralisation reaction, although the low gradient suggests that this reaction contributes substantially less to the overall $[\text{NH}_4^+]$ within the aerosol compared to NO_3^- or $2[\text{SO}_4^{2-}]$. In lieu of the $\text{NH}_3 + \text{HCl}$ reaction occurring during the BWIN daytime hours, this would suggest that almost all (if not all) of the H_2SO_4 and HNO_3 had been neutralised away by NH_3 , for which the residual NH_3 was neutralised by HCl . Furthermore, the very low temperatures allow for the NH_4Cl species to reside in the particle phase which does not occur during the other campaign seasons. In addition, the Huaneng coal power plant was still in operation in very close proximity to IAP and along with heightened biomass and coal burning in the heating season (K^+ vs Cl^- , $R^2 = 0.87$), it is likely that HCl was present in abundance. This is in agreement with the findings in section 5.3.1.7 which showed that during the BWIN daytime hours, a substantial concentration of Cl^- originated from the Huaneng power plant.

Therefore, it may be suggested that NH_3 was in excess of H_2SO_4 as well as HNO_3 . This is down to the lower production rate of H_2SO_4 and HNO_3 from SO_2 and NO_2 oxidation, due to a lower solar flux and significantly reduced temperatures occurring during the winter daytime period, compared to the other campaigns. In addition, the BWIN daytime $[\text{NO}]$ was the highest daytime $[\text{NO}]$ out of all the APHH campaigns, for which NO is known to titrate away oxidising species in the atmosphere. The higher gradient seen in the NH_4^+ vs NO_3^- trend compared to the NH_4^+ vs $2[\text{SO}_4^{2-}]$ trend is likely down to the much higher $[\text{NO}_2]$ during the BWIN daytime hours compared to the $[\text{SO}_2]$ (chapter 3). This is due to an increase in NO_2 concentrations from heating and electricity during the cooler winter months, used during the daytime hours. A higher $[\text{HNO}_3]$ is further evidenced by the $[\text{NO}_3^-]/[\text{SO}_4^{2-}]$ demonstrating the highest values across all campaign periods for the BWIN daytime hours (average of 1.45).

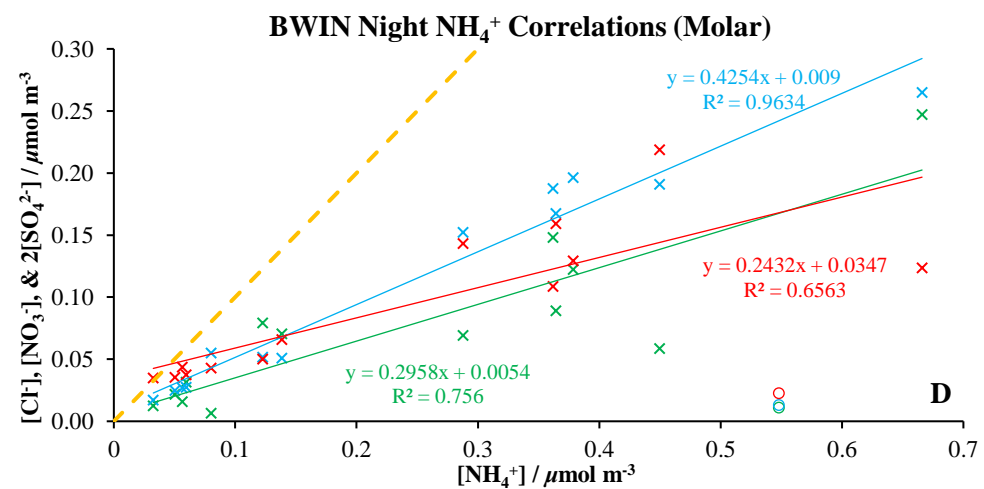
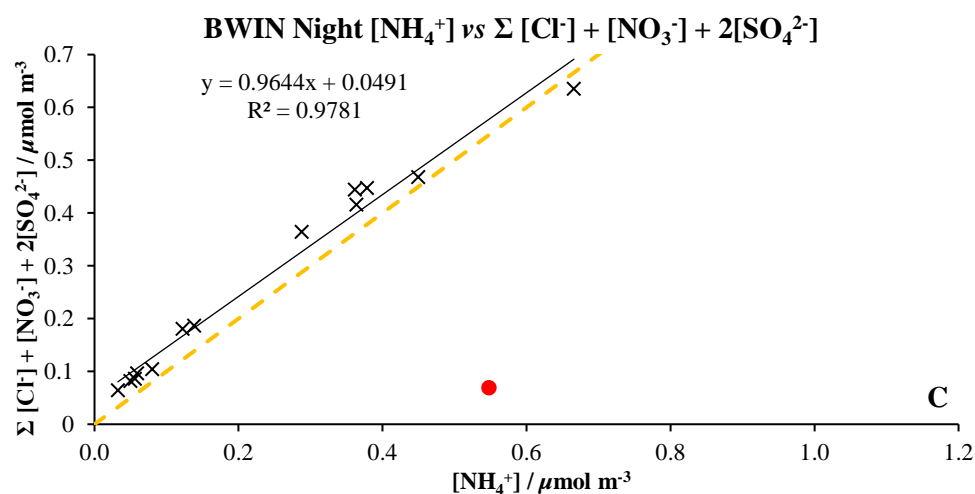
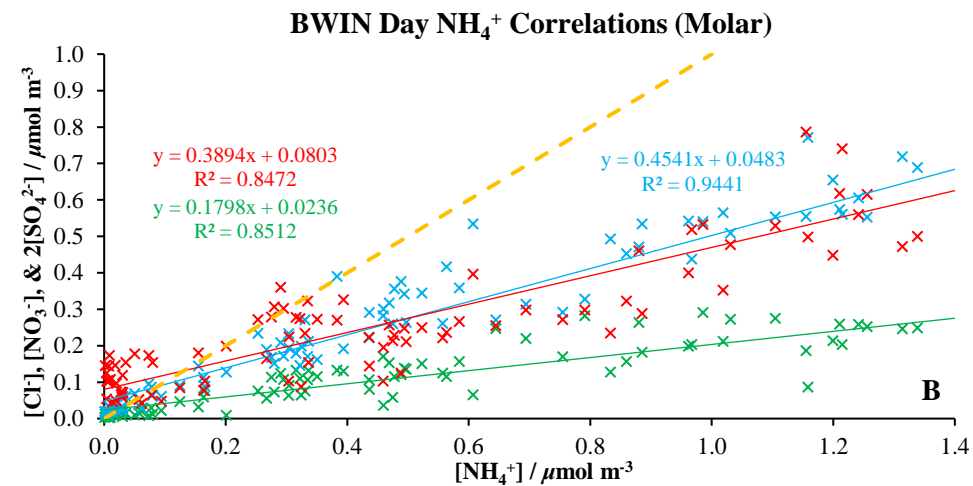
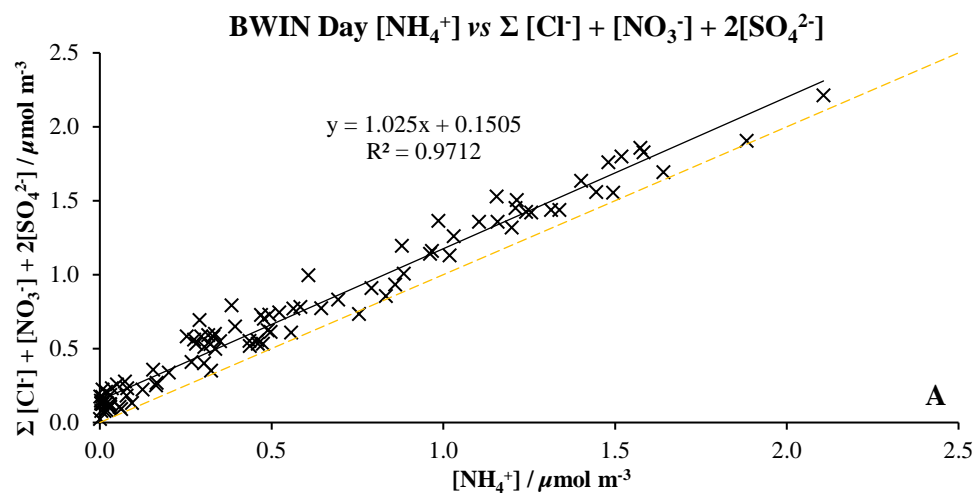


Fig. 5.18. Molar Linear Regression Correlation of NH_4^+ with the $\Sigma [\text{Cl}^-] + [\text{NO}_3^-] + 2[\text{SO}_4^{2-}]$ for the day and night periods (A and C, respectively) for the BWIN campaign. The red dot point (C) and the circle points (D) represent an anomaly. Linear regression correlation of the individual ions with $[\text{NH}_4^+]$ is also shown for the BWIN campaign day and night-time periods (B and D, respectively). The red cross points represent NH_4^+ vs $2[\text{SO}_4^{2-}]$; the blue cross points represent NH_4^+ vs NO_3^- ; and the green cross points represent NH_4^+ vs Cl^- . The solid lines show the regression analysis for each relationship with the respective regression equation shown. The 1:1 molar equivalent ratio is also presented as a yellow dashed line in all charts. Errors associated with these measurements may be found in Chapter 3.

5.3.3.2 Beijing Winter Night

During the winter night period, a potential anomaly was identified for sample #49 (21/11/2016 17:37 – 22/11/2016 08:30) and has been highlighted by representation of a red dot point in Fig. 5.18C, as well as circle points as opposed to cross points in Fig. 5.18D. This is most likely down to contamination.

Fig. 5.18C shows the molar correlation regression analysis between NH_4^+ vs $\Sigma [\text{Cl}^-] + [\text{NO}_3^-] + 2[\text{SO}_4^{2-}]$. The gradient here is 0.96 and therefore indicates that almost all of the NH_4^+ was neutralised by acidic gases and that the NH_4^+ aerosol was fully neutralised (within error). The NH_4^+ vs $\Sigma [\text{Cl}^-] + [\text{NO}_3^-] + 2[\text{SO}_4^{2-}]$ gradient in Fig. 5.18C is *ca.* 1 (0.9644x) with a very high R^2 value of $R^2 = 0.9781$ which demonstrates a very small error in this regression analysis.

Inspecting the individual species, it is seen that the NH_4^+ vs $2[\text{SO}_4^{2-}]$ gradient is 1.60 times smaller compared to the daytime value. This shows that less H_2SO_4 neutralisation occurred during the night compared to during the daytime, which is most likely down to an even lower $[\text{H}_2\text{SO}_4]$ during the night due to lower temperatures and lower solar flux reducing the oxidation of SO_2 into H_2SO_4 . There is also however a lower regression coefficient associated with the NH_4^+ vs $2[\text{SO}_4^{2-}]$ BWIN night-time trend increasing the uncertainty compared to the daytime value. This is however most likely down to the fewer samples available.

For the BWIN night-time NH_4^+ vs NO_3^- correlation however, the gradient decreases marginally compared to the daytime and Fig. 5.18D shows that the reaction between $\text{NH}_3 + \text{HNO}_3$ is the dominant formation pathway of NH_4^+ into the particle phase during the BWIN night-time periods also. As solar flux and temperatures decrease further during night-time hours, it is strange that this hasn't appeared to have affected the NH_4^+ vs NO_3^- gradient significantly, considering that the majority of the daytime HNO_3 was likely neutralised by NH_3 (section 5.3.3.1). The production of HNO_3 during the night must have taken an alternative pathway such as through the production of N_2O_5 , followed by N_2O_5 hydrolysis to produce HNO_3 ⁴⁷². The result of this process may have allowed NO_3^- to be the continuing neutralising species for NH_4^+ during the night-time hours. The fewer samples available for the night-time period however make this hypothesis speculative, for which more samples would be needed to confirm this argument.

Adversely, the NH_4^+ vs Cl^- gradient is even stronger during the night by *ca.* 60 % compared to the daytime. This may be explained by the even lower night-time temperatures reducing the NH_4Cl evaporation back into the gas phase for which the equilibrium position resides in the particle phase. Furthermore, significantly low HNO_3 as well as H_2SO_4 night-time concentrations produces a larger excess proportion of NH_3 which hadn't been neutralised by these acidic species. Moreover, $[\text{HCl}]$ is also likely higher during the night due to IAP being in close proximity to the Huaneng thermal power station in conjunction with a decreased boundary layer height during night-time hours. There is also likely a proportion of $[\text{HCl}]$ which was not neutralised by daytime NH_3 and passed over into the night-time period.

5.3.3.3 Beijing Summer Day

Reviewing the NH_4^+ vs $\Sigma [\text{Cl}^-] + [\text{NO}_3^-] + 2[\text{SO}_4^{2-}]$ correlation in Fig. 5.20A, the gradient is *ca.* 0.71 which initially suggests that NH_4^+ is in excess and that the aerosol is alkaline by nature. At closer inspection however, a very low R^2 ($R^2 = 0.2845$) is produced displaying high uncertainty which is due to two different regimes being taken. Inspecting the individual major anion correlations with NH_4^+ , two separate regimes are evident in the $2[\text{SO}_4^{2-}]$, $[\text{NO}_3^-]$ and $[\text{Cl}^-]$ correlations, as shown in Fig. 5.19.

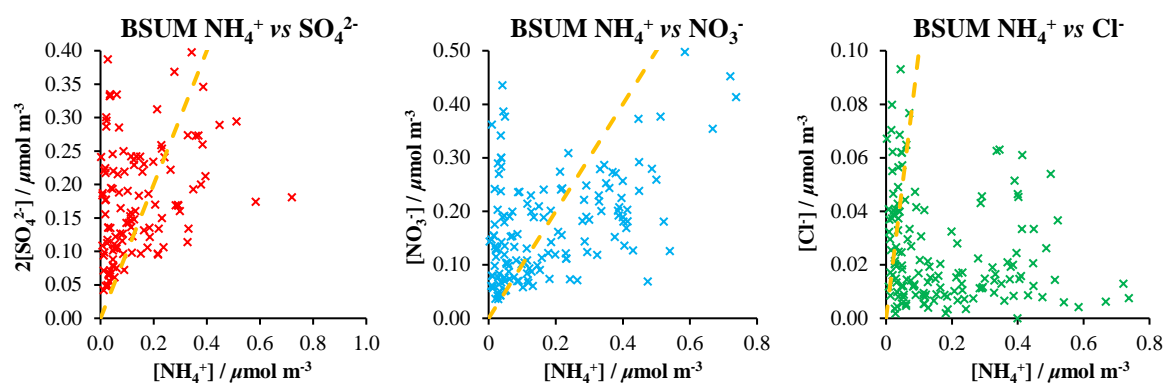


Fig. 5.19. Molar Regression Analysis of $[\text{NH}_4^+]$ vs $2[\text{SO}_4^{2-}]$, $[\text{NO}_3^-]$ and $[\text{Cl}^-]$ for the BSUM daytime hours. The 1:1 molar ratio is shown as a yellow dashed line. This is a separated-out version of Fig. 5.20B (for clarity). Errors associated with these measurements may be found in Chapter 3.

Despite the uncertainty which arises from the different regimes, the strongest gradient is nonetheless seen between NH_4^+ vs $2[\text{SO}_4^{2-}]$, followed by NH_4^+ vs $[\text{NO}_3^-]$, followed by NH_4^+ vs $[\text{Cl}^-]$, which is in agreement with the relative vapour pressures of these ammonium salts. This is likely down to the meteorology, as temperature and solar flux increase during the summer seasons which leads to significantly higher $[\text{HNO}_3]$ and $[\text{H}_2\text{SO}_4]$ to neutralise atmospheric NH_3 . In addition, the higher temperatures likely evaporate NH_4Cl from the aerosol phase and cause the equilibrium to favour the side of the gas phase constituents, which would explain the very low regression coefficient and gradient seen within the NH_4^+ vs $[\text{Cl}^-]$ analysis (Fig. 5.19). Furthermore, although HCl was not measured, the reduction in biomass burning and the closing of the Huaneng power plant are likely to have substantially reduced HCl gas-phase emissions, compared to the BWIN campaign. Due to the very high uncertainty in the regressions however, it is very difficult to make any conclusive statements.

To try and explain the two different regimes seen in Fig. 5.20A and Fig. 5.20B, it may be that on some days temperatures had increased the evaporation of NH_3 from agricultural sources producing the acid deficient schemes, and that on cooler days the reservoir of oxidants produced an abundance of H_2SO_4 and HNO_3 when NH_3 concentrations were lower. A significant amount of future work will be needed to separate these regimes using tools such as PMF with other data collected as part of the campaign. This however constitutes to future work.

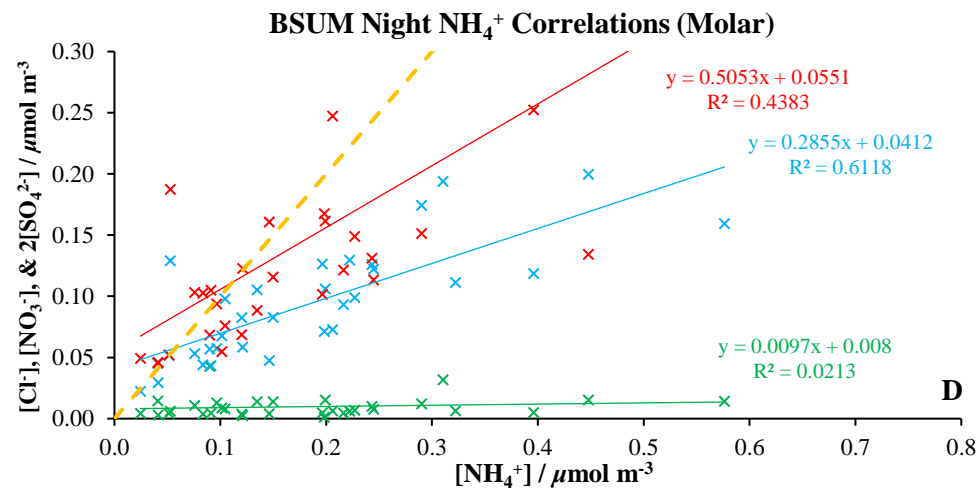
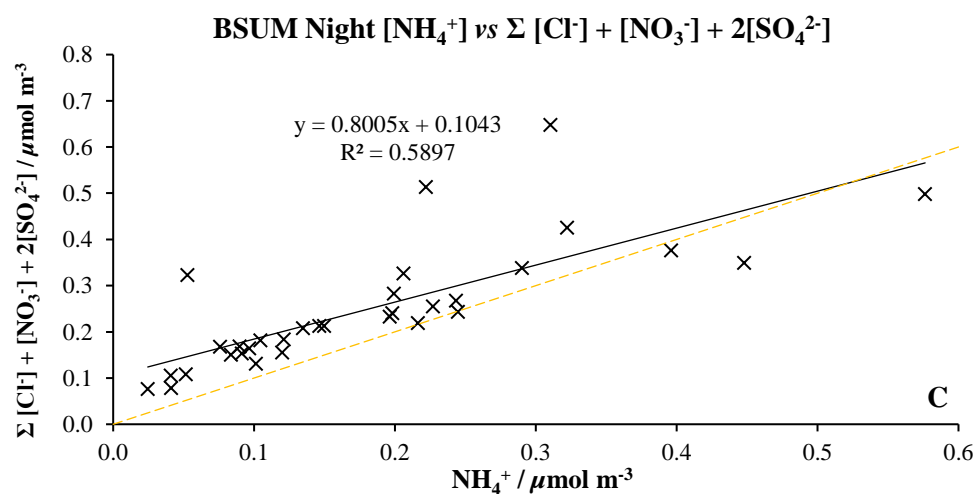
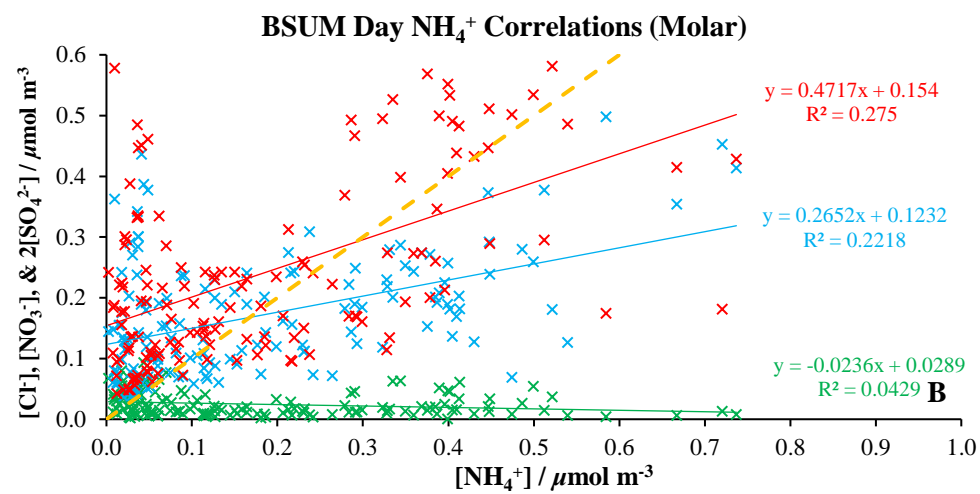
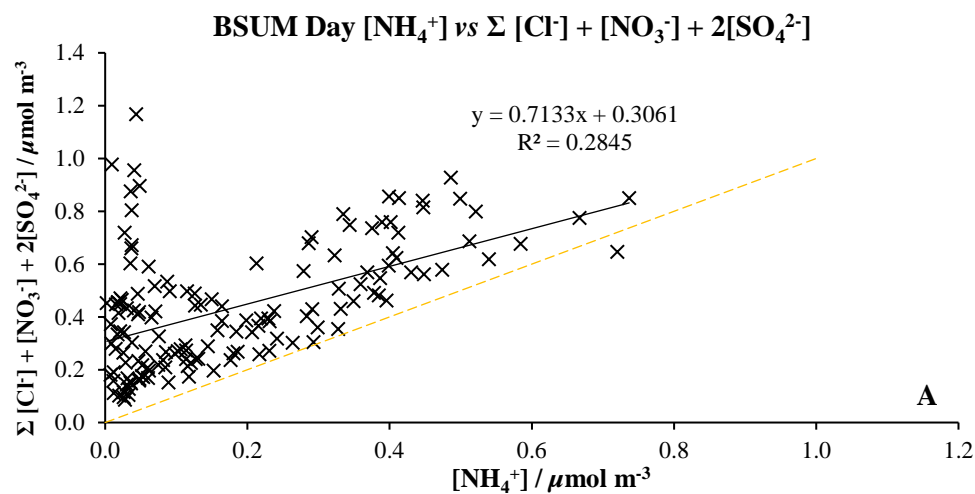


Fig. 5.20. Molar Linear Regression Correlation of NH_4^+ with the $\Sigma [\text{Cl}^-] + [\text{NO}_3^-] + 2[\text{SO}_4^{2-}]$ for the day and night periods (A and C, respectively) for the BSUM campaign. Linear regression correlation of the individual ions with $[\text{NH}_4^+]$ is also shown for the BSUM campaign day and night-time periods (B and D, respectively). The red cross points represent NH_4^+ vs $2[\text{SO}_4^{2-}]$; the blue cross points represent NH_4^+ vs NO_3^- ; and the green cross points represent NH_4^+ vs Cl^- . The solid lines show the regression analysis for each relationship with the respective regression equation shown. The 1:1 molar equivalent ratio is also presented as a yellow dashed line in all charts. Errors associated with these measurements may be found in Chapter 3.

5.3.3.4 Beijing Summer Night

For the BSUM night period, the gradient demonstrated by the NH_4^+ vs $\Sigma [\text{Cl}^-] + [\text{NO}_3^-] + 2[\text{SO}_4^{2-}]$ correlation is 0.8 which would suggest that NH_4^+ was in excess. The regression coefficient is however substantially lower (Fig. 5.20C) compared to the BWIN night-time NH_4^+ vs $\Sigma [\text{Cl}^-] + [\text{NO}_3^-] + 2[\text{SO}_4^{2-}]$ regression coefficient (Fig. 5.18).

Inspection of the correlation of NH_4^+ against the individual ions again shows the greatest gradient with $2[\text{SO}_4^{2-}]$, followed by NO_3^- , followed by Cl^- . This is what would be expected considering the vapour pressures of the ammonium salts. Similar to the daytime period, this is likely due to the relative concentrations of $[\text{H}_2\text{SO}_4]$, $[\text{HNO}_3]$ as well as $[\text{HCl}]$.

From inspection of Fig. 5.20D, $[\text{Cl}^-]$ is very low and doesn't contribute much to the NH_3 neutralisation. This is likely because the Huaneng power plant had closed between the BWIN and BSUM campaigns and during the summer season less biomass burning is expected. The heat of the summer (average night-time temperature of 25.2 °C) also will have forced the equilibrium of the NH_3 neutralisation by HCl into the gas phase. Furthermore, considerably lower $[\text{NO}]$ were present during the BSUM night-time period compared to the BWIN night-time period and therefore this particular sink for oxidants is reduced allowing for greater potential for oxidation of SO_2 and HNO_3 into H_2SO_4 and HNO_3 respectively.

5.3.3.5 Delhi Pre-Monsoon Day

The NH_4^+ vs $\Sigma [\text{Cl}^-] + [\text{NO}_3^-] + 2[\text{SO}_4^{2-}]$ correlation for the DPEM daytime period seen in Fig. 5.21A shows a gradient which is very close to 1, indicating the complete neutralisation of NH_4^+ within the particle phase by the dominant major anions SO_4^{2-} , NO_3^- , and Cl^- . Further inspection of the NH_4^+ correlations with the individual ions (Fig. 5.21B) shows a strong correlation of NH_4^+ vs $2[\text{SO}_4^{2-}]$ ($R^2 = 0.8318$), with a very high gradient (0.8202x) compared to the relationship between NH_4^+ vs Cl^- and NH_4^+ vs NO_3^- . This is indicative of SO_4^{2-} being the major neutralising species of NH_4^+ within the particle phase and that SIA formation during the DPEM daytime period is driven by the neutralisation of H_2SO_4 with NH_3 , followed by partitioning of the ammonium sulfate salt products into the particle phase. As the gradient between NH_4^+ vs $2[\text{SO}_4^{2-}]$ is below 1, this does also suggest the presence of NH_4HSO_4 as well as some NH_4^+ neutralisation by other acidic species (i.e. HNO_3).

Little correlation and a small gradient are seen between NH_4^+ vs NO_3^- , and almost no correlation or gradient is seen within the NH_4^+ vs Cl^- regression analysis (Fig. 5.21B) which indicates that HNO_3 and HCl neutralisation of NH_3 to form ammonium salts in the particle phase is negligible. The low gradient in the NH_4^+ vs NO_3^- correlation does however suggest that the residual NH_3 not neutralised by H_2SO_4 could be neutralised by HNO_3 (the uncertainty in this regression is however very high, $R^2 = 0.2147$). The NH_4^+ vs Cl^- regression in Fig. 5.21B demonstrates an even lower gradient for which there is almost no change in $[\text{Cl}^-]$ as $[\text{NH}_4^+]$ increases. The gradients presented in Fig. 5.21B is in line with the order of relative vapour pressures of the ammonium salts $(\text{NH}_4)_2\text{SO}_4 + \text{NH}_4\text{HSO}_4 > \text{NH}_4\text{NO}_3 > \text{NH}_4\text{Cl}$; an affect which becomes significantly more visible as ambient temperatures increase, and is further enhanced by lower RH%, for which the DPEM average temperature and RH%

were 36.9 °C and 41.6 %, respectively. This therefore indicates that the dominance of NH₃ neutralisation during the DPEM daytime is from H₂SO₄ to form (NH₄)₂SO₄ (and NH₄HSO₄) within the particle phase, with the (NH₄)₂SO₄ equilibrium situated towards the particle phase. The NH₄NO₃ and NH₄Cl equilibria are situated towards the gas phase species, as there is little residual NH₃ to be able to neutralise HNO₃ or HCl. Therefore, NH₃ is not a significant sink for HNO₃ or HCl during the DPEM daytime period.

Despite this, a significant proportion of NO₃⁻ is present within the DPEM daytime particle phase (average of 8.78 μg m⁻³) and the presence of detectable [Cl⁻] (daytime mean of 2.94 μg m⁻³) within the particle suggests that that NO₃⁻ and Cl⁻ entered the particle phase via a different process than acid-base neutralisation with NH₃. An alternative pathway for these species to enter the particle phase is through the neutralisation of these acidic gases with alkaline dust aerosol⁴⁷³. The concentration of cations (associated with dust) within the DPEM daytime period were 7.33 μg m⁻³ (Na⁺), 0.56 μg m⁻³ (Mg²⁺) and 8.34 μg m⁻³ (Ca²⁺), which therefore may indicate a significant level of dust; the high daytime temperatures as well as low RH% will have produced an arid and dusty climate. Therefore, the fraction of HNO₃ and HCl which had not neutralised NH₃ may react with alkaline dust species, forming NO₃⁻ independently of NH₄⁺ in the particle phase. The NO₃⁻ and Cl⁻ vs Σ [Na⁺ + K⁺ + Mg²⁺ + Ca²⁺] were however substantially low at R² = 0.28 and R² = 0.44, respectively, although there may have been other alkaline species not measured in this study which contributed to HNO₃ as well as HCl neutralisation. Other (non-neutralisation) possible pathways of NO₃⁻ and Cl⁻ into the particle phase may be via gaseous species partitioning as described by Martin., (2000)⁴⁷⁴. Furthermore, NO₃⁻ and Cl⁻ could enter the particle via organic species. Organic nitrate species are known to hydrolyse in aerosol (chapter 6). In addition, a potential route for Cl⁻ into the particle phase specifically include the dissociation of anthropogenic organochloride compounds from biomass burning¹²¹ as well as HCl dissolution into the aerosol which was directly emitted from anthropogenic activities^{475,113,25,109,476} (which are known to be ubiquitous across Delhi)³⁴⁷.

5.3.3.6 Delhi Pre-Monsoon Night

When [NH₄⁺] vs Σ [Cl⁻] + [NO₃⁻] + 2[SO₄²⁻] is plotted for the DPEM night-time data, a negative correlation is seen which is unexpected, although the uncertainty (R² = 0.5861) is also higher compared to the DPEM daytime period and is most likely down to the very low number of datapoints which were available for this analysis.

Inspecting the individual species, a very low linear regression coefficient is shown between NH₄⁺ vs 2[SO₄²⁻] (R² = 0.0246) with a very low gradient, although considerably higher correlation coefficients are seen between NH₄⁺ vs NO₃⁻ (R² = 0.6517) and NH₄⁺ vs Cl⁻ (R² = 0.7754). A potential explanation for these trends could be that little H₂SO₄ was available during the night-time hours as it had been mostly titrated away by NH₃ during the daytime, (section 5.3.3.5), with little SO₂ oxidation during the night-time hours due to reduced solar flux at night, as well as significantly reduced [SO₂] at night compared to the daytime (by *ca.* a half, chapter 3).

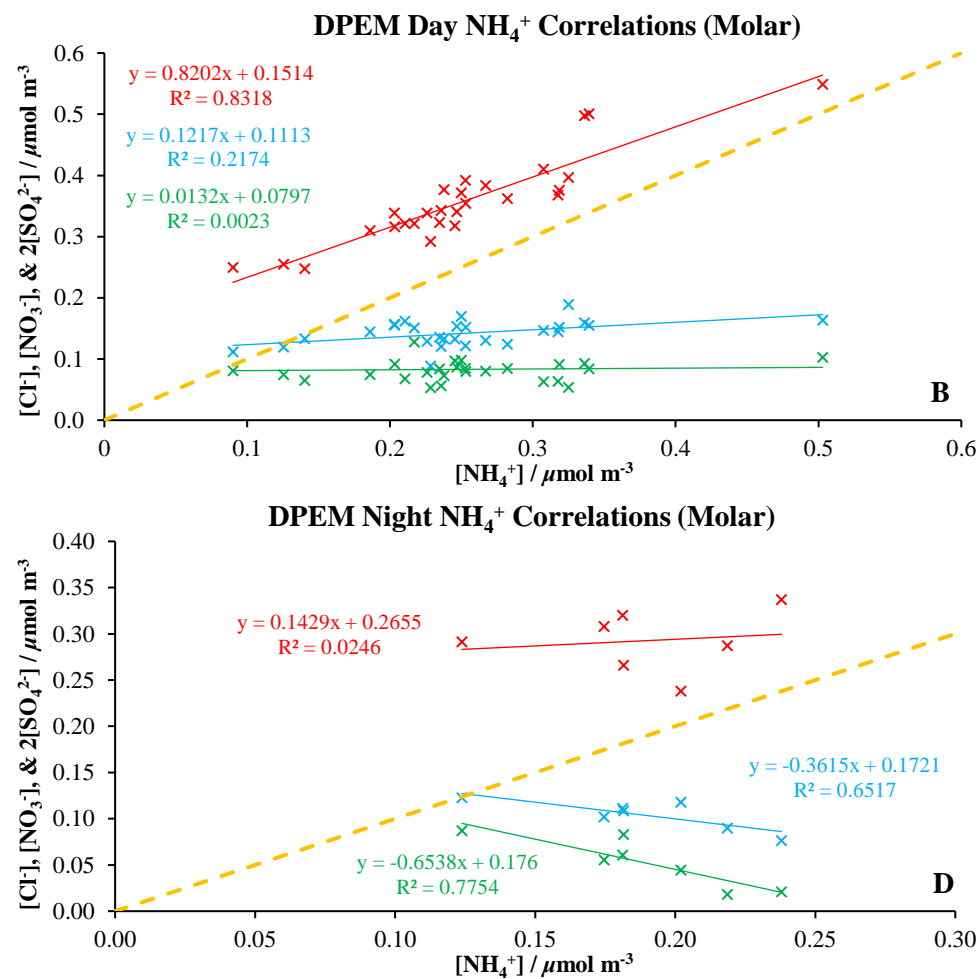
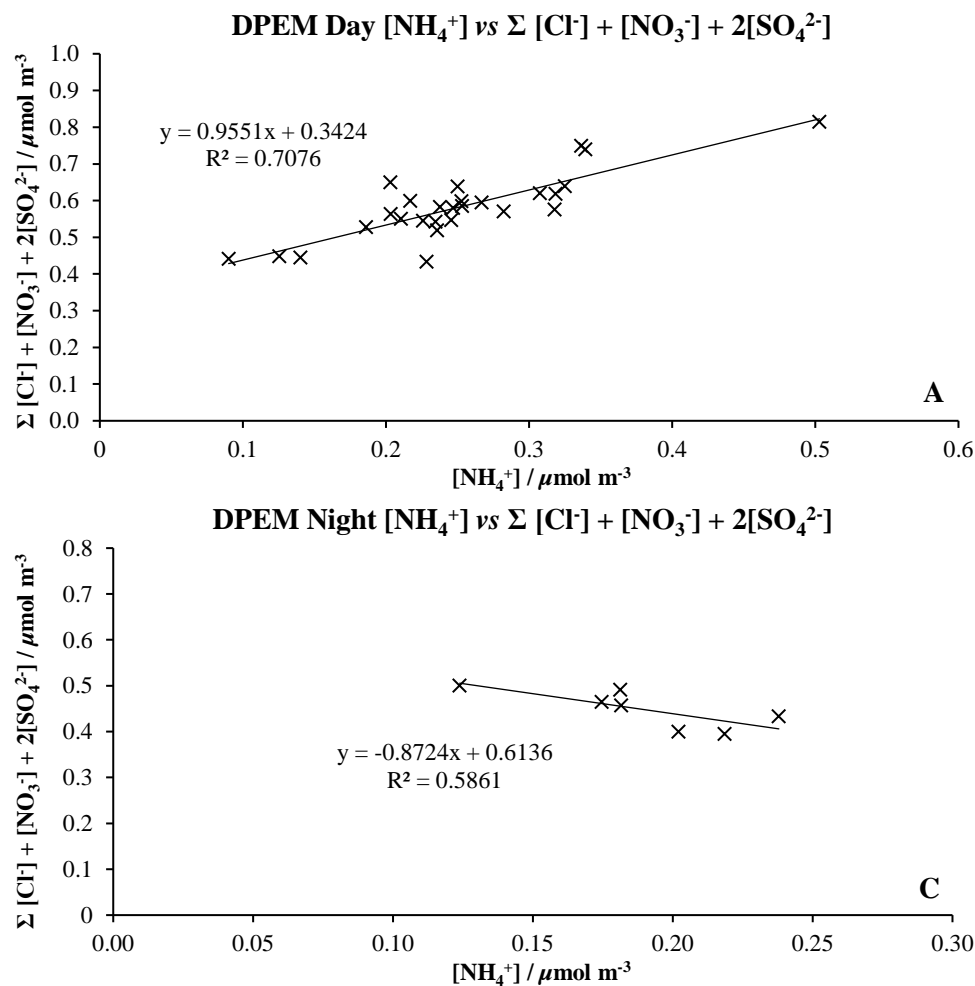


Fig. 5.21. Molar Linear Regression Correlation of NH_4^+ with the $\Sigma [\text{Cl}^-] + [\text{NO}_3^-] + 2[\text{SO}_4^{2-}]$ for the day and night periods (A and C, respectively) for the DPEM campaign. Linear regression correlation of the individual ions with $[\text{NH}_4^+]$ is also shown for the DPEM campaign day and night-time periods (B and D, respectively). The red cross points represent NH_4^+ vs $2[\text{SO}_4^{2-}]$; the blue cross points represent NH_4^+ vs NO_3^- ; and the green cross points represent NH_4^+ vs Cl^- . The solid lines show the regression analysis for each relationship with the respective regression equation shown. The 1:1 molar equivalent ratio is also presented as a yellow dashed line in all charts. Errors associated with these measurements may be found in Chapter 3.

The negative gradients observed between NH_4^+ vs NO_3^- and NH_4^+ vs Cl^- are particularly unexpected. A possible explanation for the negative correlation of NH_4^+ vs NO_3^- may be due to N_2O_5 production at night. N_2O_5 is known to be a source of NO_3^- and N_2O_5 is known to react with NH_3 ¹⁵⁵. Therefore, as N_2O_5 increases, this may increase particle NO_3^- but decrease NH_3 . This argument is however very speculative as only 7 data points were available to assess this and significantly more gas phase data (including N_2O_2 measurements are needed to confirm these hypothesis). Considerably more data would also be required to provide substantial conclusions for the negative gradient in the NH_4^+ vs Cl^- relationship.

5.3.3.7 Delhi Post-Monsoon Day

Unlike for the DPEM daytime period, the DPOM daytime NH_4^+ vs $\Sigma [\text{Cl}^-] + [\text{NO}_3^-] + 2[\text{SO}_4^{2-}]$ regression data (Fig. 5.22A) shows a gradient of below 1 (0.8221) which is indicative of NH_4^+ being in excess. This is reflected in the relative mean NH_4^+ concentrations which are an average of $3.88 \mu\text{g m}^{-3}$ and $4.20 \mu\text{g m}^{-3}$ for the DPEM and DPOM seasons, respectively (which is also indicative of an increase in NH_3 emissions during the DPOM season). Despite the correlation in Fig. 5.22A suggesting an excess of $[\text{NH}_4^+]$, the linear regression correlation coefficient obtained ($R^2 = 0.5299$) was noticeably lower for the DPOM daytime period compared to the DPEM daytime period, increasing the uncertainty surrounding this correlation. Therefore, it may be suggested that SO_4^{2-} , NO_3^- and Cl^- mostly neutralised NH_4^+ within the particle phase, although there may be an excess of NH_4^+ .

Inspecting the individual trends in Fig. 5.22B, the NH_4^+ vs $2[\text{SO}_4^{2-}]$ trend has a very low $R^2 = 0.2389$ and therefore a large uncertainty is associated with this correlation. The gradient is also very low (compared to NH_4^+ vs NO_3^-) and therefore shows that as NH_4^+ increases, the concentration of SO_4^{2-} does not substantially increase suggesting that NH_4^+ is likely in vast excess of SO_4^{2-} in the particle phase and that the ammonium sulphate species are predominantly in the form $(\text{NH}_4)_2(\text{SO}_4)$. This relationship also suggests that the equilibrium of the NH_3 neutralisation with H_2SO_4 is towards the products side, with NH_4^+ in excess. In addition to this however, it was also found in chapter 3 that a potential interference of primary cement dust may be present during the DPOM daytime hours. This would explain the low regression coefficient calculated for the NH_4^+ vs $2[\text{SO}_4^{2-}]$ correlation observed and explains the high average SO_4^{2-} mean ($17.00 \mu\text{g m}^{-3}$) detected during the DPOM daytime period.

With NH_4^+ in excess of SO_4^{2-} , this therefore suggests the presence of a reservoir of NH_3 to neutralise HNO_3 and then HCl . The gradient of NH_4^+ vs NO_3^- is 0.443 with an $R^2 = 0.7592$. This is a strong positive correlation and could indicate that HNO_3 neutralises the majority of the residual NH_3 after H_2SO_4 has been titrated out of the atmosphere. Therefore, this analysis suggests that the equilibrium position of the ammonium nitrate reversible reaction is towards the products side while NH_3 is in excess although residual HNO_3 likely remains in the gas phase after NH_3 has been titrated away.

There is also a positive gradient associated with Cl^- , although the correlation coefficient is very low ($R^2 = 0.1691$) and like $2[\text{SO}_4^{2-}]$ indicates very little increase with increasing NH_4^+ . Like the DPEM

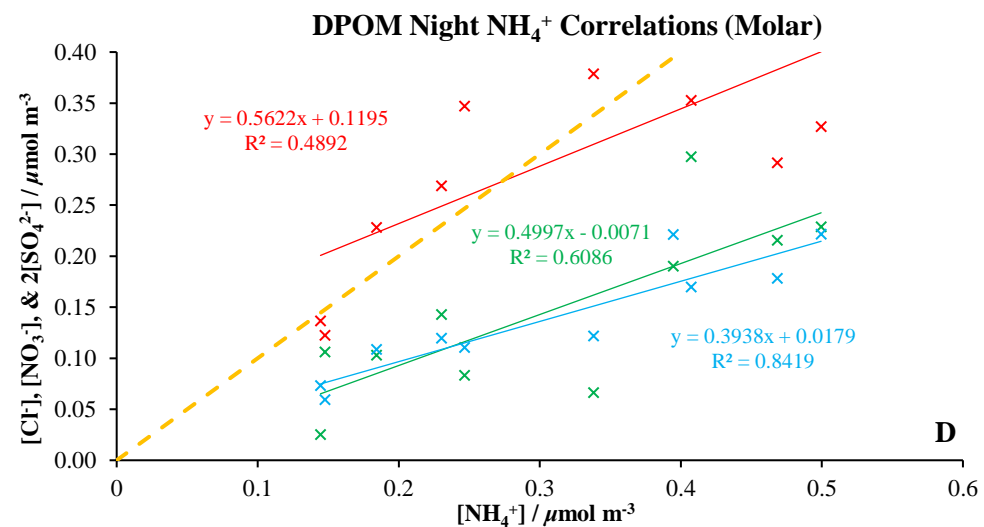
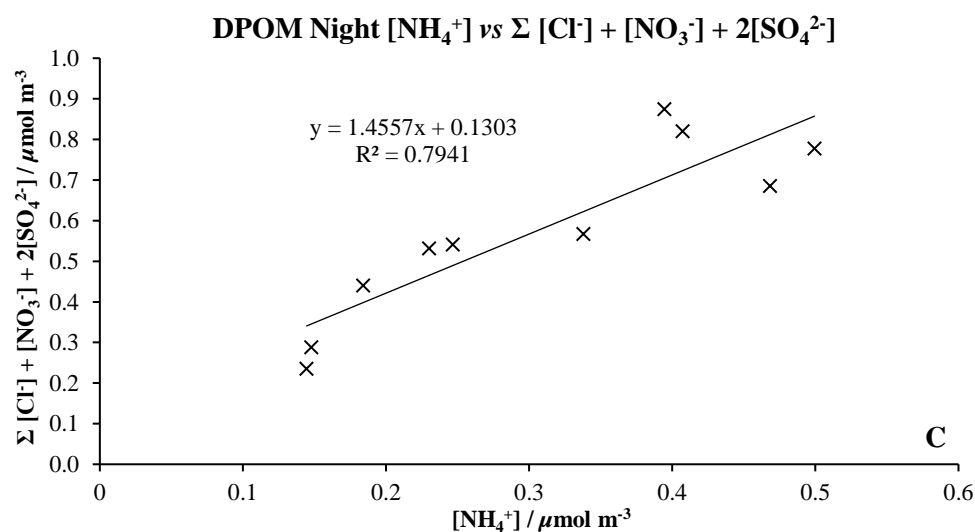
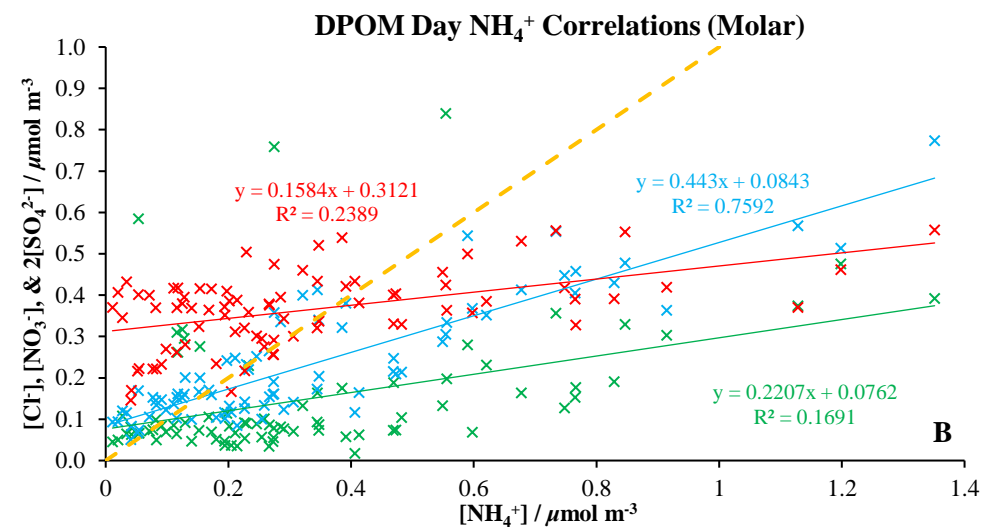
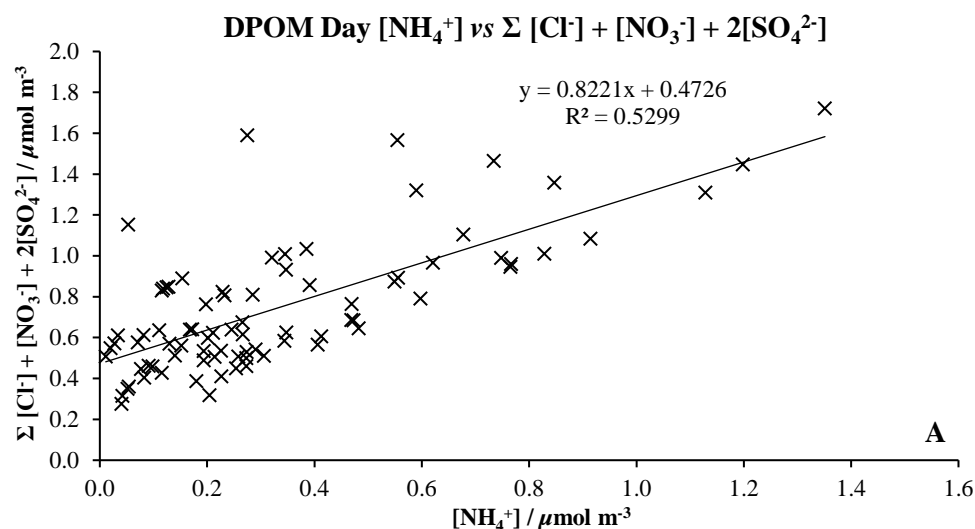


Fig. 5.22. Molar Linear Regression Correlation of NH_4^+ with the $\Sigma [\text{Cl}^-] + [\text{NO}_3^-] + 2[\text{SO}_4^{2-}]$ for the day and night periods (A and C, respectively) for the DPOM campaign. Linear regression correlation of the individual ions with $[\text{NH}_4^+]$ is also shown for the DPOM campaign day and night-time periods (B and D, respectively). The red cross points represent NH_4^+ vs $2[\text{SO}_4^{2-}]$; the blue cross points represent NH_4^+ vs NO_3^- ; and the green cross points represent NH_4^+ vs Cl^- . The solid lines show the regression analysis for each relationship with the respective regression equation shown. The 1:1 molar equivalent ratio is also presented as a yellow dashed line in all charts. Errors associated with these measurements may be found in Chapter 3.

campaign, this is attributed to the higher daytime temperatures (average of 28.6 °C) seen during the DPOM campaign, volatilising NH_4Cl into the gas phase and causing the equilibrium to dominate on the side of HCl . Fig. 5.22B therefore suggests that H_2SO_4 and HNO_3 are the driving force behind aerosol neutralisation during the DPOM daytime period at low NH_3 , with HNO_3 being the driving force behind aerosol neutralisation when H_2SO_4 has been titrated away by NH_3 .

5.3.3.8 Delhi Post-Monsoon Night

The DPOM night-time NH_4^+ vs $\Sigma [\text{Cl}^-] + [\text{NO}_3^-] + 2[\text{SO}_4^{2-}]$ regression correlation shows a gradient of $1.4557x$, with a high $R^2 = 0.7941$ (Fig. 5.22C). This therefore indicates that there is an excess of the conjugate base anions compared to NH_4^+ , which indicates an excess in $[\text{H}^+]$ not taken up by NH_3 to form NH_4^+ . The aerosol is therefore NH_4^+ deficient and acidic with respect to the inorganic species.

Inspecting the individual correlations however, the NH_4^+ vs $2[\text{SO}_4^{2-}]$ correlation shows a gradient of *ca.* 0.5 which suggests that H_2SO_4 does not saturate the NH_4^+ (Fig. 5.22D). Therefore, this indicates that NH_3 is likely to be in higher concentration compared to H_2SO_4 during the DPOM night periods. There is however a substantial uncertainty attributed to this correlation ($R^2 = 0.4892$) down to the low number of data points available. The higher regression coefficient value during the DPOM night-time compared to the daytime period is however likely down to a reduction in the concentration of primary cement species due to industrial activities ceasing at night next to the IGDTUW site (chapter 3).

NH_4^+ vs NO_3^- has a very low gradient (0.3938, although has a considerably higher R^2 value) compared to the NH_4^+ vs $2[\text{SO}_4^{2-}]$ trend. This is expected as SO_4^{2-} binds to NH_4^+ first, followed by NO_3^- . What is unexpected however is that a larger gradient ($0.4997x$) and a stronger positive correlation ($R^2 = 0.6086$) is seen between NH_4^+ vs Cl^- (Fig. 5.22D). This correlation also has a significantly higher gradient and R^2 value compared to the other periods across the APHH campaigns for the NH_4^+ vs Cl^- correlation. This therefore demonstrates a significant interaction between NH_3 and HCl which is indicative of an NH_3 reservoir left over from insufficient H_2SO_4 and HNO_3 concentrations for HCl to react with, which suggests that NH_3 had not been fully neutralised by H_2SO_4 or HNO_3 .

These correlations may be further explained by the relative concentrations of the gas phase species (chapter 3). As previously described, the very high $[\text{NO}]$ (average of 268 ppbv) during the DPOM night-time period titrates the majority of the oxidising species out of the atmosphere which is reflected in the average $[\text{O}_3]$ for the DPOM night-time period (average of 7 ppbv). This therefore reduces the oxidation of NO_2 and SO_2 species significantly, inherently reducing the concentrations of HNO_3 and H_2SO_4 , respectively, allowing NH_3 to be in excess of these species. Furthermore, HCl is expected to be abundant during the DPOM night-time period. This is because HCl is known to be released from activities such as biomass burning⁴⁷⁷ which were prevalent during the DPOM night-time period across the campaign (lead up to Diwali.)

5.3.3.9 Role of Weak Acids

Work by Meng et al., (2018)⁴⁶⁹ evaluate the importance of minor acids (such as oxalic acid, which may also be incorporated into the E-AIM⁴⁷¹ model) on the interaction with NH₃ in the production of NH₄⁺ and minor conjugate base anions (such as C₂O₄²⁻). Meng et al., (2018)⁴⁶⁹ correlate the major conjugate bases (Cl⁻, NO₃⁻, and SO₄²⁻) with NH₄⁺ to estimate the proportion of NH₄⁺ which was produced by the presence of weaker acids. They present regressions of NH₄⁺ vs [SO₄²⁻], NH₄⁺ vs Σ [SO₄²⁻ + NO₃⁻] and NH₄⁺ vs Σ [Cl⁻ + NO₃⁻ + SO₄²⁻]. They suggest that as their correlation of NH₄⁺ vs Σ [Cl⁻ + NO₃⁻ + SO₄²⁻] is less than a gradient of 1.00x but still represents a strong R² value, the gradient of their NH₄⁺ vs Σ [Cl⁻ + NO₃⁻ + SO₄²⁻] represents the number of moles of NH₄⁺ which are produce by interaction of NH₃ with Σ [HCl + HNO₃ + H₂SO₄]. They suggest that the other proportion of NH₄⁺ may have originated from the interaction of weak acids, (such as methanesulfonic acid and oxalate), with NH₃.

The theory by Meng et al., (2018)⁴⁶⁹ was applied to the data presented in this thesis to try and interpret the role of weak acids on NH₄⁺ neutralization and transformation into the particle phase. The relative regression coefficients, gradients (resembling % of NH₄⁺ neutralization contribution) and estimated % NH₄⁺ neutralization from weak acids are shown in rows 1, 2 and 3 of Table 5.6, respectively. Underneath, the regression coefficients, and gradients of regressions for three potential minor acids is also shown. Atmospheric concentrations of $\mu\text{g m}^{-3}$ had been converted to $\mu\text{mol m}^{-3}$ for this analysis.

Table 5.6. The Role of Weak Acids in NH₄⁺ Neutralization during the day and night of the DPEM, DPOM, BWIN and BSUM Campaigns.

Regression	DPEM		DPOM		BWIN		BSUM	
	D	N	D	N	D	N	D	N
NH ₄ ⁺ vs Σ [Cl ⁻ + NO ₃ ⁻ + SO ₄ ²⁻] (R ²)	0.56	0.83	0.54	0.82	0.98	0.98	0.26	0.63
NH ₄ ⁺ vs Σ [Cl ⁻ + NO ₃ ⁻ + SO ₄ ²⁻] (Gradient)	0.55	-0.94	0.74	1.17	0.83	0.84	0.48	0.55
NH ₄ ⁺ Neutralization by Weak Acids	0.45	1.94	0.26	-0.17	0.17	0.16	0.52	0.45
NH ₄ ⁺ vs F ⁻ (R ²)	0.12	0.72	0.14	0.53	NA	NA	NA	NA
NH ₄ ⁺ vs F ⁻ (Gradient)	0.02	-0.15	-0.01	0.01	NA	NA	NA	NA
NH ₄ ⁺ vs CH ₃ SO ₃ ⁻ (R ²)	0.03	0.03	0.02	0.66	0.53	0.93	0.05	0.03
NH ₄ ⁺ vs CH ₃ SO ₃ ⁻ (Gradient)	0.00	0.00	0.00	0.01	0.00	0.00	0.00	0.00
NH ₄ ⁺ vs C ₂ O ₄ ²⁻ (R ²)	0.26	0.56	0.31	0.58	0.63	0.77	0.14	0.18
NH ₄ ⁺ vs C ₂ O ₄ ²⁻ (Gradient)	0.03	-0.02	0.01	0.03	0.00	0.00	0.01	0.00

Table 5.6 shows that for the DPEM daytime hours, 55 % of NH₄⁺ is neutralised by the major acidic gases with ca. 45 % suspected to have been neutralised by minor acids. No regression was seen between NH₄⁺ and either F⁻, CH₃SO₃⁻ or C₂O₄²⁻ and therefore neither of these conjugate bases are likely to have been produced by NH₄⁺ neutralization. For the DPOM daytime period, ca. 26 % NH₄⁺ is suspected to have been neutralised by minor acids, although this is unlikely to have been either HF, CH₃SO₃H or C₂O₄H₂. According to the theory by Meng et al., (2018)⁴⁶⁹, the BSUM periods

observed a higher contribution from minor acidic species compared to the BWIN campaign which might be explained by higher oxidation occurring during the summer period producing organic acids.

Table 5.6 however demonstrates that the theory described by Meng et al., (2018)⁴⁶⁹ is inconsistent. For example, the gradient observed of NH_4^+ vs $\Sigma [\text{Cl}^- + \text{NO}_3^- + \text{SO}_4^{2-}]$ for the DPEM and DPOM night-time periods was $-0.94x$ (DPEM night) $1.17x$ (DPOM night). This would suggest that minor acids neutralised over 100 % of the NH_4^+ during the DPEM night-time period as well as -17 % of the DPOM night-time period, which is false. The role of minor acids however cannot be ruled out, as Table 5.6 does show that during some periods, strong correlation coefficients are observed between NH_4^+ vs F^- , CH_3SO_3^- and $\text{C}_2\text{O}_4^{2-}$.

5.3.3.10 Challenges in Analysis

An evaluation of the possible ammonium formation pathways have been conducted across the APHH campaigns for day and night-periods. Several uncertainties however arise. Major uncertainties revolve around the number of available datapoints. Within the night-time periods of the DPEM and DPOM only 7 and 10 datapoints were available for analysis, respectively. Therefore evaluations of these night-time periods are speculative. In addition, ideally, the $[\text{NH}_3]$, $[\text{HNO}_3]$, $[\text{H}_2\text{SO}_4]$, and $[\text{HCl}]$ gas phase concentrations are required for all campaigns to comprehensively assess and conclude the most likely NH_4^+ formation routes across the separate campaign periods. Furthermore, in some cases (such as for the BSUM day period), there are visually two different regimes between NH_4^+ and the major anions. Future work constitutes to the identification and separation of datapoints which take two separate regimes.

For diurnal profiles, loss of data occurred by the presence of five 12-hour to 24-hour daytime filter samples which were omitted during the DPOM campaign. In addition, 11 samples were omitted from the BWIN campaign for the use in diurnal averaging as these were 7-8 hours in length. For times in which very few samples were observed (1 – 2 samples), these points were omitted from the diurnal profiles. Furthermore, because of this (and blocked filters etc.) the number of samples used to average for a single diurnal average were not consistent throughout the times of day. For a larger number of samples, the variance is likely to be larger and is suspected to be the reason for some very large SD values.

5.4 Conclusion

In summary, the major Cl^- sources in Delhi and Beijing most likely originate from industrial emissions as well as coal power plants. There was a notable change in Cl^- concentrations and source origins during the summer months due to the closure of the Huaneng power station. In Delhi, much higher Cl^- was observed generally due to a considerably larger number of anthropogenic HCl emission sources from unofficial industries across the city. The main uncertainty which arises in this analysis however is the averaging of meteorological data to the HiVol sampling times needed to produce the contour plots.

The $[\text{NO}_3^-]/[\text{SO}_4^{2-}]$ ratio calculated in each city showed that generally, Delhi may have a larger contribution to $\text{PM}_{2.5}$ from stationary sources and Beijing has a larger contribution to $\text{PM}_{2.5}$ from mobile sources. The SOR and NOR were calculated and the DPEM campaign showed a significant increase in SOR after the 1st Jun which was put down to a significant wind direction change. During the DPOM campaign, the NOR and SOR were seen to generally increase on the lead up to Diwali which was attributed to very high NO_x potentially producing significant levels of organic nitrates which hydrolyse to NO_3^- , as well as increased SO_2 oxidation by NO_2 . During the BWIN season, the NOR and SOR generally followed the pattern of the pollution events which is down to increased NO_2 and SO_2 occurring during haze events. The BSUM campaign showed significantly higher daytime NOR and SOR values compared to the night-time hours which is attributed to a higher solar flux and increased $[\text{OH}]$ during daytime hours. Across the campaigns, the SOR showed that SO_4^{2-} was predominantly from secondary sources. According to the NOR campaign averages, the NO_3^- was predominantly secondarily formed during daytime hours across the APHH campaigns (although the DPEM and BWIN night-time NOR values may suggest that a higher fraction of NO_3^- is from primary sources. Major uncertainties however arise in these analyses, due to the over-simplification of the $[\text{NO}_3^-]/[\text{SO}_4^{2-}]$, NOR and SOR ratios.

The analysis of the major anions with NH_4^+ showed that the neutralisation of acidic gases with NH_3 was a substantial pathway to Cl^- , NO_3^- , SO_4^{2-} and NH_4^+ production within these Asian megacities, although further work is required to decipher which oxidation mechanisms in particular may be contributing to the Cl^- , NO_3^- , SO_4^{2-} and NH_4^+ fractions within Beijing and Delhi. It was also concluded that minor acids may contribute to NH_3 neutralisation in Delhi and Beijing.

6 The quantification of Organo-Nitrate species using a PILS-IC method at the SAPHIR smog Chamber during the NO₃ISOP campaign

6.1 Introduction

Isoprene is known to constitute *ca.* 50% of all non-methane Biogenic Volatile Organic Compounds (BVOCs) emissions into the atmosphere^{478,479,480,481}. Estimates have been reported at *ca.* 450 Tg year⁻¹ – 750 Tg year⁻¹^{482,483,484,485,480,486,487}. Due to the substantial emission of this BVOC, it has been suggested that isoprene is a significant contributor to Secondary Organic Aerosol (SOA), which in turn is to be expected to induce impacts on climate variability as well as air quality^{487,488,489}. In addition to isoprene, other VOCs which are of biogenic nature include monoterpenes and sesquiterpenes⁴⁹⁰. It is also widely acknowledged that these biogenic VOCs are readily oxidised in the atmosphere by the NO₃ radical, O₃ and OH^{490,485,486}.

NO₃ is known to be a particularly significant oxidant for BVOCs, primarily due to BVOC abundance in the atmosphere and their unsaturated nature⁴⁹¹. The nature and scale of these processes causes a significant influence on visibility and climate, as well as air quality and impact on human health through their secondary effect on O₃, NO_x and organic particulate species⁴⁹². NO₃ radical concentrations are known to increase at night⁴⁷⁸ due to a loss in concentrations during daytime hours from photolysis^{478,481,493,494,495}. NO₃ concentrations have been reported up to 350 ppt within the troposphere and have therefore indicated a possible domination of NO₃ oxidation of isoprene during night-time hours⁴⁹⁶. The NO₃ radical may be produced from either the reaction between NO₂ and O₃^{481,484} (at a rate which is related to NO₂, O₃ and temperature)⁴⁹⁷, or from the decomposition of N₂O₅⁴⁹⁵ (which has been used as the method of NO₃ radical production in previous chamber experiments^{485,497,491}).

Isoprene is known to readily react with the NO₃ radical, especially at night^{491,478,479,498,499}, and it has been estimated that the reaction between isoprene and NO₃ may produce *ca.* 50 % of the regional Organic Nitrate compounds (Org-NO₃) from isoprene origin⁴⁹⁸. It has also been reported that Org-NO₃ yields from oxidation by NO₃ are between 60-100%^{498,500}. High yields of Org-NO₃ are known to be produced from the interaction of NO₃ with BVOCs generally (in the particle and gas phases) and these reactions comprise a significant fraction of provincial and global [Org-NO₃]⁵⁰¹. The conversion of NO_x and BVOCs into Org-NO₃ species produces a transition from volatile species to species that exhibit a much lower vapour pressure and may therefore partition into the aerosol phase much more readily, forming SOA, and in turn may influence the absorbance and release of NO_x species, which in turn affects the production of O₃ and OH⁴⁷⁸. The Org-NO₃ species within SOA therefore behave as a NO_x reservoir which in turn effects the concentration of NO_x and O₃ regionally and across regions through transportation processes^{478,479}. Model simulations have also suggested that Org-NO₃ from isoprene influences ambient [NO_x] and [O₃]⁴⁹⁸. On partitioning of Org-NO₃ from

the gas to the particle phase, it has been widely acknowledged that Org-NO₃ will undergo hydrolysis to form Inorganic NO₃⁻ (Inorg-NO₃⁻) species, which in turn promotes SOA growth and also permanently removes isoprene (and other BVOCs) from the atmosphere^{479,348,502,498,276,503}. The hydrolysis of these species also allows for the estimation of the Org-NO₃ using Ion Chromatography (IC) when comparing to Aerosol Mass Spectrometer (AMS) data.

The accurate measurement and understanding of the Σ [Org-NO₃] concentrations (as opposed to individual Org-NO₃ species) within PM in the atmosphere is vital for many reasons. Firstly, Org-NO₃ species have been reported to comprise a significant fraction of organic aerosol^{269,270,272,287,504} (as well as the NO_y budget)^{505,287} and therefore the gas phase production as well as condensation into the particle phase of these species is significant in influencing the mass concentration of SOA and therefore PM. This is particularly true for areas with larger emissions of isoprene and monoterpenes. Furthermore, the Σ [Org-NO₃] affects the chemical and physical properties exhibited by the aerosol in which the OA fraction in aerosol has a direct impact on climate and radiative forcing potential of the aerosol^{506,271,272}. Moreover, the production of Org-NO₃ species acts as a sink (and reservoir) for NO_x^{273,271,272}, and therefore the production of Σ Org-NO₃ directly impacts the relative concentrations of NO_x as well as O₃ which goes on to affect the other chemistry occurring in the ambient atmosphere, as well as reducing the concentration of these toxic gases^{507,274,508,509}. Adversely, as Org-NO₃ also act as a reservoir for NO_x, these species may release as well as transport NO_x to and from different areas²⁷¹, as well as vertically through the troposphere²⁷¹ which may cause additional affects, such as changing the efficiency of O₃ production at different altitudes^{510,511} due to the release of NO_x from Org-NO₃. More work is however needed regarding the extent to which the vertical transport of Org-NO₃ (releasing NO_x) may affect O₃ production at different elevations.

Σ [Org-NO₃] data from ambient atmospheric air samples will likely be useful for future modelling studies which calculate OA formation as well as the loss of NO₃ and other key atmospheric radical species. Similarly, the ability to be able to measure Σ [Org-NO₃] will be useful for future modelling studies investigating the affect of Org-NO₃ production on the relative NO_x and O₃ concentrations and to help forecast the Air Quality Index within Asian megacities, as well as the impact of these species within aerosol on climate and the environment⁵⁰⁷.

The NO3ISOP campaign (August 2018) was an intensive smog chamber study based at the SAPHIR (Simulation of Atmospheric PHotochemistry In a large Reaction) smog chamber at the Jülich Forschungszentrum, Germany. The campaign was a collaboration between several institutions who all investigated the interaction between isoprene and the NO₃ radical under varying experimental conditions to evaluate the possible mechanisms between this interaction^{512,513,514,481}.

A Particle-Into-Liquid-Sampler coupled to Ion Chromatography (PILS-IC) system was used to investigate the production of Org-NO₃ species from the direct interaction of the NO₃ radical with isoprene (and other VOCs) as part of the NO3ISOP campaign. Sampling was conducted during the last two weeks of sampling (15th – 23rd Aug 2018) and the PILS-IC system was used to measure

[NO₃⁻] and [SO₄²⁻] within PM₁ size segregated aerosol. By measuring total NO₃⁻ species using a PILS-IC method and comparing this to AMS methods (which are known to destroy Org-NO₃ species in particular at the vaporizer stage of AMS analysis)⁴⁹⁰, an estimation of the overall Org-NO₃ fraction of species within these chamber experiments was conducted (as demonstrated in Fig. 6.1).

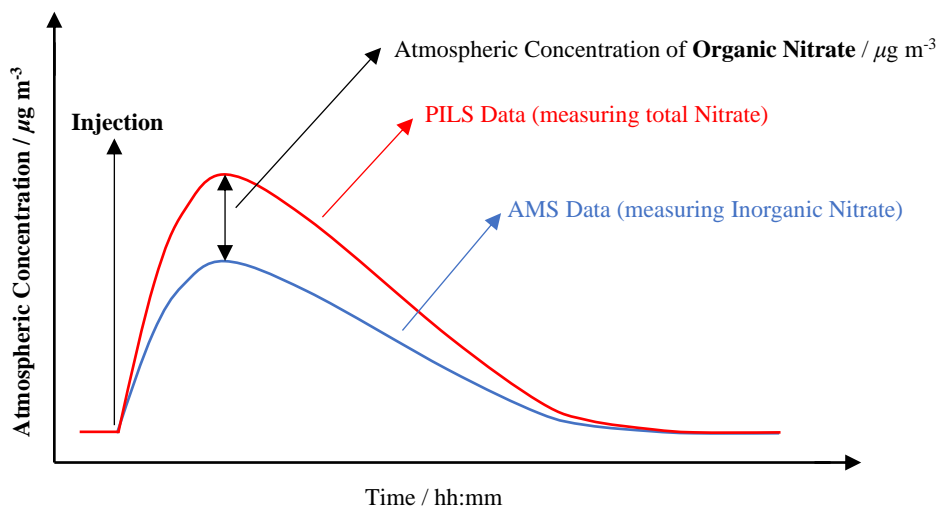


Fig. 6.1. Calculating the concentration of organic nitrate using the AMS and PILS times series.

The direct reaction between the NO₃ radical and isoprene under atmospherically relevant conditions (and RO₂ lifetimes) is a not much explored pathway. It was the focus of the NO₃ISOP study to evaluate the reaction kinetics and products which underpin Org-NO₃ formation, for use in future models. Much more sophisticated thermal instrumental methods such as Chemical Ionization Mass Spectrometry (CIMS), Gas Chromatography (GC), Proton-Transfer-Reaction Mass Spectrometry (PTR-MS), and Long Path Absorption Photometer (LOPAP) etc., which measured organic nitrate species were used as part of this campaign, but significant errors are associated with these techniques. Therefore, simpler techniques such as the PILS-IC method could provide useful information to test the trends and concentrations seen using these other instrumentation systems, although this type of analysis has not been carried out previously.

Org-NO₃ produced from isoprene oxidation may be either primary, secondary, or tertiary nitrates, of which tertiary species are known to hydrolyse most rapidly^{507,276}. A set of hydrolysis experiments using primary and secondary species was therefore initially conducted to assure that all Org-NO₃ species would have hydrolysed within the PILS samples prior to analysis by IC and [NO₃⁻] quantification. The PILS-IC times series have then been presented in comparison to the AMS values and an estimation of the Org-NO₃ fraction during the chamber experiments is shown, with possible reasoning for the behaviour of NO₃⁻ species. Significant trends were observed, although uncertainties in this technique have resulted in offsets of trends.

6.2 Experimental

6.2.1 Sampling Site and SAPHIR Smog Chamber

PILS-IC sampling was conducted at the SAPHIR chamber located at the Jülich Forschungszentrum, Germany (50.9053° N, 6.4048° E) as part of the NO3ISOP campaign during experiments performed between 15th Aug – 23rd Aug 2018. The SAPHIR chamber^{515,516} allows for the investigation of controlled chemistry at atmospherically relevant concentrations of species⁵¹⁷. The outdoor chamber⁴⁸¹ is of cylindrical shape and faces in the north-south direction^{481,517,515,516}. The length of the chamber has been reported as 18 m⁵¹⁷, with an internal diameter reported as 5 m^{517,515,516}. The volume inside the chamber accounts for 270 m³ (also reported as 268 ± 25 m³)⁵¹⁵, with a 320 m² surface area^{481,517,516} (also reported as 324 m²)⁵¹⁵ and a *ca.* 1 m⁻¹ (also reported at 0.8 m⁻¹)⁵¹⁵ surface/volume ratio value⁵¹⁶. The wall of the chamber constitutes two layers of Teflon (fluorinated ethylene propylene foil⁴⁸¹) encased within steel frames^{515,517}. The inner layer has a reported thickness of 125 μm (with a 500 μm thickness across the 52 m² floor of the reaction chamber) and an outer layer thickness of 250 μm^{515,516}. The volume of space in between the two layers is also purged with either N₂ or high-purity air to avoid any contamination from ambient air outside the chamber leaching in^{516,517}.

A pressure of *ca.* 30 Pa over ambient is the estimated running pressure inside the chamber⁴⁸¹. Furthermore, the consumption of air by instrumentation and from loss process (small leaks) is compensated by zero air^{515,517}. Shutters are also installed on the SAPHIR chamber which are able to expose the whole chamber to ambient solar radiation within 60s (for photolysis investigation) or cover the chamber for complete darkness^{481,517,516}. Due to the shadowing effect from the steel frame surrounding the Teflon chamber and due to the Teflon chamber itself, it is estimated that *ca.* 80% of ambient solar intensity is able to reach inside the chamber⁵¹⁶.

Milli-Q (MQ) grade water is heated up to produce water vapour which is mixed with synthetic air until the desired humidity of the chamber is accomplished⁵¹⁶. NO₂ is from a pre-prepared gas-mixture and O₃ concentrations are produced by a discharge ozoniser⁵¹⁷. BVOCs were also either injected from standards or from the plants themselves with coverings over the soil (SAPHIR-PLUS)⁵¹⁸.

Within the chamber, two large fans allowed for very fast mixing of gases (*ca.* 2 mins)⁴⁸¹. Flushing was carried out by using synthetic air (high purity O₂ and N₂ mixture^{481,516}) at a rate of 250 m³ over a prolonged period in the morning before the experimental runs⁴⁸¹. The work by Dewald et al., (2020)⁴⁸¹ is based on the NO3ISOP campaign also and workers report the concentrations of [NO₂], [O₃], [isoprene], as well as the Relative Humidity (RH %) ⁴⁸¹. These values have been taken from the work of Dewald et al., (2020)⁴⁸¹ and are shown in Table 6.1 (along with the experimental dates, PILS sampling times and other material details) to give an overview of the chamber reaction conditions for each day. The seed particles used for each day (except for the 17th Aug when no seed was used) was (NH₄)₂SO₄⁴⁸¹.

Table 6.1. Evaluation of Chamber conditions during the NO₃ISOP campaign as taken from Dewald et al., (2020)⁴⁸¹ over the PILS sampling period.

Date	PILS Start	PILS Stop	Isoprene / ppb	NO ₂ / ppb	O ₃ / ppb	RH %	Other Materials Injected
15 th	09:48	16:52	9	8 - 21	80 - 115	1.3 - 2.0	-
16 th	07:51	17:02	3	2 - 5	80 - 115	1.6	-
17 th	08:38	16:58	0	0 - 17	0 - 400	1.2 - 1.7	No Seed; Isobutyl nitrate; Acetaldehyde
18 th	07:00	16:20	3.5	2 - 5	80 - 110	1.3 - 1.4	Caryophyllene
19 th	08:00	16:35	3	0 - 20	0 - 110	0.07	N ₂ O ₅ ; MVK
20 th	09:00	17:04	6	3 - 5	85 - 130	1.2 - 1.9	Caryophyllene;
21 st	09:00	17:04	4.5	2 - 5	55 - 130	1.5 - 1.9	CO; Propene
22 nd	08:00	17:07	5	2.5 - 8.5	75 - 110	1.3 - 1.7	-
23 rd	08:38	17:27	4	3.5 - 5	45 - 100	1.5 - 2.2	-

* Methyl Vinyl Ketone (MVK)

6.2.2 PILS Denuder Preparation

A glass bottle was cleaned using washing up liquid and tap water, followed by rinsing the flask multiple times with 18.2 MΩ water to rid the flask of any contaminants. 15.0478 g of H₃PO₄ was weighed into a beaker on a mass balance. This was added to 700 ml 18.2 MΩ water in a 1 L flask. 50 ml of 18.2 MΩ water was also used to wash out the beaker of the residual H₃SO₄, and these washings were also added to the flask, producing a 2% H₃PO₄ solution. A mixture of 500 ml 2% H₃PO₄ solution, 20 ml glycerol and 750 ml methanol (HPLC grade) was mixed together in a glass winchester, producing the base removal denuder solution. To produce the acid removal denuder solution, 15.0174 g of Na₂CO₃ was dissolved in 750 ml 18.2 MΩ water to produce a 2% Na₂CO₃ solution. 500 ml of this solution was then measured out and added to a glass winchester, along with 750 ml of MeOH and 20 ml glycerol. The separate winchesters were vigorously shaken and the end caps were removed from the denuders. 50 ml of the basic denuder solution was added to the bases denuder and 50 ml of acidic denuder solution was added to the acids denuder. The caps of each denuder were then replaced and each denuder was inverted 60 times for coating. The denuders were then left on the side in the fume-hood to dry overnight. The coated denuders were installed into the PILS before shipment.

6.2.3 Sample Collection and IC Analysis

Sample collection was conducted at the Jülich Forschungszentrum using a PILS system. A solution of LiF (*ca.* 25 ppm) was produced (using 18.2 MΩ deionised water) and sonicated in a sonic bath for *ca.* 1 hour (referred to as ‘LIF PILSpot’ in this work). An aliquot sample of this was taken and ran on IC for determination of exact F⁻ concentration. This solution was then transferred to the LiF reservoir in the PILS. The MQ reservoir was also filled with 18.2 MΩ deionised water. A 2 m copper pipe was used to connect the SAPHIR chamber to the PILS (a 1.0 μm impactor was used on the PILS inlet). The PILS carousel was loaded with labelled glass collection vials (with crimped-on caps). The LiF solution reservoir had a flow rate of 0.237 ml min⁻¹ and the flow of air entering the PILS from the chamber was 11.6 L min⁻¹.

The flow rate of the air entering the impactor was measured using a flow meter (Alicat Scientific) attached to the copper pipe. The flow rate of LiF solution through the PILS was calculated by mass, assuming that the density of LiF (*ca.* 25 ppm) was very similar to that of water. Six empty PILS vials were pre-weighed, and then run on the PILS under very similar conditions to those during the NO3ISOP campaign. The PILS vials were weighed after sampling, and the average mass of LiF solution obtained was calculated over the six samples. This average mass of LiF was then divided by the run time of each sample (15 minutes), to give the flow rate of LiF through the PILS.

During chamber preparation, a flush was conducted on the PILS for *ca.* 1 hour. The PILS was set to run continuously sampling every 15 minutes, for 15 minutes. 3 ml of sample was produced and these samples were taken to the wet-lab shipping container beside the SAPHIR chamber where IC was conducted. The PILS solutions were then transferred to 15 ml plastic falcon vials, ready for analysis on IC. 0.5 ml of sample was transferred to IC poly vials and caps (Thermo, UK) and these were loaded into the IC carousel.

LiF, Na₂NO₃, and Na₂SO₄ were used to produce *ca.* 1000 ppm salt stock solutions. 50 ppm solution mixes were produced from these stocks of each salt, with subsequent dilutions of 25 ppm, 10 ppm, 5 ppm, 2.5 ppm, 1 ppm, 0.5 ppm, 0.25 ppm, 0.1 ppm, 0.05 ppm, 0.01 ppm (by salt concentration). In Jülich, 0.5 ml of each standard and sample was injected into the IC and each day one calibration was completed for between 30 and 40 PILS samples. Sufficient blank runs were inserted in between samples and standards to avoid carry over of material. The IC instrument method was identical to that described in chapter 2. The response of NO₃⁻ from the PILS-IC system during the campaign was too low for data manipulation and therefore the PILS samples were re-analysed after a further pre-concentration step (section 6.2.4).

6.2.4 Sample Evaporation and Reanalysis on the IC

2 ml of each sample was pipetted into a pre-washed (and dried) Thermo Bio Evaporation vial (20 ml). The sample was set to evaporate to dryness on a Biotage Evaporator (Biotage® V-10 Evaporator) in aqueous mode (temperature of 36 °C, pressure of 8 mb). 0.5 ml of 18.2 MΩ water was then added to the sample vial and the vial was set to the re-dissolve function on the Biotage (speed of 4000 rotations per minute, 10 re-dissolve cycles). The 50, 25, 10, 5, 2.5, 1, 0.5, 0.25, 0.1, 0.05, 0.01 ppm calibration solutions of mixed salt standards (LiF, NaNO₃ and Na₂SO₄) underwent the same evaporation process and extracts were run on IC to produce the calibration curves. On some occasion, < 2 ml of PILS sample was available. In this instance concentrations were corrected.

6.2.5 IC Analysis and Atmospheric Concentration Calculation

To calculate the atmospheric concentration of [NO₃⁻] and [SO₄²⁻] in the chamber, the calculation from Orsini et al., (2003)²⁶⁶ was used. This calculation also corrects for aerosol dilution during the PILS sampling method (Eq. 6.1). [C_g] is the atmospheric aerosol concentration (μg m⁻³); [C_L] is the concentration of ionic species in the sample solution detected by IC (μg L⁻¹); q_{in} is the flow of the LiF solution (ml min⁻¹); R is the dilution factor; and Q_a is the flow rate of air into the PILS impactor (L min⁻¹). The dilution factor R is calculated through Eq. 6.2.

$$[C_g] = \frac{[C_L]q_{in}R}{Q_a}$$

Eq. 6.1. Atmospheric concentration calculation using the PILS method as described by Orsini et al., (2003)²⁶⁶.

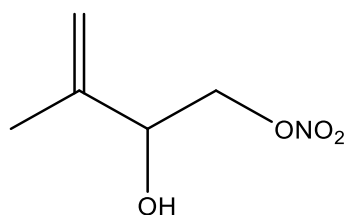
$$R = \frac{[\text{LiF}] \text{ before impactor (LiF PILSpot, ppm)}}{[\text{LiF}] \text{ detected after impactor (in the sample, ppm)}}$$

Eq. 6.2. Dilution factor calculation for the PILS method.

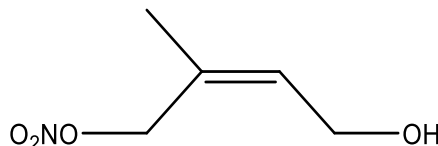
R is the ratio of the LiF solution concentration before and after the impactor stage (collection of aerosol). The concentration of LiF before the impactor is equal to the concentration of LiF within the PILS reservoir²⁶⁶. This concentration is divided by the [LiF] detected by the IC and accounts for the dilution from the deposition of particles that have grown via water condensation on the PILS head.

6.2.6 Org-NO₃ Hydrolysis in Water

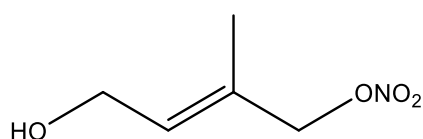
ca. 100 μl of four Org-NO₃ compounds synthesised by the University of East Anglia (UEA) (Fig. 6.2) in separate 1 ml GC vials were brought back from UEA to the University of York (UoY) in dry ice. These were synthesised by UEA for their work in the Beijing APHH campaign⁵¹⁹.



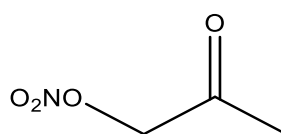
Compound 1
147.13 g mol⁻¹



Compound 2
147.13 g mol⁻¹



Compound 3
147.13 g mol⁻¹



Compound 4
199.07 g mol⁻¹

Fig. 6.2. Structures of the four Org-NO₃ compounds investigated for hydrolysis rates in this study.

10 μl of Org-NO₃ compound was transferred into a clean and pre-weighed 50 ml Falcon vial (vial A) using a 10 μl Eppendorf pipette. The Org-NO₃ contents was then weighed. A 25.4 ppm solution of LiF was produced in the same manner as for the PILS-IC runs described in section 6.2.3. Aliquots of the LiF solution (ca. 50 ml) were transferred into 50 ml falcon vials (vial B) ready for direct

transfer into vial A. The mass of LiF solution was recorded. The *ca.* 50 ml of LiF solution (25.4 ppm) was transferred from vial B to Vial A and the time was recorded at the point of mixing. The contents was shaken by hand for *ca.* 2 minutes. Vial A was then weighed again to observe the mass of 25.4 ppm LiF solution which had been transferred. 0.5 ml aliquots of the shaken solution were pipetted into numerous IC Polyvials (Thermo Scientific, UK). These were then loaded into the IC and were run on the IC in anion mode (method described in chapter 2). Structures of the four Org-NO₃ compounds investigated for hydrolysis are shown in Fig. 6.2. These runs were repeated using 18.2 MΩ water as the solvent.

6.3 Results and Discussion

6.3.1 Org-NO₃ Hydrolysis

6.3.1.1 Org-NO₃ Dissociation in 25 ppm LiF

The NO₃ISOP campaign was conducted to investigate the production of Org-NO₃ species within smog chamber experiments from the reaction between the NO₃ radical and isoprene. Atmospherically relevant concentrations and RH levels were used during these experiments. It is known from previous studies that Org-NO₃ species undergo hydrolysis to form HNO₃ and the organic alcohol derivative, a process which is known to increase under higher RH conditions^{503,520}. Org-NO₃ compounds may have an NO₃ group in either a primary, secondary, or tertiary position.

Inorg-NO₃⁻ (such as from the dissociation of HNO₃ in the aerosol phase) may be directly sampled and analysed by the IC. Tertiary Org-NO₃ compounds are known to hydrolyse very readily^{478,502} (on a scale of seconds) under atmospheric conditions^{503,348,507} and are very likely to have already hydrolysed in the particle phase during the course of the experiments^{348,276,503}. Primary and secondary nitrate species are however thought to be much more stable to hydrolysis (under atmospheric conditions)^{507,276,521}.

It was necessary to investigate whether primary species would hydrolyse into NO₃⁻ and subsequently be quantifiable by the PILS-IC method within the time taken between PILS sampling and running species on the IC. Four primary Org-NO₃ species were investigated for hydrolysis rates. For the success of quantification of Org-NO₃ species during the NO₃ISOP campaign (section 6.3.2) it was necessary that all Org-NO₃ was hydrolysed within the PILS samples. The hydrolysis rate experiments were conducted in the bulk (*ca.* 25 ppm) LiF solution like the aerosol PILS liquid samples (*ca.* 3 ml) and the results are shown in Fig. 6.3.

On retrieving the aerosol samples from the PILS at the chamber, these were transferred to plastic Falcon Vials. 0.5 ml was initially taken from the 3ml samples and run-on IC in Jülich. After observing that the Limit of Detection (LOD) of the PILS-IC method was too high for the low ambient isoprene concentrations used during most of the smog chamber experiments (except the 15th August), the samples were kept in the plastic falcon vials and were shipped back to York. Samples were concentrated up using an evaporation process (see section 6.2.4) at the beginning of January 2019. Therefore, the Org-NO₃ compounds within the aerosol samples were in the bulk aqueous phase in the plastic sample vials for *ca.* 4-5 months, prior to evaporation and being run on the IC.

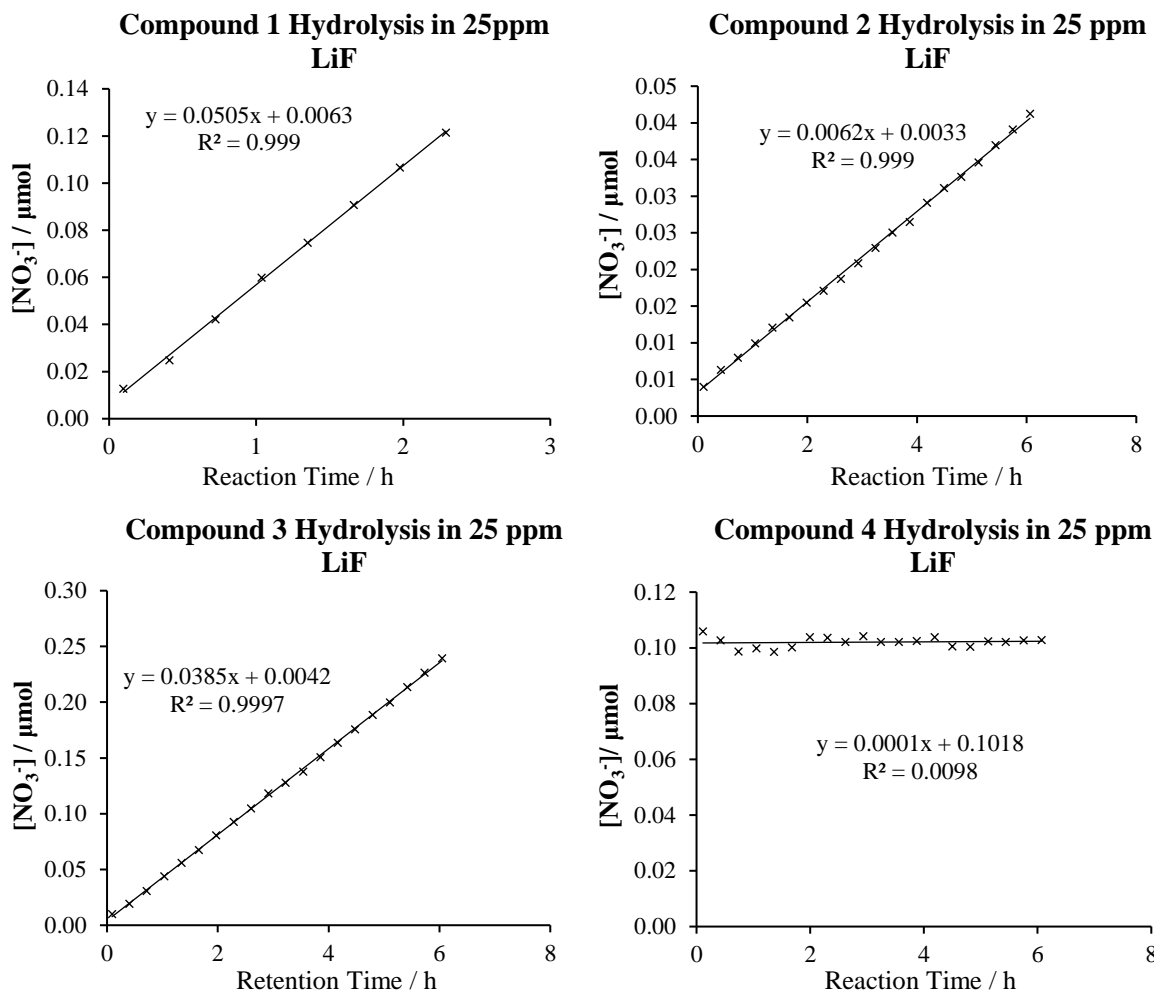


Fig. 6.3. $[NO_3^-]$ (μmol) production as a function of time (in 25.4 ppm LiF) from various Org- NO_3 compounds synthesised by UEA. The error associated with these measurements was $\pm 1.95\%$. The error was calculated based on the IC instrument reproducibility of $[NO_3^-]$. The concentration of NO_3^- produced from Org- NO_3 hydrolysis (y-axis) is plotted against time of reaction (x-axis).

The results of Org- NO_3 hydrolysis of the four compounds (Fig. 6.3) analysed were used as an indication as to whether the NO_3^- sampled during PILS-IC measurements would have originated from Org- NO_3 species or whether they were of inorganic origin (such as from N_2O_5 hydrolysis)⁵²¹. These experiments were also conducted to observe the kinetic order of reaction of the four compounds (Fig. 6.3) and rate constants of hydrolysis which would in turn suggest how many moles of Org- NO_3 (for each compound) would hydrolyse within the period of *ca.* 4 months.

Table 6.2. Hydrolysis reaction kinetics of a range of Org- NO_3 (compounds 1-4) synthesised by UEA.

Compound	Order of Reaction	$k / \text{nmol min}^{-1}$	$[NO_3^-]$ after 4 months / μmol	Equivalent Atmos Concentration / g m^{-3}
1	0	0.842	147	0.125
2	0	0.103	18	0.015
3	0	0.642	113	0.095
4	Unknown	Unknown	Unknown	Unknown

Table 6.2 shows the observed order of reaction; calculated rate constants; an estimated number of μmoles of $[\text{NO}_3^-]$ each compound could produce after *ca.* 4 months (*average of* 1.75×10^5 minutes) of hydrolysis; and the equivalent atmospheric concentration that would have needed to have been present in the chamber to produce this $[\text{NO}_3^-]$ concentration in the PILS-IC vials.

Table 6.2 shows that the compound with the fastest hydrolysis rate of reaction was compound 1 ($0.842 \text{ nmol min}^{-1}$), followed by 3 ($0.642 \text{ nmol min}^{-1}$) and 2 ($0.103 \text{ nmol min}^{-1}$). The hydrolysis rate of compound 4 could not be determined. Each of compounds 1-3 show a linear increase of $[\text{NO}_3^-]$ concentration (analogous to Org- NO_3 loss) as a function of time, suggesting the hydrolysis reactions were zero order. It has however been widely acknowledged in the literature that the neutral hydrolysis of primary Org- NO_3 species predominantly undergoes a first order substitution mechanism⁵²² (unimolecular, $\text{S}_\text{N}1$). To investigate this further, hydrolysis experiments of compounds 1-4 in 18.2 M Ω water were also conducted (section 6.3.1.3).

Using 1.75×10^5 minutes as an estimate and knowing that zero order rate constants indicate that the rate of hydrolyses does not depend on the concentration of Org- NO_3 , it was estimated that the number of μmoles of Org- NO_3 that could be hydrolysed after 4 months was *ca.* 147 μmol , 18 μmol , and 113 μmol for compounds 1, 2, and 3, respectively. Using the Relative Molecular Mass (RMM) values of each compound (Fig. 6.2) in conjunction with the volume of air sampled (for each PILS-IC sample), the corresponding [Org- NO_3] atmospheric concentrations that would have needed to have been present within the chamber for which 4 months would not have resulted in complete Org- NO_3 hydrolysis in the PILS samples were estimated (Equivalent Atmos Concentration / g m^{-3} , Table 6.2). These values correspond to 0.125 g m^{-3} , 0.015 g m^{-3} and 0.095 g m^{-3} for compounds 1, 2 and 3, respectively. Therefore, it may be safely assumed that all Org- NO_3 (primary and tertiary species in ng-mg m^{-3} levels) within the PILS samples would have hydrolysed by the beginning of January 2019 (when the sample concentration and workup took place). It was also important that complete hydrolysis had occurred, as NO_3^- is less volatile than Org- NO_3 and therefore this avoids Org- NO_3 evaporating away leading to extra uncertainty at the evaporation stage (section 6.2.4). It must however be highlighted that full hydrolysis is assumed, as long as the equilibrium of hydrolysis causes the reactants to hydrolyse to completion.

Previous work by Darer et al., (2011)²⁷⁶ who also investigated Org- NO_3 hydrolysis in bulk water found that tertiary Org- NO_3 compounds hydrolysed within minutes, whereas primary nitrates undergo hydrolysis over the course of months. Work by Baker et al., (1952)⁵²³ also report much faster hydrolysis rates (in neutral solutions but with varying temperatures) for tertiary Org- NO_3 species compared to primary and secondary structures. Hu et al., (2011)⁵⁰³ needed to use acid catalysis for the hydrolysis of primary and secondary Org- NO_3 in their study, measuring the hydrolysis of Org- NO_3 species using NMR techniques.

It has been mentioned in previous studies that Org-NO₃ species may undergo first order substitution reactions^{522,502,276,503}. An example first step (rate determining step producing the carbonium ion) for compound 1 is shown in Fig. 6.4.

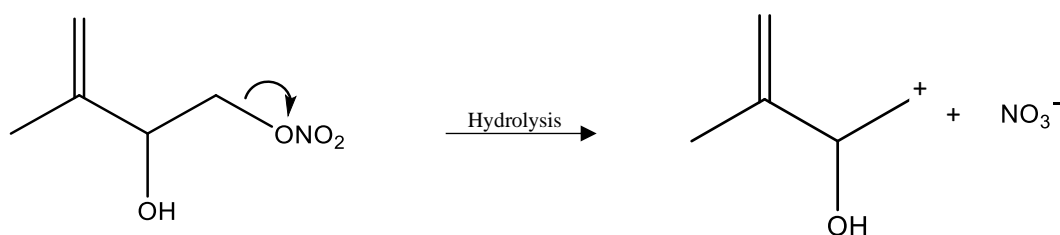


Fig. 6.4. Possible formation of carbocation via Org-NO₃ hydrolysis (compound 1).

Compound 1 has a rate which is 1.31 times faster than compound 3 and 8.19 times faster than compound 2. Based on the first order kinetics observed in neutral solution⁵⁰³, this could be explained by the increased dipole produced in compound 1 between the NO₃ and the α -carbon, making the NO₃ leaving group more favourable to be lost in compound 1 compared to compound 2 or 3. This therefore creates a faster rate determining step through an S_N¹ or E¹ pathway forming nitrate (Fig. 6.4). The α -carbon in compound 1 is bonded to an electronegative NO₃ group and the $\delta+$ on this carbon is increased due to the -I inductive effect induced by the OH group attached to the β -carbon drawing more electron density away from the α -carbon in this system (compared to compounds 2 and 3 which don't have this). Therefore, the C-NO₃ dipole is strongest in compound 1 which loses the NO₃⁻ leaving group most readily to produce the carbocation intermediate.

Compound 3 has a slower reaction compared to compound 1. This could be explained by the reduced dipole observed between the α -carbon – NO₃ bond (compared to compound 1) which less readily allows for the loss of the NO₃⁻ leaving group (rate determining step in S_N¹), leading to a slower rate of NO₃⁻ ejection from the Org-NO₃.

The carbocations produced in compounds 2 and 3 may have some resonance stabilisation due to a double bond being attached to the β -carbon, creating a more stabilised carbocation intermediate^{348,524}. This is in line with the observations of Jacobs et al., (2014)³⁴⁸ who state that the rate of hydrolysis observed for a primary Org-NO₃ compound of an unsaturated molecule is faster compared to similar saturated compounds, due to resonance stabilisation. The positive charge on the carbocations in compounds 2 and 3 therefore become delocalised, enhancing the stability of the carbocation intermediates. This in turn reduces the activation energy required for this carbocation formation and therefore the fission of the α C-NO₃ bond. Based on the reaction rates however shown in Table 6.2, the stabilisation of the intermediates produced by compounds 2 and 3 does not lower the activation energy as much as the influence of the OH group on the β -carbon in compound 1.

Compounds 2 (*Z*) and 3 (*E*) are isomers of one another with compound 3 having a rate that is 6.23 times larger than compound 2. The reason for the much-increased rate in compound 3 is potentially down to steric effects. As the CH₂OH group in compound 3 is on the opposite side of the CH₂ONO₂ group in the *E* isomer, more space is made available for the attack of an OH⁻ nucleophile to hydrolyse the αC-NO₃ bond. In compound 2 however, the CH₂OH and CH₂ONO₂ groups are on the same side of the molecule. This therefore produces a significant level of sterical hindrance for the attacking OH⁻ molecule via the S_N¹ mechanism. This would therefore lead to a higher energy barrier in producing this carbocation intermediate in compound 2.

Compound 4 had an almost zero gradient over the course of the hydrolysis experiment, which could suggest a very rapid rate of hydrolysis that was not possible to measure using the IC method (as the IC method applied only took a measurement every 20 minutes). The mass of compound 4 which underwent hydrolysis in 49.40 ml of *ca.* 25.4 ppm LiF solution was 15560 μg. This therefore corresponded to 78.16 μmol compound 4 in the bulk vial. This therefore corresponded to 0.79 μmol compound 4 in each 0.5 ml aliquot for the IC analyses. Assuming complete hydrolysis, 0.79 μmol of [NO₃⁻] would be expected as the Org-NO₃ and NO₃⁻ are equimolar in the dissociation process. The average amount of [NO₃⁻] observed for compound 4 (Fig. 6.3) across the readings was 0.102 μmol with Standard Deviation (SD) ± 0.002 μmol. The expected amount of [NO₃⁻] assuming complete dissociation is therefore ~8 times higher than the average observed.

It must however also be noted that the synthesis of compound 4 by Bew et al., (2016)⁵¹⁹ involved the reaction of chloroacetone with silver nitrate. If the purification step still left a proportion of silver nitrate behind, this Inorg-NO₃⁻ would be detected by the IC. There are therefore different possible explanations to the trend of NO₃⁻ observed within compound 4. Either compound 4 has not dissociated at all and the average NO₃⁻ value of 0.102 μmol is from the AgNO₃ left over from the synthesis process; the hydrolysis does occur although is so slow that the AgNO₃ concentration hides any observation of the Δ [NO₃⁻] from Org-NO₃ as a function of time; or instant hydrolysis occurs producing [NO₃⁻], no AgNO₃ is present, and the much lower [NO₃⁻] present is due to a very low equilibrium constant in the direction of NO₃⁻ causing incomplete dissociation.

In addition to the presence of NO₃⁻, NO₂⁻ was also observed for compound 4. Fig. 6.5 shows the μmols of NO₂⁻ as a function of time that compound 4 is dissolved in *ca.* 25.4 ppm LiF. Like [NO₃⁻] (Fig. 6.3), the Δ [NO₂⁻] as a function of time has almost no gradient ($y = -0.0022x$). The average NO₂⁻ reading across 20 samples was 0.571 μmol (SD ± 0.007 μmol) which is 5.60 times larger than the average of [NO₃⁻] observed in the sample. Therefore, the presence of NO₂⁻ was much more prominent compared to NO₃⁻.

In the work by Bew et al., (2016)⁵¹⁹, there is no mention of nitrite salts being used in the synthesis of compound 4. A potential explanation for the presence of NO₂⁻ in abundance as described by Baker et al., (1950)³⁴⁹ may be due to the oxidation of the resulting alcohol by the HNO₃ produced during

the reaction. Other work has however suggested that nitrite can be produced during Org-NO₃ hydrolysis, as opposed to the reaction between HNO₃ and the resultant alcohol^{522,523}.

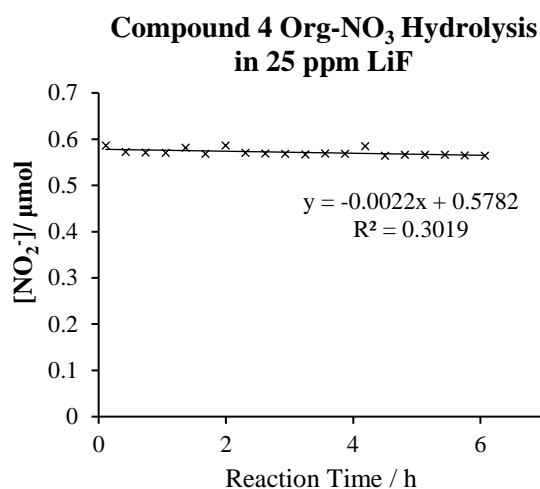


Fig. 6.5. [NO₂⁻] (μmol) as a function of time (in 25.4 ppm LiF) from compound 4 synthesised by UEA. The error associated with these measurements was ±4.78 %. The error was calculated based on the IC instrument reproducibility of [NO₂⁻]. The concentration of NO₂⁻ present (y-axis) is plotted against time of experiment (x-axis).

Although no carbonyl measurements are available for compound 4 in this study, the production of NO₂⁻ may suggest a possible Org-NO₃ hydrolysis elimination mechanism shown in Fig. 6.6, as described by Boschan et al., (1955)⁵²². It has been reported that this mechanism is of second order (first order w.r.t Org-NO₃ and 1st order w.r.t OH⁻)^{522,523}. There is also a requirement for a hydrogen atom to be attached to the α-carbon for the elimination pathway to take place to produce NO₂⁻⁵²². If the elimination reaction occurred at the β-hydrogen (in other Org-NO₃ compounds), H₂O and NO₃⁻ would be among the products of hydrolysis⁵²². It is possible that no second order trend was seen in Fig. 6.5 due to the reaction taking place on a time scale faster than the IC could measure or because the amount of water was much greater compared to the concentration of compound 4 in this study.

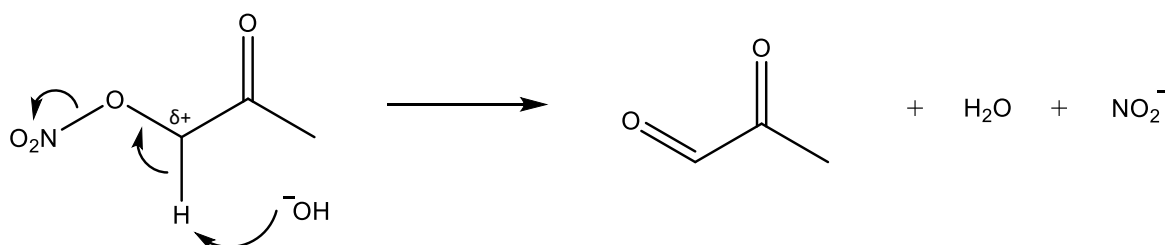


Fig. 6.6. Nitrite formation from the hydrolysis of Compound 4 through a possible elimination reaction.

Fig. 6.6 demonstrates the widely accepted sequence for the hydrolysis of nitrate esters (such as compound 4) through an elimination reaction⁵²². The yield of nitrite has been shown to be very variable across differing organo-nitrate esters⁵²². The percentage (by μmol) of nitrite produced during

the hydrolysis of compound 4 was $0.57 \mu\text{mol}$ ($\text{SD} \pm 0.01 \mu\text{mol}$) which compares to $0.10 \mu\text{mol}$ ($\text{SD} \pm 0.00 \mu\text{mol}$) NO_3^- produced. Therefore, the average % molar equivalent of nitrite from hydrolysis of Org- NO_3 was $7.31 \times 10^{-1} \%$ compared to nitrate which had a % molar yield of $1.31 \times 10^{-1} \%$. This compares to 35 % nitrite from isobutyl nitrate hydrolysis⁵²² and trace amounts of NO_2^- from the hydrolysis of methyl nitrate⁵²³ which has previously been observed⁵²². (In contradiction however, hydrolysis isobutyl nitrate was analysed during these experiments for this thesis and no NO_2^- or NO_3^- species were formed on IC).

6.3.1.2 Effect of light on Org- NO_3 Dissociation in 25 ppm LiF (Pilot Tests)

To continue the work of studies which have investigated Org- NO_3 hydrolysis rates, pilot experiments were conducted to observe whether temperature and light would affect the rate of hydrolysis of Org- NO_3 species. These experiments were conducted using compound 1 and the results are shown in Fig. 6.7. The time in hours is shown along the x -axis and the amount of NO_3^- (μmol) produced is plotted up the y -axis. The vertical grey lines correspond to 24-hour periods. The same solution was used for this study as for the Compound 1 hydrolysis experiment in section 6.3.1.1. After shaking the vial for 2 mins, the solution was dispensed into IC vials, for which the results are shown by the black points (1) in Fig 6.7 and Fig. 6.3 (section 6.3.1.1). After setting off the analysis on the IC instrument, the stock solution was placed into the fridge for a night. The solution was retrieved the next morning (2) and was dispensed into polyvials to be run on the IC (orange data points, Fig. 6.7). On completing this, the stock solution was then placed back into the fridge and was left over the weekend. The vial was retrieved from the fridge and the contents were run on the IC. The results of this are shown by the blue data points (5) in Fig. 6.7.

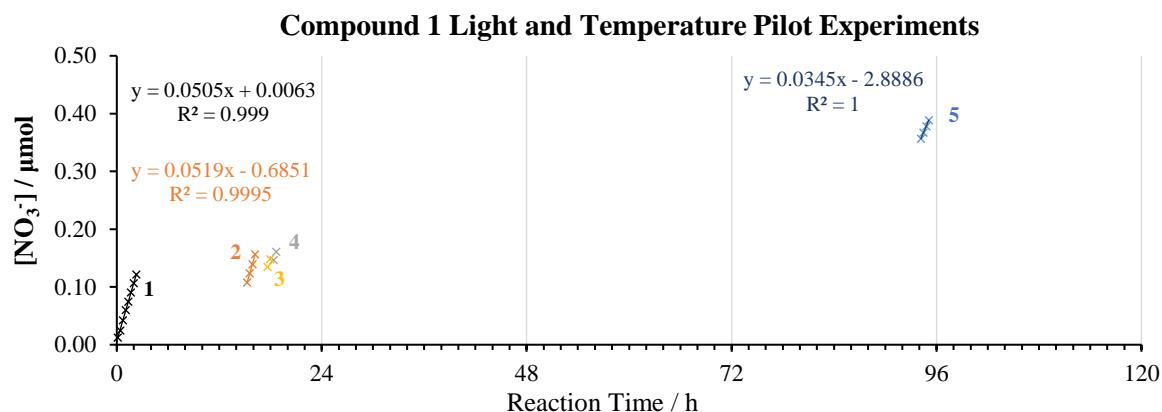


Fig. 6.7. Pilot tests observing the light and temperature dependence on $[\text{NO}_3^-]$ (μmol) production as a function of time from compound 1 hydrolysis. The vertical grey lines correspond to 24-hour periods. The black data (1) corresponds to Org- NO_3 hydrolysis directly from the stock; the orange data points demonstrate the progress of Org- NO_3 hydrolysis after the sample had spent a night in the fridge; the blue data points (5) show the progress of Org- NO_3 hydrolysis after the sample solution had spent a weekend in the fridge. Group 3 (yellow) and Group 4 (grey) results are from a light and dark experiment, respectively. The error associated with these measurements was $\pm 1.95 \%$. The error was calculated based on the IC instrument reproducibility of $[\text{NO}_3^-]$. The concentration of NO_3^- produced from Org- NO_3 hydrolysis (y -axis) is plotted against time of reaction (x -axis).

The gradients of groups 1 and 2 are very similar, $0.0505x$ and $0.0519x$, respectively. Although there is a slightly higher gradient value observed for group 2, this is likely down to the uncertainty in measurements. After the solution was left in the fridge over the weekend, the gradient of the trend for group 5 was $0.0345x$, which was 32% lower than the group 1 gradient and 34% lower than the group 2 gradient. Therefore, the shallower gradient (group 5) was either due to the solution being kept in the dark, the much lower temperature or the progress of reaction starting off a plateau.

It was however noticed that the intercept values of the linear regressions of group 1, 2 and 5 increased throughout the experiment. The initial intercept for group 1 was $c = 0.0063$ which was very close to zero and the offset from zero is likely due to systematic error. Group 2 however has an intercept value of $c = -0.6851$ and group 5 has an intercept value of $c = -2.8886$. The decreasing intercepts and visual inspection of the graph shows that a much-reduced rate of hydrolysis is seen once compound 1 is subject to a substantial reduction in temperature and light, as to pause the hydrolysis process. Furthermore, the first data point of group 2 ($0.108 \mu\text{mol}$ at 15.26 h) has a lower $[\text{NO}_3^-]$ than the last data point of group 1 ($0.121 \mu\text{mol}$ at 2.29 h). This therefore poses the question as to whether the hydrolysis process is reversible to some extent, as the error from the IC was $\pm 1.95 \%$ for NO_3^- (Fig. 6.8). The investigation into the reversibility and equilibrium of Org- NO_3 constitutes future work and would increase the understanding of Org- NO_3 within SOA in much cooler climates. This is a potential research area which has not yet been investigated with regard to Org- NO_3 hydrolysis and is likely crucial to understanding the atmospheric implications of temperature on Org- NO_3 and SOA.

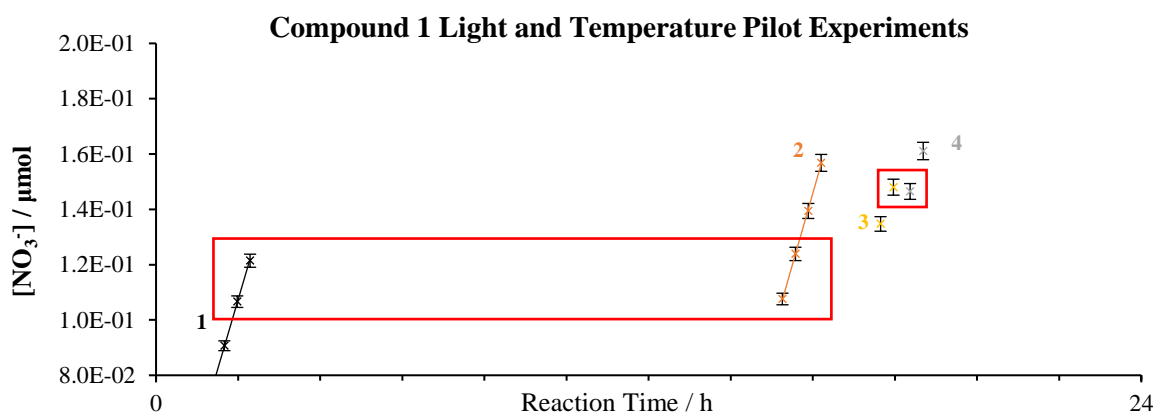


Fig. 6.8. Reduction in $[\text{NO}_3^-]$ for cooler temperatures and darker conditions. The black data (1) corresponds to Org- NO_3 hydrolysis directly from the stock; the orange data points (2) demonstrate the progress of Org- NO_3 hydrolysis after the sample had spent a night in the fridge; the yellow data points (3) show the progress of Org- NO_3 hydrolysis for an Org- NO_3 sample which had been exposed to a bright light for 1 hour and the grey data points (4) show the progress of Org- NO_3 hydrolysis from samples which had been wrapped in foil and placed into the fridge for an hour (at the same time as the light experiment). The error associated with these measurements was $\pm 1.95 \%$. The error was calculated based on the IC instrument reproducibility of $[\text{NO}_3^-]$.

Further (although much less comprehensive) pilot experiments were also conducted for the investigation of hydrolysis rates of compound 1 on exposure to light. These are shown by groups 3 and 4 in Fig. 6.8. Once the compound 1 stock solution was taken out of the fridge from the first night, 10 ml aliquots of this solution were pipetted into two separate vials (Sarstedt, Germany). One vial was wrapped in foil (dark, group 4) and the other was placed in front of a very bright visible light

source (light, group 3). The vials were kept at room temperature. After *ca.* an hour, the samples were run on the IC, in which the light experiments were run first. The samples in group 3 and 4 were run consecutively after each other with *ca.* 18 minutes intervals between each sample.

Although this was a very brief experiment, there is a small amount of evidence to suggest that the dark reaction (4) exhibited a reduced rate compared to the light reaction (3). Fig. 6.8 demonstrates an offset seen between group 3 and group 4, with a delay in group 4. A potential reason for this delay in the dark experiment may be due to a possible lack of dissociation of the $\alpha\text{C-NO}_3$ bond via photolysis. Photolysis would increase the rate of the rate determining step ($\alpha\text{C-NO}_3$ fission) as it is known that primary Org- NO_3 species follow a unimolecular S_N^1 hydrolysis mechanism^{502,522}. Although no definite conclusions may be made from the work shown here (due to the lack of samples), these pilot runs pose the question as to whether hydrolysis of Org- NO_3 may be affected by $\alpha\text{C-NO}_3$ bond photolysis from ambient light. This is also an area that is crucial to investigate to enhance the understanding of the role of Org- NO_3 within SOA.

6.3.1.3 Comparison of Org- NO_3 Dissociation in Water and LiF solution (compounds 1-3)

Previous literature indicates that hydrolysis of organic nitrates is most likely via a substitution mechanism with reaction rates in the 1st order (S_N^1), for which tertiary species are hydrolysed orders of magnitude faster compared to primary Org- NO_3 species. The results of this study (in section 6.3.1.1 and Fig. 6.3) indicate that the hydrolysis reactions of compounds 1-3 within LiF are zero order and therefore this does not agree with the literature. The hydrolysis experiments were therefore repeated in 18.2 M Ω water to try and observe whether the presence of LiF would influence the order of reaction observed of Org- NO_3 hydrolysis in this study. The results of the hydrolysis reaction rates for compounds 1-3 (w.r.t NO_3^-) are shown as the percentage molar yield of $[\text{NO}_3^-]$ as a function of time in Fig. 6.9. Fig. 6.9 also displays a direct comparison (w.r.t % molar yield of NO_3^-) between the hydrolysis experiments in 25.4 ppm LiF and 18.2 M Ω water. As zero order rates are demonstrated in the hydrolysis of compounds 1-3 in 25.4 ppm LiF and in 18.2 M Ω water, there is still a discrepancy between this study and the literature regarding order of reactions.

The % molar yield was calculated by dividing the number of $\mu\text{mol } [\text{NO}_3^-]$ calculated to have been produced by a sample, by the total number of μmol Org- NO_3 which had been added to the stock vial. The direct comparison between the hydrolysis of compounds 1-3 in LiF and water demonstrates that a faster hydrolysis reaction occurs in the presence of LiF.

Fig. 6.9 shows that the rates of $[\text{NO}_3^-]$ as a molar percentage (equimolar to the loss of Org- NO_3) for compounds 1, 2, and 3 are $9.08 \times 10^{-4} \% \text{ min}^{-1}$, $1.28 \times 10^{-4} \% \text{ min}^{-1}$, and $9.83 \times 10^{-4} \% \text{ min}^{-1}$, in a solvent of 25.4 ppm LiF, respectively. In a solvent of neutral 18.2 M Ω water, the hydrolysis rates were $5.11 \times 10^{-4} \% \text{ min}^{-1}$, $5.66 \times 10^{-5} \% \text{ min}^{-1}$, and $4.38 \times 10^{-4} \% \text{ min}^{-1}$, respectively. Therefore, for compounds 1, 2 and 3, a faster rate is observed in the presence of LiF by multiples of 1.78, 2.26 and 2.24, respectively. These results are summarised in Table 6.3.

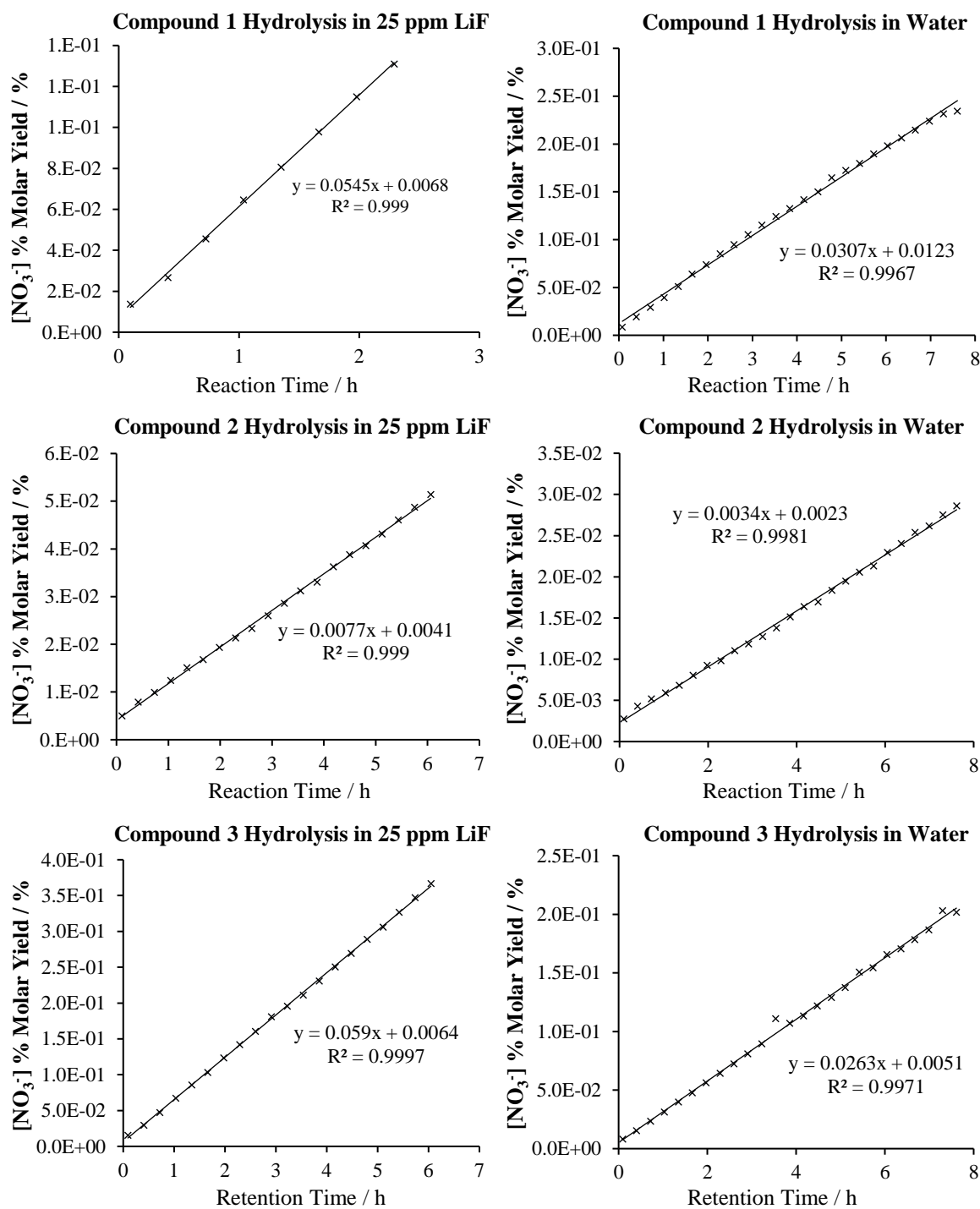


Fig. 6.9. Direct comparison of rates of reactions and kinetic orders between *Org-NO₃* hydrolysis in 25.4 ppm LiF and 18.2 MΩ water for compounds 1-3. The error associated with these measurements was ±1.95 %. The error was calculated based on the IC instrument reproducibility of [NO₃⁻]. The % [NO₃⁻] molar yield (y-axis) is plotted against time (x-axis).

Table 6.3. Comparison to orders of reaction and hydrolysis rates between the *Org-NO₃* hydrolysis experiments within an LiF (25.4 ppm) and neutral water (18.2 MΩ) for compounds 1-3.

Org-NO ₃ Compound	LiF 25.4 ppm (in 18.2 MΩ Water)		18.2 MΩ Water	
	Order of Reaction	Δ [NO ₃ ⁻] / % min ⁻¹	Order of Reaction	Δ [NO ₃ ⁻] / % min ⁻¹
1	0	9.08×10^{-4}	0	5.11×10^{-4}
2	0	1.28×10^{-4}	0	5.66×10^{-5}
3	0	9.83×10^{-4}	0	4.38×10^{-4}

6.3.1.4 Hydrolysis Reaction Kinetic Orders and possible Mechanisms for compounds 1-3

It is widely suggested in the literature that the hydrolysis of Org-NO₃ species follows first order kinetics. The Org-NO₃ hydrolysis kinetics in this study however follow a zero order for compounds 1-3 as well. To investigate why this discrepancy occurs, 6 separate possible Org-NO₃ hydrolysis mechanisms have been hypothesised and are shown in mechanisms A-D (Fig. 6.10 - Fig. 6.13).

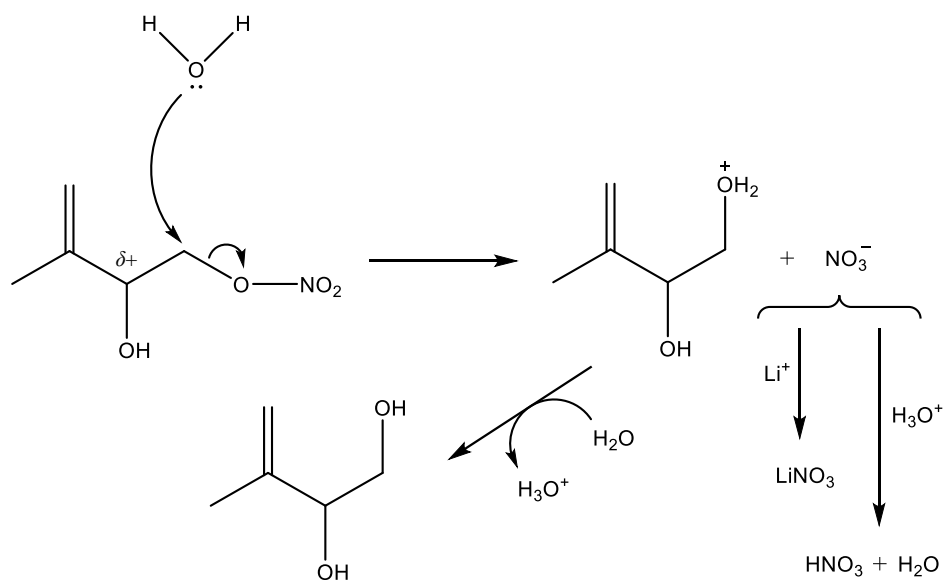


Fig. 6.10. Possible S_N² substitution mechanism during Org-NO₃ hydrolysis (mechanism A).

Mechanism A (Fig. 6.10) represents a substitution reaction⁵²². The negatively charged lone pair of electrons on the water molecule is attracted to the δ⁺ charge located on the α-carbon. In one step through a transition state, the water molecule acts as a nucleophile and the lone pair located on the oxygen atom attacks the α-carbon. As a result, the α-C–O bond breaks producing nitrate. The organic cation produced is neutralised by a water molecule (in vast excess) producing H₃O⁺, leaving an alcohol group. As this mechanism involves a transition state as the rate determining step, the process is bimolecular and of second order reaction kinetics ($k = [\text{Org-NO}_3][\text{H}_2\text{O}]$). As a substitution is involved, this therefore labels this reaction mechanism as an S_N² pathway. As water is however in vast excess, the reaction is dependant only on [Org-NO₃] and therefore pseudo first order reaction kinetics are expected (pseudo S_N¹). This mechanism would therefore be in line with literature studies which observe first order Org-NO₃ hydrolysis kinetics.

It is strange that first order kinetics are not observed in this study, due to H₂O being in vast excess and previous studies displaying first order kinetics for Org-NO₃ hydrolysis systems. Most other studies however measure Org-NO₃ by proportion of Org-NO₃ loss compared to NO₃⁻ formation^{275,503,276}. Zero order kinetics may however occur in the presence of a catalyst, as a limiting factor may be the number of molecules in a specific state required for a successful reaction to occur, as opposed to the concentration of each reactant⁵²⁵. The limiting factor in this case would therefore

be the catalyst being saturated, with [Org-NO₃] being in great excess to the catalyst. Possible catalysts at very low concentrations in this study may be either [H₃O⁺] or [OH⁻] produced from water dissociation.

For first order kinetics to be observed, the catalyst concentration (and therefore either [H₃O⁺] or [OH⁻]) need to be in excess of [Org-NO₃], so that the diminishing Org-NO₃ concentration is the one possible species to control the rate. For zero order kinetics, the [Org-NO₃] would need to be in excess of either [H₃O⁺] or [OH⁻].

To investigate the hypothesis of an acid or base catalysed mechanism occurring, several possible acid and base catalysed mechanisms have been evaluated. As an excess of water is present, a very low although replenishing concentration H₃O⁺ and OH⁻ (*ca.* 1.0 × 10⁻⁷ M, affected by the Org-NO₃ slightly) are produced at a constant concentration which does not change and is at a much lower concentration compared to Org-NO₃, allowing for the rate to be controlled. As either the H₃O⁺ or OH⁻ ions are at a very low concentration and one is required to be present to allow for primary Org-NO₃ hydrolysis, this may explain the zero-order kinetics observed in this study. This is because the reaction rate is not determined by the [H₂O] or the [Org-NO₃], but the [H₃O⁺] or [OH⁻] which is constant with the H₂O in excess and in equilibrium with these species. As the [Org-NO₃] is in excess of [H₃O⁺] or [OH⁻] and saturates either of these ions, a consistent [NO₃⁻] is produced as a function of time leading to the zero-order reaction.

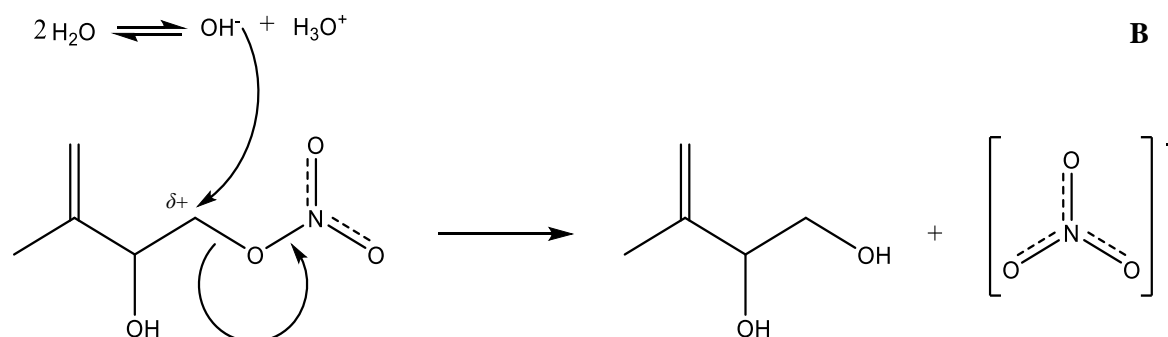


Fig. 6.11. Possible S_N² nucleophilic substitution by OH⁻ (mechanism B).

Mechanism B in Fig. 6.11 demonstrates a possible base catalysed reaction from OH⁻ produced through the dissociation of water⁵²² in this study. The OH⁻ nucleophile is electrostatically attracted to the positive charge located on the α-carbon which it attacks. In the same step (and therefore forming a bimolecular transition state), the αC–O bond breaks, producing nitrate and attaches an alcohol group to the organic. This mechanism is similar to that which is represented in mechanism A in which a bimolecular transition state is formed.

Another possible mechanism is that of C, demonstrated in Fig. 6.12. Similar to mechanism B, mechanism C is base catalysed⁵²² although follows an elimination pathway. The OH⁻ nucleophile

produced by H_2O dissociation is electrostatically attracted to the β -hydrogen and abstracts it, reforming water. In doing so, the previous bond between $\beta\text{C-H}$ breaks and the electrons are shifted to the adjacent bond forming an alkene group. At the same time, the $\alpha\text{C-O}$ bond between the organic and the NO_3 group breaks and the electrons from this bond localise onto NO_3^- , ejecting this group. This results in the introduction of an alkene group into the organic and the NO_3^- in solution. As this reaction occurs in one step and involves a single transition state, this reaction would be zero order at low enough $[\text{OH}^-]$ and first order when $[\text{OH}^-]$ overtakes the $[\text{Org-NO}_3]$ (for which the rate of this mechanism would then be dependant on just the concentration of $[\text{Org-NO}_3]$ as H_2O is in vast excess). This reaction is a bi-molecular elimination reaction and at high enough $[\text{OH}^-]$, this is therefore an E^2 mechanism with second order kinetics. As the H_2O is in vast excess, the reaction would therefore appear as pseudo first order (E^1).

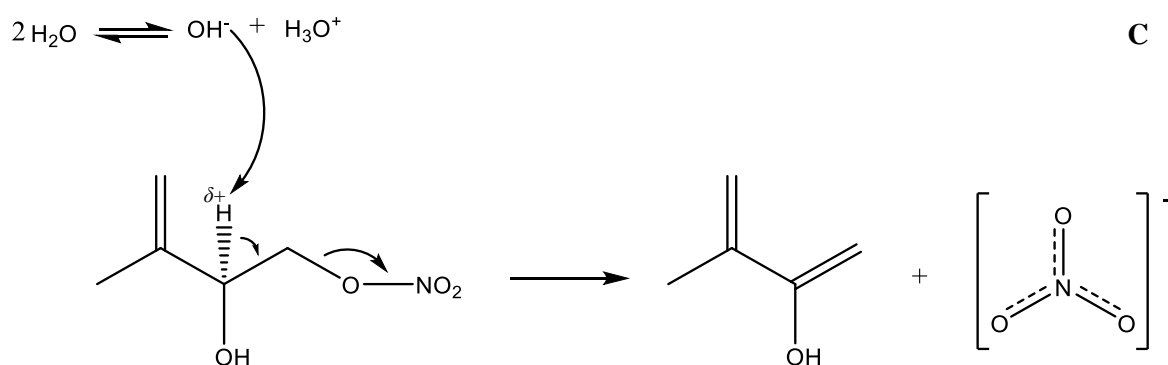


Fig. 6.12. Possible base catalysed β -hydride E^2 elimination reaction for Org-NO_3 hydrolysis (mechanism C).

Many of the previous studies described in the literature investigate the hydrolysis of Org-NO_3 species in the presence of acid. Therefore, an acid catalysed reaction was also considered and is shown in Fig. 6.13 (mechanism D), based on the work of Rindelaub et al., (2016)⁵²⁴. In this mechanism, two molecules of water react and dissociate into H_3O^+ and OH^- . The negative charge localised on the NO_3 group on the Org-NO_3 molecule is electrostatically attracted to a hydrogen located on the hydronium ion. The O-H bond on the hydronium ion breaks and water is reformed. An O-H bond is formed to produce an ONO_2H^+ group on the organic compound. The $\alpha\text{C-O}$ bond subsequently breaks and HNO_3 is ejected from the Org-NO_3 molecule. This produces a primary carbocation which may convert to a tertiary carbocation through a 1, 2-shift⁵²⁴, increasing stability and making this process more energetically favourable. Mechanism D therefore demonstrates an acid catalysed mechanism from a protonated leaving group. OH^- from water dissociation may be attracted to the tertiary carbocation causing nucleophilic substitution (S_N^1), or a lone pair of electrons located on the oxygen atom of water may be attracted to an adjacent C-H hydrogen, reforming the hydronium ion, breaking the C-H bond and shifting the electrons to form an $\alpha\text{C}=\beta\text{C}$ double bond.

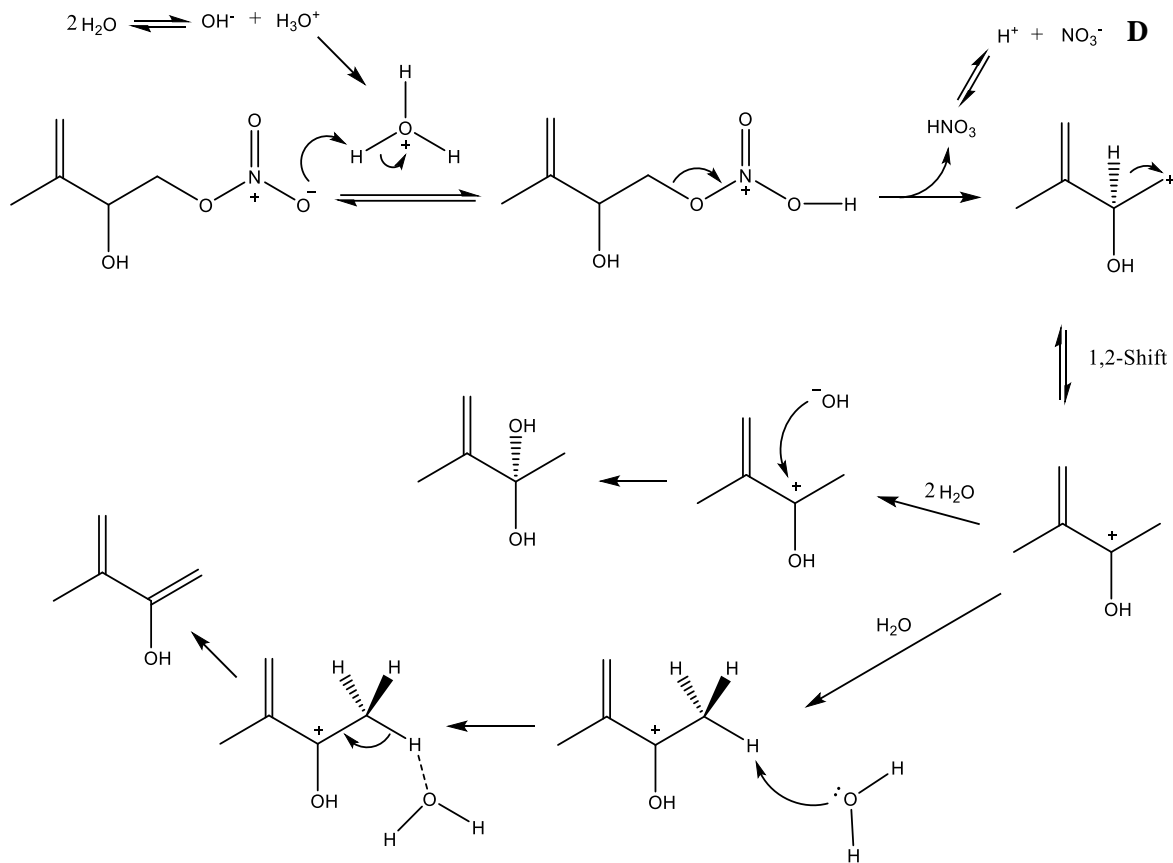


Fig. 6.13. Acid catalysed reaction mechanism for the hydrolysis of compound 1 (mechanism D).

A base or acid catalysed reaction pathway would also agree with the observation in this study that the presence of LiF causes an increase in the rate of hydrolysis. As F^- is a weak conjugate base, it will be able to deprotonate water and form a small amount of HF and OH^- . HF may then go onto protonate water producing H_3O^+ . This therefore increases the amount of acid and therefore $[H_3O^+]$ or $[OH^-]$ within the solution. As the $[H_3O^+]$ or $[OH^-]$ increases, the rate also increases although as $[H_3O^+]$ or $[OH^-]$ are still below $[Org-NO_3]$, the order of reaction remains zero-order. Li^+ does not ionically bond with OH^- and both ions behave independently of one another. This is because LiOH is a very strong base and Li^+ in water is essentially neutral.

To summarise the possible discrepancy between the literature (first order)^{276,503,348} and this study (zero order), the most likely reason for this is the presence of a high enough concentration of acid within previous studies. Previous studies which have reported first order kinetics for $Org-NO_3$ hydrolysis report the hydrolysis in the presence of acid and use NMR solvents (which may sometime be contaminated with trace levels of acid). The evidence of an increased zero order reaction rate in this study from the addition of LiF producing a small amount of H_3O^+ further explains the discrepancy. On this basis, it is very likely that mechanism D occurs in the $Org-NO_3$ hydrolysis in this study and through a first order acid catalysed S_N^1 mechanism (which agrees with the literature). In this study however, the acid concentration is low enough to demonstrate pseudo zero-order kinetics. Mechanisms B and C however cannot be discounted until base catalysed $Org-NO_3$

experiments are conducted. If B and C do occur in conjunction with mechanism D, further analytical techniques such as Gas Chromatography - Mass Spectrometry (GC-MS) or Liquid Chromatography - Mass Spectrometry (LC-MS) may need to be used to investigate the organic by-products produced to observe which pathways are predominant. These analytical techniques could also be used to further substantiate the argument that an acid catalysed reaction is present.

In addition, however, mechanisms B and C have a transition state and therefore follow S_N^2 kinetics (which would be observed as pseudo first order in a vast excess of water). H_2O is a polar protic solvent which stabilises a carbocation intermediate through an S_N^1 pathway although is much less favourable for the S_N^2 reactions as the polar water would solvate and crowd around the incoming OH^- nucleophile. Therefore, it could be that D is more likely to occur compared to B and C. Based on the IC NO_3^- experimental data, mechanism D is very likely to be occurring in the Org- NO_3 hydrolysis and mechanisms B and C may be present also and therefore a mixture of hydrolysis experiments may be occurring.

6.3.1.5 Compound 4 Hydrolysis Mechanism

Compound 4 is unique in which NO_3^- and NO_2^- are detected. In section 6.3.1.1 it was speculated (based on the literature) that compound 4 may hydrolyse to produce NO_2^- through a base catalysed elimination reaction (Fig. 6.6) as suggested in the work by Boschan et al., (1955)⁵²². The hydrolysis time series for compound 4 displaying the % molar yield of NO_2^- and NO_3^- as a result of compound 4 hydrolysis in *ca.* 25 ppm LiF and H_2O is shown in Fig. 6.14. Unlike compounds 1-3, the hydrolysis of compound 4 causes a stable NO_2^- reading as a function of time within the LiF and water solvents and a stable NO_3^- reading in LiF. A zero-order reaction is however observed for NO_3^- production as a function of time within the 18.2 M Ω water solvent.

With regards to the nitrate production, in section 6.3.1.4 it was described how LiF may speed up the hydrolysis for compounds 1-3. For compound 4 however, the opposite is true for NO_3^- . When LiF is removed from the solvent, a first order rate of reaction appears (Fig. 6.14B) as opposed to no apparent reaction within the LiF solvent (Fig. 6.14A). This therefore indicates that for compound 4, hydrolysis can take place and that the presence of NO_3^- is not just from $AgNO_3$ impurities from the synthesis protocol⁵¹⁹.

The average % molar yield [NO_3^-] in the presence of LiF is 1.31×10^{-1} % (SD $\pm 2.41 \times 10^{-3}$ %). The intercept (starting [NO_3^-] concentration) observed in the neutral water hydrolysis experiment is 5.68×10^{-2} %. Therefore, the average concentration observed in the LiF experiment is 2.30 times larger compared to the neutral water hydrolysis starting % molar yield.

As LiF is observed to catalyse the hydrolysis reactions in compounds 1-3 (w.r.t. NO_3^- production), this may be in agreement with compound 4. The phenomenon observed in the LiF experiment may be a plateau to a very fast reaction (with LiF catalysis) and the gradient observed in the water experiment may be the zero-order reaction occurring, to achieve the plateau (end of reaction) concentration of 1.31×10^{-1} % (SD $\pm 2.41 \times 10^{-3}$ %) seen in the LiF experiment. If this is the case,

this would suggest that the Org-NO₃ hydrolysis of compound 4 does not go to completion, but is at a constant equilibrium in the ratio of 99.87 % [Org-NO₃] : 0.13 % [NO₃⁻].

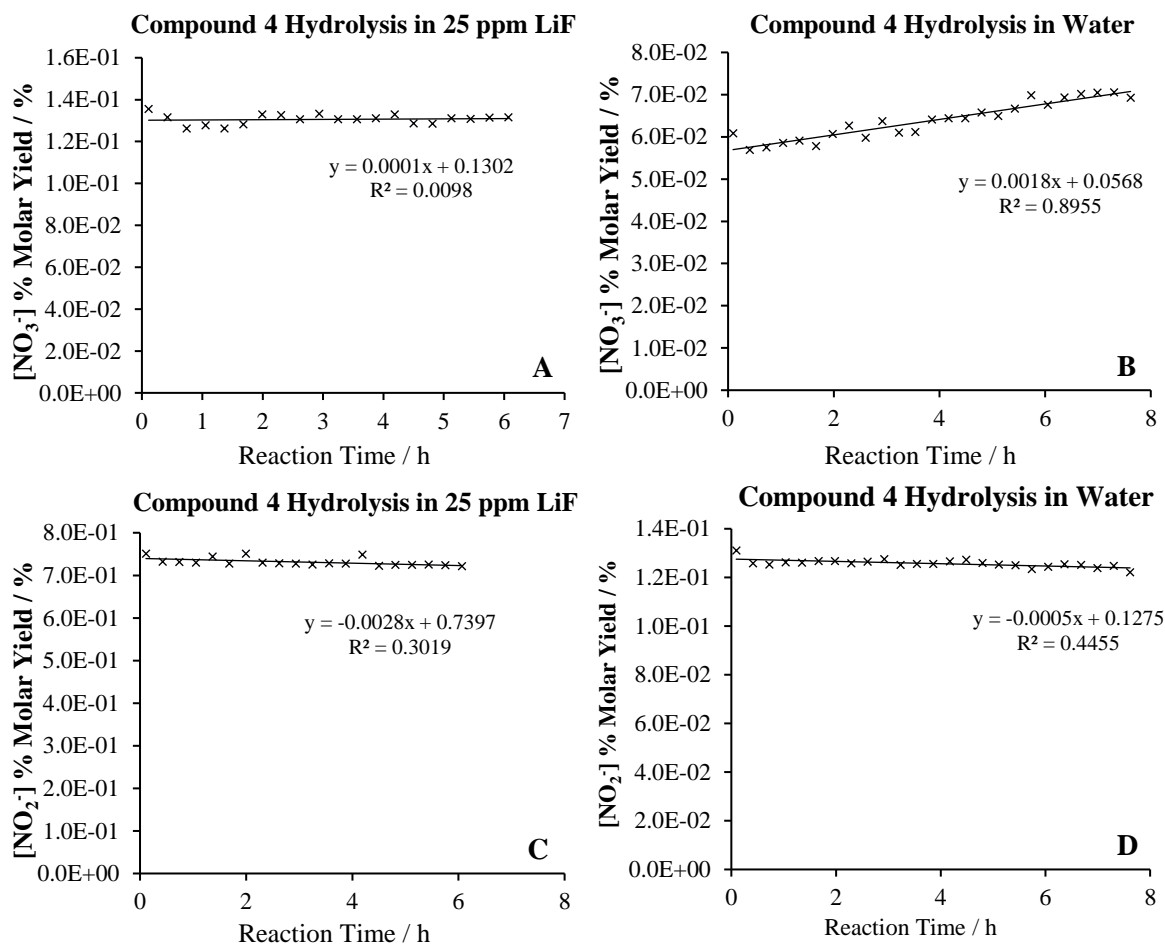


Fig. 6.14. Direct comparison of total % [NO₃⁻] and % [NO₂⁻] molar yield between Org-NO₃ (compound) hydrolysis in 25.4 ppm LiF and 18.2 MΩ water. The error associated with the [NO₃⁻] measurements was ±1.95 % and with the [NO₂⁻] measurements was ±4.78 %. The error was calculated based on the IC instrument reproducibility of these species.

Using the linear correlation regression of compound 4 for the neutral water hydrolysis ($y = 0.0018x + 0.0568$), it is estimated that it would take *ca.* 40.3 hours to achieve the average concentration of the plateau (1.31×10^{-1} [NO₃⁻] Molar % yield). Finally, the ratio of the intercept / gradient in compounds 1, 2 and 3 were 4.00×10^{-1} , 6.69×10^{-1} and 1.96×10^{-1} for the neutral water hydrolysis experiments. This compares to 31.03 observed by the neutral hydrolysis of compound 4. These ratios for compounds 1, 2 and 3 are very close to zero (the origin), whereas four is three orders of magnitude higher. This suggests that in the samples of compounds 1-3 no (or very little NO₃⁻) was present in the stock Org-NO₃, whereas for compound 4 the linear regression does not come close to passing through the origin. Therefore, it is likely that the relatively higher starting NO₃⁻ concentration may have been due to some AgNO₃ impurity.

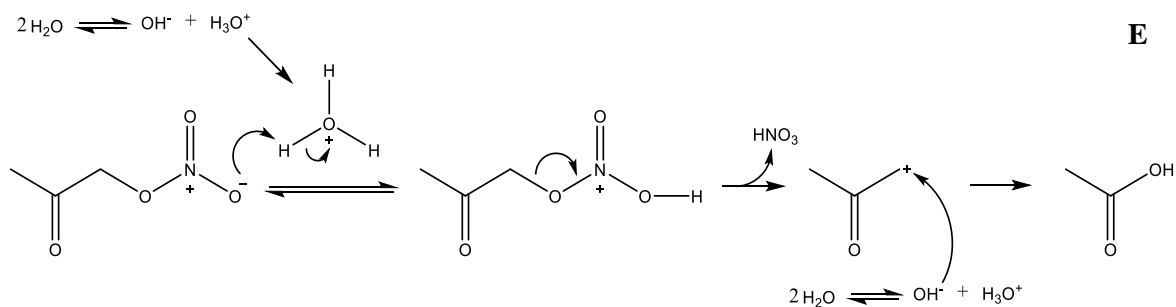


Fig. 6.15. Possible acid catalysed S_N1 hydrolysis pathway of compound 4 with OH^- as the nucleophile producing NO_3^- (mechanism E).

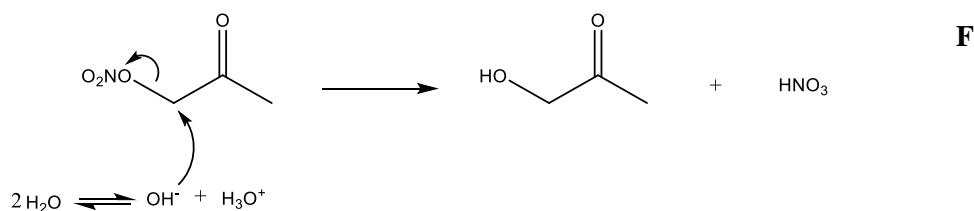


Fig. 6.16. Possible nucleophilic substitution reaction (S_N2) reaction of compound 4 producing NO_3^- (mechanism F).

Based on the findings in section 6.3.1.3 and that Org- NO_3 hydrolysis in compounds 1-3 were likely acid or base catalysed, two mechanisms have been considered for the production of NO_3^- from compound 4. These are mechanisms E and F shown in Fig. 6.15 and Fig. 6.16, respectively.

In mechanism E, the negative charge on the NO_3^- group oxygen attacks a hydrogen within a hydronium produced from water dissociation. This produces the ONO_2H^+ group on compound 4. The $\alpha\text{C-O}$ bond dissociates in compound 4 releasing HNO_3 and the formaldehyde carbocation. To finish the reaction, an OH^- group from the dissociated water acts as a nucleophile and attacks the carbocation, producing the alcohol. The production of the primary carbocation intermediate formed in mechanism E is very unfavourable, as a positive charge is located on a carbon which is directly bonded to a carbonyl (electron withdrawing) group.

The base catalysed reaction (mechanism F) is more favourable as no primary carbocation intermediate is produced. In this mechanism, an OH^- from dissociated water acts as a nucleophile and attacks the δ^+ charge located on the α -carbon. In the same step, the $\alpha\text{C-O}$ bond dissociates to eject the NO_3^- group. A transition state therefore occurs in this bimolecular pathway and this is therefore representative of an S_N2 mechanism. The very low concentration of catalytic OH^- however would make this reaction pseudo zero order.

A key observation of Fig. 6.14 is the zero-order observed in the production of NO_3^- in water, although in LiF it seems as though the reaction has reached equilibrium for compound 4 hydrolysis. Therefore, this indicates that the addition of LiF to the solvent increases the rate of hydrolysis of compound 4 somewhat. LiF releases F^- into the solution which is a weak base and therefore produces HF which is acidic. As the addition of this acid seems to increase the rate of reaction, this may indicate that the

acid catalysed reaction mechanism (F) is the predominant mechanism for compound 4. As the acid increases, the neutralisation of OH^- also increases, reducing the possibility for the base catalysed mechanism to occur.

Mechanisms G (Fig. 6.17) and H (Fig. 6.18) have been proposed as possible acid and base catalytic pathways for the formation of NO_2^- in solution. In mechanism G, the nitrate group in compound 4 has a negative charge located on an oxygen which is electrostatically attracted to a hydronium ion. This produces an ONO_2H^+ . Following this, an elimination pathway is required to produce NO_2^- in which the $\alpha\text{C-H}$ bond breaks, regenerating H^+ . This is followed by $\text{O-NO}_2\text{H}^+$ bond breakage which produces HNO_2 .

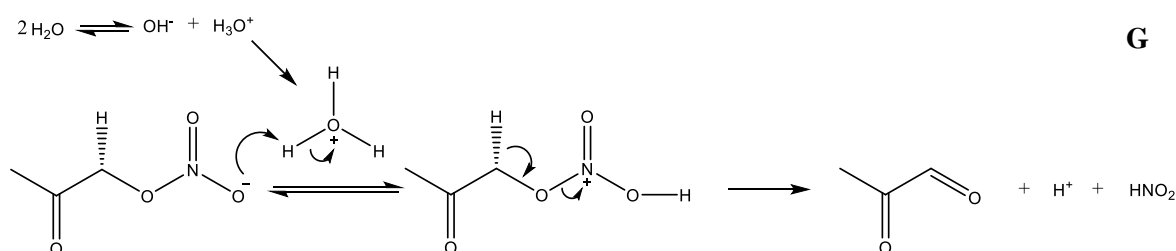


Fig. 6.17. Possible acid catalysed elimination hydrolysis reaction (E^2) of compound 4 producing NO_2^- (mechanism G).

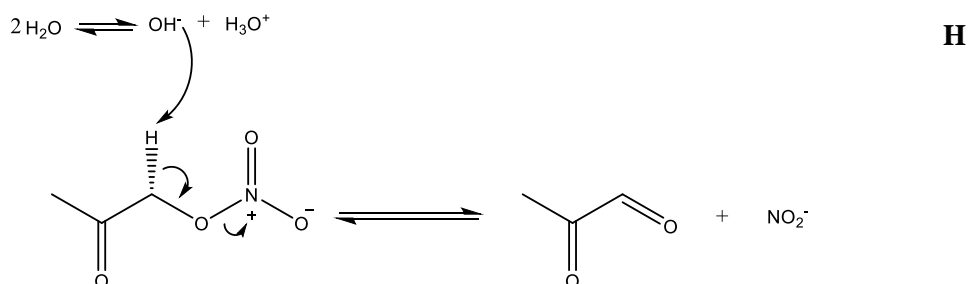


Fig. 6.18. Possible base catalysed α -hydrogen elimination hydrolysis reaction (E^2) producing NO_2^- (mechanism H).

Mechanism H involves a base catalysed reaction in which a hydroxyl group is attracted to the αH atom. This produces water and causes the $\alpha\text{C-H}$ bond to break. In the same step, the O-NO_2 bond also breaks to produce the carbonyl observed in the methylglyoxal by product, ejecting NO_2^- . The completed hydrolysis equilibrium % yield observed from hydrolysis within the 25.4 ppm LiF solvent was 5.60 times higher for NO_2^- compared to NO_3^- . Therefore, this shows that the pathway to produce NO_2^- was much more dominant compared to the NO_3^- production pathway. In addition, The % molar yield was 5.82 times larger for NO_2^- in the LiF solvent compared to the 18.2 M Ω water solvent. This therefore indicates that the lowering of the pH from the addition of LiF enhances the reaction by shifting the equilibrium more to the products (NO_2^-) side compared to in the neutral water solvent system.

In summary, the hydrolysis of compound 4 is more complicated due to both NO_3^- and NO_2^- being detected. Further investigation is required for definite conclusions as to the exact mechanisms occurring for compound 4 hydrolysis and this constitutes to future work.

6.3.2 PILS IC results from the SAPHIR Chamber

During the experiments at Jülich, the initial analysis obtained by the IC produced poor data for NO_3^- as the concentration was below the LOD for the IC. Therefore, left over sample was re-run on the IC system back at the UoY after the campaign, after cleaning the column and concentrating up samples (by a factor of 4) via evaporation (section 6.2.4).

6.3.2.1 Limit of Detection

The detection limits for NO_3^- and SO_4^{2-} were 0.048 ppm and 0.120 ppm, respectively. Table 6.4 demonstrates the proportion of samples (%) obtained on each sampling day which were < LOD, for $[\text{NO}_3^-]$ and $[\text{SO}_4^{2-}]$. All $[\text{F}^-]$ (ca. 17 – 19 ppm) within the PILS samples were > LOD (0.175 ppm). Table 6.4 shows that after evaporation, a substantial number of samples were > LOD on the 15th, 16th, 18th, 19th and 21st Aug chamber days, for NO_3^{3-} . For SO_4^{2-} , almost all samples were > LOD. On days for which a substantial number of samples are < LOD, it is difficult to correct for these very low levels. On some days, the concentrations are very low and due to the positive intercept observed in many of the calibrations, a negative concentration is obtained.

6.3.2.2 Uncertainty of PILS-IC Measurements

The errors of the PILS-IC NO_3^- and SO_4^{2-} measurements from the NO3ISOP chamber studies were calculated by propagating the substantial errors associated with this technique through Eq. 6.1.

6.3.2.2.1 Uncertainty of Dilution Factor, R

Firstly, the error associated with the dilution factor R (Eq. 6.2), was calculated. The dilution factor R may be summarised in Eq. 6.3, where R is the dilution factor, Q is the $[\text{F}^-]$ before entering the impactor (from reservoir, PILSpot) and P is the $[\text{F}^-]$ of the LiF exiting the impactor and entering the sample.

$$R = \frac{Q}{P}$$

Eq. 6.3. Algebraic version of the Orsini et al., (2003)²⁶⁶ Calculation.

An error was first calculated for the concentration of F^- exiting the impactor (P). For these values, the total calibration error (δP) was calculated by summing the calibration curve error, δP_1 (SD) and the SD associated with the reproducibility of the IC instrument (δP_2). For this process, 2 ml of sample was pipetted into each vial (section 6.2.4), although in some cases less sample was available and concentrations therefore needed to be corrected by dividing the measured concentration by the actual volume of sample pipetted, and then multiplying this by 2000 μl . The δP_1 was therefore corrected for the volume of sample which was pipetted into the sample vial for evaporation on the biotage

evaporator ($\delta P_1'$). This is outlined in Eq. 6.4 and produced the total corrected calibration error, $\delta P'$ associated with the denominator of Eq. 6.3.

$$\delta P' = \delta P_1' + \delta P_2$$

Eq. 6.4. Calculation of the absolute total concentration error for $[F^-]$ entering the impactor ($\delta P'$) which is calculated by summing the corrected calibration absolute SD uncertainty ($\delta P_1'$) with the IC reproducibility uncertainty SD (δP_2).

To solve the error of the numerator, a similar calculation was completed in which the total calibration error of the PILSpot (LiF reservoir in PILS system, $[F^-]$ before impactor stage) concentrations was calculated for each PILSpot solution. The error associated with the PILSpot calibration (δQ_1) was added to the reproducibility error of the IC instrument for F^- (δP_2) to produce the total error of the concentration for the PILSpot (δQ). As the PILSpot $[F^-]$ is associated with a solution which was a reservoir of F^- for the impactor stage of the PILS, no volume correction was needed here. Therefore, the error of the numerator (Q, the concentration of F^- entering the impactor) in calculating the value of R (Eq. 6.3) is summarised in Eq. 6.5.

$$\delta Q = \delta Q_1 + \delta P_2$$

Eq. 6.5. Calculation of the absolute total concentration error for $[F^-]$ exiting the impactor (δQ) which is calculated by summing the absolute SD error of the calibration (δQ_1) and the reproducibility SD of the IC response for $[F^-]$ (δP_2).

Finally, to calculate the error associated with the dilution factor R, the division rule of propagation of errors was taken. This is shown in Eq. 6.6 and is rearranged in Eq. 6.7 to produce the error associated with R (δR).

$$\left(\frac{\delta R}{R}\right)^2 = \left(\frac{\delta Q}{Q}\right)^2 + \left(\frac{\delta P'}{P'}\right)^2$$

Eq. 6.6. Propagation of Errors Division Rule applied to calculating the Dilution Factor, R.

$$\delta R = R \times \sqrt{\left(\frac{\delta Q}{Q}\right)^2 + \left(\frac{\delta P'}{P'}\right)^2}$$

Eq. 6.7. Re-arrangement of the division rule for propagation of errors to calculate the total error of the Dilution Factor, δR .

6.3.2.2.2 Uncertainty of NO_3^- and SO_4^{2-} Atmospheric Chamber Concentrations

The calculation of errors for the NO_3^- and SO_4^{2-} atmospheric concentrations was conducted, based on Eq. 6.1. Firstly, the error associated with the concentration measurements from the IC for NO_3^- and SO_4^{2-} were conducted. This was completed in the same manner as for $[F^-]$ in section 6.3.2.2.1.

The calibration error (δA_1) was first volume corrected to produce $\delta A_1'$, which was subsequently summed with the absolute reproducibility error of NO_3^- or SO_4^{2-} (δA_2), to produce the total corrected concentration error of NO_3^- or SO_4^{2-} ($\delta A'$), where A' is the corrected concentration of $[\text{NO}_3^-]$ or $[\text{SO}_4^{2-}]$. A' is however multiplied by 1000 to obtain the concentration in $\mu\text{g L}^{-1}$ and therefore $\delta A'$ is also multiplied by 1000 to obtain the correct units ($\mu\text{g L}^{-1}$).

The corrected concentration measurement from the IC for NO_3^- or SO_4^{2-} is subsequently multiplied by the flow rate of the LiF solution into the PILS vials, as well as the dilution factor, R . At this step, the product of this (B) is represented in Eq. 6.8. The LiF flow rate was calculated by measuring the volume of liquid given by the PILS across a 15-minute sampling period for 6 separate samples. The SD of these flow rates was calculated (across six repeats) and is used as the absolute error of the flow rate ($\delta \text{LiF}_{\text{FlowRate}}$).

$$B = A' \times \text{LiF}_{\text{FlowRate}} \times R$$

Eq. 6.8. The calculation of the product of the numerator of the Atmospheric Concentration Calculation (Eq. 6.1) using the PILS method where A' is the corrected IC concentration of NO_3^- or SO_4^{2-} , $\text{LiF}_{\text{FlowRate}}$ is the flow rate of LiF through the PILS, and R is the dilution factor.

Therefore, to propagate the errors at this step, the multiplication rule of propagation is taken and is shown in Eq. 6.9 for this instance.

$$\delta B = B \times \sqrt{\left(\frac{\delta A'}{A'}\right)^2 + \left(\frac{\delta \text{LiF}_{\text{FlowRate}}}{\text{LiF}_{\text{FlowRate}}}\right)^2 + \left(\frac{\delta R}{R}\right)^2}$$

Eq. 6.9. Re-arranged equation of the propagation of error in calculating the total δB , where δB is the total error of the numerator calculated in Eq. 6.1, and where A' , $\text{LiF}_{\text{FlowRate}}$ and R have been previously defined.

Finally, the numerator, B , is divided by the flow rate of air into the impactor, for which the error associated with the Alicat Flow Meter (section 6.2.3) is negligible compared to the other variables used in this calculation. Therefore, the numerator B is simply divided by the flow rate of air entering the PILS (constant), to produce the atmospheric chamber concentrations of NO_3^- and SO_4^{2-} , C (Eq. 6.10, where the flow rate of air entering the PILS is given as AirFlow).

$$C = \frac{B}{\text{AirFlow}}$$

Eq. 6.10. Simplified Algebraic version of Eq. 6.1 to calculate the final Atmospheric Concentration of NO_3^- or SO_4^{2-} , where C is the final Atmospheric Concentration of NO_3^- or SO_4^{2-} , B is the product of the numerator of Eq. 6.1, and AirFlow is the flow rate of air into the PILS impactor during sampling.

Therefore, as the AirFlow (Q_a , Eq. 6.1) is a constant, the δB is simply divided by this constant to produce the error of the chamber atmospheric concentrations, δC (Eq. 6.11).

$$\delta C = \frac{\delta B}{AirFlow}$$

Eq. 6.11. Simplified version of the calculation of error of the atmospheric concentrations of NO_3^- or SO_4^{2-} (δC), where δB is the product of the numerator error of Eq. 6.1 and AirFlow is a constant.

6.3.2.2.3 Uncertainty of PILS-IC Org- NO_3 Atmospheric Chamber Concentrations

To calculate the total PILS-IC [Org- NO_3] during the experiments, the AMS [NO_3^-] was subtracted from the PILS-IC [NO_3^-] (section 6.1). Therefore, to calculate the total error of the [Org- NO_3], the propagation of errors rule for addition or subtraction is taken. This was conducted by calculating the absolute error (SD) of the AMS measurements from the percentage error ($\pm 20\%$) and combining this with the absolute error (δC , SD, section 6.3.2.2.2) calculated for each sample from the PILS-IC [NO_3^-] measurements. The calculation of the total Org- NO_3 error measured from the PILS-IC is summarised in Eq. 6.12, where [$NO_3^-_{AMS}$] is the AMS [NO_3^-], and C is the final PILS-IC [NO_3^-].

$$\delta[Org - NO_3] = \sqrt{(\delta[NO_3^-_{AMS}])^2 + (\delta C)^2}$$

Eq. 6.12. Calculation of the propagated total [Org- NO_3] uncertainty where $\delta[Org-NO_3]$ is the total error of the PILS-IC [Org- NO_3] concentrations; $\delta[NO_3^-_{AMS}]$ is the error associated with the AMS [NO_3^-] ($\pm 20\%$); and δC is the error associated with the PILS-IC [NO_3^-].

6.3.2.3 Quantitative Inorganic AMS Measurement and Uncertainty Evaluation

The accurate measurement of inorganic and organic nitrogen species is vital for air quality and human health research, as well as for modelling and regulatory applications surrounding PM⁵²⁶. Several studies have used AMS^{527,528} to quantify inorganic NO_3^- within ambient aerosol including Allan et al., (2004)⁵²⁹, Farmer et al., (2010)²⁸⁷ and Bae et al., (2007)⁵²⁶. It is generally assumed that the predominant fraction of nitrogen found in the atmosphere is inorganic^{530,526}, although it is also reported that organic nitrogen species account for a significant fraction of aerosol^{526,531}. There are methods to try and separate the inorganic and organic nitrogen within AMS using multiple methods including the comparison to IC methods, such as the use of NH_4^+ balance, the identification of HNO_3 , as well as the identification of minor ions from organic nitrogen species. These methods were specifically conducted by Farmer et al., (2010)²⁸⁷ during the measurement of ambient aerosol in Riverside (California). Work by Xu et al., (2021)⁵⁰⁹ also used positive matrix factorization.

Σ [Org- NO_3] within each of the chamber studies was calculated by subtracting the AMS [NO_3^-] concentrations from the Σ [NO_3^-] measured by the PILS-IC system (see section 6.1, Fig. 6.1). Therefore, the accurate measurement of inorganic NO_3^- from the AMS is crucial.

The advantages in using AMS for inorganic NO_3^- measurements include the ability of AMS to measure real-time aerosols at a considerably higher time resolution compared to bulk HiVol filter measurements²⁸⁷ or PILS measurements, reducing the potential for artefact formation. Disadvantages however include the complicated nature of splitting inorganic from interfering organic nitrogen species⁵²⁶ as well as the very unstable nature of Org- NO_3 with regard to temperature (vaporization and ionisation stages of some AMS systems)²⁸⁷. The measurement of inorganic nitrate relies on the accurate measurement of the NO_x^+ ion²⁸⁷, although interferences arise from the presence of organic nitrogen species (including Org- NO_3 ²⁸⁷, which are more prevalent in a rural setting with higher BVOCs⁵²⁶) which produce fragment ions CH_2O^+ , C_2H_6^+ and CH_4^+ which also have m/z 30 (identical to NO_x^+)^{526,532}. This issue was specifically highlighted in the work of Bae et al., (2007)⁵²⁶ in which a correlation between the PILS and AMS nitrate in their study was poor ($R^2 = 0.34$) at Pinnacle State Park in New York and the m/z 30 to m/z 46 ratio was significantly larger than 2.4 (the ratio for pure NH_4NO_3)⁵²⁶, for which Bae et al., (2007)⁵²⁶ concluded the substantial presence of organic nitrogen species. As a result of the interference of organic nitrogen species, the relative quantification of inorganic nitrate may be overestimated in the presence of a substantial fraction of nitrogenated or oxygenated organic species within OA, particularly in a rural setting⁵²⁶, or in the case of the NO3ISOP campaign. Due to this uncertainty, this increases the error of the inorganic NO_3^- AMS measurements to $\pm 20\%$ (as reported for the data from collaborative partners during the NO3ISOP campaign who took their method from Kiendler-Scharr et al., (2016)²⁷²). For the calculation of the PILS-IC [Org- NO_3] errors, the PILS-IC NO_3^- measurement error has been propagated with the AMS NO_3^- error to calculate the total error of the PILS-IC [Org- NO_3] species.

6.3.2.4 NO3ISOP Experimental Results

The results for the time series of NO_3^- , SO_4^{2-} and Org- NO_3 are shown in Fig. 6.20 - Fig. 6.31. In each time series, the time of day is shown along the x -axis, with species concentration shown on the y -axis. The NO_3^- , SO_4^{2-} and Org- NO_3 (PILS-IC NO_3^- minus AMS total NO_3^-) time series are shown in blue, red, and bright blue, respectively, for each day. The solid green line represents the AMS time series. The errors (for PILS-IC) associated with each time series are shown as error bars in the y -axis which have been calculated using the methods described in section 6.3.2.2. The coloured lines represent the times of injection of various materials into the smog chamber. In addition, samples which had been through a UV-Vis analysis (from a collaboration with the Weizmann Institute of Science in Israel) prior to the concentration step have been marked with a large red spot on each time series for NO_3^- and Org- NO_3 , as well as a blue spot for the SO_4^{2-} time series. These specific samples had an extra step of passing the sample through the quartz UV- Vis cuvettes, which in some cases showed contamination or losses of NO_3^- and SO_4^{2-} . These values should therefore be taken with caution. The green time series on each plot demonstrates the AMS total NO_3^- and total SO_4^{2-} values (averaged to the PILS sampling times). For any potential anomalies, the values have been shown in the PILS-IC time series, although have not been linked with the time series line. Based on section 6.3.1, it is likely that the majority of Org- NO_3 had hydrolysed in the PILS samples, irrespective of primary, secondary, or tertiary structure.

Table 6.4. Percentage of samples (out of the sample set) that were below LOD for $[NO_3^-]$ and $[SO_4^{2-}]$ for each day, as well as the Correlation Regression Coefficient values for each day between the PILS-IC values and the time averaged AMS values for $[NO_3^-]$ and $[SO_4^{2-}]$.

		15 th Aug	16 th Aug	17 th Aug	18 th Aug	19 th Aug	20 th Aug	21 st Aug	22 nd Aug	23 rd Aug
<LOD N%	NO_3^-	17.9	3.33	100	10.8	15.6	56.3	12.5	52.8	94.3
	SO_4^{2-}	17.9	0.00	0.00	0.00	0.00	0.00	0.00	5.56	25.7
AMS R ²	NO_3^-	0.79	0.07	0.00	0.27	0.12	0.00	0.05	0.41	0.68
	SO_4^{2-}	0.98	0.80	0.01	0.50	0.97	0.56	0.70	0.98	0.84

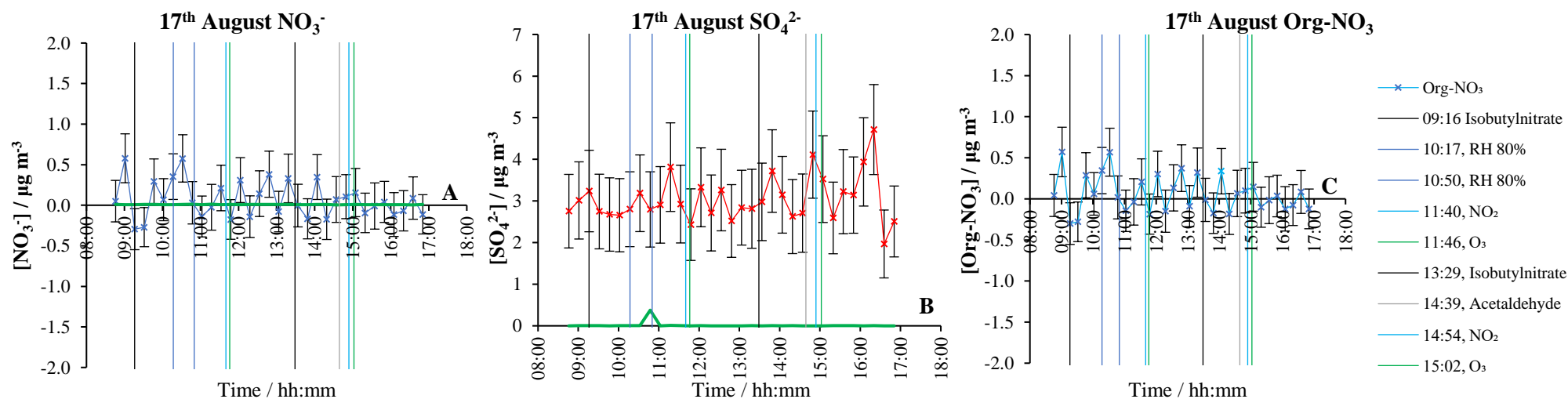


Fig. 6.19. Time series for $[NO_3^-]$ (A), $[SO_4^{2-}]$ (B) and estimated $[Org-NO_3]$ (C) measured by the PILS-IC (cross points), as well as the AMS data (green time series) on the 17th August. The injection of species into the chamber is shown as vertical lines across the x-axis which are summarised in the legend on the right. The error associated with the PILS-IC measurements are shown as error bars in the y-axis.

Therefore, the nitrate may be treated as inorganic and it is unlikely that any intact organic nitrates were present in the PILS samples.

6.3.2.4.1 17th August (Blank Chamber)

The experiment run on the 17th Aug was an aerosol blank chamber run, in which only RH, NO₂, O₃, as well as the VOCs isobutyl nitrate and acetaldehyde were added to the chamber. This experiment allowed for the noise of the PILS-IC system to be evaluated. For [NO₃⁻], the concentrations fluctuate around an average of 0.07 μg m⁻³ (SD ± 0.23 μg m⁻³) and for [SO₄²⁻] this blank average was 3.04 μg m⁻³ (SD ± 0.55 μg m⁻³). This compares to the AMS [NO₃⁻] and [SO₄²⁻] blank averages of 0.01 μg m⁻³ (SD ± 0.00 μg m⁻³) and 0.01 μg m⁻³ (SD ± 0.07 μg m⁻³). Therefore, the background seen in the PILS-IC was larger compared to the AMS for both NO₃⁻ and SO₄²⁻. As shown in Table 6.4, all NO₃⁻ values were < LOD and all SO₄²⁻ values were > LOD for the PILS-IC. Although the blank average for the PILS-IC was higher compared to that of the AMS, the PILS-IC does demonstrate a relatively clean chamber blank compared to the actual data from isoprene experiments on other days.

Possible reasons for the higher PILS-IC chamber blank concentrations in both NO₃⁻ and SO₄²⁻ are most likely down to the leaching of these ions from the glassware used during the sample preparation. A downfall to the use of the PILS sampling method, is that the only vials available for this method are made from glass. The larger variability seen in the PILS-IC may be due a different extent of leaching from the different vials used, as it is unlikely that the concentration of NO₃⁻ and SO₄²⁻ is not consistent through all vials produced by the manufacturer. In future for this type of experiment to work, it is essential that no glass is used and that an updated version of the PILS instrument is created to allow plastic vials for the benefit of IC analyses. This larger variation was also caused by the evaporator shutting down prematurely in evaporation runs, which results in two evaporation cycles being required for specific samples. The variation observed in the PILS-IC produced some problems when needing to measure at very low realistic atmospheric concentrations in the following chamber experiments.

6.3.2.4.2 15th August (High Concentration Experiment Example)

The experiment conducted on the 15th Aug was a night-time experiment in which the shutters on the SAPHIR chamber remained closed and was the only experiment conducted with significantly higher concentrations of precursors injected into the chamber. 3 ppbv of isoprene was injected into the chamber at 11:47 and 13:50, respectively. This day of results is significant as it is the only day in which an obvious trend in [NO₃⁻] may be seen without the post campaign concentration process (Fig. 6.20). For both NO₃⁻ and SO₄²⁻, 82.1% of the samples were observed to be > LOD (Table 6.4). Furthermore, a very good R² correlation was observed for SO₄²⁻ (R² = 0.98) between the PILS-IC and total AMS concentrations. Although the PILS-IC and AMS show very good temporal agreement in the SO₄²⁻ time series, an obvious offset is shown in the NO₃⁻ differences between the two instruments. This offset is likely due to the presence of Org-NO₃ species which are not measured by the AMS due to destruction at the vaporisation stage⁴⁹⁰. The estimated time series of the Org-NO₃

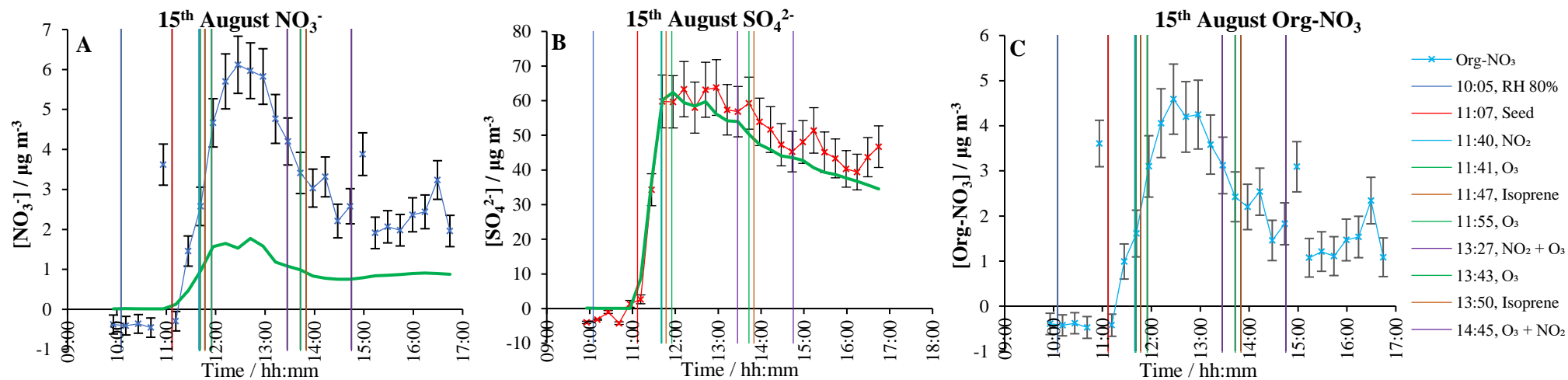


Fig. 6.20. Time series for $[NO_3^-]$ (A), $[SO_4^{2-}]$ (B) and estimated $[Org-NO_3]$ (C) measured by the PILS-IC (cross points), as well as the AMS data (green time series) on the 15th August. The injection of species into the chamber is shown as vertical lines across the x-axis which are summarised in the legend on the right. The error associated with the PILS-IC measurements are shown as error bars in the y-axis.

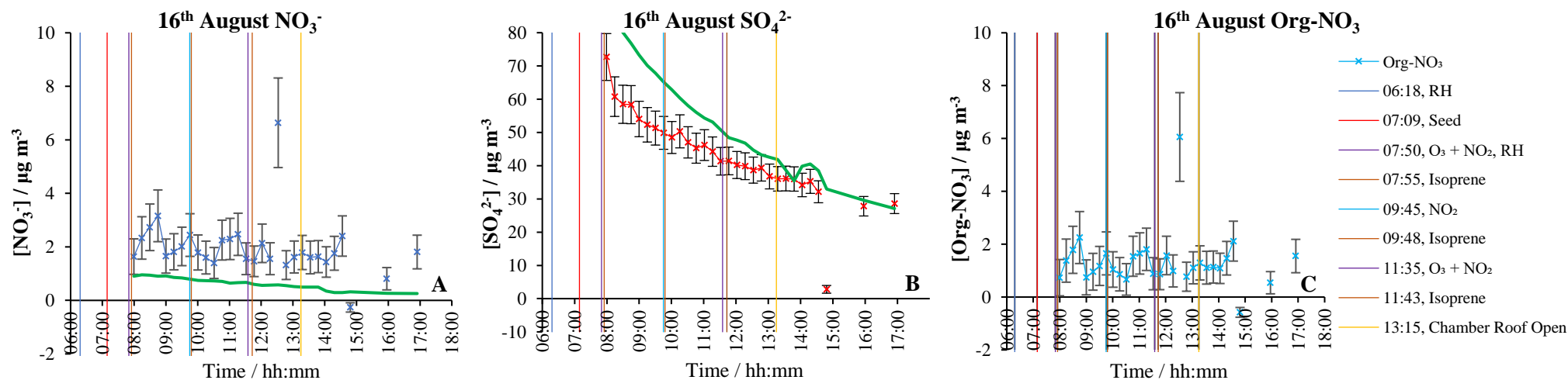


Fig. 6.21. Time series for $[NO_3^-]$ (A), $[SO_4^{2-}]$ (B) and estimated $[Org-NO_3]$ (C) measured by the PILS-IC (cross points), as well as the AMS data (green time series) on the 16th August. The injection of species into the chamber is shown as vertical lines across the x-axis which are summarised in the legend on the right. The error associated with the PILS-IC measurements are shown as error bars in the y-axis.

component is shown in Fig. 6.20C by subtracting the AMS values from the corresponding PILS-IC values.

The first few values of $[\text{NO}_3^-]$ and $[\text{SO}_4^{2-}]$ (Fig. 6.21) have negative concentrations due to being < LOD. In the $[\text{NO}_3^-]$ time series, an anomalously high value is observed at 11:11 ($3.62 \mu\text{g m}^{-3}$). On the addition of seed aerosol ($(\text{NH}_4)_2\text{SO}_4$) into the chamber at 11:07, a very clear rise in $[\text{NO}_3^-]$ is observed. This is because the nitrate species in the chamber have a surface to be able to partition into the aerosol from the gas-phase. As the NO_3^- and SO_4^{2-} content of particles increases, the inorganic fraction and therefore the hygroscopicity increases which makes Org- NO_3 deposition into the particles more prominent.

NO_2 , O_3 and isoprene are all added between 11:40 – 11:55. A rapid increase in particle phase concentration of NO_3^- is observed after addition of these gases. This is due to the formation of the NO_3 radical from the reaction between NO_2 and O_3 , which may further react with isoprene to form Org- NO_3 ^{493,490,484}, or inorganic HNO_3 ⁴⁹⁵/ N_2O_5 which can condense into the aerosol phase⁵²⁰ and produce NO_3^- on hydrolysis^{490,503,276,478,348,275,520}. It may however also be due to an initial reaction of isoprene with O_3 ^{501,478,481}, followed by reaction with NO ^{479,493} (produced from the dissociation of NO_3 into NO and NO_2), although this reaction is much slower. It is however unclear as to why NO_3^- concentrations start to rise once the seed aerosol has been injected in, as opposed to when the NO_2 and O_3 have been added to the chamber (later than the seed). Possible reasons for this may be the ineffective flushing of the chamber contents from the previous day.

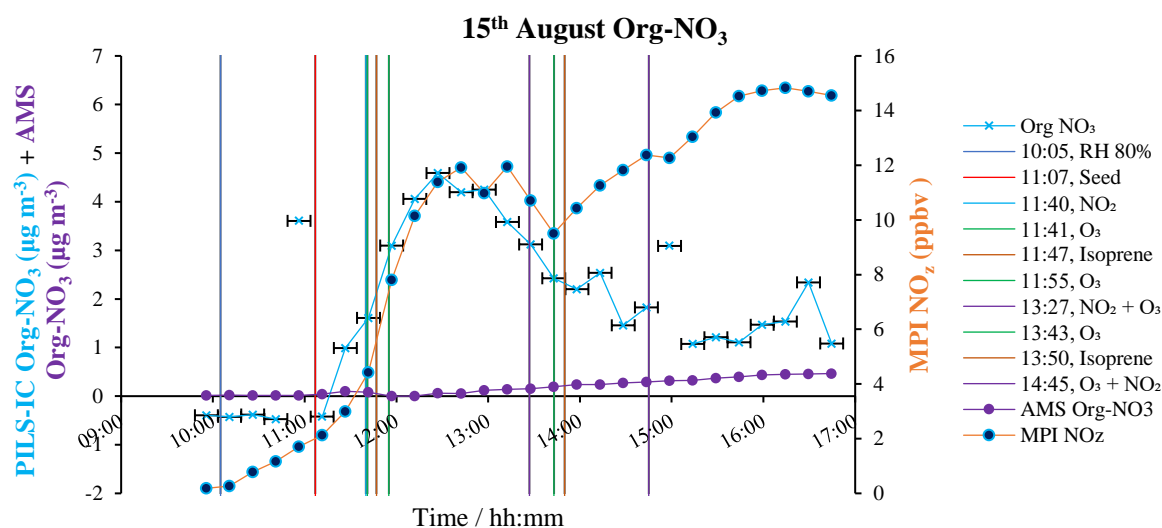


Fig. 6.22. The PILS-IC Org- NO_3 time series plotted against AMS Org- NO_3 and MPI NO_z concentrations for the 15th Aug. The injection of species into the chamber is shown as vertical lines across the x-axis which are summarised in the legend on the right. The uncertainty in the PILS-IC [Org- NO_3] can be found in Fig. 6.20C.

No correlations of significance were seen between the PILS-IC Org- NO_3 fraction and the other parameters measured during this day. The PILS-IC Org- NO_3 was however compared to the AMS Org- NO_3 (purple) in Fig. 6.22. A possible way to calculate $[\text{Org-NO}_3]$ and inorganic $[\text{NO}_3^-]$ using AMS is outlined in the work of Rollins et al., (2010)⁵³³. The $[\text{Org-NO}_3]$ from AMS may be calculated

by nebulising synthesised organic nitrate standards and sampling these into the AMS. The mass spectrums produced may be used to decipher calibration factors to generate an Org-NO₃ signature for AMS analysis. The PILS-IC Org-NO₃ showed a very different trend to the estimated AMS Org-NO₃. To investigate this further, the NO_z concentrations measured by the Max Planck Institute (MPI) were also compared (blue and orange) in Fig. 6.22. The PILS-IC trend is very similar to the MPI NO_z (NO_x reaction products e.g. NO_y - NO_x)⁵³⁴ trend up until *ca.* 12:30, although the trends deviate after this point. The AMS Org-NO₃ does not show the same increase at the beginning of the experiment as for the PILS-IC Org-NO₃ and MPI NO_z but instead shows a small linear increase over time.

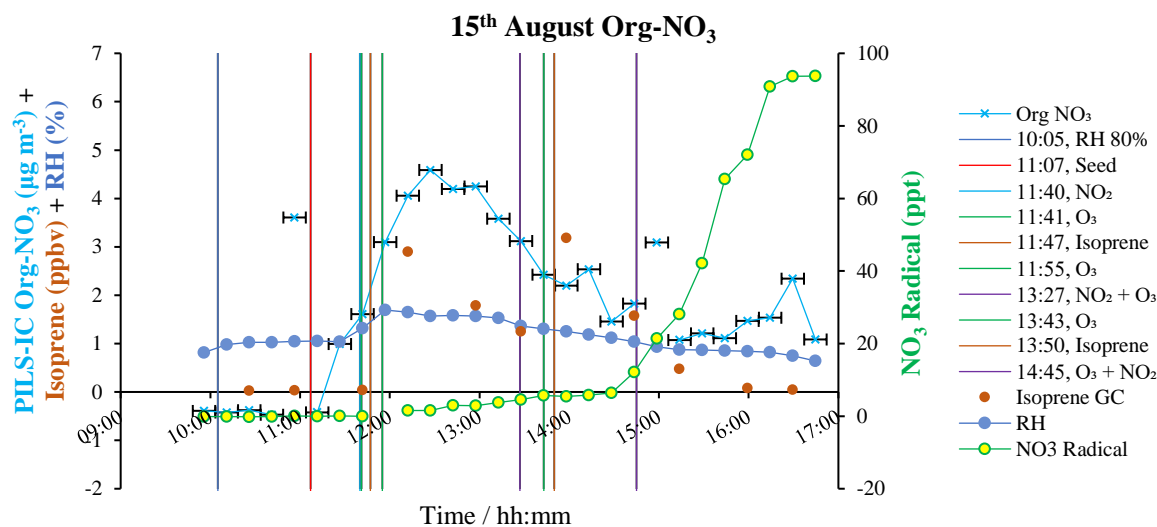


Fig. 6.23. The PILS-IC Org-NO₃ plotted against isoprene, RH and the NO₃ radical concentrations for the 15th Aug. The injection of species into the chamber is shown as vertical lines across the x-axis which are summarised in the legend on the right. The uncertainty in the PILS-IC [Org-NO₃] can be found in Fig. 6.20C.

To investigate further, the PILS-IC Org-NO₃ was therefore plotted against the most likely parameters to affect the concentration of Org-NO₃. These were the GC isoprene concentration (brown point), the RH (dull blue) and the NO₃ (yellow and green) radical concentration (Fig. 6.23). The PILS-IC Org-NO₃ generally followed the isoprene concentrations, in which peaks were seen in the PILS-IC Org-NO₃ time series at 12:17 and 14:13, just after the injection of isoprene. The [NO₃] remained low during the start of the experiment, although increased as Org-NO₃ and isoprene started to decrease. This suggests that NO₃ was in excess of isoprene during the latter half of the experiments. In general, the increase in AMS Org-NO₃ trend is inconsistent with both the PILS and NO_z measurements.

The PILS-IC does however match the trend in NO₂ up until the isoprene mixing ratios are depleted, after which the MPI shows a second increase later in the experiment when NO₃ radicals increase due to further additions of NO₂ and O₃ at very low isoprene mixing ratios. This indicates additional NO_z species are observed from the MPI instrument that do not lead to significant enhancement of NO₃ in the particle phase.

6.3.2.4.3 16th August (Low Concentration Experiment Example)

All the $[\text{SO}_4^{2-}]$ values and all but one sample for $[\text{NO}_3^-]$ were observed to be >LOD (table 6.4). Very good agreement in the trends between the PILS-IC and AMS SO_4^{2-} time series ($R^2 = 0.80$) was observed. The last three points of SO_4^{2-} in the 16th Aug time series may be down to a malfunction in the PILS sampler.

O_3 , NO_2 and RH were injected into the chamber at 07:50, followed by injection of isoprene at 07:55. In this experiment, the chamber had already been injected with NO_3 precursors (O_3 , NO_2 , RH) as well as isoprene to produce Org- NO_3 prior to the first PILS sample. $[\text{NO}_3^-]$ increased from $1.64 \mu\text{g m}^{-3}$ to $3.16 \mu\text{g m}^{-3}$ between 07:59 to 08:44 resulting in a calculated increase in the PILS-IC Org- NO_3 concentrations from $0.73 \mu\text{g m}^{-3}$ to $2.25 \mu\text{g m}^{-3}$.

The PILS-IC time series for the experiment on the 16th Aug (bright blue) is shown in Fig. 6.24, in conjunction with the time series of the NO_3 radical (green and yellow), N_2O_5 (orange), isoprene (brown) and RH % (dull blue). The times and colours of species injection and the opening of the chamber roof are shown in the legend in Fig. 6.24. For clarity, the isoprene and RH % time series have been placed into a second panel Fig. 6.24B.

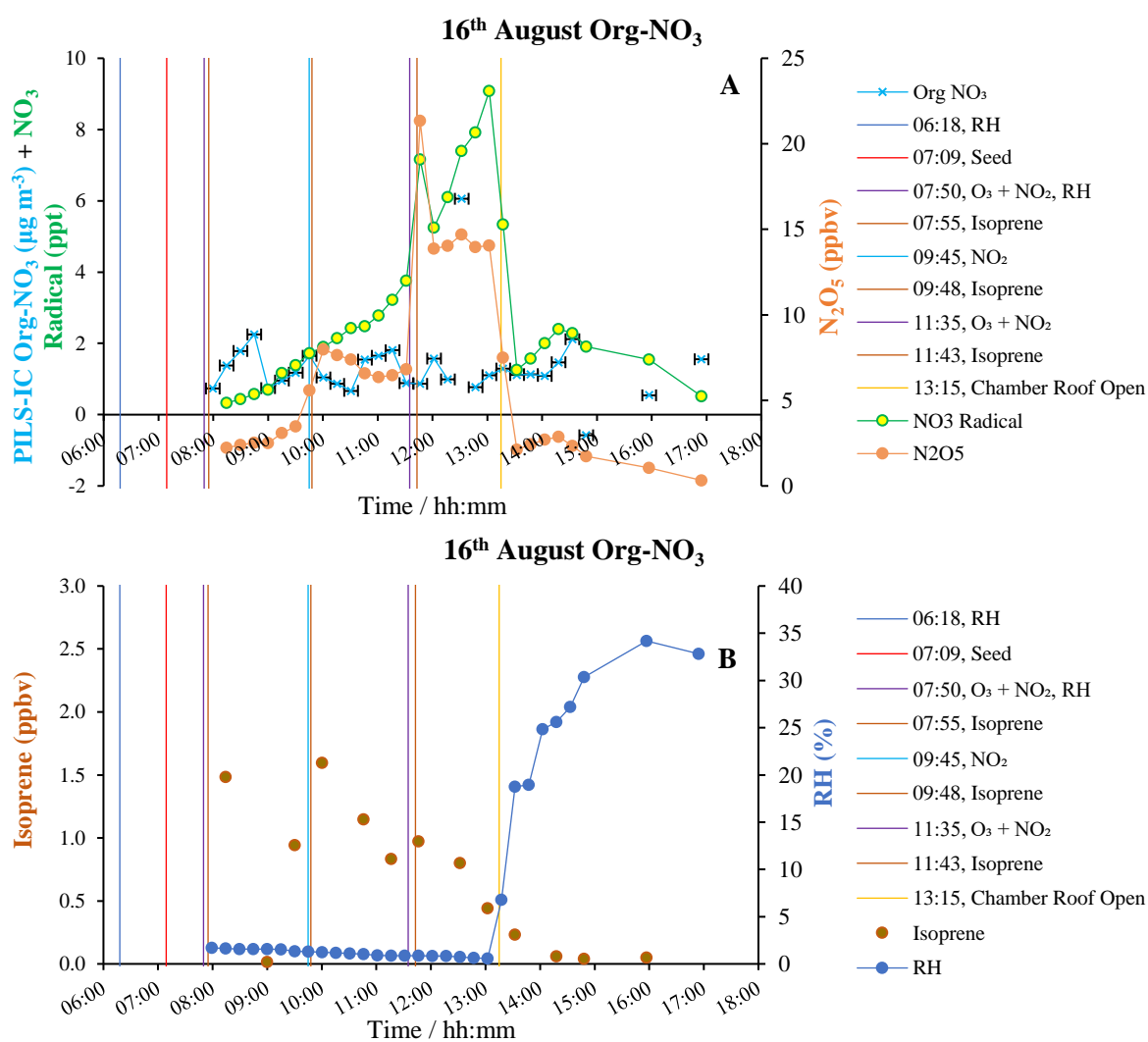


Fig. 6.24. The PILS-IC Org- NO_3 plotted against isoprene, RH and the NO_3 radical and N_2O_5 concentrations for the 16th Aug. The injection of species into the chamber is shown as vertical lines across the x-axis which are summarised in the legend on the right. The uncertainty in the PILS-IC [Org- NO_3] can be found in Fig. 6.21C

Fig. 6.24 also demonstrates an increase in PILS-IC Org-NO₃ from 09:00 (0.74 μg m⁻³) until 09:45 (1.65 μg m⁻³). This is due to an increase in isoprene which is also seen within this time, as well as an increase in NO₃ radicals. At 11:35, O₃ + NO₂ are added together simultaneously, followed by the addition of isoprene at 11:43. From these injections, it is observed that a small increase in PILS-IC Org-NO₃ occurs from 0.86 μg m⁻³ (11:46) to 1.57 μg m⁻³ (at 12:01). On opening the chamber roof at 13:15, there is a general decrease in PILS-IC Org-NO₃ from 2.29 μg m⁻³ (13:17) to 1.09 μg m⁻³ at 14:02. This can be explained by photolysis, in which N₂O₅ and NO₃ are photolyzed and destroyed^{497,535}. N₂O₅ is also known to be unstable and in a reversible reaction with NO₂ and NO₃⁴⁸⁸, in which under higher temperatures N₂O₅ will reproduce NO₂ and NO₃⁴⁸¹. This therefore would reduce the production of Org-NO₃ and in turn Inorg-NO₃⁻ species in the PILS. The trends of these species are shown in Fig. 6.24.

At 14:02 to 14:33, the PILS-IC Org-NO₃ values increase from 1.09 μg m⁻³ to 2.12 μg m⁻³. This may be due to the NO₃ radical increase from ca. 13:30 (with a delay in Org-NO₃ increase due to the time required for gaseous constituents to mix in the chamber). Furthermore, the RH increase may enhance the formation of Org-NO₃ by deposition/hydrolysis on the particle surface.

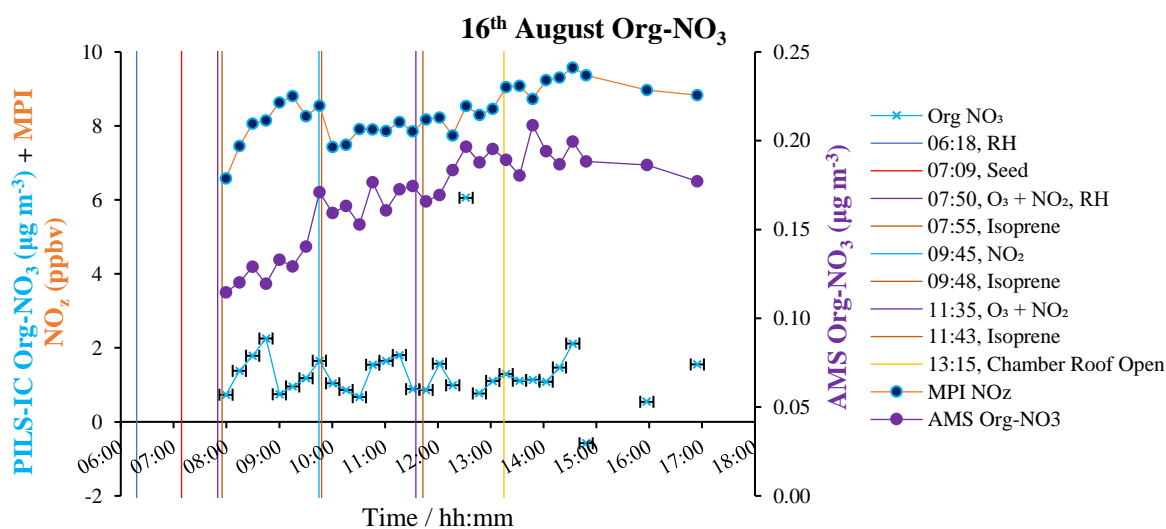


Fig. 6.25. The PILS-IC Org-NO₃ plotted against AMS Org-NO₃ and MPI NO_z concentrations for the 16th Aug. The injection of species into the chamber is shown as vertical lines across the x-axis which are summarised in the legend on the right. The uncertainty in the PILS-IC [Org-NO₃] can be found in Fig. 6.21C.

The PILS-IC Org-NO₃ was also compared to the AMS Org-NO₃ and MPI NO_z trends (Fig. 6.25). Similar to the results of the 15th Aug, the MPI NO_z mimics the increase in the PILS-IC Org-NO₃ trend, although observes a general increase in NO_z after 10:15. In addition, the AMS Org-NO₃ trend is inconsistent with the general decrease in isoprene concentrations during the experiment (Fig. 6.24).

6.3.2.4.4 18th – 23rd August

Sections 6.3.2.4.2 and 6.3.2.4.3 demonstrate examples of a high and low concentration experiment, respectively. The remaining experiments were also conducted at atmospheric relevant concentrations

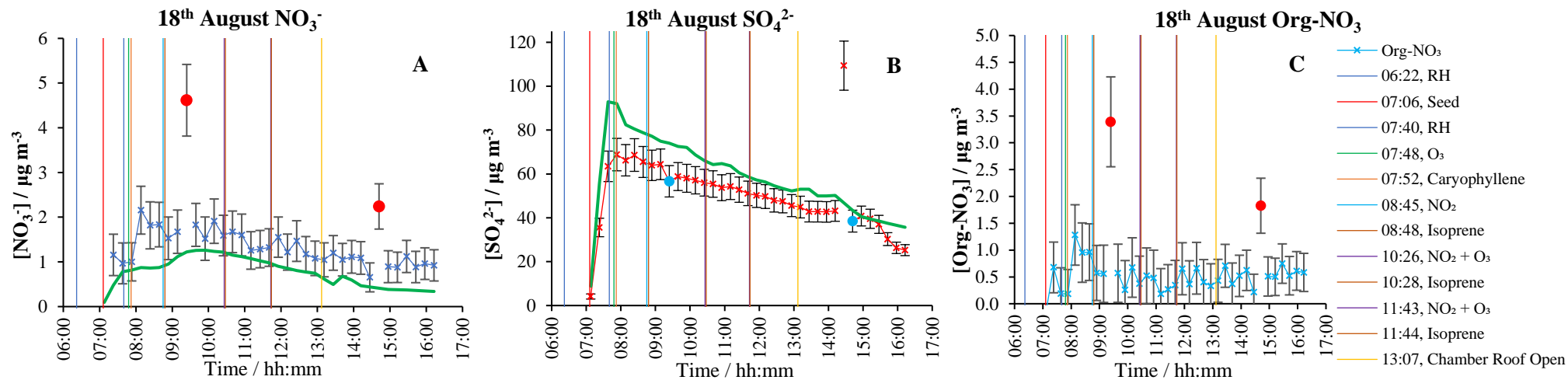


Fig. 6.26. Time series for $[NO_3^-]$ (A), $[SO_4^{2-}]$ (B) and estimated $[Org-NO_3]$ (C) measured by the PILS-IC (cross points), as well as the AMS data (green time series) on the 18th August. The injection of species into the chamber is shown as vertical lines across the x-axis which are summarised in the legend on the right. The error associated with the PILS-IC measurements are shown as error bars in the y-axis.

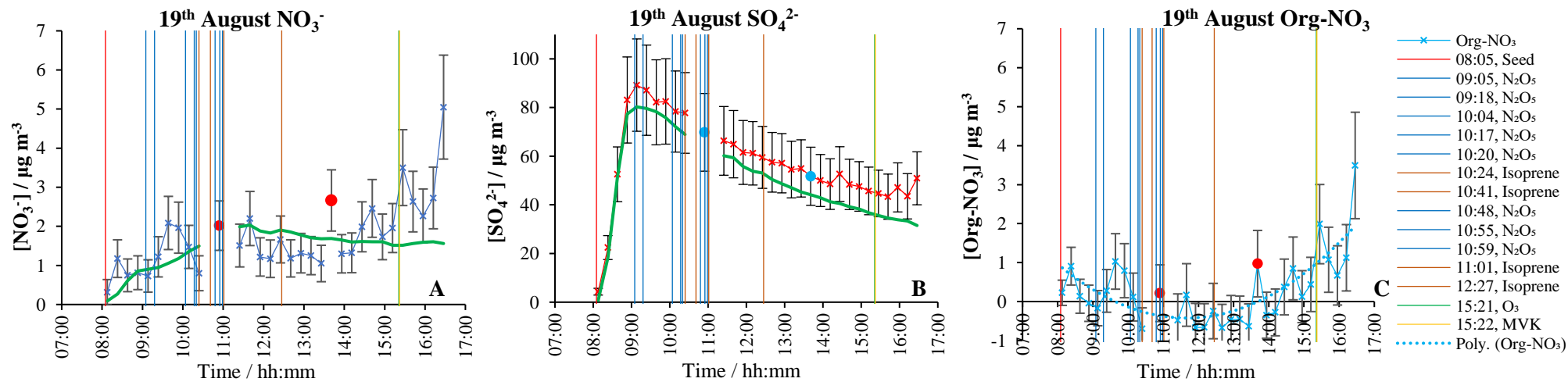


Fig. 6.27. Time series for $[NO_3^-]$ (A), $[SO_4^{2-}]$ (B) and estimated $[Org-NO_3]$ (C) measured by the PILS-IC (cross points), as well as the AMS data (green time series) on the 19th August. The injection of species into the chamber is shown as vertical lines across the x-axis which are summarised in the legend on the right. The error associated with the PILS-IC measurements are shown as error bars in the y-axis.

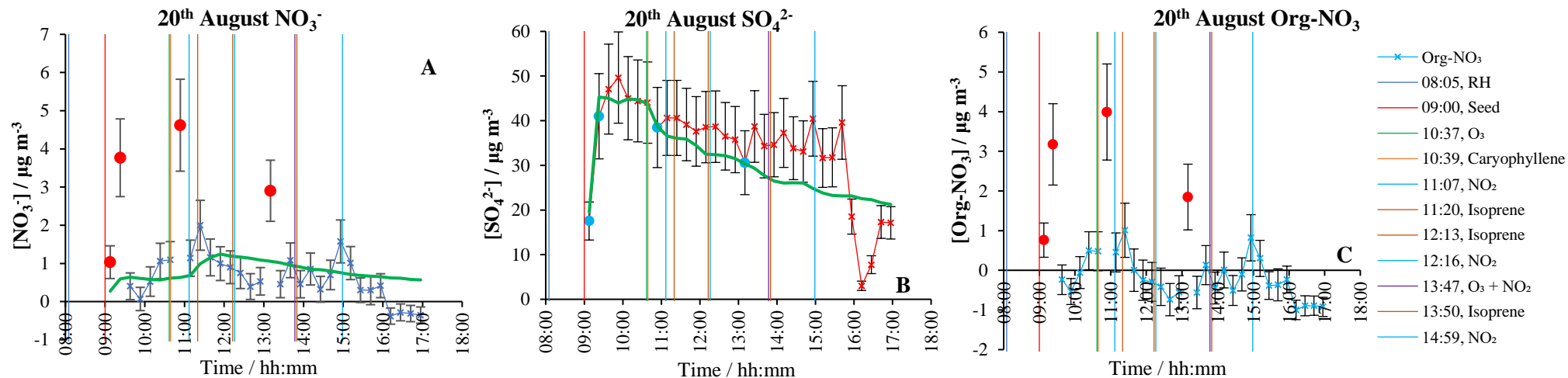


Fig. 6.28. Time series for $[\text{NO}_3^-]$ (A), $[\text{SO}_4^{2-}]$ (B) and estimated $[\text{Org-NO}_3]$ (C) measured by the PILS-IC (cross points), as well as the AMS data (green time series) on the 20th August. The injection of species into the chamber is shown as vertical lines across the x-axis which are summarised in the legend on the right. The error associated with the PILS-IC measurements are shown as error bars in the y-axis.

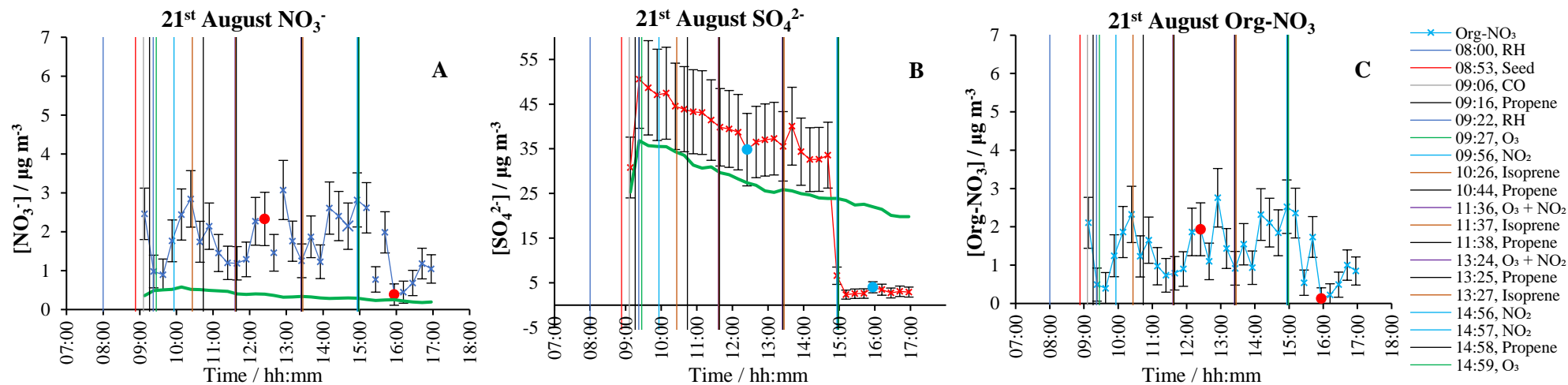


Fig. 6.29. Time series for $[\text{NO}_3^-]$ (A), $[\text{SO}_4^{2-}]$ (B) and estimated $[\text{Org-NO}_3]$ (C) measured by the PILS-IC (cross points), as well as the AMS data (green time series) on the 21st August. The injection of species into the chamber is shown as vertical lines across the x-axis which are summarised in the legend on the right. The error associated with the PILS-IC measurements are shown as error bars in the y-axis.

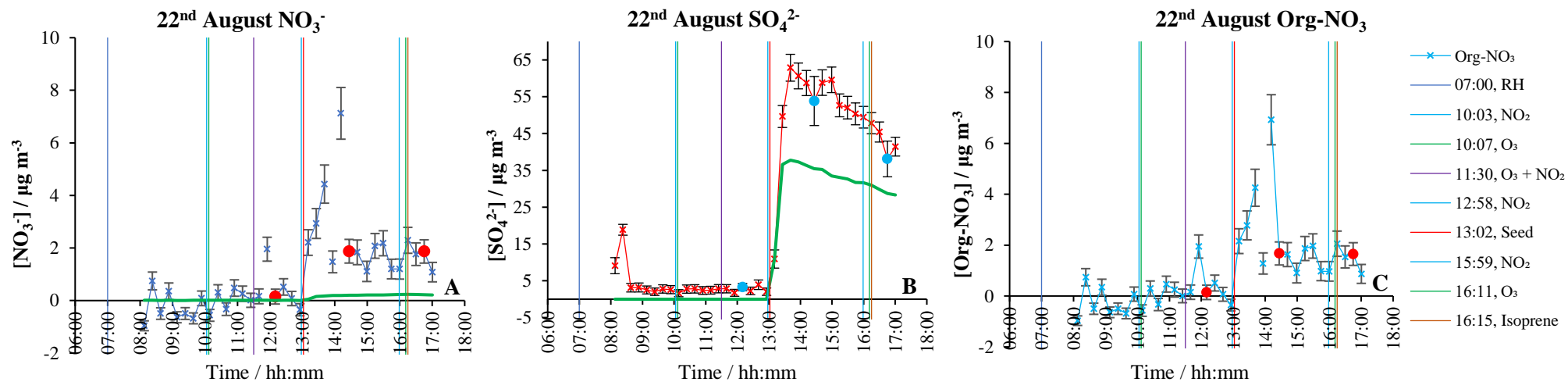


Fig. 6.30. Time series for $[NO_3^-]$ (A), $[SO_4^{2-}]$ (B) and estimated $[Org-NO_3]$ (C) measured by the PILS-IC (cross points), as well as the AMS data (green time series) on the 22nd August. The injection of species into the chamber is shown as vertical lines across the x-axis which are summarised in the legend on the right. The error associated with the PILS-IC measurements are shown as error bars in the y-axis.

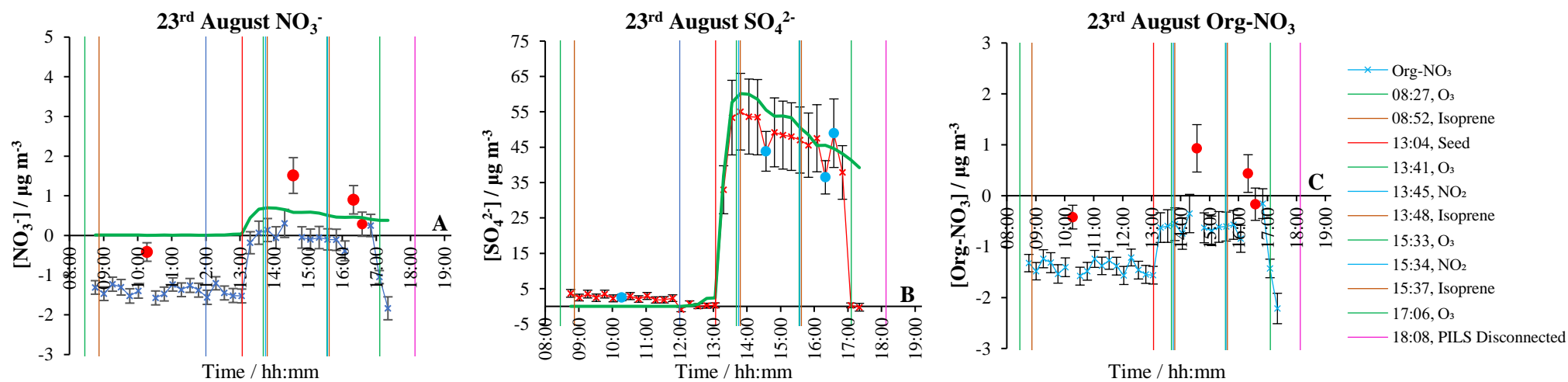


Fig. 6.31. Time series for $[NO_3^-]$ (A), $[SO_4^{2-}]$ (B) and estimated $[Org-NO_3]$ (C) measured by the PILS-IC (cross points), as well as the AMS data (green time series) on the 23rd August. The injection of species into the chamber is shown as vertical lines across the x-axis which are summarised in the legend on the right. The error associated with the PILS-IC measurements are shown as error bars in the y-axis.

which resulted in sporadic time series, as the $[\text{NO}_3^-]$ was either below or very close to the detection limit for the remaining samples. Table 6.4 shows that experimental days 20th, 22nd and 23rd Aug showed a considerable number of $[\text{NO}_3^-] < \text{LOD}$. Despite over 85 % of samples on the 18th, 19th and 21st Aug displaying $[\text{NO}_3^-] > \text{LOD}$, the inconsistent time series displayed on these days are most likely the result of atmospheric relevant concentrations of precursors added to the chamber, the use of glass and the concentration step described in section 6.2.4. The time series for $[\text{NO}_3^-]$, $[\text{SO}_4^{2-}]$ and $[\text{Org-NO}_3]$ for the remaining sampling days are shown in Fig. 6.26 - Fig. 6.31.

In particular, there were issues which arose in the comparison between the PILS-IC and AMS $[\text{SO}_4^{2-}]$ concentration values. On some days (15th, 19th, 20th and 23rd Aug), the PILS-IC and AMS SO_4^{2-} values were in relatively good agreement with each other. On some days, the PILS-IC values were significantly higher compared to the AMS (17th, 21st, and 22nd Aug). On other days, the AMS results were significantly higher than the PILS-IC $[\text{SO}_4^{2-}]$ values (16th and 18th Aug). There was however a $\pm 20\%$ error on the AMS instrument as well as a $\pm 3.13 \mu\text{g m}^{-3}$ error on the PILS-IC SO_4^{2-} values (shown by beige lines in Fig. 6.26 - Fig. 6.31).

Potential reasons of the PILS-IC observing higher $[\text{SO}_4^{2-}]$ could be down to the presence of organic-sulfate species. Isoprene oxidation products (such as epoxides) are known to be a precursor for organo-sulfate species. In addition, the literature also describes the formation of organo-sulfate species from the interactions of BVOCs with acidified ammonium sulfate aerosols, such as the work by Duporté et al., (2020)⁵³⁶ who demonstrated the formation of organo-sulfates from the interaction of ammonium sulfate particles with α -pinene oxidation products. Furthermore, SO_4^{2-} is known to be able to displace the NO_3^- within Org-NO_3 species through a nucleophilic substitution pathway²⁷⁶. This would cause the production of Organic Sulfates Org-SO_4 within the aerosol which are known to break down at the vaporizer within the AMS and may explain why on selected days the PILS-IC $[\text{SO}_4^{2-}]$ are slightly higher than those of the AMS. Similar to Org-NO_3 species, Org-SO_4 are unstable⁵³⁷ and have been shown to hydrolyse in water²⁷⁶ and may be destroyed by the AMS at the vaporizer stage leading to an underestimation of these species²⁸⁷.

Another possible reason for the higher PILS-IC values may be if the denuders had not worked properly, although all days would be expected to see higher PILS-IC $[\text{SO}_4^{2-}]$ if this was the case and it is unlikely significant gas phase H_2SO_4 would be present in the chamber.

In the cases where the PILS-IC values are lower, a possibility for this may be if there was a malfunction in the PILS instrument due to the increased heat. Lower PILS-IC $[\text{SO}_4^{2-}]$ could be down to a malfunction in the steam generator which is required to increase the size of aerosol in the PILS-Head. Another possible malfunction which would lead to lower PILS-IC $[\text{SO}_4^{2-}]$ could be an unexpected change in flow rate of the either the AMS or PILS-IC instruments. Despite the instrumental and low concentration difficulties, closer inspection of the PILS-IC Org-NO_3 data and evaluation of the overall trends may however reveal some potential information.

On the 20th Aug, it is unclear as to why the last 5 values in the PILS-IC time series show a large drop with a gradual increase from 16:11 ($3.03 \mu\text{g m}^{-3}$) until 16:42 ($17.31 \mu\text{g m}^{-3}$). The most likely explanation for this may be due to a malfunction in the pump, as the PILS sampling instrument was known to fault when overheated. On the 21st Aug (Fig. 6.29), a large drop in $[\text{SO}_4^{2-}]$ is observed from 14:40 until 15:11 at which the $[\text{SO}_4^{2-}]$ stabilises at *ca.* $2\text{-}4 \mu\text{g m}^{-3}$. This corresponds to the evaporation of the LiF solution away from the PILS reservoir (at *ca.* 14:56). Due to the heat in the PILS sampling area next to the SAPHIR chamber, the LiF solution had started to evaporate away, therefore altering the dilution factor significantly. Up until this point, the R^2 observed between the PILS-IC and AMS methods was $R^2 = 0.90$ and therefore the trends of the two methods were in very good agreement on this day for SO_4^{2-} . However, the trends do not appear to be replicated in NO_3 on both days and so maybe a result of other unknown factors. In addition, a large drop was seen in the PILS-IC SO_4^{2-} time series on the 23rd Aug as a result of the PILS sampler being disconnected from the chamber and these data points should be ignored. (Fig. 6.31).

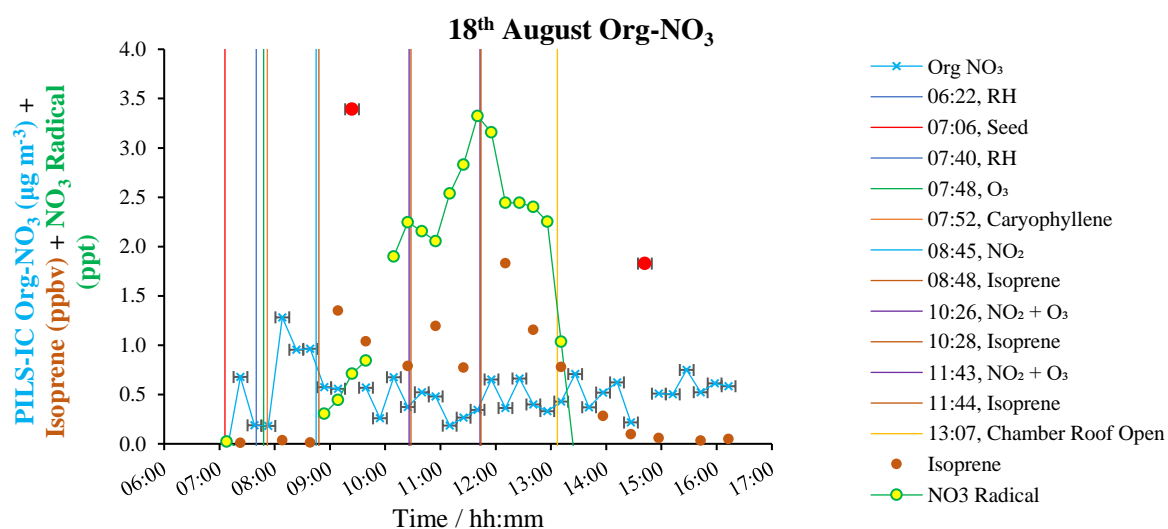


Fig. 6.32. The PILS-IC Org-NO_3 plotted against isoprene and the NO_3 radical concentrations for the 18th Aug. The injection of species into the chamber is shown as vertical lines across the x-axis which are summarised in the legend on the right. The uncertainty in the PILS-IC $[\text{Org-NO}_3]$ can be found in Fig. 6.26C.

On the 18th Aug, β -caryophyllene was added to coat the ammonium sulfate seed particles with SOA to investigate the impact of a mixed phase/coated particle. The PILS-IC $[\text{Org-NO}_3]$ increases substantially at the start of the experiment on addition of RH, O_3 and β -caryophyllene as shown in Fig. 6.32. This is most likely down to the formation of the NO_3 radical, from O_3 and residual NO_2 in the chamber, which then reacts with β -caryophyllene. β -caryophyllene has also been shown to react with NO_3 radicals in previous works, such as that by Fry et al., (2014)⁵³⁸ who measured a SOA yield of 86% ($10 \mu\text{g m}^{-3}$ mass loading) in a simulation Teflon chamber during continuous flow experiments. However, over the rest of the experiment, the Org-NO_3 estimates from the PILS are noise and close to the detection limit.

Although most of the $[\text{NO}_3^-]$ measured by the PILS on the 19th Aug was above LOD (Table 6.4), the time series for PILS-IC was too sporadic (Fig. 6.27) and therefore little information could be obtained from this experimental day.

The final experimental day to observe a significant proportion of PILS-IC $[\text{NO}_3^-] > \text{LOD}$ was the 21st Aug. A comparison of the PILS-IC $[\text{Org-NO}_3]$ to [isoprene], $[\text{NO}_3 \text{ Radical}]$ and RH% is shown in Fig. 6.33. In this experiment propene was added to change the $\text{HO}_2:\text{RO}_2$ ratio in the isoprene NO_3 experiment. A large increase occurs in the PILS-IC $[\text{Org-NO}_3]$ from 09:38 ($0.90 \mu\text{g m}^{-3}$) to 10:23 ($2.84 \mu\text{g m}^{-3}$) occurs after the injection of propene (09:16), RH (09:22), O_3 (09:27) and NO_2 (09:56). This therefore suggests that Org-NO_3 species were produced as a result of propene and NO_3 interaction. The work by Dlugokencky et al., (1989)⁴⁹⁵ compared rate constants of between H-abstraction of alkanes from the work of Atkinson et al., (1984)⁵³⁹ to that of alkenes in their work⁴⁹⁵. The reaction rate constants of alkenes by NO_3 were *ca.* three orders of magnitude faster than for alkanes in the work of Atkinson et al., (1984)⁵³⁹. Dlugokencky et al., (1989)⁴⁹⁵ therefore concluded that the $\text{NO}_3 + \text{alkene}$ reaction pathway does not occur via H-abstraction but that NO_3 adds across the π -bond within the alkene (based on the work of Japar et al., (1975)⁵⁴⁰). Furthermore, Dlugokencky et al., (1989)⁴⁹⁵ propose a mechanism for the reaction between propene and the NO_3 radical. Therefore, there is evidence in the literature to argue in favour of the alkene (propene) in this study undergoing a reaction with NO_3 . The Org-NO_3 decreases until isoprene and propene are replenished at 11:37, which leads to further increases. The signal is noisy but well above the LOD. This suggests that the PILS-IC may also be able to measure some of the organic nitrates produced from propene + NO_3 .

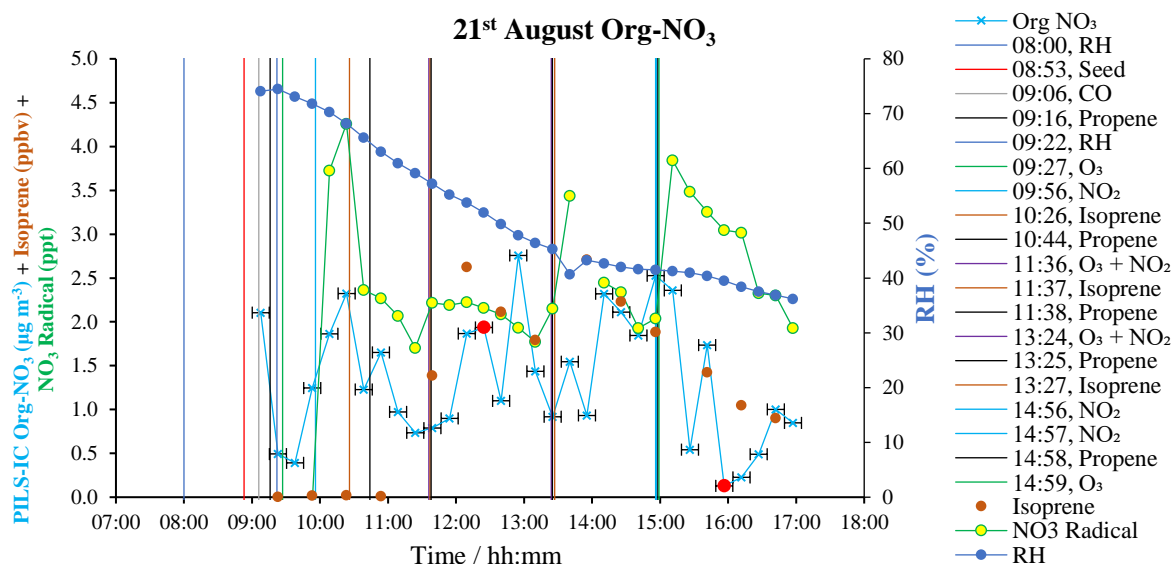


Fig. 6.33. The PILS-IC Org-NO_3 plotted against isoprene, RH and the NO_3 radical concentrations for the 21st Aug. The injection of species into the chamber is shown as vertical lines across the x-axis which are summarised in the legend on the right. The uncertainty in the PILS-IC $[\text{Org-NO}_3]$ can be found in Fig. 6.29C.

After injection of the seed aerosol (08:53), a large drop is observed from the first sample taken at 09:07 ($2.46 \mu\text{g m}^{-3}$) and 09:22 ($0.98 \mu\text{g m}^{-3}$). This is most likely either due to NO_3^- contamination

during the sample preparation process, or some residual NO_3^- species left over from the previous experiment which had not effectively been flushed out (especially if the PILS pump had faulted the previous day).

6.3.2.4.5 Ratio of Organic to Inorganic Nitrate

A comparison was completed between the experimental days in order to assess which days observed the most Org- NO_3 by mass and percentage of Inorg- NO_3^- . This was completed to assist other researchers as part of the campaign in deciphering the relative ratio of Org- NO_3 to Inorg- NO_3^- species as the AMS split into Org- NO_3 is highly uncertain. This work was also completed to investigate which conditions and species concentrations would be most favourable for Org- NO_3 atmospheric production. Fig. 6.34 shows a summary of the average concentrations of Org- NO_3 , Inorg- NO_3^- and the relative percentage fractions of these species out of $\Sigma[\text{NO}_3^-]$ for each experiment day. The heights of bars represent concentrations of $\Sigma[\text{NO}_3^-]$; the light blue bars represent the concentrations of Org- NO_3 ; and the dark blue bars present the concentrations of inorganic $[\text{NO}_3^-]$. The percentages of Org- NO_3 fractions are presented as data labels beside each bar and the dates of each experiment are shown along the x-axis. The experiment of the 23rd was omitted as concentration values were too low and gave negative averages for both the Org- NO_3 and Inorg- NO_3^- .

These results have been compared to the average concentrations of isoprene (and the maximum isoprene), and the NO_3 Radical, as well as the average RH %. The experimental day averages of these experiments are shown in Fig. 6.35, in which the average isoprene (brown), RH % (blue) and NO_3 Radical (green), as well as the maximum isoprene measured (dark red) are shown by the heights of each bar. The averages are from across all available data which matched the PILS sampling times for each experimental day.

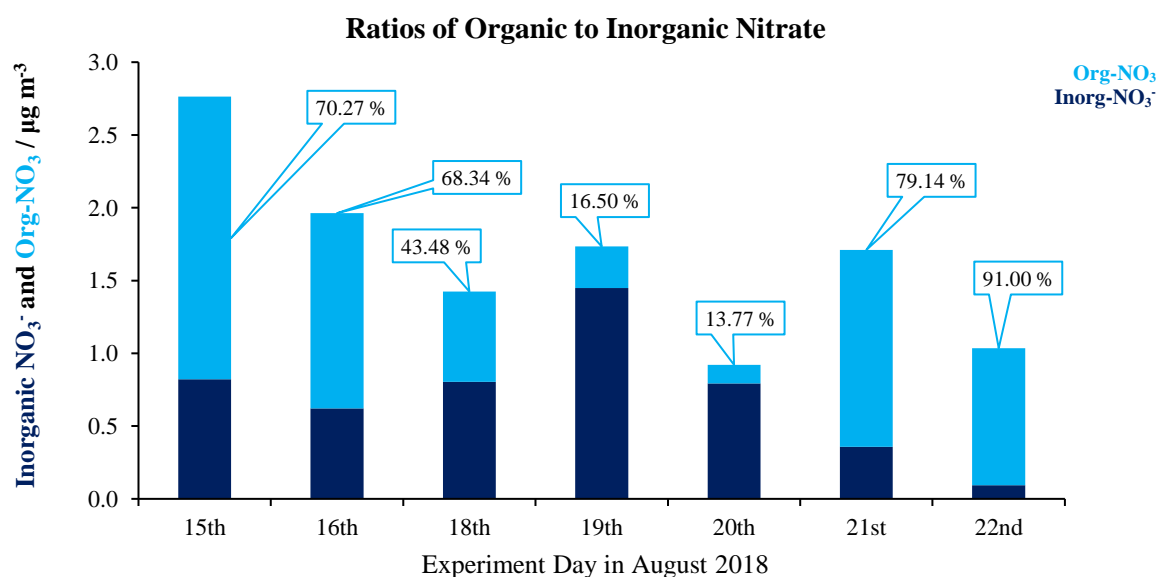


Fig. 6.34. Ratios of Organic to Inorganic Nitrate in each NO3ISOP Experiment as determined by PILS-IC for each experiment. The errors associated with these data can be found in sections 6.3.2.4.1 - 6.3.2.4.4.

Average Isoprene, RH and NO₃ Radical

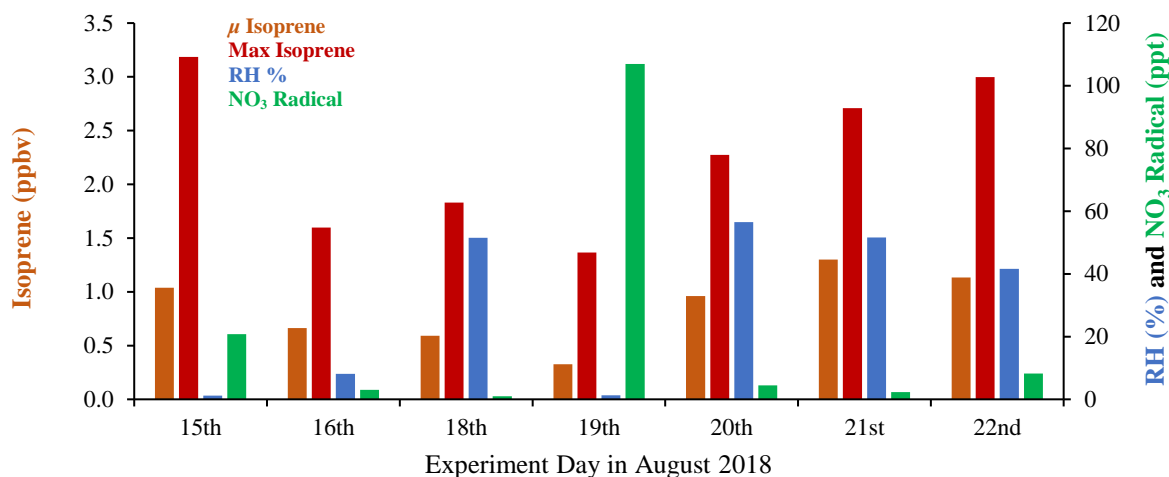


Fig. 6.35. Average Isoprene, RH and NO₃ Radical in each NO₃ISOP campaign Experiment.

The experiment on the 15th Aug had the highest concentrations of species injected into the chamber and Fig. 6.34 shows that this resulted in the highest average concentration of $\Sigma[\text{NO}_3^-]$. Although the 15th did not observe the highest average isoprene concentration, it did observe the max with a substantial NO₃ radical concentration allowing for significant Org-NO₃ production is seen. On this day the RH was however very low and therefore this may also have increased the relative concentration of Org-NO₃ as a lower RH results in less Org-NO₃ hydrolysis before the materials reach the AMS. The results on the 16th demonstrate a very similar mean proportion of Org-NO₃ to Inorg-NO₃⁻ to the 15th Aug. The lower isoprene concentration and considerably lower NO₃ radical concentrations however resulted in a lower $\Sigma[\text{NO}_3^-]$. *N.B.* The experiment on the 17th Aug was removed from Fig. 6.34 and Fig. 6.35 as this was a blank chamber experiment day.

On the 18th Aug, a surprisingly large amount of $\Sigma[\text{NO}_3^-]$ was produced despite the very low average NO₃ radical concentration. Fig. 6.26 shows that at the start of the experiment, O₃ and β -caryophyllene were added to the chamber close in proximity to each other, followed by the addition of NO₂ *ca.* an hour later. As discussed earlier, the β -caryophyllene and oxidised products could potentially react with NO₃ to produce the Org-NO₃. This reaction is extremely fast ($1.9 \times 10^{-11} \text{ molecules}^{-1} \text{ s}^{-1} \text{ cm}^3$)²⁸⁵ and would rapidly scavenge any NO₃ radical produced, which could account for the low NO₃ levels observed.

The proportions of Org-NO₃ on the 19th and 20th Aug were relatively low. On the 19th and 20th, the majority of PILS-IC [NO₃⁻] were too close to the LOD (and a substantial proportion were below LOD for the 20th Aug, Table 6.4) which resulted in very sporadic time series for the PILS-IC [Org-NO₃] for these experiments. This therefore makes it challenging to state any conclusions for these particular experiments.

Large fractions of Org-NO₃ were estimated on the 21st and 22nd Aug. This may be attributed to the substantially higher concentrations of isoprene used on these days. On the 21st, the substantially high

fraction of Org-NO₃ may be attributed to the very high isoprene concentrations in addition to propene (average of 18 ppbv) which had been added to the chamber, with sufficient mixing time for NO₂ and NO₃ to produce the NO₃ radical. On the 22nd, a slightly lower isoprene concentration is measured, although biogenic emissions from live plants were released into the chamber and therefore other BVOCs are also likely to have been present. In addition, the average [NO₃] on the 22nd was 3 times higher compared to that of the 21st and this may therefore explain the higher proportion of Org-NO₃ on the 22nd compared to the 21st.

6.3.2.5 Comparison of PILS-IC [Org-NO₃] concentrations to Speciated Measurements

To give further context to the PILS-IC [Org-NO₃] species measurements, the PILS-IC [NO₃⁻] and PILS-IC [Org-NO₃] time-series were compared to speciated gas phase measurements. These were the total Isoprene Hydroxy Nitrate (IHN), Isoprene (hydro)Peroxide Nitrate (IPN) and Isoprene Carbonyl Nitrate (ICN)⁴⁷⁸ measured by the VOCUS PTR-ToF-MS instrument used during the NO₃ISOP campaign, and are shown by a black line in Fig. 6.36, for the experiment which was run on the 15th August 2018. This day was picked for inter-comparison of the PILS-IC data with the Σ [IHN + IPN + ICN] VOCUS PTR-ToF-MS data, as high enough concentrations of NO₃⁻ were present in the PILS-IC samples to be able to conduct a comparison within a reasonable degree of certainty. The sum of Σ [IHN + IPN + ICN] gives a good indication as to the general trend of the gas phase Org-NO₃ species concentrations.

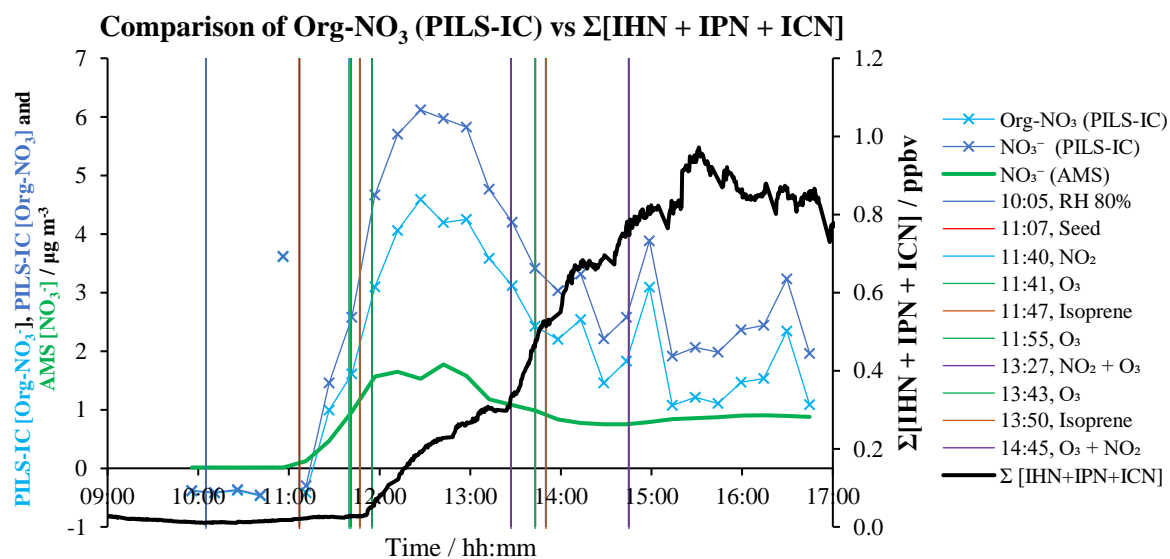


Fig. 6.36. Time series comparison of the PILS-IC [NO₃⁻] and [Org-NO₃] as well as the AMS [NO₃⁻] results from the experiment which was conducted on the 15th August (see legend). The time during the experiment is given on the x-axis with the aerosol concentrations being displayed on the primary y-axis and the gas-phase concentrations displayed on the secondary y-axis. The injection of species into the smog chamber is shown as vertical lines along the x-axis which are summarised in the legend on the right. The error associated with the PILS-IC [NO₃⁻] and [Org-NO₃] can be found in Fig. 6.20A and Fig. 6.20C, respectively.

Fig. 6.36 demonstrates that the Σ [IHN + IPN + ICN] rises after the addition of isoprene (and previous NO₂ and O₃), causing an increase in the concentrations of gas-phase Org-NO₃ species. The start of this increase occurs later compared to the PILS-IC [NO₃⁻], [Org-NO₃], as well as the AMS [NO₃⁻]

concentrations, once isoprene has been added. The increase in the PILS-IC and AMS $[\text{NO}_3^-]$ and PILS-IC $[\text{Org-NO}_3]$ measurements increase once the seed aerosol has been added, before isoprene is added to the chamber. This therefore confirms that the initial rise in the PILS-IC $[\text{NO}_3^-]$ and $[\text{Org-NO}_3]$ is due to the partitioning of inorganic NO_3^- into the aerosol phase, from residual inorganic NO_3^- leftover in the chamber from a previous experiment. Fig. 6.36 does however show a steeper incline in the PILS-IC $[\text{NO}_3^-]$ and $[\text{Org-NO}_3]$ concentrations after the addition of isoprene, which is at the same time as the increase in the gas-phase $\Sigma [\text{IHN} + \text{IPN} + \text{ICN}]$ time-series. By the fact that the PILS-IC $[\text{Org-NO}_3]$ increases before the addition of isoprene and the increase in $\Sigma [\text{IHN} + \text{IPN} + \text{ICN}]$, therefore highlights further areas of improvements (such as application of an aerosol chamber blank) which could be implemented to increase the accuracy of this technique in future.

A further discrepancy is seen between the PILS-IC $[\text{Org-NO}_3]$ trend and the VOCUS PTR-ToF $\Sigma [\text{IHN} + \text{IPN} + \text{ICN}]$ data after the PILS-IC sample taken at 12:27 (Fig. 6.36). Fig. 6.36 demonstrates that after 12:27, a decrease is seen in the PILS-IC $[\text{NO}_3^-]$ and $[\text{Org-NO}_3]$, as well as the AMS $[\text{NO}_3^-]$ time series, although a continuous increase is seen in the gas-phase $\Sigma [\text{IHN} + \text{IPN} + \text{ICN}]$ time series. This may however be explained by the loss of aerosol species throughout the experiment to the walls and internal surfaces of the reaction chamber. This is further evidenced by the fact that between the sample taken at 12:27 and the end of the experiment, the R^2 in the correlation between $[\text{NO}_3^-]$ vs $[\text{SO}_4^{2-}]$ in the PILS-IC is $R^2 = 0.65$. Therefore, the drop in Org-NO_3 in the PILS-IC as well as the AMS $[\text{NO}_3^-]$ is due to the drop in aerosol content, despite gas-phase concentrations increasing after 12:27.

6.3.2.6 Comparison of Techniques and Uncertainties in Measuring Org-NO_3

The major uncertainties in measuring Org-NO_3 by PILS-IC surrounds the sample collection stage of PILS, in which uncertainty is incorporated from the use of glass which leaches NO_3^- and SO_4^{2-} into the PILS samples causing vast fluctuations as observed in the results presented in this chapter (section 6.3.2.4). In addition, the significantly longer sampling times (15 mins) compared to high resolution AMS makes this technique lose detail in sampling. The use of an organic denuder in the system (chapter 1) could also potentially remove some gas-phase Org-NO_3 resulting in the partitioning (in equilibrium) and removal of Org-NO_3 from the aerosol phase⁵⁰⁴, an effect which would also be magnified by the longer sampling times compared to the AMS. Moreover, the adverse effect of these combined uncertainties on the quality of data and clarity in time series obtained is magnified by the presence of low $[\text{Org-NO}_3]$ and higher LODs associated with the IC method (0.048 ppm for NO_3^- and 0.12 ppm for SO_4^{2-}), compared to other instruments such as the AMS. Another critique of the PILS-IC system is that it is only able to measure inorganic nitrate and therefore the accurate measurement of Org-NO_3 is based on the reliability of the AMS to accurately measure inorganic NO_3^- (discussed in section 6.3.2.3).

There are however less potential positive and negative artefacts from inorganic species which could occur due to the presence of acid and base denuders as well as the presence of a constant flow of ambient air and LiF solution through the PILS in acquiring the sample. Furthermore, lower

temperatures associated with the collection of Org-NO₃ species compared to the very high temperatures associated with the AMS²⁸⁷ avoids errors which are associated with Org-NO₃ breakdown before reaching the detector²⁸⁷.

To compare, AMS methods for [Org-NO₃] quantification may be conducted by different methods, although there is often a compromise between time resolution and chemical specificity²⁸⁷. These include the comparison of the NO⁺ to NO₂⁺ signal (analogous to *m/z* 30 to *m/z* 46 comparison)^{272,541,527,509} as well as the use of Positive Matrix Factorization (PMF)^{509,542,543}, which are the two most common types of method used to differentiate the Org-NO₃ signal from within the total NO₃⁻.

Specifically, the major errors which surround the NO⁺/NO₂⁺ ratio include the incorporation of interferences from fragment ions of identical mass (*m/z* 30 and *m/z* 46, respectively) from ions such as CH₂O⁺ at *m/z* 30, for example⁵²⁹. HR-ToF-AMS may unambiguously separate these species, although Quadrupole AMS may not²⁷². Furthermore, it has been reported that the accurate quantification of Org-NO₃ from a nitrate signal using AMS is difficult due to measurement in the presence of a high [NO₃⁻] load, which interferes with the NO⁺ and NO₂⁺ peaks⁵³³. In addition, the use of a single marker for the identification of Org-NO₃ within a mass spectra does not exist which gives rise to ambiguity when identifying the Org-NO₃ concentration⁵³³. Rollins et al., (2010)⁵³³ do however suggest a potential method of estimating the Org-NO₃ by conducting the ion balance between NH₄⁺ and neutralising ions, although dictate that it would be difficult to arrive at an accurate measurement of Org-NO₃ and imply a significant uncertainty through this technique. Another predominant uncertainty regarding the estimation of Org-NO₃ concentration measurements using AMS is the large dependence on the conditions of reaction⁵⁰⁹ and which Org-NO₃ are produced, in conjunction with the efficacy of a particular AMS method to measure said specific species. Further uncertainties surrounding the NO⁺/NO₂⁺ method include the dependence of the conditions of reaction which may greatly affect the NO⁺/NO₂⁺ ratio, such as in very cold environments (i.e. during China Winter when the majority of NO₃⁻ is inorganic) where negative estimates of Org-NO₃ may occur^{543,544,509}. Moreover, the NO⁺/NO₂⁺ ratio has been shown to differ between AMS instruments, as well as between specific tunings of a single AMS instrument, for the same compound⁵³³.

The errors surrounding the PMF method are also closely linked to that of the NO⁺ and NO₂⁺ ratios with regard to the incorrect assignment of NO⁺ and NO₂⁺ required for PMF, as described by Xu et al., (2021)⁵⁰⁹, for example. In addition, Org-NO₃ have been reported as to be very unstable at high temperatures and have been reported to decompose in the region of *ca.* 300 – 400 °C⁵⁴⁵ and therefore would likely lead to the underestimation of Org-NO₃ species when using electrospray ionisation or flash volatilisation techniques⁵³³. This was also seen by Rollins et al., (2010)⁵³³ for n-propyl nitrate at 600 °C. Furthermore, Rollins et al., (2010)⁵³³ acknowledge that the AMS detect O and N at a lower efficiency compared to C and H which induces error. Finally, a unique signature of Org-NO₃ was

mentioned by Rollins et al., (2010)⁵³³ in their work, although this was also reported to be very small which incurs a high percentage error.

Other potential methods which could be used for Org-NO₃ identification include the use of a highly selective and sensitive technique, such as comprehensive two-dimensional gas chromatography coupled to nitrogen chemiluminescence detection (GC × GC - NCD), although significant challenges are also associated within this technique (explored in chapter 7) including the issue of changing retention times requiring the Kovats retention indices method in the correct identification of species. Furthermore, for this type of GC method, individual standards are required which would make the accurate characterisation and quantification of the Σ [Org-NO₃] species very challenging and time consuming due to the number of standards which would be required to produce an estimate of Σ [Org-NO₃]. In addition, the Org-NO₃ standards which would be required are mostly not available commercially and are mostly explosive⁵⁴⁶. Furthermore, the GC × GC – NCD system is highly challenging to use, and this method would be very work intensive. The advantages of using this technique however are the very low detection limits capable for experiments such as the NO3ISOP campaign which used atmospherically relevant concentrations.

6.3.2.7 Improved Future Methods of [Org-NO₃] Analysis

The simplicity of the PILS-IC method is one of the key advantages of this technique (on the condition that the considerable yet easy to fix errors highlighted by this thesis are addressed i.e. use of plastic instead of glass) as significant errors arise in the AMS method in [Org-NO₃] calculation surrounding the assumptions used in order to estimate the Σ [Org-NO₃] (described in section 6.3.2.3 and 6.3.2.6). The online high time resolution aspect of the AMS method however is also a key advantage. Therefore, with the intention of Σ [Org-NO₃] quantification, the PILS-IC method could be adjusted as to incorporate some of the advantages of the AMS system (such as a lower LOD and higher frequency of sampling). For the purposes of measuring the Σ [Org-NO₃], it is therefore recommended that an improved version of the simpler PILS-IC method (by incorporating the AMS advantages) is used which avoids the need of complicated AMS assumptions in Org-NO₃ quantification (section 6.3.2.3 and 6.3.2.6), if the aim of the experiment is to quantify the Σ [Org-NO₃] in aerosol.

Firstly, a much greater LOD should be acquired for the IC system connected to the PILS in order to reduce the standard deviation of the blank signal and therefore the relative amount of deviation found within a time series during an experiment. This could be reached by using a newer model of IC detector, column, as well as suppressor. Alternatively, higher concentrations could be added into the chamber, although this could alter the chemistry and is not representative if the objectives of the study are to evaluate the Σ [Org-NO₃] at atmospherically relevant concentrations (NO3ISOP campaign). Additionally, significantly smaller sampling times should be incorporated to increase the detail and number of datapoints in the [Org-NO₃] time series obtained by PILS-IC which would also need a lower LOD for IC. Moreover, a lower LOD would also reduce the need for the evaporation stage of samples which reduces the incorporation of negative artefacts from the evaporation and concentration stage.

Furthermore, altering the PILS-IC as to make the system online (like AMS) would be desirable as this would significantly reduce manual labour in processing samples and would take out the need for glass vials which inconsistently produce positive NO_3^- and SO_4^{2-} artefacts. Additionally, by conducting the PILS-IC process online, initial inorganic $[\text{NO}_3^-]$ may be quantified. At a later date when the Org- NO_3 species have been hydrolysed, offline samples which could also be gathered (in plastic vials) could be run on the IC to gather the measurement of the $\Sigma [\text{NO}_3^-]$ from both organic and inorganic species. By subtracting the initial $[\text{NO}_3^-]$ from the $\Sigma [\text{NO}_3^-]$, the $\Sigma [\text{Org-NO}_3]$ would be evaluated using the same instrument as opposed to needing AMS $[\text{NO}_3^-]$ for PILS-IC $[\text{Org-NO}_3]$ estimation.

Alternatively to PILS-IC or AMS methods, CIMS or PTR-MS methods could be used to measure the loss of gaseous isoprene and monoterpenes (as well as other BVOCs) and Cavity-Ring-Down Spectroscopy (CRDS) could be used to measure the loss of the NO_3 radical to form an estimate of the $\Sigma [\text{Org-NO}_3]$ formation, and would also incorporate the formation for tertiary Org- NO_3 species which hydrolyse quickly in the aerosol phase and may have already hydrolysed before entering the PILS-IC or AMS instruments. It would however be a requirement to know the exact concentrations of these species injected into the chamber, initially. Using the loss of the gas phase species to calculate the production of Org- NO_3 however incorporates significant uncertainty with regard to gas phase species being lost to the walls of the chamber as well as the equilibrium of Org- NO_3 species into the aerosol phase.

In summary, it is recommended that online and offline PILS-IC measurements are taken if the LOD and frequency of PILS measurements can be improved as to sample at significantly higher frequencies. Plastic vials should also be used for the offline measurements. This would allow for the difference between the inorganic $[\text{NO}_3^-]$ (to be measured for online analysis) and total $[\text{NO}_3^-]$ (to be measured for offline analysis at a later date when all of the Org- NO_3 will have hydrolysed) to be measured, giving an answer for the $\Sigma[\text{Org-NO}_3]$. Another technique which could be used is the thermal dissociation coupled to laser induced fluorescence detection, which is capable of achieving very high frequency $[\text{Org-NO}_3]$ measurements (on the scale of seconds) for which inorganic NO_3^- interference is avoided⁵⁰⁴. All of these techniques described in this section could be used in tandem for cross reference of accurate and consistent data sets.

6.3.2.8 Work Intensity to Data Benefit Analysis of PILS-IC vs AMS Methods

During the NO3ISOP campaign, the PILS-IC system was conducted offline in which samples were manually removed from the PILS system and transported to the IC within another shipping container at the Jülich Forschungszentrum site. They were subsequently pipetted into vials and ran on the IC (along with MQ blanks and calibration standard mixes which were frequently made up freshly). In comparison, the AMS was measuring species online and was therefore significantly less work intensive over the course of each sampling day during the campaign.

The PILS-IC method is a significantly simpler technique, although the data acquisition frequency is also much lower compared to the AMS. Furthermore, some of the significant errors associated with the PILS-IC technique (i.e. positive artefacts from leaching from glass vials) could be avoided in future by making simple changes (i.e. making the system online or using plastic vials). An increase in data acquisition for the PILS-IC method could also be achieved if a significantly lower LOD is firstly attained. In comparison, the AMS relies on assumptions and incorporates multiple calculation stages and numerous uncertainties (as described in section 6.3.2.3 and 6.3.2.6) in estimating the Σ [Org-NO₃] from aerosol species. The AMS does however record measurements at a much greater frequency. Finally, as the AMS set-up is substantially more complicated compared to the PILS-IC set-up. There are a greater number of potential problems which could be incurred using AMS compared to PILS-IC which would possibly make the AMS process more work intensive, during a campaign.

The data benefit to work intensity balance and therefore the choice of technique resides with the objectives of an experiment. In the case of the NO₃ISOP campaign, using simple instrumentation which was easy to fix and would give an accurate estimation of [Org-NO₃] on the condition of the improvements outlined in this thesis, would be preferential. Therefore, in measuring Σ [Org-NO₃], it is recommended that the PILS-IC is used, although the work intensity may be considerably reduced and data improved by developing the PILS-IC method as to make this an online technique. Sampling at higher frequencies with a considerably lower LOD than used during the NO₃ISOP campaign would also be essential. There would however be the necessity of a re-run of offline PILS-IC samples at a later date, in addition to the considerably improved online PILS-IC method for this to function. Although much less work intensive during a campaign, the use of AMS to calculate Org-NO₃ incorporates substantial errors (sections 6.3.2.3 and 6.3.2.6) regarding Org-NO₃ separation from inorganic NO₃⁻. It is therefore recommended that an improved PILS-IC method is used in future studies of this sort, if presented with the choice of using either a PILS-IC system or an AMS system, for the measurement of Σ [Org-NO₃].

6.4 Conclusion

Initial hydrolysis experiments of primary Org-NO₃ compounds were conducted in order to establish whether all Org-NO₃ species within the PILS samples would have resulted in complete hydrolysis (as tertiary compounds are known to undergo rapid hydrolysis). Developing on from the work by Darer et al., (2011)²⁷⁶, Hu et al., (2011)⁵⁰³ and Jacobs et al., (2014)³⁴⁸, four primary Org-NO₃ compounds were investigated for their hydrolysis rates within 25.4 ppm LiF (in 18.2 MΩ water).

Due to the LOD of the IC for NO₃⁻ being too high for the low atmospheric concentrations used in the chamber studies, the samples were left in the PILS vials for a minimum of four months before they were re-analysed. The work presented in this chapter suggests that full hydrolysis (depending on relative equilibrium constants) was likely to have occurred within the PILS sample vials before sample concentration and preparation. This therefore made it viable to assume that Σ [Org-NO₃]

corresponded to all isomers in an experiment and that a large fraction of the total possible Org-NO₃ in the aerosol had been measured (assuming a favourable equilibrium constant).

Zero order kinetics observed in this study did not agree with the literature and so the hydrolysis experiments were repeated in 18.2 MΩ water. Compounds 1-3 observed a slower rate of hydrolysis ($5.11 \times 10^{-4} \text{ \% min}^{-1}$, $5.66 \times 10^{-5} \text{ \% min}^{-1}$ and $4.38 \times 10^{-4} \text{ \% min}^{-1}$ for compounds 1, 2 and 3, respectively) in pure water (compared to the 25.4 ppm LiF solvent). This was attributed to a very likely acid catalysed S_N¹ reaction mechanism from the formation of a small quantity of HF (as F⁻ is a weak conjugate base). An acid catalysed mechanism also explained why a zero-order reaction was observed for hydrolysis of primary Org-NO₃ compounds. It was concluded that the acid was at a lower concentration in this study < [Org-NO₃], which led to the rate of hydrolysis being controlled by the acid catalyst. These were different conditions compared to the literature in which higher acid concentrations were most likely used^{276,348}. It is also speculated that the use of D₂O NMR solvents may have been contaminated with acid (as is often the case depending on the age of the solvent), which may induce a high enough acid concentration to cause first order rate kinetics in these studies. Compound 4 however observed a different behaviour in the two solvents, in which both NO₂⁻ and NO₃⁻ were produced as opposed to just NO₃⁻ (as with compounds 1-3).

This work has also demonstrated the possibility of using a PILS-IC method to produce the [Org-NO₃] concentration values for comparison to the much more sophisticated analytical instrumentation during the NO₃ISOP campaign. A method was successfully developed in quantifying the Σ[Org-NO₃] species within aerosol samples from chamber experiments investigating the reactions between NO₃ and BVOCs at atmospherically relevant concentrations.

The data presented in this chapter demonstrates that the use of PILS-IC in chamber experiments using very low atmospheric concentrations of gaseous precursors is mostly unsuitable for accurate Org-NO₃ quantification. The main issues regarding accuracy in the PILS-IC method surrounded the concentrations being very close to detection limit and therefore the need for evaporation to dryness of samples via a concentration step, as well as the need to use glass during the sample preparation on two separate occasions. The concentration step used for the PILS-IC method in this work was however successful on most days and allowed for the evidence of an increase in [Org-NO₃] from the reactions of ambient atmospheric relevance (NO₂ + O₃ + isoprene). A greater variation was however exhibited in the PILS-IC time series compared to the AMS. Furthermore, the clearest time series of NO₃⁻ from the PILS-IC occurred on the 15th Aug in which the highest concentrations of nitrate precursors were used.

When comparing the [SO₄²⁻] time series between the PILS-IC and the AMS, excellent agreement (R² > 0.8) was observed on most days in which R² > 0.50 was observed on all days apart from the 17th Aug (when no seed was added). The offset demonstrated on the 21st and 22nd Aug however is most likely down to either a calibration issue, the particle size, or the potential production of Org-SO₄ from the nucleophilic substitution of Org-NO₃ species. In the event that the PILS-IC method would be

used in future chamber studies analysing $[\text{NO}_3^-]$ and $[\text{SO}_4^{2-}]$, this work has highlighted the need for a number of crucial changes including the use of plastic in sample collected and preparation for IC analysis; using high enough concentrations within the chamber for inorganic species to be detected by the IC; and the absence of a concentration step (involving evaporation to dryness) in sample preparation; and the calculation using a quadratic fit described in chapter 2.

Comparing the estimated PILS-IC $[\text{Org-NO}_3]$ to $[\text{Inorg-NO}_3^-]$ in each experiment, it has been shown that a substantial fraction PILS-IC $\Sigma[\text{NO}_3^-]$ was consistently comprised of PILS-IC $[\text{Org-NO}_3]$ when PILS-IC $[\text{NO}_3^-]$ values were $> \text{LOD}$. This in turn indicates that Org-NO_3 production represented a large fraction of $\Sigma[\text{NO}_3^-]$ on these experimental days.

An evaluation of the major uncertainties using both the PILS-IC as well as the AMS method in quantifying $\Sigma [\text{Org-NO}_3]$ has been given in this chapter, in which it is concluded that although more work intensive than the AMS method during the campaign, an improved version of the PILS-IC incorporating both online and offline analysis of chamber samples with significantly improved LOD, a higher frequency of sampling and the use of plastic vials is recommended. This chapter discusses the uncertainties and challenges associated with $\Sigma [\text{Org-NO}_3]$ quantification using the AMS, with the major uncertainties surrounding with the ambiguity of organic and inorganic NO_3^- identification, as well as the interference of organic fragments to the NO^+ peak at m/z 30.

Finally, future work could compare to higher resolution online (CIMS) or offline Mass – Spectrometry (MS) data to identify the exact ions and structures contributing to the PILS-IC Org-NO_3 signal to try and decipher which compounds in particular are contributing most to the Org-NO_3 products from the interaction of the NO_3 radical with BVOCs.

7 Time-resolved characterization of Organic Nitrogen in PM_{2.5}: An Investigation into Beijing's Air Quality and Cancer Risk

7.1 Introduction

Organic Nitrogen (ON) compounds are a class of chemical species which are known to be present in urban PM_{2.5} and gases^{547,548,277}. They have been reported to be ubiquitously present in the atmosphere²⁷⁸ and within atmospheric particles in significant concentrations²⁷⁸. ON compounds are released both naturally, anthropogenically, as well as being formed in the atmosphere and exist over a range of chemical classifications²⁷⁷ incorporating many different N functionalities. The incorporation of a nitrogen atom into these organic species introduces dipoles into the molecules, resulting in many ON compounds being hydrophilic and in turn alters the surface tension and hygroscopicity of an aerosol particle^{278,549}. These compounds are known to be of importance environmentally²⁶² as ON acts as a source of nutrients to various ecosystems^{550,277}, although they may also induce adverse environmental affects^{278,551,552} in excess²⁶². Their toxic nature arises from the integration of a nitrogen atom into an organic molecule^{278,553,262}. An example of this in the literature reports 6-nitrochrysene having a cancer Potential Equivalency Factor (PEF) three orders of magnitude higher compared to the parent molecule, chrysene^{278,554}.

Some ON compound groups have been reported to be extremely carcinogenic and mutagenic, such as nitrosamines^{277,555,556,557,558,559,560}. This evidence of toxicity is based on animal studies^{558,561,557} in which enzyme processing of nitrosamine species forms metabolites and DNA adducts^{562,563}. Nitrosamines have specifically been reported to effect numerous vital organs such as the liver and kidneys^{262,564} and in particular Tobacco Specific Nitrosamines (TSNA) species have been reported to induce cancers to the pancreas, lungs, mouth and oesophagus, for example²⁷⁷. Due to the extreme toxicity of these species, it has been recommended by the Norwegian Institute of Public Health (NIPH) that human exposure to atmospheric nitrosamines should not be in excess of 0.3 ng m⁻³ (2011), on a daily basis^{565,277,557}.

Nitrosamines are a compound class which incorporate an amine group with a -N=O directly attached^{557,547} and some examples are shown in Fig. 7.2. Nitrosamines may either be tobacco specific (TSNAs) or non-specific (non-TSNAs)²⁷⁷. Tobacco specific nitrosamines (TSNAs) are known to originate solely from tobacco sources^{277,566,567} and have been reported to be present in burnt and unburnt tobacco products⁵⁶⁸, as well as tobacco smoke²⁷⁷. TSNAs are derived from nicotine which may react with oxidants such as HONO and O₃ to form TSNAs^{277,569,570}. Non-specific nitrosamines are known to be produced via the oxidation or nitrosation of secondary amines^{277,558,556,571,559,572}. The production of nitrosamines may also be derived from tertiary amines^{557,572} (although primary amines lack ability to produce nitrosamines⁵⁷¹). Nitrosating agents include oxides of nitrogen^{558,547}, nitrites and nitrates⁵⁵⁶. Precursor amines may be released from activities such as coal burning, for example,

which presents an environment of secondary amines, NO_x ⁵⁷³ and heat to form nitrosamines^{558,574}. Combustion sources are generally a dominant emitter of NO_x which increases the level of nitrosating agents in the atmosphere⁵⁷². Hong et al., (2017)⁵⁵⁶ suggested in their study that the detected nitrosamines had formed in the gaseous phase and carcinogens had then condensed into the aerosol phase.

A schematic is presented in Fig. 7.1 taken from the work of Choi et al., (2020)⁵⁴⁷. It shows an example of amine oxidation (Diethylamine) by OH forming an amine radical. The amine radical then reacts with NO to form the nitrosamine, N-Nitrosodimethylamine (NDMA). Nitrosamines may also be formed in the particle phase via heterogenous aqueous phase oxidation of amines with oxidants such as NO_2^- , HONO, N_2O_4 and N_2O_3 .

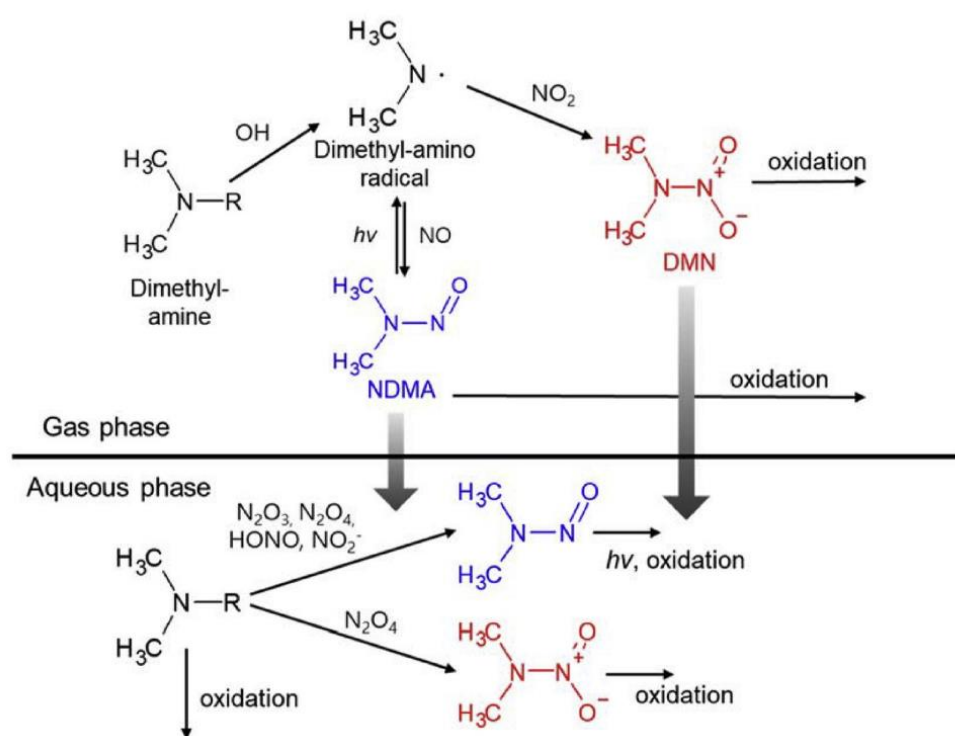
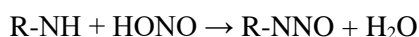


Fig. 7.1. Schematic of NDMA formation taken from Choi et al., (2020)⁵⁴⁷.

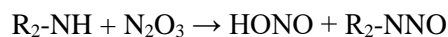
In addition Choi et al., (2018)⁵⁵⁷ describe how nitrosamines may also be produced at night, by reaction with HONO as shown in Eq. 7.1 - Eq. 7.3.



Eq. 7.1. Potential night-time nitrosamine formation pathway.



Eq. 7.2. N_2O_3 production.



Eq. 7.3. Nitrosamine formation via N₂O₃ oxidation.

Other sources of atmospheric nitrosamines and precursors include rubber and plastic combustion^{547,557}, landfill emissions^{547,557}, waste incineration emissions⁵⁵⁷, chemical manufacturer emissions⁵⁵⁷, biomass burning^{575,557}, vehicle exhaust fumes^{547,576,556,577,557,277}, cooking^{547,576,557,277}, sewage⁵⁷⁶, leather tanneries⁵⁷⁶, rubber industries^{576,556}, polymer industries⁵⁵⁶ and smoking^{547,557,277}. In more recent years, there have also been growing concerns over the release of nitrosamines and nitrosamine precursor species from carbon capture storage initiatives^{547,578,579,580}. Despite abundant literature of the presence of nitrosamines in other forms such as water supplies and treated water^{581,582,583,559,584,585}, foods and drink^{581,586,587,588}, tobacco produce and smoke^{277,569,581,566,589,566,557}, house-dust^{570,590,591,592,559,277}, cosmetics^{593,594,581}, soils⁵⁹⁵, latex items⁵⁹⁶, plastics and rubbers⁵⁵⁷ and others, relatively little work (to date)⁵⁵⁶ has focused on the identification of nitrosamine species within urban PM_{2.5} despite the extreme carcinogenic behaviour of these species.

Some of the most recent studies of nitrosamine characterisation and quantification in PM_{2.5} have taken place in London by Farren et al., (2015)²⁷⁷; in Zonguldak (Turkey) by Akyüz et al., (2013)⁵⁵⁸; and in Seoul by Hong et al., (2017)⁵⁵⁶, Choi et al., (2018)⁵⁵⁷ and Choi et al., (2020)⁵⁴⁷. Farren et al., (2015)²⁷⁷ used their calculated nitrosamine concentrations to estimate the cancer burden to the population of London induced by these highly mutagenic and carcinogenic species in the atmosphere. Although ON has been previously studied in Beijing⁵⁹⁷, there is no mention in the literature (to date and to best knowledge) of nitrosamines having been reported in Beijing. In addition to nitrosamines, other ON species such as nitro-PAHs are also known to be carcinogenic⁵⁹⁸. Evaluating which species are most abundant and carcinogenic is a vital field of study and will further enable specific ON groups to be targeted and prioritised for reduction in PM_{2.5} through policy initiatives. Reducing the concentration of such ON species may reduce the burden on human health from an air pollution perspective and in turn reduce the impact on state economies.

In this study, for the first time, 90 ON compounds (the maximum which were commercially available and suitable for analysis) were used to produce a ‘MegaMix’ standard and were successfully identified using an orthogonal comprehensive Two-dimensional Gas Chromatography coupled to Nitrogen Chemiluminescence Detection technique (GC × GC – NCD)^{277,262,599,590,588}. GC × GC – NCD is a highly selective and sensitive analytical technique and the two-dimensional character allows for the separation of over 700 ON species²⁷⁷. The NCD detector enables greater sensitivity and specificity compared to traditional Time of Flight - Mass Spectrometry (ToF-MS) detectors²⁶² and single GC methods^{277,262}. Out of these ON compounds, 13 nitrosamines have been characterized and quantified from 38 filter samples taken in Beijing over a 7-day period during the winter of the APHH campaign in 2016. These nitrosamines included 9 non-TSNAs (N-Nitrosodimethylamine (NDMA); N-nitrosomethylethylamine (NMEA); N-nitrosodiethylamine (NDEA); N-nitrosodi-n-propylamine (NDPA); N-nitrosopyrrolidine (Npyr); N-nitrosomorpholine (Nmor); N-

nitrosopiperidine (Npip); N-nitrosodi-n-butylamine (NDBA) and N-nitrosodiphenylamine (NDPhA) as well as 4 TSNA compounds (N'-nitrosornicotine (NNN); N'-nitrosoanatabine (NAT); N'-nitrosoanabasine (NAB); and 4-(methylnitrosoamino)-1-(3-pyridyl)-1-butanone (NNK)). The structures of these species are shown in Fig. 7.2. This study aims to produce a time series of these nitrosamines and uses the measurements to apply a cancer risk factor assessment to evaluate the burden of these species within PM_{2.5} to the urban population of Beijing. Furthermore, the time series developed for each species may be useful for future model studies.

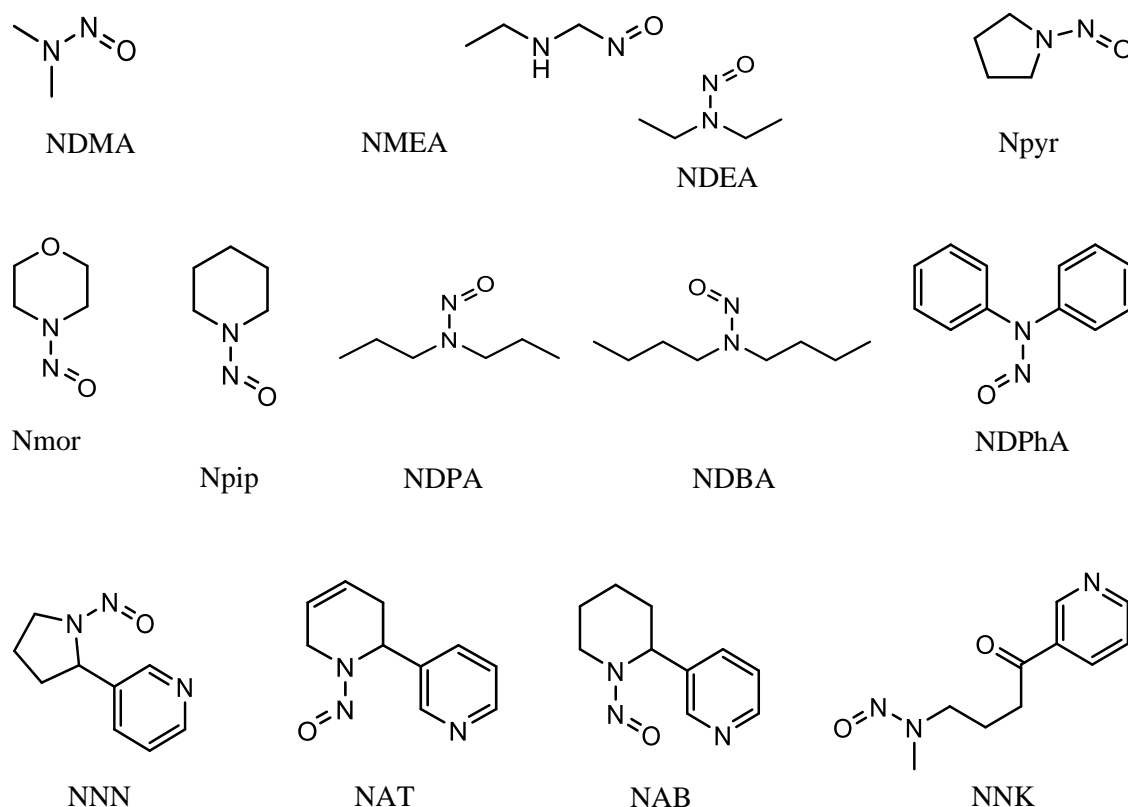


Fig. 7.2. Structures of the Nitrosamine species analysed in Beijing.

7.2 Experimental

7.2.1 Sampling Site Method and Meteorology

An in-depth description of the sampling site and method for the Beijing APHH campaign may be found in Chapter 3 of this thesis. Detail about the meteorology is also found in chapter 3. The blank filter samples used for analysis at the Beijing site had been pre-conditioned for 5 hours at 550 °C (to evacuate the filter pieces from any VOCs). This pre-conditioning method is further described in (Chapter 2).

7.2.2 Formation of GC × GC – NCD MegaMix Standard

Using previous studies which investigated ON compounds within Particulate Matter (PM) (using GC × GC – NCD and GC × GC – ToF MS)^{277,278,262} and by considering the potential secondary reaction processes that could take place between anthropogenically emitted materials (from dominant sources

Table 7.1. Table of contributing mixes to MegaMix standard. N.B. Mix 8 and Mix 10 have been removed from the table as these compounds were not suitable for GC × GC – NCD analysis.

Mix 1	Mix 2	Mix 3
Nitroethane	2-methyl-4-nitrophenol	5-Methyl-2-nitrophenol
Nitropropane	2-Nitrophenol	4-nitro-m-cresol
Nitrobutane	4-Methyl-2-nitrophenol	4-methyl-3-nitrophenol
Nitropentane	2,4-Dinitrophenol	2-fluoro-4-nitrophenol
Nitrohexane	2-Chloro-4-Nitrophenol	2-Bromo-4-nitrophenol
Nitrooctane	2,6-Dimethyl-4-nitrophenol	4-Fluoro-2-nitrophenol
Nitrodecane		3-Methyl-2-Nitrophenol
Nitrododecane		
Mix 4	Mix 5	Mix 6
2-Methyl-1-nitronaphthalene	Tetradecanamide	Trans-beta-nitrostyrene
2-Nitrobiphenyl	N-tert-butylformamide	3-Nitrostyrene
3-Nitrobiphenyl	ε-caprolactam	1,1-bis(methylthio)-2-nitroethylene
4-Nitrobiphenyl	N,N-Diethyl-3-methylbenzamide (DEET)	Nitrobenzol
4-Nitrodiphenylmethane	N-Ethylformamide	4-Nitrophenylacetate
2-Nitrofluorene	N,n-Di-n-butylformamide	1,2-Dimethyl-3-nitrobenzene
	1-Methyl-2-pyrrolidinone	4-nitro-o-xylene
		2-nitro-p-xylene
		1,3-Dimethyl-5-nitrobenzene
Mix 7	Mix 9	Mix 11
3-Butenenitrile	N-nitrosodimethylamine (NDMA)	Butyronitrile
6-Heptenenitrile	N-nitrosomethylethylamine (NMEA)	Valeronitrile
1-Cyclohexenylacetoneitrile	N-nitrosodiethylamine (NDEA)	Hexanenitrile
5-Hexenenitrile	1-nitrosopyrrolidine (Npyr)	Heptylcyanide
2-Methyl-3-butenenitrile	Nitrosomorpholine (Nmor)	Octylcyanide
1-Cyclopenteneacetoneitrile	N-nitrosodi-n-propylamine (NDPA)	Decanenitrile
4-Cyano-1-cyclohexene	1-nitrosopiperidine (Npip)	Dodecanenitrile
	N-nitrosodibutylamine (NDBA)	Pentadecanenitrile
	N-nitrosodiphenylamine (NDPhA)	Sebaconitrile
		Pyrrole-2-carbonitrile
Mix 12	Mix 13	Mix 14
Nitromethane	2-Nitrobutane	Caffeine
N-butylacetamide	2,3-Lutidine	Cotinine
1-cyclohexene-1-carbonitrile	4-Methoxy-2-nitrophenol	1-Nitronaphthalene
Undecanenitrile	2-Methyl-3-nitrophenol	3-Nitrodibenzofuran
3-Nitrophenol	1,4-Dinitrosopip	6-Nitrochrysene
3-Chloro-2-nitrobenzylalcohol	4-Nitrophenol	4-Nitroguaiacol
2-Methyl-5-nitrophenol	Tridecanenitrile	2-Nitro-1-naphthol
Tetradecanenitrile	N-Nitrososornicotine ketone (NNK)	N-Nitrososornicotine (NNN)
5-Nitroacenaphthene	1-Nitropyrene	N-nitrosoanabasine (NAB)
9-Nitroanthracene		N'-nitrosoanatabine (NAT)
		Nicotine
		4-Nitrocatechol
		Heptanenitrile

in Beijing), a list of over 100 potential PM ON compounds was initially prepared. ON compounds were chosen based on their suitability for GC × GC – NCD analysis and likelihood of detection in

the filter samples. These compounds were initially prepared individually at a concentration of 1 ppm to be run on a GC × GC – NCD method to check for suitability (signal strength, retention time, peak shape etc.). All standards were created using ethyl acetate (EtOAc, >= 99.8%, Fisher) as the solvent of choice.

To produce the MegaMix standard, 12 separate mixes of ON species were first produced to 50 ppm (of each species). The constituents of each mix were as shown in Table 7.1. *N. B.*, 4-(methylnitrosoamino)-1-(3-pyridyl)-1-butanol (NNAL) was unavailable. These 12 mixes were mixed together to produce a ‘MegaMix’ at concentrations of 4.5 ppm, 2.5 ppm, 1 ppm, 0.5 ppm, 0.25 ppm, 0.1 ppm and 0.05 ppm. 1 ml of each concentration was pipetted into a 2 ml GC vial (Supelco) to produce the set of calibrations. Mix 1 was required as an internal standard in conjunction with the Kovats retention indices method (section 7.3.2). 50 µl of Mix 1 at 10 ppm was added to each sample and calibration vial ran on the GC × GC – NCD. This therefore produced calibration standards with a volume of 1050 µl and ON compound concentrations of 4.29 ppm, 2.38 ppm, 0.95 ppm, 0.48 ppm, 0.24 ppm, 0.10 ppm, and 0.05 ppm. Mix 8 consisted of amines (Triethylamine, N,N-Dimethylethylamine, N,N-Dimethylbenzylamine, N,N-Dimethylethanolamine and 3-Dimethylamino-1-propanol) which were unsuitable for this GC × GC – NCD method due to tailing in the chromatographic peaks from their very sticky nature. Mix 8 was therefore removed from further analysis. Mix 10 consisted of only very few species (NNN, NAB and NAT) which were later incorporated into the other mixes. The nitrosamine mix (EPA 8270/Appendix IX Nitrosamines Mix, Sigma) included NDMA, NMEA, NDEA, Npyr, Nmor, NDPA, Npip, NDBA and NDPhA and was run as the mix at 1 ppm (diluted from 2000 ppm) for suitability assessment.

7.2.3 Filter Extraction and sample preparation

7.2.3.1 Preparation of ASE Extraction Cells and Vials

Prior to use Accelerated Solvent Extraction (ASE) cells were completely taken apart and each section was washed in ethyl acetate (the caps and the cell body were washed with acetone). These were then left to dry. The cells were then put back together and were run on the ASE (see section 7.2.3.2). Once the extraction cells had cooled, the bottom cap was then removed and taken apart. Two glass microfibre filter papers (Fisher Scientific, U.K) were then inserted at the bottom of the extraction cell, placed on the frit. The cap insert (with seal) and snap ring were then positioned over the frit, holding the filter pieces in place. The bottom cap was then re-inserted back onto the cell body. The ASE vials were prepared by rinsing each vial with 18.2 MΩ water (three times), followed by rinsing with EtOAc (three times). This was to rid the vials of inorganic and organic species, respectively.

7.2.3.2 Sample Preparation with Accelerated Solvent Extraction

Filter samples were prepared by cutting out a 46.9 cm² aliquot of the HiVol filter piece using a conventional kitchen duty square cookie cutter. The filter sample squares were cut into small pieces. In addition, 100 µl of 10 ppm caffeine (within EtOAc) was pipetted onto a separate circular piece of 5.7 cm² blank pre-conditioned filter. The EtOAc was left to evaporate away (while holding the filter

in the tweezers) and the spiked filter piece was chopped into four. All filter pieces were inserted into the pre-prepared 5 ml stainless steel extraction cells (section 7.2.3.1). Accelerated Solvent Extraction, (ASE 350, Dionex, Sunnyvale, CA) was the extraction method of choice. The extraction cells were run on the ASE using an extraction solvent of ethyl acetate (GC grade, 99.9% purity) under a pressure of 1500 psi and temperature of 80 °C over three consecutive cycles (5 min cycles). A 60 s purge time with a 50 % flush volume was also used. The ASE collection vials were pre-frozen before acquisition of filter extract and on completion of the ASE runs, the samples were placed into the freezer. The extracts were then evaporated under a very low flow of nitrogen (within the collection bottles) in an ice bath for *ca.* 4 hours until the extracts reached *ca.* 1 ml. The extracts were then transferred with glass pipettes into pre-weighed GC vials. 50 μ l of 10 ppm nitroalkane mix (Mix 1) was added to each vial. The final mass of the GC vial plus extract was then taken and the samples were run on GC \times GC – NCD. A calibration was run for every ten samples.

7.2.4 GC \times GC – NCD Method

A GC \times GC system (7890, Agilent Technologies) coupled to NCD (255, Agilent Technologies) via a Dual Plasma Controller (DPC, Agilent technologies) method was used in conjunction with the LECO ChromaToF[®] software. The inlet was set to splitless mode and had a temperature of 250 °C (septum purge flow at 3 ml min⁻¹). The carrier gas used during the analyses was H₂ (produced from a hydrogen generator, PEAK Scientific) which was set to a flow of 1.4 ml min⁻¹ for the entire GC \times GC run. The primary column was a DB-5 phase column 30 m in length with an internal diameter of 320 μ m and film thickness of 0.25 μ m. The oven equilibration time was 60 s and the initial oven temperature was 40 °C. At the start of the method, this temperature was held for 2 minutes, followed by a ramp of 3.50 °C min⁻¹ until 300 °C. The temperature was then held at 300 °C for 5 minutes. The secondary column was a BPX50 phase column with a length of 2.6 m, internal diameter of 100 μ m and film thickness of 0.10 μ m. The inlet purge time, purge flow and total flow for the 2D column was 120 s, 20 ml min⁻¹ and 21.4 ml min⁻¹, respectively. The secondary oven temperature offset was +12 °C. A modulator was also enabled in which the temperature started at 55 °C for 2 minutes, followed by a temperature ramp of 3.50 °C min⁻¹ until 315 °C. The modulator temperature was then held at 315 °C for 5 minutes. The modulation period was 7.50 s with a hot pulse time of 0.6 s. The cool time between stages was 3.15 s. The total time taken for the GC \times GC method was 4877.14 s, for which the data collection rate was 200 Hz with an acquisition delay of 60 s. The DPC burner was set to a temperature of 900 °C and pressure of 129 Torr. The oxidiser and H₂ flow rates were 9.1 and 5.5 sccm, respectively. The oxidiser pressure at the front of the detector was set to 4 psig.

7.2.5 Data Quality Assurance

The methods presented in this study have been based on and developed further from the previous works by Farren et al., (2015)²⁷⁷ and Ozel et al., (2011)²⁶².

7.2.5.1 Method Blank Correction

Blank correction was completed by conducting the same method as described in section 7.2.3.2, with the identical area (46.90 cm²) of pre-conditioned filter (550 °C for 5 hours) used instead. This was repeated 6 times and no extra peaks were observed in the chromatograms.

7.2.5.2 Method Recovery Correction

A 46.9 cm² piece of pre-conditioned filter paper was cut out using a square cookie cutter. This was chopped into much smaller pieces which were inserted in a pre-prepared (section 7.2.3.1) ASE extraction cell. A 5.7 cm² piece of pre-conditioned filter paper was also charged with 100 µl of 10 ppm caffeine (in EtOAc). The EtOAc was left to evaporate (while waving the filter piece around in a fume hood with tweezers). The filter piece was then chopped into four and was also inserted into the ASE extraction cell. 90 µl of mixes 2, 3, 4, 5, 6, 7, 9, 11, 12, 13 and 14 (each at 50 ppm) were pipetted into the ASE extraction cell. The cell was then closed and loaded onto the ASE to be run using the method described in section 7.2.3.2. This was repeated six times for which the average values were taken. Recoveries were calculated as NDMA (81.8 %, %RSD 11.8 %), NMEA (90.8 %, %RSD 10.7 %), N-tert-butylformamide + NDEA (99.3 %, %RSD 13.4%), Npyr (114.7 %, %RSD 23.9%), Nmor (82.8 %, %RSD 20.9 %), NDPA (99.4 %, %RSD 10.2 %), Npip (98.6 %, %RSD 10.6 %), NDBA (98.8 %, %RSD 9.4 %), NDPhA (81.9 %, %RSD 13.6 %), NNN (89.2 %, 5.8 %), NAT (91.5 %, %RSD 5.6 %) and NAB (93.8 %, %RSD 5.9 %). The recovery value for NNK was inconclusive and a value of 100 % was applied to these values.

7.2.5.3 Limit of Detection

The GC × GC – NCD method Limit of Detection (LOD) was initially calculated in the same manner as for the Ion Chromatography (IC) method for the Beijing and Delhi APHH campaigns (Chapter 2). Ten repeat runs of the 4.5 ppm MegaMix standard were conducted consecutively. The standard deviation of the instrument response for each compound was recorded over the ten repeats. This value was then multiplied by three to observe the LOD and multiplied by ten to acquire the Limit of Quantification (LOQ).

This method however gave unrealistic and non-representative values for the LOD. An alternative method was however discovered through the LECO software which uses an algorithm designed by LECO to measure the signal to noise (S/N) ratio for each individual peak. If the signal to noise ratio was above 3, this constituted to a peak being above the LOD. All nitrosamine peaks from the samples were checked that the S/N ratios were above 3 and it was found that all peaks present were S/N > 3. In the event that a peak was not present on the LECO software, a value of 0 was taken.

7.3 Results

7.3.1 ON MegaMix

The MegaMix solution produced was run on GC × GC – NCD, separating compounds by boiling point along the *x*-axis in the first dimension (Rt₁) and by polarity (and boiling point) along the *y*-axis (Rt₂). Fig. 7.3 displays a scatter plot of the retention times of the ON compounds analysed within the

MegaMix of ON Compounds as presented on a 2D GC × GC – NCD plot

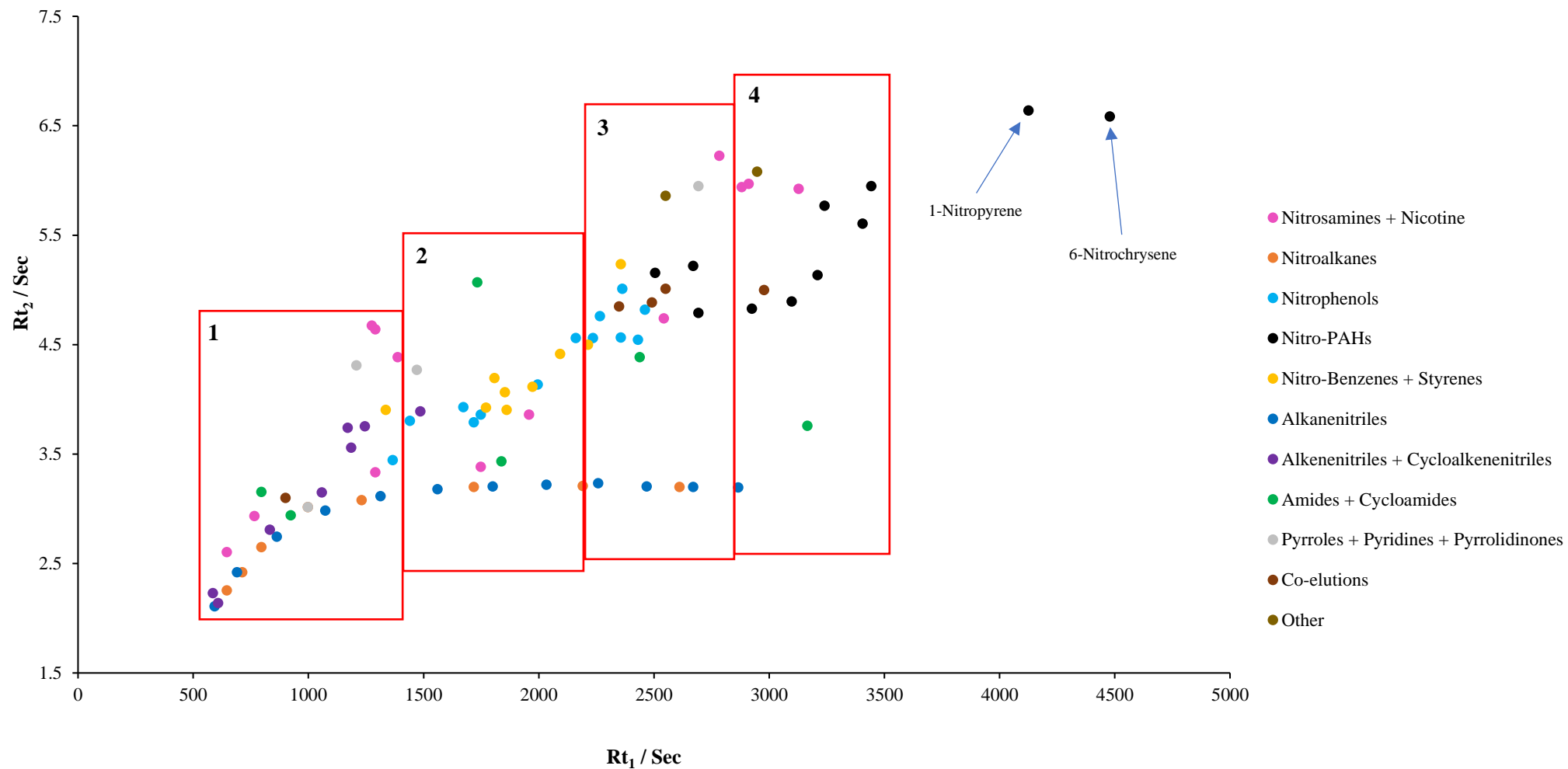


Fig. 7.3. GC × GC – NCD plot of the ON MegaMix Standard showing the distribution of different ON compounds classes. The 1D retention time (Rt_1) is given on the x-axis and the 2D retention time (Rt_2) is given on the y-axis. A key showing the ON chemical classifications for each species colour is shown in the legend on the right. The red boxes outline arbitrary slices (numbered) of the chromatogram for discussion later in this section.

MegaMix. The compounds were classed into their chemical groups, for which the nitrosamines and nicotine (pink), nitroalkanes (orange), nitrophenols (blue), nitro-PAHs (black), nitro-benzenes and styrenes (yellow), alkanenitriles (dark blue), alkenenitriles and cycloalkenenitriles (purple), amides and cycloamides (green), pyrroles and pyridines and pyrrolidinones (grey), coelutions (brown) and other (gold) are presented.

Although the method reported produced good separation for most of the ON compounds, there were some coeluting peaks. These were observed for N-tert-butylformamide + NDEA (R_{t1} 900, R_{t2} 3.1); 2-Bromo-4-nitrophenol + 4-Nitrophenol (R_{t1} 2347.5, R_{t2} 4.85); 2-Methyl-4-nitrophenol + Sebaconitrile (R_{t1} 2490, R_{t2} 4.885); 2-Methyl-1-nitronaphthalene + 2,6-Dimethyl-4-nitrophenol (R_{t1} 2550, R_{t2} 5.01); and 2-Fluoro-4-nitrophenol + 4-Nitrobiphenyl (R_{t1} 2977.5, R_{t2} 5). The predominant problem that arises with coelution is the loss of accuracy within the data as it is unclear what proportion of peak area has been produced in the chromatogram from each relative species. This issue was also encountered and described by Farren et al., (2015)²⁷⁷ regarding the coelution of NMEA with other ON species. Furthermore, due to the proximity of some peaks which the ChromaToF software had separated sufficiently, the issue of changing R_{t1} retention times (section 7.3.2) and some species (such as Npyr and Nmor) would sometimes co-elute.

As shown in Fig. 7.3, the nitroalkanes (orange) and alkanenitriles (purple) are observed in a linear trend at R_{t2} values of *ca.* 3.2 ($R_{t1} > 1500$) towards the bottom of the chromatograph. As the carbon chain on each chemical class increases, the R_{t1} increases although the R_{t2} stays constant. This indicates that the polarity of these species remains relatively constant with increasing chain length, and the polarities of linear nitroalkanes and alkanenitriles were similar.

The straight chain alkenenitriles investigated here are 3-butenitrile (R_{t1} 585, R_{t2} 2.23), 5-hexenenitrile (R_{t1} 832.5, R_{t2} 2.81) and 6-heptenenitrile (R_{t1} 1057.5, R_{t2} 3.15). This compares to the nitroalkanes of nitrobutane (R_{t1} 795, R_{t2} 2.65) and nitrohexane (R_{t1} 1230, R_{t2} 3.08). Nitroheptane was not commercially available. Therefore, for the same carbon chain length comparing 3-butenitrile (C4, R_{t1} 585, R_{t2} 2.23) with nitrobutane (C4, R_{t1} 795, R_{t2} 2.65) and 5-hexenenitrile (C6, R_{t1} 832.5, R_{t2} 2.81) with nitrohexane (C6, R_{t1} 1230, R_{t2} 3.08), the alkenenitriles have substantially lower R_{t1} values. This is likely due to the replacement of the NO_2 group with a single N atom (attached via a triple bond with carbon in the nitrile group). This change produces a more volatile molecule which explains the lower R_{t1} values in the first dimension for the alkenenitriles.

Furthermore, 3-butenitrile and 5-hexenenitrile have a shorter R_{t2} time compared to nitrobutane and nitrohexane, respectively. The NO_2 group comprises of three very electronegative atoms which produces a very strong dipole within the C-N bond which is stronger than a dipole which could be produced within a CN triple bond (with only one electronegative constituent). Finally, the cycloalkenenitriles have both larger R_{t1} (ranging from 1170 - 1485) and R_{t2} (3.74 – 3.89) values which is due to their generally larger Relative Molecular Mass (RMM). The RMMs for the alkenenitriles are 67.09 g mol^{-1} (3-Butenenitrile), 81.12 g mol^{-1} (2-Methyl-3-butenenitrile), 95.14 g mol^{-1} (5-

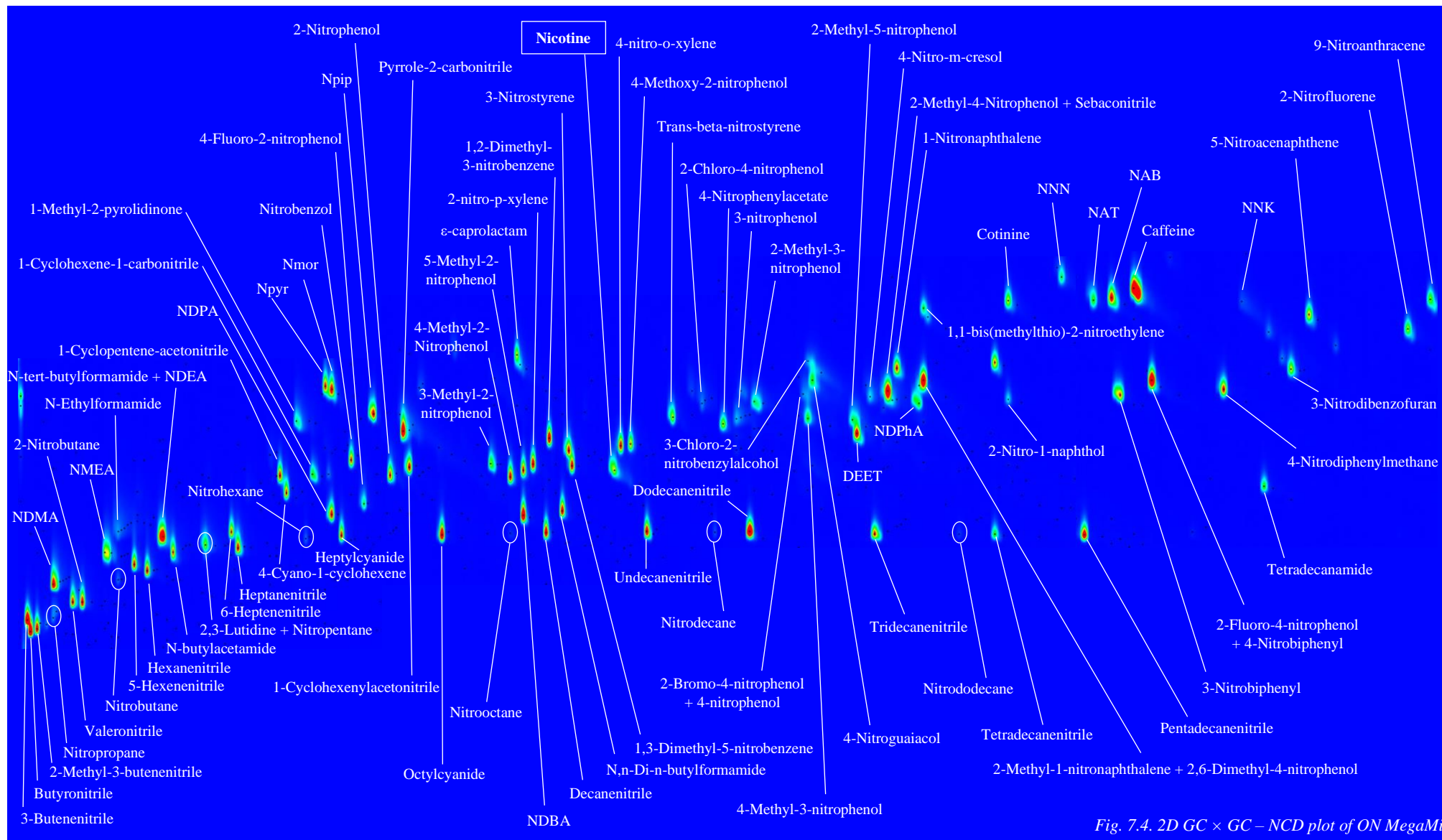


Fig. 7.4. 2D GC x GC - NCD plot of ON MegaMix.

Hexenenitrile), and $109.17 \text{ g mol}^{-1}$ (6-Heptenenitrile). For the cycloalkenenitriles these are $107.15 \text{ g mol}^{-1}$ (for 4-cyano-1-cyclohexene, 1-cyclopenteneacetonitrile and 1-cyclohexene-1-carbonitrile) and $121.18 \text{ g mol}^{-1}$ (1-cyclohexenyl-acetonitrile).

Three of the most important and atmospherically relevant ON chemical groups as indicated by their measurements within Secondary Organic Aerosol (SOA) are nitrosamines, nitrophenols and nitro-PAHs. The nitrosamines (pink) measured in this study have a variety of molecular masses and polarities and thus they do not form a band (as seen for the nitroalkanes) but are scattered throughout the chromatogram (Fig. 7.3). The nitrosamines measured generally fall into three structural categories which are aromatic (NDPhA, NNN, NAT, NAB and NNK), branched (NDMA, NMEA, NDEA, NDPA, NDBA) and cyclic compounds (Npyr, Nmor and Npip). The tobacco-specific nitrosamines (TSNAs) fall into the aromatic category and the non-TSNA species analysed in this study and have either aromatic or branched structures. The TSNAs are produced from the nitration of nicotine^{277,569,570} and therefore incorporate the nicotine back-bone which produces compounds which are inherently larger than the non-TSNAs. As expected, the larger the mass of the compound, the later the compound will elute from the column due to its smaller vapour pressure. This is observed for NNN (R_{t1} 2782.5, R_{t2} 6.225, RMM $177.21 \text{ g mol}^{-1}$); NAT (R_{t1} 2880, R_{t2} 5.94, RMM $189.09 \text{ g mol}^{-1}$); NAB (R_{t1} 2910, R_{t2} 5.97, RMM $191.23 \text{ g mol}^{-1}$); and NNK (R_{t1} 3127.5, R_{t2} 5.925 RMM $207.23 \text{ g mol}^{-1}$). For the non-TSNAs, the cyclic non-aromatic nitrosamines incorporated Npyr (R_{t1} 1275, R_{t2} 4.675, RMM $100.12 \text{ g mol}^{-1}$); Nmor (R_{t1} 1290, R_{t2} 4.64, RMM $116.12 \text{ g mol}^{-1}$) and Npip (R_{t1} 1387.5, R_{t2} 4.385, RMM $114.15 \text{ g mol}^{-1}$).

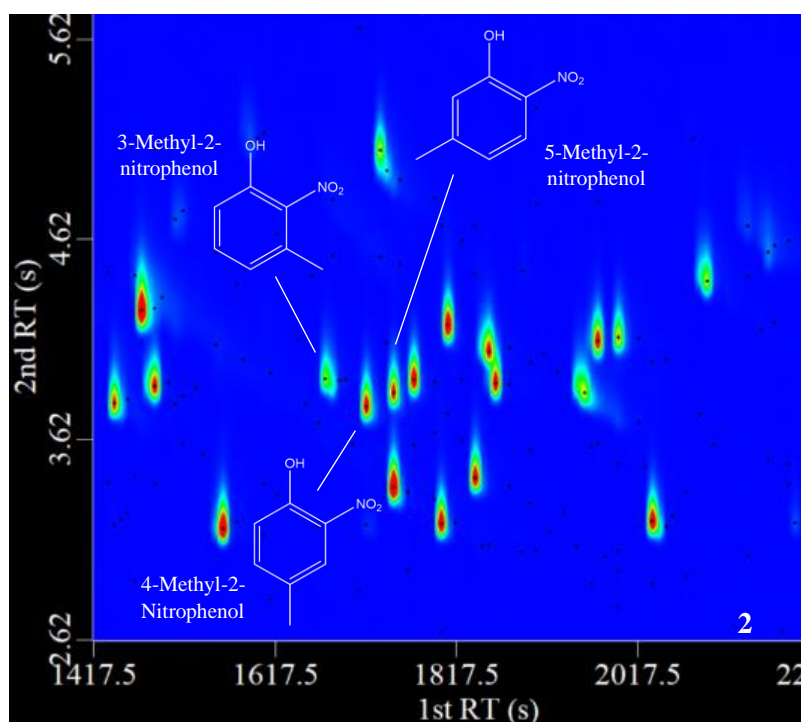


Fig. 7.5. Zoom in of section 2 (Fig. 7.3) in the MegaMix chromatogram ().

NDPhA (R_{t1} 2542.5, R_{t2} 4.74, RMM 198.22 gmol^{-1}) is the largest non-TSNA compound incorporating two phenyl rings. The branched non-TSNA compounds were NDMA (R_{t1} 645, R_{t2} 2.605, RMM 74.083 gmol^{-1}), NMEA (R_{t1} 765, R_{t2} 2.935, RMM 88.11 gmol^{-1}), NDPA (R_{t1} 1290, R_{t2} 3.335, RMM 130.19 gmol^{-1}), NDBA (R_{t1} 1747.5, R_{t2} 3.385, RMM 158.24 gmol^{-1}). These were molecules of lighter masses compared to the TSNA species and therefore eluted earlier. Finally, nicotine (an amine) eluted at (R_{t1} 1957.5, R_{t2} 3.86, RMM 162.23 gmol^{-1}) and from visualisation of the nicotine peak in Fig. 7.4, the very high affinity between nicotine and the R_{t1} column caused tailing of the nicotine peak (nicotine is bolded in Fig. 7.4). Nicotine observed less peak tailing compared to the other smaller amines. A comprehensive plot labelling all compounds (excluding 1-nitropyrene and 6-nitrochrysene) are shown on the GC \times GC – NCD chromatogram shown in Fig. 7.4.

The nitrophenols (bright blue points, Fig. 7.3) are generally found in the centre of the chromatogram. It is also worthy to note the relationship between individual isomers and their positioning on the GC \times GC plot. For 3-methyl-2-nitrophenol (R_{t1} 1673, R_{t2} 3.93, RMM 153.14 gmol^{-1}); 4-methyl-2-nitrophenol (R_{t1} 1718, R_{t2} 3.79, RMM 153.14 gmol^{-1}); and 5-methyl-2-nitrophenol (R_{t1} 1748, R_{t2} 3.86, RMM 153.14 gmol^{-1}). Here, it is seen that the R_{t1} values increase as the position of the methyl group is situated further away from the NO_2 and OH groups. This suggests that the boiling point of species increases with distance between the chemical groups. This is demonstrated in Fig. 7.5.

A likely reason for this is due to having less sterical hindrance surrounding the very electronegative NO_2 and OH groups. Therefore, the electronegative groups can get closer to each other in proximity and produce stronger intermolecular bonding, resulting in lower vapour pressures. This phenomenon was also seen in the work of Dang et al., (2019)⁶⁰⁰ who reported that the vapour pressures of methylpyridine carboxylic acids decreased when the methyl group was one carbon atom further away (from being adjacent) from the carboxylic acid group in these compounds. They attributed this to less sterical hinderance and increasing hydrogen bonding between molecules⁶⁰⁰. Furthermore, the work by Shelley et al., (2020)⁶⁰¹ specifically describe how the clustering of functional groups in 3-methyl-2-nitrophenol causes a significant increase in solid state saturation vapour pressure compared with 4-methyl-2-nitrophenol. Shelley et al., (2020)⁶⁰¹ describe how the bulky methyl group in 3-methyl-2-nitrophenol induces sterical hinderance and reduces the capability of hydrogen bond formation between molecules in 3-methyl-2-nitrophenol compared to 4-methyl-2-nitrophenol.

Furthermore, a stronger positive charge would be associated with the CH_3 group (+I inducting effect) if it is situated closer to the NO_2 and OH groups (on the benzene ring). This would produce stronger positively and negatively charged substituents on the benzene in very close proximity. Therefore, stronger intermolecular forces may be produced between molecules if the CH_3 is positioned further away from the NO_2 and OH groups. This phenomenon is also seen for the species 2-methyl-3-nitrophenol (R_{t1} 2265, R_{t2} 4.76, RMM 153.14 gmol^{-1}) and 4-methyl-3-nitrophenol (R_{t1} 2355, R_{t2} 4.57, RMM 153.14 gmol^{-1}). Another example in which sterics play a role is in the comparison

between 2-nitrophenol (R_{t1} 1440, R_{t2} 3.81, RMM 139.11 gmol^{-1}) and 3-nitrophenol (R_{t1} 2235, R_{t2} 4.56, RMM 139.11 gmol^{-1}). These species also indicate that the increased distance between the OH and NO_2 groups produces a lower vapour pressure and an increased polarity within the molecule. Finally, it could be suggested that the integration of a halocarbon into the structure of a nitrophenol reduces both the R_{t1} and R_{t2} when comparing 2-nitrophenol (R_{t1} 1440, R_{t2} 3.81, RMM 139.11 gmol^{-1}) and 4-Fluoro-2-nitrophenol (R_{t1} 1365, R_{t2} 3.45, RMM 157.10 gmol^{-1}). This is possibly due to the negative inductive effect induced by F, pulling electron density away from the OH and NO_2 groups (also inducing -I inductive effects) through the aromatic system. This therefore reduces the polarity of the entire molecule and therefore the value of R_{t2} for 4-Fluoro-2-nitrophenol (R_{t2} 3.45 s). In addition, the reduced polarity causes weaker dipole-dipole bonds to occur between the molecules, causing a higher vapour pressure and a reduced R_{t1} value for 4-Fluoro-2-nitrophenol (R_{t1} 1365 s) compared to 2-nitrophenol (R_{t1} 1440 s).

Lastly, the nitro-PAHs are situated towards the end of the chromatogram (R_{t1}) and elute much later compared to the other ON molecules due to their heavy mass. The elution times for these species were therefore larger: 1-Nitronaphthalene (R_{t1} 2505, R_{t2} 5.155, RMM 173.17 gmol^{-1}); 2-Nitrobiphenyl (R_{t1} 2670, R_{t2} 5.22, RMM 199.21 gmol^{-1}); 2-Nitro-1-naphthol (R_{t1} 2692.5, R_{t2} 4.79, RMM 189.17 gmol^{-1}); 3-Nitrobiphenyl (R_{t1} 2925, R_{t2} 4.83, RMM 199.21 gmol^{-1}); 4-Nitrodiphenylmethane (R_{t1} 3097.5, R_{t2} 4.895, RMM 213.23 gmol^{-1}); 3-Nitrodibenzofuran (R_{t1} 3210, R_{t2} 5.135, RMM 213.194 gmol^{-1}); 5-Nitroacenaphthene (R_{t1} 3240, R_{t2} 5.77, RMM 199.21 gmol^{-1}); 2-Nitrofluorene (R_{t1} 3405, R_{t2} 5.605, RMM 211.22 gmol^{-1}); 9-Nitroanthracene (R_{t1} 3442.5, R_{t2} 5.95, RMM 223.23 gmol^{-1}); 1-Nitropyrene (R_{t1} 4125, R_{t2} 6.64, RMM 247.25 gmol^{-1}); and 6-Nitrochrysene (R_{t1} 4477.5, R_{t2} 6.585, RMM 273.29 gmol^{-1}). 1-nitropyrene (R_{t1} 4125, R_{t2} 6.64) and 6-nitrochrysene (R_{t1} 4477.5, R_{t2} 6.585) are particularly low volatility and are off the scale in the chromatogram above in Fig. 7.4.

7.3.2 Kovats Retention Indices

A fundamental issue which arose during the GC \times GC – NCD analysis of ON compounds on the instrumental system was the changing retention times observed of species in the 1st dimension (R_{t1}). Changing retention times in gas chromatography systems is not uncommon and can cause major issues in species identification. This problem seems to be particularly bad with the NCD system used here and has been seen in previous studies, however the reasons have not been identified. To overcome this problem, the Kovats Retention Index (KRI)⁶⁰² is a formula used to estimate the R_{t1} of unknown species within spiked samples using known internal standards. The KRI principle is based on the spiking of known standards (with a series of nitroalkanes in this study) which are clearly shown on a chromatogram. Species within the standard are placed through the KRI equation to produce a KRI constant (Eq. 7.4). Samples are also spiked with the same mix of nitroalkanes and the KRI constants for all peaks present may be calculated. Although the R_{t1} may have shifted within the samples, the KRI remains constant and therefore matching KRI values between the standards and samples allows for the identification of peaks. KRI have been used frequently throughout the

literature^{603,604,605}, including the use of nitroalkane species with Flame Ionisation Detection (FID)⁶⁰⁶. The KRI formula for an iso-thermal and non-isothermal temperature gradient are different^{607,608,609}.

$$I^T = 100 \left[\frac{(t_{Ri} - t_{Rz})}{(t_{R(z+1)} - t_{Rz})} \right] + Z$$

Eq. 7.4. Kovats Retention Indices.

Eq. 7.4 represents the non-isothermal formulae which has been used in this work^{607,610,608,609}, where I^T is the KRI, t_{Ri} is the retention time of the compound of interest, t_{Rz} is the retention time of the nitroalkane before the compound of interest, $t_{R(z+1)}$ is the retention time of the nitroalkane after the ON compound of interest, and Z is the carbon number of the nitroalkane before the ON of interest⁶⁰⁹. In this study, standards and samples were spiked with 50 μ l of a mix of nitroalkanes (mix 1) at 10 ppm. In this study, the KRI method has been used between nitroethane and nitrododecane which cover the retention time were shifting occurred. After nitrododecane, the Rt_1 values in all samples and standards were observed to be stable.

Although in theory the KRI values should remain constant, slight deviations may be observed depending on the concentrations of samples (and therefore peak shape and size) and the modulation period set on the GC method. For larger peaks which span over modulation periods, the LECO GC ChromaToF software used may have centered the peak into an adjacent modulation pulse. Therefore, in this study, the KRI values were calculated across the 7 calibration standards specific to the corresponding samples. The KRI values for each ON compound were averaged, and an error of ± 3 s produced a window of possible KRI values associated with a specific compound. The samples corresponding to the same calibration (used to calculate the KRI windows) were also spiked with Mix 1 and ran on GC \times GC – NCD. The ChromaToF software peak picked the top 1000 most abundant peaks and the nitroalkanes were identified. For all peaks with Rt_1 values within the appropriate Rt range, KRI values were calculated. The KRI windows determined from the calibration standards were then matched to the KRI values from the samples for peak selection.

Similarly, the 2D (Rt_2) retention times were averaged within the standards and ± 0.25 s was the error assigned. This window was then applied to the peaks which had been filtered for agreement based on their KRI values. When analysing data, only peaks which agreed with the KRI and Rt_2 ranges were selected. Fig. 7.6 presents an example chromatogram of sample #88, using the KRI method to assign the nitrosamines in this sample.

On occasion more than one peak was observed and therefore these peaks were visually inspected and often were the result of one peak spanning multiple modulation cuts. On other occasions however, there may have been multiple peaks within a window which were clearly not part of the same peak.

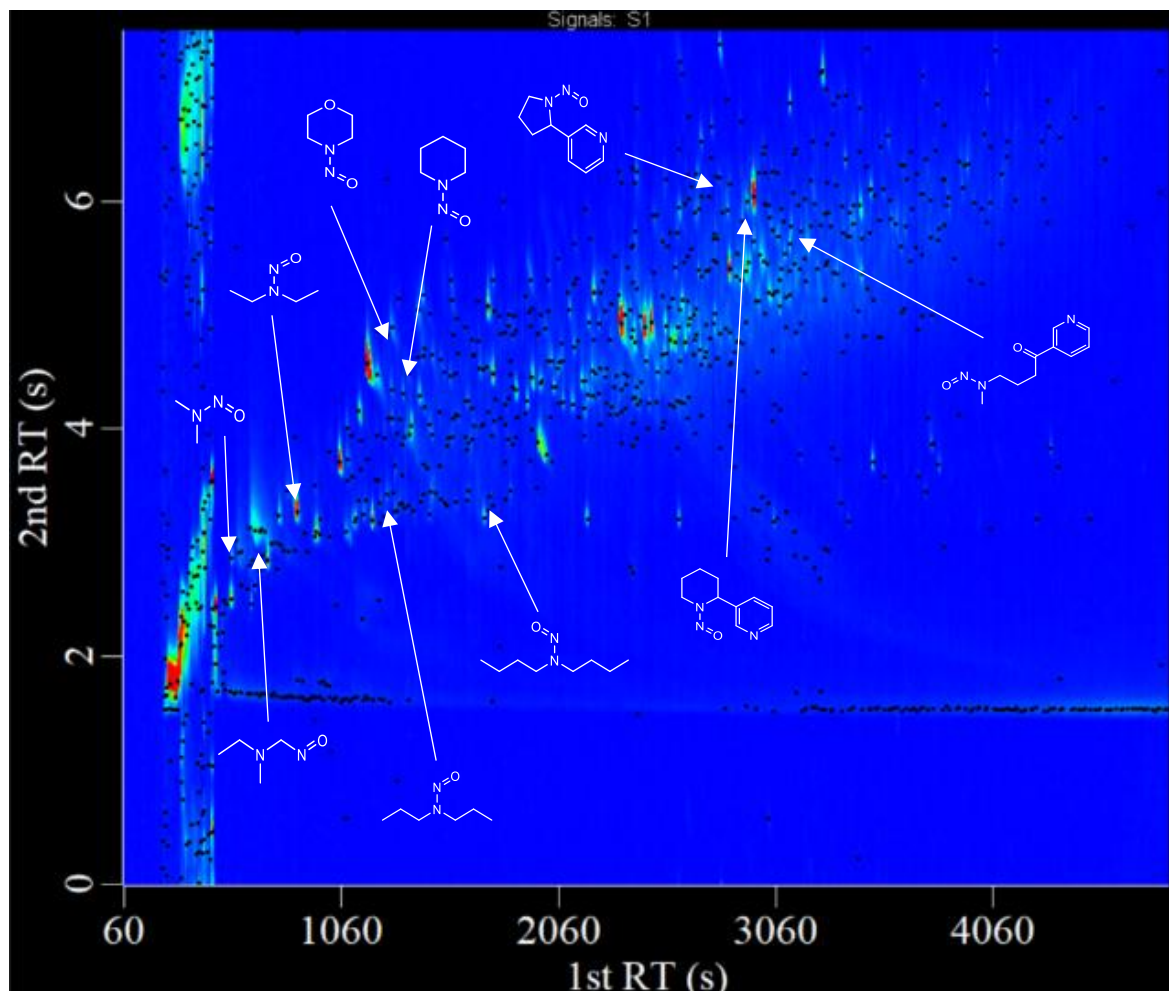


Fig. 7.6 . GC × GC – NCD Chromatogram of sample #88 representing the identification of nitrosamines using the Kovats Retention Index method (using nitroalkane mix from C₂ - C₁₂).

Here, the previous retention times in both the R_{t1} and R_{t2} dimensions (within standards) needed to be assessed to make a judgement. Further challenges arose on the occasion that the R_{t2} values also shifted. In this event, the KRI values were established and compared, and the chromatograms were visually inspected for comparison to the relative calibration chromatograms (e.g. sample #66). Ideally, the nitroalkane mix should also incorporate all straight chain nitro-alkanes spanning the R_{t1} range in which shifting retention times poses an issue. Due to the lack of availability on the global market for nitroheptane, nitrononane, nitroundecane and nitrotridecane, KRI values from nitrohexane until nitrododecane were calculated using a two-carbon gap. This is not ideal and produces a source of error at the peak selection stage.

7.3.3 ON Time Series and Concentrations

Although the MegaMix comprises of 90 different ON compounds, only the nitrosamine species are presented here as these species in particular are used within the cancer risk factor assessment calculation (see section 7.3.8). The APHH winter campaign started on 9th Nov 2016 17:30 and ended on 9th Dec 2016 17:30. 39 samples were selected which spanned a 7-day snap-shot period in Beijing between 22nd Nov 2016 08:37 until 28th Nov 2016 11:30. This section of samples encompasses one of three major pollution events observed in Beijing during the APHH winter campaign. The 39 samples selected demonstrate clean days on the 22nd – 23rd and 27th and 28th Nov and polluted days

on 24th – 26th Nov as to give a 7-day snapshot of the BWIN period. These 39 samples were selected very carefully as to incorporate a 7-day period of both clean and polluted days which average to give a reasonable indication of nitrosamine exposure during the winter period, as the pollution cycles are frequent and are shown within the [PM_{2.5}] (beginning of chapter 3) to repeat themselves throughout the winter campaign. The time series for the nitrosamines NDMA, NMEA, N-tert-butylformamide + NDEA, Npyr, Nmor and Npip are shown in Fig. 7.7; NDPA, NDBA, NDPhA, NNN, NAT, and NAB are shown in Fig. 7.8; and NNK is shown in Fig. 7.9. As in other sections, the *x*-axis represents the time, the *y*-axis represents the [ON] concentration, the red horizontal lines represent the time of sampling, the blue error bars show the uncertainty in the concentration measurements, and the grey lines represent 00:00 for a specific date. Samples included 5 night-time samples and 34 daytime samples.

The majority of these time series were very inconsistent due to the LOD exhibited by the NCD. The times series of NDMA, NMEA, [N-tert-butylformamide + NDEA] and Npip (Fig. 7.7) however had a higher number of data points and clearer time-series. What is key out of all the time series is that higher nitrosamine concentrations were generally seen in the middle of the 7-day period (25th – 26th Nov). This is most likely down to much increased atmospheric oxidation causing a higher [PM_{2.5}] loading. In addition (as has been discussed), Secondary Inorganic Aerosol (SIA) and other inorganic species are significant contributors to aerosol during haze events and increase the hygroscopicity of the aerosol. Another key aspect of the nitrosamine time-series is that significant drops are seen on the 26th Nov which coincides with a decrease in [PM_{2.5}]. Furthermore, nitrosamines are known to be destroyed by solar radiation and therefore a build up of these species is more likely during haze events when solar light is attenuated⁵⁵⁶.

Nitrosamine concentrations were also generally larger during the daytime compared to the night-time period. For non-TSNAs, this is down to secondary formation from amine oxidation by OH to form the amine radical followed by reaction with NO to form the nitrosamine (see section 7.1)⁵⁴⁷. TSNAs are also generally higher during daytime hours (Fig. 7.8 and Fig. 7.9) which may be down to a higher amount of tobacco smoking during the daytime.

A summary of the nitrosamines concentrations and statistical analysis over the 7 day window analysed are shown in Table 7.2. These data were not split into day and night due to the short sampling period and fewer samples. In most of the nitrosamine time series, the largest values are observed during the middle of the 7-day period with most maximums occurring on *ca.* 25th – 26th Nov.

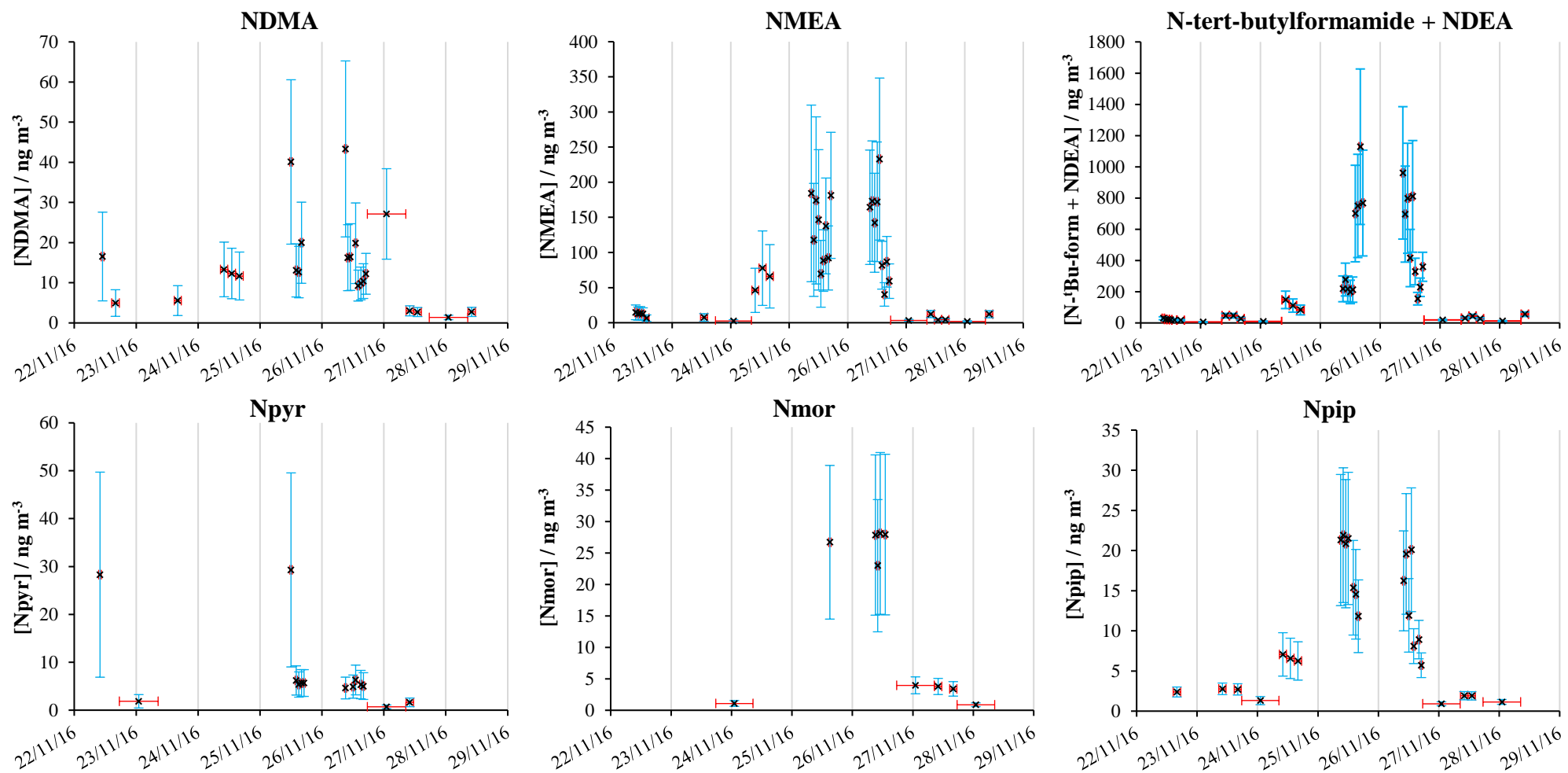


Fig. 7.7. Time series of NDMA, NMEA, N-tert-butylformamide + NDEA, Npyr, Nmor and Npip during a 7-day period during the Beijing APHH winter campaign. The black cross datapoints show the atmospheric nitrosamine concentrations in $\text{PM}_{2.5}$, with the uncertainty represented by the blue error bars in the y-axis (section 7.3.4). The red horizontal error bars demonstrate the time of sampling. The grey vertical lines show the time at 00:00.

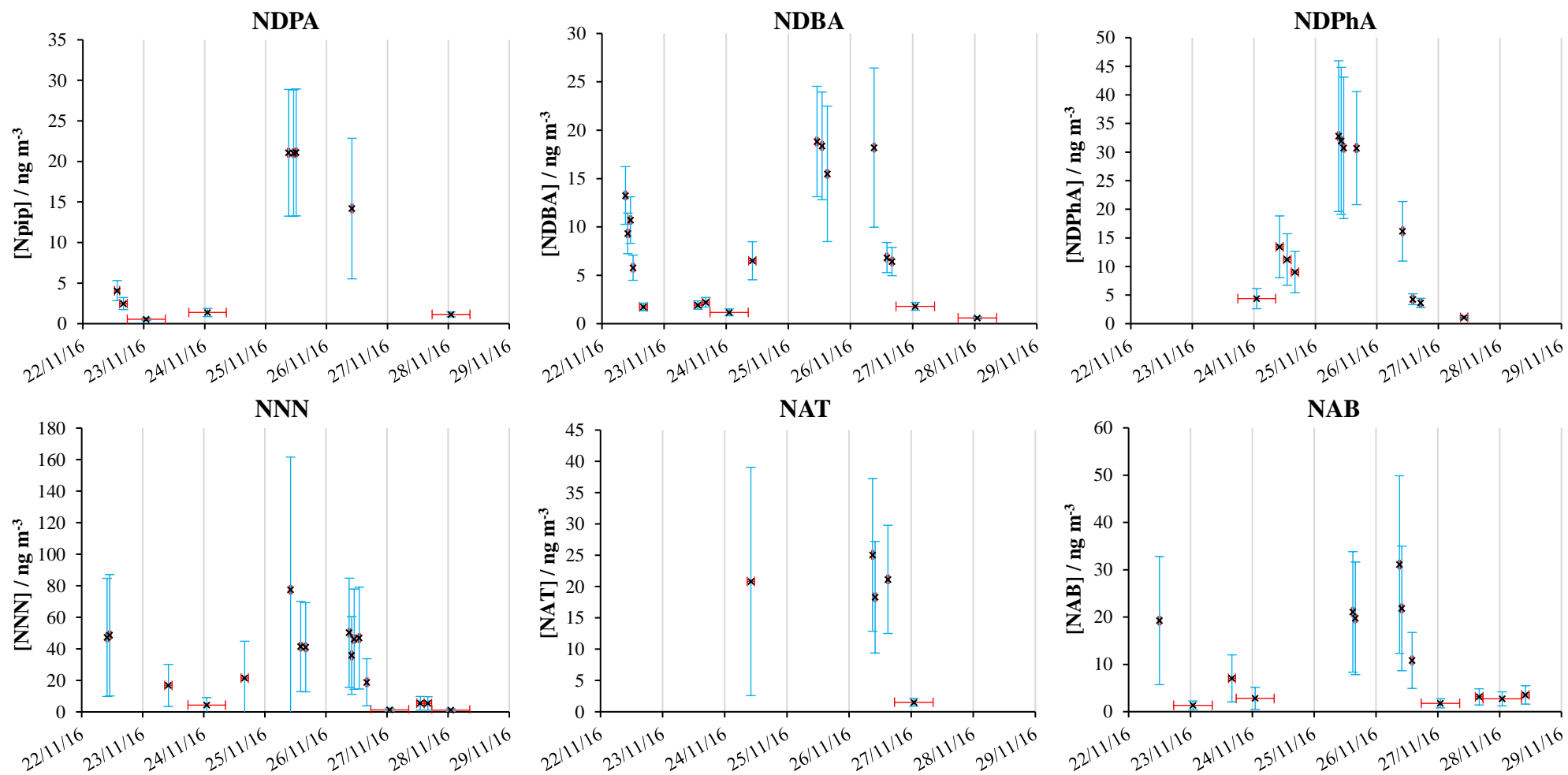


Fig. 7.8. Time series of NDPA, NDBA, NDPhA, NNN, NAT and NAB during a 7-day period during the Beijing APHH winter campaign. The black cross datapoints show the atmospheric nitrosamine concentrations in $\text{PM}_{2.5}$, with the uncertainty represented by the blue error bars in the y-axis (section 7.3.4). The red horizontal error bars demonstrate the time of sampling. The grey vertical lines show the time at 00:00.

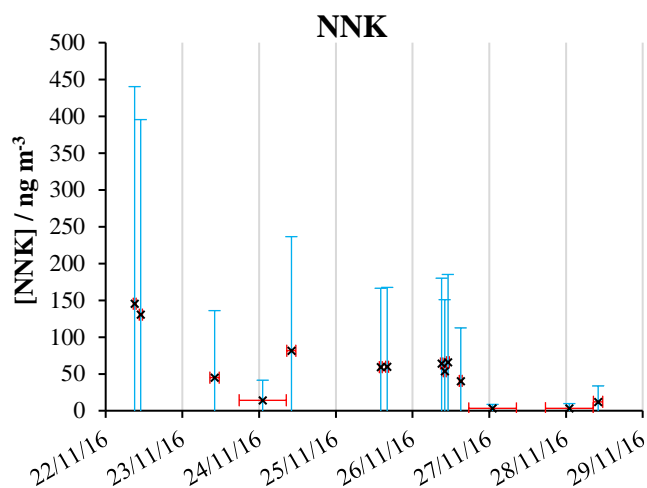


Fig. 7.9. Time series of NNK during a 7-day period during the Beijing APHH winter campaign. The black cross datapoints show the atmospheric nitrosamine concentrations in $PM_{2.5}$, with the uncertainty represented by the blue error bars in the y-axis (section 7.3.4). The red horizontal error bars demonstrate the time of sampling. The grey vertical lines show the time at 00:00.

The [N-tert-butylformamide + NDEA] time series are significantly higher compared to the other studies. This is because these species coelute and a combined concentration is observed to reach values in the $\mu\text{g m}^{-3}$ level. N-tert-butylformamide + NDEA were also the species for which the maximum number of responses from the NCD instrument were recorded ($N=39$). Although these species have been combined, there is only 1 mention (to best knowledge) in the literature of N-tert-butylformamide within aerosol in the work of Farren., (2017)⁶¹¹ who reported this species within chamber studies. Therefore, [N-tert-butylformamide + NDEA] is presented as solely NDEA in Table 7.2. In addition, Table 7.2 demonstrates that NDMA is one of the most abundant nitrosamines present in Beijing which is in-line with other urban cities²⁷⁷.

Table 7.2. Summary of the statistical parameters for nitrosamines species within the 7-day period sampled for the APHH Beijing winter campaign (ng m^{-3}).

Compound	Mean	SD	Median	Max	Min	Range	P ₁₀	P ₉₀	N
NDMA	7.03	10.78	12.32	43.35	1.35	41.99	2.80	25.72	24
NMEA	25.63	69.92	67.87	232.98	1.97	231.01	4.14	173.86	35
NDEA*	94.58	319.49	129.66	1128.68	5.97	1122.72	17.83	777.21	39
Npyr	1.23	9.02	5.35	29.30	0.70	28.59	1.70	21.70	15
Nmor	1.97	12.82	13.47	28.11	0.88	27.24	1.06	27.94	11
NDPA	1.15	9.48	4.07	21.11	0.55	20.56	1.03	21.08	10
Npip	2.95	7.63	8.09	21.91	0.92	20.99	1.55	21.13	26
NDBA	1.76	6.53	6.50	18.83	0.60	18.23	1.51	18.27	18
NDPhA	2.64	12.42	12.32	32.79	1.10	31.69	3.70	31.85	13
NNN	5.73	22.39	35.79	77.42	1.15	76.27	3.13	49.22	18
NAT	1.20	9.18	20.81	25.06	1.53	23.52	8.24	23.50	6
NAB	2.44	10.06	7.05	31.10	1.33	29.77	1.96	21.68	14
NNK	11.15	42.92	56.49	145.26	3.10	142.16	6.06	115.76	15

*NDEA represents [NDEA + N-tert-butylformamide].

Table 7.3. Comparison of mean nitrosamine concentrations (ng m^{-3}) during the clean and polluted period within the 7-day period sampled (between 22nd - 28th Nov).

	Clean		Polluted	
	Mean	SD	Mean	SD
NDMA	5.60	9.10	12.22	10.41
NMEA	3.38	4.77	106.15	54.61
N-tert-butylformamide + NDEA	18.83	14.16	368.75	319.68
Npyr	0.81	13.46	2.78	7.56
Nmor	1.23	1.52	4.67	2.16
NDPA	0.69	1.39	2.80	3.44
Npip	0.95	0.71	10.22	6.11
NDBA	1.21	4.62	3.76	6.05
NDPhA	0.76	2.31	9.42	11.93
NNN	3.12	20.12	15.17	17.18
NAT	0.26	-	4.61	2.79
NAB	2.10	5.93	3.65	7.20
NNK	8.27	61.44	21.58	12.45
$\Sigma(\text{nitrosamine})$	47.22	62.72	565.78	393.27
$\Sigma(\text{non-TSNAs})$	33.46	18.73	520.77	360.23
$\Sigma(\text{TSNAs})$	13.75	57.14	45.01	50.78

Finally, inspecting the time series Fig. 7.7 - Fig. 7.9 shows that significantly higher nitrosamines concentrations were seen during the pollution episode (24th – 26th Nov) compared to the clean periods. As would be expected, the nitrosamine concentrations seen during the pollution episode are significantly larger than those of the clean period on either side.

7.3.4 Calculating Nitrosamine Concentration Error

To calculate the error associated with the nitrosamine concentration results shown in Fig. 7.7, Fig. 7.8 and Fig. 7.9, the calibration error for each species was first calculated by calculating the %RSD across the response factors of each calibration point. The absolute (SD) error of the calibration was subsequently calculated, for which the %RSD could be converted to the absolute calibration error in terms of the SD (δA_1). The %RSD of the instrument response across 10 replicates was also calculated to account for the uncertainty surrounding the reproducibility of the peak response for a particular species from the instrument (δA_2). To find the total error (δA) of the raw nitrosamine concentration, the calibration and reproducibility absolute errors (SD) were summed together. This is summarised in Eq. 7.5.

$$\delta A = \delta A_1 + \delta A_2$$

Eq. 7.5. Calculation of the absolute calibration error of ambient samples from GC \times GC - NCD analysis, where δA is the total concentration error of the analysed species concentration deduced from GC \times GC - NCD analysis, δA_1 is the calibration absolute error for each particular sample concentration, and δA_2 represent the reproducibility error of the GC \times GC - NCD associated with a particular ON species.

Following the concentration calculation of the raw sample from the GC × GC – NCD system, the recovery correction was applied by dividing the raw concentration detected, by the recovery percentage, R. This produced the recovery corrected concentration, C. This is summarised in Eq. 7.6, where A is the raw concentration of species calculated from the GC × GC – NCD analysis.

$$C = \frac{A}{R}$$

Eq. 7.6. Recovery correction step in calculating the recovery corrected ambient PM_{2.5} nitrosamine concentrations, where C is the recovery corrected concentration, A is the raw concentration of nitrosamine calculated from GC × GC – NCD analysis and R is the recovery percentage.

As a division is used for the calculation of the recovery corrected species, the calculation of the associated error for this step involves the division rule for the propagation of error, which for these variables is summarised in Eq. 7.7.

$$\delta C = C \times \sqrt{\left(\frac{\delta A}{A}\right)^2 + \left(\frac{\delta R}{R}\right)^2}$$

Eq. 7.7. The calculation of the propagated error re-arranged as to find the error of the recovery corrected concentration of a nitrosamine species from GC × GC – NCD analysis, where A is the raw concentration of nitrosamine species, R is the percentage recovery and C is the recovery corrected value.

Once the recovery corrected concentration had been calculated (C), this was multiplied by the volume of sample present in the GC vial to calculate the mass of species which was extracted from the filter piece. The measurement of the volume of sample was conducted by measuring the mass of the sample using a mass balance. The error of the mass balance was however negligible compared to the other uncertainties relevant to this calculation, and therefore the recovery corrected concentration (C) was simply multiplied by the volume of sample (Vol_{Sample}) determined, to produce the mass of nitrosamine species, D. Therefore, δC was also multiplied by this constant, to produce the associated error, δD . This is summarised in Eq. 7.8.

$$\delta D = \delta C \times Vol_{\text{Sample}}$$

Eq. 7.8. Calculation of the error of the mass of nitrosamine species which was present on the filter sample, where δC is the recovery corrected concentration error of nitrosamine species, Vol_{Sample} is the sample volume (constant) and δD is the error of the mass of nitrosamine species which was present on the filter sample.

The volume of air sampled (AirVol) was calculated by multiplying the flow rate of the HiVol (HiVol_{FlowRate}, 80 m³ h⁻¹) by the fraction of filter piece taken (FilterPiece_{Fraction}) as well as the sampling time (Time_{Sampling}). The error associated with the volume of air sampled (δ AirVol) was therefore evaluated by calculating the absolute error of the HiVol flow rate (δ HiVol_{FlowRate}, SD across 141 replicate measurements of flow rate which had passed through HiVol at 80 m³ h⁻¹), and multiplying this by FilterPiece_{Fraction} and Time_{Sampling}, to produce δ AirVol. This is evaluated in Eq. 7.9. The FilterPiece_{Fraction} and Time_{Sampling} measurements were determined to contribute negligibly to the overall uncertainty and therefore these remain as constants in Eq. 7.9.

$$\delta AirVol = \delta HiVol \times FilterPiece_{Fraction} \times Time_{Sampling}$$

Eq. 7.9. Calculation of the corrected AirVol uncertainty, δ AirVol, where δ AirVol is the absolute error of the HiVol instrument, Area_{FilterPiece} is the fraction of filter taken from the whole filter area which was in contact with the HiVol air flow, and Time_{Sampling} is the sampling time.

Subsequently, the mass of nitrosamine species extracted from the filter sample (D) was divided by the volume of air sampled (AirVol) to calculate the atmospheric concentration of species (E). This is evaluated in Eq. 7.10.

$$E = \frac{D}{AirVol}$$

Eq. 7.10. Simplified algebraic version of the calculation of particulate nitrosamine species' atmospheric concentration within PM_{2.5}, where D is the mass of nitrosamine extracted from the filter piece, AirVol is the volume of air which was sampled that passed through the filter piece, and E is the Atmospheric Concentration of species associated with a specific sample.

To propagate the error for the calculation of the atmospheric concentration of nitrosamine (E), the division rule for error propagation is taken, and is evaluated in Eq. 7.11.

$$\delta E = E \times \sqrt{\left(\frac{\delta D}{D}\right)^2 + \left(\frac{\delta AirVol}{AirVol}\right)^2}$$

Eq. 7.11. Evaluation of the error propagation in calculating the atmospheric concentration of nitrosamine species uncertainty (δ E), where E is the atmospheric concentration of nitrosamine species, D is the mass of nitrosamine species which was extracted from the filter piece, and AirVol is the volume of air which had passed through the specific area of the filter piece which had been extracted in sample preparation.

Finally, the nitrosamine concentrations are multiplied by 1000, to convert from μ g m⁻³ to ng m⁻³, which is also applied to δ E.

7.3.5 Comparison to Other Studies

A summary of the concentrations of individual nitrosamines (as well as total nitrosamine concentration) within other studies is shown in Table 7.4. Underneath each reference the sampling city for each city is given as Zonguldak (ZGD), London (LDN), Seoul Roadside (SERO), Seoul Residential site (SERE), Seoul (SEO) and Beijing (BEJ).

Table 7.4. Summary of the mean and standard deviations of nitrosamines within atmospheric aerosol (ng m^{-3}) within the literature.

Study		Akyüz et al., (2013) ⁵⁵ ₈	^a Farren et al., (2015) ²⁷ ₇	Hong et al., (2017) ⁵⁵⁶	Hong et al., (2017) ⁵⁵⁶	^c Choi et al., (2018) ⁵⁵⁷	Choi et al., (2020) ⁵⁴⁷	Swift et al., (2019)
Site		ZGD	LDN	SERO	SERE	SEO	SEO	BEJ
Season		Winter	Winter	Autumn	Autumn	Winter	Winter	Winter
Time		Oct 08 - May 09	Jan 12 - Feb 12	Oct-Nov ^b	Oct-Nov ^b	Jan - Feb 14	Jan - Feb 18	Nov - Dec 16
NDMA	μ	9.43	1.36	0.55	0.30	-	8.76	7.03
	σ	4.99	8.60	0.51	0.30	-	14.48	10.78
NMEA	μ	5.72	-	0.01	0.01	0.19	-	25.63
	σ	3.14	-	-	-	0.09	-	69.92
NDEA	μ	5.77	0.89	0.41	0.31	0.82	1.95	94.58 ^d
	σ	2.49	8.70	0.14	0.14	0.54	3.20	319.49 ^d
Npyr	μ	10.08	0.08	0.30	0.43	0.82	0.14	1.23
	σ	5.10	8.30	-	-	0.41	0.13	9.02
Nmor	μ	10.54	0.32	1.02	0.70	-	0.38	1.97
	σ	4.63	11.10	1.13	0.85	-	0.54	12.82
NDPA	μ	6.42	0.07	0.01	0.01	-	0.02	1.15
	σ	3.19	8.30	-	-	-	0.01	9.48
Npip	μ	7.38	0.04	0.04	0.04	0.23	0.09	2.95
	σ	2.13	8.60	-	-	0.08	0.10	7.63
NDBA	μ	7.83	0.18	0.29	0.22	0.94	0.36	1.76
	σ	4.50	8.50	0.12	0.22	0.56	0.47	6.53
NDPhA	μ	5.20	1.22	0.18	0.07	-	-	2.64
	σ	1.85	9.10	-	-	-	-	12.42
NNN	μ	-	0.21	-	-	-	-	5.73
	σ	-	7.80	-	-	-	-	22.39
NAT	μ	-	0.31	-	-	-	-	1.20
	σ	-	6.80	-	-	-	-	9.18
NAB	μ	-	0.14	-	-	-	-	2.44
	σ	-	7.50	-	-	-	-	10.06
NNK	μ	-	0.57	-	-	-	-	11.15
	σ	-	13.80	-	-	-	-	42.92
Σ	μ	84.01	5.40	2.70	2.00	2.79	9.95	159.46
	σ	36.60	-	1.70	1.20	1.41	17.77	420.09

^aErrors given as %RSD as opposed to SD; ^bNo year reported in study; ^cThis study investigated PM₁₀;

^dThis study reported NDEA and N-tert-butylformamide together.

There are relatively few studies which characterize and quantify nitrosamines within PM_{2.5} (and PM₁₀) despite vast interest in nitrosamine production and measurements within other media. There are currently therefore few atmospheric studies to compare the results from this study to.

Furthermore, each study focuses on a different set of nitrosamines and were conducted in different megacities around the world in different years. These changing factors make the direct comparison of nitrosamine concentrations between the few conducted studies very challenging. Nonetheless, nitrosamines are measured in all studies on the order of ng m⁻³. Generally, the concentrations of each nitrosamine (as well as Σ [nitrosamines]) varies significantly between studies as a function of time, city and local environment. Furthermore, for the non-TSNAs, the values were generally much larger in Zonguldak⁵⁵⁸ and Beijing which is likely down to the higher concentrations of amines being emitted from these more industrialised cities, reacting with nitrosating agents (such as NO_x) to produce nitrosamines^{556,571,612,613}.

The TSNAs were only measured in this study (Beijing) and in that of Farren et al., (2015)²⁷⁷. Overall, generally much higher concentrations of TSNAs were observed in Beijing compared to London. The Beijing means were 27.3, 3.9, 17.4, and 19.6 times higher than London NNN, NAT, NAB and NNK concentrations, respectively.

Comparing the mean NDPhA of Beijing to other studies, the only study which has an atmospheric concentration higher was Zonguldak by Akyüz et al., (2013)⁵⁵⁸. This was 1.97 times larger than the [NDPhA] mean demonstrated in Beijing. The other studies in the literature however observe lower values. A reason for this may be due to the release of diphenylamine from industry. Diphenylamine has been identified to be a precursor to form NDPhA⁶¹⁴. NDPhA is known to be used in a wide variety of industrial applications such as in the synthesis of azo-dyes as well as an industrial antioxidant⁶¹⁵. This may also explain the larger concentration of NDPhA found in Beijing and Zonguldak (more industry), compared to the other studies presented in Table 7.4.

Much lower values of NDBA were found in London by Farren et al., (2015)²⁷⁷ for which Beijing was ~10 times larger. Out of all studies for NDBA, London was found to have the lowest average concentration, for which the highest value in Zonguldak reported by Akyüz et al., (2013)⁵⁵⁸ was 43.5 times larger. A detailed description of the production of NDBA (specifically) within the atmosphere has not been reported to date within the literature (to best knowledge), although is likely to be formed from the nitrosation of dibutylamine (originating from industrial sources). Dibutylamine is known to have industrial applications, such as in the synthesis of emulsifiers⁶¹⁶. Industry is therefore the most likely source of dibutylamine which may undergo nitrosation to form NDBA.

Literature values for NDPA were relatively low compared to other nitrosamine compounds. Akyüz et al., (2013)⁵⁵⁸ reported 6.42 ng m⁻³ (SD \pm 3.19 ng m⁻³) in Zonguldak, which like other nitrosamines, had the highest concentration out of all sampling sites and was 5.58 times larger than in Beijing. A possible candidate amine released from industry in Zonguldak may be from dipropylamine which is

known to be released from industrial effluents⁶¹⁷, which may react with nitrosating species to produce nitrosamines⁶¹⁸.

The mean [Npip] of 2.95 ng m⁻³ (SD ± 7.63 ng m⁻³) observed in Beijing was much lower compared to the value of 7.38 ng m⁻³ (SD ± 2.13 ng m⁻³) reported by Akyüz et al., (2013)⁵⁵⁸ in the Zonguldak province. It is likely that Akyüz et al., (2013)⁵⁵⁸ found the highest production of Nmor due to the release of piperidine from industrial processes, which underwent nitrosation in the atmosphere to produce Npip.

The mean [Nmor] seen in Zonguldak by Akyüz et al., (2013)⁵⁵⁸ was 5.35 times larger compared to that observed in Beijing. This is likely down to the specific presence of the rubber industry in Zonguldak⁵⁵⁸, as morpholine (which is the precursor of nitrosomorpholine) is known to be used in the rubber industry as an intermediate during polymerization⁶¹⁸. It is however also used in a number of other industrial applications such as in the manufacture of domestic products⁶¹⁸. Zonguldak is also a centre for the iron-steel and coal industries^{558,619} and nitrosomorpholine may be a by-product in which morpholine released from coal combustion reacts with NO_x to produce nitrosomorpholine.

The largest concentration of [Npyr] was also reported in Zonguldak and was 8.20 times larger compared to Beijing. The mean value reported for Beijing was however larger compared to all other studies. Zonguldak is a major industrial area for which coal combustion may be a major contributor to the concentration of Npyr. [Npyr] is also known to be associated with cooking aerosol⁶²⁰ and is likely to be a dominant contributor to the [Npyr] values obtained in Beijing.

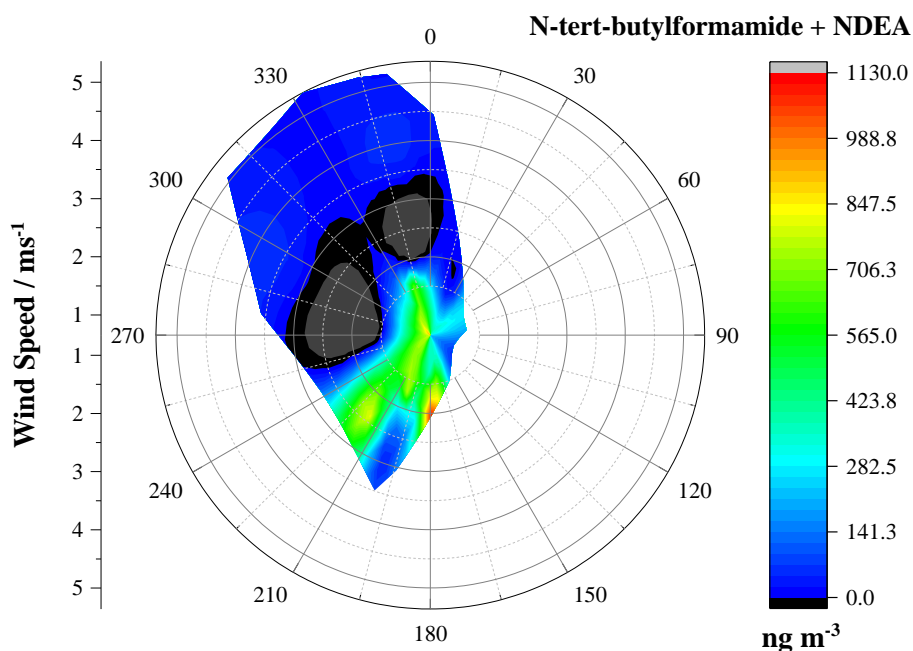


Fig. 7.10. [N-tert-butylformamide + NDEA] contour plot for the 7-day period analysed. The concentration of [N-tert-butylformamide + NDEA] (ng m⁻³) is given by the colour scale shown on the right.

The concentration of [NDEA + N-tert-butylformamide] in Beijing is much larger compared to the other megacities compared in Table 7.4. In addition, N-tert-butylformamide is not a typical compound to be expected in high abundance within the atmosphere and it is probable that most of the Beijing [NDEA + N-tert-butylformamide] mean of 94.58 ng m^{-3} ($SD \pm 319.49 \text{ ng m}^{-3}$) is made up of NDEA. A possible source of NDEA may be from carbon capture storage facilities⁶²¹ coupled with power plants. When plotting the [NDEA + N-tert-butylformamide] however in conjunction with wind data (Fig. 7.10), the highest [NDEA + N-tert-butylformamide] come from the south, for which the Huaneng thermal power station is to the SE of Beijing (chapter 5). Another possible reason for these significantly high NDEA values may be down to the industrial release of diethylamine (DEA). DEA is known to have significant emissions source from industries such as those synthesising herbicides (such as 2,4-dichlorophenoxy acetic acid⁶²²) and industrial activity is also found to the south of the Institute of Atmospheric Physics (IAP)²⁸³.

The Beijing [NMEA] was also higher compared to the other studies. As NMEA is a non-TSNA, the much larger values of [NMEA] in both Beijing and Zonguldak are most likely down to industrial emissions as both Beijing and Zonguldak⁵⁵⁸ are both highly industrialised areas with substantial coal burning.

The largest average [NDMA] out of all studies reviewed was reported by Akyüz et al., (2013)⁵⁵⁸, for which the average was 1.34 times larger than that for Beijing. The Beijing average calculated in this study was also relatively similar to the work of Choi et al., (2020)⁵⁴⁷. The values reported by Hong et al., (2017)⁵⁵⁶, at both the road and residential sites were generally much lower compared to the other Asian sites, although this study was conducted during the Autumn as opposed to the winter months. Furthermore, the value reported by Farren et al., (2015)²⁷⁷ was also much lower although the sampling site was conducted in London as opposed to an Asian megacity. Another factor which may affect the formation of NDMA is the Relative Humidity (RH), as NDMA may form either in the gas or aqueous (in cloud) phases⁶²³. The only other study (apart from this study) to report RH out of the reviewed [NDMA] values is that of Akyüz et al., (2013)⁵⁵⁸ who reported an RH of 75 %. This compares to an average of 49 % RH during the Beijing winter campaign. Therefore, in this instance, a larger RH % in Zonguldak was also associated with a larger [NDMA], which is comparable to this work in Beijing.

7.3.6 Coelution of N-tert-butylformamide and NDEA

It must be highlighted that the particularly high NDEA signal seen within the Beijing dataset from the work conducted in this thesis is orders of magnitude higher compared to the other NDEA concentration values measured by the other studies reviewed in Table 7.4.

A possible explanation for the much higher Beijing NDEA measurement is possibly down to a high presence of N-tert-butylformamide present in the atmosphere, as these species were found to co-elute when run separately on the GC × GC – NCD, despite best efforts to try and modify the instrument method to separate these species. Furthermore, running each standard individually brings further

challenges in speciation of these two molecules due to the shifting retention times experienced by the GC × GC – NCD system. Therefore, to investigate the likelihood of a significant contribution of N-tert-butylformamide to the [NDEA + N-tert-butylformamide] measurement, the most likely formation routes of N-tert-butylformamide within the atmosphere were taken into consideration.

N-tert-butylformamide presence in the atmosphere is scarcely reported in the literature and to best knowledge, the only reported studies in the literature which describe the detection of N-tert-butylformamide from filter samples is in the work of Tan et al., (2018)⁶²⁴ as well as the PhD thesis of Farren., (2017)⁶¹¹. In the work of Farren., (2017)⁶¹¹, N-tert-butylformamide was reported to have formed from the photooxidation of *tert*-butylamine (*t*BA) during chamber experiments, in which the study reports a percentage yield of 0.16 % in the presence of medium NO_x (*ca.* 45 ppbv) and 0.21 % in the presence of low NO_x (*ca.* 10 ppbv). These yields are however exceptionally low. In the work of Tan et al., (2018)⁶²⁴, N-tert-butylformamide was also detected on filter samples at the European Photoreactor (EUPHORE) smog chamber when investigating the reaction between *t*BA and OH radicals in the presence of NO_x. The authors also however reported a very low concentration of N-tert-butylformamide formed. Therefore, a possible pathway of N-tert-butylformamide formation in the atmosphere or as a positive artefact on the filter samples could be from the photooxidation of *t*BA in the presence of NO_x, although it must be emphasised that this is a very inefficient process (based on the minimal literature available). Furthermore, the higher yield of N-tert-butylformamide was obtained at the lower [NO_x] in the work of Farren., (2017)⁶¹¹ and for which the average BWIN [NO_x] was 74 ppbv, *ca.* 7.4 times larger.

A maximum possible contribution of N-tert-butylformamide could have been estimated in assuming the full photooxidation of *t*BA which could have been deducted from the [NDEA + N-tert-butylformamide] results in Beijing, although *t*BA data was not available for the BWIN APHH campaign. The presence of *t*BA in the atmosphere however cannot be ruled out as *t*BA is known to be released from chemical industries including pesticide synthesis processes, dye production, pharmaceuticals synthesis, rubber manufacturing as well as potential use in carbon capture technologies^{625,626}. Diethylamine (precursor to NDEA) is however also used in these commercial industries with the addition of emulsifying agent, metal preservative and textile auxiliary synthesis⁶²⁷. A significant amount of chemical industry is located towards the south of the IAP site²⁸³, for which the Beijing Xingyi Rubber and Plastic Manufacture Factory is located *ca.* 30 km directly south of IAP⁴⁰³, which could be a significant source of either *t*BA or DEA.

In spite of the lack of N-tert-butylformamide or *t*BA data available from the APHH BWIN campaigns, further inspection of Table 7.4 could indicate that N-tert-butylformamide contributed negligibly to the overall [NDEA + N-tert-butylformamide] measurement. When comparing the [NDEA + N-tert-butylformamide] within this study to the NDEA measurement to the other studies, a similar factor difference is seen for other nitrosamine species between the work of this study and said respective studies, in some cases. For example, comparing the NDEA measurement in the work

of Choi et al., (2018)⁵⁵⁷ who reported 0.82 ng m^{-3} to their measured [NMEA] (0.19 ng m^{-3}), a factor difference of 4.31 is observed. Comparing the [NDEA + N-tert-butylformamide] result from this thesis (94.58 ng m^{-3}) with the measured [NMEA] (25.63 ng m^{-3}) from this thesis, a similar factor difference of 3.69 is seen. In addition to this, the atmosphere of Beijing is expected to be significantly more polluted compared to the other sites reported in Table 7.4 (based on city population)²⁵⁹ and realistically, the atmosphere of the BWIN APHH campaign is not comparable to these other sites (or seasons i.e. during the Autumn for Hong et al., (2017)⁵⁵⁶; or timings i.e. the sampling by Farren et al., (2015)²⁷⁷ took place in 2012).

To summarise, the minimal data available (to date) from the literature would suggest that the [NDEA + N-tert-butylformamide] peak observed during the BWIN campaign is most likely predominantly NDEA, due to the very low efficiency of N-tert-butylformamide production in the atmosphere^{611,624}, which during the BWIN campaign is further reduced due to the very low temperatures experienced. The presence of N-tert-butylformamide however cannot be ruled out. Additionally however, the presence of further compounds co-eluting at the same 1D and 2D retention times also cannot be ruled out, although is unlikely. The presence of co-eluting peaks is simply a limitation of using a two-dimensional gas chromatographic system which was also seen by Farren et al., (2015)²⁷⁷ in the co-elution of NMEA with other species.

7.3.7 Total Nitrosamine Concentration

The overall average Σ [nitrosamines] was calculated by summing the individual nitrosamine averages together and the SD was calculated by taking the SD across the averages of the individual nitrosamines. The individual averages were calculated using the time weighted average. The total average nitrosamine concentration observed in this study was 159.46 ng m^{-3} ($\text{SD} \pm 25.63 \text{ ng m}^{-3}$). This compares to the total nitrosamine concentrations of 84.01 ng m^{-3} ($\text{SD} \pm 36.60 \text{ ng m}^{-3}$) measured in Zonguldak (Turkey), reported by Akyüz et al., (2013)⁵⁵⁸; 5.40 ng m^{-3} (error not reported for Σ [nitrosamines] reported by Farren et al., (2015)²⁷⁷ in Kensington, London (UK)); 2.70 ng m^{-3} ($\text{SD} \pm 1.70 \text{ ng m}^{-3}$) reported by Hong et al., (2017)⁵⁵⁶ from sampling by the roadside in Seoul; 2.00 ng m^{-3} ($\text{SD} \pm 1.20 \text{ ng m}^{-3}$) reported by Hong et al., (2017)⁵⁵⁶ sampling at the residential site in Seoul; Choi et al., (2018)⁵⁵⁷ who reported a total of 2.79 ng m^{-3} ($\text{SD} \pm 1.41 \text{ ng m}^{-3}$) in Seoul; and Choi et al., (2020)⁵⁴⁷ who reported a total nitrosamine concentration of 9.95 ng m^{-3} ($\text{SD} \pm 17.77 \text{ ng m}^{-3}$) in Seoul.

The average Σ [nitrosamine] value in this study (159.46 ng m^{-3} , $\text{SD} \pm 25.63 \text{ ng m}^{-3}$) was found to be larger than all other studies. The likely reasoning for the Σ [nitrosamines] having a much larger average compared to the other studies shown in Table 7.4 is likely down to the analysis of the short time-period in which a major pollution event passed over Beijing. This compares to the other averages observed in Table 7.4, which report the Σ [nitrosamines] values as an average across a whole campaign. In addition, each study focuses on a different set of nitrosamines and the only other study to measure the TSNAs, for example, is Farren et al., (2015)²⁷⁷.

The average Σ [nitrosamine] calculated in Zonguldak by Akyüz et al., (2013)⁵⁵⁸ was the second largest total nitrosamine concentration after Beijing during the winter. This is most likely down to Zonguldak being a major centre for the iron-steel and coal mining industries⁵⁵⁸. NO_x is formed during combustion of all fuels⁵⁷³ and secondary amines may also be produced from coal combustion^{558,574}. As these react together, nitrosamines are formed^{573,574}. Akyüz et al., (2013)⁵⁵⁸ do however also imply that a significant fraction of nitrosamine detection was due the polymer industry as well as plastic material and rubber combustion⁵⁵⁸. In contrast, the lowest Σ [nitrosamine] values were observed in Seoul in the work of Hong et al., (2017)⁵⁵⁶, Choi et al., (2018)⁵⁵⁷ and Choi et al., (2020)⁵⁴⁷. The total nitrosamine concentration in this study and the reviewed studies in Table 7.4 substantially exceed the concentration of 0.3 ng m^{-3} , which is the recommended limit of Σ [nitrosamines + nitramines] as recommended by the Norwegian Institute of Public Health⁵⁶⁵.

7.3.8 Cancer Risk Factor

Comparing this work to the work of Farren et al., (2015)²⁷⁷, it can be seen that in both London and Beijing that the non-TSNAs concentrations were much larger generally. Each nitrosamine is however sorted into a separate International Agency for Research on Cancer (IARC) classification describing its cancer risk. It is therefore associated with a different hazard and the level of danger imposed by the nitrosamines cannot purely be associated with their relative concentration levels in the atmosphere. This therefore indicates the necessity of calculating the cancer risk factor to help indicate where the most influential action needs to be taken regarding the reduction of species.

The classifications have been authenticated by the World Health Organisation's (WHO) IARC. Chemicals may fall into either Group 1, a known human carcinogen; Group 2A a probable human carcinogen; Group 2B, a possible human carcinogen; or Group 3, carcinogenicity to humans is not classified⁵⁵⁵. For the nitrosamines in this study according to the IARC (last updated 2nd Dec 2020 at 2.39pm, CEST)⁶²⁸, Group 1 included NNN and NNK; Group 2A included NDMA and NDEA; Group 2B included NMEA, NDPA, Npyr, Nmor, Npip and NDBA; and Group 3 included NDPhA, NAT and NAB^{629,628,555}. For the 7-day period in Beijing analysed in this study, the Σ (Group 1), Σ (Group 2A), Σ (Group 2B) and Σ (Group 3) were evaluated and compared to the values reported in London by Farren et al., (2015)²⁷⁷. These concentrations are shown in Table 7.5.

Table 7.5. Comparison of the mean and standard deviation of Σ [nitrosamines] concentrations between the WHO IARC groups between Beijing and London.

IARC Classification	Beijing		London	
	Mean	StDev	Mean	StDev
Σ (Group 1)	16.88	65.31	0.78	21.60
Σ (Group 2A)	101.61	330.27	2.25	17.30
Σ (Group 2B)	34.70	115.39	0.69	44.80
Σ (Group 3)	6.28	31.65	1.67	23.40

Table 7.5 demonstrates that for each group, Beijing has much larger concentrations of nitrosamines associated with each IARC group (note the different y-axis for each data set). For each of group 1, group 2A, group 2B and group 3, Beijing was 21.64, 45.16, 50.28 and 3.76 times larger. The largest differences between Beijing and London were therefore observed in groups 2A and 2B.

Although Beijing had much larger values compared to London in each IARC class, the distribution of nitrosamines within classes within a study was different. It must however be acknowledged that this comparison is not a direct like-for-like comparison between London and Beijing. The reason for this is that in this study the NDEA and N-tert-butylformamide coeluted and the [NDEA] in Beijing is strictly [NDEA + N-tert-butylformamide] (although N-tert-butyl formamide is a very unlikely atmospheric species). In addition, Farren et al., (2015)²⁷⁷ reported coelution of NMEA with other compounds. The issue of NMEA coelution with other ON compounds was not seen in this work and therefore NMEA was measured for this thesis and included in the Beijing group 2B classification. Farren et al., (2015)²⁷⁷ did however report considerably lower LOD values compared to this work. Furthermore, the data shown for Beijing represents the mean concentration from a relatively short period containing both clean and polluted air whereas in Farren et al., (2015)²⁷⁷ average nitrosamine concentrations were reported over across a longer period of sampling.

There are numerous ways to conduct a cancer risk assessment dependant on method and level of exposure as outlined by the “Risk Assessment Guidance for Superfund Volume I: Human Health Evaluation Manual (Part F, Supplemental Guidance for Inhalation Risk Assessment)” report by the USA Environmental Protection Agency (EPA)⁶³⁰. The method used to calculate the cancer risk in Beijing for this study was the method also used by Farren et al., (2015)²⁷⁷ in London. This method was based on the Inhalation Unit Risk (IUR) metric^{630,277}. The cancer risk assessment was calculated by working out the cumulative frequency of the product of the IUR_x and Exposure Concentration (EC_x), specific to species x and the Age Dependant Adjustment Factor ($ADAF_y$) specific to age group y in question (Eq. 7.12). The age groups are defined by the Environmental Protection Agency, U.S., Exposure Factors Handbook: 2011 ed.⁶³¹ as $0 < y < 2$, $2 < y < 16$ and $16 < y$.

The IUR is given in units of $(\mu\text{g m}^{-3})^{-1}$ and is defined by the USA EPA as “The unit inhalation risk is the upper-bound excess lifetime cancer risk estimated to result from continuous exposure to an agent at a concentration of 1 mg m^{-3} ”^{632,277}. The IUR values are specific to a carcinogen and were sourced from the USA EPA Integrated Risk Information System (IRIS) A to Z List of Chemical Assessments⁶³³. If unavailable from IRIS, IUR values were sourced from the California Office of Environmental Health Hazard Assessment (OEHHA) Toxicity Criteria Database⁶³⁴. This is in a similar manner to Farren et al., (2015)²⁷⁷. NAT, NAB and NNK were unavailable from either IRIS or OEHHA and were therefore not included in the cancer risk assessment. A further description of IUR values and their derivation is found in section 2.2 of USA EPA., (2009)⁶³⁰.

$$Cancer\ Risk = \sum_{i=1}^n IUR_x \times EC_x \times ADAF_y$$

Eq. 7.12. Cancer Risk Factor Equation.

$$EC_x = \frac{(CA_x \times ET \times EF \times ED_y)}{AT}$$

Eq. 7.13. Exposure Concentration Calculation.

The EC element in Eq. 7.12 represents the Exposure Concentration in $\mu\text{g m}^{-3}$ specific for a compound and is calculated through Eq. 7.13⁶³⁰, where CA is defined as the Concentration of the contaminant species x ($\mu\text{g m}^{-3}$); ET is the exposure time (hours day⁻¹), which is an independent variable; EF is the exposure frequency and is fixed at a constant of 365 days year⁻¹; ED is the exposure duration (years) and equates to the range of the age group defined by the Environmental Protection Agency, U.S., Exposure Factors Handbook: 2011 ed.⁶³¹; and AT is defined as the Averaging Time which equates to the product of the life expectancy multiplied by 24 hours day⁻¹ multiplied by 365 days year⁻¹ and is equal to an estimate of the number of hours a human is alive in a specific region based on that area's life expectancy. For Beijing in 2016, the life expectancy was *ca.* 82 years; and for a person living and working in London, the life expectancy in 2012 was 70 years. Therefore, the AT values in Beijing and London were 718320 h and 613200 h, respectively.

The ADAF is only applied for a specific species, x , if is known to cause cancer through a mutagenic mode of action mechanism^{277,635,630}. These species are specifically known to be more harmful to humans during the early stages of development⁶³⁰. Therefore, to correct for the extra risk imposed by these species, an extra constant ADAF_y (which is specific to the age group in question) is integrated into the cumulative cancer risk factor product (Eq. 7.2). These constants have been updated since the work of Farren et al., (2015)²⁷⁷ and correspond to a value of 10 for ages $0 < y < 2$; 3 for ages $2 < y < 16$; and 1 for $16 < y$ (no adjustment required)⁶³¹. For the species investigated in this study, ADAF_y values were only applicable to NDMA and NDEA^{635,636}.

Due to the ADAF_y incorporation^{631,630,277}, three different scenarios of cancer risk have been evaluated and are shown in Fig. 7.11A for Beijing. The mean nitrosamine concentrations from Farren et al., (2015)²⁷⁷ has been re-calculated using the updated ADAF group signatures⁶³¹ for ages $0 < y < 2$; $2 < y < 16$; and $16 < y$ and is also presented in Fig. 7.11B. The cancer risk values have been plotted as a function of the estimated exposure time (ET) which ranges from 0 to 24 hours day⁻¹.

The line graphs in Fig. 7.11 show the cumulative lifetime cancer risk caused by the carcinogenic and mutagenic toxicological effects of the nitrosamines analysed in these studies (to those exposed), as a function of the ET (along the x -axis). The blue, orange and grey lines represent the $0 < y < 2$, $2 < y < 16$ and $16 < y$ age brackets, respectively. Overall, a much larger increase in the cumulative cancer

risk factor is observed in Beijing compared to London, by a factor of 62-63 for all age groups. *N.B.* as a short time-period of samples was used for Beijing during the winter to calculate the cancer risk, Fig. 7.11 shows a worst-case scenario for Beijing (Fig. 7.11A). For comparison, the winter averages were also taken from Farren et al., (2015)²⁷⁷ as to give a worst-case estimation for London as well (Fig. 7.11B). The worst-case scenario for Beijing also assumes that no N-tert-butylulformamide was present (section 7.3.6).

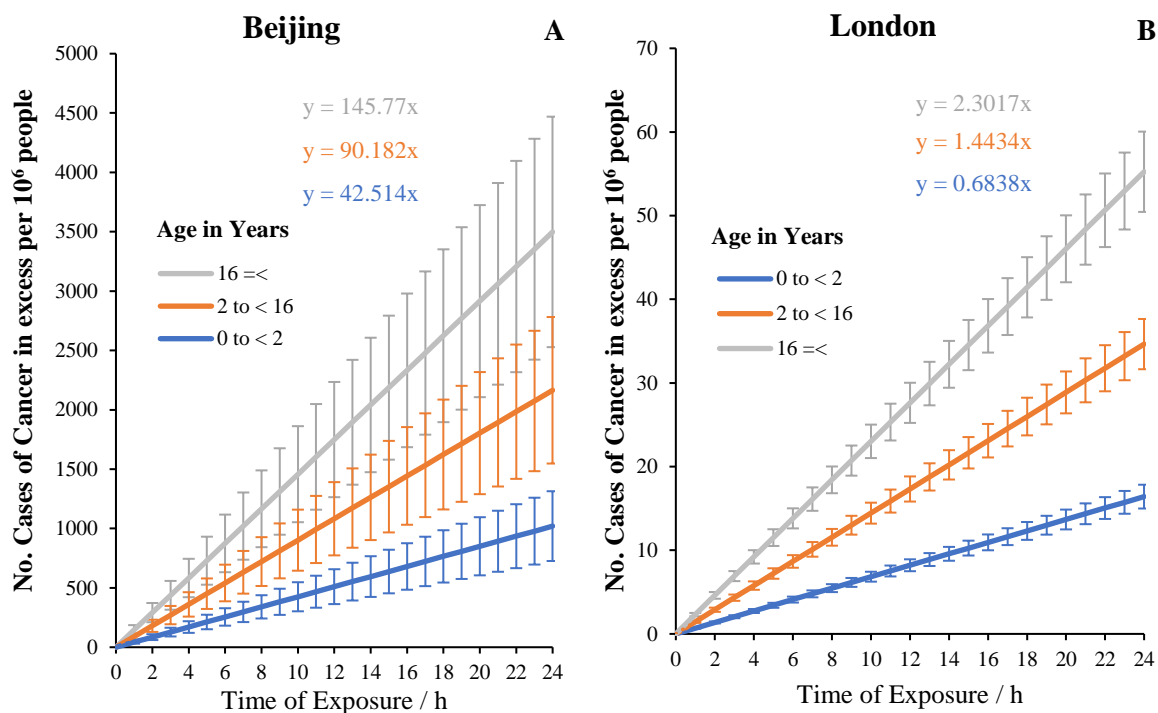


Fig. 7.11. Cancer Risk factor Assessment of Beijing and London imposed by the nitrosamines within $PM_{2.5}$ as a function of the Exposure Time (ET) for different age groups. The blue, orange and grey lines show the cancer risk imposed on the 0 to < 2, 2 to < 16 and 16 =< age brackets, against the amount of time an individual is exposed to (A) Beijing and (B) London [$PM_{2.5}$] (worst case scenarios). The vertical error bars demonstrate the uncertainty as calculated in section 7.3.8.

The errors associated with the cancer risk factor for each species (δCR_x) were calculated by using the nitrosamine errors calculated in section 7.3.4 (δE) and propagating these through the constants found in Eq. 7.12 and Eq. 7.13. These products were then summed together, using the addition rule for error propagation to calculate the summed cancer risk associated with each nitrosamine ($CR_{Nitrosamines}$). This is evaluated in Eq. 7.14.

$$\delta CR_{Nitrosamines} = \sqrt{(\delta CR_{NDMA})^2 + (\delta CR_{NMEA})^2 + (\delta CR_x)^2 + \dots}$$

Eq. 7.14. Propagation of error of the summer Cancer Risk Factors from individual species, where $\delta CR_{Nitrosamines}$ is the total error associated with the cancer risk factor calculation and δCR_x is the cancer risk factor associated with a specific nitrosamine, x.

In Beijing (in a worst-case scenario), every extra hour day⁻¹ spent outside in the $0 < y < 2$, $2 < y < 16$ and $16 < y$ age groups, increases the number of excess cancer cases by 42.5, 90.8 and 145.8 per one million people, respectively, over the course of their lifetime if exposed to these values. According to the World Population Review website²⁵⁹, the urban population of Beijing in 2016 was 18,812,324 inhabitants⁶³⁷. This therefore equates to an estimated *ca.* 799.78, 1696.53 and 2742.24 extra cancer cases (a total of 5238.56), over the lifetimes of the inhabitants in the $0 < y < 2$, $2 < y < 16$ and $16 < y$ age brackets, respectively, in Beijing per extra hour spent outside (ET), from the nitrosamines alone (which have been included in the equation), over the lifetime of those exposed. London (worst-case scenario) demonstrates that for every extra hour day⁻¹ spent outside (ET) for the $0 < y < 2$, $2 < y < 16$ and $16 < y$ age groups, the cumulative cancer risk increases by 0.68, 1.44 and 2.30 per one million people, respectively, over the lifetime of the inhabitants. In 2012, the population of London (urban area, according to world population review²⁵⁹) was 8,293,332⁶³⁸, which therefore equates to an estimated *ca.* 5.67, 11.97 and 19.09 extra cancer cases (a total of 36.73), over the lifetimes of the inhabitants in the $0 < y < 2$, $2 < y < 16$ and $16 < y$ age brackets, respectively, if exposed to these values, in London per extra hour day⁻¹ spent outside, from the nitrosamines alone (which have been included in the equation).

Although the cumulative cancer risk factor calculated in this study for Beijing (and London using the data from Farren et al., (2015)²⁷⁷) gives an insight into the excess burden of cancer imposed on a population from nitrosamines within PM_{2.5}, the calculation is not exact and is accompanied by several sources of error. One of the largest sources of error is the multiple assumptions which need to be made. Exposure depends on lifestyle, and realistically most inhabitants spend the majority of their time indoors, for which in some cases (especially in Beijing where the number of smokers is much higher), the nitrosamine levels may increase substantially from the exposure to tobacco smoke and second and third hand smoke⁵⁷⁰. This then produces further pathways of exposure including dermal and non-dietary ingestion⁵⁷⁰. In addition, several studies have reported the presence of nitrosamines within the water supply sourced from water treatment activities^{587,639,640,641}, within food^{642,643,644}, cosmetics^{593,645} as well as smoking^{566,589}, and may even be formed in the body⁶⁴⁶.

Further errors arise from the availability of data required for the cancer risk assessment, such as the IUR values. IUR values were taken from the IRIS database preferentially and if unavailable the OEHHA database was used. IUR values were however unavailable from either database for NAT, NAB and NNK, and therefore these constituents were not used in the assessment²⁷⁷. NNK is also in group 1 of the IARC assessment. In this regard, the cancer risk values are therefore underestimated. It must also be highlighted that nitrosamines are present and often formed in the gas phase and therefore calculating the cancer risk factor from PM_{2.5} samples alone also produces an underestimation⁵⁴⁷.

Furthermore, some pieces of toxicological evidence have not been updated since the 1980's. For example, the IUR value for NDEA was taken from section II of the report on N-

Nitrosodiethylamine⁶⁴⁷ from the IRIS A to Z List of Chemical Assessments⁶³³, which was last revised on the 31st Jan 1987. For greater accuracy, the IUR values need to be updated. Further inaccuracies arise from the EF, ED and AT assumptions. For the exposure frequency (24 hours day⁻¹) and exposure duration (365 days year⁻¹) constants, it is assumed that everyone in Beijing or London never leaves the city which is very unlikely for the great majority of inhabitants. The averaging lifetime (AT) is essentially the number of hours the average person is alive during one lifetime based on the life expectancy in an area. This is the product of 24 hours day⁻¹ multiplied by 365 days year⁻¹ multiplied by the average life expectancy for an area. Like EF and ED, the 24 hours day⁻¹ and 365 days year⁻¹ constants assume 100% of one's life spent in one city. In addition, however, the average life expectancy is constantly changing and over the course of time changes the cancer risk factor and the estimate of the excess number of cancer cases expected. The life expectancy used is also an average across a normally distributed set of lifetimes in an area, which further incorporates error.

It must also be highlighted that it is not only nitrosamines which impose a cancer hazard within urban PM_{2.5}. Other species such as PAHs, for example, are also known to be carcinogenic and mutagenic and present in megacity PM_{2.5}^{277,598,372}. Therefore, to improve the accuracy of the estimated cancer risk inflicted by PM_{2.5} in a megacity, other such species need to also be included. On a sampling level, it must be highlighted that the atmosphere is not homogenous and that the cancer risk factor calculation is representative of the area in close proximity to the sampler as well as the specific sampling time. The level of carcinogens will not be the same concentration or distribution across an entire megacity. It does however give a general idea and comparison of nitrosamine levels and cancer risk hazards between cities. A direct comparison between Beijing and London, specifically, is also challenging due to the different sampling times. In Beijing, much fewer samples were available, whereas in London the averages of nitrosamines were taken across an entire winter campaign. Furthermore, Farren et al., (2015)²⁷⁷ did not include NMEA within their study, whereas in Beijing NMEA was included.

7.3.9 Cancer Risk Assessment assuming low [NDEA]

In section 7.3.6, the challenges surrounding the separation of NDEA from N-tert-butylformamide were evaluated. With the data available during the BWIN campaign as well as the instrumentation available for this project, it is not possible to quantify whether any N-tert-butylformamide was present, and if so, what proportion of this species contributed to the overall [NDEA + N-tert-butylformamide]. Therefore, as a comparison, the cancer risk factor was calculated with the deduction of the [NDEA + N-tert-butylformamide] data, in the assumption that the [NDEA + N-tert-butylformamide] peak was purely from N-tert-butylformamide. The results of this analysis are shown in Fig. 7.12.

The uncertainty demonstrated in Fig. 7.12 was calculated in the same manner as previously in section 7.3.8 (Eq. 7.14), although with the exclusion of the error associated with the [NDEA + N-tert-butylformamide] values. Fig. 7.12 shows that the gradients of the cancer risk factors as a function of

exposure time are *ca.* 15 times smaller compared to the cancer risk factor calculation in Beijing when the [NDEA + N-tert-butylformamide] values are included.

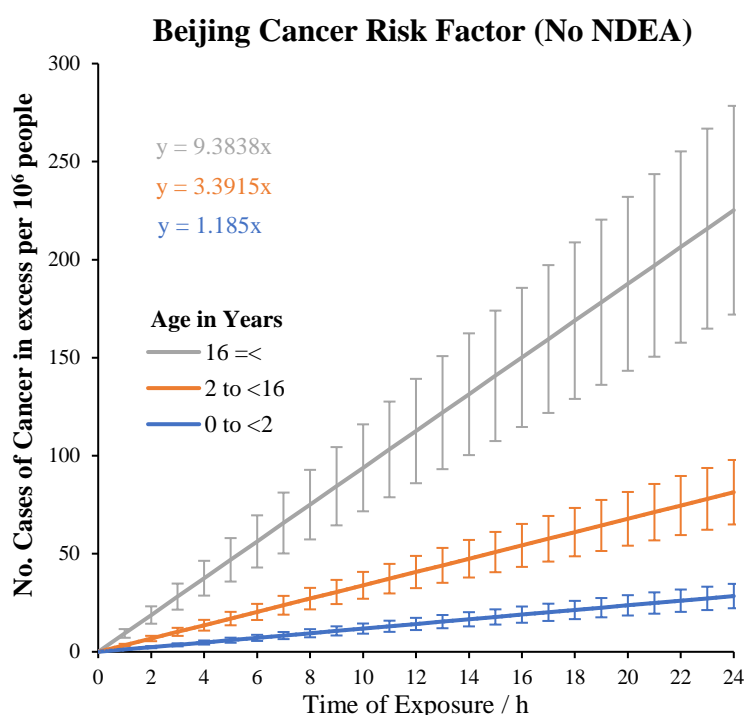


Fig. 7.12. Cancer Risk factor Assessment of Beijing imposed by the nitrosamines within PM_{2.5} (assuming no NDEA is present) as a function of the Exposure Time (ET) for different age groups. The blue, orange and grey lines show the cancer risk imposed on the 0 to < 2, 2 to < 16 and 16 =< age brackets, against the amount of time an individual is exposed to Beijing's [PM_{2.5}] (assuming no NDEA is present). The vertical error bars demonstrate the uncertainty as calculated as described in section 7.3.8.

Further work is however required in future campaigns to be able to accurately conclude (within an acceptable degree of certainty) that this is the case, by successfully separating the NDEA + N-tert-butylformamide species using GC × GC – NCD, by using a technique such as GC × GC – ToF-MS. Even if no NDEA was present and the [NDEA + N-tert-butylformamide] peak could be solely attributed to [N-tert-butylformamide], the cancer risk factor in Beijing is nevertheless higher than in London and it may therefore be concluded that the cancer risk factor in Beijing is at least 4 times larger compared to London, for the data sets analysed.

7.4 Conclusion

The use of comprehensive two-dimensional chromatography coupled to nitrogen chemiluminescence detection (GC × GC - NCD) has been successfully applied to quantify and characterize nitrosamine species in 38 filter samples taken over a 7-day period in Beijing during the winter season of 2016, using a MegaMix solution of 90 ON compounds. Both TSNAs and non-TSNAs were found to contribute to the cancer risk factor during the 7-day period examined in Beijing. It was found that the cumulative lifetime cancer risk in Beijing for inhabitants exposed to these particles was *ca.* 62 – 63 times higher compared to London (worst-case scenario). It is therefore concluded that inhabitants

in Beijing exposed to PM_{2.5} based on the samples collected are at a significantly higher risk from exposure to nitrosamines compared to people living and working in London in 2016.

Nitrosamines were found to be generally higher in concentration during the daytime based on the time series established. This has been thought to be down to a higher level of oxidation from the OH radical on amine precursors and a higher proportion of people smoking during daytime hours. In addition, nitrosamine values were found to follow the general [PM_{2.5}] trend of the 7-day period sampled. Concentrations in Beijing were generally much larger compared to London and Seoul. They were however comparable to Zonguldak in Turkey. The similarity between Beijing and Zonguldak is high industrialisation. Non-TSNAs are known to be formed from the nitrosation of amines which are released from industrial processes. The reason for the much higher nitrosamine concentrations in Beijing compared to London and Seoul may therefore be down to a higher level of industrialisation found in Beijing.

8 Conclusions

8.1 Findings and Conclusions

8.1.1 Use of Ion Chromatography for Inorganic PM_{2.5} Quantification

To accurately characterise and quantify the inorganic fraction (and CH_3SO_3^- and $\text{C}_2\text{O}_4^{2-}$) within ambient PM_{2.5} filter samples, an IC method was developed. This highlighted several data accuracy challenges which are essential for future IC users to be aware of.

It was found that using a mixed calibration standard involving both NO_2^- and NO_3^- caused partitioning between these species which caused an alteration in their respective concentrations within solution which was significant after *ca.* 3 days. Furthermore, in producing the calibration standard, cross contamination of ionic species from commercially available standards showed conductivity signals within the separate salts standard solutions, although ultimately the contribution of these contaminants to the mixed standard was deemed negligible.

At the blank correction stage of IC analysis, QMA filters were found to be sufficient for use in IC analysis for most ions, although they inconsistently leach PO_4^{3-} and Na^+ into the IC solutions. This introduced high ion concentration variability between filter sheets, which increases uncertainty in the final dataset. This also produced negative concentrations at the blank correction stage for Na^+ and PO_4^{3-} , leading to an inability to accurately assess the sea-salt contribution of anions to the final dataset.

The QMA filters also had an adverse effect on $[\text{Ca}^{2+}]$ in which Ca^{2+} was lost by adsorption onto the filter pieces via the complexes $\text{Ca}(\text{H}_2\text{O})_4$ and $\text{Ca}(\text{OH})(\text{H}_2\text{O})_3$, causing low recovery results for Ca^{2+} . The recovery results of NO_2^- were also found to be particularly low (4.0 %) when analysis was conducted using the mixed solution which was ascribed to the production of HONO which subsequently evaporates away in the gas phase from the filter piece. Improvement of recovery results was also observed using higher concentrations of solutions and pipetting smaller volumes onto filters during the protocol. This is down to ion loss through the absorption of filter paper through the foil used underneath.

Salt concentrations > 200 ppm were found to skew the chromatographic peak shape and likely damage the IC instrument. The analysis of very high loaded PM_{2.5} filter samples also caused noticeable degradation to the column and suppressor which adversely affects the LOD and LOQ. Changing the suppressor was however seen to vastly improve the LOD and LOQ for the anions analysed. Additionally, it was found that LOD and LOQ values may vary significantly depending on the method of calculation and concentration of standard used. It was found that if the concentration of calibration solutions is too high, the LOD and LOQ become unrealistically high and are not representative of the actual value. Furthermore, it was found that by implementing all the correct standard procedures in IC ion quantification does not make a substantial difference to the overall IC results (i.e. the salt cross contamination step; splitting up the calibration; not passing the calibration

equation through zero etc.) and therefore indicates that preliminary results given by the IC are already a very good representation of the final dataset. Finally, an inter-laboratory comparison was conducted between IC instruments across 10 separate laboratories world-wide, which showed good agreement between the instruments although demonstrated a higher level of uncertainty at increased solution concentrations.

8.1.2 Inter-Instrument Comparison

Inter-instrument comparisons were conducted as part of the APHH and NO3ISOP campaigns for IC measurements and were additionally compared to the AMS instrument, for data quality assurance purposes. An inter-instrument comparison of ionic concentration data during the APHH campaigns showed that across the campaigns, the work presented in this thesis was mostly in good agreement with the other IC instrument (IC_{Birm}), although comparison of the IC results to the AMS results was extensively challenging. This is predominantly down to the AMS and IC sampling different size fractions. The long duration HiVol sampling was also found to considerably affect the production of positive (acidic gas or NH_3 accumulation) and negative (ammonium salt evaporation) filter artefacts especially in these highly polluted and very hot Asian megacities. Too short a sampling time (*ca.* 30 minutes) however demonstrated $[Cl^-]$ which were very close to the LOD in many samples, artificially increasing these atmospheric concentrations for the BSUM campaign. Further difficulties in comparison arose regarding data availability between the two methods, as down-time of a single instrument causes a loss in comparison data between both instruments.

During the NO3ISOP campaign however, both the PILS and AMS were sampling $PM_{1.0}$. For the SO_4^{2-} measurements taken during this campaign, mostly excellent agreement was seen between the IC and AMS trends based on the R^2 values. However, some discrepancies were seen in the relative concentrations of SO_4^{2-} for PILS-IC and AMS methods. These discrepancies were due to either a calibration issue, particle size or the potential for Org- SO_4 formation within the chamber.

8.1.3 Inorganic Aerosol Formation in Delhi and Beijing

The ionic $PM_{2.5}$ species concentrations within Delhi and Beijing were characterised and quantified for the APHH campaigns using the experimental method developed. In both Asian megacities it was found that the change in temperatures between seasons substantially changed the overall composition of $PM_{2.5}$ aerosol. It was seen that during the warmer months in both cities, an increased proportion of the inorganic fraction was seen (78.5 % for DPEM and 62.5 % for BSUM). This was attributed to higher solar flux and temperatures causing more photooxidation during the warmer months. During the cooler months, a substantially higher fraction of organic was seen which was attributed to the DPOM campaign occurring on the lead up to Diwali with very low boundary layer heights and the BWIN campaign occurring during the heating season. During the DPOM season specifically, this was likely predominantly primary emitted organic species due to the significantly increased NO (and therefore lack of oxidising species) seen during the DPOM season compared to the other APHH campaigns. Akin to this, daytime periods in all campaigns were found to have higher SIA concentrations compared to the night-time period which was attributed to a lower solar flux, lower

temperatures, lower oxidant concentrations (from a higher [NO], [Primary Organics] and lower boundary layer height). These conditions reduced the formation of NO₂ and SO₂ to HNO₃ and H₂SO₄, respectively, during the night, inherently reducing neutralisation with NH₃.

Specifically, in Delhi the major ion concentrations were generally seen to be higher during the daytime compared to night-time hours across both the DPEM and DPOM campaigns. This was attributed to higher photooxidation levels occurring during the day causing an increase in acidic gas production which neutralises with NH₃. An exception to this general trend was the Cl⁻ DPOM average night-time concentrations which was higher compared to daytime hours. This was attributed to the reduced nocturnal boundary layer height in conjunction with significantly increased biomass burning and fireworks emissions from Diwali celebrations. In addition, a significant increase in NO_x was thought to reduce the oxidation of SO₂ and NO₂ producing less H₂SO₄ and HNO₃, respectively, therefore reducing NH₃ neutralisation by these gases, but increasing HCl + NH₃ neutralisation. These are also likely the reasons for the generally increased Cl⁻ concentrations seen during the DPOM campaign compared to the DPEM.

Generally, much higher concentrations were seen during the BWIN campaign compared to the BSUM campaign across ions. This was attributed to the considerably lower temperatures locking NH₄⁺ salts in the particle phase. Particularly for Cl⁻, a significantly lower BSUM concentration was due to the closing of the Huaneng thermal power station in very close proximity to IAP. Like Delhi, the daytime inorganic species concentrations were generally higher than the night due to increased photooxidation processes.

Further analysis of the APHH data was conducted specifically to try and identify the pathways and sources of the major atmospheric ions Cl⁻, NO₃⁻, SO₄²⁻, and NH₄⁺ into the aerosol phase. It was found that for both Delhi and Beijing, industrial emissions, garbage burning as well as coal burning were likely the predominant sources of Cl⁻. In Delhi, much higher [Cl⁻] were observed due to a considerably larger number of anthropogenic HCl emission sources from unofficial industries across the city. The BSUM campaign however showed particularly low [Cl⁻] which could potentially be attributed to the closing of the Huaneng power plant between the two campaigns. The [NO₃⁻]/[SO₄²⁻] ratio showed that Delhi has a larger contribution to PM_{2.5} from stationary sources whereas Beijing has a larger contribution from mobile sources. The NOR and SOR demonstrated that higher values were consistently seen during the day-time due to increased photooxidation. In addition, large differences in ambient temperature and solar flux caused significantly lower BWIN NOR and SOR values compared to the BSUM campaign. Particularly for the SOR during the DPEM season, it was seen that a clear increase in SOR value occurred when the wind directions had originated from the south-west of the city and had not circled around Delhi (in slower shorter trajectories) before reaching IGD TUW. This showed that the wind direction had a significant effect on the level of oxidation observed in PM_{2.5}. In addition, all SOR values across the campaigns were > 0.1 indicating that the SO₄²⁻ present in Delhi and Beijing was predominantly formed secondarily. This compares to the NOR

values which showed that during daytime hours, NO_3^- was also predominantly formed secondarily, although during night-time hours primarily emitted NO_3^- dominates the detected $[\text{NO}_3^-]$ during the DPEM and BWIN campaigns.

Although the $[\text{NO}_3^-]/[\text{SO}_4^{2-}]$, NOR and SOR give an indication as to the general sources and formation pathways to acidic gases, these provide a simplistic description. Therefore, further analysis of the pathway of production for NH_4^+ , NO_3^- , SO_4^{2-} and Cl^- in aerosol across for both megacities was conducted. Regression analysis of NH_4^+ vs [major anions] showed that neutralisation of NH_3 with the major acidic gases occurred in both megacities, for which season and temperatures greatly affected equilibria. Minor acidic gases may contribute to NH_3 neutralisation although based on the relative day and night concentrations of these anions in Delhi and Beijing, this is likely negligible.

Results from the NH_4^+ vs [major anions] regression analysis showed that the production of SIA contributing to $\text{PM}_{2.5}$ mass loading varied depending on seasons, meteorology, culture (i.e. festivals) and respective emissions. During the DPEM campaign, NH_4^+ neutralisation was dominated by SO_4^{2-} during daytime hours and was attributed to the much greater number of stationary industries scattered across Delhi releasing high concentrations of SO_2 (average of 8.0 ppbv for DPEM daytime) in conjunction with very high temperatures and solar flux inducing a high oxidation capacity of the atmosphere (where $[\text{O}_3]$ was an average of 74 ppbv during the daytime periods). $[\text{NO}_3^-]$ and $[\text{Cl}^-]$ observed almost no change within increase NH_4^+ which indicated no residual NH_3 left over to react with HNO_3 or HCl after H_2SO_4 neutralisation. Too little data was available for the DPEM night-time period to make any substantial conclusions.

During the DPOM campaign, the SIA contribution to $\text{PM}_{2.5}$ was predominantly driven by NH_4^+ neutralisation with NO_3^- during the daytime which has been attributed to high $[\text{NO}_2]$ from increased transport for Diwali celebrations, along with increased concentrations of oxidising species during the daytime. NH_4^+ neutralisation by SO_4^{2-} was also present but considerably less substantial and NH_4^+ neutralisation by Cl^- was negligible. During the DPOM night-time period, it was found that the very high $[\text{NO}]$ and [Primary Organic] provides a major sink for oxidising species reducing NO_2 and SO_2 oxidation to HNO_3 and H_2SO_4 , respectively. This resulted in primary HCl emissions contributing substantially to NH_3 neutralisation and $\text{PM}_{2.5}$ formation. In addition, it was found that during the night-time periods, the gradient of $[\text{NH}_4^+] \text{ vs } \Sigma [\text{Cl}^-] + [\text{NO}_3^-] + 2[\text{SO}_4^{2-}]$ neutralisation was 1.46 and therefore demonstrated a large excess of acidic species within the aerosol.

The BWIN campaign exhibited substantially lower temperatures compared to the other APHH campaigns and as a result the equilibrium of ammonium salt partitioning resided in the particle phase. During the day and night periods, all of SO_4^{2-} , NO_3^- and Cl^- contributed to NH_4^+ neutralisation. The largest contribution to NH_4^+ was from NO_3^- which was attributed to a larger proportion of HNO_3 from increased BWIN NO_2 from domestic heating, as well as transport.

For the BSUM campaign, increased solar flux and temperatures were found to increase NO_2 and SO_2 oxidation to HNO_3 and H_2SO_4 , respectively, neutralising NH_3 . The high temperatures caused the

NH_4Cl equilibrium to remain in the dissociated state ($\text{NH}_3 + \text{HCl}$). Insufficient HNO_3 and H_2SO_4 , as well as high temperatures, caused a minor alkaline characteristic in the BSUM night aerosol for which the $[\text{NH}_4^+] \text{ vs } \Sigma [\text{Cl}^-] + [\text{NO}_3^-] + 2[\text{SO}_4^{2-}]$ neutralisation gradient was < 1 . Therefore, this indicated that a reduction in both SO_2 and NO_2 would contribute significantly to a reduction in NO_3^- , SO_4^{2-} and NH_4^+ .

The equilibrium analysis explored within these Asian megacities however assumed that all the SIA detected was produced inorganically which is known to be the prominent pathway of SIA formation. These megacities however also comprise of large green spaces dispersed across each city (as seen in chapter 4) and therefore the presence of BVOC emissions as well as the interaction of these species with the inorganic nitrate radical could not be ignored.

To further examine the possible pathways of SIA into the aerosol phase, the formation and hydrolysis of organic nitrates during chamber experiments (SAPHIR chamber, Jülich Forschungszentrum, Germany) was investigated as part of the NO3ISOP campaign using PILS-IC. Lab experiments showed that primary organic nitrates were hydrolysable in water and likely hydrolysed via acid catalysis in an S_N^1 reaction mechanism. Zero order reaction kinetics were observed, contradicting the previous literature, although this was attributed to the [acid catalyst] being lower than the [Org- NO_3], causing the rate to be controlled by the acid catalyst.

During the chamber studies it was found that a substantial fraction of PILS $[\text{NO}_3^-]$ was comprised of [Org- NO_3]. Therefore, this indicates that the reaction between the nitrate radical and BVOCs is significant. Based on the work presented in this thesis, it is possible that some of the NO_3^- detected from Delhi and Beijing may have entered the aerosol via this organic pathway as BVOCs (as well as other unsaturated organics), NO_2 and O_3 are known to be in significant concentrations in Asian megacities.

However, substantial errors are associated with the use of PILS-IC in Org- NO_3 species detection, and therefore this method is not suitable for use during chamber studies at atmospherically relevant conditions. This is primarily due to the concentrations being mostly either below or very close to the detection limits of the IC system. It was additionally found that the use of glass during PILS sampling induced inconsistent leaching of NO_3^- and SO_4^{2-} into the PILS samples. Further significant uncertainties in the PILS-IC method in [Org- NO_3] analysis discovered in this work surround the use of AMS $[\text{NO}_3^-]$ results in calculating the PILS-IC [Org- NO_3] which is down to the interferences the AMS experiences from the inefficient Org- NO_3 species contribution to the NO^+ signal (m/z 30).

To summarise, the warmer seasons as well as daytime periods in both megacities contribute to a larger fraction of SIA in aerosol, which heavily controls $\text{PM}_{2.5}$ particle loading of the atmosphere, especially during the summer months. The SIA fraction within $\text{PM}_{2.5}$ has been shown to be strongly dependant on precursor gaseous emissions (NO_2 and NO_2) as well as meteorology and therefore this implies that SIA precursors should be the target during the warmer seasons and daytime periods, in trying to reduce atmospheric $\text{PM}_{2.5}$ mass loading. Furthermore, the fraction of inorganic species

within $PM_{2.5}$ directly alters a particle's chemical and physical properties which directly affects its radiative forcing properties, as well as its ability to absorb toxins such as nitrosamines.

To explore the impact on human health of such absorbed toxins, a GC \times GC – NCD method (in conjunction with an in lab produced 90 mixed standard of 90 ON species) was successfully applied to quantify and characterize nitrosamine species across a 7-day period in Beijing during the winter season of 2016. The nitrosamine time series developed showed that [nitrosamines] followed [$PM_{2.5}$] trends and that higher concentrations of these species were present during the daytime compared to the night. This is attributed to more cigarettes smoked and a higher level of oxidation from the OH radicals on amine precursors during daytime hours. Using this data, the cancer risk factor was calculated to estimate the excess number of cancer cases using the calculated nitrosamine concentrations. It was found that inhabitants in Beijing were at significantly higher risk of developing cancer (*ca.* 62 – 63 times higher in the worst-case scenario) in 2016 from their $PM_{2.5}$ exposure, compared to the inhabitants of London in 2012.

8.2 Recommendations

In lieu of the findings and conclusion outlined in this chapter, recommendations are put forward for IC users in data quality, as well as how to lower [$PM_{2.5}$] from the inorganic contribution.

For IC standard preparation, it is recommended to future IC users that ionic stock solutions are removed from the fridge within 30 minutes of being used to create fresh mixed standards, due to the volume of solution being temperature dependant. A fresh set of mixed salt standards should be produced *ca.* every 3 days if both NO_2^- and NO_3^- are added to the standard (due to NO_2^- and NO_3^- partitioning). It is advised that NO_2^- is removed to produce a separate single salt calibration due to the additional interaction of NO_2^- with acidic species forming HONO which may alter the [NO_2^-] within the standard. It is also recommended that salt solutions do not exceed *ca.* 200 ppm for NaCl, $NaNO_2$ and Na_2SO_4 , as to avoid skewing of the chromatographic peaks. In addition, running samples at too high concentrations is likely destructive to the instrument.

Future IC users should also be vigilant regarding their choice in filter type and brand with respect to their use case. This work highlights the issues surrounding the inconsistent contamination of Na^+ and PO_4^{3-} from Whatman (QMA) filters to ionic sample solutions during sample preparation which made sea-salt correction very challenging for the major anions. Furthermore, QMA filters were also found to bind with Ca^{2+} through complexes substantially reducing the recovery of Ca^{2+} . For ionic $PM_{2.5}$ analysis in an Asian megacity using a HiVol in future studies, it is recommended that alternative filters (such as Teflon) are considered and tested before analysis.

In the recovery analysis of ionic species, it is strongly advised that NO_2^- is removed from the anion mix to avoid losses from HONO formation and evaporation in the presence of methanesulfonic and oxalic acids in the mixture. It is also suggested to future users to aim for *ca.* 1000 ppm anion and 500 ppm cation solutions and $\leq 100 \mu l$ pipetted onto a filter piece in recovery analysis as this avoids losses of ions to the filter pieces underneath.

In quantifying the LOD and LOQ, future IC users should prepare a special anion mix for the purposes of LOD analysis in which each ion is at the lowest possible for IC analysis. Additionally, the inter-comparison work presented in this thesis with other IC instruments highlights the need for a universal calculation to be established for LOD and LOQ. Furthermore, the LOD and LOQ analyses conducted in this thesis emphasise the potential for the LOD and LOQ to degrade significantly when very high loaded PM_{2.5} samples are passed through the column and suppressor. Owing the relatively rapid column and suppressor degradation for anion mode IC and to potential instrument flux, it is recommended that the LOD and LOQ measurements are much more frequently calculated. It is also heavily suggested to future IC users to critically consider the state of their IC instrument and whether changing the column and suppressor would be beneficial, before conducting their analyses.

To improve the accuracy of this work in IC concentration calculation, it is also recommended that a quadratic fit is not used during analysis, but that a linear fit is implemented with dilution of samples if necessary. To further improve analyses, field blanks are also highly recommended

The inter-instrument comparison work over the APHH campaigns underlines the issues associated with the direct comparison of the AMS and IC instruments and it is proposed that future investigators find alternative comparison methods (such as with another IC) due to the number of caveats which are associated with sampling different size fractions. Additional outcomes of this inter-comparison brings forth the recommendation that HiVol samples in highly polluted environments are taken *ca.* every 1 – 3 hours, as to avoid the significant incorporation of positive and negative artefacts. This thesis does however also highlight that filter sampling could be particularly useful for longer term sampling or in remote locations, if an automated filter sampling system is used.

Concerning atmospheric analysis of data, chapter 4 attempted to add the APHH concentrations to an historical plot of previous measurements from publications in the effort to find trends overtime. This however proved to be extremely challenging due to limited data availability as well as large variability in the types of sampling sites; sampling locations; heights of samplers; different classification of season dates between studies; averaging methods; sampling times; sampling frequencies; sampling methods; atmospheric conditions; instruments used; quality of publication analyses; etc. There was therefore too much uncertainty to make any conclusive remarks. Moreover, the age of instrumentation and scientific techniques have also vastly improved in the past 20 years and therefore earlier studies are likely to be associated with higher error. It is recommended to future investigators that data is retrieved from modelling studies as opposed to previous publications of offline filter sampling.

The equilibrium conditions investigated of the ammonium salts in Delhi and Beijing clearly indicated which inorganic aerosol species contributed predominantly to SIA and Cl⁻ formation and therefore recommendations could be drawn out from these conclusion as to potential methods which could be implemented to reduce [PM_{2.5}] for the day and night-time periods for each city and season. During the warmer seasons (DPEM and BSUM), it is recommended that NO₂ and SO₂ are reduced as to

reduce overall HNO_3 and H_2SO_4 neutralisation with NH_3 species, reducing SIA and therefore $\text{PM}_{2.5}$ mass loading. During the cooler seasons, Cl^- was also found to contribute significantly to NH_4^+ neutralisation and therefore reductions in HCl should also be targeted during the winter seasons to further reduce NH_3 neutralisation which would in turn reduce $[\text{PM}_{2.5}]$.

The possibility of using PILS-IC as a technique to quantify the $[\text{Org-NO}_3]$ has been established for use as a comparison for much more sophisticated instrumental techniques, although significant alterations to the methods described in this thesis must be conducted by future investigators for more accurate analysis. These alterations include the use of much higher chamber concentrations which will remove the need for the concentration step. The removal of glass from the sampling technique is also necessary to avoid inconsistent leaching of NO_3^- and SO_4^{2-} from glass vials into the IC solutions, for which plastic vials are a suitable alternative. It is also advised that a PILS-IC method is not used during chamber experiments unless high enough concentrations of species are guaranteed. Moreover, the quantification of $[\text{Org-NO}_3]$ by the subtraction of the AMS $[\text{NO}_3^-]$ is advised against due to the error associated with the interferences at the NO^+ (m/z 30) peak ambiguity in AMS to correctly separate NO_3^- and Org-NO_3 . Future investigators should also be vigilant that the chamber is completely clean of the species of interest before starting the experiment. The cleaning procedure used at the chamber may not be completely effective for one's species of interest.

Finally, in order to complete an accurate assessment of cancer risk, carcinogenic data from all species in both the gas and aerosol phase is ideal, although very challenging. It is also recommended that the limit of detection of the NCD is reduced further as to conduct an even more accurate analysis. This may be achieved manually by cleaning the NCD reaction chamber as to allow a higher proportion of light to the photomultiplier tube. Future investigators must however be very careful as to avoid exposure of the photomultiplier tube to light, as this will destroy the photomultiplier tube.

8.3 Future Work

This thesis has demonstrated the successful use of offline HiVol filter sampling in conjunction with IC and $\text{GC} \times \text{GC} - \text{NCD}$ to determine the inorganic fraction of $\text{PM}_{2.5}$, as well as some of the most carcinogenic and mutagenic organic nitrogen species found within the organic fraction of aerosol, within two of the world's most polluted megacities. To develop this research further however, the IC and $\text{GC} \times \text{GC} - \text{NCD}$ instruments should be enhanced as to automate results and uncertainty analysis. By doing so, this technique could even be modified as to produce online measurements of aerosol species. This would enable a much larger time frame to be sampled giving a more representative insight into the atmospheres of these polluted megacities, as well as avoid positive and negative artefacts from filter samples.

Furthermore, these techniques should also be enhanced as to make them suitable for use within less polluted environments, incorporating lower limits of detection, as well as eliminating the caveats described in this thesis. This would allow for a direct comparison of aerosol composition and would in-turn give further insight into under which conditions and atmospheric compositions nitrosamines

and SIA preferentially form, helping to create clearer targets for governments to reduce specific emissions, as to improve air quality. Additionally, this would create the scope for these instruments to be able to measure in the countries where funding for these projects is sourced.

This thesis has also highlighted the importance of requiring aerosol size distribution data for accurate instrument inter-comparison, which is essential for any field campaign. In future field studies, the presence of a size distribution instrument which is able to measure distribution up to $PM_{2.5}$ is vital. Improvements in the understanding of inorganic aerosol formation may also be enhanced by using models such as ISORROPIA II as well as the E-AIM model to give a greater understanding of the role of ionic species found in these polluted megacities to the acidity of aerosol.

In quantifying the Org- NO_3 contribution in aerosol, an improved method to separate inorganic and Org- NO_3 should be developed as to allow for quantitative statements to be made within a smaller error. This is an important area of research, as Org- NO_3 species are known to be a sink and reservoir for NO_x and also directly affect the aerosol's chemical and physical properties. On improving the PILS-IC method to a satisfactory standard to be able to measure atmospherically relevant concentrations of species (without the need for AMS), the system should take part in field campaigns measuring ambient $PM_{2.5}$ as to try and work out under which conditions most prevalent Org- NO_3 formation occurs in a real life setting under much more complicated conditions. Knowing the key formation pathways of these species into aerosol would be very useful for modelling studies and Org- NO_3 contribution to the aerosol's radiative forcing potential.

To improve the cancer risk factor estimation, future studies should incorporate both the aerosol and gas phases into the calculation as to produce a more accurate estimation. With funding availability, a continuous measurement system of nitrosamines (as well as other carcinogenic ON compounds such as nitro-PAHs) would allow for a longer period of time to be sampled making a much more representative judgment of the cancer risk imposed by these species. In the short-term however, to develop the cancer risk estimation work further from this thesis, a complete set of ON species incorporated into the MegaMix should be quantified and characterised across the APHH Beijing winter and summer campaigns. On retrieving this data, samples should be split into day and night for further analysis. Correlations of these species to one another and the library of data obtained from the Beijing campaign will give further insight into the chemistry and formation processes of these species in Beijing's urban atmosphere. Following this, the cancer risk assessment for Delhi should also be examined. This is because Delhi showed significantly higher $PM_{2.5}$ concentrations compared to Beijing, and as nitrosamine concentrations have been shown in this study (as well as by Farren et al., (2015)²⁷⁷) to follow $PM_{2.5}$ trends, the investigation into the carcinogenicity of Delhi's $PM_{2.5}$ is vital.

Appendix

Ap Table. A. Specification of Reviewed Studies (India).

Study	Time	Season	City / Site
I1	Dec 2015–Dec 2016	Annual	Srinagar City Hemwati Nandan Bahuguna Garhwal University (HNBGU)
I2A	Oct 2007 – Mar 2008 (Urban Indoor)	Post Monsoon - Winter	Agra
I2B	Oct 2007–Mar 2008 (Urban Outdoor)	Post Monsoon - Winter	Agra
I2C	Oct 2007–Mar 2008 (Rural Indoor)	Post Monsoon - Winter	Agra
I2D	Oct 2007–Mar 2008 (Rural Outdoor)	Post Monsoon - Winter	Agra
I2E	Oct 2007–Mar 2008 (Roadside Indoor)	Post Monsoon - Winter	Agra
I2F	Oct 2007–Mar 2008 (Roadside Outdoor)	Post Monsoon - Winter	Agra
I3 + I4	8 th Dec 2006 - 7 th Jan 2007	Post-Monsoon - Winter	Ahmedabad
I5	Jan - Dec 2005	Annual	Darjeeling
I6	Jul 2009 - Jun 2010	Annual	Raipur Pt. Ravishankar Shukla University Raipur
I7A	Jan 2013 - Dec 2014; Apr - Jun	Summer	CSIR-National Physical Laboratory, New Delhi
I7B	Jan 2013 - Dec 2014; Jul - Sep	Monsoon	CSIR-National Physical Laboratory, New Delhi
I7C	Jan 2013 - Dec 2014; Oct - Jan	Post-Monsoon - Winter	CSIR-National Physical Laboratory, New Delhi
I7D	Jan 2013 - Dec 2014; Feb - Mar	Winter - Summer	CSIR-National Physical Laboratory, New Delhi
I7E	Jan 2013 - Dec 2014	Annual	CSIR-National Physical Laboratory, New Delhi
I8A	Dec 2011 - Feb 2012	Post-Monsoon - Winter	Amristar Science Building, Guru Nanak Dev University, Amritsar
I8B	Dec 2011 - Feb 2012	Post-Monsoon - Winter	School of Environmental Science Jawaharlal Nehru University Delhi
I9A	15 th - 30 th Jun 2014	Monsoon	Mathura Road, Delhi
I9B	15 th Dec 2013 - 15 th Jan 2014)	Post-Monsoon - Winter	Mathura Road, Delhi
I10	Jul 2009 - Jun 2010	Annual	Durg

I11A	Apr 2015 - Apr 2016 (Total Average)	Annual	Pune
I11B	Feb – May 2016	Summer	Pune
I11C	Jun - Sep 2015	Monsoon	Pune
I11D	Oct 2015 - Jan 2016	Post-Monsoon - Winter	Pune
I12A	Apr - Jun 2009 (Overall)	Summer	Kanpur Indian Institute of Technology, Kanpur, India
I12B	Apr - Jun 2009 (Day)	Summer	Kanpur Indian Institute of Technology, Kanpur, India
I12C	Apr - Jun 2009 (Night)	Summer	Kanpur Indian Institute of Technology, Kanpur, India
I13A	Jan 2007 - Jan 2008; Nov, Dec, Jan, Feb	Post-Monsoon - Winter	Jorhat
I13B	Jan 2007 - Jan 2008; May, Jun, Jul, Aug	Summer - Monsoon	Jorhat
I14A	8 th Apr - 30 th Jun 2007	Summer - Monsoon	Kanpur Indian Institute of Technology, Kanpur
I14B	1 st Dec 2007 - 31 st Jan 2008	Post-Monsoon - Winter	Kanpur Indian Institute of Technology, Kanpur
I14C	Overall	Annual	Kanpur Indian Institute of Technology, Kanpur
I14D	8 th Apr - 30 th Jun 2007	Summer - Monsoon	Dadanagar
I14E	1 st Dec 2007 - 31 st Jan 2008	Post-Monsoon - Winter	Dadanagar
I14F	Overall	Annual	Dadanagar
I14G	8 th Apr - 30 th Jun 2007	Summer - Monsoon	Colonelganj
I14H	1 st Dec 2007 - 31 st Jan 2008	Post-Monsoon - Winter	Colonelganj
I14I	Overall	Annual	Colonelganj
I14J	8 th Apr - 30 th Jun 2007	Summer - Monsoon	Ramadevi
I14K	1 st Dec 2007 - 31 st Jan 2008	Post-Monsoon - Winter	Ramadevi
I14L	Overall	Annual	Ramadevi
I15A	Jan 2007 - Dec 2008; May, Jun, Jul, Aug	Summer - Monsoon	Jorhat
I15B	Jan 2007 - Dec 2008; Nov, Dec, Jan, Feb	Post-Monsoon - Winter	Jorhat

I16 + I17	1 st Jan 2012 – 31 st Dec 2013	Annual	Van Vihar National Park, Bhopal
I18	Jan – Dec 2016	Annual	Indian Institute of Tropical Meteorology, Pune
I19	Apr 2013 – Nov 2014	Annual	Chemistry Department, Savitribai Phule University, Pune
I20	Jul - Nov 2011	Monsoon - Post-Monsoon	Mahabubnagar
I21	1 st Apr - 15 th Jul 2011	Summer - Monsoon	Kanpur Indian Institute of Technology, Kanpur
I22	8 th - 29 th Dec 2014	Post-Monsoon	Centre for Environmental Science and Engineering (CESE), Kanpur
I23A	Jun - Aug 2013	Monsoon	Science Block, Yogi Vemana University, Kadapa
I23B	Sept - Nov 2013	Post-Monsoon	Science Block, Yogi Vemana University, Kadapa
I23C	Dec, Jan, Feb 2014	Winter	Science Block, Yogi Vemana University, Kadapa
I23D	Mar, Apr, May 2014	Summer	Science Block, Yogi Vemana University, Kadapa
I23E	Jun - Aug 2014	Monsoon	Science Block, Yogi Vemana University, Kadapa
I23F	Sept - Nov 2014	Post-Monsoon	Science Block, Yogi Vemana University, Kadapa
I23G	Dec, Jan, Feb 2015	Winter	Science Block, Yogi Vemana University, Kadapa
I24A	Oct 2008 - Oct 2009	Annual	Raipur
I24B	Oct 2008 - Oct 2009; Oct - Jan	Post-Monsoon - Winter	Raipur
I24C	Oct 2008 - Oct 2009; Feb - Mar	Winter - Summer	Raipur
I24D	Oct 2008 - Oct 2009; Apr - Jun	Summer	Raipur
I24E	Oct 2008 - Oct 2009; Jul - Sep	Monsoon	Raipur
I25	Apr 2005 - March 2006	Annual	Raipur
I26A	12 th – 22 nd March 2013	Summer	Palampur
I26B	12 th – 22 nd March 2013	Summer	Kullu
I26C	12 th – 22 nd March 2013	Summer	Shimla

I26D	12 th – 22 nd March 2013	Summer	Solan
I26E	12 th – 22 nd March 2013	Summer	Nahan
I26F	12 th – 22 nd March 2013	Summer	Average
I27A	19 th - 30 th Oct 2008 (Day)	Post-Monsoon	Kanpur
I27B	19 th - 30 th Oct 2008 (Night)	Post-Monsoon	Kanpur
I27C	19 th - 30 th Oct 2008 (Normal)	Post-Monsoon	Kanpur
I27D	30 th Oct 2008 (Haze Event)	Post-Monsoon	Kanpur

Ap Table. B. India PM_{2.5} and Major Anion concentrations in Reviewed studies.

Study	India PM _{2.5}		India Major Anions					
	PM _{2.5}	PM _{2.5} SD	Cl ⁻	Cl ⁻ SD	NO ₃ ⁻	NO ₃ ⁻ SD	SO ₄ ²⁻	SO ₄ ²⁻ SD
I1	78.70	25.10	7.09	-	2.70	-	8.00	-
I2A	153.50	29.30	6.40	-	9.40	-	9.30	-
I2B	170.40	54.90	8.60	-	9.80	-	11.20	-
I2C	191.40	54.90	14.90	-	8.10	-	17.30	-
I2D	184.50	30.40	5.60	-	17.80	-	8.40	-
I2E	189.10	16.80	6.60	-	12.10	-	2.40	-
I2F	231.90	45.70	2.80	-	16.90	-	5.10	-
I3 + I4	55.70	17.00	0.08	0.05	1.20	0.40	9.70	4.90
I5	29.50	20.80	1.21	1.00	3.31	2.30	3.80	2.90
I6	150.90	78.60	2.10	1.82	3.12	2.63	7.86	5.86
I7A	83.66	33.12	6.92	3.63	3.76	2.16	8.38	4.30
I7B	41.62	24.10	6.47	6.18	3.56	2.70	9.90	5.01
I7C	189.84	101.05	12.54	7.08	16.46	10.85	16.16	9.48
I7D	96.80	48.52	6.59	4.35	7.19	2.33	9.83	3.62
I7E	108.00	86.50	9.46	9.17	9.49	9.18	12.62	11.21
I8A	154.76	78.78	1.08	1.11	5.99	4.62	23.25	16.09
I8B	357.30	175.00	5.27	7.03	2.49	1.98	53.19	67.23
I9A	58.20	35.00	2.14	1.54	4.37	2.14	9.97	6.25
I9B	276.90	99.90	27.80	18.10	32.80	20.10	26.10	15.30
I10	135.00	76.20	2.06	2.10	3.16	3.62	6.75	6.04
I11A	37.30	12.20	3.42	1.59	0.98	0.78	4.80	3.16
I11B	41.70	10.80	3.20	2.09	1.45	0.86	4.90	2.10
I11C	26.40	4.80	3.98	1.28	0.46	0.31	2.22	1.29
I11D	43.90	11.10	3.09	1.17	1.08	0.72	7.16	3.28
I12A	142.70	43.20	1.30	0.40	12.90	4.20	19.70	7.60
I12B	163.30	51.90	1.30	0.50	10.60	3.20	22.50	8.60
I12C	122.10	34.20	1.20	0.40	15.10	4.30	16.80	6.50

I13A	143.50	24.00	0.14	0.02	5.52	1.49	18.17	6.31
I13B	108.00	19.00	0.12	0.02	3.62	1.29	10.70	3.81
I14A	136.00	23.00	0.60	0.10	5.20	0.90	19.40	3.50
I14B	172.00	46.00	1.70	0.50	8.10	2.20	22.70	6.30
I14C	154.00	-	1.10	-	6.60	-	21.00	-
I14D	232.00	68.00	3.60	1.10	16.90	5.20	38.90	11.20
I14E	304.00	69.00	5.20	1.20	29.10	6.70	45.90	10.70
I14F	268.00	-	4.40	-	22.90	-	42.40	-
I14G	218.00	54.00	1.80	0.50	29.20	7.50	27.80	7.60
I14H	215.00	47.00	2.40	0.50	32.30	7.30	24.60	5.40
I14I	216.00	-	2.10	-	30.80	-	26.20	-
I14J	170.00	50.00	0.90	0.30	15.90	4.80	19.20	5.70
I14K	207.00	59.00	2.30	0.60	22.50	6.60	22.40	6.20
I14L	188.00	-	1.60	-	19.20	-	20.80	-
I15A	132.10	18.00	-	-	3.87	0.73	4.67	2.22
I15B	143.50	23.00	-	-	4.87	0.48	5.74	3.84
I16 + I17	44.00	41.00	1.46	1.89	3.02	3.93	3.35	2.23
I18	40.00	-	-	-	1.06	-	3.95	-
I19	97.70	-	6.10	-	3.50	-	5.70	-
I20	50.00	10.00	12.72	12.49	6.39	13.43	19.76	14.65
I21	37.61	-	2.06	1.82	3.10	2.83	5.38	2.51
I22	240.00	72.00	4.50	1.60	10.50	6.00	23.50	8.70
I23A	21.70	4.80	6.67	-	3.15	-	7.10	-
I23B	31.60	4.40	3.78	-	3.68	-	11.29	-
I23C	33.10	0.10	1.35	-	3.41	-	13.32	-
I23D	24.70	3.20	1.76	-	5.08	-	12.08	-
I23E	17.50	1.90	4.28	-	5.36	-	13.96	-
I23F	37.20	8.50	8.86	-	2.18	-	3.99	-
I23G	35.50	3.20	1.40	-	3.87	-	17.94	-
I24A	185.90	66.90	9.72	3.14	13.45	5.66	36.75	9.91
I24B	268.20	27.00	12.02	3.41	18.21	7.77	48.04	3.26
I24C	197.80	18.60	10.92	0.11	12.57	1.52	33.19	7.64
I24D	128.30	13.80	8.51	2.07	11.67	1.88	30.42	6.18
I24E	126.00	15.40	7.07	2.78	9.44	2.43	28.01	8.64
I25	167.00	75.30	6.83	3.55	8.16	7.08	46.50	32.80
I26A	47.50	7.13	5.84	1.21	1.72	0.39	2.27	0.52
I26B	34.32	1.32	5.43	1.33	0.82	0.35	1.16	0.23
I26C	32.13	2.65	5.08	2.08	0.75	0.32	1.86	0.72
I26D	53.33	5.57	3.52	0.99	1.03	0.44	2.07	0.83
I26E	41.63	4.49	3.76	1.05	1.33	0.54	1.23	0.36
I26F	41.78	7.92	4.69	0.84	1.13	0.36	1.76	0.45
I27A	133.00	61.00	0.05	0.02	2.10	2.10	13.60	8.80
I27B	192.00	83.00	1.30	1.80	9.40	4.60	13.50	6.10
I27C	127.20	37.20	-	-	3.40	2.90	11.60	4.70
I27D	295.80	24.80	-	-	13.00	4.90	24.90	8.70

Ap Table. C. India Minor Anion concentrations in Reviewed studies.

Study	India Minor Anions					
	F ⁻	F ⁻ SD	NO ₂ ⁻	NO ₂ ⁻ SD	PO ₄ ³⁻	PO ₄ ³⁻ SD
I1	0.03	-	0.07	-	-	-
I2A	1.60	-	-	-	-	-
I2B	4.80	-	-	-	-	-
I2C	0.40	-	-	-	-	-
I2D	0.80	-	-	-	-	-
I2E	0.80	-	-	-	-	-
I2F	0.40	-	-	-	-	-
I3 + I4	-	-	-	-	-	-
I5	-	-	-	-	-	-
I6	-	-	-	-	-	-
I7A	0.84	0.62	-	-	-	-
I7B	0.53	0.65	-	-	-	-
I7C	0.85	0.66	-	-	-	-
I7D	0.92	0.65	-	-	-	-
I7E	0.90	0.88	-	-	-	-
I8A	0.01	0.03	-	-	-	-
I8B	0.10	0.10	-	-	-	-
I9A	-	-	-	-	-	-
I9B	-	-	-	-	-	-
I10	-	-	-	-	-	-
I11A	-	-	-	-	-	-
I11B	-	-	-	-	-	-
I11C	-	-	-	-	-	-
I11D	-	-	-	-	-	-
I12A	-	-	-	-	-	-
I12B	-	-	-	-	-	-
I12C	-	-	-	-	-	-
I13A	-	-	-	-	-	-
I13B	-	-	-	-	-	-
I14A	-	-	-	-	-	-
I14B	-	-	-	-	-	-
I14C	-	-	-	-	-	-
I14D	-	-	-	-	-	-
I14E	-	-	-	-	-	-
I14F	-	-	-	-	-	-
I14G	-	-	-	-	-	-
I14H	-	-	-	-	-	-
I14I	-	-	-	-	-	-
I14J	-	-	-	-	-	-
I14K	-	-	-	-	-	-
I14L	-	-	-	-	-	-
I15A	-	-	-	-	-	-
I15B	-	-	-	-	-	-

I16 + I17	0.35	0.58	0.30	0.55	0.31	0.35
I18	-	-	-	-	-	-
I19	-	-	-	-	-	-
I20	-	-	-	-	-	-
I21	-	-	-	-	-	-
I22	-	-	-	-	-	-
I23A	2.88	-	-	-	1.03	-
I23B	1.72	-	2.46	-	1.00	-
I23C	0.82	-	-	-	2.22	-
I23D	0.24	-	1.16	-	2.42	-
I23E	0.08	-	-	-	3.74	-
I23F	2.36	-	0.88	-	3.21	-
I23G	0.56	-	-	-	-	-
I24A	-	-	-	-	-	-
I24B	-	-	-	-	-	-
I24C	-	-	-	-	-	-
I24D	-	-	-	-	-	-
I24E	-	-	-	-	-	-
I25	-	-	-	-	-	-
I26A	1.13	0.61	0.84	0.23	0.80	0.21
I26B	0.16	0.08	0.90	0.41	0.35	0.15
I26C	0.72	0.13	0.70	0.35	0.56	0.31
I26D	0.88	0.18	0.36	0.12	0.97	0.32
I26E	1.01	0.32	0.83	0.24	0.77	0.28
I26F	0.78	0.34	0.73	0.20	0.69	0.22
I27A	-	-	-	-	-	-
I27B	-	-	-	-	-	-
I27C	-	-	-	-	-	-
I27D	-	-	-	-	-	-

Ap Table. D. India Cation concentrations in Reviewed studies.

Study	India Cations									
	Na ⁺	Na ⁺ SD	NH ₄ ⁺	NH ₄ ⁺ SD	K ⁺	K ⁺ SD	Mg ²⁺	Mg ²⁺ SD	Ca ²⁺	Ca ²⁺ SD
I1	5.49	-	3.61	-	2.43	-	0.40	-	3.85	-
I2A	7.60	-	0.40	-	1.10	-	9.90	-	9.60	-
I2B	13.50	-	0.50	-	3.50	-	11.80	-	9.90	-
I2C	10.90	-	0.80	-	6.80	-	7.90	-	14.50	-
I2D	5.90	-	0.90	-	9.60	-	5.90	-	11.90	-
I2E	2.70	-	0.30	-	1.20	-	7.00	-	14.20	-
I2F	5.50	-	3.50	-	2.50	-	8.20	-	12.30	-
I3 + I4	0.44	0.20	3.20	1.40	0.90	0.30	0.04	0.02	0.50	0.20
I5	0.66	0.43	0.88	0.76	1.20	0.80	0.12	0.06	0.13	0.01
I6	0.92	0.67	1.94	1.28	0.52	0.35	0.26	0.17	0.91	0.74
I7A	3.40	1.75	7.14	2.29	3.30	1.62	0.40	0.29	3.23	2.80
I7B	7.28	4.54	2.89	2.51	2.47	2.38	1.02	0.69	2.12	1.64
I7C	6.08	3.70	12.91	9.15	5.29	3.06	1.03	0.93	3.09	2.67

I7D	3.50	2.85	8.60	4.23	2.86	1.22	0.33	0.29	2.10	0.94
I7E	5.52	4.17	8.85	8.38	3.68	2.57	0.81	0.80	2.68	2.24
I8A	0.60	0.17	7.54	6.87	2.85	1.44	0.09	0.09	0.91	0.92
I8B	1.38	1.31	10.90	7.70	7.70	1.70	0.20	0.10	3.06	2.58
I9A	0.41	0.38	4.94	2.87	0.86	0.49	-	-	-	-
I9B	0.64	0.30	34.20	17.00	3.83	1.63	-	-	-	-
I10	1.08	1.19	2.13	1.04	0.87	0.70	0.18	0.20	0.70	0.52
I11A	1.98	0.53	0.51	0.80	0.47	0.53	0.28	0.08	0.51	0.40
I11B	2.05	0.73	1.07	1.16	0.42	0.18	0.30	0.10	0.71	0.59
I11C	2.04	0.49	0.16	0.33	0.13	0.06	0.29	0.07	0.52	0.28
I11D	1.87	0.28	0.38	0.38	0.79	0.73	0.25	0.06	0.33	0.11
I12A	2.10	1.40	13.10	3.80	1.50	0.80	1.10	0.40	2.90	1.50
I12B	2.20	1.50	13.50	4.50	1.10	0.60	1.40	0.50	4.20	2.10
I12C	1.90	1.10	12.70	4.80	1.80	1.00	0.80	0.40	1.80	0.90
I13A	-	-	2.13	0.40	-	-	-	-	-	-
I13B	-	-	2.53	0.50	-	-	-	-	-	-
I14A	1.30	0.20	9.40	1.70	2.10	0.40	1.00	0.20	2.70	0.50
I14B	1.80	0.50	10.30	2.80	3.20	0.90	1.30	0.30	2.30	0.60
I14C	1.50	-	9.80	-	2.60	-	1.20	-	2.50	-
I14D	3.40	1.10	20.20	6.10	2.00	0.60	0.90	0.30	5.20	1.60
I14E	4.50	1.10	24.10	5.30	3.60	0.60	0.50	0.10	3.90	0.80
I14F	4.00	-	22.10	-	2.80	-	0.70	-	4.50	-
I14G	3.60	0.90	18.40	4.70	2.60	0.70	1.70	0.40	4.40	1.00
I14H	4.40	1.00	16.50	3.70	3.50	0.80	0.90	0.20	3.80	0.80
I14I	4.00	-	17.40	-	3.00	-	1.30	-	4.10	-
I14J	1.40	0.50	12.50	3.60	1.90	0.60	1.80	0.60	4.10	1.30
I14K	2.10	0.60	14.70	4.00	2.60	0.60	1.10	0.40	3.40	1.00
I14L	1.80	-	13.60	-	2.20	-	1.40	-	3.80	-
I15A	-	-	2.32	0.60	-	-	-	-	-	-
I15B	-	-	2.42	0.50	-	-	-	-	-	-
I16 + I17	0.96	1.60	2.07	2.56	0.98	1.07	0.18	0.14	0.77	0.82
I18	-	-	0.34	-	0.43	-	0.32	-	0.60	-
I19	7.90	-	3.40	-	3.80	-	2.00	-	3.10	-
I20	9.76	3.61	-	-	4.79	3.88	0.90	0.78	2.72	1.71
I21	-	-	2.54	1.87	-	-	-	-	-	-
I22	0.30	0.20	12.80	4.90	1.80	1.00	-	-	0.70	0.40
I23A	6.43	-	-	-	2.38	-	1.06	-	7.49	-
I23B	8.59	-	-	-	10.40	-	1.00	-	3.88	-
I23C	3.43	-	0.23	-	1.07	-	0.85	-	2.59	-
I23D	5.10	-	3.05	-	1.66	-	0.86	-	2.44	-
I23E	5.25	-	0.46	-	1.94	-	1.12	-	1.56	-
I23F	2.99	-	15.93	-	2.76	-	0.97	-	1.75	-
I23G	2.90	-	10.64	-	4.98	-	1.22	-	10.80	-
I24A	4.12	2.06	13.41	4.20	7.69	2.05	1.69	0.35	18.67	5.40
I24B	3.71	1.53	17.67	3.35	9.38	1.80	1.73	0.44	16.71	6.14
I24C	4.98	1.15	10.48	0.21	7.68	0.39	1.87	0.10	22.29	7.84
I24D	6.53	0.57	13.43	3.43	7.45	1.91	1.90	0.10	22.39	3.08

I24E	1.68	0.33	9.66	1.52	5.68	1.64	1.29	0.16	15.15	1.78
I25	7.41	3.55	8.76	7.67	5.90	3.43	1.69	0.58	10.20	2.98
I26A	1.27	0.37	4.96	1.32	0.50	0.19	0.57	0.19	3.23	1.01
I26B	0.94	0.44	1.28	0.37	2.21	0.52	0.22	0.11	1.54	0.68
I26C	0.70	0.29	1.51	0.53	1.79	0.58	0.38	0.12	0.65	0.25
I26D	0.73	0.35	4.05	1.22	0.41	0.17	0.03	0.01	2.27	0.98
I26E	1.77	0.54	2.32	0.97	1.01	0.52	0.28	0.09	1.64	0.83
I26F	1.08	0.41	2.82	1.44	1.18	0.71	0.30	0.17	1.85	0.87
I27A	0.20	0.10	5.20	3.70	2.20	1.80	0.05	0.02	0.30	0.10
I27B	0.30	0.10	5.30	3.70	2.60	0.70	0.04	0.02	0.30	0.10
I27C	-	-	4.40	1.80	1.90	0.80	-	-	-	-
I27D	-	-	9.10	4.10	4.20	2.30	-	-	-	-

Ap Table. E. Specification of Reviewed Studies (China).

Study	Time	Season	Site
C1A	1 st Aug - 21 st Aug 2009	Summer	Taiyuan
C1B	29 th Sep - 27 th Oct 2009	Autumn	Taiyuan
C1C	16 th Nov - 9 th Dec 2009	Winter	Taiyuan
C1D	26 th Mar - 18 th Apr 2010	Spring	Taiyuan
C1E	Aug 2009 - Apr 2010	Annual	Taiyuan
C2A	9 th Mar - 20 th Apr 2004 (Day)	Spring	Fudan University, Shanghai
C2B	15 th Jul - 16 th Aug 2004 (Day)	Summer	Fudan University, Shanghai
C2C	4 th Sep - 10 th Oct 2003 (Day)	Autumn	Fudan University, Shanghai
C2D	24 th Nov 2004 - 4 th Jan 2005 (Day)	Winter	Taopu, Shanghai
C2E	24 th Nov 2004 - 4 th Jan 2005 (Night)	Winter	Taopu, Shanghai
C2F	2004 - 2005 (Total Study)	Total	Shanghai
C3A	29 th Jun - 2 nd Aug 2005	Summer	Hei Shan Zhai, Beijing (40°21'00.0"N 116°18'00.0"E)
C3B	5 th May - 15 th Jun 2005	Summer	Tai Cang, Shanghai
C3C	18 th Jun - 17 th Jul 2006	Summer	Renshoushan Park, Lanzhou
C3D	15 th - 27 th May 2004	Spring	Wan Qing Sha, Guangzhou

C4A	17 th Jul - 26 th Jul 2010	Summer	Information Science and Engineering School, Shandong University, Jinan
C4B	11 th Oct - 27 th Oct 2010	Autumn	Information Science and Engineering School, Shandong University, Jinan
C5A	18 th Oct 2013 – 17 th Nov 2014	Annual	Meteorology building, University of Information Science & Technology, Nanjing
C5B	18 th Oct 2013 – 17 th Nov 2014; Mar - May	Spring	Meteorology building, University of Information Science & Technology, Nanjing
C5C	18 th Oct 2013 – 17 th Nov 2014; Jun - Aug	Summer	Meteorology building, University of Information Science & Technology, Nanjing
C5D	18 th Oct 2013 – 17 th Nov 2014; Sep - Nov	Autumn	Meteorology building, University of Information Science & Technology, Nanjing
C5E	18 th Oct 2013 – 17 th Nov 2014; Dec - Feb	Winter	Meteorology building, University of Information Science & Technology, Nanjing
C6A	Dec 2014 - Feb 2015	Winter	The University of Nottingham, Ningbo (UNNC)
C6B	Mar - May 2015	Spring	The University of Nottingham, Ningbo (UNNC)
C6C	Jun - Aug 2015	Summer	The University of Nottingham, Ningbo (UNNC)
C6D	Sep - Nov 2015	Autumn	The University of Nottingham, Ningbo (UNNC)
C6E	Dec 2014 - Nov 2015	Annual	The University of Nottingham, Ningbo (UNNC)
C6F	Dec 2014 - Feb 2015	Winter	Meteorological Bureau, Ningbo (NMB)
C6G	Mar - May 2015	Spring	Meteorological Bureau, Ningbo (NMB)
C6H	Jun - Aug 2015	Summer	Meteorological Bureau, Ningbo (NMB)
C6I	Sep - Nov 2015	Autumn	Meteorological Bureau, Ningbo (NMB)
C6J	Dec 2014 - Nov 2015	Annual	Meteorological Bureau, Ningbo (NMB)
C6K	Dec 2014 - Feb 2015	Winter	Regional Atmospheric Background Station, Lin'an (LRABS)
C6L	Mar - May 2015	Spring	Regional Atmospheric Background Station, Lin'an (LRABS)
C6M	Jun - Aug 2015	Summer	Regional Atmospheric Background Station, Lin'an (LRABS)
C6N	Sep - Nov 2015	Autumn	Regional Atmospheric Background Station, Lin'an (LRABS)
C6O	Dec 2014 - Nov 2015	Annual	Regional Atmospheric Background Station, Lin'an (LRABS)

C6P	Dec 2014 - Feb 2015	Winter	Meteorological Bureau, Hangzhou (HMB)
C6Q	Mar - May 2015	Spring	Meteorological Bureau, Hangzhou (HMB)
C6R	Jun - Aug 2015	Summer	Meteorological Bureau, Hangzhou (HMB)
C6S	Sep - Nov 2015	Autumn	Meteorological Bureau, Hangzhou (HMB)
C6T	Dec 2014 - Nov 2015	Annual	Meteorological Bureau, Hangzhou (HMB)
C7A	1 st Jan - 31 st Dec 2011; Mar - May	Spring	Shanghai Academy of Environmental Sciences, Shanghai (SAES)
C7B	1 st Jan - 31 st Dec 2011; Jun - Aug	Summer	Shanghai Academy of Environmental Sciences, Shanghai (SAES)
C7C	1 st Jan - 31 st Dec 2011; Sep - Nov	Autumn	Shanghai Academy of Environmental Sciences, Shanghai (SAES)
C7D	1 st Jan - 31 st Dec 2011; Jan, Feb, Dec	Winter	Shanghai Academy of Environmental Sciences, Shanghai (SAES)
C8	Jan 2016 - Jan 2017	Annual	Chifeng
C9A	Mar 2013 - Feb 2014	Annual	E-Waste Centre, near Qingyuan (N 23.59°, E 113.03°)
C9B	Mar 2013 - Feb 2014	Annual	Guangzhou (Urban), (N 23.25°, E 113.60°)
C9C	Mar 2013 - Feb 2014	Annual	Dinghushan Mountain National Nature Reserve (Background) (N 23.20°, E 112.52°)
C10A	May 2012 - May 2013	Annual	Chengdu (104°60' E, 30°36' N)
C10B	May 2012 - May 2013	Annual	Rooftop of Neijiang Environmental Monitoring Center, Neijiang
C10C	May 2012 - May 2013	Annual	Chongqing (29°370' N, 106°30'E)
C11A	28 th Dec 2006 - 31 st Jan 2007	Winter	Tianjin (Urban)
C11B	28 th Dec 2006 - 31 st Jan 2007	Winter	Tianjin (Industrial)
C11C	28 th Dec 2006 - 31 st Jan 2007	Winter	Tianjin (Coastal)
C11D	28 th Dec 2006 - 31 st Jan 2007	Winter	Tianjin (Average)
C12	15 th Oct - 5 th Nov 2004	Autumn	Guangzhou (Centre)
C13A	Jan - Feb 2002	Winter	Polytechnic University, Hong Kong
C13B	Jan - Feb 2002	Winter	Baptist University, Hong Kong
C13C	Jan - Feb 2002	Winter	Hok Tsui, Hong Kong
C13D	Jan - Feb 2002	Winter	Sun Yat-Sen University, Guangzhou

C13E	Jan - Feb 2002	Winter	Huangpu District, Guangzhou
C13F	Jan - Feb 2002	Winter	Longgui, Guangzhou
C13G	Jan - Feb 2002	Winter	Luohu, Honghu Park, ShenZhen
C13H	Jan - Feb 2002	Winter	1st Middle School of Zhuhai, Xiangzhou, Zhuhai
C13I	Jun - Jul 2002	Summer	Polytechnic University, Hong Kong
C13J	Jun - Jul 2002	Summer	Baptist University, Hong Kong
C13K	Jun - Jul 2002	Summer	Hok Tsui, Hong Kong
C13L	Jun - Jul 2002	Summer	Sun Yat-Sen University, Guangzhou
C13M	Jun - Jul 2002	Summer	Huangpu District, Guangzhou
C13N	Jun - Jul 2002	Summer	Longgui, Guangzhou
C13O	Jun - Jul 2002	Summer	Luohu, Honghu Park, ShenZhen
C13P	Jun - Jul 2002	Summer	1st Middle School of Zhuhai, Xiangzhou, Zhuhai
C14	13 th Nov - 23 rd Dec 2016	Winter	Railway Vocational School, Xi'an
C15A	Nov & Dec; 2009 & 2010	Winter	Suburb of Shenzhen (22°35'N, 113°58'E)
C15B	Jul & Aug; 2009 & 2010	Summer	Suburb of Shenzhen (22°35'N, 113°58'E)
C16A	Mar - May 2012	Spring	Institute of Earth Environment, Chinese Academy of Sciences, Xi'an High-Tech Zone
C16B	Jun - Aug 2012	Summer	Institute of Earth Environment, Chinese Academy of Sciences, Xi'an High-Tech Zone
C16C	Sep - Nov 2012	Autumn	Institute of Earth Environment, Chinese Academy of Sciences, Xi'an High-Tech Zone
C16D	Dec 2012 - Feb 2013	Winter	Institute of Earth Environment, Chinese Academy of Sciences, Xi'an High-Tech Zone
C16E	Mar 2012 - Mar 2013	Annual	Institute of Earth Environment, Chinese Academy of Sciences, Xi'an High-Tech Zone
C16F	Mar - May 2012	Spring	Jiaotong University, Xi'an
C16G	Jun - Aug 2012	Summer	Jiaotong University, Xi'an
C16H	Sep - Nov 2012	Autumn	Jiaotong University, Xi'an
C16I	Dec 2012 - Feb 2013	Winter	Jiaotong University, Xi'an
C16J	Mar 2012 - Mar 2013	Annual	Jiaotong University, Xi'an
C16K	Mar - May 2012	Spring	North Third Ring, Wei Shui Campus, Chang'an University, Xi'an
C16L	Jun - Aug 2012	Summer	North Third Ring, Wei Shui Campus, Chang'an University, Xi'an

C16M	Sep - Nov 2012	Autumn	North Third Ring, Wei Shui Campus, Chang'an University, Xi'an
C16N	Dec 2012 - Feb 2013	Winter	North Third Ring, Wei Shui Campus, Chang'an University, Xi'an
C16O	Mar 2012 - Mar 2013	Annual	North Third Ring, Wei Shui Campus, Chang'an University, Xi'an
C16P	Mar - May 2012	Spring	Municipal Environmental Protection Bureau, Weinan
C16Q	Jun - Aug 2012	Summer	Municipal Environmental Protection Bureau, Weinan
C16R	Sep - Nov 2012	Autumn	Municipal Environmental Protection Bureau, Weinan
C16S	Dec 2012 - Feb 2013	Winter	Municipal Environmental Protection Bureau, Weinan
C16T	Mar 2012 - Mar 2013	Annual	Municipal Environmental Protection Bureau, Weinan
C16U	Mar - May 2012	Spring	Municipal Environmental Protection Bureau, Baoji
C16V	Jun - Aug 2012	Summer	Municipal Environmental Protection Bureau, Baoji
C16W	Sep - Nov 2012	Autumn	Municipal Environmental Protection Bureau, Baoji
C16X	Dec 2012 - Feb 2013	Winter	Municipal Environmental Protection Bureau, Baoji
C16Y	Mar 2012 - Mar 2013	Annual	Municipal Environmental Protection Bureau, Baoji
C16Z	Mar - May 2012	Spring	Cuihua Mountain, Qinling Mountains
C16AA	Jun - Aug 2012	Summer	Cuihua Mountain, Qinling Mountains
C16AB	Sep - Nov 2012	Autumn	Cuihua Mountain, Qinling Mountains
C16AC	Dec 2012 - Feb 2013	Winter	Cuihua Mountain, Qinling Mountains
C16AD	Mar 2012 - Mar 2013	Annual	Cuihua Mountain, Qinling Mountains
C17A	Apr 2009 - Jan 2010	Total	Science Building, Peking University, Beijing (116.30° E, 39.99° N)
C17B	Apr 2009 (high-speed winds, low rainfall)	Spring	Science Building, Peking University, Beijing (116.30° E, 39.99° N)
C17C	Jul 2009 (high temp, frequent rain)	Summer	Science Building, Peking University, Beijing (116.30° E, 39.99° N)
C17D	Oct 2009 (sunny days, northwest winds)	Autumn	Science Building, Peking University, Beijing (116.30° E, 39.99° N)

C17E	Jan 2010 (cold, dry air)	Winter	Science Building, Peking University, Beijing (116.30° E, 39.99° N)
------	--------------------------	--------	---

Ap Table. F. China PM_{2.5} and Major Anion concentrations in Reviewed studies.

Study	China PM _{2.5}		China Major Anions							
	PM _{2.5}	PM _{2.5} SD	Cl ⁻	Cl ⁻ SD	NO ₃ ⁻	NO ₃ ⁻ SD	SO ₄ ²⁻	SO ₄ ²⁻ SD	C ₂ O ₄ ²⁻	C ₂ O ₄ ²⁻ SD
C1A	135.78	-	1.57	0.86	8.88	3.26	28.35	13.68	-	-
C1B	182.24	-	3.87	2.62	9.16	7.38	15.77	12.27	-	-
C1C	257.29	-	13.50	5.50	13.71	6.99	57.21	39.67	-	-
C1D	251.17	-	5.69	5.11	12.99	11.71	19.62	16.98	-	-
C1E	209.54	-	6.48	6.15	11.64	8.75	29.97	28.02	-	-
C2A	134.77	34.01	5.28	-	9.05	-	11.73	-	0.33	-
C2B	71.66	28.20	0.50	-	2.59	-	5.43	-	0.34	-
C2C	96.38	28.54	0.93	-	3.70	-	8.70	-	0.29	-
C2D	76.09	40.97	3.40	-	8.53	-	12.79	-	0.25	-
C2E	89.16	59.93	4.55	-	6.96	-	13.06	-	0.23	-
C2F	94.64	45.52	3.00	-	6.23	-	10.39	-	0.30	-
C3A	68.00	61.00	0.40	-	9.90	12.00	22.60	26.10	-	-
C3B	67.00	28.00	1.90	-	7.10	6.70	15.80	9.80	-	-
C3C	65.00	29.00	5.50	-	3.20	2.00	9.80	5.60	-	-
C3D	55.00	28.00	0.90	-	5.20	3.80	13.10	5.50	-	-
C4A	115.92	44.84	0.50	0.37	22.41	10.96	53.72	16.35	-	-
C4B	150.88	73.07	2.56	3.22	18.46	15.66	25.56	17.47	-	-
C5A	83.58	46.94	3.74	3.38	18.85	17.66	28.31	19.83	-	-
C5B	80.06	25.60	3.28	3.17	17.81	14.19	29.79	18.25	-	-
C5C	69.85	40.60	1.96	1.50	11.65	10.16	20.05	14.24	-	-
C5D	73.04	34.90	3.10	1.83	15.25	11.58	22.17	13.47	-	-
C5E	123.38	62.08	6.79	4.32	32.95	24.75	44.27	23.58	-	-
C6A	74.40	30.30	2.50	1.60	10.60	5.20	8.10	4.10	-	-
C6B	44.00	17.40	2.20	3.20	6.60	3.40	7.40	4.10	-	-
C6C	27.70	8.50	0.40	0.70	2.30	1.30	6.40	3.40	-	-
C6D	50.10	27.70	0.80	0.90	5.40	3.90	6.40	3.50	-	-
C6E	51.20	29.10	1.50	2.00	6.50	4.90	7.10	3.80	-	-
C6F	98.10	36.40	3.50	2.30	10.30	7.60	10.70	4.00	-	-
C6G	79.30	26.70	0.90	0.80	5.50	4.00	8.80	4.60	-	-
C6H	33.60	11.00	0.30	0.30	1.70	1.40	7.60	3.10	-	-
C6I	71.20	47.50	1.10	0.90	10.30	12.40	11.20	6.70	-	-
C6J	70.40	40.60	1.50	1.80	7.00	8.30	9.60	4.80	-	-
C6K	93.70	36.40	1.30	1.10	15.20	8.70	12.50	7.10	-	-
C6L	59.00	36.40	0.50	0.60	8.50	9.30	9.00	4.80	-	-
C6M	42.60	18.50	0.20	0.10	2.40	2.00	11.80	7.40	-	-
C6N	60.70	29.70	0.30	0.30	6.70	5.30	10.90	4.70	-	-
C6O	66.30	36.60	0.60	0.80	8.70	8.50	11.20	6.30	-	-
C6P	108.40	44.20	3.40	2.30	21.90	12.60	16.50	9.60	-	-
C6Q	82.60	24.50	1.00	0.80	13.30	8.10	12.80	6.10	-	-
C6R	48.40	17.60	0.40	0.50	5.70	5.80	11.90	6.20	-	-
C6S	68.00	29.70	0.90	0.60	12.30	8.90	12.70	6.00	-	-

C6T	80.00	39.60	1.70	1.90	14.20	11.30	13.80	7.60	-	-
C7A	55.00	35.00	3.50	1.60	12.07	9.93	11.29	7.71	-	-
C7B	34.00	26.00	2.21	1.20	6.43	7.58	9.54	6.99	-	-
C7C	40.00	39.00	1.20	1.28	7.67	10.66	9.67	8.78	-	-
C7D	65.00	55.00	4.21	6.21	13.33	11.23	11.70	10.16	-	-
C8	36.69	27.56	1.00	2.18	2.49	4.06	4.96	5.54	-	-
C9A	182.00	62.00	1.77	1.43	6.28	5.90	14.77	7.30	-	-
C9B	73.00	31.00	0.69	0.77	5.45	5.87	10.84	6.50	-	-
C9C	80.80	31.70	0.48	0.47	4.51	5.62	11.13	5.97	-	-
C10A	86.70	49.70	2.46	2.17	11.90	10.30	17.70	11.20	-	-
C10B	78.60	36.80	0.95	0.88	7.10	7.10	18.10	10.00	-	-
C10C	71.70	36.90	0.69	0.75	7.80	6.50	17.60	9.60	-	-
C11A	206.60	143.40	8.50	5.10	17.10	16.90	40.90	45.50	-	-
C11B	248.20	170.80	11.10	6.10	13.60	16.70	32.50	42.40	-	-
C11C	215.60	193.90	8.60	7.20	16.80	20.10	45.60	75.70	-	-
C11D	223.00	-	9.30	-	15.90	-	39.70	-	-	-
C12	153.90	-	1.20	-	8.80	-	38.60	-	-	-
C13A	60.40	22.90	1.40	0.70	6.10	3.60	10.70	4.20	-	-
C13B	48.50	24.70	1.80	0.90	4.20	2.50	8.10	4.10	-	-
C13C	41.30	20.00	1.40	0.60	3.50	1.20	11.80	2.60	-	-
C13D	90.50	41.00	2.70	1.40	10.20	2.30	15.00	6.00	-	-
C13E	104.00	77.80	5.30	2.10	4.70	3.80	12.90	5.40	-	-
C13F	138.60	111.60	6.30	5.60	11.20	9.70	17.30	6.70	-	-
C13G	60.80	18.00	2.10	0.60	4.40	1.80	13.00	3.00	-	-
C13H	59.30	23.70	2.10	0.50	8.60	2.50	17.10	4.80	-	-
C13I	40.10	19.70	0.50	0.20	1.70	1.10	9.10	3.70	-	-
C13J	30.80	7.60	0.40	0.10	1.50	0.50	5.70	2.20	-	-
C13K	15.80	2.40	0.80	0.50	0.60	0.10	3.20	1.20	-	-
C13L	66.30	18.90	0.80	0.50	2.90	1.30	15.70	6.40	-	-
C13M	101.70	11.40	2.50	1.90	4.70	1.70	22.40	3.00	-	-
C13N	78.20	46.90	1.20	0.50	4.60	3.50	13.60	7.20	-	-
C13O	47.10	16.70	1.00	0.40	2.50	1.70	8.70	2.80	-	-
C13P	31.00	20.00	0.50	0.30	1.40	1.20	11.20	7.40	-	-
C14	182.00	-	2.04	-	31.63	-	33.01	-	-	-
C15A	101.60	27.50	2.56	0.85	8.25	2.29	20.27	4.22	-	-
C15B	32.70	19.70	1.12	0.20	1.98	0.56	3.72	0.92	-	-
C16A	151.70	56.60	3.00	1.80	16.10	13.10	18.40	11.20	-	-
C16B	108.30	40.50	0.60	0.40	9.80	8.90	23.40	13.40	-	-
C16C	160.70	89.30	3.30	3.50	15.30	13.20	17.30	11.50	-	-
C16D	263.40	132.90	8.40	4.70	29.20	25.30	31.70	25.10	-	-
C16E	169.30	101.70	3.80	4.10	17.10	17.30	22.20	16.80	-	-
C16F	156.70	49.50	2.60	1.40	14.20	11.70	17.00	10.70	-	-
C16G	90.70	30.80	0.80	0.60	9.40	8.00	23.70	14.00	-	-
C16H	127.90	66.40	4.30	3.70	16.80	13.50	18.80	11.50	-	-
C16I	222.60	114.30	8.50	5.20	30.40	20.20	34.20	20.70	-	-
C16J	149.10	85.60	3.90	4.50	17.20	15.70	22.80	15.60	-	-
C16K	183.90	67.00	3.10	2.00	15.40	11.50	18.00	9.70	-	-
C16L	126.80	44.50	1.50	1.10	11.00	8.20	27.80	15.40	-	-

C16M	176.80	84.30	5.40	4.40	17.30	12.70	19.90	13.40	-	-
C16N	245.50	105.20	8.10	5.40	28.30	18.70	30.40	17.40	-	-
C16O	184.30	89.60	4.50	4.40	17.80	14.70	23.70	15.00	-	-
C16P	118.50	34.00	1.80	1.00	12.20	10.40	18.40	10.90	-	-
C16Q	102.80	33.60	0.90	0.40	9.90	8.00	28.50	13.30	-	-
C16R	126.90	83.50	3.00	2.00	21.00	20.00	21.30	17.40	-	-
C16S	196.20	80.00	6.90	3.60	31.50	20.70	34.10	21.10	-	-
C16T	135.50	70.00	3.00	3.10	18.00	17.50	24.70	16.80	-	-
C16U	128.00	54.30	1.80	1.10	10.80	11.80	15.00	11.00	-	-
C16V	89.20	46.90	1.00	0.60	10.50	11.30	25.20	19.20	-	-
C16W	105.50	59.40	2.20	2.00	12.00	10.10	13.50	8.50	-	-
C16X	204.70	98.20	4.50	1.80	28.60	27.20	28.70	20.20	-	-
C16Y	132.00	78.50	2.30	1.90	14.80	17.70	19.80	16.30	-	-
C16Z	79.00	31.00	0.70	0.30	7.10	5.50	11.60	6.60	-	-
C16AA	66.40	20.20	0.40	0.10	5.50	5.70	18.50	8.50	-	-
C16AB	114.60	70.30	1.30	1.30	18.60	17.90	17.30	10.20	-	-
C16AC	215.20	93.00	5.40	3.00	33.00	12.10	37.60	14.90	-	-
C16AD	120.30	83.80	1.70	2.50	14.80	15.60	19.30	13.60	-	-
C17A	135.00	63.00	1.42	2.18	11.30	10.80	13.60	12.40	-	-
C17B	126.00	59.00	0.72	0.81	15.50	13.70	14.70	11.50	-	-
C17C	138.00	48.00	0.30	0.56	11.80	8.20	23.50	14.50	-	-
C17D	135.00	55.00	1.12	0.98	10.70	11.00	7.90	7.40	-	-
C17E	139.00	86.00	3.52	3.32	7.30	8.10	8.50	8.60	-	-

Ap Table. G. China Minor Anion concentrations in Reviewed studies.

Study	China Minor Anions							
	F ⁻	F ⁻ SD	CH ₃ SO ₃ ⁻	CH ₃ SO ₃ ⁻ SD	NO ₂ ⁻	NO ₂ ⁻ SD	PO ₄ ³⁻	PO ₄ ³⁻ SD
C1A	0.04	0.05	-	-	-	-	-	-
C1B	0.21	0.26	-	-	-	-	-	-
C1C	0.27	0.14	-	-	-	-	-	-
C1D	0.21	0.08	-	-	-	-	-	-
C1E	0.19	0.18	-	-	-	-	-	-
C2A	0.87	-	0.26	-	0.26	-	0.42	-
C2B	0.49	-	0.27	-	0.19	-	0.71	-
C2C	0.35	-	0.48	-	0.52	-	0.30	-
C2D	0.39	-	0.44	-	0.31	-	-	-
C2E	0.50	-	0.52	-	0.46	-	-	-
C2F	0.55	-	0.34	-	0.36	-	0.44	-
C3A	-	-	-	-	0.70	-	-	-
C3B	-	-	-	-	0.20	-	-	-
C3C	-	-	-	-	2.30	-	-	-
C3D	-	-	-	-	0.60	-	-	-
C4A	-	-	-	-	-	-	-	-
C4B	-	-	-	-	-	-	-	-
C5A	-	-	-	-	2.59	1.98	-	-
C5B	-	-	-	-	2.73	2.21	-	-
C5C	-	-	-	-	2.47	2.00	-	-

C5D	-	-	-	-	2.28	1.77	-	-
C5E	-	-	-	-	2.96	1.92	-	-
C6A	0.10	0.10	-	-	0.00	0.00	0.00	0.00
C6B	0.10	0.10	-	-	0.10	0.10	0.00	0.00
C6C	0.00	0.00	-	-	0.10	0.10	0.00	0.00
C6D	0.00	0.00	-	-	0.00	0.00	0.00	0.00
C6E	0.00	0.10	-	-	0.00	0.10	0.00	0.00
C6F	0.00	0.00	-	-	0.10	0.20	0.00	0.00
C6G	0.10	0.40	-	-	0.70	0.70	0.10	0.40
C6H	0.20	0.50	-	-	0.20	0.30	0.00	0.00
C6I	0.00	0.00	-	-	0.30	0.30	0.00	0.00
C6J	0.10	0.30	-	-	0.30	0.40	0.00	0.20
C6K	0.10	0.10	-	-	0.10	0.10	0.20	0.10
C6L	0.00	0.10	-	-	0.20	0.10	0.00	0.10
C6M	0.00	0.00	-	-	0.20	0.20	0.10	0.20
C6N	0.00	0.00	-	-	0.10	0.10	0.00	0.00
C6O	0.00	0.10	-	-	0.10	0.10	0.10	0.20
C6P	0.20	0.00	-	-	0.00	0.10	0.10	0.10
C6Q	0.00	0.10	-	-	0.20	0.30	0.00	0.10
C6R	0.00	0.00	-	-	0.10	0.10	0.00	0.10
C6S	0.00	0.00	-	-	0.10	0.10	0.20	0.30
C6T	0.10	0.10	-	-	0.10	0.20	0.10	0.20
C7A	-	-	-	-	-	-	-	-
C7B	-	-	-	-	-	-	-	-
C7C	-	-	-	-	-	-	-	-
C7D	-	-	-	-	-	-	-	-
C8	-	-	-	-	-	-	-	-
C9A	0.12	0.23	-	-	-	-	-	-
C9B	0.04	0.04	-	-	-	-	-	-
C9C	0.08	0.04	-	-	-	-	-	-
C10A	-	-	-	-	-	-	-	-
C10B	-	-	-	-	-	-	-	-
C10C	-	-	-	-	-	-	-	-
C11A	-	-	-	-	-	-	-	-
C11B	-	-	-	-	-	-	-	-
C11C	-	-	-	-	-	-	-	-
C11D	-	-	-	-	-	-	-	-
C12	-	-	-	-	2.90	-	-	-
C13A	-	-	-	-	-	-	-	-
C13B	-	-	-	-	-	-	-	-
C13C	-	-	-	-	-	-	-	-
C13D	-	-	-	-	-	-	-	-
C13E	-	-	-	-	-	-	-	-
C13F	-	-	-	-	-	-	-	-
C13G	-	-	-	-	-	-	-	-
C13H	-	-	-	-	-	-	-	-
C13I	-	-	-	-	-	-	-	-
C13J	-	-	-	-	-	-	-	-

C13K	-	-	-	-	-	-	-	-
C13L	-	-	-	-	-	-	-	-
C13M	-	-	-	-	-	-	-	-
C13N	-	-	-	-	-	-	-	-
C13O	-	-	-	-	-	-	-	-
C13P	-	-	-	-	-	-	-	-
C14	-	-	-	-	-	-	-	-
C15A	-	-	-	-	-	-	-	-
C15B	-	-	-	-	-	-	-	-
C16A	0.20	0.10	-	-	-	-	-	-
C16B	0.03	0.03	-	-	-	-	-	-
C16C	0.20	0.30	-	-	-	-	-	-
C16D	0.60	0.40	-	-	-	-	-	-
C16E	0.30	0.30	-	-	-	-	-	-
C16F	0.20	0.10	-	-	-	-	-	-
C16G	0.20	0.10	-	-	-	-	-	-
C16H	0.30	0.20	-	-	-	-	-	-
C16I	0.50	0.40	-	-	-	-	-	-
C16J	0.30	0.20	-	-	-	-	-	-
C16K	0.20	0.10	-	-	-	-	-	-
C16L	0.10	0.10	-	-	-	-	-	-
C16M	0.30	0.20	-	-	-	-	-	-
C16N	0.40	0.30	-	-	-	-	-	-
C16O	0.20	0.20	-	-	-	-	-	-
C16P	0.10	0.10	-	-	-	-	-	-
C16Q	0.10	0.10	-	-	-	-	-	-
C16R	0.10	0.10	-	-	-	-	-	-
C16S	0.30	0.20	-	-	-	-	-	-
C16T	0.10	0.10	-	-	-	-	-	-
C16U	0.10	0.10	-	-	-	-	-	-
C16V	0.10	0.00	-	-	-	-	-	-
C16W	0.10	0.10	-	-	-	-	-	-
C16X	0.20	0.20	-	-	-	-	-	-
C16Y	0.10	0.10	-	-	-	-	-	-
C16Z	0.20	0.10	-	-	-	-	-	-
C16AA	0.10	0.10	-	-	-	-	-	-
C16AB	0.10	0.20	-	-	-	-	-	-
C16AC	0.50	0.20	-	-	-	-	-	-
C16AD	0.20	0.20	-	-	-	-	-	-
C17A	-	-	-	-	-	-	-	-
C17B	-	-	-	-	-	-	-	-
C17C	-	-	-	-	-	-	-	-
C17D	-	-	-	-	-	-	-	-
C17E	-	-	-	-	-	-	-	-

Ap Table. H. China Cation concentrations in Reviewed studies.

Study	China Cations									
	Na ⁺	Na ⁺ SD	NH ₄ ⁺	NH ₄ ⁺ SD	K ⁺	K ⁺ SD	Mg ²⁺	Mg ²⁺ SD	Ca ²⁺	Ca ²⁺ SD
C1A	10.10	0.64	7.74	4.41	1.06	0.35	0.54	0.24	1.82	0.96
C1B	1.67	3.26	5.57	5.37	1.67	0.70	0.92	0.85	3.19	1.59
C1C	9.52	2.62	19.56	12.54	2.48	1.24	0.99	0.56	1.37	1.12
C1D	0.85	0.48	7.34	6.90	1.46	0.69	0.96	0.39	4.41	1.49
C1E	5.06	4.81	10.18	9.56	1.71	0.94	0.88	0.60	2.75	1.70
C2A	0.57	-	4.05	-	0.53	-	0.27	-	1.45	-
C2B	0.51	-	2.44	-	0.23	-	0.28	-	1.55	-
C2C	0.41	-	3.60	-	0.34	-	0.19	-	0.79	-
C2D	0.55	-	4.38	-	0.85	-	0.37	-	1.34	-
C2E	0.79	-	4.36	-	1.20	-	0.32	-	1.17	-
C2F	0.57	-	3.78	-	0.63	-	0.28	-	1.25	-
C3A	0.10	-	4.70	3.30	1.30	-	0.03	-	0.20	-
C3B	0.40	-	4.10	1.50	2.30	-	0.06	-	0.20	-
C3C	0.50	-	4.10	2.50	0.80	-	0.40	-	1.30	-
C3D	0.40	-	4.80	2.10	1.00	-	0.03	-	0.30	-
C4A	0.21	0.10	26.86	9.01	1.16	0.50	0.06	0.04	0.32	0.87
C4B	0.67	0.24	19.88	10.28	2.07	0.99	0.19	0.11	1.94	1.95
C5A	0.46	0.20	21.02	10.42	1.90	2.23	0.11	0.06	0.66	0.48
C5B	0.43	0.21	19.09	8.72	2.61	3.46	0.12	0.08	0.82	0.71
C5C	0.47	0.19	20.88	9.60	2.02	2.37	0.09	0.05	0.77	0.41
C5D	0.47	0.20	18.75	8.39	1.18	0.75	0.11	0.05	0.58	0.36
C5E	0.49	0.20	25.86	13.19	1.94	1.22	0.11	0.06	0.47	0.30
C6A	0.50	0.10	5.00	1.80	0.90	0.30	0.10	0.00	1.10	1.10
C6B	0.50	0.30	4.00	2.00	0.50	0.30	0.10	0.10	0.90	0.70
C6C	0.50	0.20	2.40	1.40	0.40	0.10	0.10	0.10	0.50	0.40
C6D	0.40	0.10	3.80	1.70	0.60	0.30	0.10	0.10	0.50	0.40
C6E	0.50	0.20	3.90	2.00	0.60	0.30	0.10	0.10	0.80	0.80
C6F	0.70	0.30	9.40	4.40	0.90	0.40	0.10	0.00	0.80	0.80
C6G	0.40	0.10	5.90	3.80	0.50	0.20	0.10	0.00	0.50	0.40
C6H	0.70	0.50	3.20	1.80	0.30	0.30	0.10	0.00	0.20	0.30
C6I	0.60	0.20	7.50	7.20	0.80	0.70	0.00	0.00	0.20	0.40
C6J	0.60	0.40	6.60	5.10	0.60	0.50	0.10	0.00	0.40	0.50
C6K	0.50	0.20	10.20	5.60	1.00	0.40	0.20	0.20	0.30	0.20
C6L	0.40	0.20	7.50	3.90	0.90	1.50	0.10	0.10	0.20	0.10
C6M	0.30	0.10	4.90	3.20	0.40	0.20	0.00	0.00	0.20	0.10
C6N	0.30	0.10	5.90	2.50	0.70	0.30	0.10	0.10	0.20	0.20
C6O	0.40	0.20	7.30	4.50	0.80	0.70	0.10	0.10	0.20	0.20
C6P	0.70	0.30	13.50	6.70	1.60	0.70	0.10	0.00	0.60	0.50
C6Q	0.50	0.20	7.70	3.20	0.60	0.30	0.50	0.30	0.80	0.40
C6R	0.40	0.30	5.50	3.20	0.40	0.30	0.20	0.20	0.50	0.50
C6S	0.40	0.30	7.30	3.30	0.90	0.40	0.10	0.00	0.40	0.20
C6T	0.50	0.30	9.10	5.70	0.90	0.70	0.20	0.20	0.60	0.40
C7A	0.36	0.22	6.53	5.73	0.92	0.99	0.19	0.16	1.36	1.09
C7B	0.39	0.23	5.41	4.75	1.39	1.20	0.08	0.06	0.45	0.25

C7C	0.42	0.20	5.62	6.26	1.57	0.91	0.11	0.06	0.39	0.19
C7D	0.43	0.18	8.11	6.05	2.46	8.03	0.17	0.34	0.48	0.28
C8	-	-	2.92	2.77	-	-	-	-	-	-
C9A	1.74	0.37	5.51	3.78	1.17	0.76	0.43	0.56	2.05	1.16
C9B	1.04	0.44	5.29	3.52	0.71	0.45	0.09	0.03	0.75	0.46
C9C	1.33	0.36	5.42	3.45	0.59	0.40	0.08	0.04	0.64	0.30
C10A	0.45	0.23	9.00	5.10	1.23	1.22	0.07	0.04	0.44	0.28
C10B	0.21	0.09	8.20	3.60	1.17	0.94	0.06	0.06	0.35	0.21
C10C	0.25	0.12	8.00	3.50	0.77	0.45	0.04	0.03	0.32	0.17
C11A	1.00	0.60	11.30	8.80	3.30	2.40	0.10	0.10	0.90	0.50
C11B	1.10	0.60	11.50	8.90	4.50	3.60	0.20	0.10	1.40	0.90
C11C	1.00	0.60	10.90	11.70	4.20	3.30	0.20	0.10	1.70	1.00
C11D	1.00	-	11.20	-	4.00	-	0.20	-	1.30	-
C12	0.80	-	13.60	-	2.60	-	-	-	-	-
C13A	4.20	1.40	2.80	1.30	0.90	0.30	-	-	-	-
C13B	4.80	0.40	1.50	0.70	1.20	0.40	-	-	-	-
C13C	4.50	1.00	2.10	2.10	1.10	0.50	-	-	-	-
C13D	4.60	1.20	3.90	2.90	1.90	1.20	-	-	-	-
C13E	4.50	1.40	1.90	1.70	2.50	1.00	-	-	-	-
C13F	5.30	0.80	7.40	7.00	2.20	0.70	-	-	-	-
C13G	4.40	0.40	2.00	1.70	1.40	0.70	-	-	-	-
C13H	5.00	1.50	4.50	2.00	1.60	0.60	-	-	-	-
C13I	3.60	0.90	1.80	1.90	0.40	0.20	-	-	-	-
C13J	3.10	0.50	0.10	0.00	0.20	0.10	-	-	-	-
C13K	2.10	0.20	0.10	0.10	0.10	0.00	-	-	-	-
C13L	3.50	0.50	0.60	0.70	1.90	1.10	-	-	-	-
C13M	3.80	0.10	2.70	1.90	3.80	1.60	-	-	-	-
C13N	3.70	0.60	2.00	3.20	1.90	0.90	-	-	-	-
C13O	3.60	0.90	0.40	0.40	0.30	0.20	-	-	-	-
C13P	1.70	0.50	1.00	1.50	0.30	0.30	-	-	-	-
C14	0.28	-	22.18	-	0.83	-	0.07	-	1.24	-
C15A	4.85	1.43	9.88	2.09	1.75	0.92	0.28	0.12	3.41	2.44
C15B	3.05	1.13	1.38	0.41	1.50	0.28	0.29	0.07	1.32	0.34
C16A	1.60	0.70	7.50	5.90	0.90	0.70	0.30	0.20	3.40	1.90
C16B	1.00	0.60	7.20	5.70	0.60	0.50	0.10	0.10	2.10	1.10
C16C	0.90	1.50	7.90	5.90	1.20	0.90	0.20	0.20	1.70	1.60
C16D	2.80	1.20	17.10	12.10	2.80	1.90	0.50	0.20	2.50	1.60
C16E	1.70	1.20	9.60	8.70	1.30	1.40	0.30	0.20	2.50	1.70
C16F	1.80	0.70	5.60	5.60	0.90	0.60	0.30	0.20	3.60	2.00
C16G	1.70	1.10	6.00	5.10	0.90	0.40	0.20	0.10	2.20	1.50
C16H	0.70	0.50	8.50	6.40	1.50	0.90	0.10	0.10	1.60	1.30
C16I	2.20	1.00	17.50	10.50	3.20	3.10	0.60	0.40	2.20	1.40
C16J	1.60	1.00	9.10	8.60	1.50	1.80	0.30	0.30	2.50	1.70
C16K	1.20	0.40	6.30	5.20	1.00	0.60	0.40	0.30	4.50	2.90
C16L	1.50	0.40	6.50	5.50	1.00	0.60	0.20	0.10	1.80	1.00
C16M	0.40	0.30	8.30	6.30	1.70	1.00	0.20	0.10	2.10	1.90
C16N	1.00	1.00	15.80	9.10	2.80	1.60	0.70	0.30	2.50	2.20
C16O	1.10	0.70	9.20	7.70	1.60	1.30	0.40	0.30	2.80	2.40

C16P	1.40	0.70	5.60	5.00	0.80	0.60	0.20	0.10	2.10	1.40
C16Q	1.40	0.60	7.00	5.10	0.90	0.60	0.10	0.10	0.80	0.50
C16R	0.50	0.30	10.70	9.70	1.20	1.00	0.10	0.10	1.20	0.90
C16S	1.50	0.80	18.30	10.10	2.60	1.80	0.30	0.20	1.10	0.70
C16T	1.30	0.70	10.00	9.10	1.30	1.30	0.20	0.10	1.60	1.00
C16U	1.30	0.80	4.70	5.60	0.60	0.30	0.20	0.20	1.70	0.80
C16V	1.00	0.50	7.00	7.30	0.70	0.50	0.10	0.10	0.80	0.50
C16W	0.90	0.60	5.40	5.10	0.70	0.70	0.10	0.10	1.10	0.70
C16X	1.60	0.70	14.20	11.40	1.80	1.50	0.40	0.10	1.60	1.00
C16Y	1.20	0.70	7.50	8.30	0.90	1.00	0.20	0.20	1.30	0.80
C16Z	1.80	1.10	1.20	0.80	0.40	0.30	0.20	0.10	1.70	1.00
C16AA	0.80	0.40	3.60	2.90	0.50	0.30	0.10	0.00	0.50	0.40
C16AB	0.90	1.40	7.80	6.80	1.00	0.90	0.10	0.20	0.70	1.20
C16AC	3.00	0.90	20.20	7.60	2.80	1.50	0.50	0.10	1.80	0.60
C16AD	1.50	1.30	7.20	8.70	1.00	1.30	0.20	0.20	1.10	1.00
C17A	0.46	0.55	6.90	7.10	0.92	0.75	0.16	0.13	1.60	1.50
C17B	0.31	0.18	7.50	8.10	1.08	0.71	0.24	0.20	2.60	2.20
C17C	0.17	0.09	11.00	6.90	0.66	0.47	0.07	0.03	0.60	0.30
C17D	0.30	0.22	4.70	5.80	1.13	0.90	0.16	0.07	1.70	1.00
C17E	1.08	0.80	4.50	5.70	0.81	0.77	0.18	0.09	1.50	0.90

Ap Table. I. Specification of Reviewed Studies (Delhi).

Study	Time	Season	Site
D1A	Jan 2013 - Dec 2015; Nov - Feb	Post-Monsoon - Winter	NPL
D1B	Jan 2013 - Dec 2015; Mar - Jun	Summer	NPL
D1C	Jan 2013 - Dec 2015; Jul - Sep	Monsoon	NPL
D1D	Jan 2013 - Dec 2015	Annual	NPL
D2	Jan - Dec 2011	Annual	NPL
D3A	Jan - Dec 2012; Dec - Feb (Day)	Winter	IITM
D3B	Jan - Dec 2012; Mar - Jun (Day)	Summer	IITM
D3C	Jan - Dec 2012; Jul - Sep (Day)	Monsoon	IITM
D3D	Jan - Dec 2012; Oct - Nov (Day)	Post-Monsoon	IITM
D3E	Jan - Dec 2012; Dec - Feb (Night)	Winter	IITM
D3F	Jan - Dec 2012; Mar - Jun (Night)	Summer	IITM
D3G	Jan - Dec 2012; Jul - Sep (Night)	Monsoon	IITM
D3H	Jan - Dec 2012; Oct - Nov (Night)	Post-Monsoon	IITM
D3I	Jan - Dec 2012 (Total Day)	Annual	IITM
D3J	Jan - Dec 2012 (Total Night)	Annual	IITM
D3K	Jan - Dec 2012 (Total)	Annual	IITM
D4	Jan - Dec 2007	Annual	IITM
D5	Oct - Dec 1998	Post-Monsoon	NPL

D6A	Jan 2013 - May 2014	Annual	NPL
D6B	Jan 2013 - May 2014; Nov - Feb	Post-Monsoon - Winter	NPL
D6C	Jan 2013 - May 2014; Mar - Jun	Summer	NPL
D6D	Jan 2013 - May 2014; Jul - Oct	Monsoon	NPL
D7A	Jan 2013 - Dec 2014; Apr - Jun	Summer	NPL
D7B	Jan 2013 - Dec 2014; Jul - Sep	Monsoon	NPL
D7C	Jan 2013 - Dec 2014; Oct - Jan	Post-Monsoon - Winter	NPL
D7D	Jan 2013 - Dec 2014; Feb - Mar	Winter - Summer	NPL
D7E	Jan 2013 - Dec 2014	Annual	NPL
D8	Dec 2011 - Feb 2012	Post-Monsoon - Winter	JNU
D9A	15 th - 30 th Jun 2014	Summer	Mat Rd.
D9B	15 th Dec 2013 - 15 th Jan 2014	Winter	Mat Rd.
D10A	Jan 2013 - Dec 2014	Annual	NPL
D10B	Jan 2013 - Dec 2014; Nov-Feb	Post-Monsoon - Winter	NPL
D10C	Jan 2013 - Dec 2014; Mar - Jun	Summer	NPL
D10D	Jan 2013 - Dec 2014; Jul - Oct	Monsoon	NPL
D11A	16 th - 31 st Dec 2015	Winter	IGIA
D11B	1 st - 31 st Jan 2016	Winter	IGIA
D11C	1 st - 15 th Feb 2016	Winter	IGIA
D12A	29 th Oct 3 rd , 5 th and 9 th Nov 2015 (Pre-Diwali)	Post-Monsoon	IGDTUW
D12B	11 th Nov 2015 (Diwali)	Post-Monsoon	IGDTUW
D12C	16 th , 18 th Nov 2015 (Post-Diwali)	Post-Monsoon	IGDTUW
D12D	18 th , 20 th , 25 th , 27 th Oct 2016 (Pre-Diwali)	Post-Monsoon	IGDTUW
D12E	30 th Oct 2016 (Diwali)	Post-Monsoon	IGDTUW
D12F	2 nd , 6 th Nov 2016 (Post-Diwali)	Post-Monsoon	IGDTUW
D13	8 th Dec 2017–10 th Feb 2018	Winter	IGIA
D14A	Jan 2013 - Dec 2016	Annual	NPL
D14B	Jan 2013 to Dec 2016; Jan - Feb	Winter	NPL
D14C	Jan 2013 to Dec 2016; Mar - May	Summer	NPL
D14D	Jan 2013 to Dec 2016; Jun - Sep	Monsoon	NPL
D14E	Jan 2013 to Dec 2016; Oct - Dec	Post-Monsoon	NPL

*Study D5 investigated PM₂ (not PM_{2.5})

Ap Table. J. Delhi PM_{2.5} and Anion concentrations in Reviewed studies.

Study	Delhi PM _{2.5}		Delhi Anions							
	PM _{2.5}	PM _{2.5} SD	F ⁻	F ⁻ SD	Cl ⁻	Cl ⁻ SD	NO ₃ ⁻	NO ₃ ⁻ SD	SO ₄ ²⁻	SO ₄ ²⁻ SD
D1A	196.80	74.10	-	-	16.10	10.10	22.60	13.00	19.20	12.30
D1B	82.90	28.70	-	-	7.10	3.20	3.30	2.70	8.00	3.50
D1C	64.40	41.30	-	-	6.30	6.20	4.80	5.30	10.80	7.00
D1D	114.70	48.00	-	-	9.80	6.50	10.20	7.00	12.70	7.60
D2	-	-	-	-	-	-	8.11	-	11.34	-
D3A	204.15	23.93	-	-	-	-	13.05	8.14	31.09	10.65
D3B	157.39	47.19	-	-	-	-	9.67	11.23	20.05	15.05
D3C	115.13	27.13	-	-	-	-	7.48	5.66	17.04	7.81
D3D	199.44	41.55	-	-	-	-	22.88	6.48	33.73	11.90
D3E	250.81	25.98	-	-	-	-	19.79	7.94	32.33	11.68
D3F	155.34	49.52	-	-	-	-	5.68	5.97	13.31	7.42
D3G	100.86	17.76	-	-	-	-	6.52	2.10	10.84	4.60
D3H	234.83	35.35	-	-	-	-	28.60	8.25	37.15	13.02
D3I	164.16	39.93	-	-	-	-	12.15	6.79	23.66	9.12
D3J	179.02	64.80	-	-	-	-	13.34	10.12	21.29	12.18
D3K	171.59	51.61	-	-	-	-	12.74	8.18	22.47	10.23
D4	97.00	56.00	-	-	12.70	12.50	6.40	13.40	19.80	14.60
D5	248.00	-	0.05	-	0.08	-	0.07	-	0.10	-
D6A	125.50	77.20	1.05	0.57	7.30	4.82	10.77	8.17	13.06	5.95
D6B	196.00	-	1.19	-	10.30	-	17.60	-	16.00	-
D6C	83.60	-	0.99	-	5.46	-	5.85	-	10.20	-
D6D	58.80	-	1.10	-	4.51	-	6.27	-	12.84	-
D7A	83.66	33.12	0.84	0.62	6.92	3.63	3.76	2.16	8.38	4.30
D7B	41.62	24.10	0.53	0.65	6.47	6.18	3.56	2.70	9.90	5.01
D7C	189.84	101.05	0.85	0.66	12.54	7.08	16.46	10.85	16.16	9.48
D7D	96.80	48.52	0.92	0.65	6.59	4.35	7.19	2.33	9.83	3.62
D7E	108.00	86.50	0.90	0.88	9.46	9.17	9.49	9.18	12.62	11.21
D8	357.30	175.00	0.10	0.10	5.27	7.03	2.49	1.98	53.19	67.23
D9A	58.20	35.00	-	-	2.14	1.54	4.37	2.14	9.97	6.25
D9B	276.90	99.90	-	-	27.80	18.10	32.80	20.10	26.10	15.30
D10A	122.00	94.10	0.91	0.69	7.77	5.72	10.00	9.82	12.90	8.08
D10B	216.00	93.20	1.06	0.80	10.90	6.68	18.90	11.40	16.90	11.20
D10C	81.80	24.90	0.89	0.51	5.64	3.00	5.82	2.03	10.30	3.85
D10D	67.90	56.10	0.74	0.72	6.48	5.19	4.18	3.16	11.30	5.13
D11A	196.40	98.20	-	-	39.40	36.50	-	-	27.60	22.40
D11B	232.70	83.10	-	-	36.60	21.90	-	-	45.70	64.20
D11C	163.50	32.70	-	-	30.20	15.80	-	-	24.00	16.70
D12A	160.76	-	0.31	-	1.76	-	6.43	-	3.61	-
D12B	308.82	-	2.67	-	9.00	-	33.38	-	10.48	-
D12C	222.02	-	0.31	-	3.75	-	19.98	-	2.28	-
D12D	122.15	-	0.29	-	1.92	-	7.56	-	2.09	-
D12E	766.51	-	1.92	-	29.34	-	51.41	-	84.64	-
D12F	645.18	-	1.99	-	25.08	-	90.89	-	35.84	-
D13	-	-	-	-	36.00	33.90	28.50	13.60	19.90	13.90

D14A	131.00	79.00	0.95	0.76	8.21	5.14	11.60	11.60	13.90	8.77
D14B	183.00	73.00	1.30	0.88	11.00	4.59	20.20	11.40	18.60	9.36
D14C	103.00	35.00	0.92	0.61	7.11	4.25	6.45	7.22	10.40	5.94
D14D	69.00	28.00	0.64	0.67	4.13	2.78	3.50	2.83	9.79	4.75
D14E	186.00	90.00	1.04	0.74	11.40	4.90	18.40	13.40	18.10	10.20

*Study D5 investigated PM₂ (not PM_{2.5})

Ap Table. K. Delhi Cation concentrations in Reviewed studies.

Study	Delhi Cations									
	Na ⁺	Na ⁺ SD	NH ₄ ⁺	NH ₄ ⁺ SD	K ⁺	K ⁺ SD	Mg ²⁺	Mg ²⁺ SD	Ca ²⁺	Ca ²⁺ SD
D1A	7.00	6.20	18.80	10.80	5.70	4.20	1.30	1.30	3.60	2.60
D1B	3.50	1.90	5.60	3.70	3.00	1.30	0.50	0.40	3.20	3.50
D1C	6.10	4.20	3.60	5.20	3.10	3.10	1.00	0.60	2.30	1.60
D1D	5.50	4.10	9.30	6.60	3.90	2.90	0.90	0.80	16.80	2.60
D2	-	-	1.10	-	1.35	-	0.04	-	1.66	-
D3A	-	-	-	-	-	-	-	-	-	-
D3B	-	-	-	-	-	-	-	-	-	-
D3C	-	-	-	-	-	-	-	-	-	-
D3D	-	-	-	-	-	-	-	-	-	-
D3E	-	-	-	-	-	-	-	-	-	-
D3F	-	-	-	-	-	-	-	-	-	-
D3G	-	-	-	-	-	-	-	-	-	-
D3H	-	-	-	-	-	-	-	-	-	-
D3I	-	-	-	-	-	-	-	-	-	-
D3J	-	-	-	-	-	-	-	-	-	-
D3K	-	-	-	-	-	-	-	-	-	-
D4	9.80	3.60	-	-	4.80	3.90	0.90	0.80	2.70	1.70
D5	0.06	-	0.06	-	0.05	-	0.06	-	0.14	-
D6A	4.51	1.62	10.86	8.37	4.94	1.92	-	-	-	-
D6B	4.97	-	15.90	-	5.63	-	-	-	-	-
D6C	3.95	-	8.38	-	4.36	-	-	-	-	-
D6D	4.78	-	4.89	-	4.56	-	-	-	-	-
D7A	3.40	1.75	7.14	2.29	3.30	1.62	0.40	0.29	3.23	2.80
D7B	7.28	4.54	2.89	2.51	2.47	2.38	1.02	0.69	2.12	1.64
D7C	6.08	3.70	12.91	9.15	5.29	3.06	1.03	0.93	3.09	2.67
D7D	3.50	2.85	8.60	4.23	2.86	1.22	0.33	0.29	2.10	0.94
D7E	5.52	4.17	8.85	8.38	3.68	2.57	0.81	0.80	2.68	2.24
D8	1.38	1.31	10.90	7.70	7.70	1.70	0.20	0.10	3.06	2.58
D9A	0.41	0.38	4.94	2.87	0.86	0.49	-	-	-	-
D9B	0.64	0.30	34.20	17.00	3.83	1.63	-	-	-	-
D10A	5.05	3.09	9.40	8.59	4.10	2.70	-	-	-	-
D10B	5.10	2.85	16.20	10.40	5.21	2.51	-	-	-	-
D10C	3.84	1.74	8.34	2.97	4.05	2.44	-	-	-	-
D10D	6.09	3.84	3.43	3.75	2.94	2.60	-	-	-	-
D11A	-	-	26.30	20.20	-	-	-	-	-	-
D11B	-	-	24.30	13.20	-	-	-	-	-	-

D11C	-	-	16.20	12.00	-	-	-	-	-	-
D12A	1.27	-	1.37	-	1.49	-	0.62	-	3.80	-
D12B	3.86	-	0.10	-	9.24	-	1.56	-	10.25	-
D12C	1.41	-	2.20	-	1.86	-	0.67	-	4.91	-
D12D	1.01	-	1.17	-	1.62	-	0.58	-	3.02	-
D12E	8.92	-	6.53	-	77.30	-	4.88	-	9.63	-
D12F	5.81	-	25.38	-	12.80	-	2.21	-	10.60	-
D13	0.40	0.20	32.70	17.20	2.40	1.10	0.01	0.03	0.46	0.30
D14A	4.84	3.69	9.86	9.77	4.30	2.95	0.56	0.77	3.07	1.65
D14B	5.63	4.58	16.60	9.70	5.13	2.61	0.40	0.52	2.99	2.02
D14C	3.77	2.27	6.71	6.55	3.71	1.58	0.36	0.18	3.14	1.18
D14D	4.07	2.76	3.02	2.71	2.69	2.30	0.60	0.54	2.89	1.50
D14E	6.16	4.36	14.90	11.10	5.99	3.80	0.90	1.28	3.25	1.87

*Study D5 investigated PM₂ (not PM_{2.5})

Ap Table. L. Specification of Reviewed Studies (Beijing).

Study	Time	Season	Site
B1A	30 th Nov- 9 th Dec 2004 (Haze Fog)	Winter	BNU
B1B	30 th Nov- 9 th Dec 2004 (Non-Haze Fog)	Winter	BNU
B2A	15 th Jun 2012 - 2 nd Apr 2013	Annual	BEI
B2B	15 th – 30 th Jun, 10 th – 20 th Aug 2012	Summer	BEI
B2C	15 th Sep – 21 st Oct 2012	Autumn	BEI
B2D	5 th Jan – 5 th Feb 2013	Winter	BEI
B2E	4 th Mar – 2 nd Apr 2013	Spring	BEI
B3A	29 th Jun - 2 nd Aug 2005 (Overall)	Summer	HSZ
B3B	29 th Jun - 2 nd Aug 2005 (NH4 Poor)	Summer	HSZ
B3C	29 th Jun - 2 nd Aug 2005 (NH4 Rich)	Summer	HSZ
B4A	27 th Feb - 29 th Dec 2013	Annual	DOW
B4B	27 th Feb - 10 th Mar 2013	Spring	DOW
B4C	19 th - 30 th Jun 2013	Summer	DOW
B4D	10 th - 29 th Sep 2013	Autumn	DOW
B4E	7 th - 29 th Dec 2013	Winter	DOW
B5A	12 th – 18 th Jul 2010	Summer	CERN
B5B	12 th – 18 th Jul 2010	Summer	CERN
B6A	7 th Jun 1999 - 8 th Jun 2000	Annual	CGZ
B6B	7 th Jun 1999 - 8 th Jun 2000	Annual	THU
B7	Not known	NA	NA
B8A	10 th Jun 2009 – 31 st Mar 2010	Annual	US
B8B	10 th Jun - 10 th Jul 2009	Summer	US

B8C	10 th - 30 th Sep 2009	Autumn	US
B8D	1 st - 31 st Dec 2009	Winter	US
B8E	1 st - 31 st Mar 2010	Spring	US
B9A	25 th Oct - 15 th Nov 2013 (Before Heating)	Winter	BNU
B9B	15 th Nov - 26 th Dec 2013 (During Heating)	Winter	BNU
B9C	1 st - 15 th Nov 2014 (Before Heating)	Winter	BNU
B9D	16 th Nov - 30 th Nov 2014 (During Heating)	Winter	BNU
B10A	Jan 7 th - 27 th Feb 2014 (Clean)	Winter	CNU
B10B	Jan 7 th - 27 th Feb 2014 (Haze)	Winter	CNU
B10C	Jan 7 th - 27 th Feb 2014 (Haze II)	Winter	CNU
B11A	Aug 2001 - Sep 2002; 30 th Aug 2001 - 2002	Annual	CGZ
B11B	Aug 2001 - Sep 2002; Assumed Sep - Nov	Autumn	CGZ
B11C	Aug 2001 - Sep 2002; Assumed Dec - Feb	Winter	CGZ
B11D	Aug 2001 - Sep 2002; Assumed Mar - May	Spring	CGZ
B11E	Aug 2001 - Sep 2002; Assumed Jun - Aug	Summer	CGZ
B11F	Aug 2001 - Sep 2002	Annual	THU
B12A	2001 - 2003	Spring	BNU, CSC, YG, MY, PG
B12B	2001 - 2003	Summer	BNU, CSC, YG, MY, PG
B12C	2001 - 2003	Autumn	BNU, CSC, YG, MY, PG
B12D	2001 - 2003	Winter	BNU, CSC, YG, MY, PG
B12E	2001 - 2003	Annual	BNU, CSC, YG, MY, PG
B13A	10 th Apr - 8 th Jun 2013 (Haze 1)	Spring	IAP
B13B	10 th Apr - 8 th Jun 2013 (Haze 2)	Spring	IAP
B13C	10 th Apr - 8 th Jun 2013 (Haze 3)	Spring	IAP
B13D	10 th Apr - 8 th Jun 2013 (Clean)	Spring	IAP
B14A	11 th - 19 th Jan 2004	Winter	PKU
B14B	11 th - 19 th Jan 2004	Winter	OLP
B14C	11 th - 19 th Jan 2004	Winter	MT
B14D	11 th - 19 th Jan 2004	Winter	TZ
B14E	11 th - 19 th Jan 2004	Winter	CSC
B14F	11 th - 19 th Jan 2004	Winter	FG
B14G	11 th - 19 th Jan 2004	Winter	Site Averages

B14H	11 th - 19 th Aug 2004	Summer	PKU
B14I	11 th - 19 th Aug 2004	Summer	OLP
B14J	11 th - 19 th Aug 2004	Summer	MT
B14K	11 th - 19 th Aug 2004	Summer	TZ
B14L	11 th - 19 th Aug 2004	Summer	CSC
B14M	11 th - 19 th Aug 2004	Summer	FG
B14N	11 th - 19 th Aug 2004	Summer	Site Averages
B15	10 th Oct - 4 th Nov 2016	Autumn	BNU
B16A	5 th Jun - 30 th Nov 2009	Total	CMA
B16B	5 th Jun - 31 st Aug 2009	Summer	CMA
B16C	1 st Sep - 31 st Nov 2009	Autumn	CMA
B17A	19 th Aug - 18 th Sep 2015	Summer	IGSNRR
B17B	19 th Aug - 18 th Sep 2015; Non-control (Not Sampling 20 th Aug - 4 th Sep)	Summer	IGSNRR
B17C	19 th Aug - 18 th Sep 2015; Pollution-Control (Sampling 20 th Aug - 4 th Sep)	Summer	IGSNRR
B18A	Jul 1999 - Sep 2000	Annual	CGZ
B18B	Jul 1999 - Sep 2000	Annual	THU
B18C	24 th Sep - 31 st Oct 1999	Autumn	CGZ
B18D	1 st Nov 1999 - 29 th Feb 2000	Winter	CGZ
B18E	1 st Mar 2000 - 31 st May 2000	Spring	CGZ
B18F	1 st Jun - 28 th Sep 2000	Summer	CGZ
B19A	Apr 2009 - Jan 2010	Annual	PKU
B19B	Apr 2009 (high winds, low precipitation)	Spring	PKU
B19C	Jul 2009 (high temp, rains often)	Summer	PKU
B19D	Oct 2009 (northwest winds, sunny days)	Autumn	PKU
B19E	Jan 2010 (dry, cold air)	Winter	PKU
B20A	16 th - 21 st Dec 2016 (Episode 1)	Winter	BNU
B20B	24 th - 25 th Dec 2016 (Episode 2)	Winter	BNU
B20C	30 th Dec 2016 – 7 th Jan 2017 (Episode 3)	Winter	BNU
B20D	Haze Period (Ep 1 + Ep 2 + Ep3)	Winter	BNU
B20E	15 th Dec 2016 – 15 th Jan 2017 (all other periods) Non-Haze Period	Winter	BNU
B20F	15 th Dec 2016 – 15 th Jan 2017 (Average)	Winter	BNU
B21	1 st - 31 st Jan 2013 (Severe Haze)	Winter	CRAES
B22A	18 th Jun 2002 - 15 th Jul 2002	Summer	BNU

B22B	18 th Jun 2002 - 15 th Jul 2002	Summer	CSC
B22C	18 th Jun 2002 - 15 th Jul 2002	Summer	YG
B22D	1 st Dec 2002 - 29 th Dec 2002	Winter	BNU
B22E	1 st Dec 2002 - 29 th Dec 2002	Winter	CSC
B22F	1 st Dec 2002 - 29 th Dec 2002	Winter	YG
B23A	16 th Mar - 6 th Apr 2006	Spring	Very near IAP
B23B	19 th Jul - 31 st Aug 2006	Summer	Very near IAP
B23C	23 rd Oct - 13 th Nov 2006	Autumn	Very near IAP
B23D	6 th - 29 th Dec 2006	Winter	Very near IAP
B23E	2006 (Annual Mean)	Annual	Very near IAP
B24A	4 th Aug - 3 rd Sep 2012 (All Days)	Summer	YU CAS
B24B	4 th Aug - 3 rd Sep 2012 (Haze Days)	Summer	YU CAS
B24C	4 th Aug - 3 rd Sep 2012 (Non-Haze Days)	Summer	YU CAS
B25	22 nd Jul - 12 th Aug 2014 (Hourly Mean)	Summer	CRAES
B26A	Sep 2006 - Aug 2007; Mar - May 2007	Spring	IAP
B26B	Sep 2006 - Aug 2007; Jun - Aug 2007	Summer	IAP
B26C	Sep 2006 - Aug 2007; Sep - Nov 2006	Autumn	IAP
B26D	Sep 2006 - Aug 2007; Dec 2006 - Feb 2007	Winter	IAP
B27	29 th Jun - 2 nd Aug 2005	Summer	HSZ
B28	20 th Jun - 6 th Aug 2005	Summer	HSZ
B29A	1 st Jul - 20 th Sep 2005-2007 (Reference Period)	Summer	IGSNRR
B29B	1 st Jul - 20 th Sep (Olympic Period) 2008	Summer	IGSNRR
B30A	7 th Feb - 15 th Nov 2017 (Clean)	Annual	THU
B30B	7 th Feb - 15 th Nov 2017 (Slightly Polluted)	Annual	THU
B30C	7 th Feb - 15 th Nov 2017 (Moderately Polluted)	Annual	THU
B30D	7 th Feb - 15 th March 2017 (Clean)	Winter	THU
B30E	7 th Feb - 15 th March 2017 (Slightly Polluted)	Winter	THU
B30F	7 th Feb - 15 th March 2017 (Moderately Polluted)	Winter	THU
B30G	1 st May - 30 th Sep 2017 (Clean)	Summer	THU
B30H	1 st May - 30 th Sep 2017 (Slightly Polluted)	Summer	THU
B30I	1 st May - 30 th Sep 2017 (Moderately Polluted)	Summer	THU
B30J	16 th Mar - 30 th Apr; 1 st Oct - 15 th Nov 2017 (Clean)	Spring/Autumn	THU
B30K	16 th Mar - 30 th Apr; 1 st Oct - 15 th Nov 2017 (Slightly Polluted)	Spring/Autumn	THU

B30L	16 th Mar - 30 th Apr; 1 st Oct - 15 th Nov 2017 (Moderately Polluted)	Spring/Autumn	THU
------	---	---------------	-----

Ap Table. M. Beijing PM_{2.5} and Major Anion concentrations in Reviewed studies.

Study	Beijing PM _{2.5}		Beijing Major Anions							
	PM _{2.5}	PM _{2.5} SD	Cl ⁻	Cl ⁻ SD	NO ₃ ⁻	NO ₃ ⁻ SD	SO ₄ ²⁻	SO ₄ ²⁻ SD	C ₂ O ₄ ²⁻	C ₂ O ₄ ²⁻ SD
B1A	219.96	-	5.53	-	13.78	-	21.32	-	-	-
B1B	36.73	-	0.76	-	0.94	-	1.71	-	-	-
B2A	112.40	94.40	4.33	0.61	20.30	19.10	24.20	26.10	-	-
B2B	103.30	62.20	2.37	2.08	21.60	13.50	26.30	18.30	-	-
B2C	58.30	49.20	0.99	1.61	9.12	12.50	9.38	11.50	-	-
B2D	169.10	130.40	6.45	5.33	22.70	18.60	38.90	38.90	-	-
B2E	119.60	76.10	7.62	5.02	29.50	24.00	22.80	16.70	-	-
B3A	68.00	61.00	-	-	9.70	12.00	22.50	26.00	-	-
B3B	111.00	57.00	-	-	16.80	12.90	39.40	26.50	-	-
B3C	22.00	11.00	-	-	1.90	2.50	4.00	2.50	-	-
B4A	167.00	-	5.88	-	25.06	-	17.08	-	-	-
B4B	-	-	9.60	6.64	40.38	32.66	17.11	14.00	-	-
B4C	-	-	3.43	1.33	26.94	8.02	32.52	10.68	-	-
B4D	-	-	2.05	1.01	15.43	9.38	13.80	8.01	-	-
B4E	-	-	6.48	4.12	11.73	8.35	7.99	4.29	-	-
B5A	-	-	1.40	0.80	31.10	11.90	24.40	10.80	-	-
B5B	-	-	1.20	0.80	36.20	21.30	35.70	17.90	-	-
B6A	-	-	1.60	-	10.30	-	18.40	-	0.30	-
B6B	-	-	1.80	-	9.90	-	16.90	-	0.30	-
B7	132.34	-	2.69	-	7.43	-	8.56	-	-	-
B8A	92.60	-	2.84	-	9.73	-	14.60	-	-	-
B8B	73.80	-	0.38	-	8.01	-	15.90	-	-	-
B8C	103.90	-	1.60	-	1.42	-	18.70	-	-	-
B8D	106.60	-	4.53	-	12.20	-	10.80	-	-	-
B8E	88.60	-	4.76	-	16.20	-	13.80	-	-	-
B9A	117.00	-	-	-	14.43	-	7.34	-	-	-
B9B	138.00	-	-	-	11.77	-	8.91	-	-	-
B9C	90.00	-	-	-	9.89	-	4.90	-	-	-
B9D	196.00	-	-	-	23.08	-	16.68	-	-	-
B10A	99.47	38.22	4.90	3.54	11.43	8.90	9.96	6.12	-	-
B10B	217.14	135.60	7.50	7.50	24.41	24.41	22.61	22.61	-	-
B10C	286.23	98.01	9.62	3.23	65.66	23.48	54.21	21.58	-	-
B11A	96.55	-	-	-	6.89	-	9.90	-	-	-
B11B	79.80	-	-	-	8.18	-	9.61	-	-	-
B11C	122.09	-	-	-	10.72	-	9.88	-	-	-
B11D	76.41	-	-	-	4.66	-	6.71	-	-	-
B11E	88.99	-	-	-	5.36	-	13.43	-	-	-
B11F	106.94	-	-	-	7.83	-	10.55	-	-	-
B12A	162.06	179.94	2.92	2.19	11.92	11.79	13.52	13.95	0.43	0.36
B12B	93.29	56.26	1.41	1.31	11.18	10.37	18.42	15.28	0.25	0.16
B12C	105.22	39.00	1.09	0.99	9.14	10.27	12.69	12.91	0.32	1.01

B12D	214.23	159.34	5.28	3.99	12.29	12.12	20.96	19.72	0.36	0.28
B12E	154.26	145.65	3.07	3.13	11.52	11.37	17.07	16.52	0.35	0.44
B13A	164.00	-	3.50	-	39.50	-	32.30	-	-	-
B13B	164.00	-	1.00	-	26.50	-	40.20	-	-	-
B13C	125.00	-	2.90	-	21.70	-	32.60	-	-	-
B13D	51.00	-	0.70	-	4.20	-	5.70	-	-	-
B14A	100.40	-	-	-	9.20	-	12.60	-	-	-
B14B	97.20	-	-	-	6.00	-	11.00	-	-	-
B14C	76.90	-	-	-	7.10	-	9.80	-	-	-
B14D	111.20	-	-	-	9.10	-	14.50	-	-	-
B14E	116.20	-	-	-	8.90	-	13.50	-	-	-
B14F	126.50	-	-	-	9.50	-	14.30	-	-	-
B14G	106.70	-	-	-	8.30	-	12.70	-	-	-
B14H	51.40	-	-	-	4.00	-	9.30	-	-	-
B14I	58.80	-	-	-	2.30	-	7.00	-	-	-
B14J	25.90	-	-	-	1.80	-	5.50	-	-	-
B14K	46.50	-	-	-	4.70	-	8.00	-	-	-
B14L	52.80	-	-	-	3.80	-	9.40	-	-	-
B14M	62.00	-	-	-	4.90	-	11.20	-	-	-
B14N	52.30	-	-	-	3.70	-	8.70	-	-	-
B15	95.47	-	2.00	-	16.76	-	16.76	-	-	-
B16A	115.80	77.90	2.80	1.70	9.20	10.20	23.00	17.80	-	-
B16B	129.70	82.90	2.20	1.70	12.70	12.10	26.10	19.70	-	-
B16C	114.00	74.50	3.30	1.50	6.10	6.50	20.10	15.20	-	-
B17A	-	-	0.29	0.37	6.45	9.09	6.47	8.18	-	-
B17B	-	-	0.48	0.46	9.92	11.87	9.59	10.91	-	-
B17C	19.60	10.40	0.12	0.13	3.20	3.23	3.56	2.05	-	-
B18A	115.00	-	-	-	10.30	-	14.47	-	-	-
B18B	127.00	-	-	-	9.90	-	14.08	-	-	-
B18C	111.60	-	-	-	11.16	-	12.55	-	-	-
B18D	175.90	-	-	-	15.35	-	24.87	-	-	-
B18E	88.60	-	-	-	7.26	-	10.15	-	-	-
B18F	-	-	-	-	4.59	-	17.14	-	-	-
B19A	135.00	63.00	1.42	2.18	11.30	10.80	13.60	12.40	-	-
B19B	126.00	59.00	0.72	0.81	15.50	13.70	14.70	11.50	-	-
B19C	138.00	48.00	0.30	0.56	11.80	8.20	23.50	14.50	-	-
B19D	135.00	55.00	1.12	0.98	10.70	11.00	7.90	7.40	-	-
B19E	139.00	86.00	3.52	3.32	7.30	8.10	8.50	8.60	-	-
B20A	320.27	-	7.44	-	58.19	-	33.37	-	-	-
B20B	211.28	-	5.84	-	21.92	-	13.17	-	-	-
B20C	335.60	-	6.72	-	51.83	-	41.68	-	-	-
B20D	314.94	-	6.80	-	49.54	-	35.67	-	-	-
B20E	98.97	-	1.24	-	7.93	-	5.69	-	-	-
B20F	208.78	-	4.07	-	29.09	-	20.93	-	-	-
B21	-	-	4.91	-	16.35	-	23.52	-	-	-
B22A	77.30	55.70	1.93	1.50	12.20	12.60	16.00	17.30	-	-
B22B	82.20	49.50	1.98	1.12	13.30	9.26	19.20	14.00	-	-
B22C	75.40	45.60	1.69	1.30	13.20	10.30	19.70	16.20	-	-

B22D	135.70	96.60	6.38	3.45	17.00	15.40	30.40	25.40	-	-
B22E	140.80	73.90	6.57	2.07	13.50	9.17	23.10	17.10	-	-
B22F	182.20	120.80	7.36	4.69	19.30	13.70	29.90	23.40	-	-
B23A	-	-	4.60	1.90	13.80	10.40	15.20	9.40	-	-
B23B	-	-	1.80	1.20	15.20	9.30	29.90	19.70	-	-
B23C	-	-	6.10	4.70	20.50	17.60	18.60	12.50	-	-
B23D	-	-	7.30	4.90	13.30	9.70	20.30	17.40	-	-
B23E	176.60	100.30	4.50	4.00	15.40	11.70	22.40	17.00	-	-
B24A	80.60	57.30	0.60	0.60	13.70	13.40	28.40	27.30	-	-
B24B	143.80	42.30	1.10	0.70	26.40	12.00	58.00	24.70	-	-
B24C	45.90	25.50	0.30	0.50	6.60	7.80	12.10	8.20	-	-
B25	62.16	39.37	1.04	1.49	15.18	13.12	14.80	14.53	-	-
B26A	-	-	-	-	4.80	-	10.80	-	-	-
B26B	-	-	-	-	5.30	-	12.60	-	-	-
B26C	-	-	-	-	8.70	-	18.20	-	-	-
B26D	-	-	-	-	5.30	-	43.70	-	-	-
B27	68.00	61.00	0.40	-	9.90	12.00	22.60	26.10	-	-
B28	59.20	48.50	-	-	9.90	11.90	22.60	26.00	-	-
B29A	58.50	34.30	0.39	0.22	1.50	2.20	22.30	11.30	-	-
B29B	58.50	35.80	0.47	-	3.90	1.50	13.10	4.80	-	-
B30A	32.21	-	-	-	6.64	-	4.83	-	-	-
B30B	91.84	-	-	-	22.95	-	12.96	-	-	-
B30C	167.51	-	-	-	44.52	-	17.86	-	-	-
B30D	20.96	-	-	-	7.46	-	4.23	-	-	-
B30E	91.96	-	-	-	19.02	-	8.57	-	-	-
B30F	180.53	-	-	-	45.58	-	20.07	-	-	-
B30G	34.11	-	-	-	6.06	-	5.73	-	-	-
B30H	90.12	-	-	-	17.90	-	16.13	-	-	-
B30I	186.72	-	-	-	32.37	-	20.21	-	-	-
B30J	32.49	-	-	-	7.52	-	3.43	-	-	-
B30K	93.53	-	-	-	28.49	-	11.19	-	-	-
B30L	154.75	-	-	-	50.78	-	16.19	-	-	-

Ap Table. N. Beijing Minor Anion concentrations in Reviewed studies.

Beijing Minor Anions								
Study	F ⁻	F ⁻ SD	CH ₃ SO ₃ ⁻	CH ₃ SO ₃ ⁻ SD	NO ₂ ⁻	NO ₂ ⁻ SD	PO ₄ ³⁻	PO ₄ ³⁻ SD
B1A	0.32	-	-	-	-	-	-	-
B1B	0.04	-	-	-	-	-	-	-
B2A	0.22	0.33	-	-	-	-	-	-
B2B	0.28	0.30	-	-	-	-	-	-
B2C	0.07	0.08	-	-	-	-	-	-
B2D	0.42	0.50	-	-	-	-	-	-
B2E	0.10	0.14	-	-	-	-	-	-
B3A	-	-	-	-	-	-	-	-
B3B	-	-	-	-	-	-	-	-
B3C	-	-	-	-	-	-	-	-
B4A	0.24	-	-	-	-	-	-	-

B4B	0.50	0.23	-	-	-	-	-	-
B4C	0.23	0.11	-	-	-	-	-	-
B4D	0.01	0.01	-	-	-	-	-	-
B4E	0.11	0.15	-	-	-	-	-	-
B5A	-	-	-	-	8.00	2.70	-	-
B5B	-	-	-	-	2.50	0.50	-	-
B6A	-	-	-	-	-	-	-	-
B6B	-	-	-	-	-	-	-	-
B7	0.18	-	-	-	0.00	-	0.08	-
B8A	0.11	-	-	-	-	-	-	-
B8B	0.04	-	-	-	-	-	-	-
B8C	0.08	-	-	-	-	-	-	-
B8D	0.20	-	-	-	-	-	-	-
B8E	0.11	-	-	-	-	-	-	-
B9A	-	-	-	-	-	-	-	-
B9B	-	-	-	-	-	-	-	-
B9C	-	-	-	-	-	-	-	-
B9D	-	-	-	-	-	-	-	-
B10A	-	-	-	-	0.12	0.24	-	-
B10B	-	-	-	-	0.03	0.03	-	-
B10C	-	-	-	-	0.06	0.02	-	-
B11A	-	-	-	-	-	-	-	-
B11B	-	-	-	-	-	-	-	-
B11C	-	-	-	-	-	-	-	-
B11D	-	-	-	-	-	-	-	-
B11E	-	-	-	-	-	-	-	-
B11F	-	-	-	-	-	-	-	-
B12A	0.25	0.22	0.07	0.32	0.64	0.70	0.17	0.24
B12B	0.10	0.09	0.06	0.07	0.27	0.26	0.43	0.41
B12C	0.09	0.09	0.02	0.03	0.12	0.13	0.28	0.25
B12D	0.55	0.36	0.01	0.03	0.40	0.42	0.21	0.16
B12E	0.29	0.31	0.04	0.18	0.41	0.51	0.26	0.29
B13A	-	-	-	-	-	-	-	-
B13B	-	-	-	-	-	-	-	-
B13C	-	-	-	-	-	-	-	-
B13D	-	-	-	-	-	-	-	-
B14A	-	-	-	-	-	-	-	-
B14B	-	-	-	-	-	-	-	-
B14C	-	-	-	-	-	-	-	-
B14D	-	-	-	-	-	-	-	-
B14E	-	-	-	-	-	-	-	-
B14F	-	-	-	-	-	-	-	-
B14G	-	-	-	-	-	-	-	-
B14H	-	-	-	-	-	-	-	-
B14I	-	-	-	-	-	-	-	-
B14J	-	-	-	-	-	-	-	-
B14K	-	-	-	-	-	-	-	-
B14L	-	-	-	-	-	-	-	-

B14M	-	-	-	-	-	-	-	-
B14N	-	-	-	-	-	-	-	-
B15	0.05	-	-	-	-	-	-	-
B16A	-	-	-	-	-	-	-	-
B16B	-	-	-	-	-	-	-	-
B16C	-	-	-	-	-	-	-	-
B17A	0.03	0.03	-	-	-	-	-	-
B17B	0.05	0.03	-	-	-	-	-	-
B17C	0.01	0.02	-	-	-	-	-	-
B18A	-	-	-	-	-	-	-	-
B18B	-	-	-	-	-	-	-	-
B18C	-	-	-	-	-	-	-	-
B18D	-	-	-	-	-	-	-	-
B18E	-	-	-	-	-	-	-	-
B18F	-	-	-	-	-	-	-	-
B19A	-	-	-	-	-	-	-	-
B19B	-	-	-	-	-	-	-	-
B19C	-	-	-	-	-	-	-	-
B19D	-	-	-	-	-	-	-	-
B19E	-	-	-	-	-	-	-	-
B20A	-	-	-	-	-	-	-	-
B20B	-	-	-	-	-	-	-	-
B20C	-	-	-	-	-	-	-	-
B20D	-	-	-	-	-	-	-	-
B20E	-	-	-	-	-	-	-	-
B20F	-	-	-	-	-	-	-	-
B21	-	-	-	-	-	-	-	-
B22A	0.11	0.11	-	-	-	-	-	-
B22B	0.06	0.04	-	-	-	-	-	-
B22C	0.10	0.06	-	-	-	-	-	-
B22D	0.58	0.30	-	-	-	-	-	-
B22E	0.58	0.33	-	-	-	-	-	-
B22F	0.59	0.43	-	-	-	-	-	-
B23A	-	-	-	-	-	-	-	-
B23B	-	-	-	-	-	-	-	-
B23C	-	-	-	-	-	-	-	-
B23D	-	-	-	-	-	-	-	-
B23E	-	-	-	-	-	-	-	-
B24A	-	-	-	-	-	-	-	-
B24B	-	-	-	-	-	-	-	-
B24C	-	-	-	-	-	-	-	-
B25	-	-	-	-	-	-	-	-
B26A	-	-	-	-	-	-	-	-
B26B	-	-	-	-	-	-	-	-
B26C	-	-	-	-	-	-	-	-
B26D	-	-	-	-	-	-	-	-
B27	-	-	-	-	0.70	-	-	-
B28	-	-	-	-	-	-	-	-

B29A	-	-	-	-	-	-	-	-	-
B29B	-	-	-	-	-	-	-	-	-
B30A	-	-	-	-	-	-	-	-	-
B30B	-	-	-	-	-	-	-	-	-
B30C	-	-	-	-	-	-	-	-	-
B30D	-	-	-	-	-	-	-	-	-
B30E	-	-	-	-	-	-	-	-	-
B30F	-	-	-	-	-	-	-	-	-
B30G	-	-	-	-	-	-	-	-	-
B30H	-	-	-	-	-	-	-	-	-
B30I	-	-	-	-	-	-	-	-	-
B30J	-	-	-	-	-	-	-	-	-
B30K	-	-	-	-	-	-	-	-	-
B30L	-	-	-	-	-	-	-	-	-

Ap Table. O. Beijing Cation concentrations in Reviewed studies.

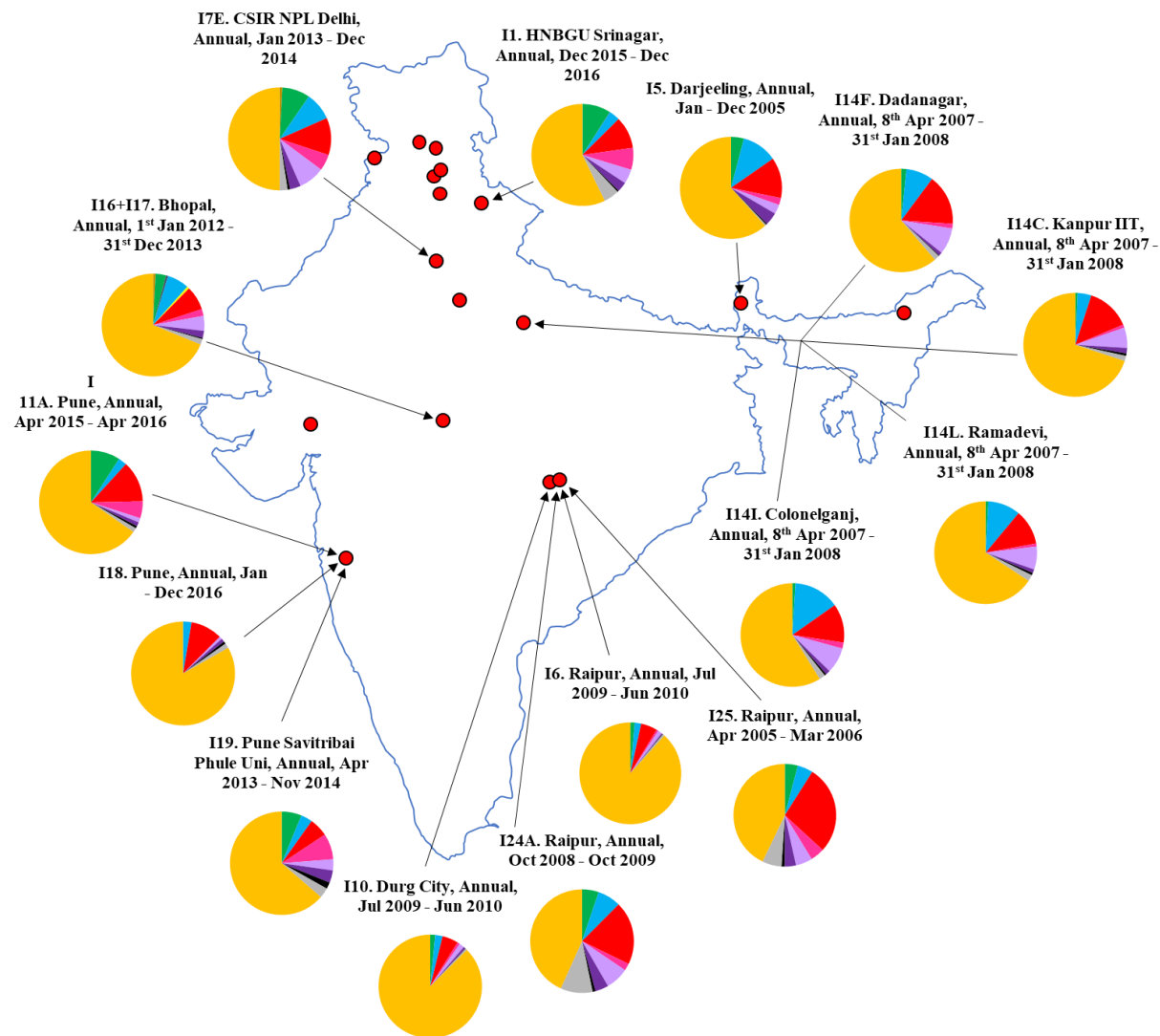
Study	Beijing Cations									
	Na ⁺	Na ⁺ SD	NH ₄ ⁺	NH ₄ ⁺ SD	K ⁺	K ⁺ SD	Mg ²⁺	Mg ²⁺ SD	Ca ²⁺	Ca ²⁺ SD
B1A	0.96	-	10.00	-	4.62	-	0.25	-	1.88	-
B1B	0.22	-	1.41	-	0.36	-	0.11	-	1.51	-
B2A	0.61	0.51	15.80	13.70	2.20	2.18	0.16	0.11	1.11	0.56
B2B	0.46	0.35	16.20	9.90	2.71	3.29	0.16	0.07	0.90	0.34
B2C	0.30	0.43	6.91	7.18	1.31	1.12	0.19	0.08	1.15	0.51
B2D	0.92	0.60	22.40	11.30	2.70	2.26	0.16	0.17	0.78	0.54
B2E	0.77	0.36	18.40	11.90	2.20	1.30	0.10	0.07	1.61	0.47
B3A	-	-	5.40	5.30	-	-	-	-	-	-
B3B	-	-	8.90	5.40	-	-	-	-	-	-
B3C	-	-	1.60	0.80	-	-	-	-	-	-
B4A	1.34	-	11.95	-	1.70	-	0.17	-	2.58	-
B4B	1.95	0.42	19.05	14.79	2.07	1.41	0.25	0.20	1.65	0.55
B4C	1.37	0.19	10.10	2.86	2.15	1.18	0.17	0.05	1.16	0.38
B4D	0.69	0.64	8.02	5.34	1.06	0.42	0.08	0.04	0.58	0.24
B4E	1.11	0.52	7.43	4.23	1.46	0.65	0.14	0.08	1.35	0.33
B5A	0.40	0.10	18.00	2.80	1.30	0.50	1.20	0.20	2.90	0.40
B5B	0.40	0.20	25.50	9.30	3.00	1.20	1.50	0.40	3.70	1.00
B6A	0.70	-	6.20	-	2.20	-	0.30	-	0.70	-
B6B	0.70	-	6.50	-	2.20	-	0.40	-	0.80	-
B7	0.54	-	4.55	-	2.23	-	0.21	-	1.76	-
B8A	0.47	-	8.33	-	1.24	-	0.11	-	0.63	-
B8B	0.18	-	6.94	-	1.21	-	0.10	-	0.18	-
B8C	0.53	-	10.70	-	1.31	-	0.13	-	0.43	-
B8D	0.73	-	6.66	-	1.26	-	0.14	-	0.11	-
B8E	0.44	-	9.62	-	1.17	-	0.09	-	0.08	-
B9A	-	-	8.34	-	-	-	-	-	-	-
B9B	-	-	7.09	-	-	-	-	-	-	-
B9C	-	-	4.15	-	-	-	-	-	-	-
B9D	-	-	11.36	-	-	-	-	-	-	-

B10A	0.54	0.68	5.13	3.19	1.23	0.64	0.51	0.21	4.43	2.90
B10B	0.56	0.56	4.50	4.50	1.67	1.67	0.26	0.26	2.59	2.59
B10C	1.84	0.49	10.82	3.55	4.05	3.82	0.55	0.40	2.94	1.21
B11A	-	-	5.78	-	1.70	-	0.16	-	-	-
B11B	-	-	5.94	-	1.75	-	0.96	-	-	-
B11C	-	-	7.13	-	2.29	-	0.16	-	-	-
B11D	-	-	4.13	-	1.99	-	0.16	-	-	-
B11E	-	-	5.90	-	1.81	-	0.10	-	-	-
B11F	-	-	5.46	-	1.44	-	0.13	-	-	-
B12A	0.61	0.64	6.47	6.75	1.09	0.97	0.24	0.20	2.54	2.46
B12B	0.24	0.17	10.10	6.97	1.29	1.25	0.10	0.07	0.73	0.60
B12C	0.21	0.15	6.33	5.80	0.76	0.74	0.06	0.06	1.16	1.70
B12D	0.88	0.52	10.64	8.83	2.48	2.16	0.20	0.17	1.68	1.67
B12E	0.55	0.54	8.72	7.66	1.55	1.63	0.17	0.16	1.63	1.90
B13A	0.48	-	20.30	-	1.20	-	0.08	-	1.00	-
B13B	0.49	-	21.80	-	1.10	-	0.15	-	1.20	-
B13C	0.41	-	21.50	-	1.20	-	0.07	-	0.50	-
B13D	0.24	-	3.20	-	0.40	-	0.12	-	1.50	-
B14A	-	-	5.40	-	-	-	-	-	-	-
B14B	-	-	5.40	-	-	-	-	-	-	-
B14C	-	-	5.30	-	-	-	-	-	-	-
B14D	-	-	5.60	-	-	-	-	-	-	-
B14E	-	-	7.30	-	-	-	-	-	-	-
B14F	-	-	6.50	-	-	-	-	-	-	-
B14G	-	-	6.00	-	-	-	-	-	-	-
B14H	-	-	3.20	-	-	-	-	-	-	-
B14I	-	-	3.10	-	-	-	-	-	-	-
B14J	-	-	2.10	-	-	-	-	-	-	-
B14K	-	-	2.80	-	-	-	-	-	-	-
B14L	-	-	3.70	-	-	-	-	-	-	-
B14M	-	-	3.90	-	-	-	-	-	-	-
B14N	-	-	3.30	-	-	-	-	-	-	-
B15	0.21	-	12.45	-	0.16	-	0.56	-	0.15	-
B16A	0.96	0.80	6.60	10.50	0.80	1.00	0.05	0.05	0.30	0.40
B16B	1.10	1.10	9.10	10.00	0.90	1.30	0.07	0.05	0.40	0.50
B16C	0.83	0.40	4.30	10.50	0.60	0.40	0.03	0.03	0.20	0.20
B17A	0.11	0.10	4.08	5.17	0.35	0.33	0.06	0.04	0.30	0.23
B17B	0.16	0.12	6.04	6.80	0.48	0.43	0.08	0.04	0.38	0.20
B17C	0.07	0.04	2.24	1.69	0.23	0.14	0.04	0.04	0.22	0.25
B18A	-	-	6.22	-	2.22	-	-	-	-	-
B18B	-	-	6.51	-	2.21	-	-	-	-	-
B18C	-	-	4.91	-	2.57	-	-	-	-	-
B18D	-	-	7.80	-	2.55	-	-	-	-	-
B18E	-	-	4.28	-	1.30	-	-	-	-	-
B18F	-	-	5.70	-	2.31	-	-	-	-	-
B19A	0.46	0.55	6.90	7.10	0.92	0.75	0.16	0.13	1.60	1.50
B19B	0.31	0.18	7.50	8.10	1.08	0.71	0.24	0.20	2.60	2.20
B19C	0.17	0.09	11.00	6.90	0.66	0.47	0.07	0.03	0.60	0.30

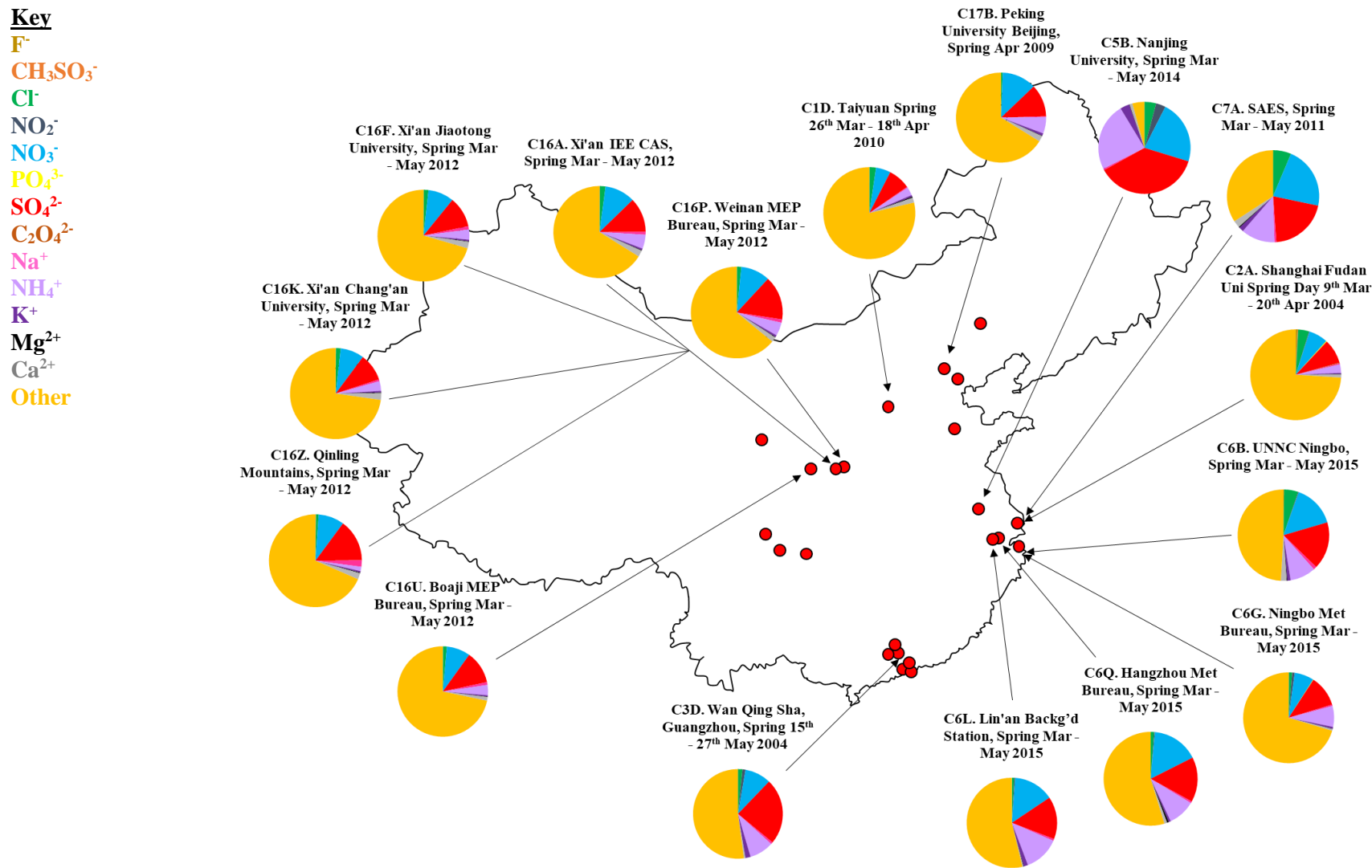
B19D	0.30	0.22	4.70	5.80	1.13	0.90	0.16	0.07	1.70	1.00
B19E	1.08	0.80	4.50	5.70	0.81	0.77	0.18	0.09	1.50	0.90
B20A	1.05	-	26.79	-	2.50	-	0.33	-	0.95	-
B20B	0.80	-	11.34	-	1.54	-	0.40	-	1.70	-
B20C	0.85	-	28.92	-	2.43	-	0.29	-	0.54	-
B20D	0.90	-	26.01	-	2.33	-	0.31	-	0.81	-
B20E	0.26	-	4.50	-	0.45	-	0.13	-	0.56	-
B20F	0.58	-	15.44	-	1.40	-	0.23	-	0.69	-
B21	2.04	-	10.48	-	1.38	-	0.71	-	1.08	-
B22A	-	-	10.40	7.74	1.20	1.32	-	-	-	-
B22B	-	-	11.00	6.59	1.53	1.24	-	-	-	-
B22C	-	-	9.75	6.78	1.21	1.64	-	-	-	-
B22D	-	-	12.90	10.70	1.94	1.80	-	-	-	-
B22E	-	-	13.30	7.18	1.88	1.33	-	-	-	-
B22F	-	-	20.30	10.40	4.23	2.10	-	-	-	-
B23A	-	-	2.90	3.70	2.20	1.10	-	-	5.80	3.10
B23B	-	-	9.30	6.60	2.10	1.30	-	-	1.20	1.50
B23C	-	-	7.70	6.60	3.70	2.70	-	-	3.30	2.90
B23D	-	-	7.30	7.30	2.90	2.30	-	-	2.30	1.90
B23E	-	-	7.30	6.70	2.60	1.90	-	-	3.40	3.00
B24A	0.40	0.60	10.50	9.30	0.90	0.60	0.30	0.60	1.20	1.70
B24B	0.50	0.30	20.80	7.40	1.50	0.40	0.40	1.00	1.20	1.90
B24C	0.30	0.70	4.80	3.40	0.60	0.50	0.20	0.40	1.10	1.60
B25	0.36	0.69	8.90	9.51	-	-	0.06	0.05	-	-
B26A	-	-	11.70	-	-	-	-	-	-	-
B26B	-	-	21.40	-	-	-	-	-	-	-
B26C	-	-	9.60	-	-	-	-	-	-	-
B26D	-	-	7.40	-	-	-	-	-	-	-
B27	0.10	-	4.70	3.30	1.30	-	0.03	-	0.20	-
B28	-	-	-	-	-	-	-	-	-	-
B29A	0.43	0.22	8.00	3.10	1.50	0.59	0.22	0.10	1.50	0.74
B29B	0.19	0.16	8.40	2.50	0.46	0.22	0.08	0.04	0.41	0.19
B30A	-	-	3.86	-	-	-	-	-	-	-
B30B	-	-	12.51	-	-	-	-	-	-	-
B30C	-	-	20.88	-	-	-	-	-	-	-
B30D	-	-	4.09	-	-	-	-	-	-	-
B30E	-	-	10.31	-	-	-	-	-	-	-
B30F	-	-	22.51	-	-	-	-	-	-	-
B30G	-	-	3.96	-	-	-	-	-	-	-
B30H	-	-	12.33	-	-	-	-	-	-	-
B30I	-	-	17.13	-	-	-	-	-	-	-
B30J	-	-	3.59	-	-	-	-	-	-	-
B30K	-	-	13.20	-	-	-	-	-	-	-
B30L	-	-	22.56	-	-	-	-	-	-	-

Key

- F^- (gold)
- $CH_3SO_3^-$ (orange)
- Cl^- (green)
- NO_2^- (dark blue)
- NO_3^- (light blue)
- PO_4^{3-} (yellow)
- SO_4^{2-} (red)
- $C_2O_4^{2-}$ (brown)
- Na^+ (pink)
- NH_4^+ (lilac)
- K^+ (purple)
- Mg^{2+} (black)
- Ca^{2+} (grey)
- Other (amber)



Ap Fig. A. Map of India showing the distribution of ionic PM_{2.5} particle composition across India (Annual) from reviewed studies. A key denoting the segment species colours is shown in the top left corner. Red markers on the map of India show the different cities. Text shown above each study presents the details of each study. The species are presented as F^- (gold), $CH_3SO_3^-$ (orange), Cl^- (green), NO_2^- (dark blue), Br^- (medium blue), NO_3^- (light blue), PO_4^{3-} (yellow), SO_4^{2-} (red), $C_2O_4^{2-}$ (brown), Na^+ (pink), NH_4^+ (lilac), K^+ (purple), Mg^{2+} (black), Ca^{2+} (grey) and other (amber) in the pie charts.

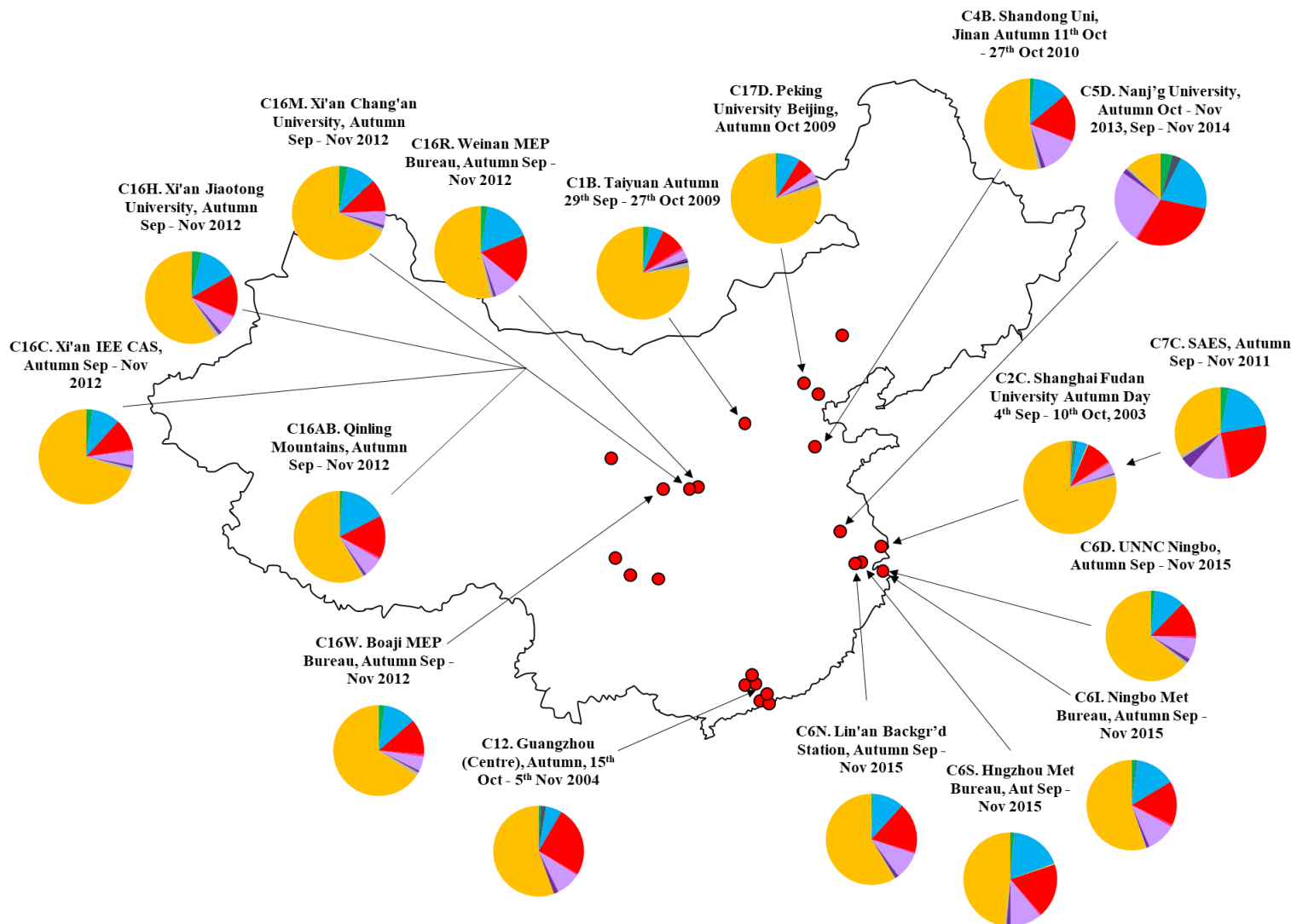


Ap Fig. B. Map of China showing the distribution of ionic $PM_{2.5}$ particle composition across China (Spring) from reviewed studies. A key denoting the segment species colours is shown in the top left corner. Red markers on the map of India show the different cities. Text shown above each study presents the details of each study. The species are presented as F^- (gold), $CH_3SO_3^-$ (orange), Cl^- (green), NO_2^- (dark blue), Br^- (medium blue), NO_3^- (light blue), PO_4^{3-} (yellow), SO_4^{2-} (red), $C_2O_4^{2-}$ (brown), Na^+ (pink), NH_4^+ (lilac), K^+ (purple), Mg^{2+} (black), Ca^{2+} (grey) and other (amber) in the pie charts.

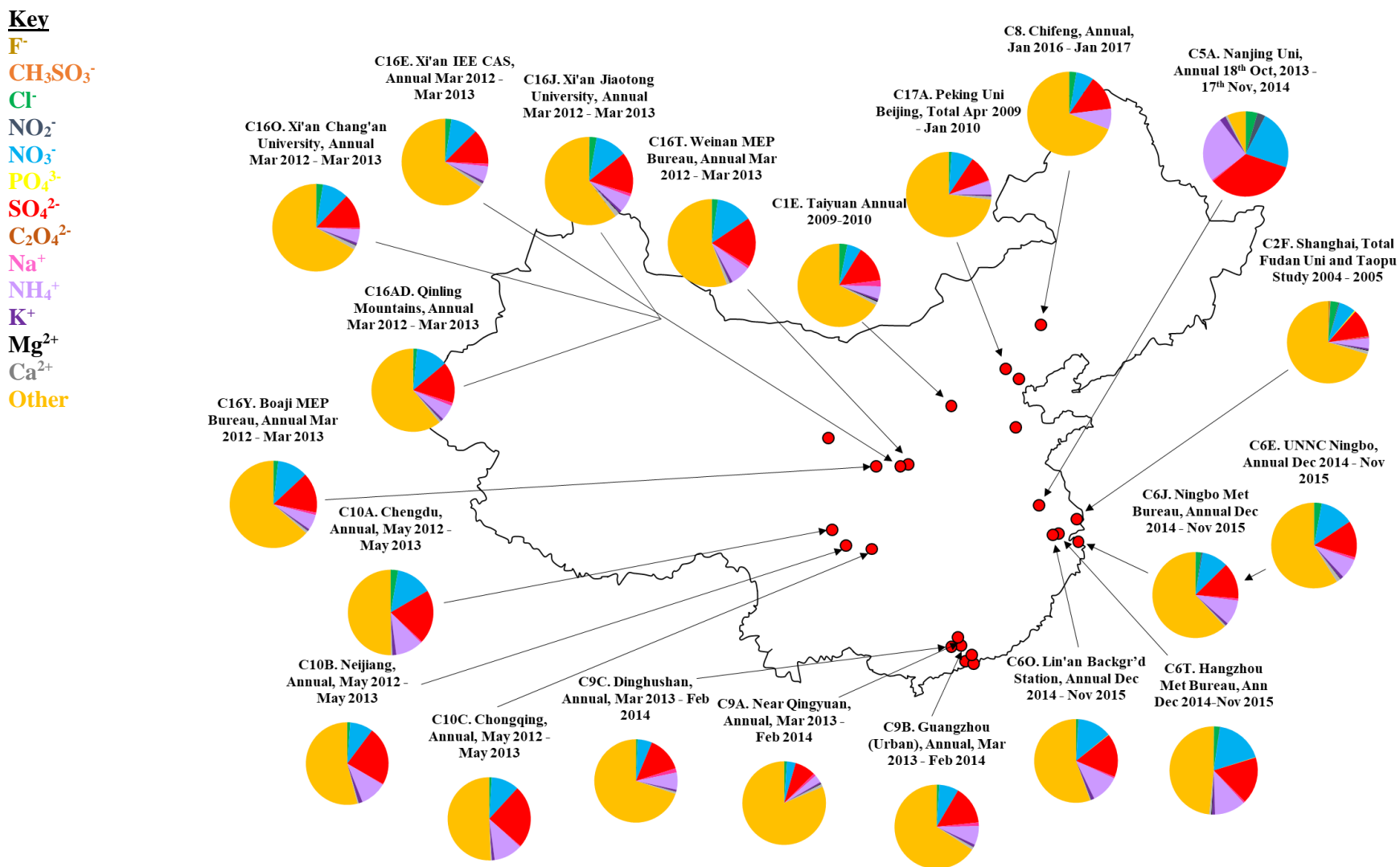
China Autumn

Key

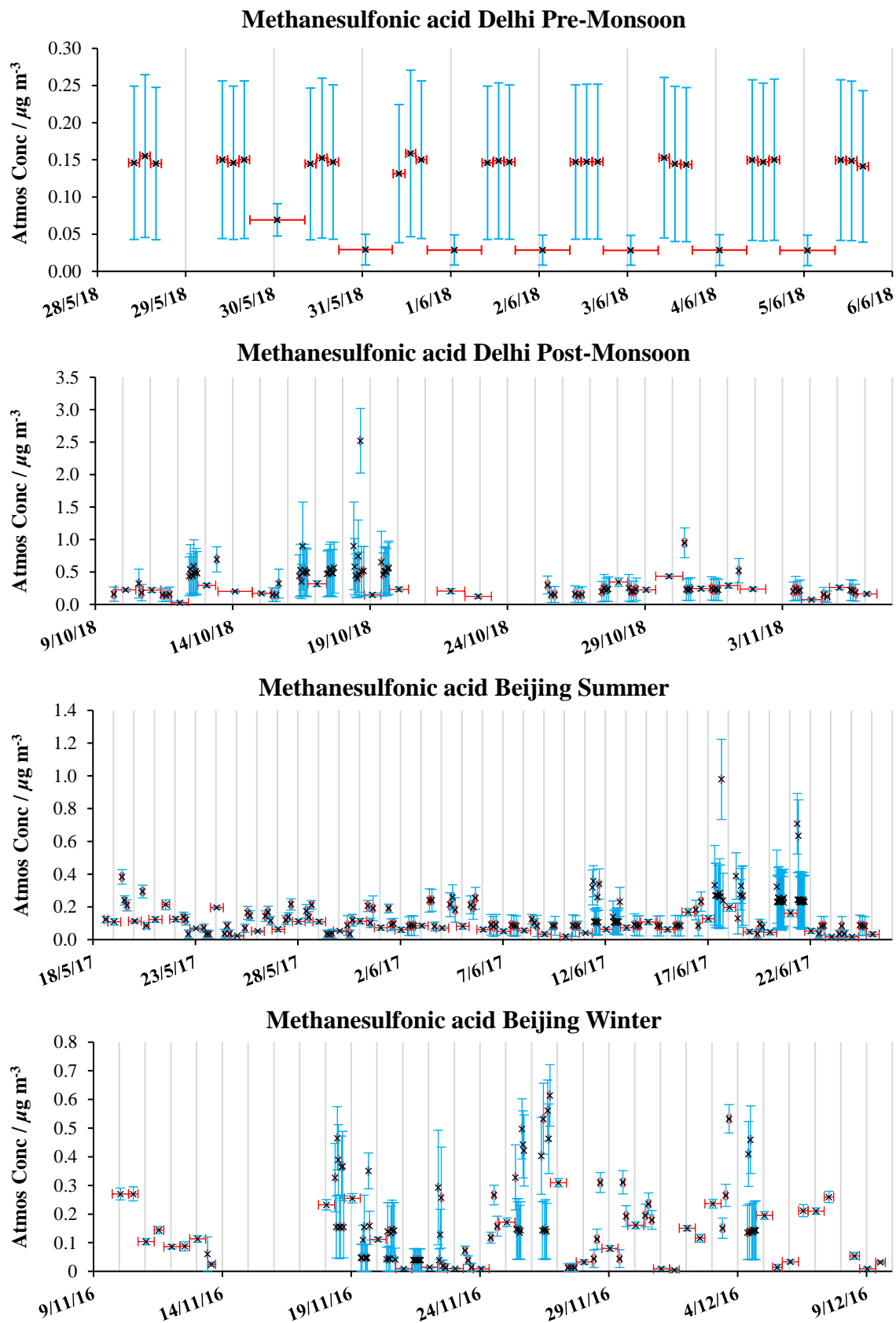
F^-
 $CH_3SO_3^-$
 Cl^-
 NO_2^-
 NO_3^-
 PO_4^{3-}
 SO_4^{2-}
 $C_2O_4^{2-}$
 Na^+
 NH_4^+
 K^+
 Mg^{2+}
 Ca^{2+}
 Other



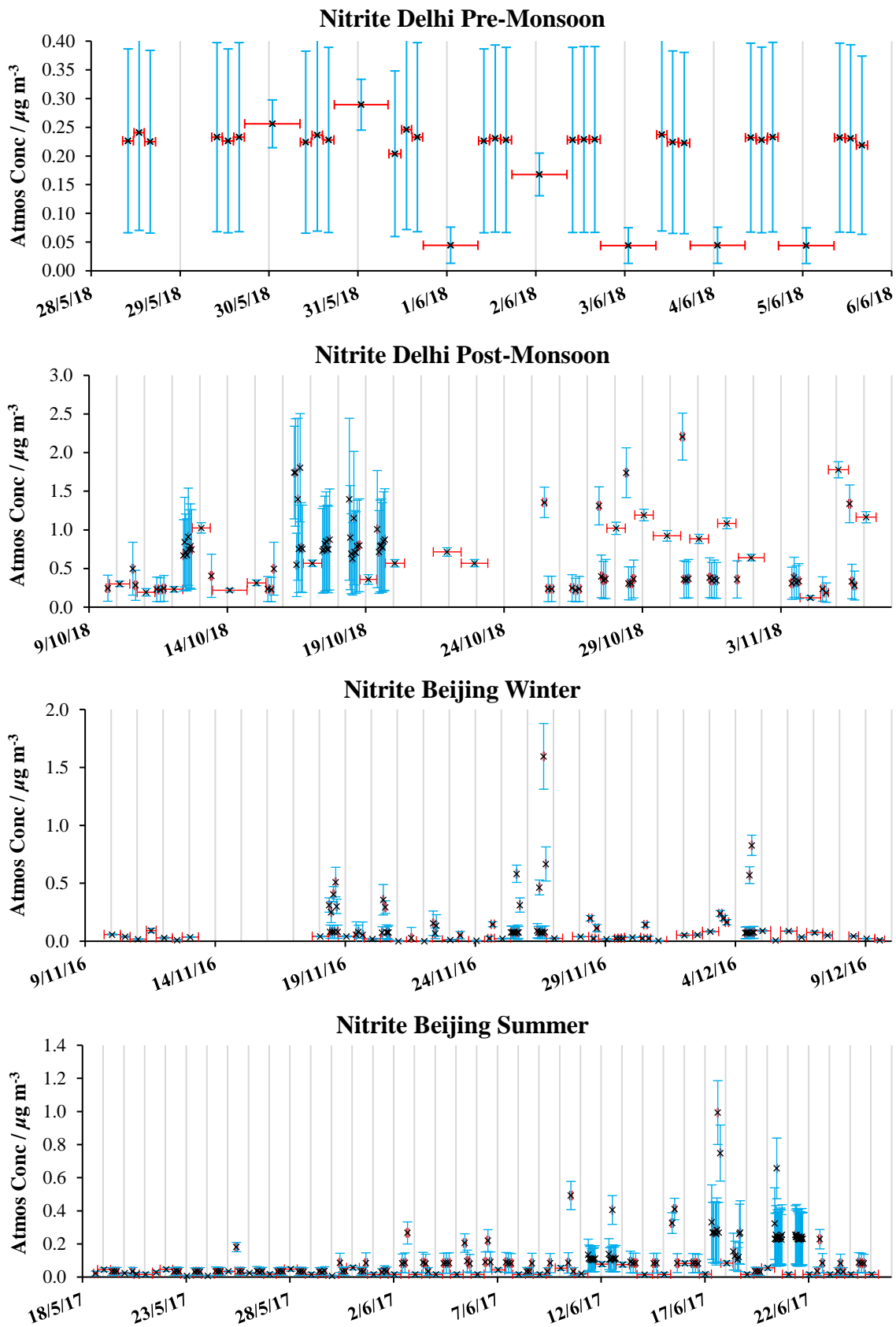
Ap Fig. C. Map of China showing the distribution of ionic $PM_{2.5}$ particle composition across China (Autumn) from reviewed studies. A key denoting the segment species colours is shown in the top left corner. Red markers on the map of India show the different cities. Text shown above each study presents the details of each study. The species are presented as F^- (gold), $CH_3SO_3^-$ (orange), Cl^- (green), NO_2^- (dark blue), Br^- (medium blue), NO_3^- (light blue), PO_4^{3-} (yellow), SO_4^{2-} (red), $C_2O_4^{2-}$ (brown), Na^+ (pink), NH_4^+ (lilac), K^+ (purple), Mg^{2+} (black), Ca^{2+} (grey) and other (amber) in the pie charts.



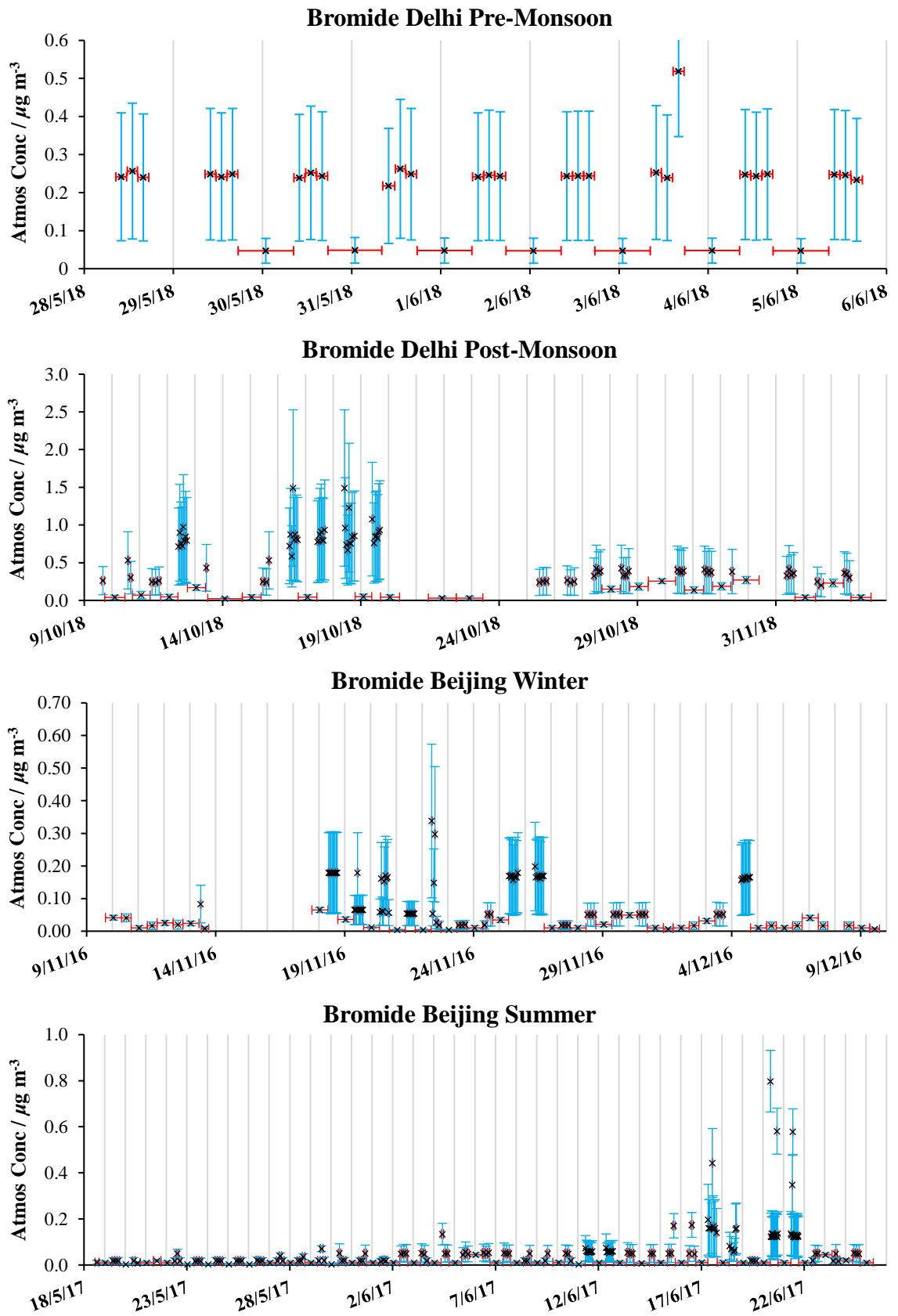
Ap Fig. D. Map of China showing the distribution of ionic PM_{2.5} particle composition across China (Annual) from reviewed studies. A key denoting the segment species colours is shown in the top left corner. Red markers on the map of India show the different cities. Text shown above each study presents the details of each study. The species are presented as F⁻ (gold), CH₃SO₃⁻ (orange), Cl⁻ (green), NO₂⁻ (dark blue), Br⁻ (medium blue), NO₃⁻ (light blue), PO₄³⁻ (yellow), SO₄²⁻ (red), C₂O₄²⁻ (brown), Na⁺ (pink), NH₄⁺ (lilac), K⁺ (purple), Mg²⁺ (black), Ca²⁺ (grey) and other (amber) in the pie charts.



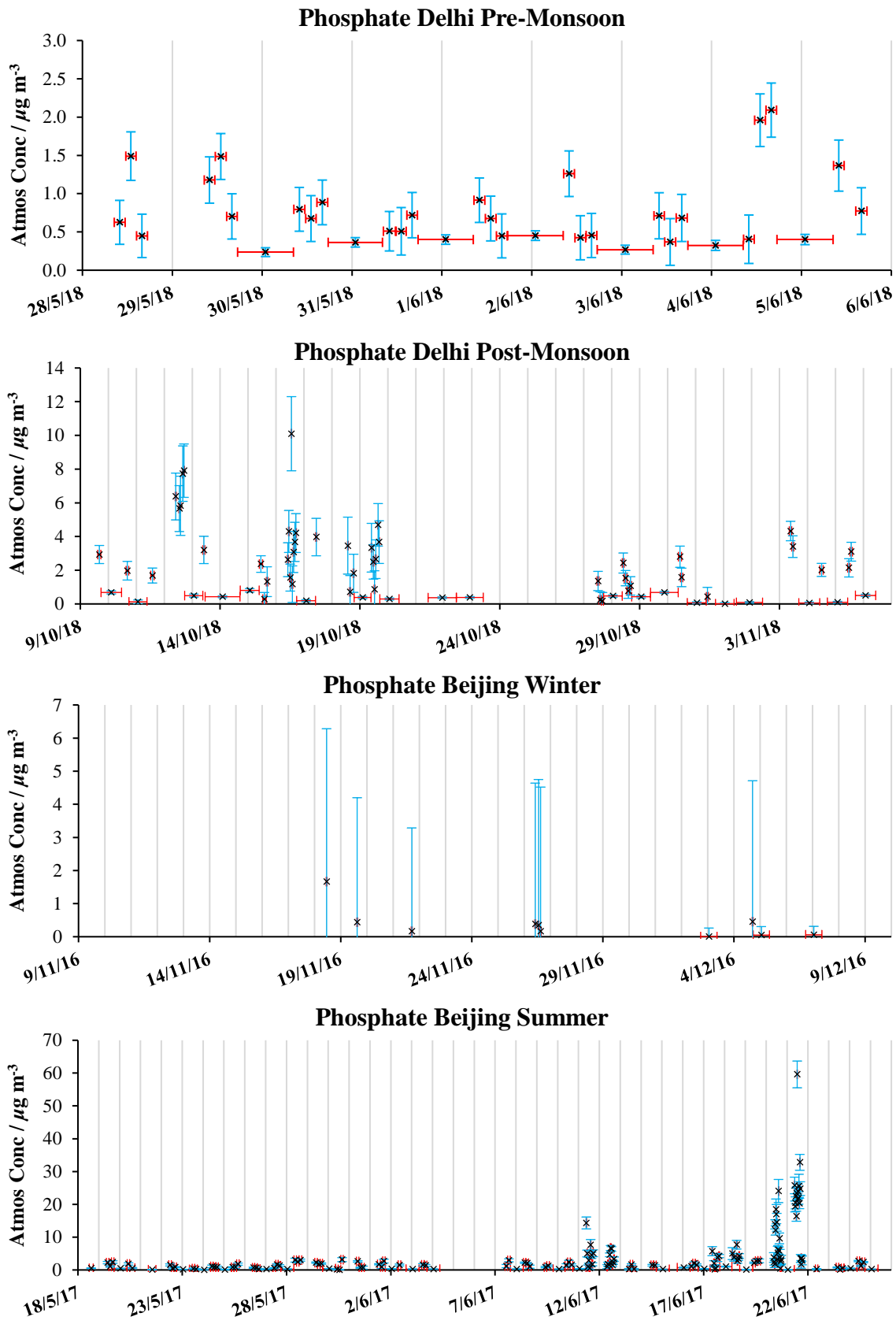
Ap Fig. E. Time series of Methanesulfonic acid measured by offline ion chromatography during the APHH Delhi pre-monsoon, Delhi Post-Monsoon, Beijing Winter and Beijing Summer campaigns. Ion concentrations are shown on the y-axis with time on the x-axis. The grey vertical lines represent midnight time points. The red error bars show the time of sampling and the blue error bars show the error of each concentration measurement in the y-axis.



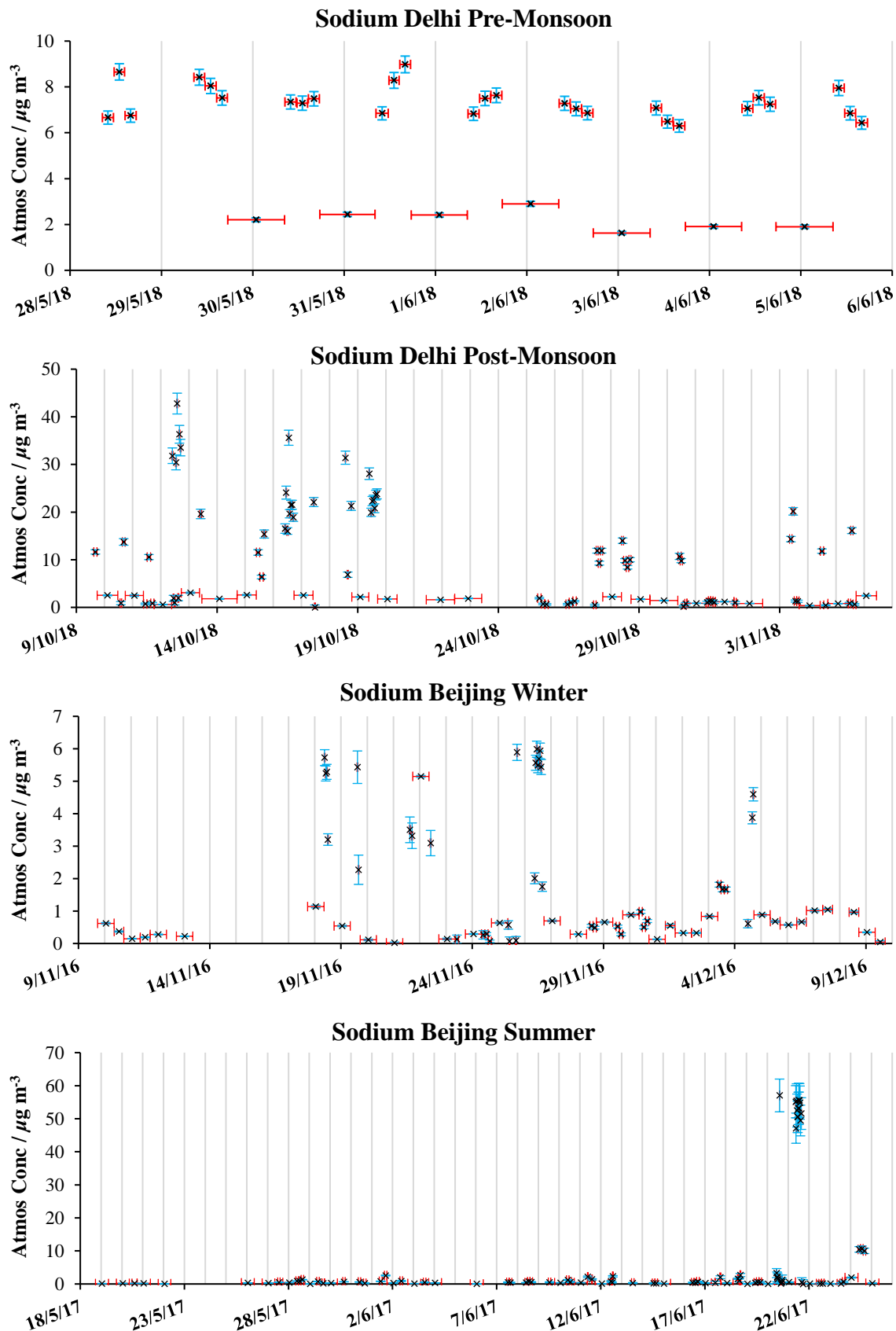
Ap Fig. F. Time series of Nitrite measured by offline ion chromatography during the APHH Delhi pre-monsoon, Delhi Post-Monsoon, Beijing Winter and Beijing Summer campaigns. Ion concentrations are shown on the y-axes with time on the x-axes. The grey vertical lines represent midnight time points. The red error bars show the time of sampling and the blue error bars show the error of each concentration measurement in the y-axis. LOD for NO_2^- is 2.6×10^{-2} ppm (BWIN), 9.2×10^{-2} ppm (BSUM) and 2.7×10^{-1} ppm for the Delhi campaigns.



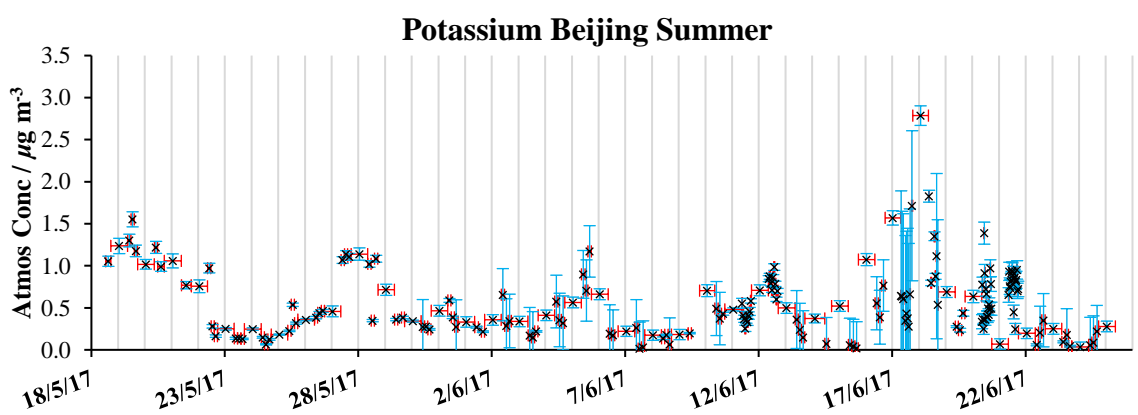
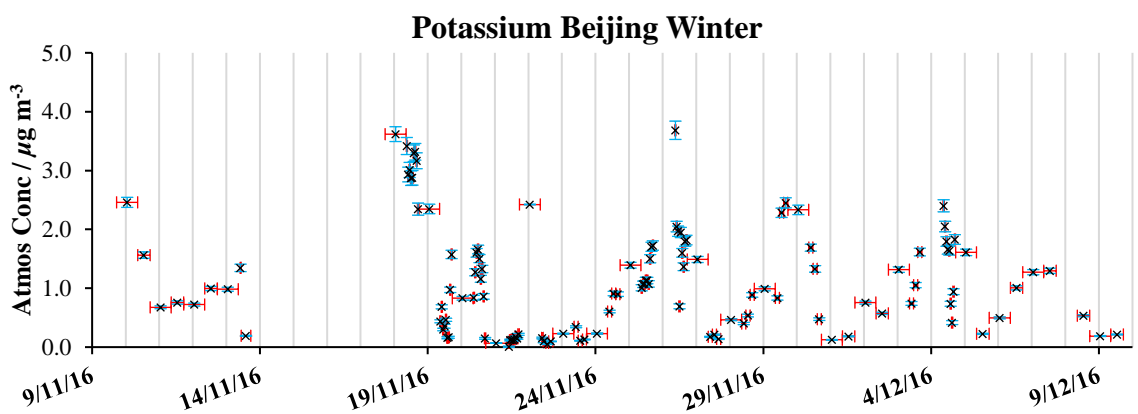
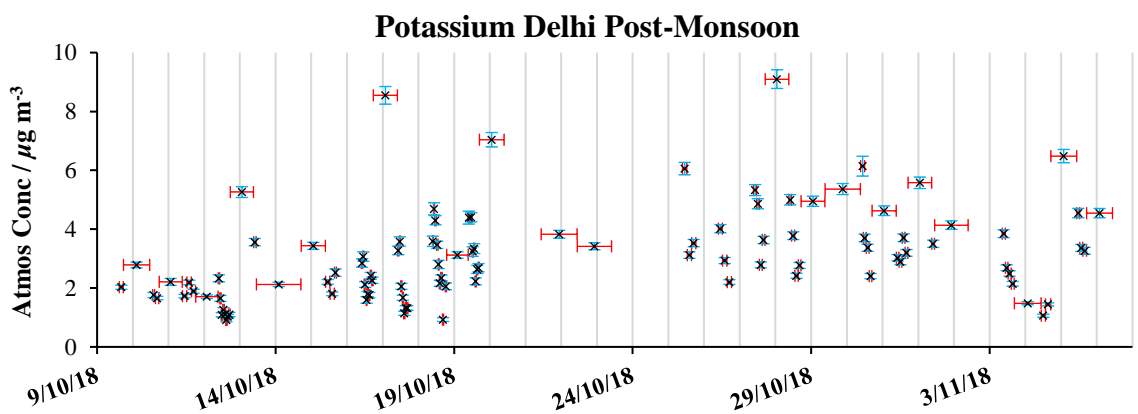
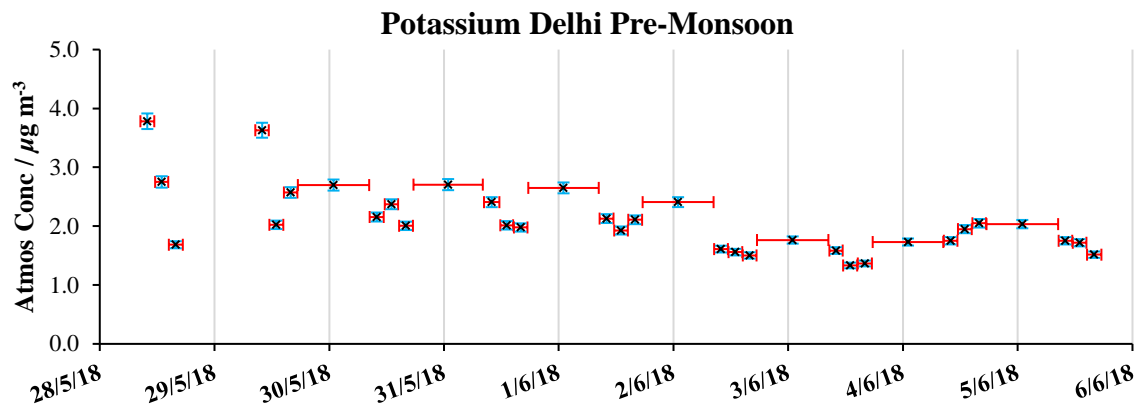
Ap Fig. G. Time series of Bromide measured by offline ion chromatography during the APHH Delhi pre-monsoon, Delhi Post-Monsoon, Beijing Winter and Beijing Summer campaigns. Ion concentrations are shown on the y-axes with time on the x-axes. The grey vertical lines represent midnight time points. The red error bars show the time of sampling and the blue error bars show the error of each concentration measurement in the y-axis. LOD for NO_2^- is 2.6×10^{-2} ppm (BWIN), 9.2×10^{-2} ppm (BSUM) and 2.7×10^{-1} ppm for the Delhi campaigns.



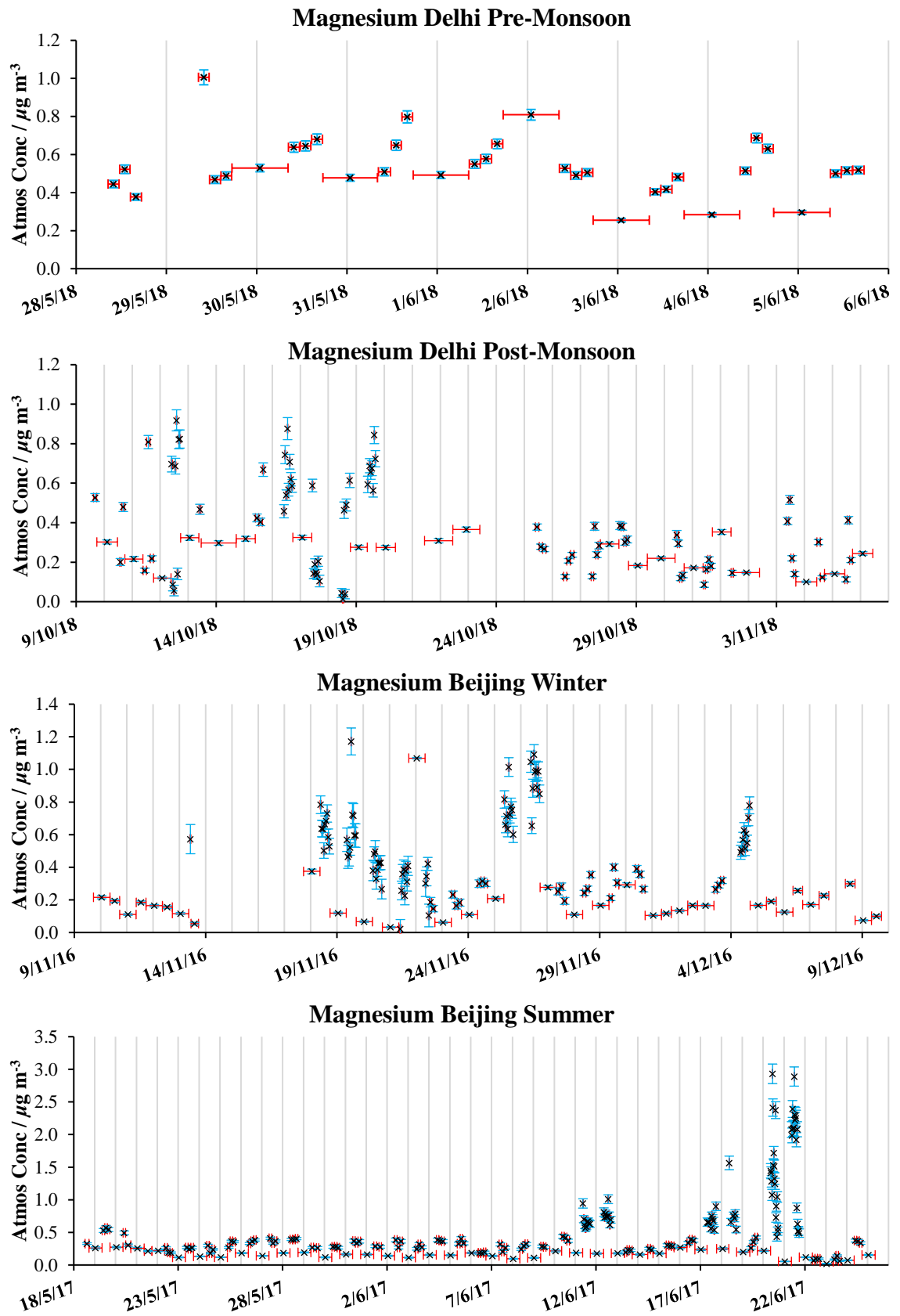
Ap Fig. H. Time series of Phosphate measured by offline ion chromatography during the APHH Delhi pre-monsoon, Delhi Post-Monsoon, Beijing Winter and Beijing Summer campaigns. Ion concentrations are shown on the y-axis with time on the x-axis. The grey vertical lines represent midnight time points. The red error bars show the time of sampling and the blue error bars show the error of each concentration measurement in the y-axis.



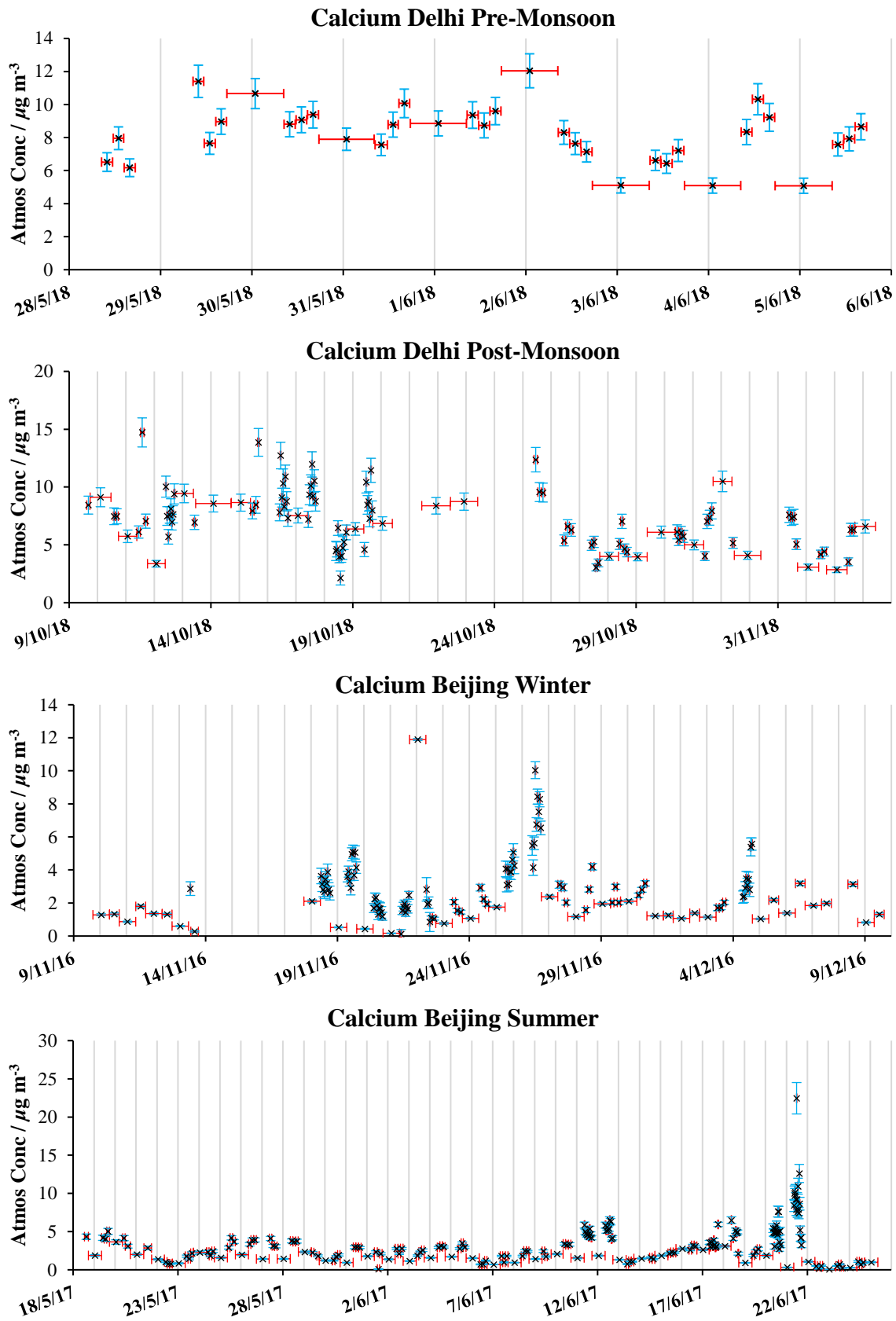
Ap Fig. 1. Time series of Sodium measured by offline ion chromatography during the APHH Delhi pre-monsoon, Delhi Post-Monsoon, Beijing Winter and Beijing Summer campaigns. Ion concentrations are shown on the y-axes with time on the x-axes. The grey vertical lines represent midnight time points. The red error bars show the time of sampling and the blue error bars show the error of each concentration measurement in the y-axis.



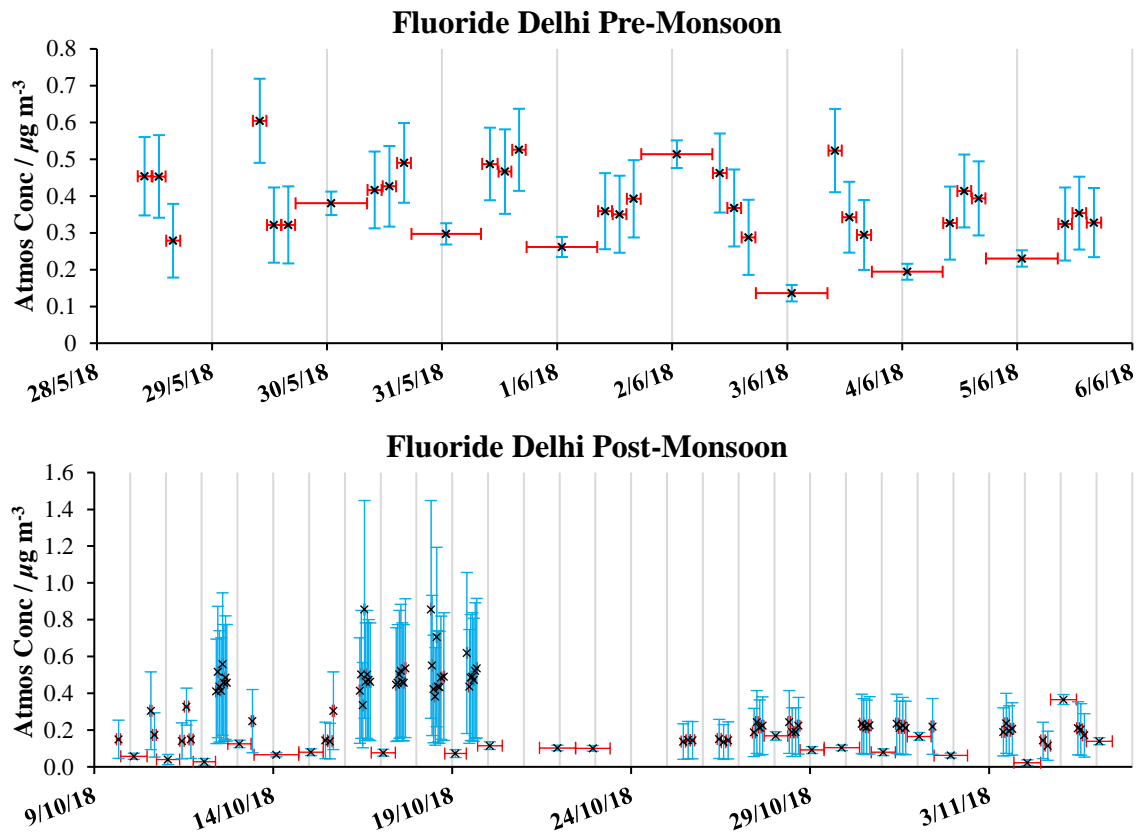
Ap Fig. J. Time series of Potassium measured by offline ion chromatography during the APHH Delhi pre-monsoon, Delhi Post-Monsoon, Beijing Winter and Beijing Summer campaigns. Ion concentrations are shown on the y-axes with time on the x-axes. The grey vertical lines represent midnight time points. The red error bars show the time of sampling and the blue error bars show the error of each concentration measurement in the y-axis.



Ap Fig. K. Time series of Magnesium measured by offline ion chromatography during the APHH Delhi pre-monsoon, Delhi Post-Monsoon, Beijing Winter and Beijing Summer campaigns. Ion concentrations are shown on the y-axis with time on the x-axis. The grey vertical lines represent midnight time points. The red error bars show the time of sampling and the blue error bars show the error of each concentration measurement in the y-axis.

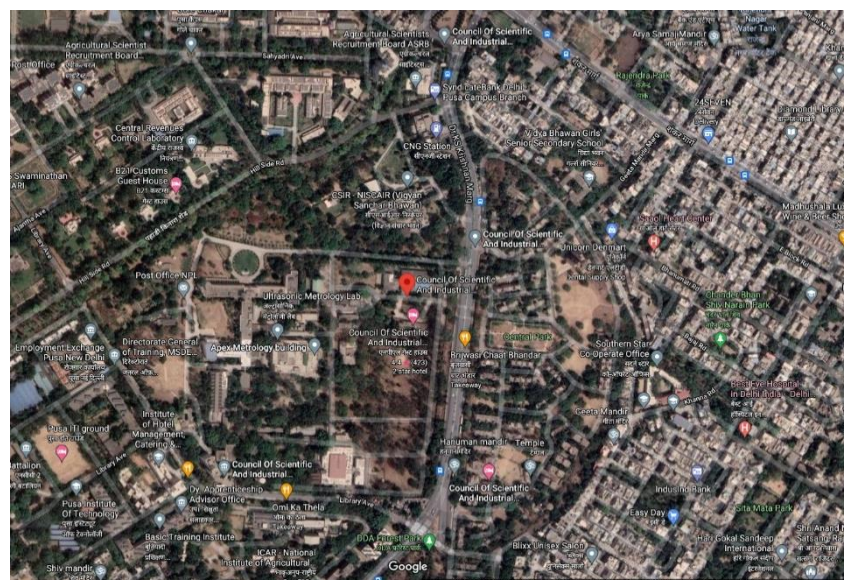


Ap Fig. L. Time series of Calcium measured by offline ion chromatography during the APHH Delhi pre-monsoon, Delhi Post-Monsoon, Beijing Winter and Beijing Summer campaigns. Ion concentrations are shown on the y-axes with time on the x-axes. The grey vertical lines represent midnight time points. The red error bars show the time of sampling and the blue error bars show the error of each concentration measurement in the y-axis.



Ap Fig. M. Time series of Fluoride measured by offline ion chromatography during the APHH Delhi pre-monsoon, Delhi Post-Monsoon, Beijing Winter and Beijing Summer campaigns. Ion concentrations are shown on the y-axes with time on the x-axes. The grey vertical lines represent midnight time points. The red error bars show the time of sampling and the blue error bars show the error of each concentration measurement in the y-axis.

National Physical Laboratory of India (NPL): Urban



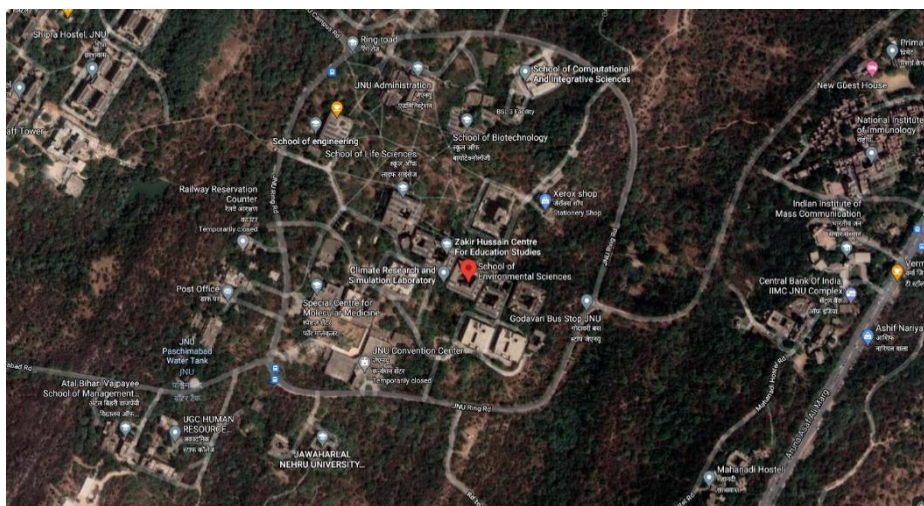
Ap Fig. N. Satellite image of the National Physical Laboratory of India (NPL) used for sampling site classification in chapter 4.

Indian Institute of Tropical Meteorology (IITM): Suburban



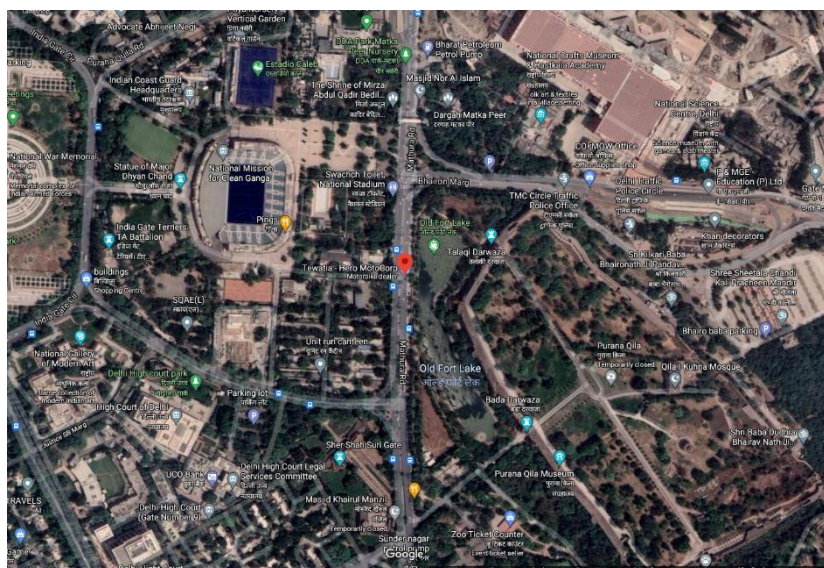
Ap Fig. O. Satellite image of the Indian Institute of Tropical Meteorology (IITM) used for sampling site classification in chapter 4.

School of Environmental Sciences, Jawaharlal Nehru University (JNU): Suburban



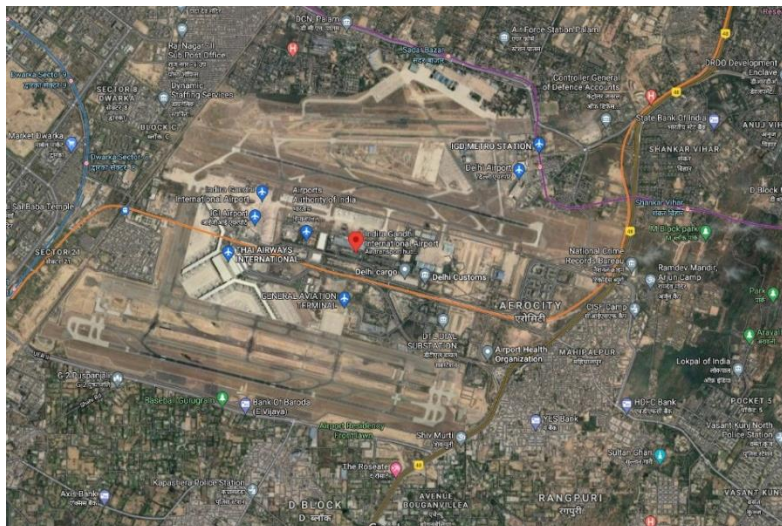
Ap Fig. P. Satellite image of the School of Environmental Sciences, Jawaharlal Nehru University (JNU) used for sampling site classification in chapter 4.

Mathura Rd. (Mat Rd.): (Roadside)



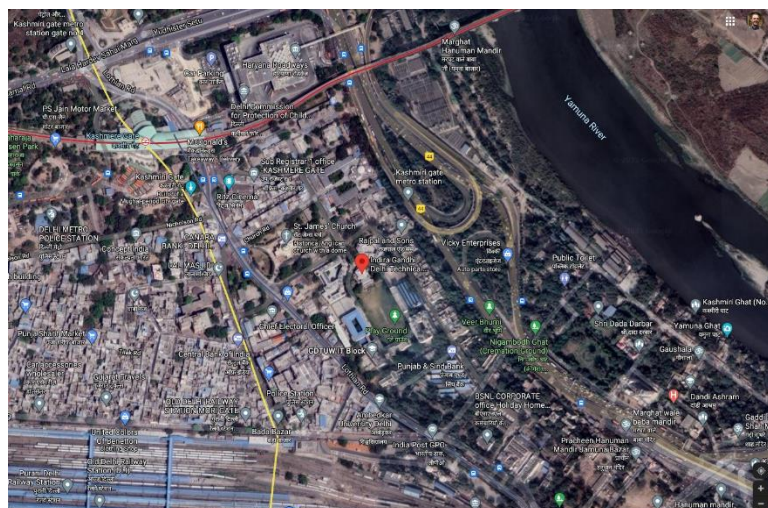
Ap Fig. Q. Satellite image of the Mathura Rd. (Mat Rd.) used for sampling site classification in chapter 4.

Indira Gandhi International Airport (IGIA): (Airport)



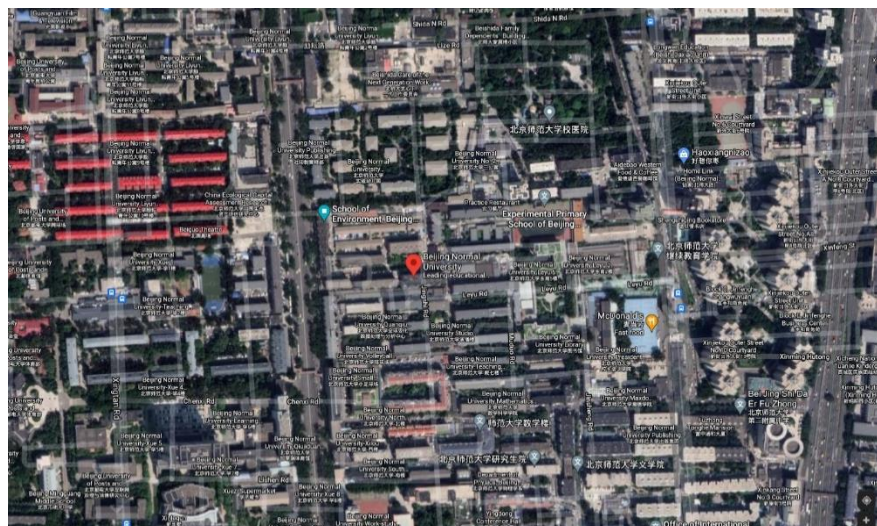
Ap Fig. R. Satellite image of the Indira Gandhi International Airport (IGIA) used for sampling site classification in chapter 4.

Indira Gandhi Delhi Technical University for Women (IGDTUW): Urban



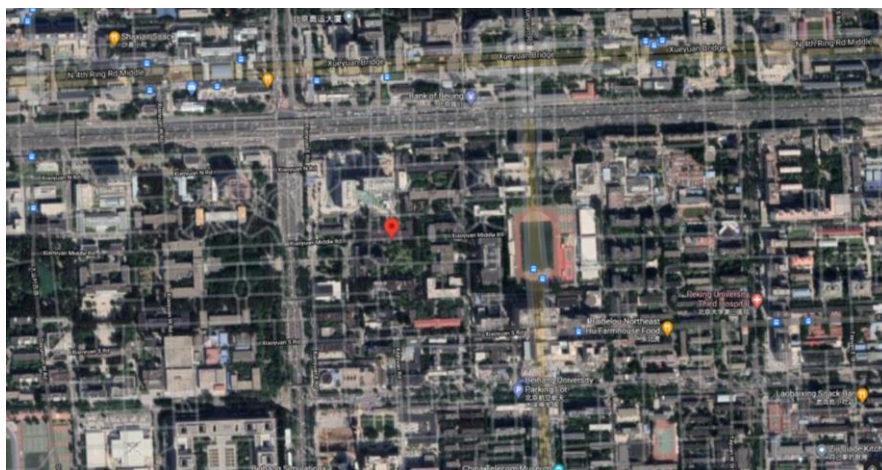
Ap Fig. S. Satellite image of the Indira Gandhi Delhi Technical University for Women (IGDTUW) used for sampling site classification in chapter 4.

Beijing Normal University (BNU): Urban



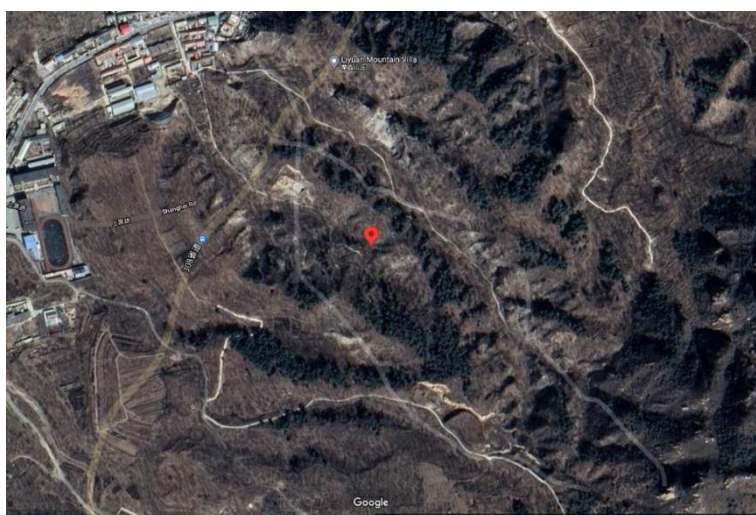
Ap Fig. T. Satellite image of the Beijing Normal University (BNU) used for sampling site classification in chapter 4.

Beihang University (BEI): Urban



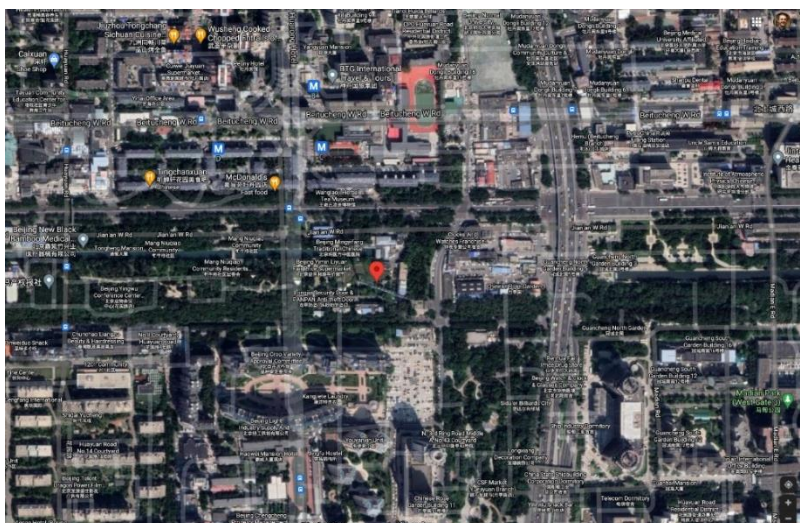
Ap Fig. U. Satellite image of the Beihang University (BEI) used for sampling site classification in chapter 4.

Hei Shan Zhai (HSZ): Rural



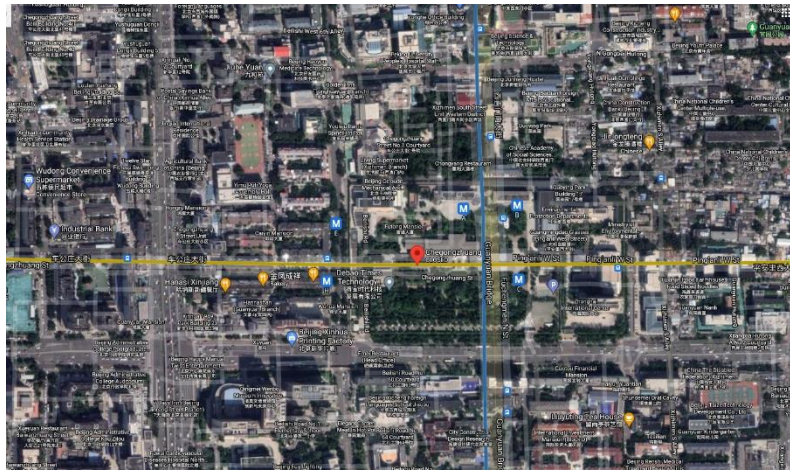
Ap Fig. V. Satellite image of the Hei Shan Zhai (HSZ) used for sampling site classification in chapter 4.

Chinese Ecosystem Research Network (CERN): Urban



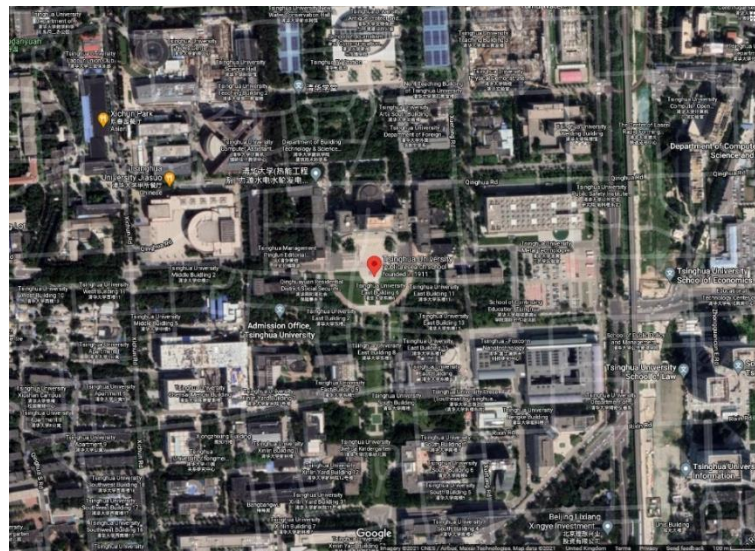
Ap Fig. W. Satellite image of the Chinese Ecosystem Research Network (CERN) used for sampling site classification in chapter 4.

Chegongzhuang (CGZ): Urban



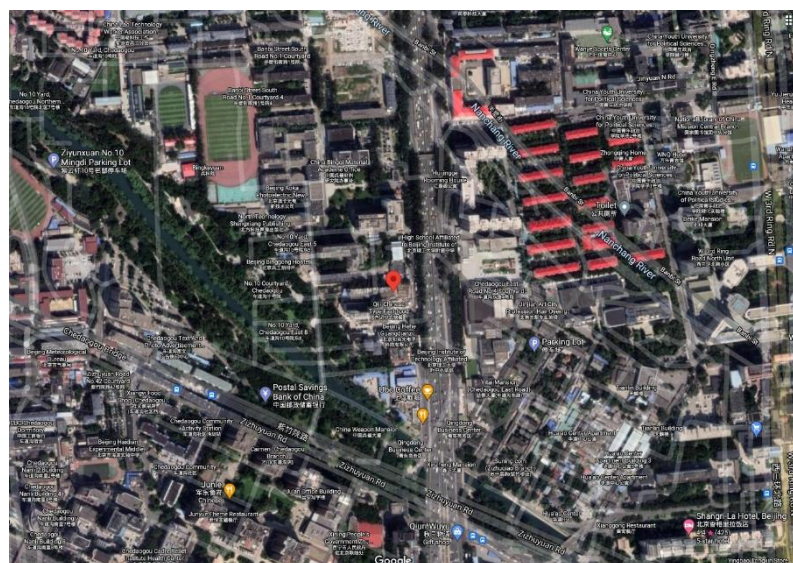
Ap Fig. X. Satellite image of the Chegongzhuang (CGZ) used for sampling site classification in chapter 4.

Tsinghua University (THU): Suburban



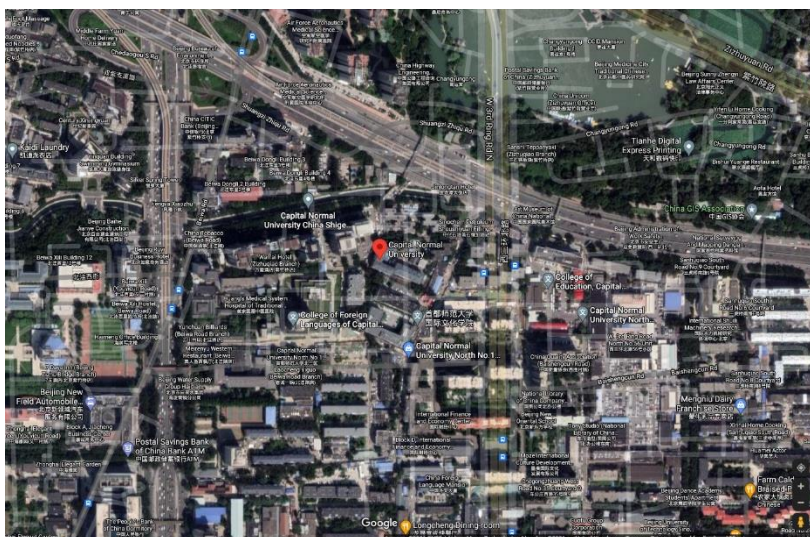
Ap Fig. Y. Satellite image of the Tsinghua University (THU) used for sampling site classification in chapter 4.

Urban Site (US): Urban



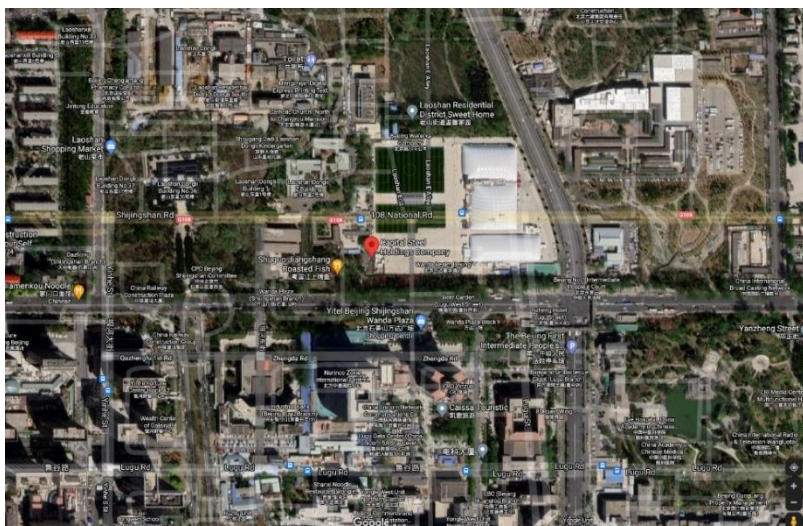
Ap Fig. Z. Satellite image of the Urban Site (US) used for sampling site classification in chapter 4.

Capital Normal University (CNU): Urban



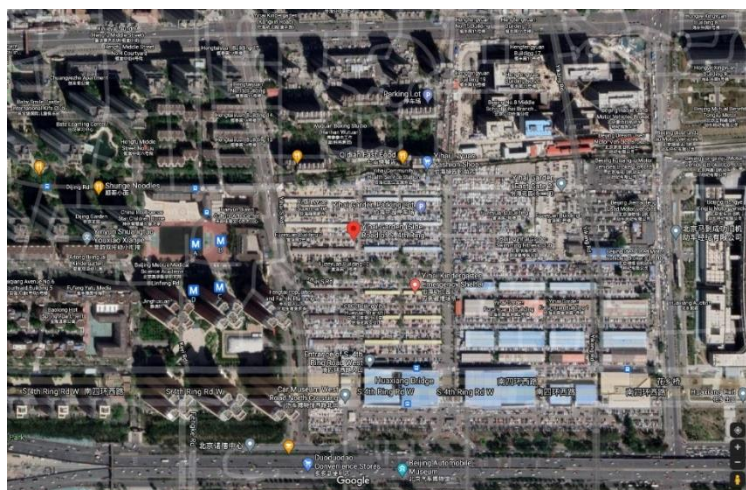
Ap Fig. AA. Satellite image of the Capital Normal University (CNU) used for sampling site classification in chapter 4.

Capital Steel Company (CSC): Industrial



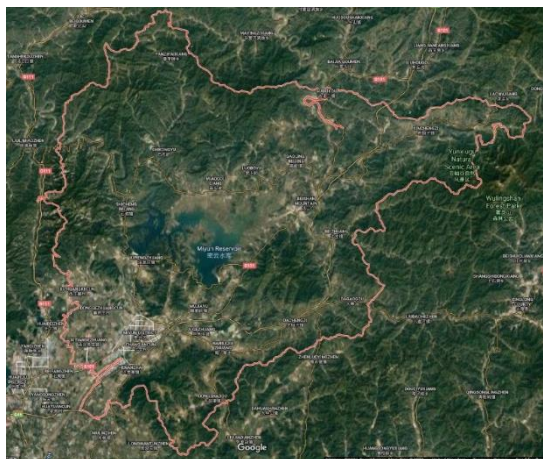
Ap Fig. BB. Satellite image of the Capital Steel Company (CSC) used for sampling site classification in chapter 4.

Yihai Garden (YG): Suburban/Residential



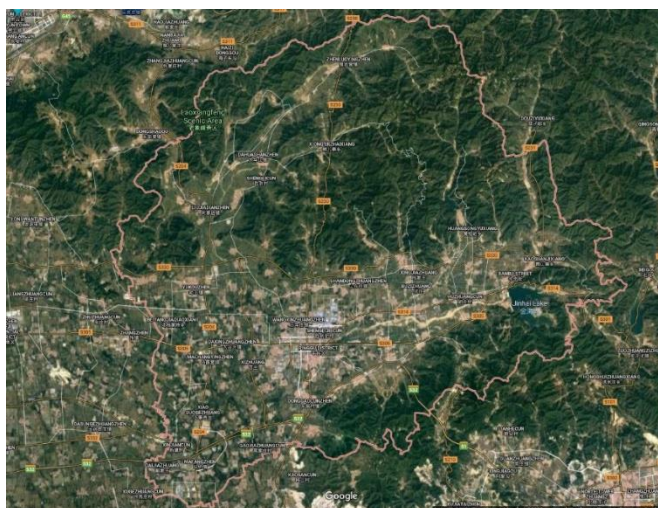
Ap Fig. CC. Satellite image of the Yihai Garden (YG) used for sampling site classification in chapter 4.

Miyun (MY): Rural



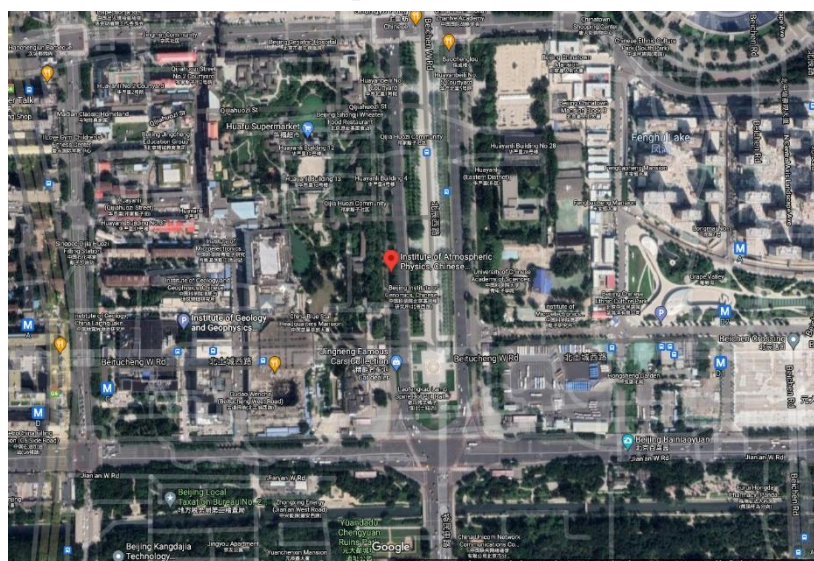
Ap Fig. DD. Satellite image of the Miyun (MY) used for sampling site classification in chapter 4.

Pinggu (PG): Rural



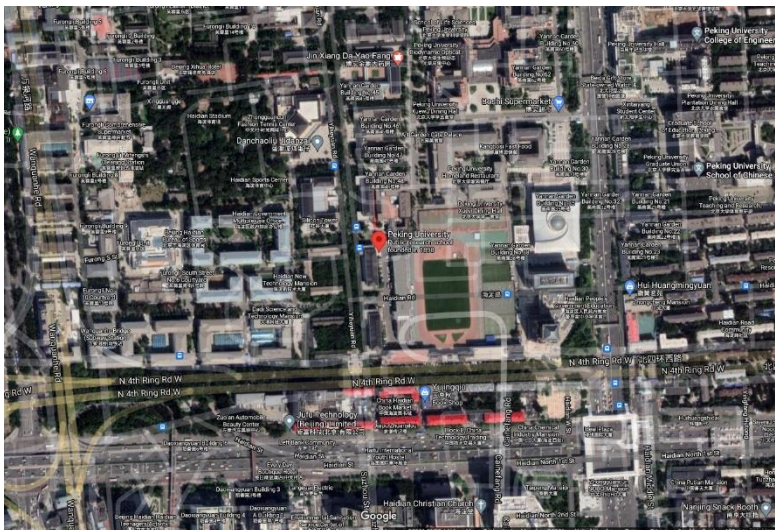
Ap Fig. EE. Satellite image of the Pinggu (PG) used for sampling site classification in chapter 4.

Institute of Atmospheric Physics (IAP): Urban



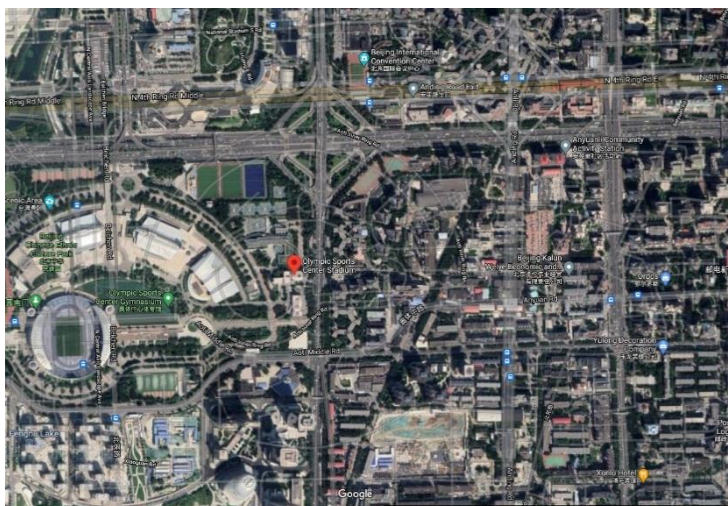
Ap Fig. FF. Satellite image of the Institute of Atmospheric Physics (IAP) used for sampling site classification in chapter 4.

Peking University (PKU): Urban



Ap Fig. GG. Satellite image of the Peking University (PKU) used for sampling site classification in chapter 4.

Olympic Park (OLP): Urban



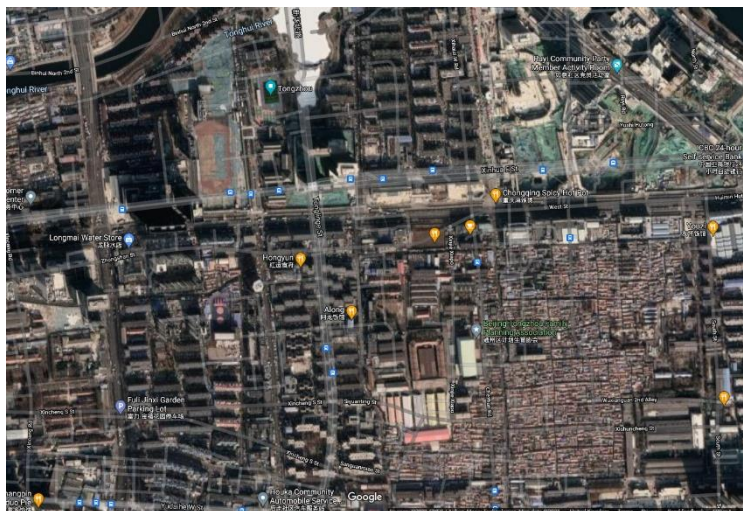
Ap Fig. HH. Satellite image of the Olympic Park (OLP) used for sampling site classification in chapter 4.

Ming Tombs (MT): Rural



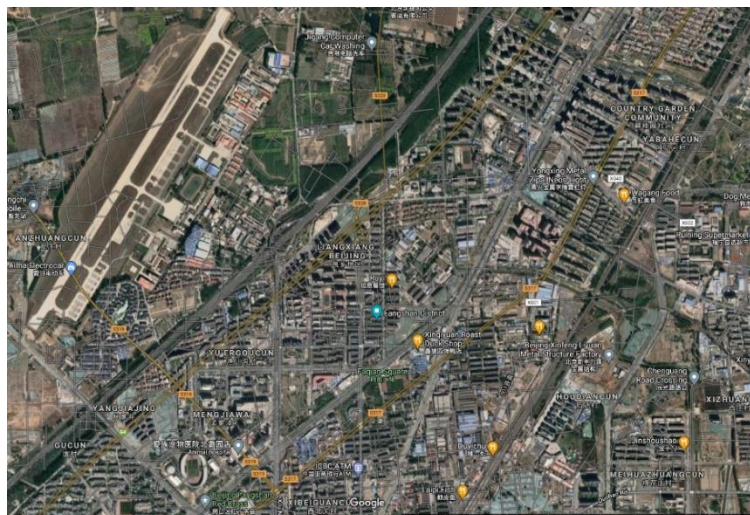
Ap Fig. II. Satellite image of the Ming Tombs (MT) used for sampling site classification in chapter 4.

Tongzhou (TZ): Urban



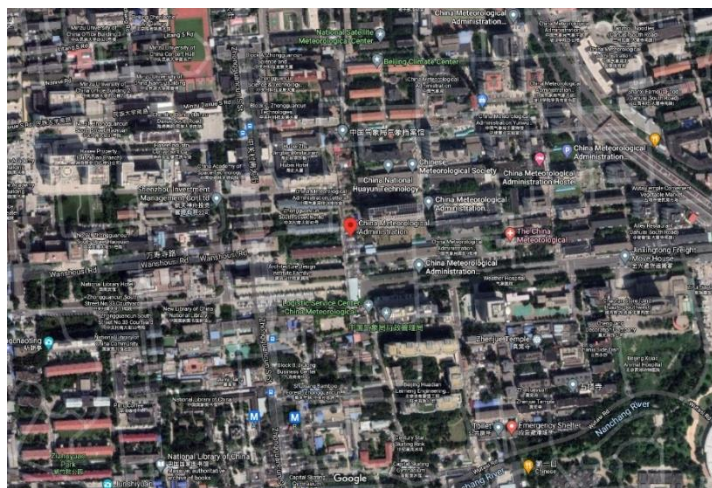
Ap Fig. JJ. Satellite image of the Tongzhou (TZ) used for sampling site classification in chapter 4.

Fangshan (FG): Urban



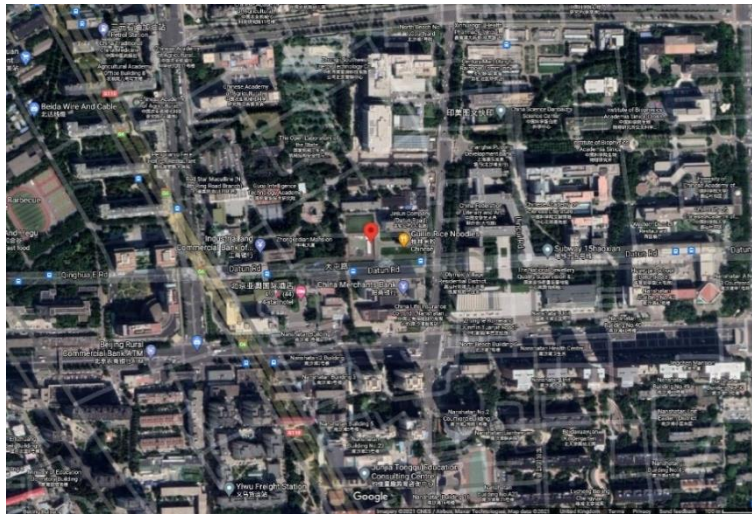
Ap Fig. KK. Satellite image of the Fangshan (FG) used for sampling site classification in chapter 4.

China Meteorological Administration (CMA): Urban



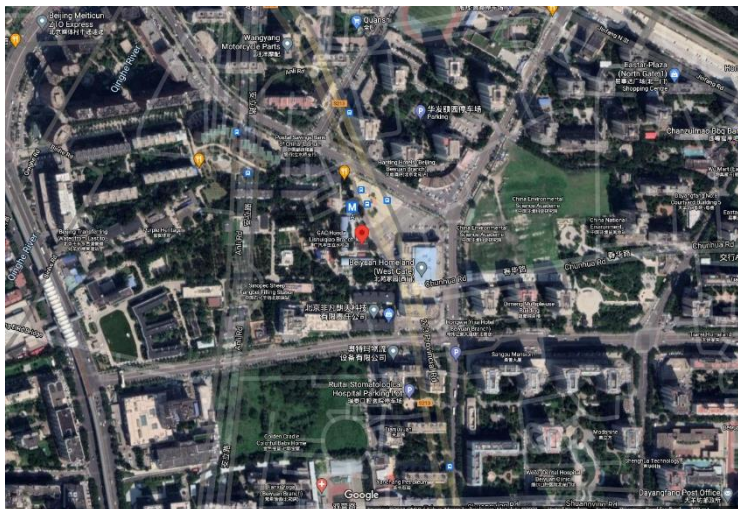
Ap Fig. LL. Satellite image of China Meteorological Administration (CMA) used for sampling site classification in chapter 4.

Institute of Geographic Sciences and Natural Resources Research (IGSNRR): Urban



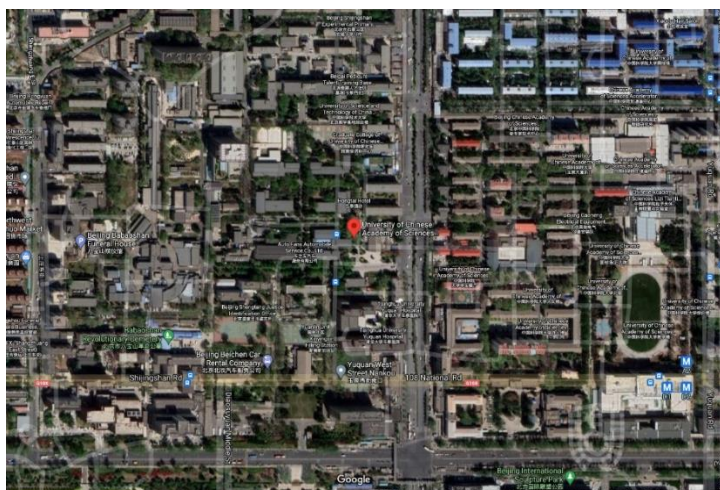
Ap Fig. MM. Satellite image of Institute of Geographic Sciences and Natural Resources Research (IGSNRR) used for sampling site classification in chapter 4.

Chinese Research Academy of Environmental Sciences (CRAES): Urban

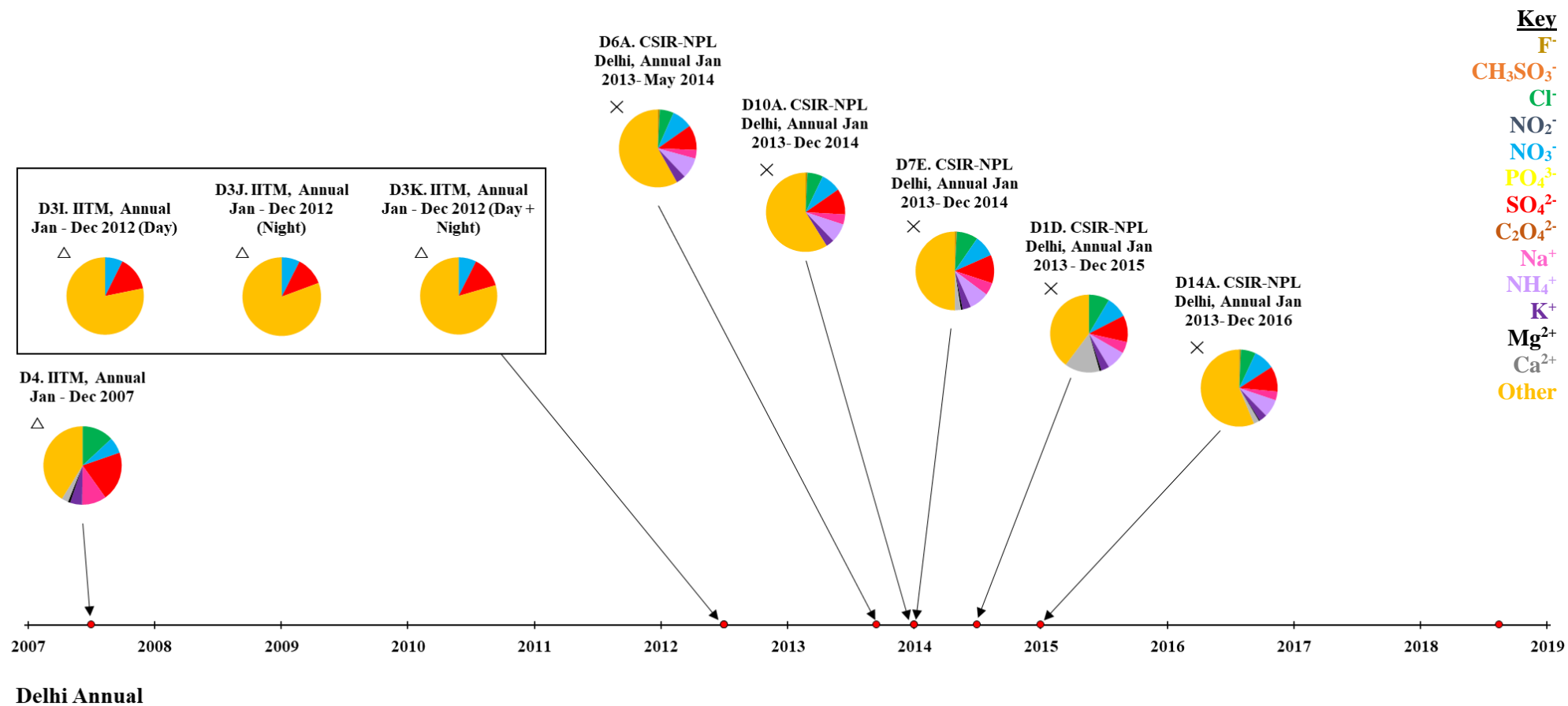


Ap Fig. NN. Satellite image of the Chinese Research Academy of Environmental Sciences (CRAES) used for sampling site classification in chapter 4.

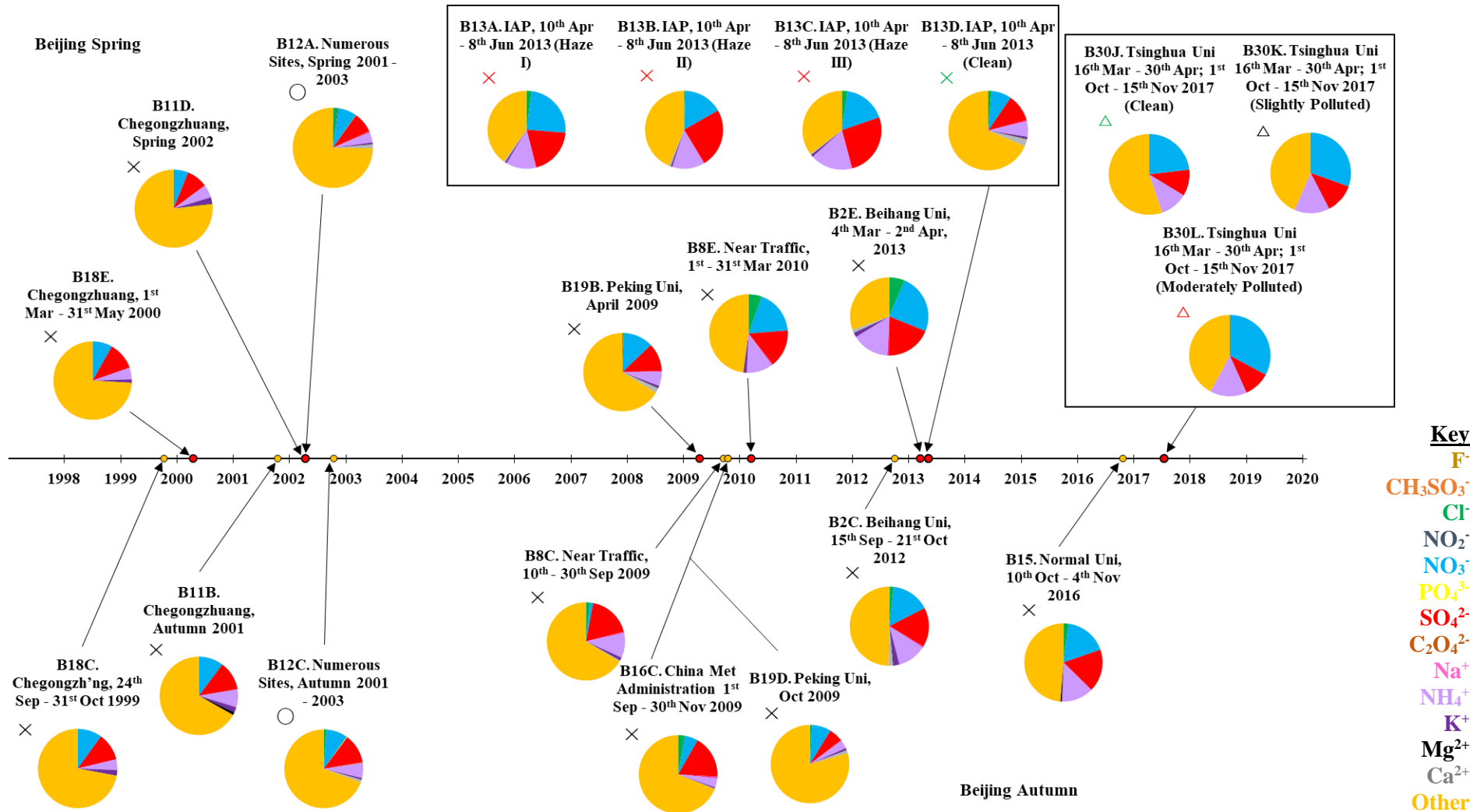
Yuquan Campus, University of Chinese Academy of Sciences (YU CAS): Urban



Ap Fig. OO. Satellite image of the Yuquan Campus, University of Chinese Academy of Sciences (YU CAS) used for sampling site classification in chapter 4.



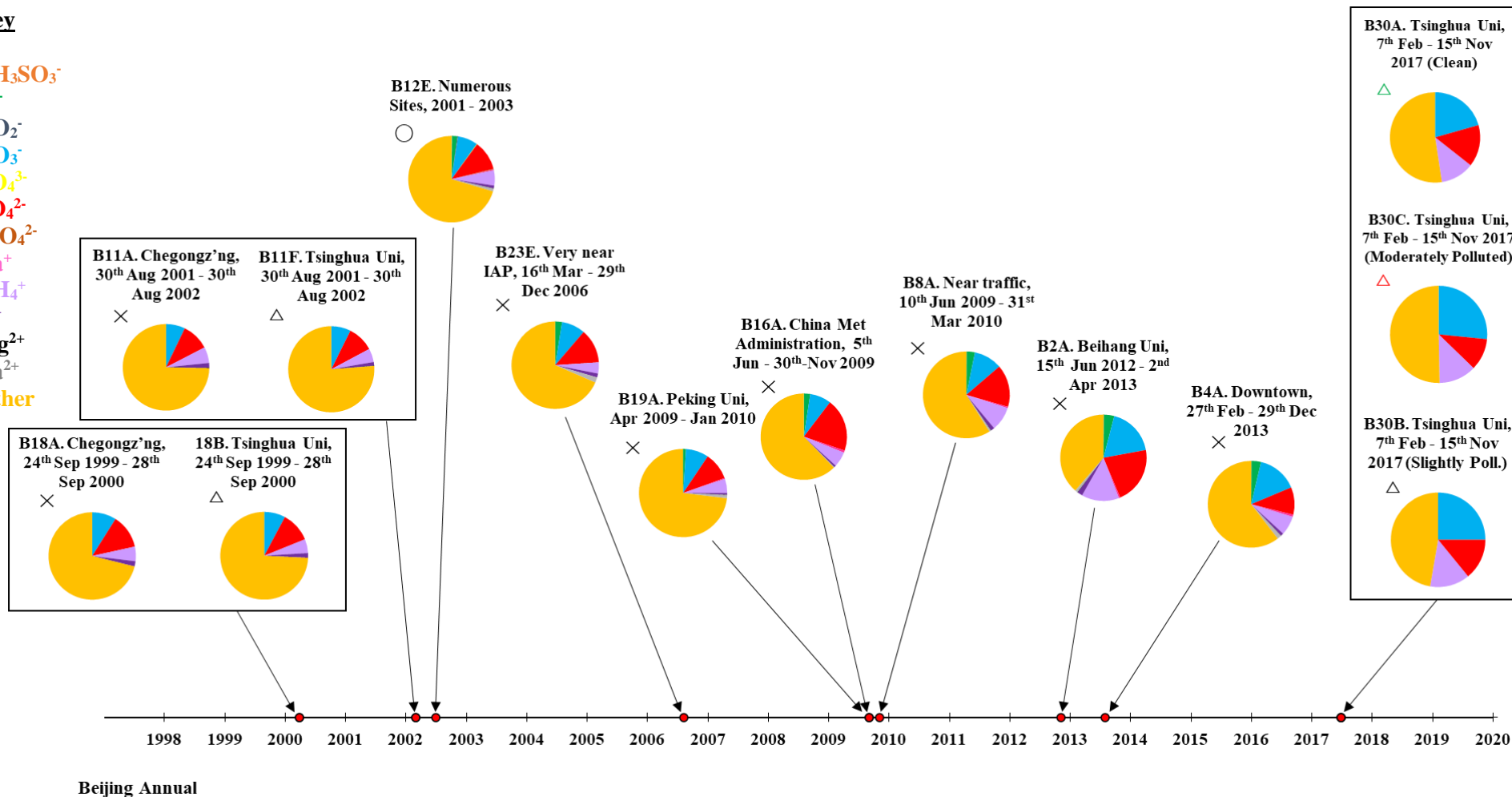
Ap Fig. PP. Timeline showing the change in PM_{2.5} particle composition as a function of time (Delhi Annual Averages). The symbols next to the pie charts represent the type of site for which Urban (×) and Suburban (Δ) are included. The symbol colours indicate atmospheric conditions including black (non-specific period). Time of sampling is shown along the x-axis. The study code along with the specific sampling site and time are also presented above each pie chart. The species presented are coloured in the pie charts, as per the key shown in the top right.



Ap Fig. QQ. Timeline showing the change in PM_{2.5} particle composition as a function of time within the Beijing Spring (top) and Autumn (bottom) seasons. The symbols next to the pie charts represent the type of site for which Urban (×), Suburban (Δ), Rural (□) and mixed (O) are included. The colours indicate atmospheric conditions including black (non-specific period), red (haze period), light blue (pollution control period) and green (clean period). Time of sampling is shown along the x-axis. The study code along with the specific sampling site and time are also presented above each pie chart. The species presented are coloured in the pie charts, as per the key shown in the bottom right.

Key

- F⁻
- CH₃SO₃⁻
- Cl⁻
- NO₂⁻
- NO₃⁻
- PO₄³⁻
- SO₄²⁻
- C₂O₄²⁻
- Na⁺
- NH₄⁺
- K⁺
- Mg²⁺
- Ca²⁺
- Other



Ap Fig. RR. Timeline showing the change in PM_{2.5} particle composition as a function of time within Beijing (Annual Averages). The symbols next to the pie charts represent the type of site for which Urban (x), Suburban (Δ), Rural (□) and mixed (O) are included. The colours indicate atmospheric conditions including black (non-specific period), red (haze period), light blue (pollution control period) and green (clean period). Time of sampling is shown along the x-axis. The study code along with the specific sampling site and time are also presented above each pie chart. The species presented are coloured in the pie charts, as per the key shown in the top left.

Abbreviations

ACSM	Aerosol Chemical Speciation Monitor
ADAF	Age Dependant Adjustment Factor
AIR-POLL	Sources and Emissions of Air Pollutants in Beijing Project (apart of APHH)
AMS	Aerosol Mass Spectrometry
APHH	Air Pollution and Human Health
ASE	Accelerated Solvent Extraction
AT	Averaging Time
BC	Black Carbon
BEI	Beihang University Beijing
BEJ	Beijing
BJ	Beijing in which exact sampling locations were not reported
BMRI	Beijing Municipal Research Institute
BNU	Beijing Normal University
BSUM	APHH Beijing summer campaign
BVOC	Biogenic Volatile Organic Compound
BWIN	APHH Beijing winter campaign
CAS	Chinese Academy of Sciences
CCN	Cloud Condensation Nuclei
CEDA	Centre for Environmental Data Analysis
CEH	Centre for Ecology and Hydrology
CERN	Chinese Ecosystem Research Network Atmospheric Sub-Centre
CEST	China Eastern Standard Time
CGZ	Chegongzhuang
CIMS	Chemical Ionization Mass Spectrometry
CMA	China Meteorological Administration (39°56'N, 116°24'E)
CNU	Capital Normal University (39°58'N, 116°22'E)
COPD	Chronic Obstructive Pulmonary Disease
CRAES	Chinese Research Academy of Environmental Sciences
CSC	Capital Steel Company (Assumed Location - Study Not Clear)
CSE	Centre for Science and Environment
DDT	Dichlorodiphenyltrichloroethane
DEA	Diethylamine
DEET	N,N-diethyl-meta-toluamide
DI	Deionised
Dia	Diameter
DL	Dingling
DOW	Downtown Beijing (Not clear exactly where)
DPC	Dual Plasma Controller
DPEM	APHH Delhi pre-monsoon campaign
DPOM	APHH Delhi post-monsoon campaign
EC	Exposure Concentration
ECMWF	European Centre for Medium-Range Weather Forecasts
ED	Exposure Duration
EF	Exposure Frequency
EPA	Environmental Protection Agency
ET	Exposure Time
EtOAc	Ethyl Acetate

FG	Fangshan
FID	Flame Ionisation Detection
GC	Gas Chromatography
GC × GC -	Two-Dimensional Gas Chromatography coupled to Nitrogen
NCD	Chemiluminescence Detection
GC-MS	Gas Chromatography - Mass Spectrometry
GDAS	Global Data Assimilation System
HCH	Hexachlorocyclohexane
HiVol	High Volume Sampler
HMS	Hydroxymethanesulfonate
HPLC	High Performance Liquid Chromatography
HSZ	Hei Shan Zhai, a rural mountainous site near Beijing (40°21'N, 116°18'E)
HYSPLIT	Hybrid Single-Particle Lagrangian Integrated Trajectory model
IAP	Institute of Atmospheric Physics
IARC	International Agency for Research on Cancer
IC	Ion Chromatography / Chromatograph
ICP-MS	Inductively Coupled Plasma Mass Spectrometry
IDL	Instrument Detection Limit
IGDTUW	Indira Gandhi Delhi Technical University for Women
IGIA	Indira Gandhi International Airport
IGSNRR	Institute of Geographic Sciences and Natural Resources Research
IITM	Indian Institute of Tropical Meteorology New Delhi Branch
Inorg-NO3-	Inorganic Nitrate
IPGCL	Indraprastha Power Generation Company Ltd.
IRIS	Integrated Risk Information System
IUR	Inhalation Unit Risk
JNU	School of Environmental Science, Jawaharlal Nehru University
KRI	Kovats Retention Index
LC-MS	Liquid Chromatography - Mass Spectrometry
LDN	London
LOD	Limit of Detection
LOPAP	LOng Path Absorption Photometer
LOQ	Limit of Quantification
Mat Rd.	Mathura Road (50 metres away)
MBEJ	Multiple sites across Beijing
MPI	Max Planck Institute
MQ	Milli-Q
MS	Mass Spectrometry
MT	Ming Tombs
MVK	Methyl Vinyl Ketone
MY	Miyun
NAAQS	National Ambient Air Quality Standard
NAB	N'-nitrosoanabasine
NAT	N'-nitrosoanatabine
NCD	Nitrogen Chemiluminescence Detection
NCT	National Capital Territory
NDBA	N-nitrosodi-n-butylamine
NDEA	N-nitrosodiethylamine
NDMA	N-Nitrosodimethylamine
NDPA	N-nitrosodi-n-propylamine

NDPhA	N-nitrosodiphenylamine
NIPH	Norwegian Institute of Public Health
NMEA	N-nitrosomethylethylamine
Nmor	N-nitrosomorpholine
NMR	Nuclear Magnetic Resonance
NNAL	4-(methylnitrosoamino)-1-(3-pyridyl)-1-butanol
NNK	4-(methylnitrosoamino)-1-(3-pyridyl)-1-butanone
NNN	N'-nitrosornicotine
NOAA	National Oceanic and Atmospheric Administration
NOR	Nitrogen Oxidation Ratio
Npip	N-nitrosopiperidine
NPL	National Physical Laboratory of India
Npyr	N-nitrosopyrrolidine
NTPC	National Thermal Power Corporation Limited
OEHHA	Office of Environmental Health Hazard Assessment
OLP	Olympic Park
ON	Organic Nitrogen
Org-NO3	Organic Nitrate
Org-SO4	Organic Sulfate
PAH	Polycyclic Aromatic Hydrocarbons
PEF	Potential Equivalency Factor
PG	Pinggu
PILS	Particle Into Liquid Sampler
PILS-IC	Particle-Into-Liquid-Sampler coupled to Ion Chromatography
PKU	Peking University
PM	Particulate Matter
PMF	Positive Matrix Factorization
POPs	Persistent Organic Pollutants
PTR-MS	Proton-Transfer-Reaction Mass Spectrometry
RH	Relative Humidity
RMM	Relative Molecular Mass
ROS	Reactive Oxygen Species
SAPHIR	Simulation of Atmospheric PHotochemistry In a large Reaction
SD	Standard Deviation
SEOU	Seoul
SERE	Seoul Residential
SERO	Seoul Roadside
SIA	Secondary Inorganic Aerosol
SMPS	Scanning Mobility Particle Sizer
SOA	Secondary Organic Aerosol
SOR	Sulfur Oxidation Ratio
SP2	Single Particle Soot Photometer
TEOM-FDMS	Tapered Element Oscillating Monitor - Filter Dynamics Measurement System
THU	Tsinghua University
TM	Transition Metal
TMI	Transition Metal Ion
ToF-MS	Time of Flight - Mass Spectrometry
TSNA	Tobacco Specific Nitrosamines
TZ	Tongzhou

UCAS	University of the Chinese Academy of Sciences
UEA	University of East Anglia
ULE	Ultra - Low Emissions
UN	United Nations
UoB	University of Birmingham
UoM	University of Manchester
UoY	University of York
US	Urban Site (116°18'10"8E, 39°56'50"7N)
UTC	Universal Time Coordinated
VOC	Volatile Organic Compound
WBJ	A western urban district of Beijing
WHO	World Health Organisation
YF	Yufa
YG	Yihai Garden
YU CAS	Yuquan Campus, University of Chinese Academy of Sciences
ZGD	Zonguldak

References

- 1 S. C. Pryor, P. Crippa and R. C. Sullivan, in *Reference Module in Earth Systems and Environmental Sciences*, Elsevier, 2015, p. <https://doi.org/10.1016/B978-0-12-409548-9.09177-6>.
- 2 Air pollution, https://www.who.int/health-topics/air-pollution#tab=tab_1, (accessed Feb 2021).
- 3 P. Tschofen, I. L. Azevedo and N. Z. Muller, *PNAS.*, 2019, **116**, 19857–19862.
- 4 European Environment Agency, *Every breath we take Improving air quality in Europe*, Publications Office of the European Union, 2013, Luxembourg, 2013.
- 5 Health and Environmental Effects of Particulate Matter (PM) | Particulate Matter (PM) Pollution | US EPA, <https://www.epa.gov/pm-pollution/health-and-environmental-effects-particulate-matter-pm>, (accessed Mar 2021).
- 6 M. El-Fadel and M. Massoud, *Sci. Total Environ.*, 2000, **257**, 133–146.
- 7 R. T. Burnett, C. Arden Pope, M. Ezzati, C. Olives, S. S. Lim, S. Mehta, H. H. Shin, G. Singh, B. Hubbell, M. Brauer, H. Ross Anderson, K. R. Smith, J. R. Balmes, N. G. Bruce, H. Kan, F. Laden, A. Prüss-Ustün, M. C. Turner, S. M. Gapstur, W. R. Diver and A. Cohen, *Environ. Health Perspect.*, 2014, **122**, 397–403.
- 8 Ambient (outdoor) air pollution, [https://www.who.int/news-room/fact-sheets/detail/ambient-\(outdoor\)-air-quality-and-health](https://www.who.int/news-room/fact-sheets/detail/ambient-(outdoor)-air-quality-and-health), (accessed Mar 2021).
- 9 Carbon Monoxide's Impact on Indoor Air Quality | Indoor Air Quality (IAQ) | US EPA, https://www.epa.gov/indoor-air-quality-iaq/carbon-monoxides-impact-indoor-air-quality#Exposure_Limits, (accessed Feb 2021).
- 10 E. K. Vakkilainen, in *Steam Generation from Biomass*, Elsevier, 2017, pp. 18–56.
- 11 H. Petetin, B. Sauvage, M. Parrington, H. Clark, A. Fontaine, G. Athier, R. Blot, D. Boulanger, J.-M. Cousin, P. Nédélec and V. Thouret, *Atmos. Chem. Phys.*, 2018, **18**, 17277–17306.
- 12 H. Topacoglu, S. Katsakoglou and A. Ipekci, *Hippokratia.*, 2014, **18**, 37–39.
- 13 R. K. Jain, Z. Cui and J. K. Domen, *Environmental Impact of Mining and Mineral Processing: Management, Monitoring, and Auditing Strategies*, Elsevier Inc., 2016.
- 14 T. Stavrou, J. F. Müller, K. F. Boersma, I. De Smedt and R. J. van der A, *Geophys. Res. Lett.*, 2008, **35**, doi:10.1029/2008GL033521.
- 15 F. S. Rowland, *Stratospheric Ozone Depletion*, Springer Science and Business Media, LLC, Dordrecht, 2009.
- 16 Ground-level Ozone Basics | Ground-level Ozone Pollution | US EPA, <https://www.epa.gov/ground-level-ozone-pollution/ground-level-ozone-basics>, (accessed Feb 2021).
- 17 K. L. Ebi and G. McGregor, *Environ. Health Perspect.*, 2008, **116**, 1449–1455.
- 18 J. Lelieveld and F. J. Dentener, *J. Geophys. Res. Atmos.*, 2000, **105**, 3531–3551.
- 19 M. Ullerstam, R. Vogt, S. Langer and E. Ljungström, *Phys. Chem. Chem. Phys.*, 2002, **4**, 4694–4699.
- 20 T. Wang, L. Xue, P. Brimblecombe, Y. F. Lam, L. Li and L. Zhang, *Sci. Total Environ.*, 2017, **575**, 1582–1596.
- 21 T. D. Gordon, A. A. Presto, A. A. May, N. T. Nguyen, E. M. Lipsky, N. M. Donahue, A. Gutierrez, M. Zhang, C. Maddox, P. Rieger, S. Chattopadhyay, H. Maldonado, M. M.

- Maricq and A. L. Robinson, *Atmos. Chem. Phys.*, 2014, **14**, 4661–4678.
- 22 T. C. Bond, D. S. Covert, J. C. Kramlich, T. V. Larson and R. J. Charlson, *J. Geophys. Res. Atmos.*, 2002, **107**, ICC 9-1-ICC 9-14.
- 23 E. Corsini, M. Marinovich and R. Vecchi, *Int. J. Mol. Sci.*, 2019, **20**, 4992.
- 24 J. Wang, J. Li, J. Ye, J. Zhao, Y. Wu, J. Hu, D. Liu, D. Nie, F. Shen, X. Huang, D. D. Huang, D. Ji, X. Sun, W. Xu, J. Guo, S. Song, Y. Qin, P. Liu, J. R. Turner, H. C. Lee, S. Hwang, H. Liao, S. T. Martin, Q. Zhang, M. Chen, Y. Sun, X. Ge and D. J. Jacob, *Nat. Commun.*, 2020, **11**, 2844.
- 25 X. Fu, T. Wang, S. Wang, L. Zhang, S. Cai, J. Xing and J. Hao, *Environ. Sci. Technol.*, 2018, **52**, 1644–1654.
- 26 S. N. Behera, R. Betha and R. Balasubramanian, *Aerosol Air Qual. Res.*, 2013, **13**, 1282–1296.
- 27 C. Mangia, M. Cervino, E. Antonio and L. Gianicolo, *Int. J. Environ. Res. Public Heal.*, 2015, **12**, 7667–7681.
- 28 G. Myhre, C. E. L. Myhre, B. H. Samset and T. Storelvmo, *Nat. Educ. Knowl.*, 2013, **4**, 7.
- 29 I. J. George and J. P. D. Abbatt, *Nat. Chem.*, 2010, **2**, 713–722.
- 30 M. Kulmala, T. Petäjä, T. Nieminen, M. Sipilä, H. E. Manninen, K. Lehtipalo, M. Dal Maso, P. P. Aalto, H. Junninen, P. Paasonen, I. Riipinen, K. E. J. Lehtinen, A. Laaksonen and V. M. Kerminen, *Nat. Protoc.*, 2012, **7**, 1651–1667.
- 31 WHO | Ambient and household air pollution and health, <https://www.who.int/airpollution/data/en/>, (accessed Mar 2021).
- 32 United Kingdom Population 2021 (Demographics, Maps, Graphs), <https://worldpopulationreview.com/countries/united-kingdom-population>, (accessed Mar 2021).
- 33 Air Quality Expert Group, *Particulate Matter in the United Kingdom Summary*, 2005.
- 34 J. Williams, M. De Reus, R. Krejci, H. Fischer and J. Ström, *Atmos. Chem. Phys.*, 2002, **2**, 133–145.
- 35 OECD, *The economic consequences of outdoor air pollution | POLICY HIGHLIGHTS*, 2016.
- 36 M. Zhang, Y. Song, X. Cai and J. Zhou, *J. Environ. Manage.*, 2008, **88**, 947–954.
- 37 S. Comunian, D. Dongo, C. Milani and P. Palestini, *Int. J. Environ. Res. Public Heal.*, 2020, **17**, 4487.
- 38 L. Setti, F. Passarini, G. De Gennaro, P. Barbieri, S. Licen, M. G. Perrone, A. Piazzalunga, M. Borelli, J. Palmisani, A. Di Gilio, E. Rizzo, A. Colao, P. Piscitelli and A. Miani, *BMJ Open*, 2020, **10**, doi:10.1136/bmjopen-2020-039338.
- 39 N. S. M. Nor, C. W. Yip, N. Ibrahim, M. H. Jaafar, Z. Z. Rashid, N. Mustafa, H. H. A. Hamid, K. Chandru, M. T. Latif, P. E. Saw, C. Y. Lin, K. M. Alhasa, J. H. Hashim and M. S. M. Nadzir, *Sci. Rep.*, 2021, **11**, 2508.
- 40 T. Barakat, B. Muylkens and B.-L. Su, *Matter.*, 2020, **3**, 977–980.
- 41 B. Wang, J. Liu, Y. Li, S. Fu, X. Xu, L. Li, J. Zhou, X. Liu, X. He, J. Yan, Y. Shi, J. Niu, Y. Yang, Y. Li, B. Luo and K. Zhang, *BMC Public Heal.*, 2020, **20**, 1585.
- 42 M. A. Zoran, R. S. Savastru, D. M. Savastru and M. N. Tautan, *Sci. Total Environ.*, 2020, **738**, 139825.
- 43 Z. S. Farhangrazi, G. Sancini, A. C. Hunter and S. M. Moghimi, *Front. Immunol.*, 2020, **11**,

- 44 Z. Shi, T. Vu, S. Kotthaus, R. M. Harrison, S. Grimmond, S. Yue, T. Zhu, J. Lee, Y. Han, M. Demuzere, R. E. Dunmore, L. Ren, D. Liu, Y. Wang, O. Wild, J. Allan, W. J. Acton, J. Barlow, B. Barratt, D. Beddows, W. J. Bloss, G. Calzolari, D. Carruthers, D. C. Carslaw, Q. Chan, L. Chatzidiakou, Y. Chen, L. Crilley, H. Coe, T. Dai, R. Doherty, F. Duan, P. Fu, B. Ge, M. Ge, D. Guan, J. F. Hamilton, K. He, M. Heal, D. Heard, C. N. Hewitt, M. Hollaway, M. Hu, D. Ji, X. Jiang, R. Jones, M. Kalberer, F. J. Kelly, L. Kramer, B. Langford, C. Lin, A. C. Lewis, J. Li, W. Li, H. Liu, J. Liu, M. Loh, K. Lu, F. Lucarelli, G. Mann, G. Mcfiggans, M. R. Miller, G. Mills, P. Monk, E. Nemitz, F. O'connor, P. I. Palmer, C. Percival, O. Popoola, C. Reeves, A. R. Rickard, L. Shao, G. Shi, D. Spracklen, D. Stevenson, Y. Sun, Z. Sun, S. Tao, S. Tong, Q. Wang, W. Wang, X. Wang, X. Wang, Z. Wang, L. Wei, L. Whalley, X. Wu, Z. Wu, P. Xie, F. Yang, Q. Zhang, Y. Zhang, Y. Zhang and M. Zheng, *Atmos. Chem. Phys.*, 2019, **19**, 7519–7546.
- 45 A. P. Ault and J. L. Axson, *Anal. Chem.*, 2017, **89**, 430–452.
- 46 E. W. Emerson, J. M. Katich, J. P. Schwarz, G. R. McMeeking and D. K. Farmer, *J. Geophys. Res. Atmos.*, 2018, **123**, 12,277–12,290.
- 47 J. P. Reid, A. K. Bertram, D. O. Topping, A. Laskin, S. T. Martin, M. D. Petters, F. D. Pope and G. Rovelli, *Nat. Commun.*, 2018, **9**, 1–14.
- 48 Particulate Matter (PM) Basics | Particulate Matter (PM) Pollution | US EPA, <https://www.epa.gov/pm-pollution/particulate-matter-pm-basics>, (accessed Feb 21).
- 49 S. C. Lee, Y. Cheng, K. F. Ho, J. J. Cao, -K Louie, J. C. Chow and J. G. Watson, *Aerosol Sci. Technol.*, 2006, **40**, 157–165.
- 50 M. Sørensen, B. Daneshvar, M. Hansen, L. O. Dragsted, O. Hertel, L. Knudsen and S. Loft, *Environ. Health Perspect.*, 2003, **111**, 161–166.
- 51 T. Wei and M. Tang, *Environ. Toxicol. Pharmacol.*, 2018, **60**, 195–201.
- 52 C. Wang, Y. Tu, Z. Yu and R. Lu, *Int. J. Environ. Res. Public Health*, 2015, **12**, 8187–8197.
- 53 W.-H. Chen, K.-H. Lee, J. Kavita Mutuku and C.-J. Hwang, *Aerosol Air Qual. Res.*, 2018, **18**, 866–883.
- 54 S. Chowdhury, S. Dey, S. Guttikunda, A. Pillarisetti, K. R. Smith and L. Di Girolamo, *PNAS.*, 2019, **116**, 10711–10716.
- 55 S. Twomey, *J. Atmos. Sci.*, 1977, **34**, 1149–1152.
- 56 B. A. Albrecht, *Science (80-)*, 1989, **245**, 1227–1230.
- 57 J. Hansen, M. Sato and R. Ruedy, *J. Geophys. Res. Atmos.*, 1997, **102**, 6831–6864.
- 58 M. Lippmann, D. B. Yeates and R. E. Albert, *Br. J. Ind. Med.*, 1980, **37**, 337–362.
- 59 R. Sturm, *AME Med. J.*, 2020, **5**, 14.
- 60 T. Zhang, B. Gao, Z. Zhou and Y. Chang, *Biomed. Eng. Online*, 2016, **15**, 138.
- 61 S. Feng, D. Gao, F. Liao, F. Zhou and X. Wang, *Ecotoxicol. Environ. Saf.*, 2016, **128**, 67–74.
- 62 X. Deng, F. Zhang, W. Rui, F. Long, L. Wang, Z. Feng, D. Chen and W. Ding, *Toxicol. Vitr.*, 2013, **27**, 1762–1770.
- 63 C. W. Liu, T. L. Lee, Y. C. Chen, C. J. Liang, S. H. Wang, J. H. Lue, J. S. Tsai, S. W. Lee, S. H. Chen, Y. F. Yang, T. Y. Chuang and Y. L. Chen, *Part. Fibre Toxicol.*, 2018, **15**, 4.
- 64 R. Li, R. Zhou and J. Zhang, *Oncol. Lett.*, 2018, **15**, 7506–7514.
- 65 T. Li, R. Hu, Z. Chen, Q. Li, S. Huang, Z. Zhu and L.-F. Zhou, *Chronic Dis. Transl. Med.*,

- 2018, **4**, 176–186.
- 66 D. Li, Y. Li, G. Li, Y. Zhang, J. Li and H. Chen, *PNAS.*, 2019, **116**, 2488–2493.
- 67 M. Brauer, C. Avila-Casado, T. I. Fortoul, S. Vedal, B. Stevens and A. Churg, *Environ. Health Perspect.*, 2001, **109**, 1039–1043.
- 68 Y. Shou, Y. Huang, X. Zhu, C. Liu, Y. Hu and H. Wang, *Ecotoxicol. Environ. Saf.*, 2019, **174**, 344–352.
- 69 J. Kavita Mutuku, W.-C. Hou and W.-H. Chen, *Aerosol Air Qual. Res.*, 2020, **20**, 1094–1110.
- 70 A. Valavanidis, K. Fiotakis and T. Vlachogianni, *J. Environ. Sci. Heal. - Part C Environ. Carcinog. Ecotoxicol. Rev.*, 2008, **26**, 339–362.
- 71 H. Zhang and G. Papadakis, *J. Biomech.*, 2010, **43**, 2453–2459.
- 72 Y.-S. Cheng, Y. Zhou and B. T. Chen, *Aerosol Sci. Technol.*, 1999, **31**, 286–300.
- 73 D. Y. H. Pui, S. C. Chen and Z. Zuo, *Particuology*, 2014, **13**, 1–26.
- 74 Y. Wei, I.-K. Han, M. Shao, M. Hu, J. Zhang and X. Tang, *Environ. Sci. Technol.*, 2009, **43**, 4757–4762.
- 75 L. Wang, D. Luo, X. Liu, J. Zhu, F. Wang, B. Li and L. Li, *Chemosphere*, 2021, **264**, 128436.
- 76 C. Potera, *Environ. Health Perspect.*, 2014, **122**, A29.
- 77 O. Raaschou-Nielsen, Z. J. Andersen, R. Beelen, E. Samoli, M. Stafoggia, G. Weinmayr, B. Hoffmann, P. Fischer, M. J. Nieuwenhuijsen, B. Brunekreef, W. W. Xun, K. Katsouyanni, K. Dimakopoulou, J. Sommar, B. Forsberg, L. Modig, A. Oudin, B. Oftedal, P. E. Schwarze, P. Nafstad, U. De Faire, N. L. Pedersen, C. G. Östenson, L. Fratiglioni, J. Penell, M. Korek, G. Pershagen, K. T. Eriksen, M. Sørensen, A. Tjønneland, T. Ellermann, M. Eeftens, P. H. Peeters, K. Meliefste, M. Wang, B. Bueno-de-Mesquita, T. J. Key, K. de Hoogh, H. Concin, G. Nagel, A. Vilier, S. Grioni, V. Krogh, M. Y. Tsai, F. Ricceri, C. Sacerdote, C. Galassi, E. Migliore, A. Ranzi, G. Cesaroni, C. Badaloni, F. Forastiere, I. Tamayo, P. Amiano, M. Dorronsoro, A. Trichopoulou, C. Bamia, P. Vineis and G. Hoek, *Lancet Oncol.*, 2013, **14**, 813–822.
- 78 E. Longhin, J. A. Holme, K. B. Gutzkow, V. M. Arlt, J. E. Kucab, M. Camatini and M. Gualtieri, *Part. Fibre Toxicol.*, 2013, **10**, 63.
- 79 C. Reche, T. Moreno, F. Amato, M. Viana, B. L. van Drooge, H. C. Chuang, K. Bérubé, T. Jones, A. Alastuey and X. Querol, *Ecotoxicol. Environ. Saf.*, 2012, **78**, 327–335.
- 80 K. S. Kouassi, S. Billet, G. Garçon, A. Verdin, A. Diouf, F. Cazier, J. Djaman, D. Courcot and P. Shirali, *J. Appl. Toxicol.*, 2010, **30**, 310–320.
- 81 K. Donaldson, D. M. Brown, C. Mitchell, M. Dineva, P. H. Beswick, P. Gilmour and W. MacNee, *Environ. Health Perspect.*, 1997, **105**, 1285–1289.
- 82 R. Habre, E. Moshier, W. Castro, A. Nath, A. Grunin, A. Rohr, J. Godbold, N. Schachter, M. Kattan, B. Coull and P. Koutrakis, *J. Expo. Sci. Environ. Epidemiol.*, 2014, **24**, 380–387.
- 83 G. Wang, J. Zhao, R. Jiang and W. Song, *Environ. Toxicol.*, 2015, **30**, 343–356.
- 84 A. P. Davel, M. Lemos, L. M. Pastro, S. C. Pedro, P. A. De André, C. Hebeda, S. H. Farsky, P. H. Saldiva and L. V. Rossoni, *Toxicology*, 2012, **295**, 39–46.
- 85 L. Nikasinovic, J. Just, F. Sahraoui, N. Seta, A. Grimfeld and I. Momas, *J. Allergy Clin. Immunol.*, 2006, **117**, 1382–1388.
- 86 W. Yue, L. Tong, X. Liu, X. Weng, X. Chen, D. Wang, S. C. Dudley, E. K. Weir, W. Ding, Z. Lu, Y. Xu and Y. Chen, *Redox Biol.*, 2019, **22**, 101161.

- 87 B. Sul, A. Wallqvist, M. J. Morris, J. Reifman and V. Rakesh, *Comput. Biol. Med.*, 2014, **52**, 130–143.
- 88 P. T. Macklem, *Am. J. Respir. Crit. Care Med.*, 1996, **153**, 83–89.
- 89 V. V. Jain, B. Abejie, M. H. Bashir, T. Tyner and J. Vempilly, *J. Asthma*, 2013, **50**, 600–605.
- 90 H. Zhao, W. Li, Y. Gao, J. Li and H. Wang, *Toxicology*, 2014, **325**, 180–188.
- 91 S. Salvi, A. Blomberg, B. Rudell, F. Kelly, T. Sandström, S. T. Holgate and A. Frew, *Am. J. Respir. Crit. Care Med.*, 1999, **159**, 702–709.
- 92 A. Peters, A. Döring, H. E. Wichmann and W. Koenig, *Lancet*, 1997, **349**, 1582–1587.
- 93 L. C. Vinikoor-Imler, J. Allen Davis and T. J. Luben, *Int. J. Environ. Res. Public Health*, 2011, **8**, 1865–1871.
- 94 S. P. Eckel, M. Cockburn, Y. H. Shu, H. Deng, F. W. Lurmann, L. Liu and F. D. Gilliland, *Thorax*, 2016, **71**, 891–898.
- 95 H. Kan, S. J. London, G. Chen, Y. Zhang, G. Song, N. Zhao, L. Jiang and B. Chen, *Environ. Int.*, 2007, **33**, 376–384.
- 96 Q. He, Y. Yan, L. Guo, Y. Zhang, G. Zhang and X. Wang, *Atmos. Res.*, 2017, **184**, 48–55.
- 97 W. Xu, X. Liu, L. Liu, A. J. Dore, A. Tang, L. Lu, Q. Wu, Y. Zhang, T. Hao, Y. Pan, J. Chen and F. Zhang, *Atmos. Environ.*, 2019, **210**, 241–252.
- 98 Q. Li, Z. Yang, X. Li, S. Ding and F. Du, *Aerosol Air Qual. Res.*, 2019, **19**, 2697–2706.
- 99 D. Hu, L. Qiao, J. Chen, X. Ye, X. Yang, T. Cheng and W. Fang, *Aerosol Air Qual. Res.*, 2010, **10**, 255–264.
- 100 Q. Yao, Z. Liu, S. Han, Z. Cai, J. Liu, T. Hao, J. Liu, X. Huang and Y. Wang, *Environ. Sci. Pollut. Res.*, 2020, **27**, 26750–26762.
- 101 G. Reshma Begam, C. Viswanatha Vachaspati, Y. Nazeer Ahammed, K. Raghavendra Kumar, R. R. Reddy, S. K. Sharma, M. Saxena and T. K. Mandal, *Environ. Sci. Pollut. Res.*, 2017, **24**, 1719–1734.
- 102 R. Beardsley, M. Jang, B. Ori, A. Y. Im, C. A. Delcomyn and N. Witherspoon, *Environ. Chem.*, 2013, **10**, 167–177.
- 103 R. Volkamer, F. San Martini, L. T. Molina, D. Salcedo, J. L. Jimenez and M. J. Molina, *Geophys. Res. Lett.*, 2007, **34**, L19807.
- 104 T. Fang, H. Guo, L. Zeng, V. Verma, A. Nenes and R. J. Weber, *Environ. Sci. Technol.*, 2017, **51**, 2611–2620.
- 105 F. Chen, X. Zhang, X. Zhu, H. Zhang, J. Gao and P. K. Hopke, *Aerosol Air Qual. Res.*, 2017, **17**, 368–380.
- 106 S. Chang and D. T. Allen, *Atmos. Environ.*, 2006, **40**, 512–523.
- 107 N. Kaneyasu, H. Yoshikado, T. Mizuno, K. Sakamoto and M. Soufuku, *Atmos. Environ.*, 1999, **33**, 1745–1756.
- 108 S. Gani, S. Bhandari, S. Seraj, D. S. Wang, K. Patel, P. Soni, Z. Arub, G. Habib, L. H. Ruiz and J. S. Apte, *Atmos. Chem. Phys.*, 2019, **19**, 6843–6859.
- 109 Jaiprakash, A. Singhai, G. Habib, R. S. Raman and T. Gupta, *Environ. Sci. Pollut. Res.*, 2017, **24**, 445–462.
- 110 P. Pant, A. Shukla, S. D. Kohl, J. C. Chow, J. G. Watson and R. M. Harrison, *Atmos. Environ.*, 2015, **109**, 178–189.

- 111 R. S. Patil, R. Kumar, R. Menon, M. K. Shah and V. Sethi, *Atmos. Res.*, 2013, **132–133**, 1–11.
- 112 X. Ren, R. Sun, H.-H. Chi, X. Meng, Y. Li and Y. A. Levendis, *Fuel.*, 2017, **200**, 37–46.
- 113 G. Li, W. Lei, N. Bei and L. T. Molina, *Atmos. Chem. Phys.*, 2012, **12**, 8751–8761.
- 114 A. McCulloch, M. L. Aucott, C. M. Benkovitz, T. E. Graedel, G. Kleiman, P. M. Midgley and Y. Li, *J. Geophys. Res. Atmos.*, 1999, **104**, 8391–8403.
- 115 T. Y. Palmer, *Nature*, 1976, **263**, 44–46.
- 116 I. Paraskaki and M. Lazaridis, *Waste Manag. Res.*, 2005, **23**, 199–208.
- 117 X. Qiu, Q. Ying, S. Wang, L. Duan, J. Zhao, J. Xing, D. Ding, Y. Sun, B. Liu, A. Shi, X. Yan, Q. Xu and J. Hao, *Atmos. Chem. Phys.*, 2019, **19**, 6737–6747.
- 118 A. Retama, A. Neria-Hernández, M. Jaimes-Palomera, O. Rivera-Hernández, M. Sánchez-Rodríguez, A. López-Medina and E. Velasco, *Atmos. Environ. X.*, 2019, **2**, 100013.
- 119 L.-H. Rivellini, I. Chiapello, E. Tison, M. Fourmentin, A. Féron, A. Diallo, P. Goloub, F. Canonaco, A. Stephan Henry Prévôt and V. Riffault, *Atmos. Chem. Phys.*, 2017, **17**, 10291–10314.
- 120 H. Chen, M. E. Varner, R. B. Gerber and B. J. Finlayson-Pitts, *J. Phys. Chem. B.*, 2016, **120**, 1526–1536.
- 121 J. M. Lobert, W. C. Keene, J. A. Logan and R. Yevich, *J. Geophys. Res. Atmos.*, 1999, **104**, 8373–8389.
- 122 S. C. Lee, W.-M. Li and L. Y. Chan, *Sci. Total Environ.*, 2001, **279**, 181–193.
- 123 P. A. Clausen, M. Frederiksen, C. S. Sejbæk, J. B. Sørli, K. S. Hougaard, K. B. Frydendall, T. K. Carøe, E. M. Flachs, H. W. Meyer, V. Schlünssen and P. Wolkoff, *Int. J. Hyg. Environ. Health*, 2020, **229**, 113592.
- 124 X. Li, B. Wu and J. Zhu, *Prog. Petrochemical Sci.*, 2018, **2**, PPS.000539.
- 125 B. Wu, Y. Li, X. Li, J. Zhu, R. Ma and S. Hu, *Energy Fuels*, 2018, **32**, 6475–6481.
- 126 E. Häsänen, P. K. G. Manninen, K. Himberg and V. Väätäinen, *J. Radioanal. Nucl. Chem.*, 1990, **144**, 367–374.
- 127 B. D. Fuqua, J. L. Sims, J. E. Leggett, J. F. Benner and W. O. Atkinson, *Can. J. Plant Sci.*, 1976, **56**, 893–899.
- 128 B. J. Novak, S. Meinardi and D. R. Blake, *Nicotine Tob. Res.*, 2008, **10**, 1621–1625.
- 129 J. Chen, C. Liu, Z. Yang and J. Wang, *Earth Sci. Front.*, 2008, **15**, 242–247.
- 130 N. Ishikawa, G. Ishioka, M. Yanaka, K. Takata and M. Murakami, *Plant Prod. Sci.*, 2015, **18**, 137–145.
- 131 S. Liu, M. Zhang, L. Yang, Y. Li, L. Wang, Z. Huang, L. Wang, Z. Chen and M. Zhou, *J. Epidemiol. Community Health*, 2017, **71**, 154–161.
- 132 Y. Yokouchi, Y. Nojiri, L. A. Barrie, D. Toom-Saunty, T. Machida, Y. Inuzuka, H. Akimoto, H. J. Li, Y. Fujinuma and S. Aoki, *Nature*, 2000, **403**, 295–298.
- 133 C. Coulter, J. T. G. Hamilton, W. C. Mcroberts, L. Kulakov, M. J. Larkin and D. B. Harper, *Appl. Environ. Microbiol.*, 1999, **65**, 4301–4312.
- 134 F. Keppler, R. Elden, V. Niedan, J. Pracht and H. F. Schöler, *Nature*, 2000, **403**, 298–301.
- 135 M. A. K. Khalil, R. M. Moore, D. B. Harper, J. M. Lobert, D. J. Erickson, V. Koropalov, W. T. Sturges and W. C. Keene, *J. Geophys. Res. Atmos.*, 1999, **104**, 8333–8346.

- 136 Y. E. Yudovich and M. P. Ketris, *Int. J. Coal Geol.*, 2006, **67**, 127–144.
- 137 K. H. Lui, T. Jones, K. BéruBé, S. S. H. Ho, S. H. L. Yim, J. J. Cao, S. C. Lee, L. Tian, D. W. Min and K. F. Ho, *Chemosphere*, 2019, **230**, 578–586.
- 138 A. Laskin, R. C. Moffet, M. K. Gilles, J. D. Fast, R. A. Zaveri, B. Wang, P. Nigge and J. Shutthanandan, *J. Geophys. Res. Atmos.*, 2012, **117**, D15302.
- 139 Y. Wang, W. Song, W. Yang, X. Sun, Y. Tong, X. Wang, C. Liu, Z. Bai and X. Liu, *J. Geophys. Res. Atmos.*, 2019, **124**, 4174–4185.
- 140 W. Song, Y.-L. Wang, W. Yang, X.-C. Sun, Y.-D. Tong, X.-M. Wang, C.-Q. Liu, Z.-P. Bai and X.-Y. Liu, *Environ. Pollut.*, 2019, **248**, 183–190.
- 141 R. K. Pathak, T. Wang and W. S. Wu, *Atmos. Environ.*, 2011, **45**, 1183–1191.
- 142 Y. Xie, G. Wang, X. Wang, J. Chen, Y. Chen, G. Tang, L. Wang, S. Ge, G. Xue, Y. Wang and J. Gao, *Atmos. Chem. Phys.*, 2020, **20**, 5019–5033.
- 143 S. K. Hassan, A. A. El-Abssawy and M. I. Khoder, *Atmos. Pollut. Res.*, 2013, **4**, 117–129.
- 144 R. Zhang, Y. Zhang, H. Lin, X. Feng, T.-M. Fu and Y. Wang, *Atmosphere (Basel)*, 2020, **11**, 433.
- 145 J. G. Calvert, *SO₂, NO and NO₂ Oxidation Mechanisms: Atmospheric Considerations*, Butterworth Publishers, University of Michigan, 1984.
- 146 L. Luo, Y.-Y. Pan, R.-G. Zhu, Z.-Y. Zhang, N.-J. Zheng, Y.-H. Liu, C. Liu, H.-W. Xiao and H.-Y. Xiao, *Atmos. Environ.*, 2020, **225**, 117371.
- 147 T. Ohara, H. Akimoto, J. Kurokawa, N. Horii, K. Yamaji, X. Yan and T. Hayasaka, *Atmos. Chem. Phys.*, 2007, **7**, 4419–4444.
- 148 L. Kong, M. Feng, Y. Liu, Y. Zhang, C. Zhang, C. Li, J. An, X. Liu, Q. Tan, N. Cheng, Y. Deng, R. Zhai and Z. Wang, *Atmos. Chem. Phys.*, 2020, **20**, 11181–11199.
- 149 J. Hao, H. Tian and Y. Lu, *Environ. Sci. Technol.*, 2002, **36**, 552–560.
- 150 J. Xue, Z. Yuan, A. K. H. Lau and J. Z. Yu, *J. Geophys. Res. Atmos.*, 2014, **119**, 4888–4902.
- 151 M. A. H. Khan, M. C. Cooke, S. R. Utembe, A. T. Archibald, R. G. Derwent, P. Xiao, C. J. Percival, M. E. Jenkin, W. C. Morris and D. E. Shallcross, *Atmos. Res.*, 2015, **164–165**, 347–357.
- 152 H. Shen, T.-M. Yang, C.-C. Lu, C.-S. Yuan, C.-H. Hung, C.-T. Lin, C.-W. Lee, G. Jing, & Gongren Hu and K.-C. Lo, *Environ. Sci. Pollut. Res.*, 2020, **27**, 6918–6935.
- 153 Z. Dong, F. Su, Z. Zhang and S. Wang, *J. Environ. Sci. (China)*, 2020, **88**, 316–325.
- 154 W. L. Chang, P. V. Bhave, S. S. Brown, N. Riemer, J. Stutz and D. Dabdub, *Aerosol. Sci. Technol.*, 2011, **45**, 665–695.
- 155 S. Sarkar and B. Bandyopadhyay, *J. Phys. Chem. A.*, 2020, **124**, 3564–3572.
- 156 X. Liu, K. Sun, Y. Qu, M. Hu, Y. Sun, F. Zhang and Y. Zhang, *Aerosol Air Qual. Res.*, 2015, **15**, 2246–2257.
- 157 X. Fu, S. Wang, X. Chang, S. Cai, J. Xing and J. Hao, *Sci. Rep.*, 2016, **6**, 35992.
- 158 M. Xia, X. Peng, W. Wang, C. Yu, P. Sun, Y. Li, Y. Liu, Z. Xu, Z. Wang, Z. Xu, W. Nie, A. Ding and T. Wang, *Atmos. Chem. Phys.*, 2020, **20**, 6147–6158.
- 159 S. Yan and G. Wu, *Sci. Rep.*, 2017, **7**, 46216.
- 160 Sulfur dioxide (SO₂) | Minnesota Pollution Control Agency, <https://www.pca.state.mn.us/air/sulfur-dioxide-so2>, (accessed Mar 21).

- 161 Sulfur Dioxide Basics | Sulfur Dioxide (SO₂) Pollution | US EPA, <https://www.epa.gov/so2-pollution/sulfur-dioxide-basics>, (accessed Mar 21).
- 162 G. Li, N. Bei, J. Cao, R. Huang, J. Wu, T. Feng, Y. Wang, S. Liu, Q. Zhang, X. Tie and L. T. Molina, *Atmos. Chem. Phys.*, 2017, **17**, 3301–3316.
- 163 G. Wang, R. Zhang, M. E. Gomez, L. Yang, M. L. Zamora, M. Hu, Y. Lin, J. Peng, S. Guo, J. Meng, J. Li, C. Cheng, T. Hu, Y. Ren, Y. Y. Wang, J. Gao, J. Cao, Z. An, W. Zhou, G. Li, J. Wang, P. Tian, W. Marrero-Ortiz, J. Secrest, Z. Du, J. Zheng, D. Shang, L. Zeng, M. Shao, W. Wang, Y. Huang, Y. Y. Wang, Y. Zhu, Y. Li, J. Hu, B. Pan, L. Cai, Y. Cheng, Y. Ji, F. Zhang, D. Rosenfeld, P. S. Liss, R. A. Duce, C. E. Kolb and M. J. Molina, *Proc Natl Acad Sci USA.*, 2016, **113**, 13630–13635.
- 164 B. J. Finlayson-Pitts and J. N. Pitts Jr., *Chemistry of the Upper and Lower Atmosphere*, Academic Press, San Diego, San Francisco, New York, Boston, London, Sydney, Tokyo, 1st edn., 2000.
- 165 E. S. Saltzman, G. W. Brass and D. A. Price, *Geophys. Res. Lett.*, 1983, **10**, 513–516.
- 166 Y. Xie, A. Ding, W. Nie, H. Mao, X. Qi, X. Huang, Z. Xu, V. M. Kerminen, T. Petäjä, X. Chi, A. Virkkula, M. Boy, L. Xue, J. Guo, J. Sun, X. Yang, M. Kulmala and C. Fu, *J. Geophys. Res. Atmos.*, 2015, **120**, 12,679–12,694.
- 167 S. N. Pandis and J. H. Seinfeld, *J. Geophys. Res. Atmos.*, 1989, **94**, 12911–12923.
- 168 C. R. Usher, H. Al-Hosney, S. Carlos-Cuellar and V. H. Grassian, *J. Geophys. Res. Atmos.*, 2002, **107**, ACH 16-1-ACH 16-9.
- 169 S. Yan and G. Wu, *Sci. Rep.*, 2017, **7**, 46216.
- 170 J. G. Calvert and W. R. Stockwell, *Environ. Sci. Technol.*, 1983, **17**, 428A-443A.
- 171 J. Shao, Q. Chen, Y. Wang, X. Lu, P. He, Y. Sun, V. Shah, R. V. Martin, S. Philip, S. Song, Y. Zhao, Z. Xie, L. Zhang and B. Alexander, *Atmos. Chem. Phys.*, 2019, **19**, 6107–6123.
- 172 Y. Fang, C. Ye, J. Wang, Y. Wu, M. Hu, W. Lin, F. Xu and T. Zhu, *Atmos. Chem. Phys.*, 2019, **19**, 12295–12307.
- 173 M. Boy, M. Kulmala, T. M. Ruuskanen, M. Pihlatie, A. Reissell, P. P. Aalto, P. Keronen, M. Dal Maso, H. Hellen, H. Hakola, R. Jansson, M. Hanke and F. Arnold, *Atmos. Chem. Phys.*, 2005, **5**, 863–878.
- 174 R. L. Mauldin III, T. Berndt, M. Sipilä, P. Paasonen, T. Petäjä, S. Kim, T. Kurtén, F. Stratmann, V. M. Kerminen and M. Kulmala, *Nature*, 2012, **488**, 193–196.
- 175 G. Sarwar, K. Fahey, R. Kwok, R. C. Gilliam, S. J. Roselle, R. Mathur, J. Xue, J. Yu and W. P. L. Carter, *Atmos. Environ.*, 2013, **68**, 186–197.
- 176 E. Harris, B. Sinha, D. Van Pinxteren, A. Tilgner, K. W. Fomba, J. Schneider, A. Roth, T. Gnauk, B. Fahlbusch, S. Mertes, T. Lee, J. Collett, S. Foley, S. Borrmann, P. Hoppe and H. Herrmann, *Science (80-.)*, 2013, **340**, 727–730.
- 177 H. He, Y. Wang, Q. Ma, J. Ma, B. Chu, D. Ji, G. Tang, C. Liu, H. Zhang and J. Hao, *Sci. Rep.*, 2014, **4**, 4172.
- 178 J. Baltrusaitis, P. M. Jayaweera and V. H. Grassian, *J. Phys. Chem. C.*, 2011, **115**, 492–500.
- 179 C. Ye, P. Liu, Z. Ma, C. Xue, C. Zhang, Y. Zhang, J. Liu, C. Liu, X. Sun and Y. Mu, *Environ. Sci. Technol. Lett.*, 2018, **5**, 757–763.
- 180 M. E. Gebel, B. J. Finlayson-Pitts and J. A. Ganske, *Geophys. Res. Lett.*, 2000, **27**, 887–890.
- 181 W. Nie, T. Wang, L. K. Xue, A. J. Ding, X. F. Wang, X. M. Gao, Z. Xu, Y. C. Yu, C. Yuan, Z. S. Zhou, R. Gao, X. H. Liu, Y. Wang, S. J. Fan, S. Poon, Q. Z. Zhang and W. X. Wang,

- Atmos. Chem. Phys.*, 2012, **12**, 11985–11995.
- 182 W. Nie, A. Ding, T. Wang, V.-M. Kerminen, C. George, L. Xue, W. Wang, Q. Zhang, T. Petäjä, X. Qi, X. Gao, X. Wang, X. Yang, C. Fu and M. Kulmala, *Sci. Rep.*, 2014, **4**, 6634.
- 183 C. George, M. Ammann, B. D’Anna, D. J. Donaldson and S. A. Nizkorodov, *Chem. Rev.*, 2015, **115**, 4218–4258.
- 184 X. Chi, P. He, Z. Jiang, X. Yu, F. Yue, L. Wang, B. Li, H. Kang, C. Liu and Z. Xie, *J. Meteorol. Res.*, 2018, **32**, 14–25.
- 185 Y. Sun, G. Zhuang, A. Tang, Y. Wang and Z. An, *Environ. Sci. Technol.*, 2006, **40**, 3148–3155.
- 186 L. Xu, F. Duan, K. He, Y. Ma, L. Zhu, Y. Zheng, T. Huang, T. Kimoto, T. Ma, H. Li, S. Ye, S. Yang, Z. Sun and B. Xu, *Environ. Pollut.*, 2017, **227**, 296–305.
- 187 J. Zhou, R. Zhang, J. Cao, J. C. Chow and J. G. Watson, *Aerosol Air Qual. Res.*, 2012, **12**, 492–502.
- 188 C. Chen, Y. L. Sun, W. Q. Xu, W. Du, L. B. Zhou, T. T. Han, Q. Q. Wang, P. Q. Fu, Z. F. Wang, Z. Q. Gao, Q. Zhang and D. R. Worsnop, *Atmos. Chem. Phys.*, 2015, **15**, 12879–12895.
- 189 J. Wang, X. Ge, Y. Chen, Y. Shen, Q. Zhang, Y. Sun, J. Xu, S. Ge, H. Yu and M. Chen, *Atmos. Chem. Phys.*, 2016, **16**, 9109–9127.
- 190 Q. Xu, S. Wang, J. Jiang, N. Bhattarai, X. Li, X. Chang, X. Qiu, M. Zheng, Y. Hua and J. Hao, *Sci. Total. Environ.*, 2019, **689**, 1293–1303.
- 191 G. J. Zheng, F. K. Duan, H. Su, Y. L. Ma, Y. Cheng, B. Zheng, Q. Zhang, T. Huang, T. Kimoto, D. Chang, U. Pöschl, Y. F. Cheng and K. B. He, *Atmos. Chem. Phys.*, 2015, **15**, 2969–2983.
- 192 Y. Zhang, W. Huang, T. Cai, D. Fang, Y. Wang, J. Song, M. Hu and Y. Zhang, *Atmos. Res.*, 2016, **174–175**, 62–69.
- 193 K. Ram, M. M. Sarin, A. K. Sudheer and R. Rengarajan, *Aerosol Air Qual. Res.*, 2012, **12**, 359–370.
- 194 Y. Wang, G. Zhuang, Y. Sun and Z. An, *Atmos. Environ.*, 2006, **40**, 6579–6591.
- 195 Z. Wang, D. Zhang, B. Liu, Y. Li, T. Chen, F. Sun, D. Yang, Y. Liang, M. Chang, L. Yang and A. Lin, *J. Atmos. Chem.*, 2016, **73**, 407–425.
- 196 X. Wang, W. Wei, S. Cheng, S. Yao, H. Zhang and C. Zhang, *Atmos. Pollut. Res.*, 2019, **10**, 1976–1984.
- 197 M. I. Khoder, *Chemosphere.*, 2002, **49**, 675–684.
- 198 M. Saxena, A. Sharma, A. Sen, P. Saxena, Saraswati, T. K. Mandal, S. K. Sharma and C. Sharma, *Atmos. Res.*, 2017, **184**, 112–125.
- 199 G. Hu, Y. Zhang, J. Sun, L. Zhang, X. Shen, W. Lin and Y. Yang, *Atmos. Res.*, 2014, **145–146**, 1–11.
- 200 Y. Wang, G. Zhuang, A. Tang, H. Yuan, Y. Sun, S. Chen and A. Zheng, *Atmos. Environ.*, 2005, **39**, 3771–3784.
- 201 X. Wang, W. Wei, S. Cheng, C. Zhang and W. Duan, *J. Environ. Sci. (China)*, 2019, **78**, 293–302.
- 202 R. Zhang, X. Sun, A. Shi, Y. Huang, J. Yan, T. Nie, X. Yan and X. Li, *Atmos. Environ.*, 2018, **177**, 275–282.
- 203 A. Chatterjee, A. Adak, A. K. Singh, M. K. Srivastava, S. K. Ghosh, S. Tiwari, P. C. S.

- Devara and S. Raha, *PLoS ONE.*, 2010, **5**, e11122.
- 204 A. Chatterjee, C. Dutta, T. K. Jana and S. Sen, *J. Atmos. Chem.*, 2012, **69**, 83–100.
- 205 Q. Fu, G. Zhuang, J. Wang, C. Xu, K. Huang, J. Li, B. Hou, T. Lu and D. G. Streets, *Atmos. Environ.*, 2008, **42**, 2023–2036.
- 206 T.-C. Li, C.-S. Yuan, H.-C. Huang, C.-L. Lee, S.-P. Wu and C. Tong, *Sci. Rep.*, 2016, **6**, 22956.
- 207 J. H. Seinfeld, *Atmospheric Chemistry and Physics of Air Pollution*, Wiley, New York, 1986.
- 208 Y. Sun, Z. Wang, P. Fu, Q. Jiang, T. Yang, J. Li and X. Ge, *Atmos. Environ.*, 2013, **77**, 927–934.
- 209 W. A. H. Asman, M. A. Sutton and J. K. Schjørring, *New Phytol.*, 1998, **139**, 27–48.
- 210 S. Wang, J. Nan, C. Shi, Q. Fu, S. Gao, D. Wang, H. Cui, A. Saiz-Lopez and B. Zhou, *Sci. Reports 2015 51*, 2015, **5**, 1–13.
- 211 H. Guo, R. J. Weber and A. Nenes, *Sci. Reports 2017 71*, 2017, **7**, 1–7.
- 212 S. N. Behera, M. Sharma, V. P. Aneja and R. Balasubramanian, *Environ. Sci. Pollut. Res.*, 2013, **20**, 8092–8131.
- 213 M. W. Shephard, E. Dammers, K. E. Cady-Pereira, S. K. Kharol, J. Thompson, Y. Gainariu-Matz, J. Zhang, C. A. McLinden, A. Kovachik, M. Moran, S. Bittman, C. E. Sioris, D. Griffin, M. J. Alvarado, C. Lonsdale, V. Savic-Jovicic and Q. Zheng, *Atmos. Chem. Phys.*, 2020, **20**, 2277–2302.
- 214 M. Van Damme, L. Clarisse, S. Whitburn, J. Hadji-Lazaro, D. Hurtmans, C. Clerbaux and P.-F. Coheur, *Nat. 2018 5647734*, 2018, **564**, 99–103.
- 215 L. Clarisse, M. Van Damme, C. Clerbaux and P. F. Coheur, *Atmos. Meas. Tech.*, 2019, **12**, 5457–5473.
- 216 J. David Felix, E. M. Elliott, T. J. Gish, L. L. McConnell and S. L. Shaw, *Rapid Commun. Mass Spectrom.*, 2013, **27**, 2239–2246.
- 217 M. A. Sutton, U. Dragosits, Y. S. Tang and D. Fowler, *Atmos. Environ.*, 2000, **34**, 855–869.
- 218 X. Huang, Y. Song, M. Li, J. Li, Q. Huo, X. Cai, T. Zhu, M. Hu and H. Zhang, *Global Biogeochem. Cycles*, 2012, **26**, GB1030.
- 219 C. Viatte, T. Wang, M. Van Damme, E. Dammers, F. Meleux, L. Clarisse, M. W. Shephard, S. Whitburn, P. François Coheur, K. E. Cady-Pereira and C. Clerbaux, *Atmos. Chem. Phys.*, 2020, **20**, 577–596.
- 220 A. S. Gautam, R. S. Negi, S. Singh, A. K. Srivastava, S. Tiwari and D. S. Bisht, *Int. J. Environ. Res.*, 2018, **12**, 681–691.
- 221 A. Kulshrestha, D. S. Bisht, J. Masih, D. Massey, S. Tiwari and A. Taneja, *J. Atmos. Chem.*, 2009, **62**, 121–138.
- 222 R. Rengarajan, A. K. Sudheer and M. M. Sarin, *Atmos. Res.*, 2011, **102**, 420–431.
- 223 R. Rengarajan, A. K. Sudheer and M. M. Sarin, *Atmos. Environ.*, 2011, **45**, 1940–1945.
- 224 D. K. Deshmukh, M. K. Deb, Y. I. Tsai and S. L. Mkoma, *J. Atmos. Chem.*, 2010, **66**, 81.
- 225 S. Kumar, S. Nath, M. S. Bhatti and S. Yadav, *Aerosol Air Qual. Res.*, 2018, **18**, 1573–1590.
- 226 D. K. Deshmukh, M. K. Deb, Y. I. Tsai and S. L. Mkoma, *Aerosol Air Qual. Res.*, 2011, **11**, 696–708.

- 227 R. D. Gawhane, P. S. P. Rao, K. B. Budhavant, V. Waghmare, D. C. Meshram and P. D. Safai, *Environ. Sci. Pollut. Res.*, 2017, **24**, 21065–21072.
- 228 S. N. Behera, M. Sharma and S. P. Shukla, *J. Hazard. Toxic Radioact. Waste.*, 2016, **20**, A4015002-1-A4015002-9.
- 229 P. Khare and B. P. Baruah, *Atmos. Res.*, 2010, **98**, 148–162.
- 230 S. N. Behera and M. Sharma, *Sci. Total. Environ.*, 2010, **408**, 3569–3575.
- 231 P. Khare, B. P. Baruah and P. G. Rao, *Tellus B. Chem. Phys. Meteorol.*, 2011, **63**, 990–1000.
- 232 S. Kumar and R. S. Raman, *Sci. Total. Environ.*, 2020, **720**, 137511.
- 233 S. Kumar and R. S. Raman, *Atmos. Environ.*, 2016, **143**, 152–163.
- 234 R. D. Gawhane, P. S. P. Rao, K. Budhavant, D. C. Meshram and P. D. Safai, *Meteorol. Atmos. Phys.*, 2019, **131**, 1497–1508.
- 235 A. S. Pipal, S. Singh and G. P. Satsangi, *Urban. Clim.*, 2019, **27**, 243–258.
- 236 D. S. Bisht, A. K. Srivastava, A. S. Pipal, M. K. Srivastava, A. K. Pandey, S. Tiwari and G. Pandithurai, *Environ. Sci. Pollut. Res.*, 2015, **22**, 5293–5304.
- 237 S. Ghosh, T. Gupta, N. Rastogi, A. Gaur, A. Misra, S. N. Tripathi, D. Paul, V. Tare, O. Prakash, D. Bhattu, A. K. Dwivedi, D. S. Kaul, R. Dalai and S. K. Mishra, *Aerosol Air Qual. Res.*, 2014, **14**, 879–891.
- 238 G. K. Singh, P. Rajput, D. Paul and T. Gupta, *J. Aerosol Sci.*, 2018, **126**, 231–241.
- 239 D. K. Deshmukh, M. K. Deb, Y. Suzuki and G. N. Kouvarakis, *Air. Qual. Atmos. Heal.*, 2013, **6**, 95–110.
- 240 S. K. Verma, M. K. Deb, Y. Suzuki and Y. I. Tsai, *Atmos. Res.*, 2010, **95**, 65–76.
- 241 S. K. Sharma, T. K. Mandal, C. Sharma, J. C. Kuniyal, R. Joshi, P. P. Dhyani, Rohtash, A. Sen, H. Ghayas, N. C. Gupta, P. Sharma, M. Saxena, A. Sharma, B. C. Arya and A. Kumar, *MAPAN-J. Metrol. Soc. I.*, 2014, **29**, 243–253.
- 242 K. Ram and M. M. Sarin, *Atmos. Environ.*, 2011, **45**, 460–468.
- 243 Y. Wang, G. Zhuang, X. Zhang, K. Huang, C. Xu, A. Tang, J. Chen and Z. An, *Atmos. Environ.*, 2006, **40**, 2935–2952.
- 244 R. K. Pathak, W. S. Wu and T. Wang, *Atmos. Chem. Phys.*, 2009, **9**, 1711–1722.
- 245 Y. Zhu, L. Yang, C. Meng, Q. Yuan, C. Yan, C. Dong, X. Sui, L. Yao, F. Yang, Y. Lu and W. Wang, *Atmos. Res.*, 2015, **153**, 276–285.
- 246 H. Wang, J. An, M. Cheng, L. Shen, B. Zhu, Y. Li, Y. Wang, Q. Duan, A. Sullivan and L. Xia, *Chemosphere.*, 2016, **148**, 526–536.
- 247 J.-S. Xu, M.-X. Xu, C. Snape, J. He, S. N. Behera, H.-H. Xu, D.-S. Ji, C.-J. Wang, H. Yu, H. Xiao, Y.-J. Jiang, B. Qi and R.-G. Du, *Chemosphere.*, 2017, **179**, 316–330.
- 248 M. Zhou, L. Qiao, S. Zhu, L. Li, S. Lou, H. Wang, Q. Wang, S. Tao, C. Huang and C. Chen, *J. Environ. Sci. (China)*, 2016, **48**, 151–160.
- 249 Y. Hao, X. Meng, X. Yu, M. Lei, W. Li, W. Yang, F. Shi and S. Xie, *Sci. Total. Environ.*, 2020, **706**, 135715.
- 250 N. Ding, S.-J. Chen, T. Wang, T. Wang and B.-X. Mai, *Environ. Pollut.*, 2018, **238**, 823–832.
- 251 Y. Chen, S.-D. Xie, B. Luo and C. Zhai, *Atmosphere.*, 2019, **10**, 78.

- 252 W. Li, Z. Bai, A. Liu, J. Chen and L. Chen, *Aerosol Air Qual. Res.*, 2009, **9**, 105–119.
- 253 S.-Y. Chang, C. C. K. Chou, S. Liu and Y. Zhang, *Aerosol Air Qual. Res.*, 2013, **13**, 1373–1383.
- 254 S.-C. Lai, S.-C. Zou, J.-J. Cao, S.-C. Lee and K.-F. Ho, *J. Environ. Sci. (China)*, 2007, **19**, 939–947.
- 255 Y. Zhang, Y. Jia, M. Li and L. Hou, *Environ. Forensics.*, 2018, **19**, 166–171.
- 256 W. Dai, J. Gao, G. Cao and F. Ouyang, *Atmos. Res.*, 2013, **122**, 391–400.
- 257 X. Niu, J. Cao, Z. Shen, S. S. H. Ho, X. Tie, S. Zhao, H. Xu, T. Zhang and R. Huang, *Atmos. Environ.*, 2016, **147**, 458–469.
- 258 R. Zhang, J. Jing, J. Tao, S.-C. Hsu, G. Wang, J. Cao, C. S. L. Lee, L. Zhu, Z. Chen, Y. Zhao and Z. Shen, *Atmos. Chem. Phys.*, 2013, **13**, 7053–7074.
- 259 World Population Review, <https://worldpopulationreview.com/>, (accessed Jan 21).
- 260 Air Pollution and Human Health in Developing Megacities | UK Centre for Ecology & Hydrology, <https://www.ceh.ac.uk/our-science/projects/air-pollution-and-human-health-developing-mega-cities>, (accessed Mar 21).
- 261 SeQuant, *A Practical Guide to Ion Chromatography*, SeQuant AB, Umeå, 2007.
- 262 M. Z. Özel, J. F. Hamilton and A. C. Lewis, *Environ. Sci. Technol.*, 2011, **45**, 1497–1505.
- 263 Agilent Technologies, *Agilent Technologies Operation and Maintenance Manual Agilent 355 Sulfur and 255 Nitrogen Chemiluminescence Detectors*, 2012.
- 264 Hamamatsu Photonics K. K. (Editorial Committee), *PHOTOMULTIPLIER TUBES Basics and Applications*, Hamamatsu Photonics K. K. (Electron Tube Division), Edition 3a., 2007.
- 265 F. J. Brechtel, *Brechtel Manufacturing Incorporated Particle into Liquid Sampler Manual v12*, Brechtel Manufacturing Inc., Hayward, CA 94544, v12 edn., 2008.
- 266 D. A. Orsini, Y. Ma, A. Sullivan, B. Sierau, K. Baumann and R. J. Weber, *Atmos. Environ.*, 2003, **37**, 1243–1259.
- 267 J. Xu, S. Song, R. M. Harrison, C. Song, L. Wei, Q. Zhang, Y. Sun, L. Lei, C. Zhang, X. Yao, D. Chen, W. Li, M. Wu, H. Tian, L. Luo, S. Tong, W. Li, J. Wang, G. Shi, Y. Huangfu, Y. Tian, B. Ge, S. Su, C. Peng, Y. Chen, F. Yang, A. Mihajlidi-Zeli, D. Đor, S. J. Swift, I. Andrews, J. F. Hamilton, Y. Sun, A. Kramawijaya, J. Han, S. Saksakulkrai, C. Baldo, S. Hou, F. Zheng, K. R. Daellenbach, C. Yan, Y. Liu, M. Kulmala, P. Fu and Z. Shi, *Atmos. Meas. Tech.*, 2020, **13**, 6325–6341.
- 268 J. Lang, Y. Zhang, Y. Zhou, S. Cheng, D. Chen, X. Guo, S. Chen, X. Li, X. Xing and H. Wang, *Aerosol. Air. Qual. Res.*, 2017, **17**, 412–425.
- 269 W. Huang, Y. Yang, Y. Wang, W. Gao, H. Li, Y. Zhang, J. Li, S. Zhao, Y. Yan, D. Ji, G. Tang, Z. Liu, L. Wang, R. Zhang and Y. Wang, *Sci. Total Environ.*, 2021, **768**, 144538.
- 270 B. R. Ayres, H. M. Allen, D. C. Draper, S. S. Brown, R. J. Wild, J. L. Jimenez, D. A. Day, P. Campuzano-Jost, W. Hu, J. De Gouw, A. Koss, R. C. Cohen, K. C. Duffey, P. Romer, K. Baumann, E. Edgerton, S. Takahama, J. A. Thornton, B. H. Lee, F. D. Lopez-Hilfiker, C. Mohr, P. O. Wennberg, T. B. Nguyen, A. Teng, A. H. Goldstein, K. Olson and J. L. Fry, *Atmos. Chem. Phys.*, 2015, **15**, 13377–13392.
- 271 L. H. Renbaum and G. D. Smith, *Phys. Chem. Chem. Phys.*, 2009, **11**, 8040–8047.
- 272 A. Kiendler-Scharr, A. A. Mensah, E. Friese, D. Topping, E. Nemitz, A. S. H. Prevot, M. Äijälä, J. Allan, F. Canonaco, M. Canagaratna, S. Carbone, M. Crippa, M. D. Osto, D. A. Day, P. De Carlo, C. F. Di Marco, H. Elbern, A. Eriksson, E. Freney, L. Hao, H. Herrmann, L. Hildebrandt, R. Hillamo, J. L. Jimenez, A. Laaksonen, G. McFiggans, C. Mohr, C.

- O'Dowd, R. Otjes, J. Ovadnevaite, S. N. Pandis, L. Poulain, P. Schlag, K. Sellegri, E. Swietlicki, P. Tiitta, A. Vermeulen, A. Wahner, D. Worsnop and H.-C. Wu, *Geophys. Res. Lett.*, 2016, **43**, 7735–7744.
- 273 B. H. Lee, C. Mohr, F. D. Lopez-Hilfiker, A. Lutz, M. Hallquist, L. Lee, P. Romer, R. C. Cohen, S. Iyer, T. Kurtén, W. Hu, D. A. Day, P. Campuzano-Jost, J. L. Jimenez, L. Xu, N. L. Ng, H. Guo, R. J. Weber, R. J. Wild, S. S. Brown, A. Koss, J. De Gouw, K. Olson, A. H. Goldstein, R. Seco, S. Kim, K. Mcavey, P. B. Shepson, T. Starn, K. Baumann, E. S. Edgerton, J. Liu, J. E. Shilling, D. O. Miller, W. Brune, S. Schobesberger, E. L. D'ambro, J. A. Thornton, R. J. Weber and R. J. Wild, 2016, **113**.
- 274 K. T. Vasquez, J. D. Crouse, B. C. Schulze, K. H. Bates, A. P. Teng, L. Xu, H. M. Allen, P. O. Wennberg, *PNAS*, 2020, **117**, 33011–33016.
- 275 S. Liu, J. E. Shilling, C. Song, N. Hiranuma, R. A. Zaveri and L. M. Russell, *Aerosol. Sci. Tech.*, 2012, **46**, 1359–1369.
- 276 A. I. Darer, N. C. Cole-Filipiak, A. E. O'connor and M. J. Elrod, *Environ. Sci. Technol.*, 2011, **45**, 1895–1902.
- 277 N. J. Farren, N. Ramírez, J. D. Lee, E. Finessi, A. C. Lewis and J. F. Hamilton, *Environ. Sci. Technol.*, 2015, **49**, 9648–9656.
- 278 M. Z. Özel, M. W. Ward, J. F. Hamilton, A. C. Lewis, T. Raventós-Duran and R. M. Harrison, *Aerosol. Sci. Technol.*, 2010, **44**, 109–116.
- 279 Air Pollution in the World, <https://aqicn.org/city/all/>, (accessed Jan 2021).
- 280 India - PM2.5 levels in Delhi 2019, <https://www.statista.com/statistics/1051325/india-pm-25-levels-in-delhi/>, (accessed Aug 2021).
- 281 Average annual PM2.5 air pollution levels in Beijing, China between 2009 and 2019, <https://www.statista.com/statistics/690823/china-annual-pm25-particle-levels-beijing/>, (accessed Mar 2021).
- 282 J. Wang and S. Xu, *Int. J. Coal Sci. Technol.*, 2014, **1**, 129–134.
- 283 F. A. Squires, E. Nemitz, B. Langford, O. Wild, W. S. Drysdale, W. J. F. Acton, P. Fu, C. S. B. Grimmond, J. F. Hamilton, C. N. Hewitt, M. Hollaway, S. Kotthaus, J. Lee, S. Metzger, N. Pinguha-Durden, M. Shaw, A. R. Vaughan, X. Wang, R. Wu, Q. Zhang and Y. Zhang, *Atmos. Chem. Phys.*, 2020, **20**, 8737–8761.
- 284 M. E. Marlier, A. S. Jina, P. L. Kinney and R. S. DeFries, *Curr. Clim. Chang. Rep.*, 2016, **2**, 15–27.
- 285 MCM Website, <http://mcm.leeds.ac.uk/MCM/>, (accessed Mar 2021).
- 286 Q. Zhang, J. L. Jimenez, M. R. Canagaratna, I. M. Ulbrich, N. L. Ng, D. R. Worsnop and Y. Sun, *Anal. Bioanal. Chem.*, 2011, **401**, 3045–3067.
- 287 D. K. Farmer, A. Matsunaga, K. S. Docherty, J. D. Surratt, J. H. Seinfeld, P. J. Ziemann and J. L. Jimenez, *P. Natl. Acad. Sci. USA.*, 2010, **107**, 6670–6675.
- 288 S. Tiwari, A. K. Srivastava, D. S. Bisht, T. Bano, S. Singh, S. Behura, M. K. Srivastava, D. M. Chate and B. Padmanabhamurty, *J. Atmos. Chem.*, 2009, **62**, 193–209.
- 289 Shivani, R. Gadi, M. Saxena, S. K. Sharma and T. K. Mandal, *Meteorol. Atmos. Phys.*, 2019, **131**, 753–764.
- 290 R. Gadi, A. K. Sarkar, B. S. Gera, A. P. Mitra and D. C. Parashar, *Indian. J. Radio Space. Phys.*, 2002, **31**, 93–97.
- 291 R. Shen, K. Schäfer, L. Shao, J. Schnelle-Kreis, Y. Wang, F. Li, Z. Liu, S. Emeis and H. P. Schmid, *Urban Clim.*, 2017, **22**, 51–63.

- 292 C. Meng-Tian, S. Yang, Z. Xiao-Wan and C. Na, *Atmos. Ocean. Sci. Lett.*, 2014, **7**, 23–27.
- 293 X. Yu, K. He, Y. Ma, F. Yang, F. Duan, A. Zheng and C. Zhao, *J. Environ. Sci. (China)*, 2004, **16**, 813–815.
- 294 R. A. Hall and T. P. Whitehead, *J. clin. Path.*, 1970, **23**, 323–326.
- 295 X. Luo, Y. Wang, S. Wen, M. Ma, C. Sun, W. Yin and Y. Ma, *Int. J. Miner. Process.*, 2016, **152**, 1–6.
- 296 X. Wang, W. Liu, H. Duan, B. Wang, C. Han and D. Wei, *Powder Technol.*, 2018, **329**, 158–166.
- 297 EPA, *ANALYTICAL DETECTION LIMIT GUIDANCE & Laboratory Guide for Determining Method Detection Limits*, Wisconsin, 1996.
- 298 J. N. Miller and J. C. Miller, *Statistics and Chemometrics for Analytical Chemistry*, Pearson Education Limited, London, 6th edn., 2010.
- 299 D. J. Anderson, *Clin. Chem.*, 1989, **35**, 2152–2153.
- 300 Harvard University, *A Summary of Error Propagation*, Harvard, 2007.
- 301 L. Wang, L. Wen, C. Xu, J. Chen, X. Wang, L. Yang, W. Wang, X. Yang, X. Sui, L. Yao and Q. Zhang, *Sci. Total Environ.*, 2015, **538**, 93–101.
- 302 C. H. Song, M. E. Park, E. J. Lee, J. H. Lee, B. K. Lee, D. S. Lee, J. Kim, J. S. Han, K. J. Moon and Y. Kondo, *Atmos. Environ.*, 2009, **43**, 2168–2173.
- 303 T. C. Vandenkoer, M. Z. Markovic, J. E. Sanders, X. Ren, S. E. Pusede, E. C. Browne, R. C. Cohen, L. Zhang, J. Thomas, W. H. Brune and J. G. Murphy, *J. Geophys. Res. Atmos.*, 2014, **119**, 9093–9106.
- 304 G. Lammel and J. N. Cape, *Chem. Soc. Rev.*, 1996, **25**, 361–369.
- 305 X. Wang, W. Wang, L. Yang, X. Gao, W. Nie, Y. Yu, P. Xu, Y. Zhou and Z. Wang, *Atmos. Environ.*, 2012, **63**, 68–76.
- 306 X. Wang, J. Chen, J. Sun, W. Li, L. Yang, L. Wen, W. Wang, X. Wang, J. L. Collett, Y. Shi, Q. Zhang, J. Hu, L. Yao, Y. Zhu, X. Sui, X. Sun and A. Mellouki, *Sci. Total Environ.*, 2014, **493**, 133–137.
- 307 X. Gao, L. Yang, S. Cheng, R. Gao, Y. Zhou, L. Xue, Y. Shou, J. Wang, X. Wang, W. Nie, P. Xu and W. Wang, *Atmos. Environ.*, 2011, **45**, 6048–6056.
- 308 B. Stieger, G. Spindler, B. Fahlbusch, K. Müller, A. Grüner, L. Poulain, L. Thöni, E. Seitzler, M. Wallasch and H. Herrmann, *J. Atmos. Chem. 2017 751*, 2017, **75**, 33–70.
- 309 J. Kleffmann and P. Wiesen, *Atmos. Chem. Phys.*, 2008, **8**, 6813–6822.
- 310 Lukas Gutzwiller, Frank Arens, Urs Baltensperger, Heinz W. Gäggeler and Markus Ammann, *Environ. Sci. Technol.*, 2002, **36**, 677–682.
- 311 J. Kleffmann, J. Heland, R. Kurtenback and J. C. Lörzer, *Environ. Sci. Pollut. Res.*, 2002, **9**, 48–54.
- 312 A. Sorooshian, J. Csavina, T. Shingler, S. Dey, F. J. Brechtel, A. E. Sáez and E. A. Betterton, *Environ. Sci. Technol.*, 2012, **46**, 9473–9480.
- 313 V. H. Grassian, *Int. Rev. Phys. Chem.*, 2010, **20**, 467–548.
- 314 C. B. Boring, Z. Genfa, P. K. Dasgupta, M. W. Martin and W. F. Smith, *Anal. Chem.*, 2002, **74**, 1256–1268.
- 315 P. K. Simon and P. K. Dasgupta, *Environ. Sci. Technol.*, 1995, **29**, 1534–1541.
- 316 P. Koutrakis, J. M. Wolfson, A. Bunyaviroch, S. E. Froehlich, K. Hirano and J. D. Mulik,

- Anal. Chem.*, 1993, **65**, 209–214.
- 317 A. P. R. Zabell, F. E. Lytle and R. K. Julian, *Clin. Mass Spectrom.*, 2016, **2**, 25–33.
- 318 EPA. CALIBRATION CURVES: PROGRAM USE/NEEDS FINAL, <https://www.epa.gov/sites/production/files/2014-05/documents/calibration-guide-ref-final-oct2010.pdf>, (accessed Jun 2021).
- 319 NIST. Models for Instrument Calibration, <https://www.itl.nist.gov/div898/handbook/mpc/section3/mpc361.htm>, (accessed Aug 2021).
- 320 M. Zheng, L. G. Salmon, J. J. Schauer, L. Zeng, C. S. Kiang, Y. Zhang and G. R. Cass, *Atmos. Environ.*, 2005, **39**, 3967–3976.
- 321 J. M. Moch, E. Dovrou, L. J. Mickley, F. N. Keutsch, Y. Cheng, D. J. Jacob, J. Jiang, M. Li, J. W. Munger, X. Qiao and Q. Zhang, *Geophys. Res. Lett.*, 2018, **45**, 11,969–11,979.
- 322 T. D. Nelin, A. M. Joseph, M. W. Gorr and L. E. Wold, *Toxicol. Lett.*, 2012, **208**, 293–299.
- 323 Y.-F. Xing, Y.-H. Xu, M.-H. Shi and Y.-X. Lian, *J. Thorac. Dis.*, 2016, **8**, E69–E74.
- 324 Y. Zhang, Z. Ding, Q. Xiang, W. Wang, L. Huang and F. Mao, *Int. J. Hyg. Environ. Heal.*, 2020, **224**, 113418.
- 325 K. J. Maji, A. K. Dikshit, M. Arora and A. Deshpande, *Sci. Total. Environ.*, 2018, **612**, 683–693.
- 326 Z. Ye, X. Guo, L. Cheng, S. Cheng, D. Chen, W. Wang and B. Liu, *Atmos. Environ.*, 2019, **219**, 116989.
- 327 I. Trebs, S. Metzger, F. X. Meixner, G. Helas, A. Hoffer, Y. Rudich, A. H. Falkovich, M. A. L. Moura, R. S. da Silva Jr., P. Artaxo, J. Slanina and M. O. Andreae, *J. Geophys. Res.*, 2005, **110**, D07303, doi:10.1029/2004JD005478.
- 328 A. Nenes, S. N. Pandis and C. Pilinis, *Aquat. Geochem.*, 1998, **4**, 123–152.
- 329 C. Fountoukis and A. Nenes, *Atmos. Chem. Phys.*, 2007, **7**, 4639–4659.
- 330 J. T. Walker, D. R. Whitall, W. Robarge and H. W. Paerl, *Atmos. Environ.*, 2004, **38**, 1235–1246.
- 331 R. Chen, J. Cheng, J. Lv, L. Wu and J. Wu, *Environ. Geochem. Hlth.*, 2017, **39**, 913–921.
- 332 Y. Yang, R. Zhou, Y. Yu, Y. Yan, Y. Liu, Y. Di, D. Wu and W. Zhang, *J. Environ. Sci. (China)*, 2017, **55**, 146–156.
- 333 E. Dovrou, C. Y. Lim, M. R. Canagaratna, J. H. Kroll, D. R. Worsnop, F. N. Keutsch and J. A. Paulson, *Atmos. Meas. Tech.*, 2019, **12**, 5303–5315.
- 334 N. Takegawa, Y. Miyazaki, Y. Kondo, Y. Komazaki, T. Miyakawa, J. L. Jimenez, J. T. Jayne, D. R. Worsnop, J. D. Allan and R. J. Weber, *Aerodyne Aerosol Mass Spectrom.*, 2005, **39**, 760–770.
- 335 Y. Xue, L. Cheng, X. Chen, X. Zhai, W. Wang, W. Zhang, Y. Bai, H. Tian, L. Nie, S. Zhang and T. Wei, *PLoS ONE.*, 2018, **13**, e0194226. <https://doi.org/10.1371/journal.pone.0194>.
- 336 ERA5 ECMWF, <https://www.ecmwf.int/en/forecasts/datasets/reanalysis-datasets/era5>, (accessed Feb 2021).
- 337 A. A. Nair and F. Yu, *Atmosphere (Basel)*, 2020, **11**, 1092.
- 338 Global Sulphur Levels | UNEP - UN Environment Programme, https://www.unep.org/global-sulphur-levels?_ga=2.57864364.78991530.1615032115-1045238511.1615032115, (accessed Mar 2021).

- 339 S. K. Sharma, A. Datta, T. Saud, M. Saxena, T. K. Mandal, Y. N. Ahammed and B. C. Arya, *J. Environ. Sci.*, 2010, **22**, 1023–1028.
- 340 Y. Zhang, S.-Y. Wu, S. Krishnan, K. Wang, A. Queen, V. P. Aneja and S. Pal Arya, *Atmos. Environ.*, 2008, **42**, 3218–3237.
- 341 Y. Zhou, X. H. Huang, Q. Bian, S. M. Griffith, P. K. K. Louie and J. Z. Yu, *J. Geophys. Res-Atmos.*, 2015, **120**, 9772–9788.
- 342 Y. Wang and Y. Chen, *Geophys. Res. Lett.*, 2019, **46**, 5535–5545.
- 343 K. Widziewicz-Rzońca and M. Tytła, *Scientometrics*, 2020, **124**, 1945–2008.
- 344 S. K. R. Boreddy, K. Kawamura, S. Bikkina and M. M. Sarin, *Sci. Total. Environ.*, 2016, **544**, 661–669.
- 345 J. Cash, B. Langford, C. Di Marco, N. Mullinger, J. Allan, E. Reyes-Villegas, R. Joshi, M. Heal, W. J. F. Acton, N. Hewitt, P. Misztal, W. Drysdale, T. Mandal, R. Gadi and E. Nemitz, *Atmos. Chem. Phys. Discuss. [preprint]*, 2020, 1–42.
- 346 H. Zhang, S. Yu, L. Shao and P. He, *J. Environ. Sci. (China)*, 2019, **75**, 370–377.
- 347 S. S. Gunthe, P. Liu, U. Panda, S. S. Raj, A. Sharma, E. Darbyshire, E. Reyes-Villegas, J. Allan, Y. Chen, X. Wang, S. Song, M. L. Pöhlker, L. Shi, Y. Wang, S. M. Kommula, T. Liu, R. Ravikrishna, G. Mcfiggans, L. J. Mickley, S. T. Martin, U. Pöschl, M. O. Andreae and H. Coe, *Nat. Geosci.*, 2021, **14**, 77–84.
- 348 M. I. Jacobs, W. J. Burke and M. J. Elrod, *Atmos. Chem. Phys.*, 2014, **14**, 8933–8946.
- 349 J. W. Baker and D. M. Easty, *Nature*, 1950, **166**, 156.
- 350 G. Prasad, *Report No. R&D/LAB/SAN/2019-20/SAN0310819/10700*, Mumbai , India, 2019.
- 351 Normet, <https://www.normet.com/>, (accessed Feb 2021).
- 352 J. W. Park, K. H. Kim and K. Y. Ann, *Adv. Mater. Sci. Eng.*, 2016, **2016**, Article ID 7179403.
- 353 C. H. Kim, Y. Choi and Y. S. Ghim, *Aerosol Air Qual. Res.*, 2015, **15**, 814–820.
- 354 C. N. Liu, S. F. Lin, A. Awasthi, C. J. Tsai, Y. C. Wu and C. F. Chen, *Atmos. Environ.*, 2014, **85**, 48–53.
- 355 W. JG, C. JC, C. LW and F. NH, *J. Air Waste Manag. Assoc.*, 2009, **59**, 898–911.
- 356 X. Zhang and P. H. McMurry, *Environ. Sci. Technol.*, 2002, **25**, 456–459.
- 357 X. Y. Yu, T. Lee, B. Ayres, S. M. Kreidenweis, W. Malm and J. L. Collett, *Atmos. Environ.*, 2006, **40**, 4797–4807.
- 358 Ravi Kant Pathak, Xiaohong Yao and Chak K. Chan, *Environ. Sci. Technol.*, 2003, **38**, 254–259.
- 359 W. C. Malm, B. A. Schichtel and M. L. Pitchford, *J. Air Waste Manage. Assoc.*, 2011, **61**, 1131–1149.
- 360 L. L. Ashbaugh and R. A. Eldred, *J. Air Waste Manage. Assoc.*, 2004, **54**, 93–104.
- 361 Y. H. Cheng and C. J. Tsai, *J. Aerosol Sci.*, 1997, **28**, 1553–1567.
- 362 S. Witz, R. W. Eden, M. W. Wadley, C. Dunwoody, R. P. Papa & Kahirup and J. J. Torre, *Waste Manag. Assoc.*, 1990, **40**, 53–61.
- 363 C. J. Tsai and S. N. Perng, *Atmos. Environ.*, 1998, **32**, 1605–1613.
- 364 W. Xu, Y. Sun, Q. Wang, J. Zhao, J. Wang, X. Ge, C. Xie, W. Zhou, W. Du, J. Li, P. Fu, Z. Wang, D. R. Worsnop and H. Coe, *J. Geophys. Res. Atmos.*, 2019, **124**, 1132–1147.

- 365 W. Xu, C. Xie, E. Karnezi, Q. Zhang, J. Wang, S. N. Pandis, X. Ge, J. Zhang, J. An, Q. Wang, J. Zhao, W. Du, Y. Qiu, W. Zhou, Y. He, Y. Li, J. Li, P. Fu, Z. Wang, D. R. Worsnop and Y. Sun, *Atmos. Chem. Phys.*, 2019, **19**, 10205–10216.
- 366 V. N. Ipatieff, B. B. Corson and H. Pines, *J. Am. Chem. Soc.*, 1936, **58**, 919–922.
- 367 C. H. Suresh, K. Nobuaki and S. R. Gadre, *J. Org. Chem.*, 2001, **66**, 6883–6890.
- 368 K. Soni, S. Singh, T. Bano, R. S. Tanwar, S. Nath and B. C. Arya, *Atmos. Environ.*, 2010, **44**, 4355–4363.
- 369 Centre for Environmental Data Analysis, <https://www.ceda.ac.uk/>, (accessed Feb 2021).
- 370 S. J. Swift, I. Andrews and J. F. Hamilton, 2020, <https://catalogue.ceda.ac.uk/uuid/f29fdcae79374754>.
- 371 S. J. Swift and J. F. Hmailton, 2019, <https://catalogue.ceda.ac.uk/uuid/df8261bae435459f>.
- 372 A. Elzein, G. J. Stewart, S. J. Swift, B. S. Nelson, L. R. Crilley, M. S. Alam, E. Reyes-Villegas, R. Gadi, R. M. Harrison, J. F. Hamilton and A. C. Lewis, *Atmos. Chem. Phys.*, 2020, **20**, 14303–14319.
- 373 Y. Sun, L. Lei, W. Zhou, C. Chen, Y. He, J. Sun, Z. Li, W. Xu, Q. Wang, D. Ji, P. Fu, Z. Wang and D. R. Worsnop, *Sci. Total. Environ.*, 2020, **742**, 140739.
- 374 Saraswati, S. K. Sharma, M. Saxena and T. K. Mandal, *Atmos. Res.*, 2019, **218**, 34–49.
- 375 S. Chandra, M. J. Kulshrestha, B. Kumar and R. K. Kotnala, *J. Earth Syst. Sci.*, 2019, **128**, 1–17.
- 376 D. S. Bisht, U. C. Dumka, D. G. Kaskaoutis, A. S. Pipal, A. K. Srivastava, V. K. Soni, S. D. Attri, M. Sateesh and S. Tiwari, *Sci. Total. Environ.*, 2015, **521–522**, 431–445.
- 377 S. K. Sharma and T. K. Mandal, *Urban Clim.*, 2017, **21**, 106–122.
- 378 S. K. Sharma, T. K. Mandal, S. Jain, Saraswati, A. Sharma and M. Saxena, *B. Environ. Contam. Tox.*, 2016, **97**, 286–293.
- 379 K. Ali, P. Acharja, D. K. Trivedi, R. Kulkarni, P. Pithani, P. D. Safai, D. M. Chate, S. Ghude, R. K. Jenamani and M. Rajeevan, *Sci. Total. Environ.*, 2019, **662**, 687–696.
- 380 P. Acharja, K. Ali, D. K. Trivedi, P. D. Safai, S. Ghude, T. Prabhakaran and M. Rajeevan, *Sci. Total. Environ.*, 2020, **729**, 138800.
- 381 S. Jain, S. K. Sharma, N. Vijayan and T. K. Mandal, *Environ. Pollut.*, 2020, **262**, 114337.
- 382 H. Wang, M. Tian, X. Li, Q. Chang, J. Cao, F. Yang, Y. Ma and K. He, *Aerosol. Air. Qual. Res.*, 2015, **15**, 2200–2211.
- 383 R. K. Pathak, T. Wang, K. F. Ho and S. C. Lee, *Atmos. Environ.*, 2011, **45**, 318–325.
- 384 X. Dao, Z. Wang, Y. Lv, E. Teng, L. Zhang and C. Wang, *PLoS ONE.*, 2014, **9**, e113831. doi:10.1371/journal.pone.0113831.
- 385 X. Yao, C. K. Chan, M. Fang, S. Cadle, T. Chan, P. Mulawa, K. He and B. Ye, *Atmos. Environ.*, 2002, **36**, 4223–4234.
- 386 Y. Liu, T. Zhang, Q. Liu, R. Zhang, Z. Sun and M. Zhang, *Aerosol. Air. Qual. Res.*, 2014, **14**, 954–969.
- 387 H. Yang, J. Chen, J. Wen, H. Tian and X. Liu, *Atmos. Environ.*, 2016, **124**, Part, 378–386.
- 388 X. Li, L. Jiang, Y. Bai, Y. Yang, S. Liu, X. Chen, J. Xu, Y. Liu, Y. Wang, X. Guo, Y. Wang and G. Wang, *Atmos. Res.*, 2019, **218**, 25–33.
- 389 F. K. Duan, K. B. He, Y. L. Ma, F. M. Yang, X. C. Yu, S. H. Cadle, T. Chan and P. A. Mulawa, *Sci. Total. Environ.*, 2006, **355**, 264–275.

- 390 Y. Song, X. Tang, S. Xie, Y. Zhang, Y. Wei, M. Zhang, L. Zeng and S. Lu, *J. Hazard. Mater.*, 2007, **146**, 124–130.
- 391 Y. Zhang, J. Lang, S. Cheng, S. Li, Y. Zhou, D. Chen, H. Zhang and H. Wang, *Sci. Total Environ.*, 2018, **630**, 72–82.
- 392 X. Han, Q. Guo, C. Liu, H. Strauss, J. Yang, J. Hu, R. Wei, L. Tian, J. Kong and M. Peters, *Environ. Pollut.*, 2016, **218**, 230–241.
- 393 K. He, F. Yang, Y. Ma, Q. Zhang, X. Yao, C. K. Chan, S. Cadle, T. Chan and P. Mulawa, *Atmos. Environ.*, 2001, **35**, 4959–4970.
- 394 P. Shao, H. Tian, Y. Sun, H. Liu, B. Wu, S. Liu, X. Liu, Y. Wu, W. Liang, Y. Wang, J. Gao, Y. Xue, X. Bai, W. Liu, S. Lin and G. Hu, *Atmos. Environ.*, 2018, **189**, 133–144.
- 395 B. Han, R. Zhang, W. Yang, Z. Bai, Z. Ma and W. Zhang, *Sci. Total Environ.*, 2016, **544**, 319–329.
- 396 Y. Sun, G. Zhuang, Y. Wang, L. Han, J. Guo, M. Dan, W. Zhang, Z. Wang and Z. Hao, *Atmos. Environ.*, 2004, **38**, 5991–6004.
- 397 J. Gao, X. Peng, G. Chen, J. Xu, G.-L. Shi, Y.-C. Zhang and Y.-C. Feng, *Sci. Total Environ.*, 2016, **542, Part**, 162–171.
- 398 X. Li, Y. Wang, X. Guo and Y. Wang, *J. Environ. Sci. (China)*, 2013, **25**, 741–750.
- 399 W. S. Wu and T. Wang, *Atmos. Environ.*, 2007, **41**, 5442–5451.
- 400 T. Okuda, S. Matsuura, D. Yamaguchi, T. Umemura, E. Hanada, H. Orihara, S. Tanaka, K. He, Y. Ma, Y. Cheng and L. Liang, *Atmos. Environ.*, 2011, **45**, 2789–2794.
- 401 Google Maps (Delhi), <https://www.google.com/maps/@28.6471948,76.9531794,11z>, (accessed Jan 2021).
- 402 Free Map Tools, <https://www.freemaptools.com/about.htm>, (accessed Aug 2021).
- 403 Google Maps (Beijing), <https://www.google.com/maps/place/Beijing,+China/@39.9375346,115.837023,9z/data=!3m1!4b1!4m5!3m4!1s0x35f05296e7142cb9:0xb9625620af0fa98a!8m2!3d39.9041999!4d116.4073963>, (accessed Jan 2021).
- 404 To meet air quality standards, Delhi needs a 65 per cent cut in pollution levels - says new CSE analysis, <https://www.cseindia.org/to-meet-air-quality-standards-delhi-needs-a-65-per-cent-cut-in-pollution-levels-says-new-cse-analysis-9666>, (accessed Mar 2021).
- 405 New Delhi US Embassy, India Air Pollution: Real-time Air Quality Index, <https://aqicn.org/city/india/new-delhi/us-embassy/>, (accessed Mar 2021).
- 406 H. Zhang, S. Wang, J. Hao, X. Wang, S. Wang, F. Chai and M. Li, *J. Clean. Prod.*, 2016, **112**, 1519–1527.
- 407 S. K. Sharma, · Saraswati, · T K Mandal and M. Saxena, *Bull. Environ. Contam. Toxicol.*, 2058, **99**, 281–285.
- 408 J. Suneja, G. Kotnala, A. Kaur, T. K. Mandal and S. K. Sharma, *Mapan - J. Metrol. Soc. India*, 2020, **35**, 125–133.
- 409 New Delhi, Delhi, India Weather Averages | Monthly Average High and Low Temperature | Average Precipitation and Rainfall days | World Weather Online, <https://www.worldweatheronline.com/new-delhi-weather-averages/delhi/in.aspx>, (accessed Mar 2021).
- 410 Department of Animal Husbandry & Dairying releases 20th Livestock Census; Total Livestock population increases 4.6% over Census-2012, Increases to 535.78 million, <https://pib.gov.in/PressReleasePage.aspx?PRID=1588304>, (accessed Mar 2021).

- 411 K. Vohra, E. A. Marais, S. Suckra, L. Kramer, W. J. Bloss, R. Sahu, A. Gaur, S. N. Tripathi, M. Van Damme, L. Clarisse and P. F. Coheur, *Atmos. Chem. Phys.*, 2021, **21**, 6275–6296.
- 412 EDGARv5.0 air pollutants, https://edgar.jrc.ec.europa.eu/overview.php?v=50_AP, (accessed Aug 2021).
- 413 M. Crippa, D. Guizzardi, M. Muntean, E. Schaaf, F. Dentener, J. A. Van Aardenne, S. Monni, U. Doering, J. G. J. Olivier, V. Pagliari and G. Janssens-Maenhout, *Earth Syst. Sci. Data*, 2018, **10**, 1987–2013.
- 414 L. Luo, Y.-Y. Zhang, H.-Y. Xiao, H.-W. Xiao, N.-J. Zheng, Z.-Y. Zhang, Y.-J. Xie and C. Liu, *Atmosphere.*, 2019, **10**, 505; <https://doi.org/10.3390/atmos10090505>.
- 415 K. R. Kolesar, C. N. Mattson, P. K. Peterson, N. W. May, R. K. Prendergast and K. A. Pratt, *Atmos. Environ.*, 2018, **177**, 195–202.
- 416 K. Li, D. J. Jacob, H. Liao, L. Shen, Q. Zhang and K. H. Bates, *Proc. Natl. Acad. Sci. U. S. A.*, 2019, **116**, 422–427.
- 417 Y. Li, M. Cheng, Z. Guo, Y. He, X. Zhang, X. Cui and S. Chen, *Aerosol Air Qual. Res.*, 2020, **20**, 2170–2184.
- 418 W. Dui, B. Xueyan, D. Xuejiao, L. Fei, T. Haobo, L. Guolian and H. Jian, *J. Meteorol. Res-PRC.*, 2007, **21**, 215–223.
- 419 W. Xu, Q. Wu, X. Liu, A. Tang, A. J. Dore and M. R. Heal, *Environ. Sci. Pollut. Res.*, 2016, **23**, 1158–1172.
- 420 S. N. Behera and M. Sharma, *Atmos. Environ.*, 2011, **45**, 4015–4024.
- 421 H. Du, L. Kong, T. Cheng, J. Chen, X. Yang, R. Zhang, Z. Han, Z. Yan and Y. Ma, *Aerosol. Air. Qual. Res.*, 2010, **10**, 589–595.
- 422 K. Matsumoto and H. Tanaka, *Atmos. Environ.*, 1996, **30**, 639–648.
- 423 I. J. Ackermann, H. Hass, M. Memmesheimer, C. Ziegenbein and A. Ebel, *Meteorol. Atmos. Phys.*, 1995, **57**, 101–114.
- 424 A. Gupta, R. Kumar, K. M. Kumari and S. S. Srivastava, *Atmos. Environ.*, 2003, **37**, 4837–4846.
- 425 C. L. Blanchard, P. M. Roth, S. J. Tanenbaum, S. D. Ziman and J. H. Seinfeld, *J. Air. Waste. Manag.*, 2000, **50**, 2073–2084.
- 426 L. Xiaoxiu, Z. Xiaoshan, M. Yujing, N. Anpu and J. Guibin, *Atmos. Environ.*, 2003, **37**, 2581–2588.
- 427 I. Mori, M. Nishikawa and Y. Iwasaka, *Sci. Total. Environ.*, 1998, **224**, 87–91.
- 428 O. Boucher and U. Lohmann, *Tellus B Chem Phys Meteorol.*, 1995, **47**, 281–300.
- 429 Y.-C. Lin, M.-T. Cheng, W.-Y. Ting and C.-R. Yeh, *Atmos. Environ.*, 2006, **40**, 4725–4733.
- 430 S. Kadowaki, *Environ. Sci. Technol.*, 1986, **20**, 1249–1253.
- 431 N. J. Farren, R. E. Dunmore, M. I. Mead, M. S. M. Nadzir, A. A. Samah, S.-M. Phang, B. J. Bandy, W. T. Sturges and J. F. Hamilton, *Atmos. Chem. Phys.*, 2019, **19**, 1537–1553.
- 432 V. Singh, S. Singh and A. Biswal, *Sci. Total. Environ.*, 2021, **750**, 141461.
- 433 A. F. Stein, R. R. Draxler, G. D. Rolph, B. J. B. Stunder, M. D. Cohen and F. Ngan, *Bull. Am. Meteorol. Soc.*, 2015, **96**, 2059–2077.
- 434 G. Rolph, A. Stein and B. Stunder, *Environ. Model. Softw.*, 2017, **95**, 210–228.
- 435 HYSPLIT AIR RESOURCES LAB (NOAA), https://www.ready.noaa.gov/HYSPLIT_traj.php, (accessed Mar 2021).

- 436 H. Wang and C. Wang, *Waste Manag. Res.*, 2013, **31**, 67–72.
- 437 K. E. R. R. Dawe, T. C. Furlani, S. F. Kowal, T. F. Kahan, T. C. VandenBoer and C. J. Young, *Indoor Air.*, 2019, **29**, 70–78.
- 438 H. Wang, X. Wang, X. Yang, W. Li, L. Xue, T. Wang, J. Chen and W. Wang, *Aerosol Air Qual. Res.*, 2017, **17**, 878–887.
- 439 F. Drewnick, S. S. Hings, J. Curtius, G. Eerdekens and J. Williams, *Atmos. Environ.*, 2006, **40**, 4316–4327.
- 440 A. L. H. Müller, C. C. Müller, F. G. Antes, J. S. Barin, V. L. Dressler, E. M. M. Flores and E. I. Müller, *Anal. Lett.*, 2012, **45**, 1004–1015.
- 441 N. Gysel, W. A. Welch, C.-L. Chen, P. Dixit, D. R. Cocker III and G. Karavalakis, *J. Environ. Sci. (China)*, 2018, **65**, 162–170.
- 442 A. Ooki and M. Uematsu, *J. Geophys. Res. Atmos.*, 2005, **110**, D03201, doi:10.1029/2004JD004737.
- 443 Y. Tobo, D. Zhang, N. Nakata, M. Yamada, H. Ogata, K. Hara and Y. Iwasaka, *Geophys. Res. Lett.*, 2009, **36**, L05817, doi:10.1029/2008GL036883.
- 444 H.-H. Yang, K.-T. Lee, Y.-S. Hsieh, S.-W. Luo and R.-J. Huang, *Aerosol Air Qual. Res.*, 2015, **15**, 1672–1680.
- 445 R. Arimoto, R. A. Duce, D. L. Savoie, J. M. Propsero, R. Talbot, J. D. Cullen, U. Tomza, N. F. Lewis and B. J. Ray, *J. Geophys. Res.*, 1996, **101**, 2011–2023.
- 446 X. Huang, Z. Liu, J. Zhang, T. Wen, D. Ji and Y. Wang, *Atmos. Res.*, 2016, **168**, 70–79.
- 447 Sulfur Dioxide Basics | Sulfur Dioxide (SO₂) Pollution | US EPA, <https://www.epa.gov/so2-pollution/sulfur-dioxide-basics>, (accessed Mar 21).
- 448 L. Tang, X. Xue, J. Qu, Z. Mi, X. Bo, X. Chang, S. Wang, S. Li, W. Cui and G. Dong, *Sci. Data*, 2020, **7**.
- 449 N. D. Ganguly, *Surface ozone pollution during the festival of Diwali, New Delhi, India*, 2009, vol. 2.
- 450 T. Liu, M. E. Marlier, A. Karambelas, M. Jain, S. Singh, M. K. Singh, R. Gautam and R. S. Defries, 2019.
- 451 H. Sembhi, M. Wooster, T. Zhang, S. Sharma, N. Singh, S. Agarwal, H. Boesch, S. Gupta, A. Misra, S. N. Tripathi, S. Mor and R. Khaiwal, *Environ. Res. Lett.*, 2020, **15**, 104067.
- 452 S. Liu, Z. Zhang, Y. Wang, Y. Hu, W. Liu, C. Chen, Y. Mei and H. Sun, *Atmos. Pollut. Res.*, 2019, **10**, 954–959.
- 453 Z. Y. Zhao, F. Cao, M. Y. Fan, W. Q. Zhang, X. Y. Zhai, Q. Wang and Y. L. Zhang, *Atmos. Environ.*, 2020, **242**, 117762.
- 454 T. Han, X. Liu, Y. Zhang, Y. Qu, L. Zeng, M. Hu and T. Zhu, *J. Environ. Sci. (China)*, 2015, **31**, 51–60.
- 455 P. S. Zhao, F. Dong, D. He, X. J. Zhao, X. L. Zhang, W. Z. Zhang, Q. Yao and H. Y. Liu, *Atmos. Chem. Phys.*, 2013, **13**, 4631–4644.
- 456 D. Liu, M. Flynn, M. Gysel, A. Targino, I. Crawford, K. Bower, T. Choularton, Z. Jurányi, M. Steinbacher, C. H. Ugglin, J. Curtius, M. Kampus, A. Petzold, E. Weingartner, U. Baltensperger and H. Coe, *Atmos. Chem. Phys.*, 2010, **10**, 7389–7407.
- 457 J. Duan, R.-J. Huang, Y. Li, Q. Chen, Y. Zheng, Y. Chen, C. Lin, H. Ni, M. Wang, J. Ovadnevaite, D. Ceburnis, C. Chen, D. R. Worsnop, T. Hoffmann, C. O'Dowd and J. Cao, *Atmos. Chem. Phys.*, 2020, **20**, 3793–3807.

- 458 J. Pal, M. C. Goswami, M. Singh and K. K. Singh, *Ironmak. Steelmak.*, 2003, **30**, 441–446.
- 459 M. Chabukdhara and O. P. Singh, *Int. J. Coal Sci. Technol.*, 2016, **3**, 87–96.
- 460 J. Yang, L. Li, S. Wang, H. Li, J. S. Francisco, X. Cheng Zeng and Y. Gao, *J. Am. Chem. Soc.*, 2019, **141**, 19312–19320.
- 461 D. Au Yang, G. Bardoux, N. Assayag, C. Laskar, D. Widory and P. Cartigny, *Atmos. Environ.*, 2018, **193**, 109–117.
- 462 Y. Cheng, G. Zheng, C. Wei, Q. Mu, B. Zheng, Z. Wang, M. Gao, Q. Zhang, K. He, G. Carmichael, U. Pöschl and H. Su, *Sci. Adv.*, 2016, **2**, e1601530.
- 463 P. He, Z. Xie, X. Chi, X. Yu, S. Fan, H. Kang, C. Liu and H. Zhan, *Atmos. Chem. Phys.*, 2018, **18**, 14465–14476.
- 464 X. J. Zhao, P. S. Zhao, J. Xu, W. Meng, W. W. Pu, F. Dong, D. He and Q. F. Shi, *Atmos. Chem. Phys.*, 2013, **13**, 5685–5696.
- 465 Z. Meng, W. Lin, R. Zhang, Z. Han and X. Jia, *Sci. Total Environ.*, 2017, **579**, 1521–1530.
- 466 J. H. Seinfeld and S. N. Pandis, *Atmospheric Chemistry and Physics: From Air Pollution to Climate Change*, John Wiley & Sons, Inc, Hoboken, New Jersey, 2nd ed., 1998.
- 467 O. V. Rattigan, J. Reilly, C. D. Judd, K. F. Moore, M. Das, D. E. Sherman, V. A. Dutkiewicz, J. L. Collett Jr. and L. Husain, *J. Geophys. Res. Atmos.*, 2001, **106**, 17347–17358.
- 468 S. Mikkonen, M. R. A. Pitkänen, T. Nieminen, A. Lipponen, S. Isokääntä, A. Arola and K. E. J. Lehtinen, *Atmos. Chem. Phys.*, 2019, **19**, 12531–12543.
- 469 Z. Meng, X. Xu, W. Lin, B. Ge, Y. Xie, B. Song, S. Jia, R. Zhang, W. Peng, Y. Wang, H. Cheng, W. Yang and H. Zhao, *Atmos. Chem. Phys.*, 2018, **18**, 167–184.
- 470 R. Vecchi, G. Valli, P. Fermo, A. D’Alessandro, A. Piazzalunga and V. Bernardoni, *Atmos. Environ.*, 2009, **43**, 1713–1720.
- 471 E. Friese and A. Ebel, *J. Phys. Chem. A*, 2010, **114**, 11595–11631.
- 472 N. Riemer, H. Vogel, B. Vogel, B. Schell, I. Ackermann, C. Kessler and H. Hass, *J. Geophys. Res. Atmos.*, 2003, **108**, 4144.
- 473 P. Gupta, M. Satsangi, G. P. Satsangi, A. Jangid, Y. Liu, S. K. Pani and R. Kumar, *Env. Geochem Heal.*, 2020, **42**, 2081–2099.
- 474 S. T. Martin, *Chem. Rev.*, 2000, **100**, 3403–3453.
- 475 G. Sharma, B. Sinha, Pallavi, H. Hakkim, B. P. Chandra, A. Kumar and V. Sinha, *Environ. Sci. Technol.*, 2019, **53**, 4765–4774.
- 476 G. Beig, *Nat. Geosci.*, 2021, **14**, 59–60.
- 477 M. O. Andreae, *Atmos. Chem. Phys.*, 2019, **19**, 8523–8546.
- 478 P. O. Wennberg, K. H. Bates, J. D. Crouse, L. G. Dodson, R. C. Mcvay, L. A. Mertens, T. B. Nguyen, E. Praske, R. H. Schwantes, M. D. Smarte, J. M. St Clair, A. P. Teng, X. Zhang and J. H. Seinfeld, *Chem. Rev.*, 2018, **118**, 3337–3390.
- 479 F. Xiong, K. M. Mcavey, K. A. Pratt, C. J. Groff, M. A. Hostetler, M. A. Lipton, T. K. Starn, J. V. Seeley, S. B. Bertman, A. P. Teng, J. D. Crouse, T. B. Nguyen, P. O. Wennberg, P. K. Misztal, A. H. Goldstein, A. B. Guenther, A. R. Koss, K. F. Olson, J. A. De Gouw, K. Baumann, E. S. Edgerton, P. A. Feiner, L. Zhang, D. O. Miller, W. H. Brune and P. B. Shepson, *Atmos. Chem. Phys.*, 2015, **15**, 11257–11272.
- 480 A. Guenther, T. Karl, P. Harley, C. Wiedinmyer, P. I. Palmer and C. Geron, *Atmos. Chem. Phys.*, 2006, **6**, 3181–3210.

- 481 P. Dewald, J. M. Liebmann, N. Friedrich, J. Shenolikar, J. Schuladen, F. Rohrer, D. Reimer, R. Tillmann, A. Novelli, C. Cho, K. Xu, R. Holzinger, F. Bernard, L. Zhou, W. Mellouki, S. S. Brown, H. Fuchs, J. Lelieveld and J. N. Crowley, *Atmos. Chem. Phys.*, 2020, **20**, 10459–10475.
- 482 R. A. Rasmussen and M. A. K. Khalil, *J. Geophys. Res.*, 1988, **93**, 1417–1421.
- 483 T. Berndt and O. Böge, *Int. J. Chem. Kinet.*, 1997, **29**, 755–765.
- 484 I. Suh, W. Lei and R. Zhang, *J. Phys. Chem. A.*, 2001, **105**, 6471–6478.
- 485 N. L. Ng, A. J. Kwan, J. D. Surratt, A. W. H. Chan, P. S. Chhabra, A. Sorooshian, H. O. T. Pye, J. D. Crouse, P. O. Wennberg, R. C. Flagan and J. H. Seinfeld, *Atmos. Chem. Phys.*, 2008, **8**, 4117–4140.
- 486 A. L. Lockwood, P. B. Shepson, M. N. Fiddler and M. Alaghmand, *Atmos. Chem. Phys.*, 2010, **10**, 6169–6178.
- 487 A. G. Carlton, C. Wiedinmyer and J. H. Kroll, *Atmos. Chem. Phys.*, 2009, **9**, 4987–5005.
- 488 A. E. Perring, A. Wisthaler, M. Graus, P. J. Wooldridge, A. L. Lockwood, L. H. Mielke, P. B. Shepson, A. Hansel and R. C. Cohen, *Atmos. Chem. Phys.*, 2009, **9**, 4945–4956.
- 489 N. L. Ng, J. H. Kroll, M. D. Keywood, R. Bahreini, V. Varutbangkul, R. C. Flagan, J. H. Seinfeld, A. Lee and A. H. Goldstein, *Environ. Sci. Technol.*, 2006, **40**, 2283–2297.
- 490 J. L. Fry, S. S. Brown, A. M. Middlebrook, P. M. Edwards, P. Campuzano-Jost, D. A. Day, J. L. Jimenez, H. M. Allen, T. B. Ryerson, I. Pollack, M. Graus, C. Warneke, J. A. De Gouw, C. A. Brock, J. Gilman, B. M. Lerner, W. P. Dubé, J. Liao and A. Welti, *Atmos. Chem. Phys.*, 2018, **18**, 11663–11682.
- 491 A. W. Rollins, A. Kiendler-Scharr, J. L. Fry, T. Brauers, S. S. Brown, H.-P. Dorn, W. P. Dubé, H. Fuchs, A. Mensah, T. F. Mentel, F. Rohrer, R. Tillmann, R. Wegener, P. J. Wooldridge and R. C. Cohen, *Atmos. Chem. Phys.*, 2009, **9**, 6685–6703.
- 492 N. L. Ng, S. S. Brown, A. T. Archibald, E. Atlas, R. C. Cohen, J. N. Crowley, D. A. Day, N. M. Donahue, J. L. Fry, H. Fuchs, R. J. Griffin, M. I. Guzman, H. Herrmann, A. Hodzic, Y. Iinuma, J. L. Jimenez, A. Kiendler-Scharr, B. H. Lee, D. J. Luecken, J. Mao, R. McLaren, A. Mutzel, H. D. Osthoff, B. Picquet-Varrault, U. Platt, H. O. T. Pye, Y. Rudich, R. H. Schwantes, M. Shiraiwa, J. Stutz, J. A. Thornton, A. Tilgner, B. J. Williams and R. A. Zaveri, *Atmos. Chem. Phys.*, 2017, **17**, 2103–2162.
- 493 J. Liebmann, N. Sobanski, J. Schuladen, E. Karu, H. Hellén, H. Hakola, Q. Zha, M. Ehn, M. Riva, L. Heikkinen, J. Williams, H. Fischer, J. Lelieveld and J. N. Crowley, *Atmos. Chem. Phys.*, 2019, **19**, 10391–10403.
- 494 T. Benter and R. N. Schindler, *Chem. Phys. Lett.*, 1988, **145**, 67–70.
- 495 E. J. Dlugokencky and C. J. Howard, *J. Phys. Chem.*, 1989, **93**, 1091–1096.
- 496 I. Barnes, V. Bastian, K. H. Becker and Z. Tong, *J. Phys. Chem.*, 1990, **94**, 2413–2419.
- 497 R. H. Schwantes, A. P. Teng, T. B. Nguyen, M. M. Coggon, J. D. Crouse, J. M. St. Clair, X. Zhang, K. A. Schilling, J. H. Seinfeld and P. O. Wennberg, *J. Phys. Chem. A.*, 2015, **119**, 10158–10171.
- 498 F. Xiong, C. H. Borca, L. V. Slipchenko and P. B. Shepson, *Atmos. Chem. Phys.*, 2016, **16**, 5595–5610.
- 499 S. S. Brown, J. A. Degouw, C. Warneke, T. B. Ryerson, W. P. Dubé, E. Atlas, R. J. Weber, R. E. Peltier, J. A. Neuman, J. M. Roberts, A. Swanson, F. Flocke, S. A. McKeen, J. Brioude, R. Sommariva, M. Trainer, F. C. Fehsenfeld and A. R. Ravishankara, *Atmos. Chem. Phys.*, 2009, **9**, 3027–3042.
- 500 J. F. Hamilton, D. J. Bryant, P. M. Edwards, B. Ouyang, T. J. Bannan, A. Mehra, A. W.

- Mayhew, J. R. Hopkins, R. E. Dunmore, F. A. Squires, J. D. Lee, M. J. Newland, S. D. Worrall, A. Bacak, H. Coe, C. Percival, L. K. Whalley, D. E. Heard, E. J. Slater, R. L. Jones, T. Cui, J. D. Surratt, C. E. Reeves, G. P. Mills, S. Grimmond, Y. Sun, W. Xu, Z. Shi and A. R. Rickard, *Cite This Environ. Sci. Technol.*, 2021, **55**, 853.
- 501 P. M. Edwards, K. C. Aikin, W. P. Dube, J. L. Fry, J. B. Gilman, J. A. de Gouw, M. G. Graus, T. F. Hanisco, J. Holloway, G. Hübler, J. Kaiser, F. N. Keutsch, B. M. Lerner, J. A. Neuman, D. D. Parrish, J. Peischl, I. B. Pollack, A. R. Ravishankara, J. M. Roberts, T. B. Ryerson, M. Trainer, P. R. Veres, G. M. Wolfe, C. Warneke and S. S. Brown, *Nat. Geosci.*, 2017, **10**, 490–495.
- 502 J. D. Rindelaub, K. M. McAvey and P. B. Shepson, *Atmos. Environ.*, 2015, **100**, 193–201.
- 503 K. S. Hu, A. I. Darer and M. J. Elrod, *Atmos. Chem. Phys.*, 2011, **11**, 8307–8320.
- 504 A. W. Rollins, J. D. Smith, K. R. Wilson and R. C. Cohen, *Environ. Sci. Technol.*, 2010, **44**, 5540–5545.
- 505 J. Sun, J. S. Fu and K. Huang, *Proc. Natl. Acad. Sci.*, 2016, **113**, E4433–E4434.
- 506 B. R. Ayres, H. M. Allen, D. C. Draper, S. S. Brown, R. J. Wild, J. L. Jimenez, D. A. Day, P. Campuzano-Jost, W. Hu, J. De Gouw, A. Koss, R. C. Cohen, K. C. Duffey, P. Romer, K. Baumann, E. Edgerton, S. Takahama, J. A. Thornton, B. H. Lee, F. D. Lopez-Hilfiker, C. Mohr, P. O. Wennberg, T. B. Nguyen, A. Teng, A. H. Goldstein, K. Olson and J. L. Fry, *Atmos. Chem. Phys.*, 2015, **15**, 13377–13392.
- 507 A. Zare, P. S. Romer, T. Nguyen, F. N. Keutsch, K. Skog and R. C. Cohen, *Atmos. Chem. Phys.*, 2018, **18**, 15419–15436.
- 508 J. A. Fisher, D. J. Jacob, K. R. Travis, P. S. Kim, E. A. Marais, C. Chan Miller, K. Yu, L. Zhu, R. M. Yantosca, M. P. Sulprizio, J. Mao, P. O. Wennberg, J. D. Crouse, A. P. Teng, T. B. Nguyen, J. M. St Clair, R. C. Cohen, P. Romer, B. A. Nault, P. J. Wooldridge, J. L. Jimenez, P. Campuzano-Jost, D. A. Day, W. Hu, P. B. Shepson, F. Xiong, D. R. Blake, A. H. Goldstein, P. K. Misztal, T. F. Hanisco, G. M. Wolfe, T. B. Ryerson, A. Wisthaler and T. Mikoviny, *Atmos Chem Phys*, 2016, **16**, 5969–5991.
- 509 W. Xu, M. Takeuchi, C. Chen, Y. Qiu, C. Xie, W. Xu, N. Ma, D. R. Worsnop, N. L. Ng and Y. Sun, *Atmos. Meas. Tech.*, 2021, **14**, 3693–3705.
- 510 E. A. Marais, D. J. Jacob, S. Choi, J. Joiner, M. Belmonte-Rivas, R. C. Cohen, S. Beirle, L. T. Murray, L. D. Schiferl and L. Jaeglé, *Atmos. Chem. Phys.*, 2018, **18**, 17017–17027.
- 511 L. Jaeglé, D. J. Jacob, W. H. Brune, I. C. Faloona, D. Tan, Y. Kondo, G. W. Sachse, B. Anderson, G. L. Gregory, S. Vay, H. B. Singh, D. R. Blake and R. Shetter, *Geophys. Res. Lett.*, 1999, **26**, 3081–3084.
- 512 P. Dewald, J. Shenolikar, N. Friedrich, F. Rohrer, R. Tillmann, D. Reimer, K. Xu, R. Holzinger, F. Bernard, L. Zhou, S. Brown, H. Fuchs, J. Crowley, P. Dewald, J. Shenolikar, N. Friedrich, F. Rohrer, R. Tillmann, D. Reimer, K. Xu, R. Holzinger, F. Bernard, L. Zhou, S. Brown, H. Fuchs and J. Crowley, in *22nd EGU General Assembly, held online 4-8 May, 2020, id.4597*, 2020, p. 4597.
- 513 B. Brownwood, A. Turdziladze, T. Hohaus, R. Wu, T. F. Mentel, P. T. M. Carlsson, E. Tsiligiannis, M. Hallquist, S. Andres, L. Hantschke, D. Reimer, F. Rohrer, R. Tillmann, B. Winter, J. Liebmann, S. S. Brown, A. Kiendler-Scharr, A. Novelli, H. Fuchs and J. L. Fry, *ACS Earth Sp. Chem.*, 2021, **X**, acsearthspacechem.0c00311.
- 514 2018 NO3-Isop SAPHIR Chamber ,
<https://www.colorado.edu/lab/browngroup/2019/01/25/2018-no3-isop-saphir-chamber>,
 (accessed Mar 2021).
- 515 R. Wegener, T. Brauers, R. Koppmann, S. Rodríguez Bares, F. Rohrer, R. Tillmann, A. Wahner, A. Hansel and A. Wisthaler, *J. Geophys. Res-Atmos.*, 2007, **112**,

- 516 F. Rohrer, B. Bohn, T. Brauers, D. Brüning, F.-J. Johnen, A. Wahner and J. Kleffmann, *Atmos. Chem. Phys.*, 2005, **5**, 2189–2201.
- 517 H. Fuchs, S. M. Ball, B. Bohn, T. Brauers, R. C. Cohen, H.-P. Dorn, W. P. Dubé, J. L. Fry, R. Häsel, U. Heitmann, R. L. Jones, J. Kleffmann, T. F. Mentel, P. M. Usger, F. Rohrer, A. W. Rollins, A. A. Ruth, A. Kiendler-Scharr, E. Schlosser, A. J. L. Shillings, R. Tillmann, R. M. Varma, D. S. Venables, G. Villena Tapia, A. Wahner, R. Wegener, P. J. Wooldridge and S. S. Brown, *Atmos. Meas. Tech.*, 2010, **3**, 21–37.
- 518 T. Hohaus, U. Kuhn, S. Andres, M. Kaminski, F. Rohrer, R. Tillmann, A. Wahner, R. Wegener, Z. Yu and A. Kiendler-Scharr, *Atmos. Meas. Tech.*, 2016, **9**, 1247–1259.
- 519 S. P. Bew, G. D. Hiatt-Gipson, G. P. Mills and C. E. Reeves, *Beilstein J. Org. Chem.*, 2016, **12**, 1081–1095.
- 520 J. A. Fisher, D. J. Jacob, K. R. Travis, P. S. Kim, E. A. Marais, C. Chan Miller, K. Yu, L. Zhu, R. M. Yantosca, M. P. Sulprizio, J. Mao, P. O. Wennberg, J. D. Crouse, A. P. Teng, T. B. Nguyen, J. M. St Clair, R. C. Cohen, P. Romer, B. A. Nault, P. J. Wooldridge, J. L. Jimenez, P. Campuzano-Jost, D. A. Day, W. Hu, P. B. Shepson, F. Xiong, D. R. Blake, A. H. Goldstein, P. K. Misztal, T. F. Hanisco, G. M. Wolfe, T. B. Ryerson, A. Wisthaler and T. Mikoviny, *Atmos. Chem. Phys.*, 2016, **16**, 5969–5991.
- 521 C. M. Boyd, J. Sanchez, L. Xu, A. J. Eugene, T. Nah, W. Y. Tuet, M. I. Guzman and N. L. Ng, *Atmos. Chem. Phys.*, 2015, **15**, 7497–7522.
- 522 R. Boschan, R. T. Merrow and R. W. van Dolah, *Chem. Rev.*, 1955, **55**, 485–510.
- 523 J. W. Baker and D. M. Easty, *J. Chem. Soc.*, 1952, **I**, 1193–1207.
- 524 J. D. Rindelaub, C. H. Borca, M. A. Hostetler, J. H. Slade, M. A. Lipton, L. V. Slipchenko and P. B. Shepson, *Atmos. Chem. Phys.*, 2016, **16**, 15425–15432.
- 525 Chemistry LibreTexts: 2.10: Zero-Order Reactions, [https://chem.libretexts.org/Bookshelves/Physical_and_Theoretical_Chemistry_Textbook_Maps/Supplemental_Modules_\(Physical_and_Theoretical_Chemistry\)/Kinetics/02%3A_Reaction_Rates/2.10%3A_Zero-Order_Reactions](https://chem.libretexts.org/Bookshelves/Physical_and_Theoretical_Chemistry_Textbook_Maps/Supplemental_Modules_(Physical_and_Theoretical_Chemistry)/Kinetics/02%3A_Reaction_Rates/2.10%3A_Zero-Order_Reactions), (accessed Jan 2021).
- 526 M.-S. Bae, J. J. Schwab, Q. Zhang, O. Hogrefe, K. L. Demerjian, S. Weimer, K. Rhoads, D. Orsini, P. Venkatchari and P. K. Hopke, *J. Geophys. Res.*, 2007, **112**, D22305.
- 527 J. T. Jayne, D. C. Leard, X. Zhang, P. Davidovits, K. A. Smith, C. E. Kolb and D. R. Worsnop, <http://dx.doi.org/10.1080/027868200410840>, 2010, **33**, 49–70.
- 528 M. R. Canagaratna, J. T. Jayne, J. L. Jimenez, J. D. Allan, M. R. Alfarra, Q. Zhang, T. B. Onasch, F. Drewnick, H. Coe, A. Middlebrook, A. Delia, L. R. Williams, A. M. Trimborn, M. J. Northway, P. F. DeCarlo, C. E. Kolb, P. Davidovits and D. R. Worsnop, *Mass Spectrom. Rev.*, 2007, **26**, 185–222.
- 529 J. D. Allan, A. E. Delia, H. Coe, K. N. Bower, M. R. Alfarra, J. L. Jimenez, A. M. Middlebrook, F. Drewnick, T. B. Onasch, M. R. Canagaratna, J. T. Jayne and D. R. Worsnop, *J. Aerosol Sci.*, 2004, **35**, 909–922.
- 530 H. O, S. JJ, D. F, L. GG, P. S, D. KL, R. K, F. HD, R. OV, H. L and D. VA, *J. Air Waste Manag. Assoc.*, 2004, **54**, 1040–1060.
- 531 S. E. Cornell, T. D. Jickells, J. N. Cape, A. P. Rowland and R. A. Duce, *Atmos. Environ.*, 2003, **37**, 2173–2191.
- 532 C. Marcolli, M. R. Canagaratna, D. R. Worsnop, R. Bahreini, J. A. De Gouw, C. Warneke, P. D. Goldan, W. C. Kuster, E. J. Williams, B. M. Lerner, J. M. Roberts, J. F. Meagher, F. C. Fehsenfeld, M. Marchewka, S. B. Bertman and A. M. Middlebrook, *Atmos. Chem. Phys.*, 2006, **6**, 5649–5666.

- 533 A. W. Rollins, J. L. Fry, J. F. Hunter, J. H. Kroll, D. R. Worsnop, S. W. Singaram and R. C. Cohen, *Atmos. Meas. Tech.*, 2010, **3**, 301–310.
- 534 R. Torres-Jardón, J. A. García-Reynoso, A. Jazcilevich, L. G. Ruiz-Suárez & Tim and C. C. Keener, *J. Air Waste Manage. Assoc.*, 2009, **59**, 1155–1172.
- 535 H. H. Holmes and D. Farrington, *J. Am. Chem. Soc.*, 1934, **56**, 630–637.
- 536 G. Duporté, P. M. Flaud, J. Kammer, E. Geneste, S. Augagneur, E. Panguì, H. Lamkaddam, A. Gratien, J. F. Doussin, H. Budzinski, E. Villenave and E. Perraudin, *J. Phys. Chem. A*, 2020, **124**, 409–421.
- 537 B. M. Connelly and M. A. Tolbert, *Environ. Sci. Technol.*, 2010, **44**, 4603–4608.
- 538 J. L. Fry, D. C. Draper, K. C. Barsanti, J. N. Smith, J. Ortega, P. M. Winkler, M. J. Lawler, S. S. Brown, P. M. Edwards, R. C. Cohen and L. Lee, *Environ. Sci. Technol.*, 2014, **48**, 11944–11953.
- 539 R. Atkinson, C. N. Plum, W. P. L. Carter, A. M. Winer and J. N. Pitts Jr., *J. Phys. Chem.*, 1984, **88**, 2361–2364.
- 540 S. M. Japar and H. Niki, *J. Phys. Chem.*, 1975, **79**, 1629–1632.
- 541 P. F. DeCarlo, J. R. Kimmel, A. Trimborn, M. J. Northway, J. T. Jayne, A. C. Aiken, M. Gonin, K. Fuhrer, T. Horvath, K. S. Docherty, D. R. Worsnop and J. L. Jimenez, *Anal. Chem.*, 2006, **78**, 8281–8289.
- 542 J. L. Fry, D. C. Draper, K. J. Zarzana, P. Campuzano-Jost, D. A. Day, J. L. Jimenez, S. S. Brown, R. C. Cohen, L. Kaser, A. Hansel, L. Cappellin, T. Karl, A. Hodzic Roux, A. Turnipseed, C. Cantrell, B. L. Lefer and N. Grossberg, *Atmos. Chem. Phys.*, 2013, **13**, 8585–8605.
- 543 K. Yu, Q. Zhu, K. Du and X. F. Huan, *Atmos. Chem. Phys.*, 2019, **19**, 5235–5249.
- 544 Q. Zhu, L. Y. He, X. F. Huang, L. M. Cao, Z. H. Gong, C. Wang, X. Zhuang and M. Hu, *Atmos. Chem. Phys.*, 2016, **16**, 10283–10297.
- 545 D. A. Day, P. J. Wooldridge, M. B. Dillon, J. A. Thornton and R. C. Cohen, *J. Geophys. Res. Atmos.*, 2002, **107**, ACH 4-1.
- 546 E. M. Johnson, *Chemistry of Organic Nitrates*, Springer, Berlin, Heidelberg, Berlin, Needleman P., 1975, vol. 40.
- 547 N. R. Choi, Y. G. Ahn, J. Y. Lee, E. Kim, S. Kim, S. M. Park, I. H. Song and Y. P. Kim, *Atmos. Environ.*, 2020, **237**, 117582.
- 548 J. N. Cape, S. E. Cornell, T. D. Jickells and E. Nemitz, *Atmos. Res.*, 2011, **102**, 30–48.
- 549 T. Novakov and J. E. Penner, *Nature*, 1993, **365**, 823–826.
- 550 J. C. Neff, E. A. Holland, F. J. Dentener, W. H. McDowell and K. M. Russell, *Biogeochemistry*, 2002, **57**, 99–136.
- 551 A. Sorteberg, Ø. Hov, S. Solberg, K. Tørseth, H. Areskoug, M. Ferm, K. Granby, H. Lättilä, K. Persson and D. Simpson, *J. Atmos. Chem.*, 1998, **30**, 241–271.
- 552 H. Sievering, D. Rusch and L. Marquez, *Atmos. Environ.*, 1996, **30**, 2527–2537.
- 553 J. Arey, B. Zielinska, W. P. Harger, R. Atkinson and A. M. Winer, *Mutat. Res. Lett.*, 1988, **207**, 45–51.
- 554 J. F. Collins, J. P. Brown, G. V. Alexeeff and A. G. Salmon, *Regul. Toxicol. Pharm.*, 1998, **28**, 45–54.
- 555 IARC Monographs on the Identification of Carcinogenic Hazards to Humans - Agents Classified by the IARC Monographs, Volumes 1–128, <https://monographs.iarc.fr/agents->

classified-by-the-iarc/, (accessed Jan 2021).

- 556 Y. Hong, K. H. Kim, B. I. Sang and H. Kim, *Environ. Pollut.*, 2017, **226**, 324–334.
- 557 N. Rae Choi, Y. Gyong Ahn, H. Bae Lim, J. Yi Lee, C. Hoon Jung and Y. Pyo Kim, *Air Qual. Atmos. Heal.*, 2018, **11**, 855–865.
- 558 M. Akyüz and Ş. Ata, *Environ. Sci. Pollut. R.*, 2013, **20**, 7398–7412.
- 559 M. Aragón, R. M. Marcé and F. Borrull, *Talanta.*, 2013, **115**, 896–901.
- 560 B. Jurado-Sánchez, E. Ballesteros and M. Gallego, *J. Chromatogr. A.*, 2009, **1216**, 1200–1205.
- 561 International Agency for Research on Cancer, *IARC Monographs on the Evaluation of the Carcinogenic Risk of Chemicals to Humans: Some N-Nitroso Compounds*, World Health Organisation, Lyon, 1978, vol. 17.
- 562 R. Montesano and J. Hall, in *Mutation, Cancer, and Malformation. Environmental Science Research.*, eds. E. H. Y. Chu and W. M. Generoso, Springer US, Boston, MA., 31st edn., 1984, pp. 447–464.
- 563 Y. Lao, P. W. Villalta, S. J. Sturla, M. Wang and S. S. Hecht, *Chem. Res. Toxicol.*, 2006, **19**, 674–682.
- 564 M. W. Byun, H. J. Ahn, J. H. Kim, J. W. Lee, H. S. Yook and S. B. Han, *J. Chromatogr. A.*, 2004, **1054**, 403–407.
- 565 CO2 capture: Health effects of amines and their derivatives, <https://www.fhi.no/en/publ/2011/co2-capture-health-effects-of-amine/>, (accessed Jan 2021).
- 566 S. S. Hecht and D. Hoffmann, *Carcinogenesis*, 1988, **9**, 875–884.
- 567 S. Fischer, B. Spiegelhalder and R. Preussmann, *Carcinogenesis*, 1989, **10**, 169–173.
- 568 E. Yalcin and S. De La Monte, *J. Physiol. Biochem.*, 2016, **72**, 107–120.
- 569 M. Sleiman, L. A. Gundel, J. F. Pankow, P. Jacob, B. C. Singer and H. Destailats, *P. Natl. Acad. Sci. USA.*, 2010, **107**, 6576–6581.
- 570 N. Ramírez, M. Z. Özel, A. C. Lewis, R. M. Marcé, F. Borrull and J. F. Hamilton, *Environ. Int.*, 2014, **71**, 139–147.
- 571 J. N. Pitts, D. Grosjean, K. Van Cauwenberghe, J. P. Schmid and D. R. Fitz, *Environ. Sci. Technol.*, 1978, **12**, 946–953.
- 572 B. Spiegelhalder and R. Preussmann, *Carcinogenesis*, 1983, **4**, 1147–1152.
- 573 M.-R. Chao, C.-J. Wang, M.-T. Wu, C.-H. Pan, C.-Y. Kuo, H.-J. Yang, L. W. Chang and C.-W. Hu, *Cancer. Epidem. Biomar.*, 2008, **17**, 3381–3389.
- 574 M. Hein, *Fuel Energy Abstr.*, 1998, **39**, 176.
- 575 V. Kumar, B. P. Chandra and V. Sinha, *Sci. REPORTS /*, 2018, **8**, 626.
- 576 X. Ge, A. S. Wexler and S. L. Clegg, *Atmos. Environ.*, 2011, **45**, 524–546.
- 577 E. Ulku Goff, J. R. Coombs, D. H. Fine and T. M. Baines, *Anal. Chem.*, 1980, **52**, 1833–1836.
- 578 X. Chen, G. Huang, C. An, Y. Yao and S. Zhao, *Chem. Eng. J.*, 2018, **335**, 921–935.
- 579 C. J. Nielsen, H. Herrmann and C. Weller, *Chem. Soc. Rev.*, 2012, **41**, 6684–6704.
- 580 K. Yu, W. A. Mitch and N. Dai, *Environ. Sci. Technol.*, 2017, **51**, 11522–11536.
- 581 A. Llop, F. Borrull and E. Pocurull, *J. Sep. Sci.*, 2010, **33**, 3692–3700.

- 582 S. D. Richardson and T. A. Ternes, *Anal. Chem.*, 2018, **90**, 398–428.
- 583 S. D. Richardson, *TrAC - Trend. Anal. Chem.*, 2003, **22**, 666–684.
- 584 C. Planas, Ó. Palacios, F. Ventura, J. Rivera and J. Caixach, *Talanta*, 2008, **76**, 906–913.
- 585 J. E. Grebel and I. H. (Mel) Suffet, *J. Chromatogr. A.*, 2007, **1175**, 141–144.
- 586 S. Ventanas and J. Ruiz, *Talanta*, 2006, **70**, 1017–1023.
- 587 C. C. Fan and T. F. Lin, *Chemosphere*, 2018, **200**, 48–56.
- 588 D. Kocak, M. Z. Özel, F. Gogus, J. F. Hamilton and A. C. Lewis, *Food. Chem.*, 2012, **135**, 2215–2220.
- 589 K. D. Brunnemann and D. Hoffmann, *Crit. Rev. Toxicol.*, 1991, **21**, 235–240.
- 590 N. Ramírez, M. Z. Özel, A. C. Lewis, R. M. Marcé, F. Borrull and J. F. Hamilton, *J. Chromatogr. A.*, 2012, **1219**, 180–187.
- 591 G. E. Matt, P. J. E. Quintana, M. F. Hovell, J. T. Bernert, S. Song, N. Novianti, T. Juarez, J. Floro, C. Gehrman, M. Garcia and S. Larson, *Tob. Control.*, 2004, **13**, 29–37.
- 592 T. Whitehead, C. Metayer, M. H. Ward, M. G. Nishioka, R. Gunier, J. S. Colt, P. Reynolds, S. Selvin, P. Buffler and S. M. Rappaport, *Am. J. Epidemiol.*, 2009, **169**, 1113–1123.
- 593 R. C. Schothorst and H. H. J. Somers, *Anal. Bioanal. Chem.*, 2005, **381**, 681–685.
- 594 C. Flower, S. Carter, A. Earls, R. Fowler, S. Hewlins, S. Lalljie, M. Lefebvre, J. Mavro, D. Small and N. Volpe, *Int. J. Cosmet. Sci.*, 2006, **28**, 21–33.
- 595 S. K. Pancholy, *Soil. Biol. Biochem.*, 1978, **10**, 27–32.
- 596 D. Feng, L. Liu, L. Zhao, Q. Zhou and T. Tan, *Chromatographia*, 2011, **74**, 817–825.
- 597 Q. Zhang, F. Duan, K. He, Y. Ma, H. Li, T. Kimoto and A. Zheng, *Front. Env. Sci. Eng.*, 2015, **9**, 1004–1014.
- 598 P. P. Fu, D. Herreno-Saenz, L. S. Von Tungeln, J. O. Lay, Y. S. Wu and F. E. Evans, *Environ. Heal. Persp.*, 1994, **102**, 177–183.
- 599 F. C.-Y. Wang, W. K. Robbins and M. A. Greaney, *J. Sep. Sci.*, 2004, **27**, 468–472.
- 600 C. Dang, T. Bannan, P. Shelley, M. Priestley, S. D. Worrall, J. Waters, H. Coe, C. J. Percival, D. Topping, S. D. Worrall and C. J. Percival, *Aerosol Sci. Technol.*, 2019, **53**, 1040–1055.
- 601 P. D. Shelley, T. J. Bannan, S. D. Worrall, M. R. Alfara, U. K. Krieger, C. J. Percival, A. Garforth and D. Topping, *Atmos. Chem. Phys*, 2020, **20**, 8293–8314.
- 602 E. Kováts, *Helv. Chim. Acta.*, 1958, **41**, 1915–1932.
- 603 J. Bermejo and M. D. Guillén, *Anal. Chem.*, 1987, **59**, 94–97.
- 604 P. Tan, A. Xichuan Wei, H. Zhang, M. Niu and D. Zhang, *Anal. Methods.*, 2019, **11**, 4868–4874.
- 605 J. R. Hobbs and E. P. Conde, in *Advances in Analysis and Detection of Explosives*, Springer Netherlands, 1993, pp. 153–164.
- 606 M. Görgényi and K. Héberger, in *J. Chromatogr. A.*, Elsevier, 2003, vol. 985, pp. 11–19.
- 607 H. van Den Dool and P. D. Kratz, *J. Chromatogr. A.*, 1963, **11**, 463–471.
- 608 Gas Chromatographic Retention Data, <https://webbook.nist.gov/chemistry/gc-ri/>, (accessed Jan 2021).
- 609 A. D. McNaught and A. Wilkinson, *IUPAC. Compendium of Chemical Terminology*,

Blackwell Scientific Publications, Oxford, 2nd edn., 1997.

- 610 M. L. Lee, D. L. Vassilaros and C. M. White, *Anal. Chem.*, 1979, **51**, 768–773.
- 611 N. J. Farren, University of York, 2017.
- 612 S. M. Murphy, A. Sorooshian, J. H. Kroll, N. L. Ng, P. Chhabra, C. Tong, J. D. Surratt, E. Knipping, R. C. Flagan and J. H. Seinfeld, *Atmos. Chem. Phys.*, 2007, **7**, 2313–2337.
- 613 Deutsche Forschungsgemeinschaft. Kommission zur Prüfung Gesundheitsschädlicher Arbeitsstoffe, in *The MAK-Collection for Occupational Health and Safety*, Wiley-VCH Verlag GmbH & Co. KGaA, Weinheim, Germany, 1990, pp. 24–37.
- 614 W.-J. Zhou, J. M. Boyd, F. Qin, S. E. Hruddy and X.-F. Li, *Environ. Sci. Technol.*, 2009, **43**, 8443–8448.
- 615 O. Drzyzga, *Chemosphere.*, 2003, **53**, 809–818.
- 616 S. Gangolli, *The Dictionary of Substances and Their Effects*, Royal Society of Chemistry, London, 1999.
- 617 P. H. Howard, *Handbook of Environmental Fate and Exposure Data for Organic Compound*, CRC Press., Florida, 2003rd edn., 1997.
- 618 D. Grosjean, *J. Air Waste Manag. Assoc.*, 1991, **41**, 306–311.
- 619 D. Turer, H. A. Nefeslioglu, K. Zorlu and C. Gokceoglu, *Environ. Geol.*, 2008, **55**, 1001–1014.
- 620 K. R. Bharucha, C. K. Cross and L. J. Rubin, *J. Agric. Food Chem.*, 1979, **27**, 63–69.
- 621 T. Spietz, S. Dobras, L. Więclaw-Solny and A. Krótki, *Ochr. Sr. i Zasobow Nat.*, 2017, **28**, 43–50.
- 622 Z. Arsenijević, B. Grbić, Ž. Grbavčić, S. Miletić, G. Savčić, N. Radić and R. Garić-Grulović, *PREVENTION AND CONTROL OF DIMETHYL-AMINE VAPORS EMISSION: HERBICIDE PRODUCTION PLANT*, 2008, vol. 14.
- 623 J. W. Hutchings, B. Ervens, D. Straub and P. Herckes, *Environ. Sci. Technol.*, 2010, **44**, 8128–8133.
- 624 W. Tan, L. Zhu, T. Mikoviny, C. J. Nielsen, A. Wisthaler, P. Eichler, M. Müller, B. D’Anna, N. J. Farren, J. F. Hamilton, J. B. C. Pettersson, M. Hallquist, S. Antonsen and Y. Stenstrøm, *J. Phys. Chem. A*, 2018, **122**, 4470–4480.
- 625 G. S. Reddy, A. S. Reddy, M. V. Subbaiah and A. Krishnaiah, *J. Solut. Chem.* 2010 393, 2010, **39**, 399–408.
- 626 S. Antonsen, A. J. C. Bunkan, B. D’Anna, P. Eichler, N. Farren, M. Hallquist, J. F. Hamilton, H. Kvarnliden, T. Mikoviny, M. Müller, C. J. Nielsen, Y. Stenstrøm, W. Tan, A. Wisthaler and L. Zhu, *Energy Procedia*, 2017, **114**, 1026–1032.
- 627 H. Zhang, Y. Luo, M. Zhuo, T. Yang, J. Liang, M. Zhang, J. Ma, H. Duan and Q. Li, *RSC Adv. Commun. Publ.*, 2016, **6**, 6511–6515.
- 628 IARC Monographs on the Identification of Carcinogenic Hazards to Humans - List of Classifications, <https://monographs.iarc.fr/list-of-classifications/>, (accessed Jan 2021).
- 629 Agents Classified by the IARC Monographs, Volumes 1-123, <https://monographs.iarc.fr/wp-content/uploads/2018/09/ClassificationsAlphaOrder.pdf>, (accessed Jan 2021).
- 630 US EPA, *Risk Assessment Guidance for Superfund Volume I: Human Health Evaluation Manual (Part F, Supplemental Guidance for Inhalation Risk Assessment)*, Washington, D.C., 2009.

- 631 US EPA, *Environmental Protection Agency, U.S., Exposure Factors Handbook: 2011 ed. National Center for Environmental Assessment: Washington, D.C.*, Washington, D.C., 2011.
- 632 Technical Appendix A. Listing of All Toxicity Weights for TRI Chemicals and Chemical Categories, https://www.epa.gov/sites/production/files/2015-12/documents/technical_appendix_a-toxicity_v2.3.4.pdf, (accessed Jan 2021).
- 633 IRIS A to Z List of Chemical Assessments, https://iris.epa.gov/AtoZ/?list_type=alpha, (accessed Jan 2021).
- 634 Chemicals (California Office of Environmental Health Hazard Assessment (OEHHA)), <https://oehha.ca.gov/chemicals>, (accessed Jan 2021).
- 635 D. C. Washington, *Memorandum: Implementation of the Cancer Guidelines and Accompanying Supplemental Guidance -Science Policy Council Cancer Guidelines Implementation Workgroup Communication II: Performing Risk Assessments that include Carcinogens Described in the Supplemental Guidance as having a Mutagenic Mode of Action*, Washington, D.C., 2006.
- 636 US EPA, *US EPA: Supplemental Guidance for Assessing Susceptibility from Early-Life Exposure to Carcinogens*, Washington, DC, 2005.
- 637 World Population Review: Beijing Population, <https://worldpopulationreview.com/world-cities/beijing-population>, (accessed Jan 2021).
- 638 World Population Review: London Population, <https://worldpopulationreview.com/world-cities/london-population>, (accessed Jan 2021).
- 639 W. Wang, J. Yu, W. An and M. Yang, *Sci. Total. Environ.*, 2016, **551–552**, 489–495.
- 640 M. R. Templeton and Z. Chen, *J. Water. Supply. Res. T.*, 2010, **59**, 277–283.
- 641 Q. Luo, D. Wang and Z. Wang, *Sci. Total. Environ.*, 2012, **437**, 219–225.
- 642 J.-E. Park, J.-E. Seo, J.-Y. Lee and H. Kwon, *Toxicol. Res.*, 2015, **31**, 279–288.
- 643 C. Crews, *Qual. Assur. Saf. Crop.*, 2010, **2**, 2–12.
- 644 P. J. Song and J. F. Hu, *Food Chem. Toxicol.*, 1988, **26**, 205–208.
- 645 N. R. Choi, Y. P. Kim, W. H. Ji, G. S. Hwang and Y. G. Ahn, *Talanta*, 2016, **148**, 69–74.
- 646 A. R. Tricker and R. Preussmann, *Mutat. Res-Genet. Tox.*, 1991, **259**, 277–289.
- 647 US EPA, *N-Nitrosodiethylamine (CASRN 55-18-5) Integrated Risk Information System (IRIS) Chemical Assessment Summary*, Washington, D.C., 1987.